

Springer Topics in Signal Processing

Shefeng Yan

Broadband Array Processing

Springer Topics in Signal Processing

Volume 17

Series Editors

Jacob Benesty, INRS-EMT, University of Quebec, Montreal, QC, Canada

Walter Kellermann, Erlangen-Nürnberg, Friedrich-Alexander-Universität,
Erlangen, Germany

More information about this series at <http://www.springer.com/series/8109>

Shefeng Yan

Broadband Array Processing

Shefeng Yan
Institute of Acoustics
Chinese Academy of Sciences
Beijing, China

ISSN 1866-2609 ISSN 1866-2617 (electronic)
Springer Topics in Signal Processing
ISBN 978-981-13-6801-1 ISBN 978-981-13-6802-8 (eBook)
<https://doi.org/10.1007/978-981-13-6802-8>

Library of Congress Control Number: 2019932604

© Springer Nature Singapore Pte Ltd. 2019

This work is subject to copyright. All rights are reserved by the Publisher, whether the whole or part of the material is concerned, specifically the rights of translation, reprinting, reuse of illustrations, recitation, broadcasting, reproduction on microfilms or in any other physical way, and transmission or information storage and retrieval, electronic adaptation, computer software, or by similar or dissimilar methodology now known or hereafter developed.

The use of general descriptive names, registered names, trademarks, service marks, etc. in this publication does not imply, even in the absence of a specific statement, that such names are exempt from the relevant protective laws and regulations and therefore free for general use.

The publisher, the authors and the editors are safe to assume that the advice and information in this book are believed to be true and accurate at the date of publication. Neither the publisher nor the authors or the editors give a warranty, express or implied, with respect to the material contained herein or for any errors or omissions that may have been made. The publisher remains neutral with regard to jurisdictional claims in published maps and institutional affiliations.

This Springer imprint is published by the registered company Springer Nature Singapore Pte Ltd.
The registered company address is: 152 Beach Road, #21-01/04 Gateway East, Singapore 189721,
Singapore

Preface

Sensor array signal processing has played an important role in various application areas such as sonar, radar, wireless communications, astronomy, seismology, medical imaging, and sound field analysis. The main purpose is to improve the signal-to-noise ratio by performing beamforming to provide spatial filtering and construct the spatial spectral estimate of the signal and noise field.

The goal of the beamformer design is to provide higher array gain and a narrower mainlobe width to provide better spectral resolution. However, the pursuit of the highest array gain in some cases may result in a large weight vector norm, a significant increase in sensitivity, and severe degradation in performance in the presence of a mismatch. Thus, improving the robustness of the beamformer is another important goal of beamformer design. The high sidelobes of a beamformer can cause severe performance degradation, especially in the presence of unexpected or suddenly appearing interferers. Sidelobe control is another important research issue in beamformer design. While reducing the sidelobes, the main beam may be widened and the array gain may be reduced. Therefore, we devote a significant amount of effort to the design of beamformers that provides a suitable compromise among these conflicting objectives.

When the signals of interest are broadband, broadband array processing is required. Sound is a natural source of broadband signals, and much of the research and development in broadband array processing has been focused on acoustic arrays, such as hydrophone arrays, microphone arrays, and so on.

Since the frequency-domain snapshot model is usually used, the frequency-domain implementation is a straightforward extension of the narrowband beamformer to broadband beamformer, in which the broadband array signals are decomposed into a lot of frequency bins using DFT, for each frequency bin, narrowband condition is satisfied and a narrowband beamformer can be used directly.

The procedure of frequency-domain implementation is block processing, which requires a block of snapshots to perform DFT. It is not suitable in many applications due to its associated time delay resulting from the block processing. Broadband beamformer can also be implemented in the time domain by placing an FIR filter at the output of each sensor. An important advantage is that the beamformer can be

updated when each new snapshot arrives. The goal is then to design the impulse responses of the FIR filters to achieve the desired beam pattern.

For both the narrowband beamformer weight vector design in the frequency-domain implementation and the FIR filter design in the time-domain implementation, the multiple-objective approach can be used, which involves trade-offs among the array gain, the robustness, the sidelobe level, the mainlobe pattern, as well as a number of other performance measures. It can not only provide the beamformer design with a high level of detail in the specification of performance but also include most of the existing beamformer design methods as its special cases. This is useful for analyzing and evaluating the advantages and disadvantages of various methods that can be regarded as special cases.

Circular arrays and spherical arrays have attracted a significant amount of interest over the past few decades. An important advantage is that the processing problem can be greatly simplified due to their symmetry property. In addition to the element-space beamformer, modal beamformer can be applied to circular arrays and spherical arrays. Modal beamformer is a two-stage beamformer that allows a very efficient implementation, where a decomposer is used to perform the spatial decomposition of the sound field into a number of harmonics (circular harmonics or spherical harmonics) using spatial (circular or spherical) Fourier transform, and an actual beamformer is used to form the beam by combining the harmonics.

Utilizing the spatial Fourier transform relationship, array processing and performance analysis can be performed in the harmonics domain. Therefore, by deriving the expressions for the harmonics domain performance measures, the modal beamformer design can be formulated as an optimization problem with a form that resembles the element-space beamformer design problem, and the techniques developed for the element-space beamformers can be extended to the case of modal beamformers.

This book is organized as follows: In Chap. 1, some backgrounds in array processing are introduced. In Chap. 2, the DFT-based frequency-domain implementation of a broadband beamformer is introduced. Chapter 3 focuses on the design of subband beamformers for frequency-domain broadband beamformer. In Chap. 4, the FIR-based time-domain implementation of the broadband beamformer is presented, where FIR beamformer is designed by separately designing the subband beamformers and the corresponding FIR filters. The techniques for optimal design of the FIR beamformer are developed in Chap. 5. Chapters 6 and 7 focus on the modal beamforming problem for circular arrays, with Chap. 6 for the frequency-domain modal beamformer and Chap. 7 for the time-domain modal beamformer. The frequency-domain and time-domain modal beamformers for spherical arrays are presented in Chaps. 8 and 9, respectively.

This work was supported in part by the National Natural Science Foundation of China under Grant 61725106.

Beijing, China
September 2018

Shefeng Yan

Contents

1	Background of Array Processing	1
1.1	Introduction	1
1.2	Array Signal Model	1
1.2.1	Signal Model	1
1.2.2	Noise Models	5
1.2.3	Data Model	7
1.3	Beamformer	9
1.3.1	Frequency-Wavenumber Response Function	9
1.3.2	Array Performance Measures	11
1.4	Traditional Beamformer	19
1.4.1	Delay-and-Sum (DAS) Beamformer	20
1.4.2	Optimum Beamformer	20
1.5	Summary	26
	References	28
2	Frequency-Domain Broadband Beamforming	29
2.1	Introduction	29
2.2	Frequency-Domain Snapshot Model	30
2.2.1	Frequency-Domain Snapshots	30
2.2.2	Covariance Matrix	33
2.3	DFT Beamformer	35
2.3.1	DFT Implementation	35
2.3.2	Broadband Beam Pattern	38
2.3.3	DFT Beamforming	39
2.3.4	Signal Not Along MRA	44
2.4	Summary	46
	Reference	46

3 Optimal Design of Subband Beamformers	47
3.1 Introduction	47
3.2 Robust Beamformers	48
3.2.1 Loaded Sample Matrix Inversion Beamformer	48
3.2.2 Norm Constrained Beamformer	52
3.2.3 Worst-Case Constrained Beamformer	56
3.2.4 Comparison of Robust Beamformers	61
3.3 Low-Sidelobe Beamformers	65
3.3.1 Windows for Uniform Linear Arrays	65
3.3.2 Low-Sidelobe Designs	69
3.3.3 Robust Against Manifold Uncertainty	75
3.4 Mainlobe Pattern Synthesis	86
3.4.1 Norms	86
3.4.2 Least Squares Error Pattern Synthesis	88
3.4.3 Minimum-Norm Pattern Synthesis	90
3.4.4 Mixed-Norm Pattern Synthesis	93
3.4.5 Frequency-Invariant Beam Pattern	96
3.5 Multiple-Objective Design	98
3.6 Summary	101
References	103
4 Time-Domain Broadband Beamforming	105
4.1 Introduction	105
4.2 FIR Beamforming	106
4.3 FIR Beamformer Design via FFT	108
4.4 FIR Filter Design for FIR Beamformer	111
4.4.1 Minimum-Norm Filter Design	112
4.4.2 Mixed-Norm Filter Design	116
4.5 FIR Beamformer via Subband Beamformers and FIR Filters Designs	119
4.5.1 Design Principles	119
4.5.2 FIR Broadband Beamformer	122
4.6 Summary	128
References	129
5 Optimal Design of Time-Domain Broadband Beamformers	131
5.1 Introduction	131
5.2 Jointly Spatial and Frequency Responses Optimization	132
5.2.1 Drawback of Two-Stage Method	132
5.2.2 FIR Beamformer Pattern	133
5.2.3 Frequency-Invariant FIR Beamformer	135

5.3	Adaptive FIR Beamformer	142
5.3.1	Data Covariance Matrix	142
5.3.2	Design of Adaptive FIR Beamformer	145
5.3.3	Adaptive FIR Beamformer with Sidelobe Control	146
5.4	Minimum Mainlobe Spatial Pattern Variation Design	152
5.4.1	Mainlobe Spatial Response Variation	152
5.4.2	Peak Sidelobes Constrained Minimax MSRV	152
5.4.3	Peak Sidelobes Constrained Least-Square MSRV	153
5.4.4	Mean-Squared MSRV Constrained Least-Square Sidelobes	155
5.4.5	Frequency-Invariant Beamformer with Interference Rejection	156
5.5	Multiple-Objective Design of FIR Beamformers	161
5.6	Summary	163
	References	164
6	Modal Beamforming for Circular Arrays	165
6.1	Introduction	165
6.2	Continuous Circular Arrays (Apertures)	166
6.2.1	Uniform Weighting	167
6.2.2	Conventional Beamformer	169
6.2.3	Phase Mode Excitation	172
6.2.4	Circular Mode	175
6.2.5	Phase-Mode Beamformer	182
6.2.6	Modal Representation of DAS Beamformer	184
6.3	Uniform Circular Arrays	186
6.3.1	Element-Space Beamformer	186
6.3.2	Circular-Harmonics-Domain (CHD) Beamformer	192
6.3.3	Performance Measures in Circular Harmonics Domain	195
6.4	Design of CHD Beamformers	201
6.4.1	Phase-Mode Beamformer	201
6.4.2	CHD DAS Beamformer	205
6.4.3	CHD MVDR Beamformer	205
6.4.4	Maximum-Directivity-Index (MDI) Beamformer	206
6.4.5	MVDR Beamformer in Planarly Isotropic Noise Field	207
6.4.6	Maximum WNG Beamformer	209
6.4.7	Multiply Constrained CHD Beamformer	211
6.5	Frequency-Domain Broadband CHD Beamforming	215
6.5.1	Implementation of CHD Beamformer	215
6.5.2	Unbaffled Circular Array	218
6.5.3	Baffled Circular Array	219
6.6	Summary	220
	References	223

7 Time-Domain Modal Beamforming for Circular Arrays	225
7.1 Introduction	225
7.2 Beamformer with Symmetric Patterns	226
7.2.1 Design of Weight Vector	226
7.2.2 Symmetric-Pattern Beamforming	231
7.3 Time-Domain CHD Beamforming Structure	232
7.4 Design of FIR Filters for Pattern Generation	234
7.5 Time-Domain Broadband CHD Beamforming	247
7.6 Summary	253
References	254
8 Modal Beamforming for Spherical Arrays	255
8.1 Introduction	255
8.2 Continuous Spherical Arrays (Apertures)	256
8.2.1 Spherical Apertures	256
8.2.2 Spherical Mode	257
8.2.3 Phase-Mode Beamformer	262
8.2.4 Modal Representation of DAS Beamformer	268
8.3 Spherical Arrays	271
8.3.1 Nearly-Uniform Spherical Arrays	271
8.3.2 Spherical-Harmonics-Domain (SHD) Beamformer	273
8.3.3 SHD Beamformer Structure	278
8.3.4 Performance Measures in Spherical Harmonics Domain	279
8.4 Design of SHD Beamformers	284
8.4.1 Multiply Constrained SHD Beamformer	284
8.4.2 SHD MVDR Beamformer	285
8.4.3 Maximum-Directivity-Index Beamformer	286
8.4.4 Maximum WNG Beamformer	288
8.4.5 Norm Constrained SHD Beamformer	290
8.5 Frequency-Domain Broadband SHD Beamforming	294
8.6 Summary	296
References	297
9 Time-Domain Modal Beamforming for Spherical Arrays	299
9.1 Introduction	299
9.2 Rotationally Symmetric SHD Beamformer	300
9.2.1 Beamforming Structure	300
9.2.2 Design of Weight Vector	303
9.3 Time-Domain SHD Beamforming Structure	308
9.4 Design of FIR Filters for Pattern Generation	311
9.5 Time-Domain Broadband SHD Beamforming	323
9.6 Summary	328
References	330
Glossary	331

Chapter 1

Background of Array Processing



1.1 Introduction

Sensor arrays have been in use in many practical applications such as sonar, radar, wireless communications, astronomy, seismology, medical imaging, sound field analysis, etc. Such an array consists of a set of sensors that are spatially distributed at known locations. The sensor array collects spatial samples of propagation wave fields. The processing of data received by the array of sensors, named as array signal processing, has been an active research area for well over several decades. The main objective of array signal processing is to estimate various parameters of the signal arriving from a desired direction in the presence of interfering signals and noise. A representative array signal processing problem is shown in Fig. 1.1.

A beamformer is an important array signal processor, which linearly combines the sensor outputs so that the signal arriving from a specific direction will pass through and those from other directions are attenuated. It provides spatial filtering to separate signals that occupy the same temporal frequency band.

The rest of this chapter is organized as follows. Some background of the array signal model is presented in Sect. 1.2. The concept and formulation of beamformer is presented in Sect. 1.3, where several commonly used array performance measures are discussed. In Sect. 1.4, two kinds of traditional beamformers, delay-and-sum beamformer and optimum beamformer, are introduced. A brief summary of this chapter is given in Sect. 1.5.

1.2 Array Signal Model

1.2.1 Signal Model

Consider the standard Cartesian (x, y, z) and spherical (r, θ, ϕ) coordinate systems, where r is the radial distance, θ and ϕ are the azimuth angle and the elevation angle,

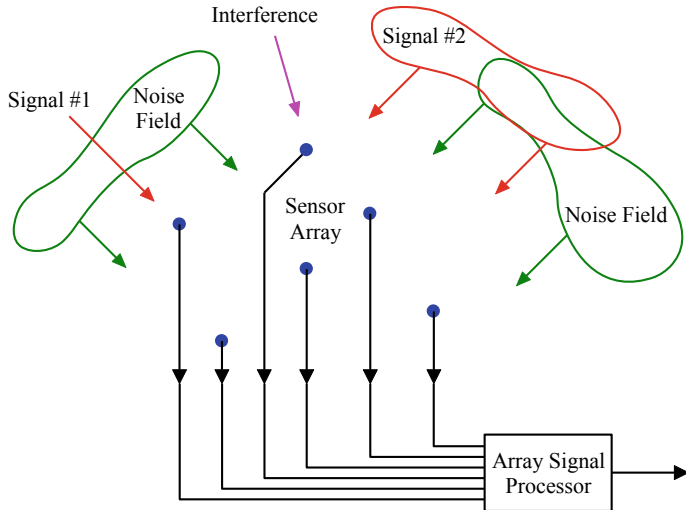
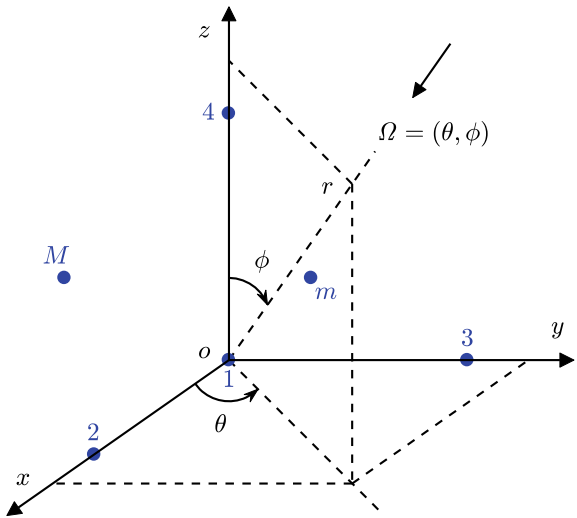


Fig. 1.1 Array signal processing problem

Fig. 1.2 Standard Cartesian and spherical coordinate system



respectively, measured from the x -axis towards the y -axis and downwards from the z -axis, as shown in Fig. 1.2. The spherical coordinate angle is defined as $\Omega = (\theta, \phi)$.

To analyze the response of an array to an external signal field, we consider an array of M isotropic sensors shown in Fig. 1.2. Assume that the sensors locate at positions

$$\mathcal{P}_m = [p_{xm}, p_{ym}, p_{zm}]^T, m = 1, \dots, M, \quad (1.1)$$

where $(\cdot)^T$ denotes the transpose, p_{xm} , p_{ym} and p_{zm} are respectively the x -, y - and z -coordinate of the m th sensor.

Usually, the origin of the coordinate system is assumed to be located at the center of gravity of the array, i.e.,

$$\sum_{m=1}^M \mathcal{P}_m = \mathbf{0}. \quad (1.2)$$

Consider a unit magnitude plane wave propagating from the direction $\Omega = (\theta, \phi)$ with temporal (radian) frequency ω . The sensors spatially sample the signal field at the locations \mathcal{P}_m , $m = 1, \dots, M$. If $s(t)$ is the signal that would be received at the origin of the coordinate system, then the signal received by the m th sensor can be written as

$$s_m(t) = s[t - \tau_m(\Omega)], \quad m = 1, \dots, M, \quad (1.3)$$

where $\tau_m(\Omega)$ is the propagation delay between the position \mathcal{P}_m and the origin of the coordinate system, which is given by

$$\tau_m(\Omega) = \mathbf{v}^T(\Omega) \mathcal{P}_m / c, \quad m = 1, \dots, M, \quad (1.4)$$

where c is the velocity of propagation in the medium and $\mathbf{v}(\Omega)$ is a unit vector that can be written as

$$\mathbf{v}(\Omega) = -[\sin \phi \cos \theta, \sin \phi \sin \theta, \cos \phi]^T. \quad (1.5)$$

The minus sign arises because of the propagation direction being opposite to Ω .

Alternatively, Eq. (1.3) can be written in the Fourier transform domain as

$$S_m(\omega) = \int_{-\infty}^{\infty} s_m(t) e^{-i\omega t} dt = \int_{-\infty}^{\infty} s[t - \tau_m(\Omega)] e^{-i\omega t} dt = S(\omega) e^{-i\omega \tau_m(\Omega)}, \quad (1.6)$$

where i is the imaginary unit and $S(\omega) = \int_{-\infty}^{\infty} s(t) e^{-i\omega t} dt$. Note that Eq. (1.6) is the frequency-domain representation of Eq. (1.3).

Define the wavenumber \mathbf{k} as

$$\mathbf{k}(\Omega) \triangleq (\omega/c) \mathbf{v}(\Omega) = k \mathbf{v}(\Omega), \quad (1.7)$$

where

$$k = \omega/c = 2\pi/\lambda \quad (1.8)$$

with λ being the wavelength corresponding to the frequency ω .

Since $\omega \tau_m(\Omega) = \mathbf{k}^T(\Omega) \mathcal{P}_m$, Eq. (1.6) can be rewritten as

$$S_m(\omega) = S(\omega) \exp(-ik^T \mathcal{P}_m), \quad (1.9)$$

where $\exp(\cdot) = e^{(\cdot)}$, and the direction dependence of \mathbf{k} is suppressed in the notation.

The signals received by the sensor array can be written in vector notation as

$$\mathbf{x}_s(t) = [s_1(t), \dots, s_m(t), \dots, s_M(t)]^T, \quad (1.10)$$

whose frequency-domain representation can be written as

$$X_s(\omega) = \begin{bmatrix} S_1(\omega) \\ \vdots \\ S_m(\omega) \\ \vdots \\ S_M(\omega) \end{bmatrix} = \begin{bmatrix} \exp(-ik^T \mathcal{P}_1) \\ \vdots \\ \exp(-ik^T \mathcal{P}_m) \\ \vdots \\ \exp(-ik^T \mathcal{P}_M) \end{bmatrix} S(\omega). \quad (1.11)$$

Defining

$$\mathbf{p}(\mathbf{k}) \triangleq [\exp(-ik^T \mathcal{P}_1), \dots, \exp(-ik^T \mathcal{P}_m), \dots, \exp(-ik^T \mathcal{P}_M)]^T, \quad (1.12)$$

Equation (1.11) can be written as

$$X_s(\omega) = \mathbf{p}(\mathbf{k}) S(\omega). \quad (1.13)$$

The vector $\mathbf{p}(\mathbf{k})$ is referred to as the array response vector or the array manifold vector, which describes all of the spatial characteristics of the sensor array.

Clearly, the array response vector $\mathbf{p}(\mathbf{k})$ satisfies

$$\|\mathbf{p}(\mathbf{k})\|^2 = \mathbf{p}^H(\mathbf{k}) \mathbf{p}(\mathbf{k}) = M, \quad (1.14)$$

where $\|\cdot\|$ denotes the Euclidean norm and $(\cdot)^H$ denotes the conjugate transpose.

The $M \times M$ spatial spectral matrix of $X_s(\omega)$ is given by

$$S_s(\omega) = E[X_s(\omega) X_s^H(\omega)] = \mathbf{p}(\mathbf{k}) E[|S(\omega)|^2] \mathbf{p}^H(\mathbf{k}), \quad (1.15)$$

where $E[\cdot]$ denotes the statistical expectation of the quantity in the brackets.

Since the signal spectrum $S_s(\omega)$ is given by

$$S_s(\omega) = E[|S(\omega)|^2], \quad (1.16)$$

the spatial spectral matrix can then be rewritten as

$$S_s(\omega) = \mathbf{p}(\mathbf{k}) S(\omega) \mathbf{p}^H(\mathbf{k}). \quad (1.17)$$

1.2.2 Noise Models

There is noise associated with the observation process in all physical systems. Assume that the noise is a sample function of a random process with known second-order statistics.

Let $n_m(t)$ be the additive noise at the m th sensor. In a vector form, we get

$$\mathbf{n}(t) = [n_1(t), \dots, n_m(t), \dots, n_M(t)]^T. \quad (1.18)$$

Let $\mathbf{N}(\omega)$ be the frequency-domain representation of $\mathbf{n}(t)$, the $M \times M$ spatial spectral matrix of the noise vector can be written as

$$\mathbf{S}_n(\omega) = \mathbf{E}[\mathbf{N}(\omega)\mathbf{N}^H(\omega)]. \quad (1.19)$$

Assume that the noise spectra at different sensors are identical. Let $S_n(\omega)$ be the noise spectrum, the spatial spectral matrix of the noise can be rewritten as

$$\mathbf{S}_n(\omega) = S_n(\omega)\boldsymbol{\rho}_n(\omega), \quad (1.20)$$

where $\boldsymbol{\rho}_n(\omega)$ is the normalized spatial spectral matrix.

In this section, we emphasize two types of noise model.

We first consider the spatially white noise, in which the additive noise is modeled as a zero-mean Gaussian random process that is temporally white and spatially uncorrelated. The spatially white noise has a diagonal spectral matrix, i.e.,

$$\boldsymbol{\rho}_{nw}(\omega) = \mathbf{I}, \quad (1.21)$$

where the subscript “nw” denotes white noise.

We next consider the isotropic noise, in which the noise is modeled as the noise sources distributed uniformly over a sphere.

Using Eq. (1.9), the spectrum correlation function of a plane wave at two different locations (e.g., \mathcal{P}_m and $\mathcal{P}_{\bar{m}}$) is given by

$$\mathbf{E}\left[S_m(\omega)S_{\bar{m}}^*(\omega)\right] = \mathbf{E}[|S(\omega)|^2]\exp[-ik^T(\mathcal{P}_m - \mathcal{P}_{\bar{m}})], \quad (1.22)$$

where the superscript “*” denotes the complex conjugate.

Isotropic noise can be viewed as that there are an infinite number of uncorrelated plane waves arriving from all directions with uniform spectral density. Thus, by integrating the spectrum correlation function Eq. (1.22) over a sphere, the spectrum correlation function of isotropic noise at locations \mathcal{P}_m and $\mathcal{P}_{\bar{m}}$ is given by

$$\varrho(\omega) = \int_0^\pi \int_0^{2\pi} \mathbf{E}[|S(\omega)|^2]\exp[-ik^T(\mathcal{P}_m - \mathcal{P}_{\bar{m}})]d\theta \sin\phi d\phi. \quad (1.23)$$

Due to the spherical symmetry of the noise field, the spectrum correlation function can be a function of the distance between \mathcal{P}_m and $\mathcal{P}_{\tilde{m}}$, i.e., $d \triangleq \|\mathcal{P}_m - \mathcal{P}_{\tilde{m}}\|$, but not a function of the locations \mathcal{P}_m and $\mathcal{P}_{\tilde{m}}$. Therefore, we can let $\mathcal{P}_m = [0, 0, d]^T$ and $\mathcal{P}_{\tilde{m}} = [0, 0, 0]^T$. Equation (1.23) reduces to

$$\begin{aligned}\varrho(\omega) &= \int_0^{2\pi} \int_0^\pi \mathbb{E}[|S(\omega)|^2] \exp(-ikd \cos\phi) d\theta \sin\phi d\phi \\ &= 2\pi \mathbb{E}[|S(\omega)|^2] \int_0^\pi \exp(-ikd \cos\phi) \sin\phi d\phi.\end{aligned}\quad (1.24)$$

Letting $\alpha = \cos\phi$, Eq. (1.24) becomes

$$\begin{aligned}\varrho(\omega) &= 2\pi \mathbb{E}[|S(\omega)|^2] \int_0^\pi e^{-ikd \cos\phi} \sin\phi d\phi = 2\pi \mathbb{E}[|S(\omega)|^2] \int_{-1}^1 e^{-ikd\alpha} d\alpha \\ &= 4\pi \mathbb{E}[|S(\omega)|^2] \frac{\sin(kd)}{kd} = 4\pi \mathbb{E}[|S(\omega)|^2] \text{sinc}(kd),\end{aligned}\quad (1.25)$$

where $\text{sinc}(\cdot) = \sin(\cdot)/(\cdot)$.

It is easy to know that the isotropic noise spectrum is

$$S_n(\omega) = 4\pi \mathbb{E}[|S(\omega)|^2]. \quad (1.26)$$

Substituting Eq. (1.26) into Eq. (1.25) gives

$$\varrho(\omega) = S_n(\omega) \text{sinc}(kd). \quad (1.27)$$

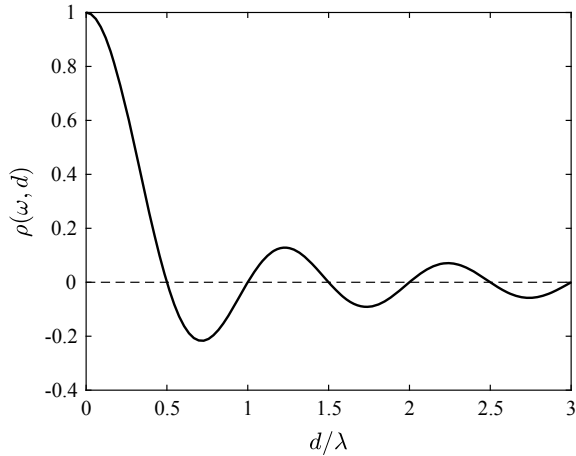
It means that spatial correlation coefficient of the noise received by two sensors spaced by d is

$$\rho(\omega, d) = \text{sinc}(kd) = \text{sinc}(\omega d/c) = \text{sinc}(2\pi d/\lambda). \quad (1.28)$$

The spatial correlation coefficient $\rho(\omega, d)$ as a function of d/λ is shown in Fig. 1.3. It is seen that $\rho(\omega, d) = 0$ when d/λ is a positive integer times of $1/2$, which means that the noises at two sensors are uncorrelated when the interelement spacing d is a positive integer times of half wavelength for the case of isotropic noise.

The $M \times M$ normalized spatial spectral matrix of isotropic noise, denoted by $\rho_{\text{niso}}(\omega)$, can be written as

Fig. 1.3 Spatial correlation coefficient $\rho(\omega, d)$ as a function of d/λ



$$\boldsymbol{\rho}_{\text{niso}}(\omega) = \begin{bmatrix} \rho(\omega, d_{1,1}) & \cdots & \rho(\omega, d_{1,\tilde{m}}) & \cdots & \rho(\omega, d_{1,M}) \\ \vdots & \ddots & \vdots & & \vdots \\ \rho(\omega, d_{m,1}) & \cdots & \rho(\omega, d_{m,\tilde{m}}) & \cdots & \rho(\omega, d_{m,M}) \\ \vdots & & \vdots & \ddots & \vdots \\ \rho(\omega, d_{M,1}) & \cdots & \rho(\omega, d_{M,\tilde{m}}) & \cdots & \rho(\omega, d_{M,M}) \end{bmatrix}, \quad (1.29)$$

where the subscript “niso” denotes isotropic noise and $d_{m,\tilde{m}}$ denotes the distance between the m th and the \tilde{m} th sensor. Note that $d_{m,m} = 0$ and $\rho(\omega, d_{m,m}) = 1$ for $m = 1, \dots, M$. Thus, the diagonal terms of $\boldsymbol{\rho}_{\text{niso}}(\omega)$ equal one.

1.2.3 Data Model

Assume that $D + 1$ plane-wave signals impinge on the array from directions Ω_d ($d = 0, 1, \dots, D$), respectively. The time series received by the m th element can be modeled as

$$x_m(t) = s_0[t - \tau_m(\Omega_0)] + \sum_{d=1}^D s_d[t - \tau_m(\Omega_d)] + n_m(t), \quad m = 1, \dots, M, \quad (1.30)$$

where $s_d(t)$, $d = 0, 1, \dots, D$ are the $D+1$ signals that would be received at the origin of the coordinate system, and $n_m(t)$ is the additive noise. In what follows we assume that the first term in Eq. (1.30) corresponds to the desired signal or signal of interest

(SOI) and the second term to D interferences. The interferences can sometimes be contained into the noise component.

In a vector form, we get

$$\mathbf{x}(t) = \mathbf{x}_s(t) + \mathbf{x}_i(t) + \mathbf{n}(t), \quad (1.31)$$

where $\mathbf{x}(t) = [x_1(t), \dots, x_m(t), \dots, x_M(t)]^T$.

Alternatively, Eq. (1.30) can be written in the Fourier transform domain as

$$\begin{aligned} X_m(\omega) &= S_0(\omega)e^{-i\omega\tau_m(\mathcal{Q}_0)} + \sum_{d=1}^D S_d(\omega)e^{-i\omega\tau_m(\mathcal{Q}_d)} + N_m(\omega), \\ m &= 1, \dots, M, \end{aligned} \quad (1.32)$$

where $X_m(\omega)$, $S_d(\omega)$ ($d = 0, 1, \dots, D$) and $N_m(\omega)$ are the frequency-domain representations of $x_m(t)$, $s_d(t)$ ($d = 0, 1, \dots, D$) and $n_m(t)$, respectively.

Equation (1.32) can be written in a vector form as

$$X(\omega) = \mathbf{p}(\mathbf{k}_0)S_0(\omega) + \sum_{d=1}^D \mathbf{p}(\mathbf{k}_d)S_d(\omega) + N(\omega), \quad (1.33)$$

where $X(\omega) = [X_1(\omega), \dots, X_m(\omega), \dots, X_M(\omega)]^T$, $\mathbf{p}(\mathbf{k}_d)$ ($d = 0, 1, \dots, D$) are the array response vectors for the desired signal and D interfering signals, and $N(\omega) = [N_1(\omega), \dots, N_m(\omega), \dots, N_M(\omega)]^T$.

The $M \times M$ spatial spectral matrix of $X(\omega)$ is given by

$$S_x(\omega) = \mathbb{E}[X(\omega)X^H(\omega)]. \quad (1.34)$$

We assume that the desired signal $\mathbf{x}_s(t)$, the interfering signals $\mathbf{x}_i(t)$, and the additive noise $\mathbf{n}(t)$ are uncorrelated with each other. The spatial spectral matrix $S_x(\omega)$ can be written as

$$\begin{aligned} S_x(\omega) &= S_s(\omega) + S_i(\omega) + S_n(\omega) \\ &= \mathbf{p}(\mathbf{k}_0)S_{s0}(\omega)\mathbf{p}^H(\mathbf{k}_0) + \sum_{d=1}^D \mathbf{p}(\mathbf{k}_d)S_{sd}(\omega)\mathbf{p}^H(\mathbf{k}_d) + S_n(\omega)\rho_n(\omega), \end{aligned} \quad (1.35)$$

where $S_i(\omega)$ is the $M \times M$ spatial spectral matrix of the interfering signals, and $S_{sd}(\omega)$ ($d = 0, 1, \dots, D$) are the spectra of the desired and interfering signals.

1.3 Beamformer

1.3.1 Frequency-Wavenumber Response Function

Using Eq. (1.32), consider the case of a single plane-wave signal in noise. Thus,

$$x_m(t) = s(t - \tau_m) + n_m(t), m = 1, \dots, M, \quad (1.36)$$

whose frequency-domain representation is given by

$$X_m(\omega) = S(\omega)e^{-i\omega\tau_m} + N_m(\omega), m = 1, \dots, M. \quad (1.37)$$

The time series from each sensor are shifted so that the signals are aligned in time and then added. This operation is shown in Fig. 1.4a, where a normalization factor $1/M$ has been included and $n_B(t)$ is the output due to the noise. This array processor is referred to as a delay-and-sum (DAS) beamformer or the conventional beamformer.

Alternatively, its complex representation in the frequency domain is shown in Fig. 1.4b. The DAS beamformer is implemented by a set of phase shifts instead of delay lines.

More generally, the received data from sensors are weighted and summed, the resulting beamformer is shown in Fig. 1.5, where $w_m^*(\omega)$, $m = 1, \dots, M$, are the complex weights.

From Fig. 1.5, the output of the beamformer can be written in the frequency domain as

$$Y(\omega) = \sum_{m=1}^M w_m^*(\omega)X_m(\omega) = \mathbf{w}^H(\omega)\mathbf{X}(\omega), \quad (1.38)$$

where $\mathbf{w}(\omega) = [w_1(\omega), \dots, w_m(\omega), \dots, w_M(\omega)]^T$.

For the special case of a DAS beamformer, the weights become

$$w_{cm}^*(\omega) = e^{i\omega\tau_m(\Omega_0)}/M, m = 1, \dots, M, \quad (1.39)$$

where the subscript “c” denotes conventional beamformer, Ω_0 is the direction-of-arrival of the desired signal.

We recognize the exponential term as the m th element of the array manifold vector $\mathbf{p}^*(\mathbf{k}_0)$. Thus, the DAS weight vector is

$$\mathbf{w}_c^*(\omega) = \mathbf{p}^*(\mathbf{k}_0)/M. \quad (1.40)$$

Consider the case of a single plane-wave signal at \mathbf{k} . Using Eqs. (1.13) and (1.38), the response of the beamformer to the plane wave is given by

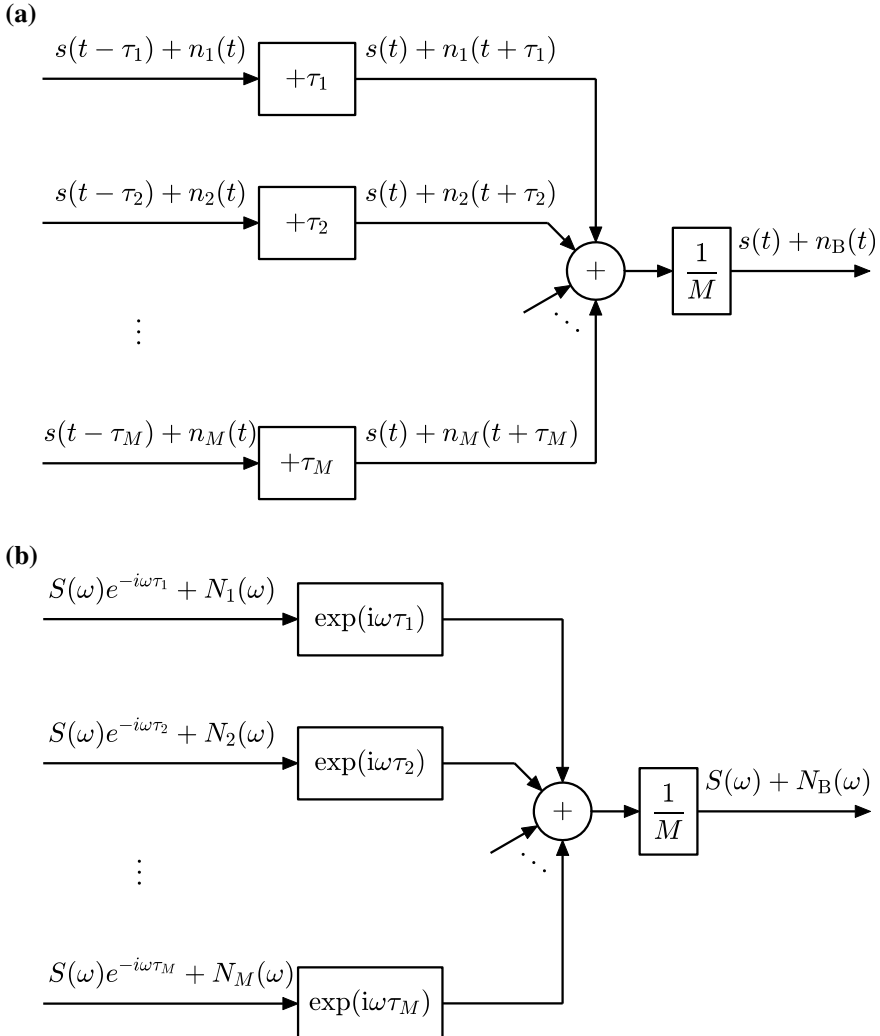


Fig. 1.4 DAS beamformer. **a** Time domain, **b** Frequency domain

$$Y(\omega) = \mathbf{w}^H(\omega) \mathbf{p}(\mathbf{k}) S(\omega). \quad (1.41)$$

Defining

$$Y(\omega, \mathbf{k}) \triangleq \mathbf{w}^H(\omega) \mathbf{p}(\mathbf{k}), \quad (1.42)$$

Equation (1.41) can be written as

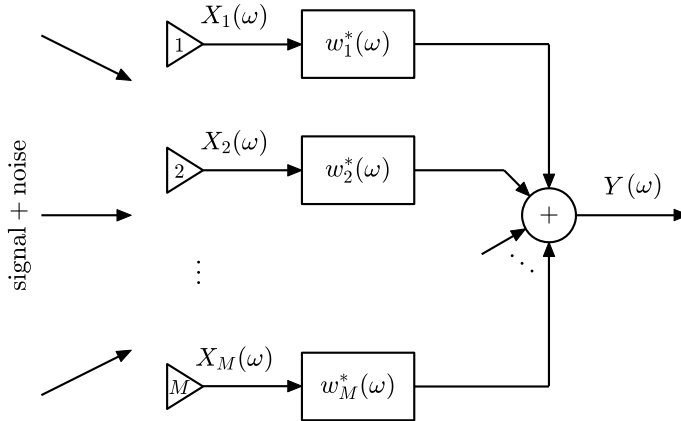


Fig. 1.5 General beamformer

$$Y(\omega) = Y(\omega, \mathbf{k})S(\omega). \quad (1.43)$$

It means that $Y(\omega, \mathbf{k})$ describes the response of the beamformer to an arbitrary plane wave. It is referred to as the frequency-wavenumber response function.

1.3.2 Array Performance Measures

There are a number of performance measures by which one can assess the capabilities of a beamformer. Several commonly used array performance measures are discussed in this section.

1. Beam Pattern, Beamwidth, and Sidelobe Level

The beam pattern, denoted by $B(\omega, \Omega)$, is the frequency-wavenumber response function evaluated versus the direction

$$B(\omega, \Omega) = Y(\omega, \mathbf{k})|_{\mathbf{k}=(\omega/c)\mathbf{v}(\Omega)} = \mathbf{w}^H(\omega)\mathbf{p}(\omega, \Omega), \quad (1.44)$$

where $\mathbf{p}(\omega, \Omega)$ is the array manifold vector which uses the frequency ω and direction Ω as arguments, i.e.,

$$\mathbf{p}(\omega, \Omega) = \mathbf{p}(\mathbf{k})|_{\mathbf{k}=(\omega/c)\mathbf{v}(\Omega)}, \quad \Omega \in \Theta, \quad (1.45)$$

where the angle set Θ is the field of view (FOV).

Frequently, the beam pattern is plotted in dB,

$$B_{\text{dB}}(\omega, \Omega) = 20\lg|B(\omega, \Omega)|, \quad \Omega \in \Theta, \quad (1.46)$$

where $\lg(\cdot) = \log_{10}(\cdot)$.

The beam pattern of a conventional DAS beamformer is referred to as a conventional beam pattern, which is given by

$$B_c(\omega, \Omega) = \mathbf{w}_c^H(\omega) \mathbf{p}(\omega, \Omega), \Omega \in \Theta, \quad (1.47)$$

where $\mathbf{w}_c(\omega)$ is the weight vector of the DAS beamformer.

In most cases of interest, the signal direction-of-arrival is unknown. The array manifold vector in the assumed signal direction $\Omega_o = (\theta_o, \phi_o)$ is used to compute the weight vector,

$$\mathbf{w}_c(\omega) = \mathbf{p}(\omega, \Omega_o)/M. \quad (1.48)$$

Thus,

$$B_c(\omega, \Omega) = \mathbf{p}^H(\omega, \Omega_o) \mathbf{p}(\omega, \Omega)/M, \quad (1.49)$$

which has its maximum value at $\Omega = \Omega_o$.

The direction $\Omega_o = (\theta_o, \phi_o)$ is referred to as the main response axis (MRA). It is also referred to as the look direction or steering direction. The array manifold vector $\mathbf{p}(\omega, \Omega_o)$ is referred to as the steering vector.

Consider a uniformly spaced linear array of $M = 10$ isotropic elements along the y -axis. The interelement spacing is d . This type of array is referred to as a uniform linear array (ULA). The steering direction is at $\Omega_o = (\theta_o, \phi_o) = (0^\circ, 90^\circ)$. The field of view Θ is located in the xy -plane (i.e., $\phi = 90^\circ$) and $\theta \in [-90^\circ, 90^\circ]$.

The conventional beam pattern in dB versus θ at frequency $\omega = \pi c/d$ (i.e., $d = \lambda/2$) is plotted in Fig. 1.6. Figure 1.6b is the zoomed-in plot of Fig. 1.6a. It is seen that the main response axis occurs at θ_o .

The sidelobe level (SL), the beamwidth (BW_{-3dB} , BW_{NN} and BW_{SL}), the mainlobe region (Θ_{ML}) and the sidelobe region (Θ_{SL}) are clearly illustrated in Fig. 1.6, where BW_{-3dB} is the -3 -dB beamwidth or half-power beamwidth, BW_{NN} is the null-to-null beamwidth, and BW_{SL} is the sidelobe-level beamwidth, which is defined to be the width between two directions where the beam powers are equal to the sidelobe level.

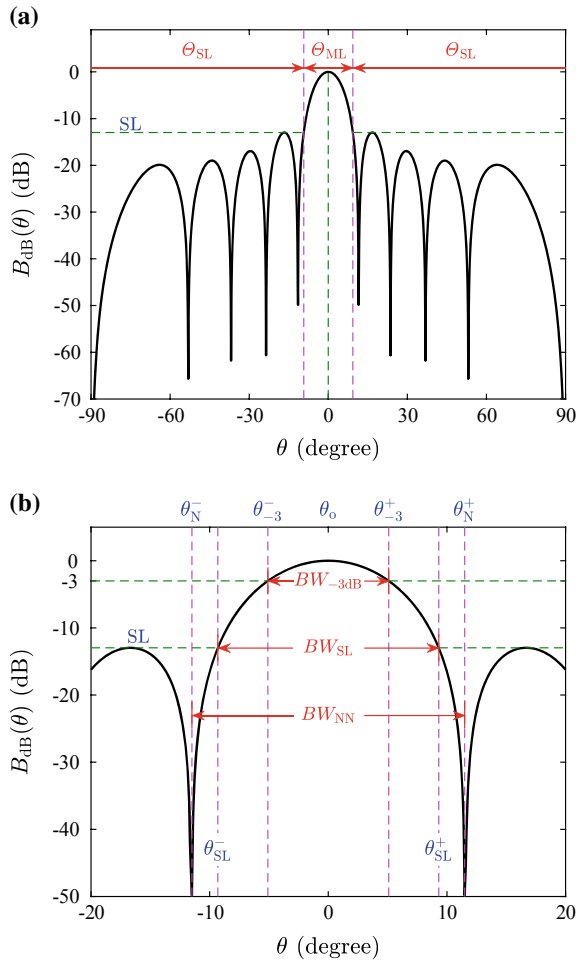
2. Array Gain, White Noise Gain, and Directivity

One of the purposes of beamforming is to improve the signal-to-interference-plus-noise ratio (SINR) or signal-to-noise ratio (SNR) when the interfering signals have been contained into the noise component. The improvement is measured by the array gain.

Consider the case of a single plane-wave desired signal, D plane-wave interfering signals, and additive noise. Then

$$\mathbf{X}(\omega) = \mathbf{p}(\omega, \Omega_0) S_0(\omega) + \sum_{d=1}^D \mathbf{p}(\omega, \Omega_d) S_d(\omega) + \mathbf{N}(\omega). \quad (1.50)$$

Fig. 1.6 Conventional beam pattern of 10-element uniform linear array at $d = \lambda/2$



Let Ω_s be the direction of desired signal, then

$$\Omega_s = \Omega_0. \quad (1.51)$$

Defining $\mathbf{p}_s(\omega) = \mathbf{p}(\omega, \Omega_s)$, $\mathbf{p}_d(\omega) = \mathbf{p}(\omega, \Omega_d)$, $d = 1, \dots, D$ and using Eq. (1.35), the spatial spectral matrix is given by

$$\begin{aligned} \mathbf{S}_x(\omega) &= S_{s0}(\omega) \mathbf{p}_s(\omega) \mathbf{p}_s^H(\omega) + \sum_{d=1}^D S_{sd}(\omega) \mathbf{p}_d(\omega) \mathbf{p}_d^H(\omega) + S_n(\omega) \mathbf{p}_n(\omega) \\ &= \mathbf{S}_s(\omega) + \mathbf{S}_i(\omega) + \mathbf{S}_n(\omega). \end{aligned} \quad (1.52)$$

The spectrum of the desired signal is

$$S_s(\omega) = S_{s0}(\omega). \quad (1.53)$$

The spectrum of the interfering signal component is given by

$$S_i(\omega) = \sum_{d=1}^D S_{sd}(\omega). \quad (1.54)$$

Assume that the noise spectra at each sensor are the same. At each sensor, the signal spectrum-to-noise spectrum ratio at frequency ω is

$$SNR_{in}(\omega) = S_s(\omega)/S_n(\omega). \quad (1.55)$$

The interfering signal spectrum-to-noise spectrum ratio at frequency ω is given by

$$INR(\omega) = S_i(\omega)/S_n(\omega). \quad (1.56)$$

The input SINR can be written as

$$SINR_{in}(\omega) = S_s(\omega)/[S_i(\omega) + S_n(\omega)] = S_s(\omega)/S_{i+n}(\omega), \quad (1.57)$$

where $S_{i+n}(\omega) = S_i(\omega) + S_n(\omega)$ is the spectrum of the interfering signal plus noise.

The spatial spectral matrix of interfering signal plus noise, denoted by $S_{i+n}(\omega)$, can be written as

$$S_{i+n}(\omega) = S_i(\omega) + S_n(\omega) = S_{i+n}(\omega)\rho_{i+n}(\omega), \quad (1.58)$$

where ρ_{i+n} is the normalized spatial spectral matrix of interfering signal plus noise.

Substituting Eq. (1.50) into Eq. (1.38) gives

$$\begin{aligned} Y(\omega) &= \mathbf{w}^H(\omega)X(\omega) \\ &= \mathbf{w}^H(\omega)\mathbf{p}_s(\omega)S_0(\omega) + \sum_{d=1}^D \mathbf{w}^H(\omega)\mathbf{p}_d(\omega)S_d(\omega) + \mathbf{w}^H(\omega)\mathbf{N}(\omega). \end{aligned} \quad (1.59)$$

Thus, the output spectrum is given by

$$\begin{aligned} S_y(\omega) &= E\{Y(\omega)Y^*(\omega)\} \\ &= \mathbf{w}^H(\omega)\mathbf{S}_x(\omega)\mathbf{w}(\omega) \\ &= \mathbf{w}^H(\omega)\mathbf{S}_s(\omega)\mathbf{w}(\omega) + \mathbf{w}^H(\omega)\mathbf{S}_i(\omega)\mathbf{w}(\omega) + \mathbf{w}^H(\omega)\mathbf{S}_n(\omega)\mathbf{w}(\omega) \end{aligned}$$

$$= S_{ys}(\omega) + S_{yi}(\omega) + S_{yn}(\omega), \quad (1.60)$$

where $S_{ys}(\omega)$, $S_{yi}(\omega)$ and $S_{yn}(\omega)$ are the spectrum output due to the desired signal, the interfering signal, and the noise, respectively.

The output SINR is given by

$$\begin{aligned} SINR_{out}(\omega) &= \frac{S_{ys}(\omega)}{S_{yi}(\omega) + S_{yn}(\omega)} \\ &= \frac{\mathbf{w}^H(\omega) \mathbf{S}_s(\omega) \mathbf{w}(\omega)}{\mathbf{w}^H(\omega) [S_i(\omega) + S_n(\omega)] \mathbf{w}(\omega)} \\ &= \frac{S_s(\omega) |\mathbf{w}^H(\omega) \mathbf{p}_s(\omega)|^2}{S_{i+n}(\omega) \mathbf{w}^H(\omega) \boldsymbol{\rho}_{i+n}(\omega) \mathbf{w}(\omega)}. \end{aligned} \quad (1.61)$$

In the absence of the interfering signals, the output SINR reduces to output SNR

$$SNR_{out}(\omega) = \frac{S_{ys}(\omega)}{S_{yn}(\omega)} = \frac{S_s(\omega) |\mathbf{w}^H(\omega) \mathbf{p}_s(\omega)|^2}{S_n(\omega) \mathbf{w}^H(\omega) \boldsymbol{\rho}_n(\omega) \mathbf{w}(\omega)}. \quad (1.62)$$

The array gain is defined to be the ratio of the SINR at the output of the beamformer to the SINR at an input sensor. Using Eqs. (1.57) and (1.61),

$$G(\omega) = \frac{SINR_{out}(\omega)}{SINR_{in}(\omega)} = \frac{|\mathbf{w}^H(\omega) \mathbf{p}_s(\omega)|^2}{\mathbf{w}^H(\omega) \boldsymbol{\rho}_{i+n}(\omega) \mathbf{w}(\omega)}. \quad (1.63)$$

The array gain can be expressed in dB as

$$G_{dB}(\omega) = 10 \lg G(\omega). \quad (1.64)$$

For the special case of a single plane-wave desired signal in the presence of spatially white noise, $\boldsymbol{\rho}_n(\omega) = \mathbf{I}$. Using Eq. (1.63), the array gain is given by

$$G_w(\omega) = \frac{|\mathbf{w}^H(\omega) \mathbf{p}_s(\omega)|^2}{\mathbf{w}^H(\omega) \mathbf{I} \mathbf{w}(\omega)} = \|\mathbf{w}(\omega)\|^{-2}. \quad (1.65)$$

The array gain against spatially white noise is referred to as the white noise gain (WNG). The WNG equals the inverse of the squared norm of the weight vector.

Note that the array gain in Eq. (1.63) is unchanged if the weight vector $\mathbf{w}(\omega)$ is multiplied by an arbitrary scale factor. Therefore, the weight vector can be normalized so that the spectrum output due to the desired signal equals the input signal spectrum

$$S_{ys}(\omega) = S_s(\omega) \mathbf{w}^H(\omega) \mathbf{p}_s(\omega) \mathbf{p}_s^H(\omega) \mathbf{w}(\omega) = S_s(\omega). \quad (1.66)$$

This equality implies

$$|\mathbf{w}^H(\omega)\mathbf{p}_s(\omega)| = 1. \quad (1.67)$$

Note that the output spectrum $\mathbf{w}^H(\omega)\mathbf{S}_x(\omega)\mathbf{w}(\omega)$ is unchanged when $\mathbf{w}(\omega)$ undergoes an arbitrary phase rotation. Therefore, the phase of $\mathbf{w}(\omega)$ can always be rotated, without affecting the output spectrum, so that $\mathbf{w}^H(\omega)\mathbf{p}_s(\omega)$ is real. Thus, $\mathbf{w}(\omega)$ can be chosen such that

$$\mathbf{w}^H(\omega)\mathbf{p}_s(\omega) = 1. \quad (1.68)$$

The constraint in Eq. (1.68) is referred to as a distortionless constraint.

From Eq. (1.67), the following inequality holds:

$$1 = |\mathbf{w}^H(\omega)\mathbf{p}_s(\omega)|^2 \leq \|\mathbf{w}(\omega)\|^2 \|\mathbf{p}_s(\omega)\|^2 = M \|\mathbf{w}(\omega)\|^2. \quad (1.69)$$

This implies

$$\|\mathbf{w}(\omega)\|^2 \geq 1/M, \quad (1.70)$$

with equality if the weight vector $\mathbf{w}(\omega)$ is in the same direction as $\mathbf{p}_s(\omega)$, which corresponds to a DAS beamformer.

Using Eqs. (1.65) and (1.70) gives

$$G_w(\omega) \leq M, \quad (1.71)$$

which implies that the maximum WNG is M and corresponds to a DAS beamformer.

The directivity is a common measure of array performance. The directivity, denoted by G_D , is defined as the ratio between the peak and the average values of the squared beam pattern.

$$G_D = \frac{|B(\theta_0, \phi_0)|^2}{\frac{1}{4\pi} \int_0^\pi \int_0^{2\pi} |B(\theta, \phi)|^2 d\theta \sin \phi d\phi}, \quad (1.72)$$

where (θ_0, ϕ_0) is the steering direction and the ω dependence has been suppressed.

Throughout the remainder of this book, the frequency dependence will be suppressed in the notation for convenience when the variable is clear.

The numerator of Eq. (1.72) is

$$G_{D,NUM} = |B(\theta_0, \phi_0)|^2 = |\mathbf{w}^H \mathbf{p}(\theta_0, \phi_0)|^2. \quad (1.73)$$

The denominator of Eq. (1.72) is given by

$$G_{D,DEN} = \frac{1}{4\pi} \int_0^\pi \int_0^{2\pi} |B(\theta, \phi)|^2 d\theta \sin \phi d\phi$$

$$\begin{aligned}
&= \mathbf{w}^H \frac{1}{4\pi} \int_0^{\pi} \int_0^{2\pi} \mathbf{p}(\theta, \phi) \mathbf{p}^H(\theta, \phi) d\theta \sin\phi d\phi \mathbf{w} \\
&= \mathbf{w}^H \mathbf{S}_{\text{iso}} \mathbf{w},
\end{aligned} \tag{1.74}$$

where

$$\begin{aligned}
\mathbf{S}_{\text{iso}} &= \frac{1}{4\pi} \int_0^{\pi} \int_0^{2\pi} \mathbf{p}(\theta, \phi) \mathbf{p}^H(\theta, \phi) d\theta \sin\phi d\phi \\
&= \frac{1}{4\pi} \int_0^{\pi} \int_0^{2\pi} \mathbf{S}_{\text{a}}(\theta, \phi) d\theta \sin\phi d\phi,
\end{aligned} \tag{1.75}$$

with

$$\mathbf{S}_{\text{a}}(\theta, \phi) = \mathbf{p}(\theta, \phi) \mathbf{p}^H(\theta, \phi). \tag{1.76}$$

The (m, \tilde{m}) th element of $\mathbf{S}_{\text{a}}(\theta, \phi)$ in Eq. (1.76) is given by

$$[\mathbf{S}_{\text{a}}(\theta, \phi)]_{m, \tilde{m}} = e^{-ik^T \mathcal{P}_m} e^{ik^T \mathcal{P}_{\tilde{m}}} = e^{-ik^T (\mathcal{P}_m - \mathcal{P}_{\tilde{m}})}. \tag{1.77}$$

Using Eq. (1.23), the (m, \tilde{m}) th element of \mathbf{S}_{iso} in Eq. (1.75) is

$$[\mathbf{S}_{\text{iso}}]_{m, \tilde{m}} = \frac{1}{4\pi} \int_0^{\pi} \int_0^{2\pi} \exp \left[-ik^T (\mathcal{P}_m - \mathcal{P}_{\tilde{m}}) \right] d\theta \sin\phi d\phi = \text{sinc} \left(kd_{m, \tilde{m}} \right), \tag{1.78}$$

where $d_{m, \tilde{m}}$ denotes the distance between the m th and the \tilde{m} th sensor.

Using Eq. (1.29) gives

$$\mathbf{S}_{\text{iso}} = \boldsymbol{\rho}_{\text{niso}}. \tag{1.79}$$

Using Eqs. (1.73), (1.74) and (1.79), Eq. (1.72) can be written as

$$G_{\text{D}} = \frac{|\mathbf{w}^H \mathbf{p}(\theta_0, \phi_0)|^2}{\mathbf{w}^H \boldsymbol{\rho}_{\text{niso}} \mathbf{w}} \triangleq G_{\text{iso}}, \tag{1.80}$$

where G_{iso} denotes the array gain against spatially isotropic noise. Thus, the directivity G_{D} can be interpreted as the array gain against spatially isotropic noise.

The directivity is usually expressed in dB and is referred to as the directivity index (DI),

$$DI = 10 \lg G_{\text{D}} = 10 \lg G_{\text{iso}}. \tag{1.81}$$

Recall that the noises are uncorrelated when the interelement spacing is a positive integer times of the half wavelength in isotropic noise case. The white noise array gain is identical to the array directivity for a uniform linear array with $d = \lambda/2$.

3. Sensitivity and Robustness

Consider the effect of weight perturbations and array location perturbations.

Assume that the nominal weight vector is $\mathbf{w}^n = [w_1^n, \dots, w_m^n, \dots, w_M^n]^T$, where $w_m^n = g_m^n e^{i\varphi_m^n}$. The actual weight is $w_m = g_m e^{i\varphi_m}$, where

$$g_m = g_m^n (1 + \Delta g_m), \quad (1.82)$$

$$\varphi_m = \varphi_m^n + \Delta \varphi_m. \quad (1.83)$$

Assume that the nominal array locations are $\mathcal{P}_m^n, m = 1, \dots, M$. The actual array locations are

$$\mathcal{P}_m = \mathcal{P}_m^n + \Delta \mathcal{P}_m. \quad (1.84)$$

Assume that the $\Delta g_m (m = 1, 2, \dots, M)$, $\Delta \varphi_m (m = 1, 2, \dots, M)$, and each component of $\Delta \mathcal{P}_m$ (i.e., $\Delta p_{xm}, \Delta p_{ym}, \Delta p_{zm}$) ($m = 1, 2, \dots, M$) are statistically independent, zero-mean, Gaussian random variables, the variances of Δg_m and $\Delta \varphi_m$ are respectively σ_g^2 and σ_φ^2 , and the variance of each component of $\Delta \mathcal{P}_m$ is equal to σ_p^2 .

The expectation of the squared magnitude of the actual beam pattern can be written as [1, 2]

$$\begin{aligned} \mathbb{E}\left\{\left|\tilde{B}(\Omega)\right|^2\right\} &= |\bar{B}(\Omega)|^2 e^{-(\sigma_\varphi^2 + \sigma_\lambda^2)} \\ &+ \sum_{m=1}^M (g_m^n)^2 \left[\left(1 + \sigma_g^2\right) - e^{-(\sigma_\varphi^2 + \sigma_\lambda^2)} \right], \end{aligned} \quad (1.85)$$

where $\tilde{B}(\Omega)$ and $\bar{B}(\Omega)$ are the actual and the nominal beam patterns, respectively, and $\sigma_\lambda = (2\pi/\lambda)\sigma_p$.

For the case of small variances, Eq. (1.85) reduces to

$$\mathbb{E}\left\{\left|\tilde{B}(\Omega)\right|^2\right\} = |\bar{B}(\Omega)|^2 e^{-(\sigma_\varphi^2 + \sigma_\lambda^2)} + \|\mathbf{w}\|^2 \left(\sigma_g^2 + \sigma_\varphi^2 + \sigma_\lambda^2\right). \quad (1.86)$$

The first term in Eq. (1.86) attenuates the beam pattern uniformly. The expected value of the beam pattern along the main response axis is less than unity, while this doesn't affect the array gain. The second term raises the expected value of the beam pattern in the sidelobe region uniformly.

The effect of the second term is more critical. Define the sensitivity function

$$T_{\text{se}} \triangleq \sum_{m=1}^M (g_m^{\text{n}})^2 = \sum_{m=1}^M |w_m^{\text{n}}|^2 = \|\mathbf{w}\|^2, \quad (1.87)$$

which equals the inverse of the WNG. As the WNG increases, the sensitivity decreases. Therefore, the robustness of a beamformer can be quantified by the WNG.

Recall that the DAS beamformer has the maximum WNG. Thus, it will be more robust to perturbations and parameter variations than the other beamformers.

4. Spatial Spectrum

For a given steering direction Ω_o , using Eq. (1.60), the output spectrum is given by

$$S_y(\Omega_o) = \mathbf{w}^H(\Omega_o) S_x \mathbf{w}(\Omega_o), \quad (1.88)$$

where $\mathbf{w}(\Omega_o)$ is the weight vector for the steering direction Ω_o .

Consider the typical application where the beamformer is scanned across the region of Θ space of interest (or field of view) by changing the steering direction in discrete steps. The output spectrum as a function of steering direction Ω_o can be used as the estimation of the spatial spectrum

$$P(\Omega_o) \triangleq \mathbf{w}^H(\Omega_o) S_x \mathbf{w}(\Omega_o), \quad \Omega_o \in \Theta, \quad (1.89)$$

where $P(\Omega_o)$ is referred to as the spatial spectrum using beamscan.

The spatial spectrum can be expressed in dB as

$$P_{\text{dB}}(\Omega_o) = 10 \lg P(\Omega_o), \quad \Omega_o \in \Theta. \quad (1.90)$$

The spatial spectrum can be used to estimate the direction-of-arrival of multiple plane-wave signals in the presence of noise.

1.4 Traditional Beamformer

Let $\bar{\mathbf{p}}$ and $\tilde{\mathbf{p}}$ be the nominal and actual steering vectors, respectively. The mismatch between the nominal and actual steering vector can be caused by signal direction mismatch, array perturbations, frequency mismatch, etc.

In practice, the actual steering vector $\tilde{\mathbf{p}}$ can not be known precisely. The nominal steering vector $\bar{\mathbf{p}}$ is used instead. Thus the distortionless constraint in Eq. (1.68) becomes

$$\mathbf{w}^H \bar{\mathbf{p}}_s = 1, \quad (1.91)$$

where $\bar{\mathbf{p}}_s$ is the nominal steering vector corresponding to the signal of interest.

1.4.1 Delay-and-Sum (DAS) Beamformer

Using $\bar{\mathbf{p}}$ instead of \mathbf{p} in Eq. (1.48), the weight vector of the conventional DAS beamformer becomes

$$\mathbf{w}_c = \bar{\mathbf{p}}_s / M. \quad (1.92)$$

The weight vector can be scaled to satisfy the distortionless constraint Eq. (1.91). Then,

$$\mathbf{w}_c = \bar{\mathbf{p}}_s / \bar{\mathbf{p}}_s^H \bar{\mathbf{p}}_s. \quad (1.93)$$

In most cases, we assume that

$$\|\bar{\mathbf{p}}_s\|^2 = \bar{\mathbf{p}}_s^H \bar{\mathbf{p}}_s = M. \quad (1.94)$$

Then, Eq. (1.93) reduces to Eq. (1.92).

Using $\tilde{\mathbf{p}}$ instead of \mathbf{p} in Eqs. (1.47) and (1.92), the actual beam pattern is given by

$$\tilde{B}_c(\Omega) = \mathbf{w}_c^H \tilde{\mathbf{p}}(\Omega) = \frac{\bar{\mathbf{p}}_s^H \tilde{\mathbf{p}}(\Omega)}{M}. \quad (1.95)$$

Substituting Eq. (1.92) into Eq. (1.60), the output spectrum of the DAS beamformer is given by

$$S_{y,c} = \mathbf{w}_c^H \mathbf{S}_x \mathbf{w}_c = \bar{\mathbf{p}}_s^H \mathbf{S}_x \bar{\mathbf{p}}_s / M^2. \quad (1.96)$$

Using Eq. (1.63), the array gain for the DAS beamformer can be written as

$$G_c = \frac{|\bar{\mathbf{p}}_s^H \tilde{\mathbf{p}}_s / M|^2}{\bar{\mathbf{p}}_s^H \rho_n \bar{\mathbf{p}}_s / M^2} = \frac{|\bar{\mathbf{p}}_s^H \tilde{\mathbf{p}}_s|^2}{\bar{\mathbf{p}}_s^H \rho_n \bar{\mathbf{p}}_s}. \quad (1.97)$$

For a given noise model, the maximum value of G_c can be obtained in the absence of mismatch, i.e., $\tilde{\mathbf{p}}_s = \bar{\mathbf{p}}_s$.

In the special case of a spatially white noise, the maximum array gain is

$$G_{cw} = M. \quad (1.98)$$

1.4.2 Optimum Beamformer

In many of the array processing applications, we want to maximize the array gain or the output SINR. From Eq. (1.63), the maximization of the array gain is equivalent to

the minimization of the output noise variance subject to a distortionless constraint [3]. This array processor is an optimum beamformer and is referred to as the minimum variance distortionless response (MVDR) beamformer or Capon beamformer.

The output noise variance is given by

$$E[S_{yn}] = \mathbf{w}^H \mathbf{S}_n \mathbf{w}. \quad (1.99)$$

Note that the interfering signals have been contained into the noise component.

Thus, the MVDR beamformer design problem can be formulated as

$$\begin{aligned} & \min_{\mathbf{w}} \mathbf{w}^H \mathbf{S}_n \mathbf{w}, \\ & \text{subject to } \mathbf{w}^H \bar{\mathbf{p}}_s = 1. \end{aligned} \quad (1.100)$$

By using Lagrange multipliers, the solution to Eq. (1.100) is given by

$$\mathbf{w}_{\text{MVDR}} = \frac{\mathbf{S}_n^{-1} \bar{\mathbf{p}}_s}{\bar{\mathbf{p}}_s^H \mathbf{S}_n^{-1} \bar{\mathbf{p}}_s} = \frac{\boldsymbol{\rho}_n^{-1} \bar{\mathbf{p}}_s}{\bar{\mathbf{p}}_s^H \boldsymbol{\rho}_n^{-1} \bar{\mathbf{p}}_s}, \quad (1.101)$$

where the denominator $\bar{\mathbf{p}}_s^H \boldsymbol{\rho}_n^{-1} \bar{\mathbf{p}}_s$ is a scale factor.

If $\boldsymbol{\rho}_n = \mathbf{I}$, the weight vector in Eq. (1.101) reduces to that in Eq. (1.93). This implies that the MVDR beamformer reduces to the DAS beamformer in the white noise environment.

Using $\tilde{\mathbf{p}}$ instead of \mathbf{p} in Eqs. (1.44) and (1.101), the actual beam pattern of the MVDR beamformer is given by

$$\tilde{B}_{\text{MVDR}}(\Omega) = \mathbf{w}_{\text{MVDR}}^H \tilde{\mathbf{p}}(\Omega) = \frac{\bar{\mathbf{p}}_s^H \boldsymbol{\rho}_n^{-1} \tilde{\mathbf{p}}(\Omega)}{\bar{\mathbf{p}}_s^H \boldsymbol{\rho}_n^{-1} \bar{\mathbf{p}}_s}. \quad (1.102)$$

Substituting Eq. (1.101) into Eq. (1.60), the output spectrum of the MVDR beamformer is given by

$$S_{y,\text{MVDR}} = \mathbf{w}^H \mathbf{S}_x \mathbf{w} = \frac{\bar{\mathbf{p}}_s^H \boldsymbol{\rho}_n^{-1} \mathbf{S}_x \boldsymbol{\rho}_n^{-1} \bar{\mathbf{p}}_s}{\bar{\mathbf{p}}_s^H \boldsymbol{\rho}_n^{-1} \bar{\mathbf{p}}_s \bar{\mathbf{p}}_s^H \boldsymbol{\rho}_n^{-1} \bar{\mathbf{p}}_s}. \quad (1.103)$$

Substituting Eq. (1.101) into Eq. (1.63), the array gain for the MVDR beamformer is given by

$$G_{\text{MVDR}} = \frac{|\mathbf{w}^H \tilde{\mathbf{p}}_s|^2}{\mathbf{w}^H \boldsymbol{\rho}_n \mathbf{w}} = \frac{|\bar{\mathbf{p}}_s^H \mathbf{S}_n^{-1} \tilde{\mathbf{p}}_s|^2}{\bar{\mathbf{p}}_s^H \mathbf{S}_n^{-1} \boldsymbol{\rho}_n \mathbf{S}_n^{-1} \bar{\mathbf{p}}_s} = \frac{|\bar{\mathbf{p}}_s^H \boldsymbol{\rho}_n^{-1} \tilde{\mathbf{p}}_s|^2}{\bar{\mathbf{p}}_s^H \boldsymbol{\rho}_n^{-1} \bar{\mathbf{p}}_s}. \quad (1.104)$$

The optimum array gain, denoted by G_{opt} , can be obtained when $\tilde{\mathbf{p}}_s = \bar{\mathbf{p}}_s$, which is

$$G_{\text{opt}} = \bar{\mathbf{p}}_s^H \boldsymbol{\rho}_n^{-1} \bar{\mathbf{p}}_s. \quad (1.105)$$

The output SNR of the optimum beamformer is

$$SNR_{\text{opt}} = (\sigma_s^2 / \sigma_n^2) \bar{\mathbf{p}}_s^H \boldsymbol{\rho}_n^{-1} \bar{\mathbf{p}}_s, \quad (1.106)$$

where SNR_{opt} can be replaced by $SINR_{\text{opt}}$ since we have included the interferences in the noise spectral matrix.

In applications where the signal is always present, the noise spectral matrix \mathbf{S}_n is unavailable, the spatial spectral matrix \mathbf{S}_x is used instead of \mathbf{S}_n . Then Eq. (1.100) becomes

$$\begin{aligned} & \min_{\mathbf{w}} \mathbf{w}^H \mathbf{S}_x \mathbf{w}, \\ & \text{subject to } \mathbf{w}^H \bar{\mathbf{p}}_s = 1. \end{aligned} \quad (1.107)$$

Using \mathbf{S}_x instead of \mathbf{S}_n in Eq. (1.101), the weight vector can be written as

$$\mathbf{w}_{\text{MVDR}} = \frac{\mathbf{S}_x^{-1} \bar{\mathbf{p}}_s}{\bar{\mathbf{p}}_s^H \mathbf{S}_x^{-1} \bar{\mathbf{p}}_s}. \quad (1.108)$$

Substituting Eq. (1.108) into Eq. (1.60), the output spectrum of the MVDR beamformer is given by

$$S_{y, \text{MVDR}} = \mathbf{w}^H \mathbf{S}_x \mathbf{w} = \frac{1}{\bar{\mathbf{p}}_s^H \mathbf{S}_x^{-1} \bar{\mathbf{p}}_s}. \quad (1.109)$$

Substituting Eq. (1.108) into Eq. (1.63), the array gain for this MVDR beamformer is given by

$$G_{\text{MVDR}} = \frac{|\mathbf{w}^H \tilde{\mathbf{p}}_s|^2}{\mathbf{w}^H \boldsymbol{\rho}_n \mathbf{w}} = \frac{|\bar{\mathbf{p}}_s^H \mathbf{S}_x^{-1} \tilde{\mathbf{p}}_s|^2}{\bar{\mathbf{p}}_s^H \mathbf{S}_x^{-1} \boldsymbol{\rho}_n \mathbf{S}_x^{-1} \bar{\mathbf{p}}_s}. \quad (1.110)$$

Consider the model

$$\mathbf{X} = \beta \tilde{\mathbf{p}}_s \mathbf{S} + \mathbf{N}, \quad (1.111)$$

where the interferences have been included in the noise, β is a binary parameter (0 or 1) indicating whether the desired signal is present.

When $\beta = 0$, the optimization problem in Eq. (1.107) reduces to that in Eq. (1.100).

When $\beta = 1$, the spatial spectral matrix \mathbf{S}_x can be written as

$$\mathbf{S}_x = \mathbf{S}_s \tilde{\mathbf{p}}_s \tilde{\mathbf{p}}_s^H + \mathbf{S}_n \boldsymbol{\rho}_n \quad (1.112)$$

Using the matrix inversion lemma

$$S_x^{-1} = S_n^{-1} \rho_n^{-1} \left\{ \mathbf{I} - \tilde{\mathbf{p}}_s \tilde{\mathbf{p}}_s^H \rho_n^{-1} (S_s/S_n) \left[1 + (S_s/S_n) \tilde{\mathbf{p}}_s^H \rho_n^{-1} \tilde{\mathbf{p}}_s \right]^{-1} \right\}, \quad (1.113)$$

and letting $\chi = (S_s/S_n) \tilde{\mathbf{p}}_s^H \rho_n^{-1} \tilde{\mathbf{p}}_s$ gives

$$S_x^{-1} = S_n^{-1} \rho_n^{-1} \left\{ \mathbf{I} - \tilde{\mathbf{p}}_s \tilde{\mathbf{p}}_s^H \rho_n^{-1} (S_s/S_n) [1 + \chi]^{-1} \right\}. \quad (1.114)$$

Then,

$$\begin{aligned} S_x^{-1} \tilde{\mathbf{p}}_s &= S_n^{-1} \rho_n^{-1} \tilde{\mathbf{p}}_s - S_n^{-1} \rho_n^{-1} \tilde{\mathbf{p}}_s \tilde{\mathbf{p}}_s^H \rho_n^{-1} \tilde{\mathbf{p}}_s (S_s/S_n) [1 + \chi]^{-1} \\ &= S_n^{-1} \rho_n^{-1} \tilde{\mathbf{p}}_s - S_n^{-1} \rho_n^{-1} \tilde{\mathbf{p}}_s [\chi / (1 + \chi)] \\ &= S_n^{-1} \rho_n^{-1} \tilde{\mathbf{p}}_s / (1 + \chi). \end{aligned} \quad (1.115)$$

Thus,

$$\tilde{\mathbf{p}}_s^H S_x^{-1} \tilde{\mathbf{p}}_s = S_n^{-1} \tilde{\mathbf{p}}_s^H \rho_n^{-1} \tilde{\mathbf{p}}_s / (1 + \chi). \quad (1.116)$$

When $\tilde{\mathbf{p}}_s = \bar{\mathbf{p}}_s$, using Eqs. (1.115) and (1.116), Eq. (1.108) can be written as

$$\mathbf{w}_{\text{MVDR}} = \frac{S_x^{-1} \bar{\mathbf{p}}_s}{\bar{\mathbf{p}}_s^H S_x^{-1} \bar{\mathbf{p}}_s} \Big|_{\tilde{\mathbf{p}}_s = \bar{\mathbf{p}}_s} = \frac{\rho_n^{-1} \bar{\mathbf{p}}_s}{\bar{\mathbf{p}}_s^H \rho_n^{-1} \bar{\mathbf{p}}_s}. \quad (1.117)$$

which is identical to the weight vector in Eq. (1.101).

It shows that, if $\tilde{\mathbf{p}}_s = \bar{\mathbf{p}}_s$, the MVDR beamformer for $\beta = 1$ case will reduce to that for $\beta = 0$ case.

To evaluate the numerator in Eq. (1.110), using Eq. (1.115), then

$$\bar{\mathbf{p}}_s^H S_x^{-1} \tilde{\mathbf{p}}_s = S_n^{-1} \bar{\mathbf{p}}_s^H \rho_n^{-1} \tilde{\mathbf{p}}_s / (1 + \chi). \quad (1.118)$$

The denominator of Eq. (1.110) is given by

$$\begin{aligned} \bar{\mathbf{p}}_s^H S_x^{-1} \rho_n S_x^{-1} \bar{\mathbf{p}}_s &= S_n^{-1} \bar{\mathbf{p}}_s^H \rho_n^{-1} \left[\mathbf{I} - \tilde{\mathbf{p}}_s \tilde{\mathbf{p}}_s^H \rho_n^{-1} (S_s/S_n) (1 + \chi)^{-1} \right] \rho_n \\ &\quad \cdot S_n^{-1} \rho_n^{-1} \left[\mathbf{I} - \tilde{\mathbf{p}}_s \tilde{\mathbf{p}}_s^H \rho_n^{-1} (S_s/S_n) (1 + \chi)^{-1} \right] \bar{\mathbf{p}}_s \\ &= S_n^{-2} \bar{\mathbf{p}}_s^H \rho_n^{-1} \left[\mathbf{I} - \tilde{\mathbf{p}}_s \tilde{\mathbf{p}}_s^H \rho_n^{-1} (S_s/S_n) (1 + \chi)^{-1} \right]^2 \bar{\mathbf{p}}_s. \end{aligned} \quad (1.119)$$

Letting

$$\frac{|\bar{\mathbf{p}}_s^H \rho_n^{-1} \tilde{\mathbf{p}}_s|^2}{(\bar{\mathbf{p}}_s^H \rho_n^{-1} \bar{\mathbf{p}}_s)(\bar{\mathbf{p}}_s^H \rho_n^{-1} \tilde{\mathbf{p}}_s)} = \cos^2(\bar{\mathbf{p}}_s, \tilde{\mathbf{p}}_s, \rho_n^{-1}), \quad (1.120)$$

Equation (1.119) reduces to

$$\begin{aligned}
& \bar{\mathbf{p}}_s^H \mathbf{S}_x^{-1} \boldsymbol{\rho}_n \mathbf{S}_x^{-1} \bar{\mathbf{p}}_s \\
&= S_n^{-2} \bar{\mathbf{p}}_s^H \boldsymbol{\rho}_n^{-1} \bar{\mathbf{p}}_s \left[1 - 2 \frac{\chi}{1 + \chi} \cos^2(\bar{\mathbf{p}}_s, \tilde{\mathbf{p}}_s, \boldsymbol{\rho}_n^{-1}) + \left(\frac{\chi}{1 + \chi} \right)^2 \cos^2(\bar{\mathbf{p}}_s, \tilde{\mathbf{p}}_s, \boldsymbol{\rho}_n^{-1}) \right] \\
&= S_n^{-2} (1 + \chi)^{-2} \bar{\mathbf{p}}_s^H \boldsymbol{\rho}_n^{-1} \bar{\mathbf{p}}_s [(1 + \chi)^2 - (2\chi + \chi^2) \cos^2(\bar{\mathbf{p}}_s, \tilde{\mathbf{p}}_s, \boldsymbol{\rho}_n^{-1})] \\
&= S_n^{-2} (1 + \chi)^{-2} \bar{\mathbf{p}}_s^H \boldsymbol{\rho}_n^{-1} \bar{\mathbf{p}}_s [1 + (2\chi + \chi^2) \sin^2(\bar{\mathbf{p}}_s, \tilde{\mathbf{p}}_s, \boldsymbol{\rho}_n^{-1})], \tag{1.121}
\end{aligned}$$

where $\sin^2(\bar{\mathbf{p}}_s, \tilde{\mathbf{p}}_s, \boldsymbol{\rho}_n^{-1}) = 1 - \cos^2(\bar{\mathbf{p}}_s, \tilde{\mathbf{p}}_s, \boldsymbol{\rho}_n^{-1})$.

Substituting Eqs. (1.118) and (1.121) into Eq. (1.110) gives [4]

$$\begin{aligned}
G_{\text{MVDR}} &= \frac{|\bar{\mathbf{p}}_s^H \mathbf{S}_x^{-1} \tilde{\mathbf{p}}_s|^2}{\bar{\mathbf{p}}_s^H \mathbf{S}_x^{-1} \boldsymbol{\rho}_n \mathbf{S}_x^{-1} \bar{\mathbf{p}}_s} \\
&= \frac{|\bar{\mathbf{p}}_s^H \boldsymbol{\rho}_n^{-1} \tilde{\mathbf{p}}_s|^2 [S_n^{-2} (1 + \chi)^{-2}]}{\bar{\mathbf{p}}_s^H \boldsymbol{\rho}_n^{-1} \bar{\mathbf{p}}_s [1 + (2\chi + \chi^2) \sin^2(\bar{\mathbf{p}}_s, \tilde{\mathbf{p}}_s, \boldsymbol{\rho}_n^{-1})] [S_n^{-2} (1 + \chi)^{-2}]} \\
&= \frac{\tilde{\mathbf{p}}_s^H \boldsymbol{\rho}_n^{-1} \tilde{\mathbf{p}}_s \cos^2(\bar{\mathbf{p}}_s, \tilde{\mathbf{p}}_s, \boldsymbol{\rho}_n^{-1})}{1 + (2\chi + \chi^2) \sin^2(\bar{\mathbf{p}}_s, \tilde{\mathbf{p}}_s, \boldsymbol{\rho}_n^{-1})} \\
&= \frac{\tilde{\mathbf{p}}_s^H \boldsymbol{\rho}_n^{-1} \tilde{\mathbf{p}}_s \cos^2(\bar{\mathbf{p}}_s, \tilde{\mathbf{p}}_s, \boldsymbol{\rho}_n^{-1})}{1 + \left\{ 2(\sigma_s^2 / \sigma_n^2) \tilde{\mathbf{p}}_s^H \boldsymbol{\rho}_n^{-1} \tilde{\mathbf{p}}_s + [(\sigma_s^2 / \sigma_n^2) \tilde{\mathbf{p}}_s^H \boldsymbol{\rho}_n^{-1} \tilde{\mathbf{p}}_s]^2 \right\} \sin^2(\bar{\mathbf{p}}_s, \tilde{\mathbf{p}}_s, \boldsymbol{\rho}_n^{-1})}. \tag{1.122}
\end{aligned}$$

We see that when $\bar{\mathbf{p}}_s = \tilde{\mathbf{p}}_s$, from Eq. (1.120), $\cos^2(\bar{\mathbf{p}}_s, \tilde{\mathbf{p}}_s, \boldsymbol{\rho}_n^{-1}) = 1$ and $\sin^2(\bar{\mathbf{p}}_s, \tilde{\mathbf{p}}_s, \boldsymbol{\rho}_n^{-1}) = 0$. Using Eq. (1.122) gives $G_{\text{MVDR}} = \bar{\mathbf{p}}_s^H \boldsymbol{\rho}_n^{-1} \bar{\mathbf{p}}_s = G_{\text{opt}}$. The array gain degrades in the presence of array manifold vector mismatch. In the presence of array manifold vector mismatch, as the SNR increases the array gain degrades.

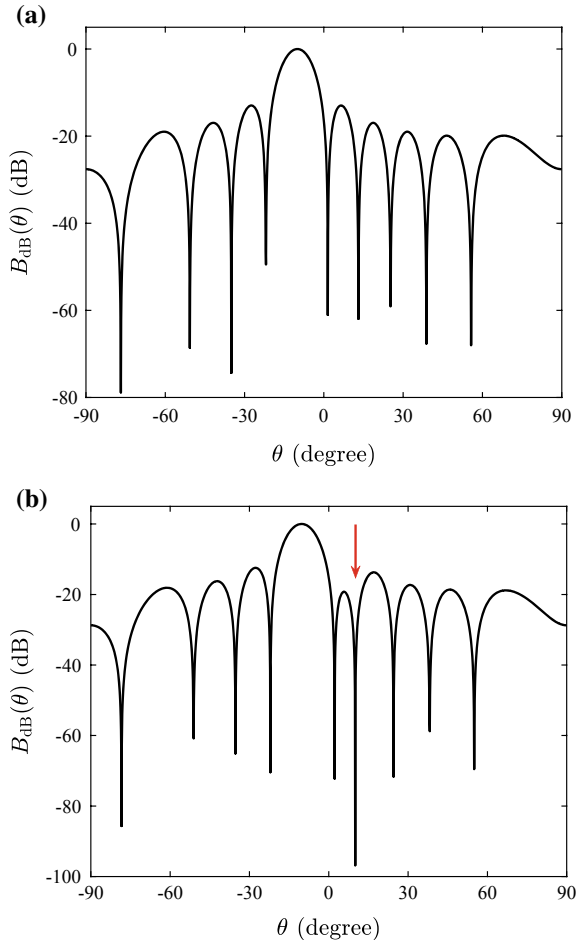
Consider a 10-element uniform linear array with $d = \lambda/2$ along the y -axis in the white noise environment. Two plane-wave signals impinge on the array from $(\theta, \phi) = (-10^\circ, 90^\circ)$ and $(10^\circ, 90^\circ)$ with $SNR = 15$ dB and 30 dB, respectively.

Both DAS beamformer and MVDR beamformer are designed for the steering direction $\Omega_o = (\theta_o, \phi_o) = (-10^\circ, 90^\circ)$. The beam patterns of both beamformers in the xy -plane are plotted in Fig. 1.7a and b, respectively.

It is seen that the main response axes of both beam patterns are at $\theta_o = -10^\circ$. The MVDR beam pattern has a null at the direction of the interferer $\theta = 10^\circ$.

Both beamformers are scanned across the region $[-90^\circ, 90^\circ]$ by changing the steering direction in 0.1° steps. Using Eq. (1.89), the resulting spatial spectrum in dB is plotted in Fig. 1.8. The small circles in the figure denote the true direction-of-arrival and powers of the signals.

Fig. 1.7 Beam patterns as functions of θ for a 10-element uniform linear array. **a** DAS beamformer, **b** MVDR beamformer



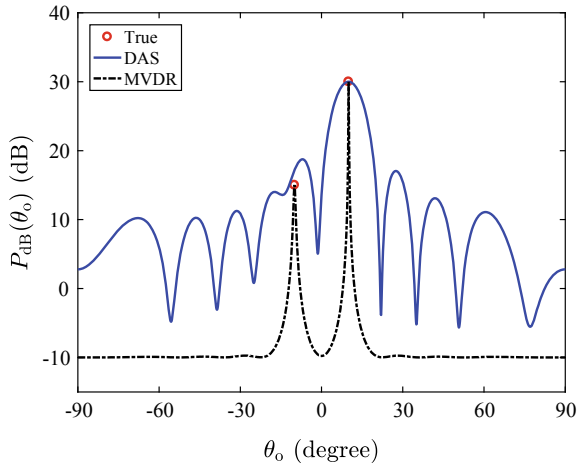
The DAS beamformer has poorer resolution than the MVDR beamformer and its sidelobes result in false peaks. The MVDR beamformer can give good direction-of-arrival estimates for the signals based on the peak locations.

Now study the effects of steering vector mismatch on the performance of MVDR beamformers. Assume that the array manifold vector is perturbed with a zero-mean complex Gaussian random variable $\mathbf{p}_\Delta(\theta) = \tilde{\mathbf{p}}(\theta) - \bar{\mathbf{p}}(\theta)$ and $\|\mathbf{p}_\Delta(\theta)\|^2 = 0.01$.

We first consider the case of the desired signal absent, i.e., $\beta = 0$. The actual MVDR beam pattern \tilde{B} is calculated using Eq. (1.102). The nominal beam pattern \bar{B} can also be calculated by using $\bar{\mathbf{p}}$ instead of $\tilde{\mathbf{p}}$ in Eq. (1.102). The actual and nominal beam patterns are shown in Fig. 1.9a.

There is only a slight variation between the actual and the nominal beam patterns. The null of the actual beam pattern at the direction $\theta = 10^\circ$ is deeper than that of

Fig. 1.8 Spatial spectrum estimation using beamscan



the nominal beam pattern because the actual steering vector is matched to spatial spectral matrix of the interference.

We next consider the case of the desired signal present, i.e., $\beta = 1$. The weight vector is calculated using Eq. (1.108). The actual and nominal beam patterns are then calculated and shown in Fig. 1.9b.

The nominal beam pattern at the direction $\theta_o = -10^\circ$ is equal to unity because of the distortionless constraint. However, the beam pattern of the beamformer degrades significantly under mismatch. The reason is that the MVDR beamformer treats the mismatched signal as an interferer and attempts to null it, which causes the degradation of the sidelobes.

Moreover, as the SNR increases the array gain degrades significantly with very small array manifold vector mismatch.

1.5 Summary

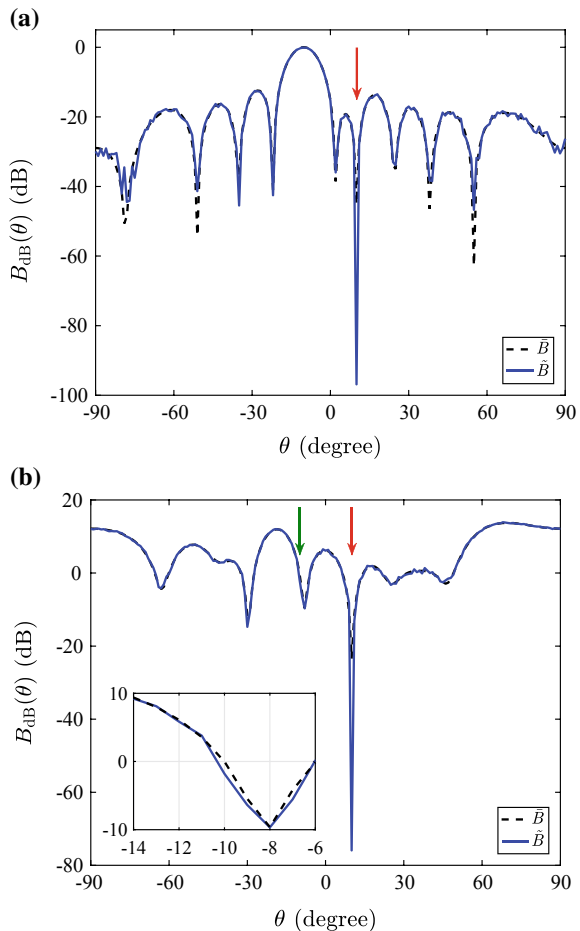
Some background in array processing have been presented in this chapter.

The general formulation of array signal model and beamforming are presented. Two traditional beamformers, i.e., the DAS beamformer and the MVDR beamformer, are introduced.

Several commonly used array performance measures are discussed, e.g., beam pattern (beamwidth, sidelobe level), array gain (directivity), WNG, sensitivity (robustness), etc. They can be used to quantify the capabilities of the beamformer. The directivity can be interpreted as the array gain against spatially isotropic noise. The sensitivity function equals the squared norm of the weight vector.

The WNG equals the inverse of the squared norm of the weight vector, which can be used to quantify the robustness of the beamformer. The DAS beamformer

Fig. 1.9 Nominal and actual MVDR beam patterns for the case **a** $\beta = 0$, and **b** $\beta = 1$



has the maximum WNG and thus is more robust to the perturbations and parameter variations than other beamformers.

The MVDR beamformer attempts to achieve the maximum output SINR. It can obtain the optimum array gain in the absence of mismatch. The array gain degrades in the presence of array manifold vector mismatch. As the SNR increases, the degradation due to mismatch increases and even very small mismatches will lead to unacceptable performance.

References

1. H.L. Van Trees, *Optimum Array Processing: Part IV of Detection, Estimation, and Modulation Theory* (Wiley, New York, 2002)
2. E.N. Gilbert, S.P. Morgan, Optimum design of directive antenna arrays subject to random variations. *Bell Syst. Tech. J.* **34**(3), 637–663 (1955)
3. J. Capon, High-resolution frequency-wavenumber spectrum analysis. *Proc. IEEE* **57**(8), 1408–1418 (1969)
4. H. Cox, Resolving power and sensitivity to mismatch of optimum array processors. *J. Acoust. Soc. Am.* **54**(3), 771–785 (1973)

Chapter 2

Frequency-Domain Broadband Beamforming



2.1 Introduction

In most applications ranging from sonar, radar, to microphone arrays, the broadband signals are of interest. Broadband beamforming has been studied extensively [1]. In particular, much of the development in broadband beamforming has been focused on the application area of various acoustic arrays because sound is a natural source of broadband signals.

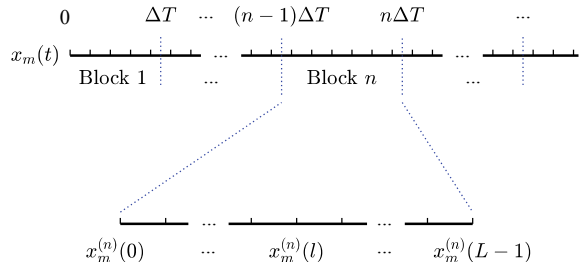
The time-domain model and its corresponding frequency-domain representation for broadband signals have been presented in Chap. 1. Since it is more convenient to design the beamformer weights in the frequency domain, the frequency-domain model is more desirable.

In practice, we usually divide the total received data by each sensor into a lot of blocks. For each block of time-domain samples, a discrete Fourier transform (DFT) is performed to obtain a set of complex frequency-domain samples that are referred to as the frequency-domain snapshots. The frequency-domain snapshot model is typically appropriate for broadband processes.

The broadband array signals have been decomposed into a lot of frequency bins using the DFT. For each frequency bin, whenever the narrowband condition is satisfied, the narrowband beamformers can be used directly.

The rest of this chapter is organized as follows. The frequency-domain snapshot model for broadband arrays is presented in Sect. 2.2. In Sect. 2.3, the frequency-domain implementation of broadband beamformer is presented. A brief summary of this chapter is given in Sect. 2.4.

Fig. 2.1 Block data from the m th sensor



2.2 Frequency-Domain Snapshot Model

2.2.1 Frequency-Domain Snapshots

In most applications, the total observation interval are divided into a lot of non-overlapping or overlapping intervals of length ΔT , as shown in Fig. 2.1. In order to sample the signal field using an array of elements, the time interval ΔT must be significantly greater than the propagation time across the array, that is

$$\Delta T \gg \Delta T_{\max}, \quad (2.1)$$

where ΔT_{\max} is the maximum propagation time across the array for any direction.

Consider a single plane-wave signal in the absence of noise. Thus,

$$x_m(t) = s[t - \tau_m(\Omega)], \quad m = 1, \dots, M. \quad (2.2)$$

The corresponding frequency-domain representation is

$$X_m(\omega) = S(\omega)e^{-i\omega\tau_m(\Omega)}, \quad m = 1, \dots, M. \quad (2.3)$$

Assume that the frequency of the signal is bandlimited to the region

$$|\omega - \omega_c| \leq 2\pi B_s/2, \quad (2.4)$$

where B_s is the bandwidth, and ω_c is the center radian frequency.

The signals of interest are broadband when the time-bandwidth product $B_s \cdot \Delta T$ is large. In practice, common $B_s \cdot \Delta T$ products are from 16 to 512.

If $s(t)$ is the signal that would be received at the origin of the coordinate system, in the time interval ΔT , the sampled signal is

$$s^{(n)}(l) = s(t)|_{t=lT_s}, \quad (n-1)\Delta T \leq t < n\Delta T, \quad (2.5)$$

where $T_s = 1/f_s$ is the sampling interval with f_s being the sampling frequency, and n is the index of the time interval.

Performing a DFT on the samples $s^{(n)}(l)$ ($l = 0, 1, \dots, L - 1$), where L is the length of the samples, gives

$$S^{(n)}(k), (k = 0, \dots, L - 1) = \text{DFT}[s^{(n)}(l), (l = 0, \dots, L - 1)], \quad (2.6)$$

or

$$\begin{aligned} S^{(n)}(k) &= \sum_{l=0}^{L-1} s^{(n)}(l) \exp(-i2\pi kl/L) \\ &= \mathbf{s}^{(n)} \mathbf{e}(k), \quad k = 0, \dots, L - 1, \end{aligned} \quad (2.7)$$

where $\mathbf{s}^{(n)}$ is a $1 \times L$ row vector

$$\mathbf{s}^{(n)} = [s^{(n)}(0), \dots, s^{(n)}(l), \dots, s^{(n)}(L - 1)], \quad (2.8)$$

and $\mathbf{e}(k)$ is an $L \times 1$ column vector, given by

$$\mathbf{e}(k) = [1, \dots, \exp(-i2\pi kl/L), \dots, \exp(-i2\pi k \frac{L-1}{L})]^T. \quad (2.9)$$

For L even, the radian frequency corresponding to k is

$$\omega_k = \begin{cases} 2\pi f_s k / L, & k = 0, \dots, L/2 - 1 \\ 2\pi f_s (k - L) / L, & k = L/2, \dots, L - 1 \end{cases}, \quad (2.10)$$

and the resolution of the transform is

$$\omega_\Delta = \frac{2\pi f_s}{L} = \frac{2\pi}{\Delta T}. \quad (2.11)$$

The DFT in Eqs. (2.6) and (2.7) can be implemented using a fast Fourier transform (FFT).

Because $s^{(n)}(l)$ is real, its DFT exhibits a conjugate symmetry. Thus,

$$S^{(n)}(L - k) = \text{conj}(S^{(n)}(k)), \quad k = 1, \dots, L/2 - 1, \quad (2.12)$$

where $\text{conj}(\cdot)$ denotes the complex conjugate.

Using inverse DFT (IDFT), $s^{(n)}(l)$ can be written in Fourier series expansion as

$$s^{(n)}(l) = \frac{1}{L} \sum_{k=0}^{L-1} S^{(n)}(k) \exp(i2\pi kl/L)$$

$$= \frac{1}{L} \sum_{k=0}^{L-1} S^{(n)}(k) \exp(i\omega_k l T_s), \quad l = 0, \dots, L-1, \quad (2.13)$$

where $S^{(n)}(k)$ is the Fourier series coefficient given in Eq. (2.7).

This means the time series $s^{(n)}(l)$ can be decomposed into a set of frequency bins with waveform

$$s_k^{(n)}(l) \triangleq S^{(n)}(k) \exp(i\omega_k l T_s), \quad l = 0, \dots, L-1, \quad (2.14)$$

whose complex envelope is $S^{(n)}(k)$ centered at ω_k with bandwidth

$$B_\Delta = \omega_\Delta / 2\pi = \frac{1}{\Delta T}. \quad (2.15)$$

Using Eq. (2.1) gives

$$B_\Delta \cdot \Delta T_{\max} \ll 1. \quad (2.16)$$

A bandpass signal whose complex envelope satisfies Eq. (2.16) is a narrowband signal. Thus, $s_k^{(n)}(l)$ is a narrowband signal.

In the time interval ΔT , the sampled data from the m th sensor is

$$\begin{aligned} x_m^{(n)}(l) &= x_m(t)|_{t=lT_s} \\ &= s[t - \tau_m(\mathcal{Q})]|_{t=lT_s}, \quad (n-1)\Delta T \leq t < n\Delta T. \end{aligned} \quad (2.17)$$

Similar to Eq. (2.13), $x_m^{(n)}(l)$ can be written in Fourier series expansion as

$$\begin{aligned} x_m^{(n)}(l) &= \frac{1}{L} \sum_{k=0}^{L-1} X_m^{(n)}(k) \exp(i2\pi k l / L) \\ &= \frac{1}{L} \sum_{k=0}^{L-1} X_m^{(n)}(k) \exp(i\omega_k l T_s), \quad l = 0, \dots, L-1, \end{aligned} \quad (2.18)$$

where $X_m^{(n)}(k)$ is the Fourier series coefficient, given by

$$\begin{aligned} X_m^{(n)}(k) &= \sum_{l=0}^{L-1} x_m^{(n)}(l) \exp(-i2\pi k l / L) \\ &= \mathbf{x}_m^{(n)} \mathbf{e}(k), \quad k = 0, \dots, L-1, \end{aligned} \quad (2.19)$$

where $\mathbf{x}_m^{(n)}$ is a $1 \times L$ row vector

$$\mathbf{x}_m^{(n)} = [x_m^{(n)}(0), \dots, x_m^{(n)}(l), \dots, x_m^{(n)}(L-1)]. \quad (2.20)$$

In Eq. (2.18), the time series $x_m^{(n)}(l)$ is decomposed into a set of narrowband frequency bins with waveform

$$x_{mk}^{(n)}(l) \triangleq X_m^{(n)}(k) \exp(i\omega_k l T_s), \quad l = 0, \dots, L-1, \quad (2.21)$$

whose complex envelope is $X_m^{(n)}(k)$.

Substituting Eq. (2.17) into Eq. (2.19) gives

$$X_m^{(n)}(k) = \sum_{l=0}^{L-1} s[t - \tau_m(\Omega)]|_{t=lT_s} \exp(-i2\pi k l / L), \quad k = 0, \dots, L-1. \quad (2.22)$$

The narrowband condition is satisfied for the complex envelopes, so the following approximation can be used

$$X_m^{(n)}(k) \approx S^{(n)}(k) \exp(-i\omega_k \tau_m(\Omega)), \quad k = 0, \dots, L-1. \quad (2.23)$$

We recognize the exponential term as the m th element of the array manifold vector $\mathbf{p}(\omega_k, \Omega)$. Thus, Eq. (2.23) can be written in matrix form as

$$X_k(n) = \mathbf{p}(\omega_k, \Omega) S_k(n), \quad (2.24)$$

where $X_k(n) = \left[X_1^{(n)}(k), \dots, X_m^{(n)}(k), \dots, X_M^{(n)}(k) \right]^T$ and $S_k(n) = S^{(n)}(k)$.

In the presence of interfering signals and noise, Eq. (2.24) becomes

$$X_k(n) = \mathbf{p}(\omega_k, \Omega_0) S_{0k}(n) + \sum_{d=1}^D \mathbf{p}(\omega_k, \Omega_d) S_{dk}(n) + N_k(n), \quad (2.25)$$

where Ω_0 and Ω_d ($d = 1, \dots, D$) are the directions-of-arrival of the desired and interfering signals, $S_{dk}(n)$ ($d = 0, \dots, D$) are their complex envelopes at frequency bin ω_k , respectively, and $N_k(n) = \left[N_1^{(n)}(k), \dots, N_m^{(n)}(k), \dots, N_M^{(n)}(k) \right]^T$ with $N_m^{(n)}(k)$ being the complex envelope of the noise at frequency bin ω_k .

Equation (2.25) is referred to as the frequency-domain snapshot model. The frequency-domain snapshot approach is typically used for broadband signals.

2.2.2 Covariance Matrix

In each frequency bin, the covariance matrix, denoted by $\mathbf{R}_x(\omega_k)$, is

$$\mathbf{R}_x(\omega_k) = \mathbb{E}[X_k(n) X_k^H(n)]. \quad (2.26)$$

For the case where the signal, interference and noise snapshots are uncorrelated, the covariance matrix can be written as

$$\begin{aligned}\mathbf{R}_x(\omega_k) &= \sigma_0^2(\omega_k) \mathbf{p}(\omega_k, \Omega_0) \mathbf{p}^H(\omega_k, \Omega_0) \\ &\quad + \sum_{d=1}^D \sigma_d^2(\omega_k) \mathbf{p}(\omega_k, \Omega_d) \mathbf{p}^H(\omega_k, \Omega_d) + \sigma_n^2(\omega_k) \mathbf{\rho}_n(\omega_k) \\ &= \mathbf{R}_s(\omega_k) + \mathbf{R}_i(\omega_k) + \mathbf{R}_n(\omega_k),\end{aligned}\quad (2.27)$$

where $\sigma_d^2(\omega_k) = E[S_{dk}(n)S_{dk}^*(n)]$ ($d = 0, \dots, D$) and $\sigma_n^2(\omega_k)$ are the variances (or powers) of the desired signal, the interferences and the noise, respectively, in the frequency bin ω_k , $\mathbf{R}_s(\omega_k)$, $\mathbf{R}_i(\omega_k)$ and $\mathbf{R}_n(\omega_k)$ are the corresponding covariance matrices, and $\mathbf{\rho}_n(\omega_k)$ is the normalized noise covariance matrix.

The powers of the desired signal and the interfering signals in the frequency bin ω_k are, respectively, given by

$$\sigma_s^2(\omega_k) = \sigma_0^2(\omega_k), \quad (2.28)$$

$$\sigma_i^2(\omega_k) = \sum_{d=1}^D \sigma_d^2(\omega_k). \quad (2.29)$$

In the frequency-domain snapshot model, the covariance matrix \mathbf{R}_x and the spatial spectral matrix \mathbf{S}_x at ω_k have the relationship

$$\mathbf{R}_x(\omega_k) = \mathbf{S}_x(\omega_k) B_\Delta. \quad (2.30)$$

In practical applications, the theoretical covariance matrix $\mathbf{R}_x(\omega_k)$ is unavailable. It can be estimated from the data samples

$$\widehat{\mathbf{R}}_x(\omega_k) = \frac{1}{N} \sum_{n=1}^N [X_k(n) X_k^H(n)], \quad (2.31)$$

where N is the number of training snapshots (also termed the training sample size). $\widehat{\mathbf{R}}_x$ is referred to as the sample covariance matrix. The sample covariance matrix $\widehat{\mathbf{R}}_x$ approaches the theoretical covariance matrix \mathbf{R}_x with $N \rightarrow \infty$.

In order for the sample covariance matrix $\widehat{\mathbf{R}}_x(\omega_k)$ to be invertible, we require

$$N \geq M. \quad (2.32)$$

2.3 DFT Beamformer

2.3.1 DFT Implementation

In Sect. 2.2, the broadband signals have been decomposed into a lot of frequency bins using the DFT. For each frequency bin, the narrowband condition is satisfied, therefore the narrowband beamformers can be applied directly.

From Eq. (2.4), defining $f_c = \omega_c/2\pi$, the frequency band of interest is given by

$$[f_l, f_u] = [f_c - B_s/2, f_c + B_s/2], \quad (2.33)$$

where f_l and f_u are the lower and upper temporal frequency, respectively. Note that the subscript “l” denotes lower and should not be confused with the number one.

The array is only required to process signals over the frequency band $[f_l, f_u]$. Therefore, using Eq. (2.10), the frequency bins of interest are

$$\omega_k = 2\pi f_s k / L \in [2\pi f_l, 2\pi f_u], \quad (2.34)$$

which requires

$$L f_l / f_s \leq k \leq L f_u / f_s. \quad (2.35)$$

Define

$$k_{\min} = \text{int}(L f_l / f_s) \quad (2.36)$$

and

$$k_{\max} = \text{int}(L f_u / f_s), \quad (2.37)$$

where $\text{int}(\cdot)$ denotes rounding towards the nearest integer.

The received data on the array can be written in a matrix form as

$$\begin{aligned} \mathbf{x}^{(n)} &= \left[\left(\mathbf{x}_1^{(n)} \right)^T, \dots, \left(\mathbf{x}_m^{(n)} \right)^T, \dots, \left(\mathbf{x}_M^{(n)} \right)^T \right]^T \\ &= \begin{bmatrix} x_1^{(n)}(0) & \dots & x_1^{(n)}(l) & \dots & x_1^{(n)}(L-1) \\ \vdots & \ddots & \vdots & & \vdots \\ x_m^{(n)}(0) & \dots & x_m^{(n)}(l) & \dots & x_m^{(n)}(L-1) \\ \vdots & & \vdots & \ddots & \vdots \\ x_M^{(n)}(0) & \dots & x_M^{(n)}(l) & \dots & x_M^{(n)}(L-1) \end{bmatrix}, \end{aligned} \quad (2.38)$$

which is a block of data.

Using Eq. (2.19), the frequency-domain data in each frequency bin can be written in an $M \times 1$ column vector as

$$\begin{aligned} \mathbf{X}^{(n)}(k) &= \left[X_1^{(n)}(k), \dots, X_m^{(n)}(k), \dots, X_M^{(n)}(k) \right]^T \\ &= \left[\mathbf{x}_1^{(n)} \mathbf{e}(k), \dots, \mathbf{x}_m^{(n)} \mathbf{e}(k), \dots, \mathbf{x}_M^{(n)} \mathbf{e}(k) \right]^T \\ &= \mathbf{x}^{(n)} \mathbf{e}(k), \quad k = k_{\min}, \dots, k_{\max}. \end{aligned} \quad (2.39)$$

Within each frequency bin, the narrowband beamformers can be used. These beamformers can also be termed subband beamformers.

Assume that the weight vector for the frequency bin ω_k is

$$\mathbf{w}(\omega_k) = [w_1(\omega_k), \dots, w_m(\omega_k), \dots, w_M(\omega_k)]^T, \quad k = k_{\min}, \dots, k_{\max}. \quad (2.40)$$

The subband beamformer output is given by

$$Y^{(n)}(k) = \mathbf{w}^H(\omega_k) \mathbf{X}^{(n)}(k), \quad k = k_{\min}, \dots, k_{\max}. \quad (2.41)$$

The outputs of the different frequency bins can be combined to synthesize the broadband beamformer output signal. Thus, an IDFT can be performed on the frequency-domain subband beamformer output.

In order that the broadband beamformer output signal is real, we require the following conjugate symmetry properties to be satisfied

$$Y^{(n)}(k) = \text{conj}\left(Y^{(n)}(L - k)\right), \quad k = L - k_{\max}, \dots, L - k_{\min}. \quad (2.42)$$

Therefore,

$$y^{(n)}(l), (l = 0, \dots, L - 1) = \text{IDFT}\left[Y^{(n)}(k), (k = 0, \dots, L - 1)\right], \quad (2.43)$$

or

$$y^{(n)}(l) = \frac{1}{L} \sum_{k=0}^{L-1} Y^{(n)}(k) \exp(i2\pi kl/L), \quad l = 0, \dots, L - 1, \quad (2.44)$$

where

$$Y^{(n)}(k) = \begin{cases} \mathbf{w}^H(\omega_k) \mathbf{X}^{(n)}(k), & k = k_{\min}, \dots, k_{\max}, \\ \text{conj}\left(Y^{(n)}(L - k)\right), & k = L - k_{\max}, \dots, L - k_{\min}, \\ 0, & \text{otherwise.} \end{cases} \quad (2.45)$$

This broadband beamformer implemented in the frequency domain using DFT is referred to as a DFT beamformer.

In the final step, the IDFT is taken to obtain L output samples in the time domain, this procedure is referred to as block processing. Alternatively, a sliding window technique can be used, in which the DFT is performed each time a new sample enters the buffer.

To summarize, the DFT beamformer consists of the following steps.

- Step 1. The output of each sensor is sampled using analog-to-digital (A/D) converter.
- Step 2. For each sensor, we buffer L samples and take the DFT of the L samples to obtain the subband frequency-domain sample vector $\mathbf{X}^{(n)}(k)$ corresponding to each frequency bin, as shown in Eq. (2.39). The buffered data are indexed with n .
- Step 3. For each frequency bin within the frequency band of interest $[f_l, f_u]$, the narrowband condition is satisfied and the narrowband beamforming methods can be used. Using Eq. (2.41), weighted combinations of the subband sample vector at each frequency bin are formed to obtain the narrowband beamformer output.
- Step 4. Using Eq. (2.43), the IDFT is performed on the narrowband beamformer outputs in all frequency bins to obtain the output samples $y^{(n)}(l)$ corresponding to the n th buffered array data.
- Step 5. The output samples $y^{(n)}(l)$ for each buffered data are combined to obtain the broadband beamformer output time series, denoted by $y(l)$.

It is convenient to index the frequency bins within the frequency band of interest from 1 to K . Defining

$$\begin{aligned} \check{k} &= k - k_{\min} + 1, \quad k = k_{\min}, \dots, k_{\max}, \\ \check{k} &= 1, \dots, K, \end{aligned} \quad (2.46)$$

where $K = k_{\max} - k_{\min} + 1$ is the number of frequency bins within the frequency band $[f_l, f_u]$.

For convenience, in what follows we use the symbol k instead of \check{k} . Thus, the center frequency of the frequency bin over the frequency band $[f_l, f_u]$ is

$$f_k = (2\pi f_s/L) \cdot (k + k_{\min} - 1), \quad k = 1, \dots, K. \quad (2.47)$$

Note that $k = 1$ corresponds to the frequency bin near the lower frequency f_l , which is different from that in Eq. (2.10). The weight vector for the frequency bin f_k is $\mathbf{w}(f_k) = [w_1(f_k), \dots, w_m(f_k), \dots, w_M(f_k)]^T$.

The DFT beamformer structure is shown in Fig. 2.2.

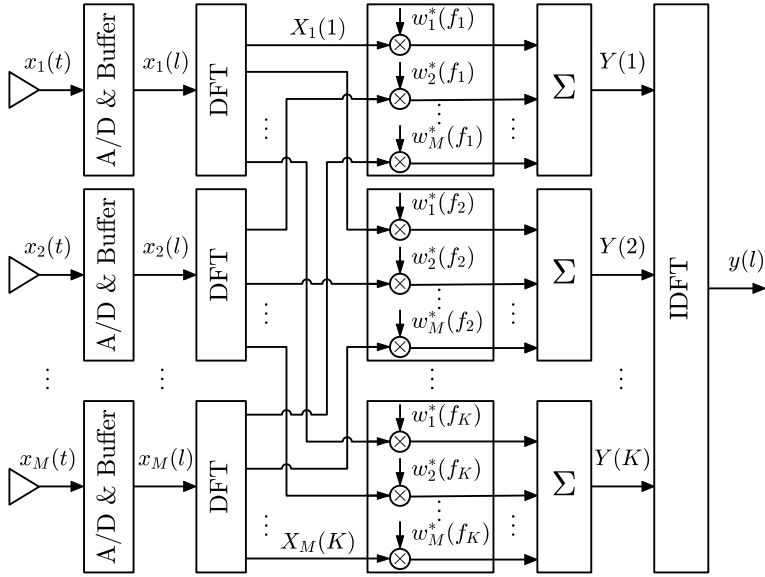


Fig. 2.2 DFT broadband beamformer

2.3.2 *Broadband Beam Pattern*

The broadband beam pattern is a function of the temporal frequency f within the frequency band of interest $[f_l, f_u]$ and the direction Ω within the field of view Θ , i.e.,

$$B(f, \Omega) = \mathbf{w}^H(f) \mathbf{p}(f, \Omega), \quad f \in [f_l, f_u], \quad \Omega \in \Theta. \quad (2.48)$$

Consider a broadband uniform linear array with $M = 12$ sensors along the y -axis. The design frequency of the array is the highest frequency of interest f_u . The corresponding design wavelength is $\lambda_u = c/f_u$ and the interelement spacing is $d = \lambda_u/2$.

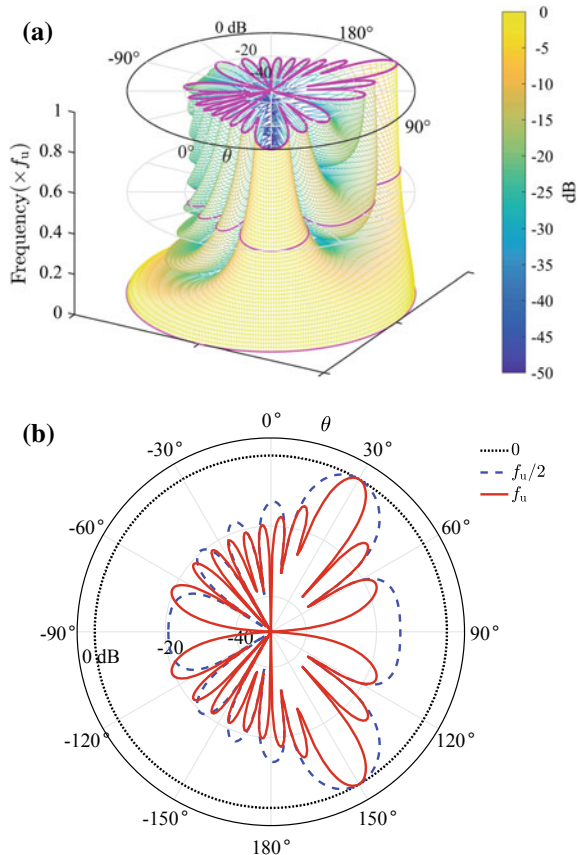
Assume that the field of view is located in the xy -plane (i.e., $\theta \in [-180^\circ, 180^\circ]$ and $\phi = 90^\circ$) and the steering direction is $\Omega_o = (\theta_o, \phi_o) = (30^\circ, 90^\circ)$.

The DAS beam pattern in dB as a function of frequency $f \in [0, f_u]$ and direction $\theta \in [-180^\circ, 180^\circ]$ is shown in Fig. 2.3a. The polar plot of the beam patterns for frequencies $f = 0, f_u/2$ and f_u are shown in Fig. 2.3b.

It is seen that the beam patterns are symmetrical about the y -axis along which the linear array is located. The main response axis occurs at 30° and 150° .

The mainlobe widens as the frequency decreases. The beamformer would have an isotropic beam pattern as the frequency approached 0. This beamwidth variation as a function of frequency will cause the signals arrived from the outer portions of the mainlobe to low-pass filtering and lead to distorted signal spectra.

Fig. 2.3 DAS beam patterns in dB for broadband array for $\theta_0 = 30^\circ$ using **a** cylindrical plot for $f \in [0, f_u]$, $\theta \in [-180^\circ, 180^\circ]$, and **b** polar plot for $f = 0, f_u/2$ and f_u



Since the beam patterns of a linear array are symmetrical, the field of view can be chosen to be $\Theta = [-90^\circ, 90^\circ]$.

Alternatively, the broadband beam patterns can be presented graphically in mesh plot or pseudocolor plot on the frequency-direction plane, as shown in Fig. 2.4.

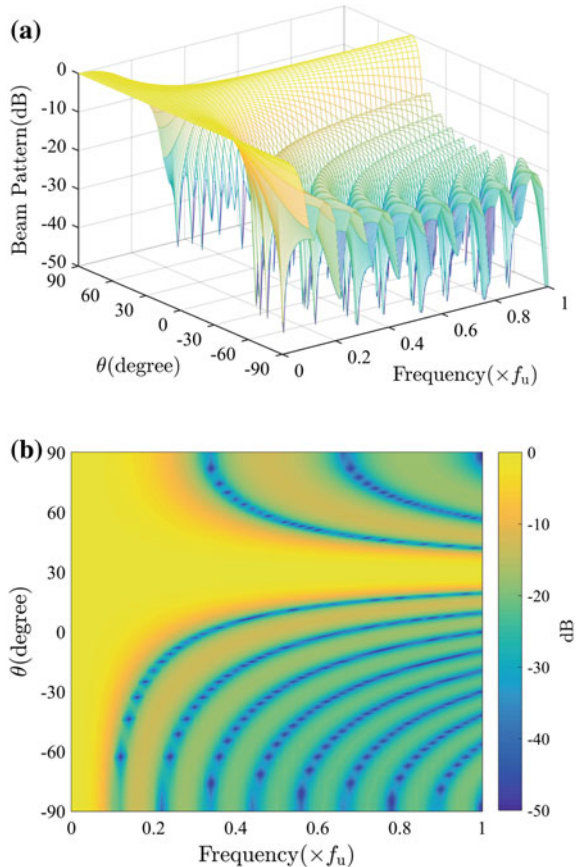
2.3.3 DFT Beamforming

Consider a linear frequency-modulated (LFM) broadband signal impinging on the 12-element uniform linear array from $\theta_s = 30^\circ$ in the absence of noise.

The LFM signal waveform is

$$s(l) = s(t)|_{t=l/f_s} = \begin{cases} \sin\left[2\pi\left(f_l + \frac{f_u-f_l}{2T}t\right)t\right] & |t| \leq l/f_s, \\ 0, & \text{otherwise,} \end{cases} \quad (2.49)$$

Fig. 2.4 DAS beam patterns in dB for broadband array for $f \in [0, f_u]$ and $\theta \in [-90^\circ, 90^\circ]$, using **a** mesh plot, and **b** pseudocolor plot



where T is the signal duration in seconds. Assume that $f_l = f_u/2$, $f_s = 5f_u$, and the sample length is $T \cdot f_s = 512$.

The instantaneous frequency of the LFM signal is

$$f(t) = f_l + \frac{f_u - f_l}{T} t. \quad (2.50)$$

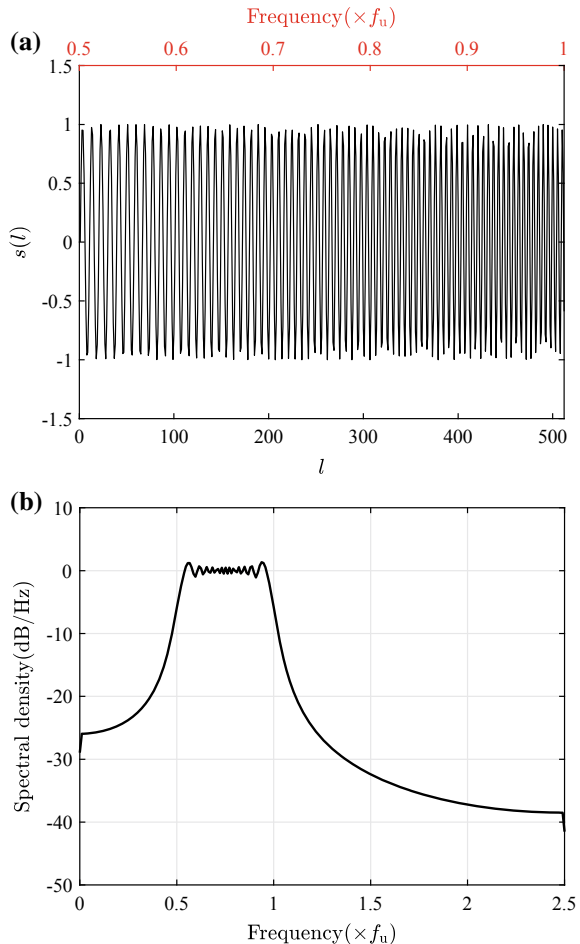
The signal waveform and its spectral density are shown in Fig. 2.5a, b, respectively. The instantaneous frequency of the LFM signal is also shown on the top of Fig. 2.5a.

The sampled signal received by the m th sensor is given by

$$s_m(l) = s[t - \tau_m(\theta_s)]|_{t=l/f_s}, \quad m = 1, \dots, M, \quad (2.51)$$

where $\tau_m(\theta_s)$ is the corresponding propagation delay.

Fig. 2.5 LFM broadband signal. **a** Time-domain waveform, and **b** spectral density



Using Eqs. (2.49) and (2.51), the sampled signals received by the sensors are shown in Fig. 2.6, where the sample length of each sensor is 512.

Assume that the length of the buffer is $L = 256$. The DFT is performed each time L new samples enter the buffer to obtain the frequency-domain samples. This implies that the received signals by each sensor are divided into 2 non-overlapping segments (indexed with n). Assume that the frequency bins of interest are $21 \leq k \leq 56$, which corresponds to the frequency band $[0.4102 f_u, 1.0938 f_u]$ that cover the frequency band $[f_1, f_u]$.

Conventional DAS beamformers with steering direction $\theta_o = \theta_s = 30^\circ$ are designed for each frequency bin. The frequency-domain samples are processed using the narrowband beamformers to obtain the subband beamformer output for each frequency bin. The amplitudes of the subband beamformer outputs $|Y^{(n)}(k)|$ in dB for each segment are shown in Fig. 2.7a.

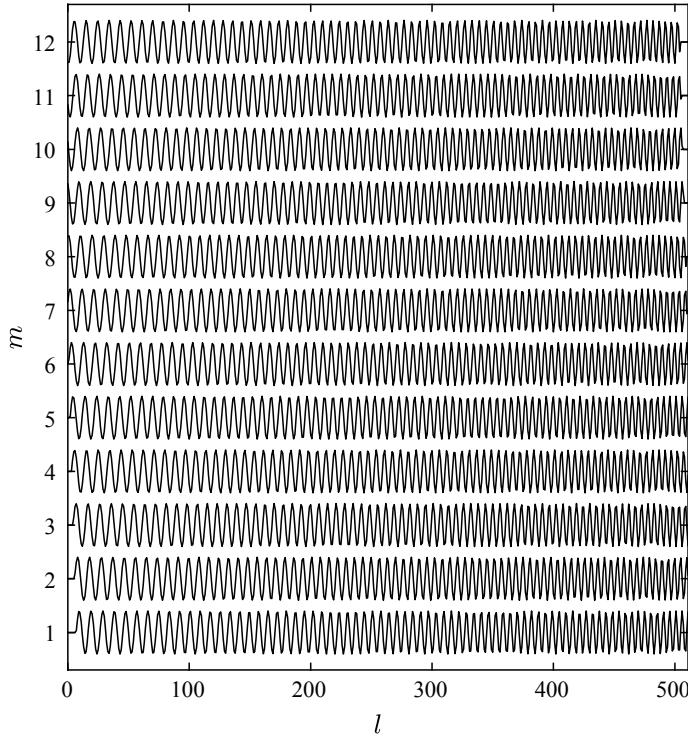


Fig. 2.6 Sampled signal waveform received by the array

The IDFT is performed on the narrowband beamformer outputs in all frequency bins to obtain the output samples $y^{(n)}(l)$ for each segment. The outputs of each segment are then connected to obtain the broadband beamformer output time series $y(l)$, as shown in Fig. 2.7b.

It is seen that the amplitude of the beamformer output becomes smaller at the head and tail of each segment. The reason for this behavior is that only limited number of frequency bins are used to synthesize the beamformer output signal. This causes the beamformer output error at the junction of the segments, which can be clearly observed from the error between the beamformer output and the desired signal, i.e., $y(l) - s(l)$, as shown in Fig. 2.8 (in solid line).

Alternatively, the DFT is performed each time $L/2$ new samples enter the buffer to obtain the frequency-domain samples. This implies that the signals received by each sensor are divided into 3 overlapping segments.

The amplitude of the subband beamformer output $|Y^{(n)}(k)|$ in dB for each segment and the broadband beamformer output time series $y(l)$ are shown in Fig. 2.9a, b, respectively. Note that when combining the output of the IDFT, $L/4$ samples of both segments at the junction are removed so that the beamformer output time series have the same size as the desired signal.

Fig. 2.7 DFT beamformer output with non-overlapping buffer. **a** The amplitude of subband beamformer output in each frequency bin $|Y^{(n)}(k)|$, and **b** broadband beamformer output time series $y(l)$

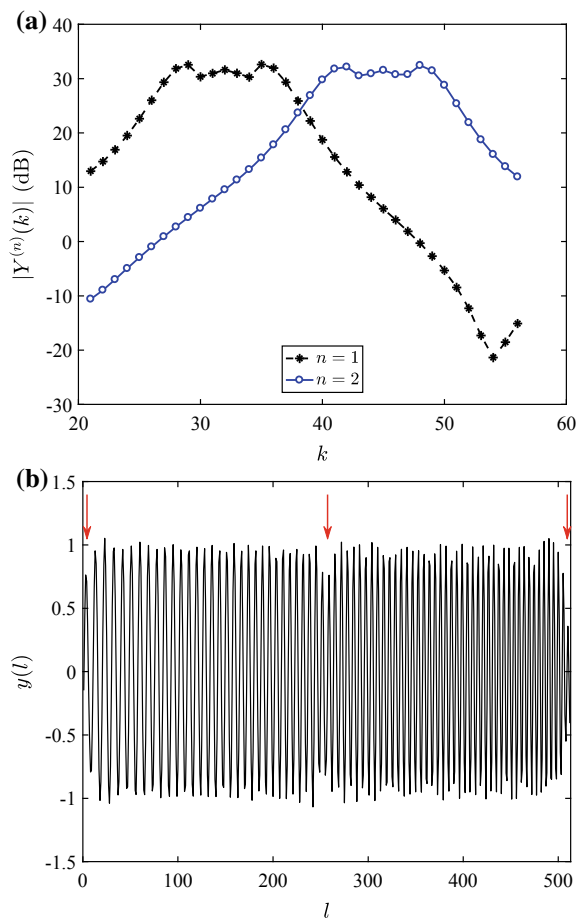


Fig. 2.8 Error between the beamformer output and the desired signal

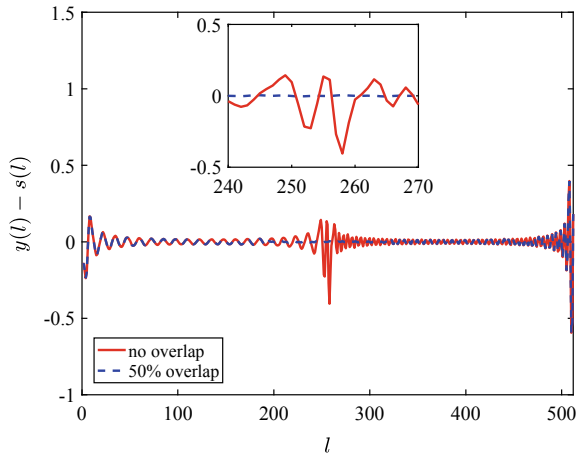
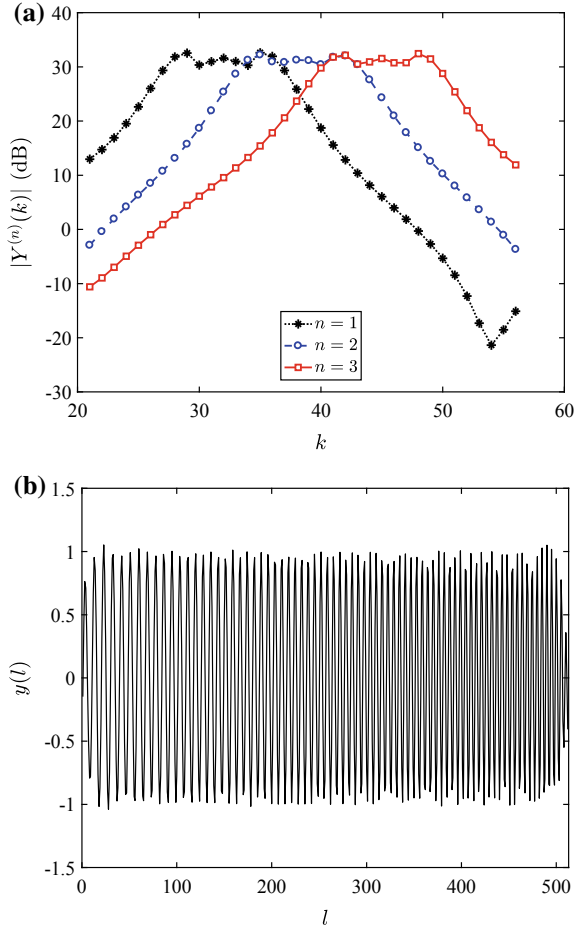


Fig. 2.9 DFT beamformer output with 50% overlapping buffer. **a** Subband beamformer output $|Y^{(n)}(k)|$, and **b** broadband beamformer output $y(l)$

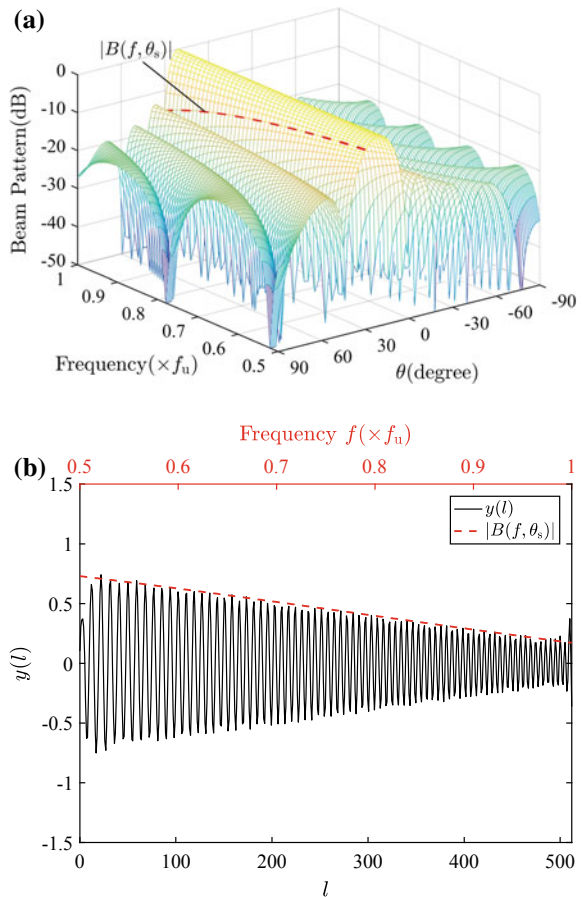


The error between the beamformer output time series and the desired signal is also plotted in Fig. 2.8 (in dashed line). It is seen that the error at the junction is small enough. Therefore, in practice, the 50% overlapping buffer is frequently used for DFT broadband beamforming.

2.3.4 Signal Not Along MRA

Consider a single plane-wave signal arriving at the 12-element broadband uniform linear array from the direction $\theta_s = 30^\circ$ in the absence of noise. Assume that the steering direction is $\theta_o = 21^\circ$.

Fig. 2.10 DFT broadband beamforming. **a** DAS beam patterns, **b** beamformer output when $\theta_0 = 21^\circ$ and $\theta_s = 30^\circ$



The conventional DAS beam pattern over the frequency band $[f_1, f_u]$ is shown in Fig. 2.10a. The main response axis occurs at $\theta_0 = 21^\circ$. The beam pattern cut at direction $\theta_s = 30^\circ$ is also plotted in this figure. The value of the pattern versus frequency along the signal direction θ_s , i.e., $|B(f, \theta_s)|$ in dB, becomes smaller as the frequency increases.

The broadband beamformer output time series is shown in Fig. 2.10b. The magnitude of $|B(f, \theta_s)|$ is also plotted. It is seen that the amplitude of beamformer output time series versus frequency is consistent with the magnitude of $|B(f, \theta_s)|$. The signal that arrives inside the main beam but not along the main response axis is low-pass filtered because the beamwidth becomes narrower as the frequency increases.

2.4 Summary

In many applications, the beamforming can be implemented in the frequency domain. The time-domain output vectors from the sensors are converted to a set of subband complex vectors in the frequency domain. The narrowband condition is satisfied for each subband and the frequency-domain snapshot model can be used.

The DFT implementation of a frequency-domain broadband beamformer is introduced. This broadband beamformer is termed DFT beamformer, whereby the signal received at each sensor is decomposed into a number of narrowband frequency bins using the DFT and each frequency bin is treated as an independent narrowband beamformer. The outputs of each narrowband beamformer are combined to synthesize the broadband beamformer output time series. The DFT beamformer is a block data processor in which a block of data are required each time to perform the DFT.

The mainlobe of the DAS beam pattern widens as the frequency decreases. This beamwidth variation as a function of frequency will cause the signals arrived from the outer portions of the mainlobe to low-pass filtering and lead to distorted signal spectra. The broadband beamformers with constant mainlobe response over the frequency of interest are desirable in many applications.

Reference

1. W. Liu, S. Weiss, *Wideband Beamforming Concepts and Techniques* (Wiley, 2010)

Chapter 3

Optimal Design of Subband Beamformers



3.1 Introduction

In Chap. 2, the frequency-domain implementation of broadband beamformer is presented, in which the broadband signals from each sensor are decomposed into a lot of subbands using the DFT. For each subband, the narrowband condition is satisfied and the narrowband beamformers can be applied directly.

Recall the discussion in Chap. 1 that commonly used performance measures by which we assess the capabilities of a narrowband beamformer are array gain, robustness, sidelobe level, beamwidth and mainlobe pattern. Optimal design of a beamformer is to find the weight vector by optimizing one or multiple performances of the beamformer under a number of criteria.

The MVDR beamformer attempts to maximize the array gain under the assumption that the signal steering vector and the covariance matrix are accurately known. Unfortunately, its performance degrades rapidly in the presence of mismatch. A beamformer that attempts to preserve good performance under mismatch is a robust beamformer. A popular approach to improve the robustness of the MVDR beamformer is diagonal loading [1, 2]. However, it is not clear how to choose the diagonal loading level. The covariance matrix error can be viewed as due to a steering vector error [3]. Several methods were proposed to obtain the diagonal loading level by making explicit use of the uncertainty of the steering vector [4–7].

The issue of sidelobe control is very important in both fixed [8] and adaptive beamformer [9] designs. The fixed beamformer design problem is also called an array pattern synthesis problem. In many cases, the MVDR beamformer can have unacceptably high sidelobes. This may cause a severe performance degradation in the presence of suddenly appearing or moving interferers because the MVDR beamformer requires some time to suppress them. The low sidelobe is typically utilized to reduce the out-of-sector interference. The sidelobes decrease may lead to the width of the mainlobe increases. One objective of beam pattern optimization is to balance the beamwidth with the desired low sidelobe level pattern.

Mainlobe pattern synthesis is another important issue. Its main task is to seek a beam pattern that approximates the desired beam pattern over the mainlobe region. Several techniques were developed using quadratic programming for finding the least squares error approximation to a desired beam pattern [10, 11]. However, they attempted to approximate the desired beam pattern over the entire visible region. This leads to larger error since the approximation over the sidelobe region is unnecessary. The sidelobes only need to be guaranteed below some prescribed threshold value besides the mainlobe pattern approximation [12].

The mainlobe pattern synthesis techniques can be used to design frequency-invariant (FI) beamformer, of which the mainlobe pattern is constant over the frequency band of interest. This beamformer is also called a constant mainlobe pattern (CMP) beamformer.

The rest of this chapter is organized as follows. In Sect. 3.2, we discuss the robust beamformer design problem. In Sect. 3.3, we discuss the low-sidelobe beamformer design problem. In Sect. 3.4, we discuss the mainlobe pattern synthesis problem. In Sect. 3.5, a unified framework for designing optimal beamformers is presented using multiple-objective design method. A brief summary of this chapter is given in Sect. 3.6.

3.2 Robust Beamformers

3.2.1 *Loaded Sample Matrix Inversion Beamformer*

In the frequency-domain snapshot model, we design the MVDR beamformer using the covariance matrix $\mathbf{R}_x(\omega_k)$ instead of the spatial spectral matrix $\mathbf{S}_x(\omega)$. Using Eq. (1.108), the weight vector for the MVDR beamformer is given by

$$\mathbf{w}_{\text{MVDR}}(\omega_k) = \alpha \mathbf{R}_x^{-1}(\omega_k) \bar{\mathbf{p}}_s(\omega_k), \quad (3.1)$$

where $\alpha = [\bar{\mathbf{p}}_s^H(\omega_k) \mathbf{R}_x^{-1}(\omega_k) \bar{\mathbf{p}}_s(\omega_k)]^{-1}$ is a scale factor in order for the distortionless constraint to be satisfied, but does not affect the array gain. In what follows we do not need to calculate its value.

The beamformer output power can be used as an estimate of the desired signal power

$$\hat{\sigma}_s^2(\omega_k) = \mathbf{w}_{\text{MVDR}}^H(\omega_k) \mathbf{R}_x(\omega_k) \mathbf{w}_{\text{MVDR}}(\omega_k) = \frac{1}{\bar{\mathbf{p}}_s^H(\omega_k) \mathbf{R}_x^{-1}(\omega_k) \bar{\mathbf{p}}_s(\omega_k)}. \quad (3.2)$$

In practice, the sample covariance matrix $\hat{\mathbf{R}}_x(\omega_k)$ in Eq. (2.31) is used instead of $\mathbf{R}_x(\omega_k)$. This leads to the sample matrix inversion (SMI) implementation of the MVDR beamformer

$$\mathbf{w}_{\text{SMI}} = \alpha_{\text{SMI}} \widehat{\mathbf{R}}_x^{-1} \overline{\mathbf{p}}_s, \quad (3.3)$$

where $\alpha_{\text{SMI}} = \left(\overline{\mathbf{p}}_s^H \widehat{\mathbf{R}}_x^{-1} \overline{\mathbf{p}}_s \right)^{-1}$ and the frequency dependence is suppressed in the notation. This beamformer is also referred to as the SMI beamformer.

Define the ratio of the output SINR of SMI beamformer due to the use of $\widehat{\mathbf{R}}_x$ to the optimum SINR which using \mathbf{R}_x as

$$\rho_0 = \frac{\text{SINR}_{\text{SMI}}}{\text{SINR}_{\text{opt}}}. \quad (3.4)$$

In the absence of desired signal (i.e., $\beta = 0$), the mean of ρ_0 is [13]

$$\mathbb{E}(\rho_0) = \frac{N - M + 2}{N + 1}, \quad (3.5)$$

where N is the number of samples. It implies that in order for the SINR loss to be less than 3 dB, we require

$$N \geq 2M - 3 \approx 2M. \quad (3.6)$$

The SMI implementation will increase the sidelobe level of the MVDR beamformer. The expected value of the sidelobe level of the SMI beam pattern is [14]

$$\mathbb{E}(SLL) = \frac{1}{N + 1}. \quad (3.7)$$

In the presence of desired signal (i.e., $\beta = 1$), in order for the SINR loss to be within 3 dB, we require [3]

$$N \geq \text{SINR}_{\text{opt}} \cdot (M - 1) \gg M, \quad (3.8)$$

which will be significantly larger than that in the signal-free training data case.

The covariance matrix mismatch causes a performance degradation similar to that in the steering vector mismatch case. The SMI implementation could suffer significant performance degradation in the presence of mismatches, particularly in the presence of desired signal, because it will treat the mismatched signal as an interferer and attempt to null it.

In order to preserve good performance in the presence of mismatch, robust beamformers are required.

For convenience, in what follows we use the symbol \mathbf{R} instead of $\widehat{\mathbf{R}}_x$ when its meaning should be clear from the context.

One of the most popular approaches to robust beamforming in the presence of mismatch and small training sample size is the diagonal loading technique, which was proposed independently by Cox et al. [1] and Carlson [2]. This beamformer is

referred to as the loaded sample matrix inversion (LSMI) beamformer, whose weight vector is given by

$$\mathbf{w}_{\text{LSMI}} = \alpha_{\text{LSMI}}(\mathbf{R} + \lambda \mathbf{I})^{-1} \bar{\mathbf{p}}_s, \quad (3.9)$$

where $\alpha_{\text{LSMI}} = [\bar{\mathbf{p}}_s^H(\mathbf{R} + \lambda \mathbf{I})^{-1} \bar{\mathbf{p}}_s]^{-1}$ and λ is the diagonal loading factor.

The load-to-white-noise ratio (LNR) in dB, which is also referred to as the diagonal loading level, can be defined as

$$LNR = 10 \lg(\lambda / \sigma_w^2), \quad (3.10)$$

where σ_w^2 is the power of the noise.

The diagonal loading can warrant the invertibility of the loaded matrix $\mathbf{R} + \lambda \mathbf{I}$ whether \mathbf{R} is singular or not. Therefore, this beamformer works even if $N < M$.

Let

$$\mathbf{R} = \mathbf{U} \boldsymbol{\Gamma} \mathbf{U}^H = \sum_{m=1}^M \gamma_m \mathbf{u}_m \mathbf{u}_m^H, \quad (3.11)$$

where $\mathbf{U} = [\mathbf{u}_1, \dots, \mathbf{u}_m, \dots, \mathbf{u}_M]$ with $\mathbf{u}_m (m = 1, 2, \dots, M)$ being the eigenvectors of \mathbf{R} , and

$$\boldsymbol{\Gamma} = \text{diag}(\gamma_1, \dots, \gamma_m, \dots, \gamma_M), \quad \gamma_1 \geq \dots \geq \gamma_m \geq \dots \geq \gamma_M \quad (3.12)$$

with $\gamma_m (m = 1, 2, \dots, M)$ being the corresponding eigenvalues.

Thus,

$$(\mathbf{R} + \lambda \mathbf{I})^{-1} = [\mathbf{U}(\boldsymbol{\Gamma} + \lambda \mathbf{I})\mathbf{U}^H]^{-1} = \mathbf{U}(\boldsymbol{\Gamma} + \lambda \mathbf{I})^{-1}\mathbf{U}^H. \quad (3.13)$$

Substituting Eq. (3.13) into Eq. (3.9) gives

$$\mathbf{w}_{\text{LSMI}} = \alpha_{\text{LSMI}} \mathbf{U}(\boldsymbol{\Gamma} + \lambda \mathbf{I})^{-1} \mathbf{U}^H \bar{\mathbf{p}}_s. \quad (3.14)$$

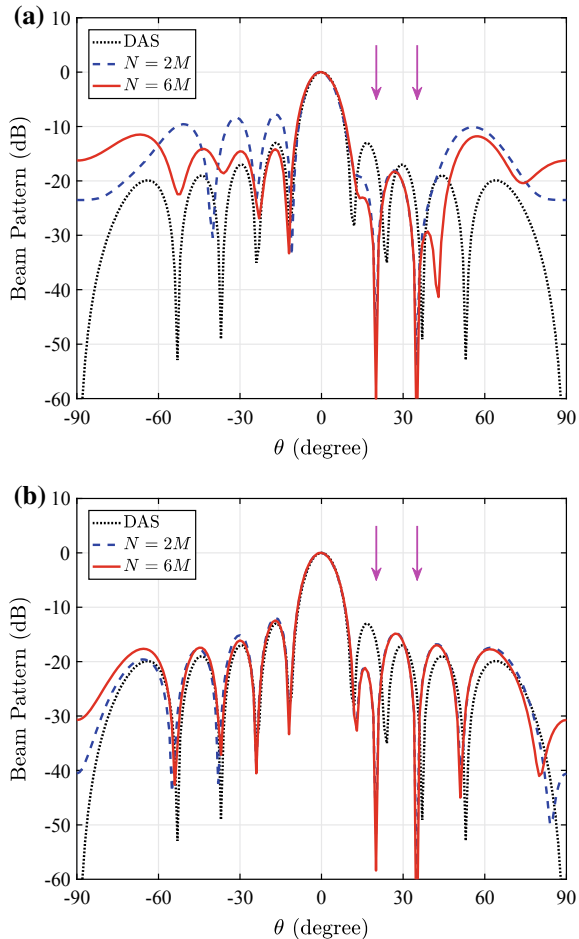
The major computational demand of Eq. (3.14) comes from the eigendecomposition of the matrix \mathbf{R} , which requires $O(M^3)$ flops.

When $N < M$, the sample covariance matrix \mathbf{R} is singular. Assume that the rank of \mathbf{R} is N . Then, \mathbf{R} can be written as

$$\mathbf{R} = \sum_{m=1}^N \gamma_m \mathbf{u}_m \mathbf{u}_m^H, \quad (3.15)$$

and the inversion of the loaded sample covariance matrix can be written as

Fig. 3.1 Adapted beam pattern with $N = 2M$ and $N = 6M$ snapshots. **a** SMI beamformer, **b** LSMI beamformer with $LNR = 10$ dB



$$(\mathbf{R} + \lambda \mathbf{I})^{-1} = \frac{1}{\lambda} \left[\mathbf{I} - \sum_{m=1}^N \frac{\gamma_m}{\gamma_m + \lambda} \mathbf{u}_m \mathbf{u}_m^H \right]. \quad (3.16)$$

Consider a 10-element uniform linear array with half-wavelength spacing along the y -axis in the white noise environment. Two plane-wave interfering signals impinge on the array from $\theta = 20^\circ$ and 35° with $LNR = 30$ and 35 dB, respectively. The steering direction is at $\theta_0 = 0^\circ$.

The adapted beam patterns of the SMI beamformers are shown in Fig. 3.1a for various values of N . For comparison, the conventional DAS beam pattern is also plotted in each figure. It is seen that the sidelobe levels of the SMI beam patterns are higher than that of the conventional DAS beam pattern. As N increases, the sidelobe level decreases.

The LSMI beamformers for various values of N are designed by choosing the diagonal loading with $LNR = 10$ dB. The corresponding beam patterns are shown in Fig. 3.1b. We observe that the sidelobe behavior can be improved significantly by using diagonal loading.

3.2.2 Norm Constrained Beamformer

LSMI beamformer has been a popular method to improve the robustness of the MVDR beamformer. However, it is not clear how to choose the diagonal loading.

Recall that the sensitivity function equals the squared norm of the weight vector, i.e., $T_{se} = \|\mathbf{w}\|^2$. Therefore, we can improve the robustness of the MVDR beamformer by imposing an additional constraint on the Euclidean norm of weight vector. This leads to the norm constrained (NC) MVDR beamformer, which we term the NC beamformer. The weight vector design problem can be formulated as

$$\begin{aligned} & \min_{\mathbf{w}} \mathbf{w}^H \mathbf{R} \mathbf{w}, \\ & \text{subject to } \mathbf{w}^H \mathbf{p}_s = 1, \quad \|\mathbf{w}\|^2 \leq \zeta_0, \end{aligned} \quad (3.17)$$

where ζ_0 is a specified value to control the norm of \mathbf{w} . The smaller the ζ_0 , the higher the robustness of resulting beamformer. From Eq. (1.70), we require

$$\zeta_0 \geq 1/M, \quad (3.18)$$

with equality corresponding to the DAS beamformer.

Since the WNG equals the inverse of the squared norm of the weight vector, the norm constraint in Eq. (3.17) is also referred to as a WNG constraint. Thus, the norm constrained beamformer is also called a WNG constrained beamformer [15].

There is loss in the WNG behavior compared to the DAS beamformer. The WNG loss can be defined as

$$G_{wd} = 10 \lg \left(\frac{\|\mathbf{w}\|^2}{1/M} \right) = 10 \lg M + 10 \lg (\|\mathbf{w}\|^2). \quad (3.19)$$

Using Eq. (3.18), we have

$$G_{wd} \leq 10 \lg M + 10 \lg (\zeta_0) \triangleq G_{wd0}, \quad (3.20)$$

where G_{wd0} is the prescribed loss value in WNG. Clearly, $G_{wd0} \geq 0$, and with equality corresponding to the DAS beamformer.

Using Eq. (3.20), we have

$$\zeta_0 = (1/M) \cdot 10^{G_{wd0}/10}. \quad (3.21)$$

For the optimization problem in Eq. (3.17), let

$$\mathbf{R} = \mathbf{V}^H \mathbf{V} \quad (3.22)$$

be the Cholesky factorization of \mathbf{R} , we obtain

$$\mathbf{w}^H \mathbf{R} \mathbf{w} = (\mathbf{V} \mathbf{w})^H (\mathbf{V} \mathbf{w}) = \|\mathbf{V} \mathbf{w}\|^2. \quad (3.23)$$

The optimization problem in Eq. (3.17) can be written as

$$\begin{aligned} & \min_{\mathbf{w}} \|\mathbf{V} \mathbf{w}\|, \\ & \text{subject to } \mathbf{w}^H \bar{\mathbf{p}}_s = 1, \|\mathbf{w}\| \leq \sqrt{\xi_0}. \end{aligned} \quad (3.24)$$

Introducing a new scalar non-negative variable σ , Eq. (3.24) can be rewritten as

$$\begin{aligned} & \min_{\mathbf{w}} \sigma, \\ & \text{subject to } \mathbf{w}^H \bar{\mathbf{p}}_s = 1, \\ & \|\mathbf{V} \mathbf{w}\| \leq \sigma, \\ & \|\mathbf{w}\| \leq \sqrt{\xi_0}. \end{aligned} \quad (3.25)$$

The optimization problem in Eq. (3.25) is a second-order cone programming (SOCP) problem, which belongs to a subclass of the well-structured convex programming problems where a linear function is minimized subject to a set of second-order cone constraints and possibly a set of linear equality constraints. An SOCP problem is computationally tractable and can be solved efficiently using an SOCP solver such as SeDuMi [16].

Alternatively, the solution to Eq. (3.17) was found in [17] using the Lagrange multiplier methodology.

Consider the condition

$$\|\mathbf{w}\|^2 \leq \xi_0. \quad (3.26)$$

When the solution to the MVDR beamformer (i.e., Eq. (3.1) or Eq. (3.3) in practice) satisfies the norm constraint in Eq. (3.26), i.e.,

$$\frac{\bar{\mathbf{p}}_s^H \mathbf{R}^{-2} \bar{\mathbf{p}}_s}{[\bar{\mathbf{p}}_s^H \mathbf{R}^{-1} \bar{\mathbf{p}}_s]^2} \leq \xi_0, \quad (3.27)$$

this MVDR (or SMI) solution is also the solution to the NC beamformer. For this case, the norm constraint in Eq. (3.26) is inactive.

Otherwise, we have the condition

$$\xi_0 < \frac{\bar{\mathbf{p}}_s^H \mathbf{R}^{-2} \bar{\mathbf{p}}_s}{[\bar{\mathbf{p}}_s^H \mathbf{R}^{-1} \bar{\mathbf{p}}_s]^2}. \quad (3.28)$$

Under Eq. (3.28), the equality constraint

$$\|\mathbf{w}\|^2 = \zeta_0 \quad (3.29)$$

should be satisfied. Then, Eq. (3.17) becomes

$$\begin{aligned} & \min_{\mathbf{w}} \mathbf{w}^H \mathbf{R} \mathbf{w}, \\ & \text{subject to } \mathbf{w}^H \bar{\mathbf{p}}_s = 1, \mathbf{w}^H \mathbf{w} = \zeta_0. \end{aligned} \quad (3.30)$$

Using the Lagrange multiplier methodology, we define

$$F(\mathbf{w}, \lambda, \mu) \triangleq \mathbf{w}^H \mathbf{R} \mathbf{w} + \lambda(\mathbf{w}^H \mathbf{w} - \zeta_0) + \mu(\mathbf{w}^H \bar{\mathbf{p}}_s - 1) + \mu^*(\bar{\mathbf{p}}_s^H \mathbf{w} - 1), \quad (3.31)$$

where λ and μ are the real-valued Lagrange multiplier.

Taking the gradient of Eq. (3.31) with respect to \mathbf{w}^H and setting the result to zero gives

$$\mathbf{R} \mathbf{w} + \lambda \mathbf{w} + \mu \bar{\mathbf{p}}_s = \mathbf{0}, \quad (3.32)$$

then,

$$\mathbf{w} = -\mu(\mathbf{R} + \lambda \mathbf{I})^{-1} \bar{\mathbf{p}}_s. \quad (3.33)$$

Using $\bar{\mathbf{p}}_s^H \mathbf{w} = 1$, we obtain

$$\mu = -[\bar{\mathbf{p}}_s^H(\mathbf{R} + \lambda \mathbf{I})^{-1} \bar{\mathbf{p}}_s]^{-1}. \quad (3.34)$$

Substituting it into Eq. (3.33) gives

$$\mathbf{w} = \frac{(\mathbf{R} + \lambda \mathbf{I})^{-1} \bar{\mathbf{p}}_s}{\bar{\mathbf{p}}_s^H(\mathbf{R} + \lambda \mathbf{I})^{-1} \bar{\mathbf{p}}_s}. \quad (3.35)$$

Substituting Eq. (3.35) into Eq. (3.29) gives

$$\mathbf{w}^H \mathbf{w} = \frac{\bar{\mathbf{p}}_s^H(\mathbf{R} + \lambda \mathbf{I})^{-2} \bar{\mathbf{p}}_s}{[\bar{\mathbf{p}}_s^H(\mathbf{R} + \lambda \mathbf{I})^{-1} \bar{\mathbf{p}}_s]^2} = \zeta_0. \quad (3.36)$$

It is seen that the weight vector in Eq. (3.35) has the form of diagonal loading, while the diagonal loading factor λ is chosen based on the weight vector norm constraint (or the WNG constraint) in Eq. (3.36).

Under Eq. (3.28), there is a unique solution $\hat{\lambda}$ to Eq. (3.36) (see also [17]) and the left side of Eq. (3.36) is a monotonically decreasing function of $\hat{\lambda}$ (see also [18, 19]). Therefore, $\hat{\lambda}$ can be obtained via, for example, a Newton's method.

Substituting Eq. (3.13) into Eq. (3.36) and using $\hat{\lambda}$ instead of λ gives

$$\frac{\bar{\mathbf{p}}_s^H \mathbf{U} (\boldsymbol{\Gamma} + \hat{\lambda} \mathbf{I})^{-2} \mathbf{U}^H \bar{\mathbf{p}}_s}{\left[\bar{\mathbf{p}}_s^H \mathbf{U} (\boldsymbol{\Gamma} + \hat{\lambda} \mathbf{I})^{-1} \mathbf{U}^H \bar{\mathbf{p}}_s \right]^2} = \xi_0. \quad (3.37)$$

Defining

$$z = \mathbf{U}^H \bar{\mathbf{p}}_s, \quad (3.38)$$

and letting z_m be the m th element of z , Eq. (3.37) can be written as

$$\frac{\sum_{m=1}^M \frac{|z_m|^2}{(\gamma_m + \hat{\lambda})^2}}{\left[\sum_{m=1}^M \frac{|z_m|^2}{\gamma_m + \hat{\lambda}} \right]^2} = \xi_0. \quad (3.39)$$

From Eq. (3.39), we have the inequality

$$\xi_0 \leq \frac{\|\bar{\mathbf{p}}_s\|^2}{(\gamma_M + \hat{\lambda})^2} \Big/ \frac{\|\bar{\mathbf{p}}_s\|^4}{(\gamma_1 + \hat{\lambda})^2} = \frac{(\gamma_1 + \hat{\lambda})^2}{M(\gamma_M + \hat{\lambda})^2}. \quad (3.40)$$

Using Eq. (3.40) and considering that $\hat{\lambda} \geq 0$, the lower and upper bounds on $\hat{\lambda}$ are given by

$$0 \leq \hat{\lambda} \leq \frac{\gamma_1 - \gamma_M \sqrt{M \xi_0}}{\sqrt{M \xi_0} - 1}. \quad (3.41)$$

Solving Eq. (3.39) for $\hat{\lambda}$ and substituting Eq. (3.13) into Eq. (3.35) gives the NC beamformer weight vector

$$\mathbf{w}_{\text{NC}} = \frac{\mathbf{U} (\boldsymbol{\Gamma} + \hat{\lambda} \mathbf{I})^{-1} \mathbf{U}^H \bar{\mathbf{p}}_s}{\bar{\mathbf{p}}_s^H \mathbf{U} (\boldsymbol{\Gamma} + \hat{\lambda} \mathbf{I})^{-1} \mathbf{U}^H \bar{\mathbf{p}}_s}. \quad (3.42)$$

To summarize, the design of weight vector for NC beamformer consists of the following steps (see also [19]).

- Step 1. Compute the eigendecomposition of \mathbf{R} using Eq. (3.11).
- Step 2. If Eq. (3.27) is satisfied, set $\hat{\lambda} = 0$. Otherwise, solve Eq. (3.39) for $\hat{\lambda}$ using a Newton's method. The lower and upper bounds on $\hat{\lambda}$ are given by Eq. (3.41).
- Step 3. Substitute $\hat{\lambda}$ into Eq. (3.42) to obtain the NC weight vector \mathbf{w}_{NC} .

For the case where \mathbf{R} is singular, the upper bound on ξ_0 corresponding to Eq. (3.28) becomes

$$\xi_0 < \frac{1}{\left\| \mathbf{U}_n^H \bar{\mathbf{p}}_s \right\|^2}, \quad (3.43)$$

and the NC beamformer still works, which means that we can allow $N < M$.

3.2.3 Worst-Case Constrained Beamformer

The NC beamformer can improve the robustness of an MVDR beamformer. It belongs to the class of diagonal loading approaches. However, it is not clear how to choose the optimal value of the diagonal loading level. Several robust beamforming methods were presented by using the information about the uncertainty of the array steering vector [4–7].

Assume that the squared norm of the error between the actual and nominal signal steering vectors can be bounded by some known constant ε ,

$$\|\mathbf{p}_\Delta\|^2 = \|\tilde{\mathbf{p}}_s - \bar{\mathbf{p}}_s\|^2 \leq \varepsilon. \quad (3.44)$$

Then, the actual signal steering vector belongs to the uncertainty set S

$$S \triangleq \left\{ \mathbf{p}_s \mid \mathbf{p}_s = \bar{\mathbf{p}}_s + \mathbf{p}_\Delta, \|\mathbf{p}_\Delta\|^2 \leq \varepsilon \right\}. \quad (3.45)$$

Based on the worst-case performance optimization, the robust beamforming problem can be formulated as

$$\begin{aligned} & \max_{\mathbf{w}} \min_{\mathbf{p}_\Delta} \frac{\sigma_s^2 |\mathbf{w}^H \mathbf{p}_s|^2}{\mathbf{w}^H \mathbf{R} \mathbf{w}}, \\ & \text{subject to } \|\mathbf{p}_s - \bar{\mathbf{p}}_s\|^2 \leq \varepsilon, \quad \text{for all } \mathbf{p}_s \in S, \end{aligned} \quad (3.46)$$

which can be rewritten as [4]

$$\begin{aligned} & \min_{\mathbf{w}} \mathbf{w}^H \mathbf{R} \mathbf{w}, \\ & \text{subject to } |\mathbf{w}^H (\bar{\mathbf{p}}_s + \mathbf{p}_\Delta)| \geq 1, \quad \text{for all } \|\mathbf{p}_\Delta\|^2 \leq \varepsilon. \end{aligned} \quad (3.47)$$

Note that Eq. (3.47) modifies the MVDR (or SMI) beamformer by using the inequality constraints instead of the distortionless constraint. These inequality constraints guarantee that

$$|\mathbf{w}^H \mathbf{p}_s| \geq 1, \quad \text{for all } \mathbf{p}_s \in S, \quad (3.48)$$

with equality corresponding to the worst case.

In practice, the steering vector error upper bound ε is unavailable and the estimated value ε_0 is used instead. The optimization problem in Eq. (3.47) becomes

$$\begin{aligned} & \min_{\mathbf{w}} \mathbf{w}^H \mathbf{R} \mathbf{w}, \\ & \text{subject to } \min_{\|\mathbf{p}_\Delta\|^2 \leq \varepsilon_0} |\mathbf{w}^H (\bar{\mathbf{p}}_s + \mathbf{p}_\Delta)| \geq 1. \end{aligned} \quad (3.49)$$

This beamformer is referred to as the worst-case constrained (WCC) beamformer. Using the Cauchy-Schwarz inequality, it is easy to verify that under

$$|\mathbf{w}^H \bar{\mathbf{p}}_s| \geq \varepsilon_0 \|\mathbf{w}\|, \quad (3.50)$$

the following equality is satisfied

$$\min_{\|\mathbf{p}_\Delta\|^2 \leq \varepsilon_0} |\mathbf{w}^H(\bar{\mathbf{p}}_s + \mathbf{p}_\Delta)| = |\mathbf{w}^H \bar{\mathbf{p}}_s| - \varepsilon_0 \|\mathbf{w}\|. \quad (3.51)$$

Therefore, Eq. (3.49) can be rewritten as

$$\begin{aligned} & \min_{\mathbf{w}} \mathbf{w}^H \mathbf{R} \mathbf{w}, \\ & \text{subject to } |\mathbf{w}^H \bar{\mathbf{p}}_s| - \varepsilon_0 \|\mathbf{w}\| \geq 1. \end{aligned} \quad (3.52)$$

Using the fact that the cost function in Eq. (3.52) is unchanged when \mathbf{w} undergoes an arbitrary phase rotation, Eq. (3.52) can be rewritten as

$$\begin{aligned} & \min_{\mathbf{w}} \mathbf{w}^H \mathbf{R} \mathbf{w}, \\ & \text{subject to } \mathbf{w}^H \bar{\mathbf{p}}_s \geq 1 + \varepsilon_0 \|\mathbf{w}\|. \end{aligned} \quad (3.53)$$

Using Eq. (3.23), Eq. (3.53) becomes

$$\begin{aligned} & \min_{\mathbf{w}} \|\mathbf{V} \mathbf{w}\|, \\ & \text{subject to } \varepsilon_0 \|\mathbf{w}\| \leq \mathbf{w}^H \bar{\mathbf{p}}_s + 1, \end{aligned} \quad (3.54)$$

which is a convex SOCP problem and it is easy to obtain the solution for the weight vector by using an SOCP solver such as SeDuMi.

Note that the inequality constraint in Eq. (3.49) is equivalent to $\min |\mathbf{w}^H(\bar{\mathbf{p}}_s + \mathbf{p}_\Delta)| = 1$. Therefore, the inequality constraint in Eq. (3.52) is equivalent to the equality constraint $|\mathbf{w}^H \bar{\mathbf{p}}_s| - \varepsilon_0 \|\mathbf{w}\| = 1$. This means that Eq. (3.52) can be rewritten as [4]

$$\begin{aligned} & \min_{\mathbf{w}} \mathbf{w}^H \mathbf{R} \mathbf{w}, \\ & \text{subject to } |\mathbf{w}^H \bar{\mathbf{p}}_s - 1|^2 = \varepsilon_0^2 \mathbf{w}^H \mathbf{w}. \end{aligned} \quad (3.55)$$

Using the Lagrange multiplier methodology, we define

$$F(\mathbf{w}, \lambda) \triangleq \mathbf{w}^H \mathbf{R} \mathbf{w} + \lambda (\varepsilon_0^2 \mathbf{w}^H \mathbf{w} - \mathbf{w}^H \bar{\mathbf{p}}_s \bar{\mathbf{p}}_s^H \mathbf{w} + \mathbf{w}^H \bar{\mathbf{p}}_s + \bar{\mathbf{p}}_s^H \mathbf{w} - 1), \quad (3.56)$$

where $\lambda \geq 0$ is the Lagrange multiplier.

Taking the gradient of $F(\mathbf{w}, \lambda)$ with respect to \mathbf{w}^H and setting the result to zero gives

$$\mathbf{R} \mathbf{w} + \lambda (\varepsilon_0^2 \mathbf{w} - \bar{\mathbf{p}}_s \bar{\mathbf{p}}_s^H \mathbf{w} + \bar{\mathbf{p}}_s) = \mathbf{0}, \quad (3.57)$$

then

$$\mathbf{w} = -\lambda (\mathbf{R} + \lambda \varepsilon_0^2 \mathbf{I} - \lambda \bar{\mathbf{p}}_s \bar{\mathbf{p}}_s^H)^{-1} \bar{\mathbf{p}}_s. \quad (3.58)$$

Using the matrix inversion lemma gives

$$\mathbf{w} = \frac{\lambda}{\lambda \bar{\mathbf{p}}_s^H (\mathbf{R} + \lambda \varepsilon_0^2 \mathbf{I})^{-1} \bar{\mathbf{p}}_s - 1} (\mathbf{R} + \lambda \varepsilon_0^2 \mathbf{I})^{-1} \bar{\mathbf{p}}_s. \quad (3.59)$$

It is seen that this beamformer also belongs to the class of diagonal loading approaches.

Stoica et al. [20] formulated the spatial spectral estimation as a covariance fitting problem

$$\begin{aligned} & \max_{\sigma^2} \sigma^2, \\ & \text{subject to } \mathbf{R} - \sigma^2 \mathbf{p}_s \mathbf{p}_s^H \succcurlyeq 0, \text{ for all } \mathbf{p}_s \in S, \end{aligned} \quad (3.60)$$

where the notation \succcurlyeq means that the matrix is semidefinite.

It can be verified that the following equivalences hold

$$\begin{aligned} & \mathbf{R} - \sigma^2 \mathbf{p}_s \mathbf{p}_s^H \succcurlyeq 0 \\ & \Leftrightarrow \mathbf{I} - \sigma^2 \mathbf{R}^{-1/2} \mathbf{p}_s \mathbf{p}_s^H \mathbf{R}^{-1/2} \succcurlyeq 0 \\ & \Leftrightarrow 1 - \sigma^2 \mathbf{p}_s^H \mathbf{R}^{-1} \mathbf{p}_s \geq 0 \\ & \Leftrightarrow \sigma^2 \leq \frac{1}{\mathbf{p}_s^H \mathbf{R}^{-1} \mathbf{p}_s}, \end{aligned} \quad (3.61)$$

where $\mathbf{R}^{-1/2}$ is the Hermitian square root of \mathbf{R}^{-1} .

Using Eq. (3.61), the optimization problem in Eq. (3.60) can be reduced to

$$\begin{aligned} & \min_{\mathbf{p}_s} \mathbf{p}_s^H \mathbf{R}^{-1} \mathbf{p}_s, \\ & \text{subject to } \|\mathbf{p}_s - \bar{\mathbf{p}}_s\|^2 \leq \varepsilon_0. \end{aligned} \quad (3.62)$$

To exclude the trivial solution $\mathbf{p}_s = \mathbf{0}$, it requires

$$\varepsilon_0 < \|\bar{\mathbf{p}}_s\|^2. \quad (3.63)$$

Clearly, the solution to Eq. (3.62) will occur on the boundary of the uncertainty set. Therefore the inequality constraint in Eq. (3.62) is equivalent to the equality constraint. This leads to

$$\begin{aligned} & \min_{\mathbf{p}_s} \mathbf{p}_s^H \mathbf{R}^{-1} \mathbf{p}_s, \\ & \text{subject to } \|\mathbf{p}_s - \bar{\mathbf{p}}_s\|^2 = \varepsilon_0. \end{aligned} \quad (3.64)$$

Using the Lagrange multiplier methodology, we define

$$F(\mathbf{p}_s, \lambda) \triangleq \mathbf{p}_s^H \mathbf{R}^{-1} \mathbf{p}_s + \lambda (\|\mathbf{p}_s - \bar{\mathbf{p}}_s\|^2 - \varepsilon_0), \quad (3.65)$$

where $\lambda \geq 0$ is the Lagrange multiplier. Taking the gradient of $F(\mathbf{p}_s, \lambda)$ with respect to \mathbf{p}_s^H and setting the result to zero gives

$$\mathbf{R}^{-1} \mathbf{p}_s + \lambda (\mathbf{p}_s - \bar{\mathbf{p}}_s) = \mathbf{0}. \quad (3.66)$$

The optimal solution $\hat{\mathbf{p}}_s$ to Eq. (3.66) is given by

$$\hat{\mathbf{p}}_s = \left(\frac{\mathbf{R}^{-1}}{\lambda} + \mathbf{I} \right)^{-1} \bar{\mathbf{p}}_s. \quad (3.67)$$

Using the matrix inversion lemma gives

$$\hat{\mathbf{p}}_s = \bar{\mathbf{p}}_s - (\mathbf{I} + \lambda \mathbf{R})^{-1} \bar{\mathbf{p}}_s. \quad (3.68)$$

Similar to Eq. (3.13), we have

$$(\mathbf{I} + \lambda \mathbf{R})^{-1} = \mathbf{U} (\mathbf{I} + \lambda \boldsymbol{\Gamma})^{-1} \mathbf{U}^H. \quad (3.69)$$

Thus, Eq. (3.68) becomes

$$\hat{\mathbf{p}}_s = \bar{\mathbf{p}}_s - \mathbf{U} (\mathbf{I} + \lambda \boldsymbol{\Gamma})^{-1} \mathbf{U}^H \bar{\mathbf{p}}_s. \quad (3.70)$$

Using $\hat{\mathbf{p}}_s$ instead of $\bar{\mathbf{p}}_s$ in Eq. (3.2) gives the estimate of signal power

$$\hat{\sigma}_s^2 = \frac{1}{\hat{\mathbf{p}}_s^H \mathbf{R}^{-1} \hat{\mathbf{p}}_s}. \quad (3.71)$$

Using Eq. (3.67), Eq. (3.71) can be written as

$$\hat{\sigma}_s^2 = \frac{1}{\bar{\mathbf{p}}_s^H \mathbf{U} \boldsymbol{\Gamma} (\lambda^{-2} \mathbf{I} + 2\lambda^{-1} \boldsymbol{\Gamma} + \boldsymbol{\Gamma}^2)^{-1} \mathbf{U}^H \bar{\mathbf{p}}_s}. \quad (3.72)$$

Using $\hat{\mathbf{p}}_s$ instead of $\bar{\mathbf{p}}_s$ in Eq. (3.1) gives the weight vector of the robust beamformer

$$\mathbf{w}_{\text{WCC}} = \frac{\mathbf{R}^{-1} \hat{\mathbf{p}}_s}{\hat{\mathbf{p}}_s^H \mathbf{R}^{-1} \hat{\mathbf{p}}_s}. \quad (3.73)$$

where the subscript ‘‘WCC’’ denotes the WCC beamformer.

Using Eq. (3.67), Eq. (3.73) can be written as

$$\mathbf{w}_{\text{WCC}} = \frac{(\mathbf{R} + \frac{1}{\lambda} \mathbf{I})^{-1} \bar{\mathbf{p}}_s}{\bar{\mathbf{p}}_s^H (\mathbf{R} + \frac{1}{\lambda} \mathbf{I})^{-1} \mathbf{R} (\mathbf{R} + \frac{1}{\lambda} \mathbf{I})^{-1} \bar{\mathbf{p}}_s}. \quad (3.74)$$

It is seen that this beamformer also belongs to the class of diagonal loading approaches, where the diagonal loading factor is $1/\lambda$. It is proved that the weight vector in Eq. (3.74) is identical to that from Eq. (3.54) [5].

Substituting Eq. (3.70) into the constraint in Eq. (3.64) gives

$$\|\mathbf{U}(\mathbf{I} + \lambda\mathbf{\Gamma})^{-1}\mathbf{U}^H\bar{\mathbf{p}}_s\|^2 = \varepsilon_0. \quad (3.75)$$

Similar to Eq. (3.39), Eq. (3.75) can be written as

$$\begin{aligned} g(\lambda) &\triangleq \|\mathbf{U}(\mathbf{I} + \lambda\mathbf{\Gamma})^{-1}\mathbf{U}^H\bar{\mathbf{p}}_s\|^2 \\ &= \sum_{m=1}^M \frac{|z_m|^2}{(1 + \lambda\gamma_m)^2} = \varepsilon_0. \end{aligned} \quad (3.76)$$

Note that the bigger the ζ_0 , the bigger the diagonal loading factor $1/\lambda$ and the higher the robustness of the resulting beamformer.

It is seen that $g(\lambda)$ is a monotonically decreasing function of λ . Using Eqs. (3.63), (3.70) and (3.76), we know that $g(0) > \varepsilon_0$. Using Eq. (3.76), we know that $\lim_{\lambda \rightarrow \infty} g(\lambda) = 0 < \varepsilon_0$. Therefore, there exists a unique solution $\hat{\lambda}$ to Eq. (3.76) which can be determined by using the Newton's method.

Using Eq. (3.76), the lower and upper bounds on $\hat{\lambda}$ can be given by

$$\frac{\|\bar{\mathbf{p}}_s\| - \sqrt{\varepsilon_0}}{\gamma_1\sqrt{\varepsilon_0}} \leq \hat{\lambda} \leq \frac{\|\bar{\mathbf{p}}_s\| - \sqrt{\varepsilon_0}}{\gamma_M\sqrt{\varepsilon_0}}. \quad (3.77)$$

To summarize, the design of weight vector for WCC beamformer consists of the following steps (see also [5]).

- Step 1. Compute the eigendecomposition of \mathbf{R} using Eq. (3.11).
- Step 2. Solve Eq. (3.76) for $\hat{\lambda}$ using a Newton's method. The lower and upper bounds on $\hat{\lambda}$ are given by Eq. (3.77).
- Step 3. Substitute $\hat{\lambda}$ into Eq. (3.70) to obtain the estimate of signal steering vector $\hat{\mathbf{p}}_s$.
- Step 4. Substitute $\hat{\mathbf{p}}_s$ into Eq. (3.73), or substitute $\hat{\lambda}$ into Eq. (3.74), to obtain the weight vector \mathbf{w}_{WCC} for WCC beamformer.

Using the knowledge that $\|\bar{\mathbf{p}}_s\|^2 = M$, we can estimate the signal steering vector as

$$\hat{\mathbf{p}}_s = M^{1/2}\hat{\mathbf{p}}_s/\|\hat{\mathbf{p}}_s\| \quad (3.78)$$

to satisfy $\|\hat{\mathbf{p}}_s\|^2 = M$.

Correspondingly, the signal power can be estimated as [20]

$$\hat{\hat{\sigma}}_s^2 = \frac{\hat{\sigma}_s^2 \|\hat{\mathbf{p}}_s\|^2}{M}. \quad (3.79)$$

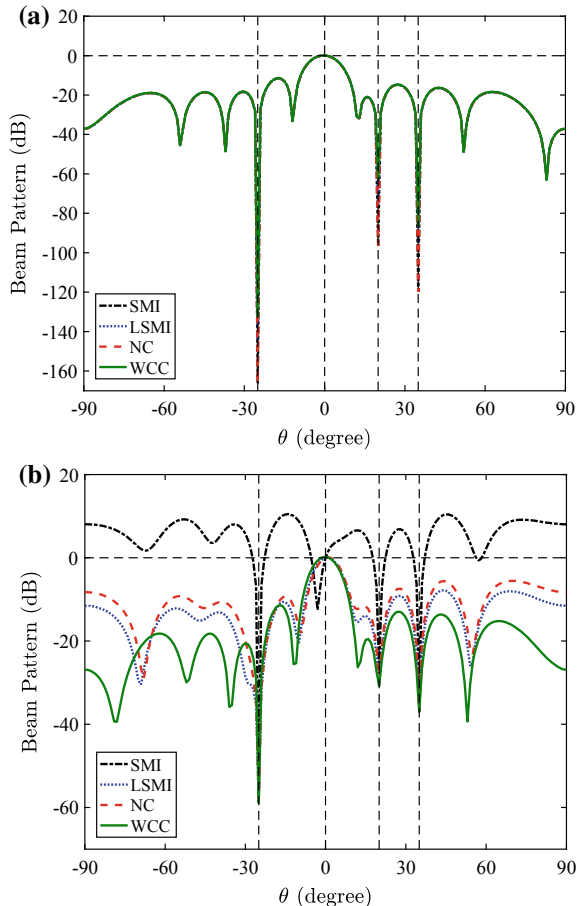
3.2.4 Comparison of Robust Beamformers

Consider the 10-element uniform linear array with half-wavelength spacing in the white noise environment. Four plane-wave signals impinge on the array from $\theta = -25^\circ, 0^\circ, 20^\circ$, and 35° , respectively, with $SNR = 60, 10, 30$ and 35 dB. The array manifold vector distortion is \mathbf{p}_Δ , which is assumed to be an unknown norm-bounded complex vector.

Assuming that the second signal is the SOI, we choose the steering direction $\theta_0 = 0^\circ$. Four beamformers (SMI, LSMI, NC and WCC) are designed. For these beamformers, we choose $LNR = 10$ dB for LSMI beamformer, $\zeta_0 = 0.6$ for NC beamformer, and $\varepsilon_0 = 1$ for WCC beamformer.

First, we assume that there is no array manifold distortion (i.e., $\|\mathbf{p}_\Delta\| = 0$), the resulting beam patterns are shown in Fig. 3.2. In Fig. 3.2a, we assume that $N = \infty$ samples are used to estimate the covariance matrix, which implies that the theoretical covariance matrix is used. In Fig. 3.2b we choose $N = 2M$.

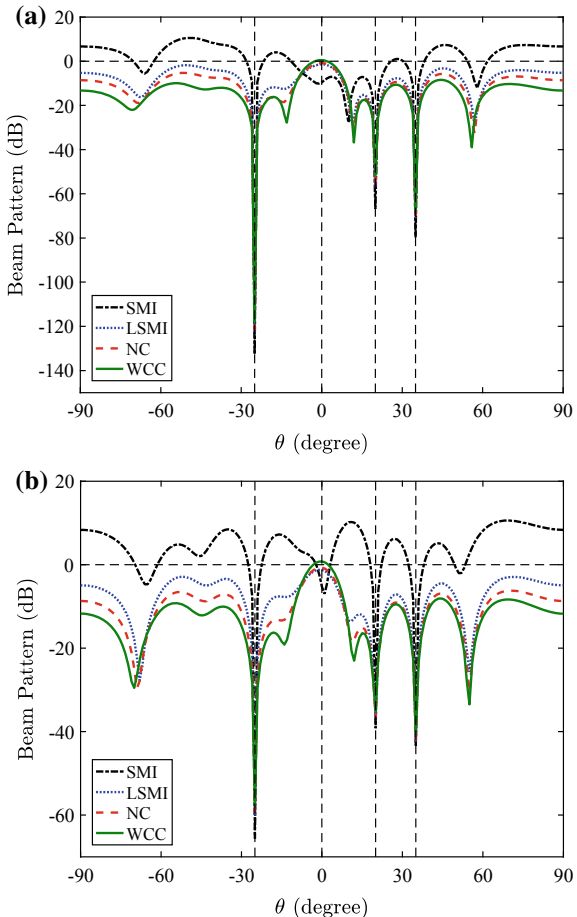
Fig. 3.2 Comparison of the beam patterns when $\|\mathbf{p}_\Delta\| = 0$ and **a** $N = \infty$, **b** $N = 2M$



In the absence of steering vector and covariance matrix mismatches as shown in Fig. 3.2a, all the beam patterns have good mainlobes and place perfect nulls at the directions of the interferers. In the presence of covariance matrix mismatch as shown in Fig. 3.2b, the beam pattern of the SMI beamformer degrades significantly by even a relatively small covariance matrix mismatch. The other three beamformers preserve good beam patterns under mismatch.

Consider the case of array manifold vector distortion $\|p_\Delta\| = \sqrt{0.5}$. The resulting beam patterns of the four beamformers using covariance matrix with $N = \infty$ and $N = 2M$ are shown in Fig. 3.3a, b, respectively. Note that the error between the sample and the theoretical covariance matrix can be viewed as due to a steering vector error [3].

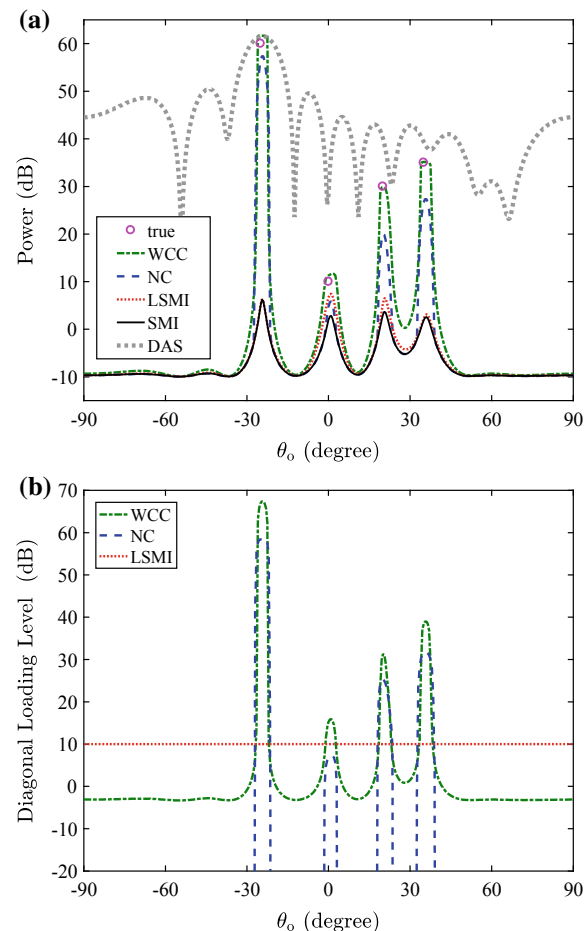
Fig. 3.3 Comparison of the beam patterns when $\|p_\Delta\| = \sqrt{0.5}$ and **a** $N = \infty$, **b** $N = 2M$



It is seen that SMI beamformer places a null at the signal direction because it treats the mismatched signal as an interferer and attempts to suppress it. The LSMI, NC, and WCC beamformers preserve good beam patterns. They improve the robustness against steering vector and covariance matrix mismatches. Among the three robust beamformers, the LSMI and NC beam patterns at the steering direction are less than unity. The WCC beam pattern maintains an approximate unity gain at the steering direction.

Assume that the array manifold vector distortion is norm-bounded by $\|\mathbf{p}_\Delta\| = 1$. Five beamforming methods (DAS, SMI, LSMI, NC and WCC) are used to estimate the spatial spectrum (i.e., power of the signals), as shown in Fig. 3.4a. The small circles in the figure denote the true directions-of-arrival and powers of the signals. For these beamformers, we have used the theoretical covariance matrix, i.e., $N = \infty$.

Fig. 3.4 Comparison of various beamformers on **a** spatial spectrum, and **b** diagonal loading level



It is seen that the DAS beamformer has poor resolution and its sidelobes result in false peaks. The other methods can provide good direction-of-arrival estimates for the incident signals based on the peak locations and the WCC method gives the best power estimates of the signals. The WCC method outperforms the other methods.

The diagonal loading levels of the LSMI, NC, and WCC methods are shown in Fig. 3.4b. The LSMI method have a fixed diagonal loading level. The NC method have a nonzero or zero diagonal loading level depending on whether the norm constraint in Eq. (3.26) is active or not. The WCC method adjusts the diagonal loading level adaptively as the signal presents or the SNR changes.

Figure 3.5 shows the output SINR of the five methods when the steering direction and the signal direction coincide. The DAS method has high output SINR for strong signal while low output SINR for weak signal. The SMI method has lower output SINR due to its sensitivity to mismatches. The LSMI method improves the output SINR when the power of the desired signal is not quite high. The output SINR of the NC method is better than that of the LSMI method when the desired signal is quite strong. The output SINR of the WCC method is in general better than that of the other methods.

Assume that the second signal is treated as the SOI and the others as the interferences. The SNR is varied between -20 and 40 dB by changing the power of the SOI. The output SINRs as functions of the SNR of the five beamforming methods with $N = \infty$ and $N = 2M$ are shown in Fig. 3.6a, b, respectively.

It is seen that the SINR curves of the robust methods (LSMI, NC, and WCC) are higher than that of the SMI method, although their SINR curves drop when the SOI SNR is quite high. Among them, the WCC method is very excellent.

Fig. 3.5 The output SINR for various signals when the steering direction coincides

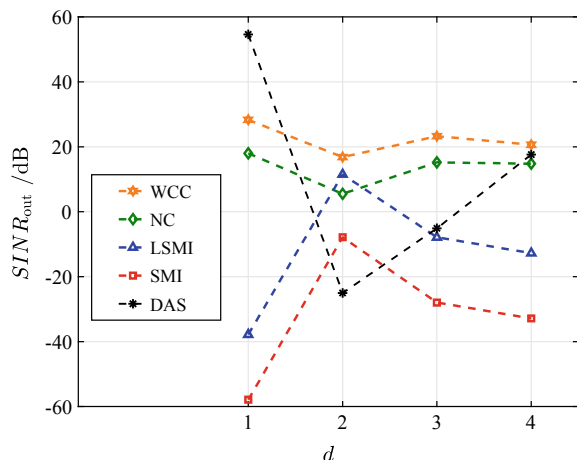
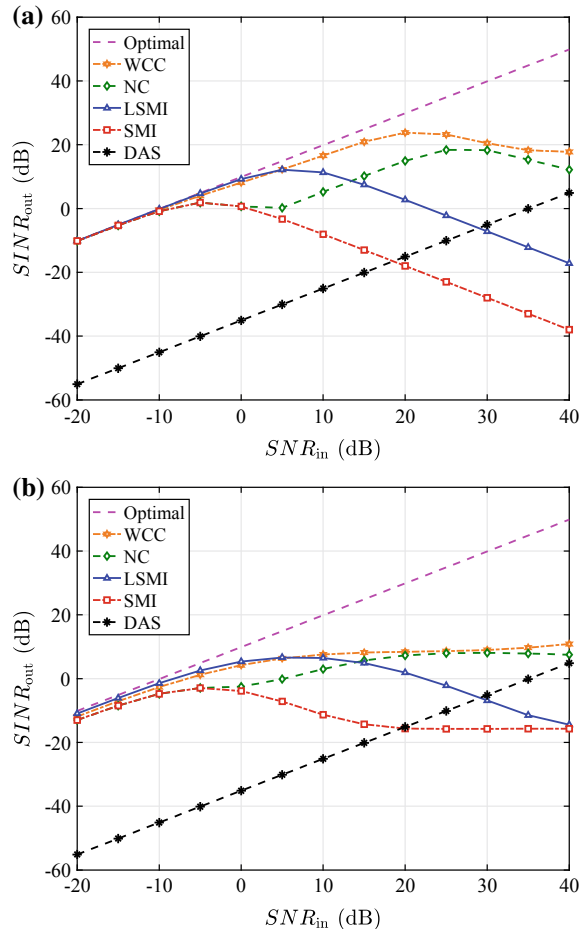


Fig. 3.6 Comparison of the beamformers as SNR varies.
a $N = \infty$, **b** $N = 2M$



3.3 Low-Sidelobe Beamformers

3.3.1 Windows for Uniform Linear Arrays

By exploiting the analogy between the array processing and the spectral analysis of time series, the techniques from finite impulse response (FIR) filters and spectral estimation windows can be used in the design of weighting for uniform linear arrays.

There are several kinds of array weightings that are equivalent to various windows used in the spectral analysis of time series.

1. Uniform weighting

Consider the case when an M -element linear array with spacing d . The uniform weighting is given by

$$w_m = 1/M, \quad m = 1, \dots, M. \quad (3.80)$$

In a vector form, we get

$$\mathbf{w}_d = [w_1, \dots, w_m, \dots, w_M]^T. \quad (3.81)$$

If we choose the array weighting to be the uniform weightings, i.e.,

$$\mathbf{w} = \mathbf{w}_d, \quad (3.82)$$

the beamformer will correspond to a conventional beamformer that is steered to broadside.

The first right null of the resulting beam pattern occurs at $\theta_N^+ = \arcsin(\lambda/Md)$ and the null-to-null beamwidth is $BW_{NN} = 2\arcsin(\lambda/Md)$.

2. Cosine^q weighting

The Cosine^q weighting is given by

$$w_m(q) = \alpha(q) \cos^q \left[\pi \frac{m - (M + 1)/2}{M} \right], \quad m = 1, \dots, M, \quad (3.83)$$

where $\alpha(q)$ is chosen so that the beam pattern at the steering direction is equal to unity. The weighting for $q = 1$ and $q = 2$ are called the cosine weighting and the Hanning weighting, respectively. For $q = 0$, it reduces to uniform weighting.

The first right null of the resulting beam pattern occurs at $\theta_N^+ = \arcsin(\lambda(q + 2)/2Md)$ and the null-to-null beamwidth is $BW_{NN} = 2\arcsin(\lambda(q + 2)/2Md)$, which is wider in comparison to the uniform weightings.

3. Raised cosine^q weighting

The family of raised cosine^q weighting is given by

$$w_m(p, q) = \alpha(p, q) \left\{ p + (1 - p) \cos^q \left[\pi \frac{m - (M + 1)/2}{M} \right] \right\}, \quad m = 1, \dots, M, \quad (3.84)$$

where $\alpha(p, q)$ is chosen so that the beam pattern at the steering direction is equal to unity. The weighting for $q = 1$ is called the raised cosine weighting.

For $q = 2$, Eq. (3.84) becomes

$$w_m(p) = \frac{\alpha(p)}{2} \left\{ (1 + p) + (1 - p) \cos \left[2\pi \frac{m - (M + 1)/2}{M} \right] \right\}, \quad m = 1, \dots, M. \quad (3.85)$$

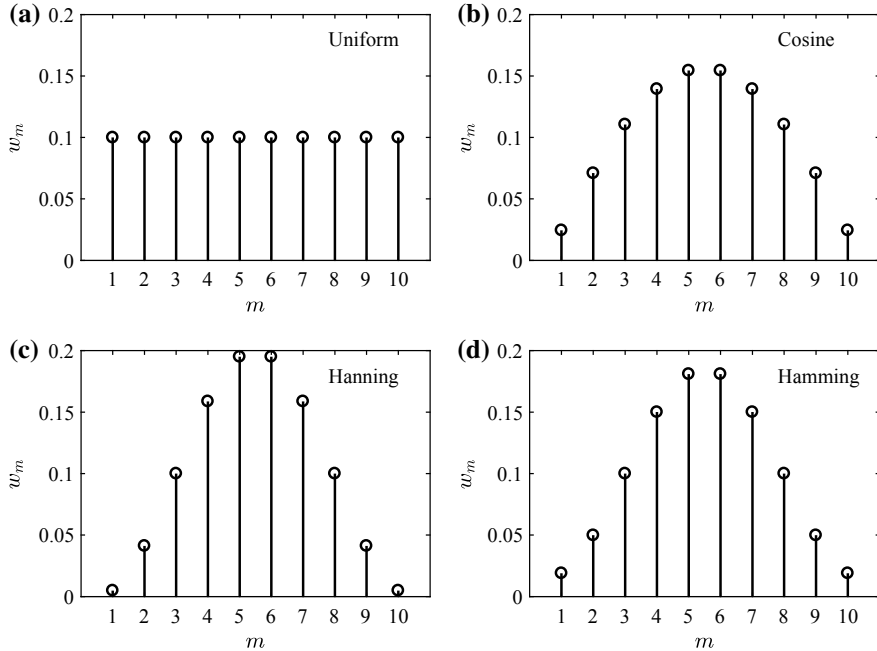


Fig. 3.7 Various array weightings (windows)

The weighting for $q = 2$ and $p = 0.08$ is called the Hamming weighting.

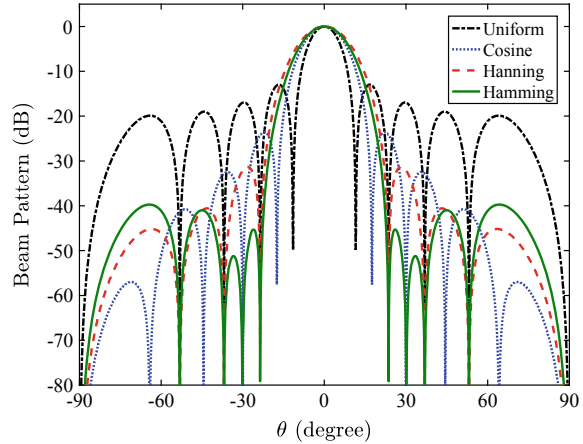
The first right null of the resulting beam pattern for the Hamming weighting occurs at $\theta_N^+ = \arcsin(2\lambda/Md)$ and the null-to-null beamwidth is $BW_{NN} = 2\arcsin(2\lambda/Md)$, which is the same as the Hanning weightings.

Assume that $M = 10$ and $d = \lambda/2$. The array weightings using various windows are shown in Fig. 3.7. The resulting beam patterns using these array weights are shown in Fig. 3.8. It is seen that the cosine, Hanning, and Hamming weightings produce beam patterns with low sidelobe level at the cost of widening beamwidth in comparison to the uniform weightings. Comparing to the Hanning weighting, the Hamming weighting achieves a lower sidelobe level for the same null-to-null beamwidth.

4. Chebyshev weighting

The previous weightings do not control the height of the sidelobes explicitly. A method was presented by Dolph to design weights that explicitly control sidelobes and beamwidths [21], which is given by

Fig. 3.8 Beam patterns for various weightings



$$w_m = \begin{cases} z^{M-1}/2, & m = 1 \\ \sum_{i=1}^{m-1} \frac{0.5(M-1)(m-2)!(M-i-1)!}{(m-i)!(i-1)!(M-i-1)!(M-m)!} z^{M-2m+1} (z^2 - 1)^{m-i}, & 2 \leq m \leq M/2 + 1, \\ w_{M+1-m}, & m \geq M/2 + 1 \end{cases} \quad (3.86)$$

where $(\cdot)!$ denotes the factorial and

$$z = \begin{cases} \frac{\cos\left[\frac{\pi}{2(M-1)}\right]}{\cos\left[\pi\frac{d}{\lambda}\sin\theta_N^+\right]}, & \text{for given } \theta_N^+ \\ \cosh\left[\frac{\operatorname{arccosh}\left(\sqrt{10^{-SLL/10}}\right)}{M-1}\right], & \text{for given } SLL \text{ (in dB)} \end{cases}, \quad (3.87)$$

where SLL is the specified sidelobe level in dB.

The weighting in Eq. (3.86) is sometimes called the Dolph-Chebyshev weighting, or simply Chebyshev weighting.

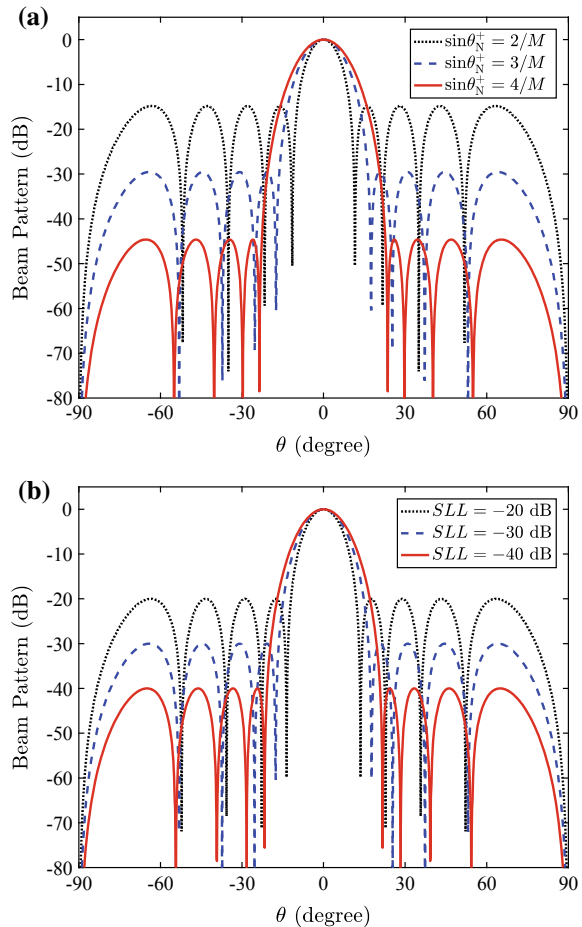
For the same uniform linear array, the resulting beam patterns for the Dolph-Chebyshev weighting with $\sin\theta_N^+ = 2/M, 3/M$ and $4/M$ (i.e., the same beamwidth as in Fig. 3.8) are shown in Fig. 3.9a. The beam patterns for the specified sidelobe levels of $-20, -30$ and -40 dB are shown in Fig. 3.9b.

For a uniform linear array with half-wavelength spacing, the Dolph-Chebyshev weighting produces a beam pattern with the minimum beamwidth for a specified sidelobe level, or a beam pattern with the minimum sidelobe level for a specified beamwidth.

5. Array steering

If we assume that the array is steered to the direction θ_0 rather than broadside, the array weight vector can be given by

Fig. 3.9 Beam patterns for Dolph-Chebyshev weightings **a** with specified beamwidths, and **b** with specified sidelobe levels



$$\mathbf{w} = \mathbf{w}_d \circ \mathbf{p}(\theta_o), \quad (3.88)$$

where “ \circ ” denotes the dot product and $\mathbf{p}(\theta_o)$ denotes the steering vector.

3.3.2 Low-Sidelobe Designs

1. Minimum sidelobes for specified beamwidth

The Dolph-Chebyshev weighting can provide an optimum beamwidth-sidelobe trade-off for a uniform linear array with half-wavelength spacing. However, it is only applicable to uniform linear arrays.

For arrays with arbitrary geometry, the low-sidelobe beamformer design problem can be formulated as minimizing the maximum sidelobe level while keeping the distortionless response at the steering direction,

$$\begin{aligned} \min_{\mathbf{w}} \max_{\theta \in \Theta_{\text{SL}}} |\mathbf{w}^H \mathbf{p}(\theta)|, \\ \text{subject to } |\mathbf{w}^H \mathbf{p}(\theta_0)| = 1, \end{aligned} \quad (3.89)$$

where Θ_{SL} is the specified sidelobe region, which is defined as

$$\Theta_{\text{SL}} \triangleq \{\theta \mid |\theta - \theta_0| \geq BW_{\text{SL}}/2\}, \quad (3.90)$$

where BW_{SL} is the specified sidelobe-level beamwidth, which is defined to be the width between two directions where the beam power equals to the sidelobe level.

Use the fact that the phase of \mathbf{w} can always be rotated, without affecting the cost function in Eq. (3.89), so that $\mathbf{w}^H \mathbf{p}(\theta_0)$ is real, i.e., $\mathbf{w}^H \mathbf{p}(\theta_0) = 1$. Thus, the optimization problem in Eq. (3.89) can be rewritten as

$$\begin{aligned} \min_{\mathbf{w}} \max_{\theta \in \Theta_{\text{SL}}} |\mathbf{w}^H \mathbf{p}(\theta)|, \\ \text{subject to } \mathbf{w}^H \mathbf{p}(\theta_0) = 1. \end{aligned} \quad (3.91)$$

The minimax criterion is used in Eq. (3.91). The resulting weight vector leads to the constant sidelobe that is the minimum possible for the given beamwidth. The beamformer is referred to as the minimum-sidelobe (MSL) beamformer. It can be viewed as extending the Dolph-Chebyshev method utilized for linear arrays to more general geometries. For this reason, the minimax criterion is also called the Chebyshev criterion.

In order to improve the robustness of the beamformer, the norm constraint on the weight vector \mathbf{w} can be imposed. Therefore the beamformer design problem becomes

$$\begin{aligned} \min_{\mathbf{w}} \max_{\theta \in \Theta_{\text{SL}}} |\mathbf{w}^H \mathbf{p}(\theta)|, \\ \text{subject to } \mathbf{w}^H \mathbf{p}(\theta_0) = 1, \\ \|\mathbf{w}\| \leq \sqrt{\xi_0}, \end{aligned} \quad (3.92)$$

where ξ_0 is a prescribed parameter.

Let

$$\theta_i \in \Theta_{\text{SL}}, \quad i = 1, 2, \dots, N_{\text{SL}} \quad (3.93)$$

be the chosen (uniform or nonuniform) grids that approximate the sidelobe region using a finite number of directions. In Eq. (3.93), N_{SL} is the number of the directions.

Introducing a new scalar non-negative variable ξ , Eq. (3.92) can be rewritten as [22]

$$\begin{aligned}
& \min_{\mathbf{w}} \xi, \\
& \text{subject to } \mathbf{w}^H \mathbf{p}(\theta_0) = 1, \\
& \quad |\mathbf{w}^H \mathbf{p}(\theta_i)| \leq \xi, \quad \theta_i \in \Theta_{\text{SL}}, \quad i = 1, 2, \dots, N_{\text{SL}}, \\
& \quad \|\mathbf{w}\| \leq \sqrt{\xi_0}.
\end{aligned} \tag{3.94}$$

This optimization problem has been reformulated as a convex SOCP problem, which is computationally tractable and can be solved efficiently using an SOCP solver.

The beamformer is referred to as the robust minimum-sidelobe (RMSL) beamformer, whose weight vector is termed as \mathbf{w}_{RMSL} .

The beam patterns of a 10-element uniform linear array using Dolph-Chebyshev weighting and minimum-sidelobe design (i.e., Eq. (3.91)) for frequencies corresponding to $d = \lambda/2$ and $d = \lambda/4$ are shown in Fig. 3.10a, b, respectively. For the Dolph-Chebyshev weighting, the specified sidelobe level is -30 dB. For the minimum-sidelobe design, the beamwidth BW_{SL} is chosen to be the same as that of the Dolph-Chebyshev weighting.

We see that for $d = \lambda/2$, the beam patterns coincide. For $d = \lambda/4$, the sidelobe level using minimum-sidelobe design is even lower than that of the Dolph-Chebyshev weighting.

Consider a 24-element uniform circular array (UCA) with radius 0.75λ located in the xy -plane. We design the beam pattern using the minimum-sidelobe design for the case when the steering direction is at $\theta_0 = 0^\circ$.

We choose $BW_{\text{SL}} = 80^\circ$. The resulting beam pattern is plotted in Fig. 3.11. This method achieves a very low sidelobe level.

The conventional DAS beam pattern is also plotted in this figure for comparison purposes. Its sidelobe level is about -7.9 dB, which may be too high for many applications.

For the MSL beamformer, the norm of the resulting weight vector in dB is 8.78 dB, which may be too high and will lead to poor robustness.

The RMSL method in Eq. (3.94) is used to design the weight vector, in which the constraint value ξ_0 is chosen to be $\xi_0 = (1/M) \times 10^{G_{\text{wd0}}/10}$ with G_{wd0} being the prescribed WNG loss as defined in Eq. (3.20). The resulting beam patterns for various values of G_{wd0} are shown in Fig. 3.12. As the prescribed WNG loss G_{wd0} increases, the sidelobe level decreases.

2. Low-sidelobe adaptive beamformer

The windows can be used to decrease the sidelobes. Using the window technique as in Eq. (3.88), the MVDR beamformer in Eq. (3.1) can be modified to

$$\mathbf{w} = \alpha \mathbf{R}^{-1} (\mathbf{w}_d \circ \bar{\mathbf{p}}_s), \tag{3.95}$$

where \mathbf{w}_d is the window as described in Sect. 3.3.1 and $\bar{\mathbf{p}}_s$ is the nominal steering vector corresponding to the signal of interest.

Fig. 3.10 Beam patterns of a 10-element ULA,
a $d = \lambda/2$, **b** $d = \lambda/4$

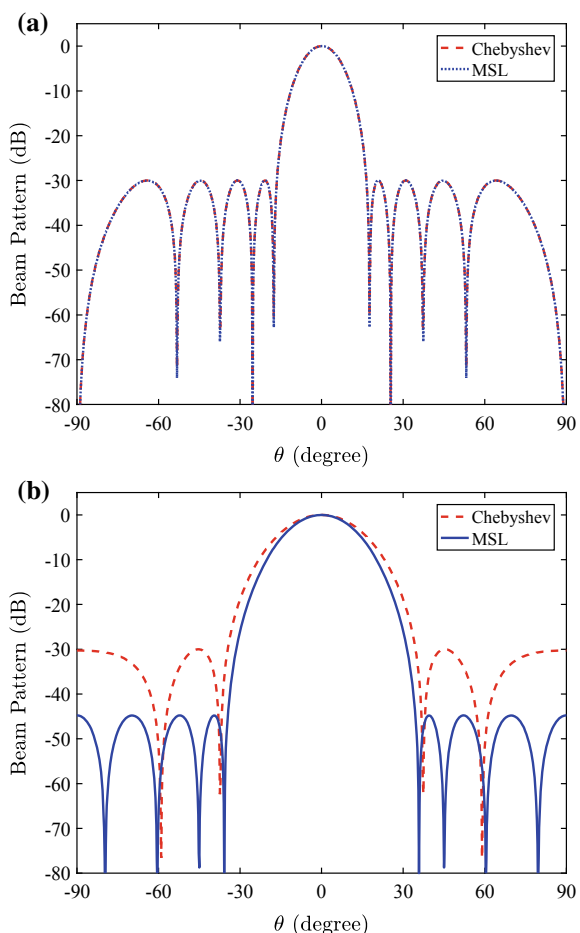


Fig. 3.11 Beam patterns of 24-element UCA

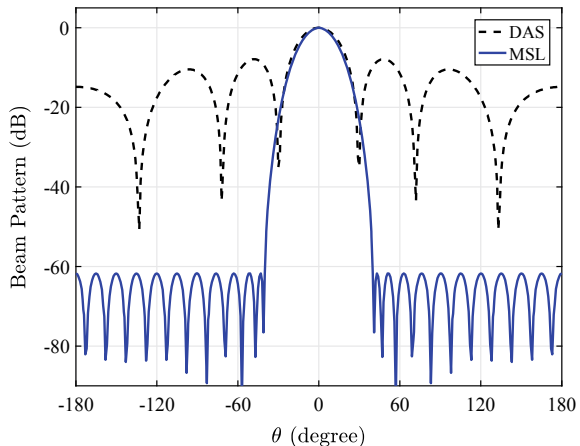


Fig. 3.12 Beam patterns of 24-element UCA using RMSL method

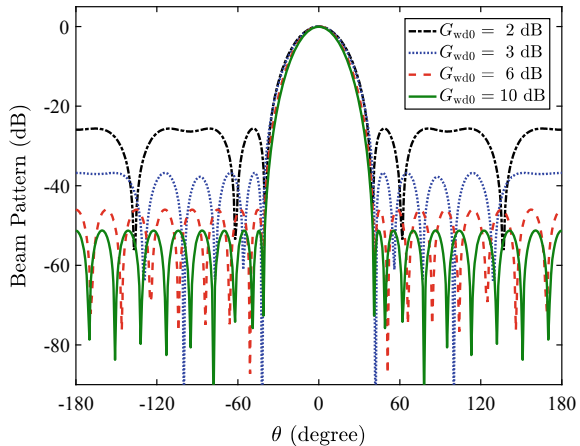
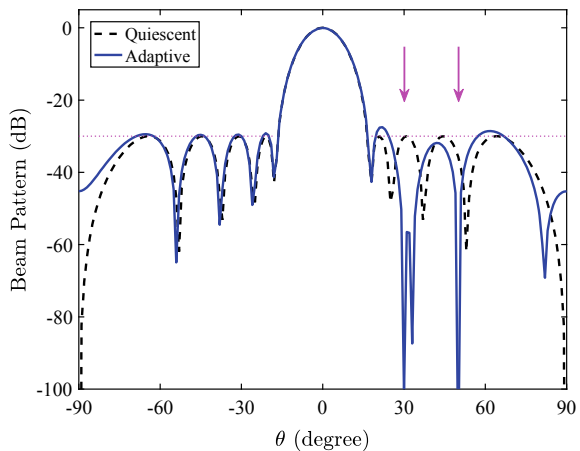


Fig. 3.13 Low-sidelobe adaptive beam pattern



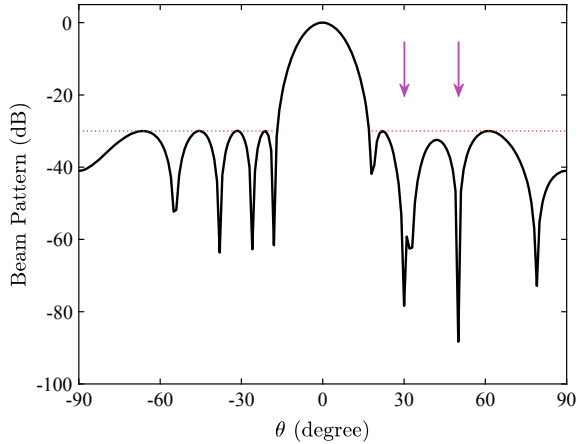
The beam pattern of an adaptive beamformer in the presence of white noise is referred to as the quiescent pattern. The quiescent weight vector corresponding to that in Eq. (3.95) is given by

$$\mathbf{w}_q = \alpha(\mathbf{w}_d \circ \bar{\mathbf{p}}_s). \quad (3.96)$$

Consider a 10-element uniform linear array with half-wavelength spacing. In addition to the white noise interference, we assume that there are two uncorrelated plane-wave interferers located at 30° and 50° , with interference-to-noise ratios (INRs) of 25 and 30 dB, respectively.

The Dolph-Chebyshev weighting with -30 -dB sidelobes is used for the quiescent pattern. The adaptive beam pattern using Eq. (3.95) is plotted in Fig. 3.13.

Fig. 3.14 Beam pattern using RSLC method



We see that the sidelobes of the adaptive beam pattern are slightly higher than -30 dB.

3. High array gain with sidelobe control

The MVDR beamformer can provide a high array gain. In order to control the sidelobes, the following multiple inequality constraints

$$|\mathbf{w}^H \mathbf{p}(\theta_i)| \leq \xi_{0i}, \quad \theta_i \in \Theta_{\text{SL}}, \quad i = 1, \dots, N_{\text{SL}} \quad (3.97)$$

can be imposed in the sidelobe region. In Eq. (3.97), ξ_{0i} ($i = 1, \dots, N_{\text{SL}}$) are the specified values to control the sidelobes. For the constant value of ξ_{0i} , the constant sidelobes can be obtained.

The constraints in Eq. (3.97) can be added to the norm constrained MVDR beamformer in Eq. (3.17) as

$$\begin{aligned} & \min_{\mathbf{w}} \mathbf{w}^H \mathbf{R} \mathbf{w}, \\ & \text{subject to } \mathbf{w}^H \mathbf{p}(\theta_s) = 1, \\ & |\mathbf{w}^H \mathbf{p}(\theta_i)| \leq \xi_{0i}, \quad \theta_i \in \Theta_{\text{SL}}, \quad i = 1, 2, \dots, N_{\text{SL}}, \\ & \|\mathbf{w}\| \leq \sqrt{\xi_0}. \end{aligned} \quad (3.98)$$

This optimization problem can be reformulated in a convex form as an SOCP problem which is computationally tractable.

The resulting beamformer is referred to as the robust sidelobe constrained (RSLC) beamformer, whose weight vector is termed as \mathbf{w}_{RSLC} .

For the same cases as in Fig. 3.13, the beam pattern using RSLC method as given by Eq. (3.98) is plotted in Fig. 3.14, in which the constraint value ξ_0 is chosen to be $\xi_0 = (1/M) \times 10^{2/10}$.

Comparing to Fig. 3.13, the sidelobes in Fig. 3.14 are strictly controlled to be below -30 dB.

In the white noise case where $\mathbf{R} = \mathbf{I}$, Eq. (3.98) reduces to

$$\begin{aligned} & \min_{\mathbf{w}} \mathbf{w}^H \mathbf{w}, \\ & \text{subject to } \mathbf{w}^H \mathbf{p}(\theta_s) = 1, \\ & |\mathbf{w}^H \mathbf{p}(\theta_i)| \leq \xi_{0i}, \quad \theta_i \in \Theta_{\text{SL}}, \quad i = 1, 2, \dots, N_{\text{SL}}. \end{aligned} \quad (3.99)$$

Note that the weight vector norm constraint is removed since the weight vector has already appeared in the cost function. The beamformer results in the robustness that is the maximum possible for the given sidelobe level.

In many cases, we would prefer that the sidelobes decay rather than remain constant. For the 10-element uniform linear array, assume that we want to obtain a beam pattern whose sidelobes satisfy the specified envelope shown by the dashed lines in Fig. 3.15. The resulting beams using the method as given by Eq. (3.99) are shown in solid lines in Fig. 3.15. The resulting beam patterns satisfy the sidelobe requirements strictly. In Fig. 3.15b, a notch with a width of 5° and a depth of -60 dB is achieved.

Consider the case of volumetric arrays.

The geometry of a 121-element hemispherical array with a radius of $(19/6)\lambda$ is shown in Fig. 3.16a. The steering direction is $\Omega_0 = (\theta_0, \phi_0) = (0^\circ, 0^\circ)$. The conventional beam pattern steered to $(0^\circ, 0^\circ)$ is shown in Fig. 3.16c. The sidelobe level is about -13.8 dB.

Assume that the design objective is to achieve a notch in the direction $(\theta, \phi) = (45^\circ, 50^\circ)$ with a width of 20° and a depth of -50 dB in addition to the sidelobe level constraint of -25 dB. The beamwidth is chosen to be $BW_{\text{SL}} = 20^\circ$. Figure 3.16b shows the desired sidelobe envelope along the plane $\theta = 45^\circ$ (the right side of the plot is $\theta = 225^\circ$).

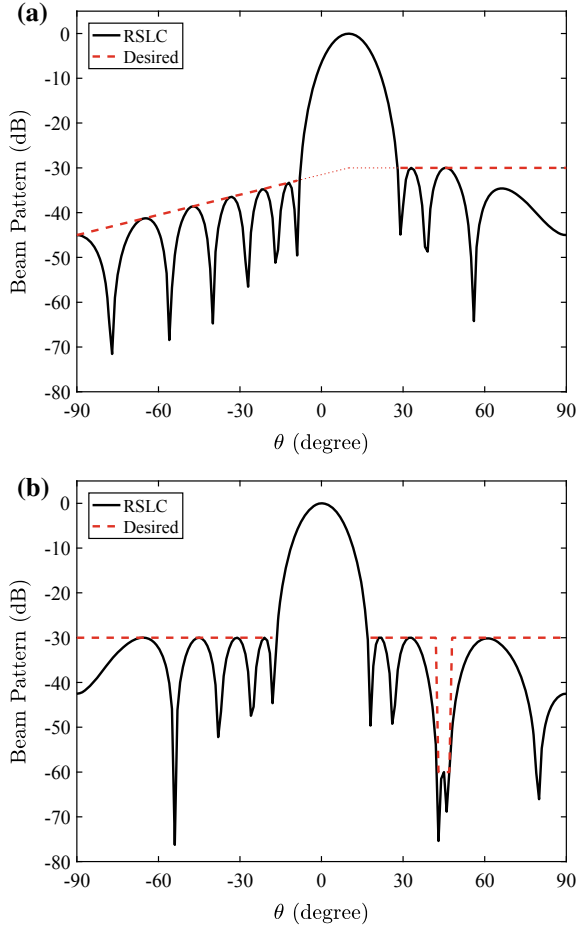
The optimal beam pattern using the method given by Eq. (3.99) is shown in Fig. 3.16d. The resulting sidelobes are strictly controlled to be below -25 dB and a notch in the direction $(45^\circ, 50^\circ)$ is achieved. The resulting WNG loss is only $G_{\text{wd}} = 1.23$ dB.

The vertical beam patterns along the planes $\theta = 45^\circ$ (or 225°) and $\theta = 135^\circ$ (or 315°) are shown in Fig. 3.16e, f, respectively. The sidelobe behavior can be seen clearly.

3.3.3 Robust Against Manifold Uncertainty

In the real-world case, the array manifold vector is generally not accurately known. When errors exist in the array manifold vector, the beam pattern designed using the ideal method will degrade, and the beamformer sidelobe level will increase. A robust pattern synthesis method for arrays with manifold vectors perturbation was developed (see also [23]).

Fig. 3.15 Nonuniform sidelobes



Let $\tilde{\mathbf{p}}(\theta) = [\tilde{p}_1(\theta), \tilde{p}_2(\theta), \dots, \tilde{p}_M(\theta)]^T$ and $\bar{\mathbf{p}}(\theta) = [\bar{p}_1(\theta), \bar{p}_2(\theta), \dots, \bar{p}_M(\theta)]^T$ be the actual and the ideal (presumed) array manifold vectors, respectively. There always exist errors between them.

If the steering direction corresponds to the actual signal direction, i.e., $\theta_o = \theta_s$, using $\bar{\mathbf{p}}(\theta)$ instead of $\mathbf{p}(\theta)$ in Eq. (3.91) and discretizing the visible region, the low-sidelobe beamformer design problem Eq. (3.91) can be rewritten as

$$\begin{aligned} & \min_{\mathbf{w}} B, \\ & \text{subject to } \mathbf{w}^H \bar{\mathbf{p}}(\theta_s) = 1, \end{aligned} \quad (3.100)$$

where $B = \max_{\theta_i \in \Theta_{SL}} |\mathbf{w}^H \bar{\mathbf{p}}(\theta_i)|$ is the sidelobe level. This beamformer is referred to as a nominal optimal beamformer.

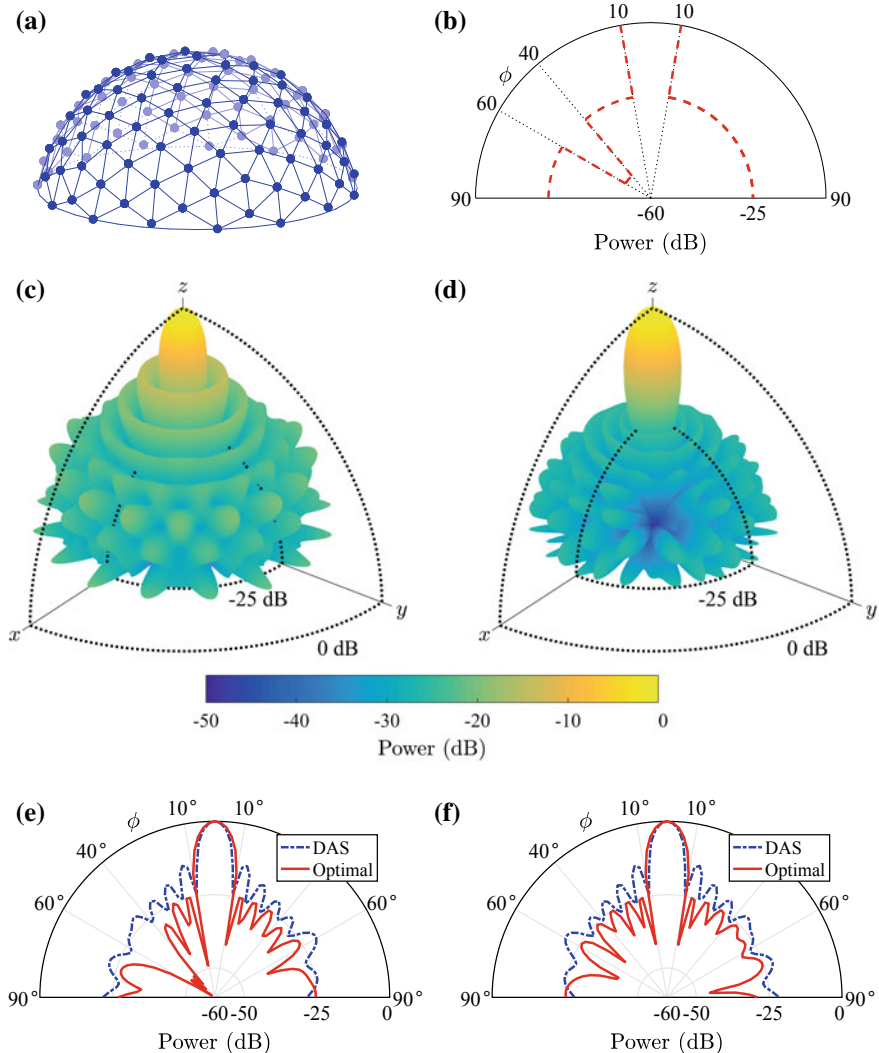


Fig. 3.16 Beam pattern design for volumetric array. **a** Geometry of a hemispherical array of 121 elements. **b** Desired sidelobe envelope in the slice plane $\theta = 45^\circ$ (or 225°). **c** Conventional DAS beam pattern steered to $(\theta_0, \phi_0) = (0^\circ, 0^\circ)$. **d** Optimal beam pattern steered to $(0^\circ, 0^\circ)$. **e** Vertical beam patterns along the plane $\theta = 45^\circ$ (or 225°). **f** Vertical beam patterns along the plane $\theta = 135^\circ$ (or 315°)

In practice, what we want is to minimize the sidelobe level while ensuring that the beam response at the steering direction is not less than unity, i.e.,

$$\begin{aligned} \min_{\mathbf{w}} \max_{\theta_i \in \Theta_{\text{SL}}} |\mathbf{w}^H \tilde{\mathbf{p}}(\theta_i)|, \quad i = 1, 2, \dots, N_{\text{SL}}, \\ \text{subject to } |\mathbf{w}^H \tilde{\mathbf{p}}(\theta_s)| \geq 1. \end{aligned} \quad (3.101)$$

Assume that the actual array manifold vector $\tilde{\mathbf{p}}(\theta)$ is unknown, and the error between $\tilde{\mathbf{p}}(\theta)$ and $\bar{\mathbf{p}}(\theta)$ is an unknown complex vector. This indicates that $\tilde{\mathbf{p}}(\theta)$ can be viewed as belonging to an uncertainty set, i.e., $\tilde{\mathbf{p}}(\theta) \in S(\theta)$. The uncertainty set $S(\theta)$ will be introduced in two cases below.

Thus, the constraint in Eq. (3.101) can be rewritten as

$$|\mathbf{w}^H \mathbf{p}(\theta_s)| \geq 1, \quad \forall \mathbf{p}(\theta_s) \in S(\theta_s). \quad (3.102)$$

Correspondingly, the worst-case sidelobe level becomes

$$B_{\text{wc}}(\mathbf{w}) = \max_{\theta_i \in \Theta_{\text{SL}}} \max_{\mathbf{p}(\theta_i) \in S(\theta_i)} |\mathbf{w}^H \mathbf{p}(\theta_i)|, \quad i = 1, 2, \dots, N_{\text{SL}}. \quad (3.103)$$

Then, using the worst-case optimization criterion, the robust low-sidelobe beam synthesis problem can be formulated as

$$\begin{aligned} \min_{\mathbf{w}} B_{\text{wc}}(\mathbf{w}), \\ \text{subject to } \min_{\mathbf{p}(\theta_s) \in S(\theta_s)} |\mathbf{w}^H \mathbf{p}(\theta_s)| \geq 1. \end{aligned} \quad (3.104)$$

1. ℓ_2 -norm regularization

Assume that the array manifold vector distortion is norm-bounded, i.e.,

$$\|\tilde{\mathbf{p}}(\theta) - \bar{\mathbf{p}}(\theta)\| \leq \varepsilon(\theta), \quad \theta \in \Theta, \quad (3.105)$$

where $\varepsilon(\theta)$ is assumed to be known.

Then, the actual array manifold vector uncertainty set $S(\theta)$ becomes the following ellipsoidal uncertainty set $S_2(\theta)$:

$$S_2(\theta) \triangleq \{\mathbf{p}(\theta) | \mathbf{p}(\theta) = \bar{\mathbf{p}}(\theta) + \mathbf{p}_\Delta(\theta), \|\mathbf{p}_\Delta(\theta)\| \leq \varepsilon(\theta)\}, \quad \theta \in \Theta. \quad (3.106)$$

For any $\mathbf{p}(\theta_s) \in S_2(\theta_s)$, we have

$$\begin{aligned} |\mathbf{w}^H \mathbf{p}(\theta_s)| &= |\mathbf{w}^H \bar{\mathbf{p}}(\theta_s) + \mathbf{w}^H \mathbf{p}_\Delta(\theta_s)| \\ &\geq |\mathbf{w}^H \bar{\mathbf{p}}(\theta_s)| - |\mathbf{w}^H \mathbf{p}_\Delta(\theta_s)| \\ &\geq |\mathbf{w}^H \bar{\mathbf{p}}(\theta_s)| - \|\mathbf{p}_\Delta(\theta_s)\| \cdot \|\mathbf{w}\| \\ &\geq |\mathbf{w}^H \bar{\mathbf{p}}(\theta_s)| - \varepsilon(\theta_s) \|\mathbf{w}\|. \end{aligned} \quad (3.107)$$

Note that $|\mathbf{w}^H \bar{\mathbf{p}}(\theta_s)| \geq \varepsilon(\theta_s) \|\mathbf{w}\|$ is required to guarantee sufficient WNG of a robust beamformer. Moreover, the equality in Eq. (3.107) holds by choosing

$$\mathbf{p}_\Delta(\theta_s) = -\varepsilon(\theta_s)(\mathbf{w}/\|\mathbf{w}\|) \exp\{\mathrm{i}\angle[\mathbf{w}^H \bar{\mathbf{p}}(\theta_s)]\}. \quad (3.108)$$

Therefore,

$$\min_{\mathbf{p}(\theta_s) \in S_2(\theta_s)} |\mathbf{w}^H \mathbf{p}(\theta_s)| = |\mathbf{w}^H \bar{\mathbf{p}}(\theta_s)| - \varepsilon(\theta_s) \|\mathbf{w}\|. \quad (3.109)$$

Similarly,

$$\max_{\mathbf{p}(\theta_i) \in S_2(\theta_i)} |\mathbf{w}^H \mathbf{p}(\theta_i)| = |\mathbf{w}^H \bar{\mathbf{p}}(\theta_i)| + \varepsilon(\theta_i) \|\mathbf{w}\|, \quad i = 1, 2, \dots, N_{\text{SL}}. \quad (3.110)$$

The equality of Eq. (3.110) holds with the choice of

$$\mathbf{p}_\Delta(\theta_i) = \varepsilon(\theta_i)(\mathbf{w}/\|\mathbf{w}\|) \exp\{\mathrm{i}\angle[\mathbf{w}^H \bar{\mathbf{p}}(\theta_i)]\}. \quad (3.111)$$

Substituting Eq. (3.110) into Eq. (3.103) gives

$$B_{\text{wc}}(\mathbf{w}) = \max_{\theta_i \in \Theta_{\text{SL}}} [|\mathbf{w}^H \bar{\mathbf{p}}(\theta_i)| + \varepsilon(\theta_i) \|\mathbf{w}\|], \quad i = 1, 2, \dots, N_{\text{SL}}. \quad (3.112)$$

Using Eqs. (3.109) and (3.112) in Eq. (3.104) gives

$$\begin{aligned} & \min_{\mathbf{w}} \max_{\theta_i \in \Theta_{\text{SL}}} [|\mathbf{w}^H \bar{\mathbf{p}}(\theta_i)| + \varepsilon(\theta_i) \|\mathbf{w}\|], \quad i = 1, 2, \dots, N_{\text{SL}}, \\ & \text{subject to } |\mathbf{w}^H \bar{\mathbf{p}}(\theta_s)| - \varepsilon(\theta_s) \|\mathbf{w}\| \geq 1. \end{aligned} \quad (3.113)$$

Although this optimization problem is non-convex, it can be converted to a convex problem. Using the fact that the cost function in Eq. (3.113) is unchanged when \mathbf{w} undergoes an arbitrary phase rotation, if \mathbf{w}_{opt} is a solution to Eq. (3.113), we can adjust its phase until $\mathbf{w}^H \bar{\mathbf{p}}(\theta_s)$ becomes a real number without affecting the value of the cost function. Thus the solution to Eq. (3.113) can be written as

$$\begin{aligned} & \min_{\mathbf{w}} \max_{\theta_i \in \Theta_{\text{SL}}} [|\mathbf{w}^H \bar{\mathbf{p}}(\theta_i)| + \varepsilon(\theta_i) \|\mathbf{w}\|], \quad i = 1, 2, \dots, N_{\text{SL}}, \\ & \text{subject to } \mathbf{w}^H \bar{\mathbf{p}}(\theta_s) \geq 1 + \varepsilon(\theta_s) \|\mathbf{w}\|. \end{aligned} \quad (3.114)$$

This is a convex problem and its solution can be obtained using an SOCP solver. The optimization problem is referred to as the ℓ_2 regularization of the robust pattern synthesis problem.

2. ℓ_1 -norm regularization

We next assume that the absolute value of each elements of the array manifold vector error is bounded by some known value. Then the actual array manifold vector belongs to the following uncertainty set $S_1(\theta)$

$$S_1(\theta) \triangleq \{ \mathbf{p}(\theta) | \mathbf{p}(\theta) = \bar{\mathbf{p}}(\theta) + \mathbf{p}_\Delta(\theta), |p_{\Delta m}(\theta)| \leq \delta_m(\theta) \}, \quad \theta \in \Theta, \quad (3.115)$$

where $\delta_m(\theta)$ is the specified upper bound on the error, and $p_{\Delta m}(\theta)$ is the m th element of the array manifold error $\mathbf{p}_\Delta(\theta)$

$$\mathbf{p}_\Delta(\theta) = [p_{\Delta 1}(\theta), \dots, p_{\Delta m}(\theta), \dots, p_{\Delta M}(\theta)]^T. \quad (3.116)$$

For the optimization problem in Eq. (3.104), similar to Eq. (3.107), for any $\mathbf{p}(\theta_s) \in S_1(\theta_s)$, we have

$$\begin{aligned} |\mathbf{w}^H \mathbf{p}(\theta_s)| &= |\mathbf{w}^H \bar{\mathbf{p}}(\theta_s) + \mathbf{w}^H \mathbf{p}_\Delta(\theta_s)| \\ &\geq |\mathbf{w}^H \bar{\mathbf{p}}(\theta_s)| - |\mathbf{w}^H \mathbf{p}_\Delta(\theta_s)| \\ &\geq |\mathbf{w}^H \bar{\mathbf{p}}(\theta_s)| - \sum_{m=1}^M [|\mathbf{w}_m^*| \cdot |p_{\Delta m}(\theta_s)|] \\ &\geq |\mathbf{w}^H \bar{\mathbf{p}}(\theta_s)| - \sum_{m=1}^M [\delta_m(\theta_s) |w_m|]. \end{aligned} \quad (3.117)$$

The equality of Eq. (3.117) holds with the choice of

$$p_{\Delta m}(\theta_s) = -\delta_m(\theta_s) (w_m / |w_m|) \exp\{i\angle[\mathbf{w}^H \bar{\mathbf{p}}(\theta_s)]\}. \quad (3.118)$$

Therefore,

$$\min_{\mathbf{p}(\theta_s) \in S_1(\theta_s)} |\mathbf{w}^H \mathbf{p}(\theta_s)| = |\mathbf{w}^H \bar{\mathbf{p}}(\theta_s)| - \sum_{m=1}^M [\delta_m(\theta_s) |w_m|]. \quad (3.119)$$

Similarly,

$$\max_{\mathbf{p}(\theta_i) \in S_1(\theta_i)} |\mathbf{w}^H \mathbf{p}(\theta_i)| = |\mathbf{w}^H \bar{\mathbf{p}}(\theta_i)| + \sum_{m=1}^M [\delta_m(\theta_i) |w_m|], \quad i = 1, 2, \dots, N_{\text{SL}}. \quad (3.120)$$

The equality of Eq. (3.120) holds with the choice of

$$p_{\Delta m}(\theta_i) = \delta_m(\theta_i) (w_m / |w_m|) \exp\{i\angle[\mathbf{w}^H \bar{\mathbf{p}}(\theta_i)]\}. \quad (3.121)$$

Substituting Eqs. (3.119) and (3.120) into Eq. (3.104) gives

$$\begin{aligned} \min_{\mathbf{w}} \max_{\theta_i \in \Theta_{\text{SL}}} & \left\{ \left| \mathbf{w}^H \bar{\mathbf{p}}(\theta_i) \right| + \sum_{m=1}^M [\delta_m(\theta_i) |w_m|] \right\}, \quad i = 1, 2, \dots, N_{\text{SL}}, \\ \text{subject to} \quad & \left| \mathbf{w}^H \bar{\mathbf{p}}(\theta_s) \right| - \sum_{m=1}^M [\delta_m(\theta_s) |w_m|] \geq 1. \end{aligned} \quad (3.122)$$

Using the fact that the cost function in Eq. (3.122) is unchanged when \mathbf{w} undergoes an arbitrary phase rotation, we can assume that $\mathbf{w}^H \bar{\mathbf{p}}(\theta_s)$ is a real number, thus Eq. (3.122) can be rewritten as

$$\begin{aligned} \min_{\mathbf{w}} \max_{\theta_i \in \Theta_{\text{SL}}} & \left\{ \left| \mathbf{w}^H \bar{\mathbf{p}}(\theta_i) \right| + \sum_{m=1}^M [\delta_m(\theta_i) |w_m|] \right\}, \quad i = 1, 2, \dots, N_{\text{SL}}, \\ \text{subject to} \quad & \mathbf{w}^H \bar{\mathbf{p}}(\theta_s) \geq 1 + \sum_{m=1}^M [\delta_m(\theta_s) |w_m|]. \end{aligned} \quad (3.123)$$

This is a convex optimization problem that can be formulated as an SOCP problem and solved using an SOCP solver. This optimization problem is referred to as the ℓ_1 regularization of the robust pattern synthesis problem.

3. A lower bound on sidelobes

The lower bounds of the worst-case sidelobe level of the two robust pattern synthesis methods are derived below.

For the ℓ_2 regularization method, assume that the upper bounds on the array manifold error norm of all directions are identical, i.e., $\varepsilon(\theta) = \varepsilon$ for all θ .

Let \mathbf{w}_{nom} be the solution to the optimization problem Eq. (3.100) and B_{nom} be the obtained highest sidelobes. Then,

$$B_{\text{nom}} = \max_{\theta_i \in \Theta_{\text{SL}}} \left| \mathbf{w}_{\text{nom}}^H \bar{\mathbf{p}}(\theta_i) \right|, \quad i = 1, 2, \dots, N_{\text{SL}}. \quad (3.124)$$

Note that an equivalent problem to Eq. (3.100) is

$$\begin{aligned} \min_{\mathbf{w}} & B, \\ \text{subject to} \quad & \mathbf{w}^H \bar{\mathbf{p}}(\theta_s) \geq 1. \end{aligned} \quad (3.125)$$

This equivalence can be proved by contradiction as follows. If the minimum value of the objective function in Eq. (3.125) is achieved when $\bar{B} \triangleq \mathbf{w}^H \bar{\mathbf{p}}(\theta_s) > 1$, by replacing \mathbf{w} with \mathbf{w}/\bar{B} , the objective function will decrease while the inequality constraint will be still satisfied. Therefore, the optimum value of the objective function is obtained when $\mathbf{w}^H \bar{\mathbf{p}}(\theta_s) = 1$. Thus the optimization problem in Eq. (3.125) is equivalent to that in Eq. (3.100).

Assume that the solution to the optimization problem Eq. (3.114) is \mathbf{w}_{rob2} . Clearly, \mathbf{w}_{rob2} satisfies the constraint in Eq. (3.125). Thus,

$$\max_{\theta_i \in \Theta_{\text{SL}}} |\mathbf{w}_{\text{rob2}}^H \bar{\mathbf{p}}(\theta_i)| \geq \max_{\theta_i \in \Theta_{\text{SL}}} |\mathbf{w}_{\text{nom}}^H \bar{\mathbf{p}}(\theta_i)|. \quad (3.126)$$

Let B_{rob2} be the resulting worst-case sidelobe level by using the ℓ_2 regularization method. Substituting \mathbf{w}_{rob2} into Eq. (3.112) gives

$$B_{\text{rob2}} \triangleq B_{\text{wc}}(\mathbf{w}_{\text{rob2}}) = \max_{\theta_i \in \Theta_{\text{SL}}} [|\mathbf{w}_{\text{rob2}}^H \bar{\mathbf{p}}(\theta_i)| + \varepsilon \|\mathbf{w}_{\text{rob2}}\|]. \quad (3.127)$$

From Eqs. (3.124), (3.126) and (3.127), we have

$$B_{\text{rob2}} - B_{\text{nom}} \geq \varepsilon \cdot \|\mathbf{w}_{\text{rob2}}\|. \quad (3.128)$$

From the constraint in Eq. (3.114), we have

$$\varepsilon \|\mathbf{w}_{\text{rob2}}\| + 1 \leq \mathbf{w}_{\text{rob2}}^H \bar{\mathbf{p}}(\theta_s) = \|\mathbf{w}_{\text{rob2}}\| \cdot \|\bar{\mathbf{p}}(\theta_s)\|. \quad (3.129)$$

Note that the equality on the right side of Eq. (3.129) holds because $\mathbf{w}_{\text{rob2}}^H \bar{\mathbf{p}}(\theta_s)$ is a positive real number. Hence, the lower bound on $\|\mathbf{w}_{\text{rob2}}\|$ is given by

$$\|\mathbf{w}_{\text{rob2}}\| \geq 1 / [\|\bar{\mathbf{p}}(\theta_s)\| - \varepsilon]. \quad (3.130)$$

Substituting Eq. (3.130) into Eq. (3.128) gives

$$B_{\text{rob2}} - B_{\text{nom}} \geq \varepsilon / [\|\bar{\mathbf{p}}(\theta_s)\| - \varepsilon]. \quad (3.131)$$

For instance, with 5% uncertainty in the manifold vectors, which corresponds to $\varepsilon = 0.05 \|\bar{\mathbf{p}}(\theta_s)\|$, then

$$B_{\text{rob2}} - B_{\text{nom}} \geq 0.0526. \quad (3.132)$$

Since $B_{\text{nom}} > 0$,

$$B_{\text{rob2}} > 0.0526. \quad (3.133)$$

This indicates that, we cannot achieve a lower worst-case sidelobe level than $20 \lg 0.0526 = -25.6$ dB in the presence of 5% array manifold mismatch, regardless of the array geometry and the number of elements.

It is worth noting that, what we mean here is that the worst-case sidelobe level B_{rob2} cannot be lower than -25.6 dB, however, the actual maximum sidelobe level $\max_{\theta \in \Theta_{\text{SL}}} |\mathbf{w}_{\text{rob2}}^H \tilde{\mathbf{p}}(\theta)|$ can be lower than -25.6 dB.

For the ℓ_1 regularization method, assume that the upper bounds on the array manifold error norm for all directions are identical, i.e., for all θ , $\delta_m(\theta) = \delta_m$, $m = 1, \dots, M$.

Let $\mathbf{w}_{\text{rob1}} = [w_{\text{rob1},1}, \dots, w_{\text{rob1},m}, \dots, w_{\text{rob1},M}]^T$ be the solution to the optimization problem Eq. (3.123). Similar to Eq. (3.127), we can define the worst-case sidelobe of the ℓ_1 regularization method as

$$B_{\text{rob1}} \triangleq B_{\text{wc}}(\mathbf{w}_{\text{rob1}}) = \max_{\theta_i \in \Theta_{\text{SL}}} \left\{ \left| \mathbf{w}_{\text{rob1}}^H \bar{\mathbf{p}}(\theta_i) \right| + \sum_{m=1}^M [\delta_m |w_{\text{rob1},m}|] \right\}. \quad (3.134)$$

Similar to Eq. (3.126), $\max_{\theta_i \in \Theta_{\text{SL}}} \left| \mathbf{w}_{\text{rob1}}^H \bar{\mathbf{p}}(\theta_i) \right| \geq \max_{\theta_i \in \Theta_{\text{SL}}} \left| \mathbf{w}_{\text{nom}}^H \bar{\mathbf{p}}(\theta_i) \right|$. Thus

$$B_{\text{rob1}} - B_{\text{nom}} \geq B_{\text{aux}}, \quad (3.135)$$

where B_{aux} is the minimum cost function of the following optimization problem

$$\begin{aligned} & \min_{\mathbf{w}} \max_{\theta_i \in \Theta_{\text{SL}}} \sum_{m=1}^M [\delta_m |w_m|], \quad i = 1, 2, \dots, N_{\text{SL}}, \\ & \text{subject to} \quad \mathbf{w}^H \bar{\mathbf{p}}(\theta_s) \geq 1 + \sum_{m=1}^M [\delta_m |w_m|]. \end{aligned} \quad (3.136)$$

Since the cost function in Eq. (3.136) is unchanged when each element w_m of \mathbf{w} undergoes an arbitrary phase rotation, we can assume that w_m is a positive real number. Moreover, the phase rotation of w_m can be included in $\bar{\mathbf{p}}_m(\theta_s)$, we can rotate until $\bar{\mathbf{p}}_m(\theta_s) = |\bar{\mathbf{p}}_m(\theta_s)|$. Thus, Eq. (3.136) can be rewritten as the following equivalent optimization problem [24]

$$\begin{aligned} & \min_{\mathbf{w}} \max_{\theta_i \in \Theta_{\text{SL}}} \sum_{m=1}^M [\delta_m w_m], \quad i = 1, 2, \dots, N_{\text{SL}}, \\ & \text{subject to} \quad \sum_{m=1}^M |\bar{\mathbf{p}}_m(\theta_s)| w_m \geq 1 + \sum_{m=1}^M [\delta_m w_m]. \end{aligned} \quad (3.137)$$

This is a linear programming problem. Ideally, $|\bar{\mathbf{p}}_m(\theta_s)| = 1$. Assuming $\delta_m = \delta$ for $m = 1, \dots, M$, the optimum cost function of Eq. (3.137) is given by

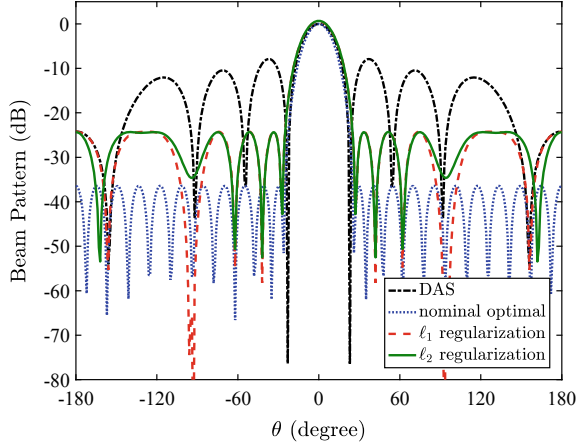
$$B_{\text{aux}} = \delta / (1 - \delta). \quad (3.138)$$

Assume that $\delta = 0.05$, i.e., there is 5% error in array manifold vector, then $B_{\text{aux}} = 0.0526$. Substituting it into Eq. (3.135) gives

$$B_{\text{rob1}} - B_{\text{nom}} \geq 0.0526. \quad (3.139)$$

From Eqs. (3.139) and (3.132), it is seen that B_{rob1} and B_{rob2} have the identical lower bounds.

Fig. 3.17 Beam patterns obtained with the error-free manifold



Consider a 24-element UCA with radius 0.96λ located in the xy -plane. The nominal optimal beamformer shown in Eq. (3.100), the ℓ_1 regularization method shown in Eq. (3.123) and the ℓ_2 regularization method shown in Eq. (3.114) are used. For the ℓ_1 and ℓ_2 regularization methods, we choose $\delta_m(\theta_i) = 0.05$ and $\varepsilon(\theta_i) = 0.05\sqrt{M}$, respectively. The steering direction is chosen to be $\theta_0 = \theta_s = 0^\circ$. The sidelobe region is chosen to be $\Theta_{SL} = [-180^\circ, -25^\circ] \cup [25^\circ, 180^\circ]$, which is sampled using 1° intervals.

In the absence of array manifold errors, the beam patterns obtained using the three methods are shown in Fig. 3.17. For comparison purposes, the conventional DAS beam pattern is also plotted in this figure.

It is seen that the obtained sidelobe level of the DAS beamformer is about 7.9 dB, which may be too high for many applications. The nominal optimal beamformer results in very low sidelobes, which is about -37 dB when there are no array manifold errors. The sidelobe levels of both robust beamformers are about -24 dB, lower than the DAS beamformer and higher than the nominal optimal beamformer.

Keep the weight vectors obtained above unchanged. Consider a case with array manifold errors and assume that each element of the manifold vector for each direction is perturbed with a zero-mean circularly symmetric complex Gaussian random variable and normalized so that $|\tilde{p}_m(\theta) - \bar{p}_m(\theta)| = 0.05$. Correspondingly, $\|\tilde{p}(\theta) - \bar{p}(\theta)\| = 0.05\sqrt{M}$. The perturbing Gaussian random variables are assumed to be independent of each other.

Monte Carlo simulations with 100 repetitions are used to compare the beam patterns of the nominal optimal method and the two robust low-sidelobe methods. The obtained beam patterns of the three beamformers are shown in Fig. 3.18a-c, respectively.

It is seen from Figs. 3.17 and 3.18 that, though the nominal optimal beamformer can obtain a very low sidelobe in the absence of array manifold errors, its sidelobe level increases significantly when errors occur in the array manifold, and its mainlobe

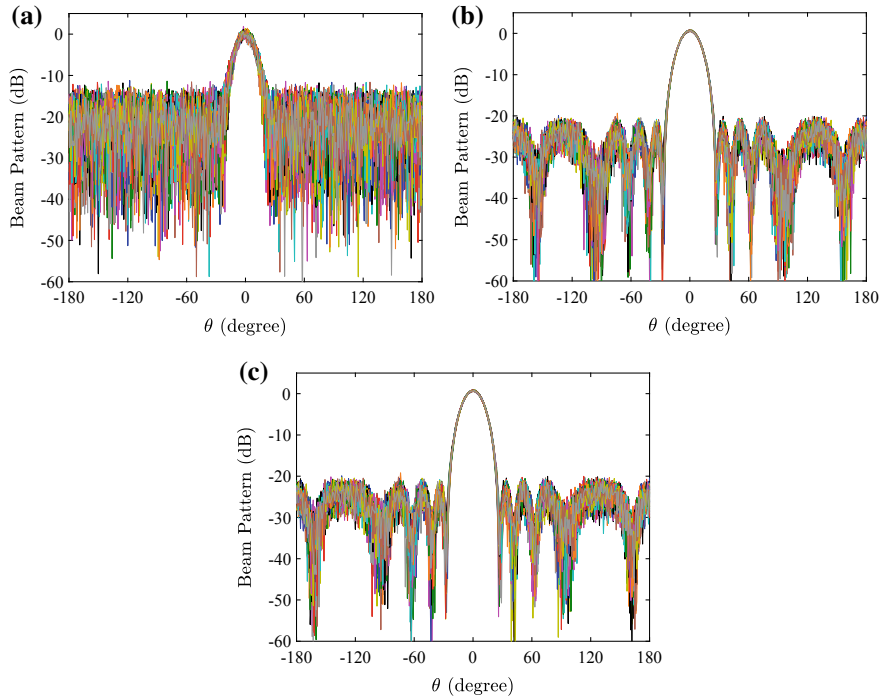


Fig. 3.18 Beam patterns of 100 Monte Carlo simulations in the presence of array manifold errors using **a** the nominal optimal method, **b** the ℓ_1 regularization method, and **c** the ℓ_2 regularization method

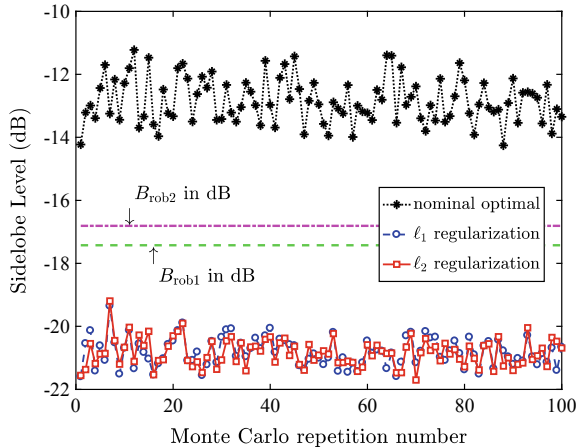
is also distorted in this case. This indicates that this method is not robust against the array manifold perturbation. The performances of beam patterns obtained by the two robust low-sidelobe methods are roughly equivalent. Their mainlobes remain roughly unchanged in the presence of array manifold error and the sidelobes are slightly increased. The two methods have enough robustness against array manifold errors.

The obtained sidelobe levels of the three methods are shown in Fig. 3.19. The worst-case sidelobe levels in dB of the two robust methods (i.e., $20 \lg B_{\text{rob1}}$ and $20 \lg B_{\text{rob2}}$) are also shown in this figure for comparison.

It is seen that, $20 \lg B_{\text{rob2}}$ is approximately 0.6 dB higher than $20 \lg B_{\text{rob1}}$. The actual sidelobe level of the nominal optimal beamformer increases to about -13 dB in the presence of manifold errors, which is approximately 24 dB higher than with no manifold errors. Moreover, in the 100 simulations, the variance of the actual sidelobe level of the nominal optimal beamformer is very high.

The actual sidelobe levels of the two robust methods are about -21 dB, which are approximately 3 dB higher than with no manifold errors. The variance of the sidelobe levels are also moderate. Hence, the results show that the ℓ_1 and ℓ_2 regularization methods improve the robustness against the array manifold perturbation significantly.

Fig. 3.19 Sidelobe levels of three beamformers



3.4 Mainlobe Pattern Synthesis

3.4.1 Norms

Consider a vector (row or column) \mathbf{z} of length N . Without loss of generality, we can let $\mathbf{z} = [z_1, \dots, z_n, \dots, z_N]$. Its ℓ_q -norm can be defined as

$$z_q = \left(\sum_{n=1}^N |z_n|^q \right)^{1/q}. \quad (3.140)$$

Typically, $q = 1, 2$ or ∞ . The ℓ_2 -norm is also referred to as the Euclidean norm, and the ℓ_∞ -norm is also referred to as the Chebyshev norm. The ℓ_2 -norm, $\|\mathbf{z}\|_2$, can also be written as $\|\mathbf{z}\|$ for simplicity. When $q = \infty$, the corresponding ℓ_∞ -norm is given by

$$\|\mathbf{z}\|_q = \max_n |z_n|. \quad (3.141)$$

The beam pattern synthesis problem is to design the weight vector \mathbf{w} of the beamformer so that the obtained beam pattern approximates the desired one, i.e.,

$$B(\theta) \approx B_d(\theta), \quad \forall \theta \in \Theta, \quad (3.142)$$

where $B(\theta) = \mathbf{w}^H \mathbf{p}(\theta)$ and $B_d(\theta)$ are the designed beam pattern (or synthesized beam pattern) and the desired beam pattern at direction θ , respectively, Θ is the visible region where the approximation processing is required to be performed.

Beam pattern synthesis requires minimal synthesis error. The synthesis error can be measured by the weighted norm of the difference between the synthesized beam

pattern and the desired beam pattern. The weighted norm of the difference is given by

$$\delta_q = \left(\int_{\Theta} \lambda(\theta) |B(\theta) - B_d(\theta)|^q d\theta \right)^{1/q}, \quad (3.143)$$

where $q = \infty, 1, 2$, and $\lambda(\theta)$ is a non-negative weighting function used for adjusting the fitting precision at various directions. The larger the weighting function, the higher the design precision at that direction.

In practical applications, the direction can be discretized, and the error norm of the discretized direction is used instead of the error norm in Eq. (3.143). Let $\theta_j \in \Theta$ ($j = 1, \dots, J$) be the discretized direction grids in the visible region Θ , and J be the number of direction grids. There is a trade-off between design precision and the number of grids. For more points, it would lead to better precision but longer computation time, and vice versa. The discretized error norm is given by

$$\delta_q = \left(\sum_{j=1}^J \lambda_j |B(\theta_j) - B_d(\theta_j)|^q \right)^{1/q}, \quad (3.144)$$

$$\theta_j \in \Theta, \quad j = 1, \dots, J.$$

The norm for $q = 2$ and $q = \infty$ corresponds to the mean-square error and the peak error, respectively.

Define the synthesized beam pattern vector $\mathbf{B}(\Theta)$ and the desired beam pattern vector $\mathbf{B}_d(\Theta)$ as

$$\mathbf{B}(\Theta) = [B(\theta_1), \dots, B(\theta_j), \dots, B(\theta_J)], \quad \theta_j \in \Theta, \quad (3.145)$$

$$\mathbf{B}_d(\Theta) = [B_d(\theta_1), \dots, B_d(\theta_j), \dots, B_d(\theta_J)], \quad \theta_j \in \Theta. \quad (3.146)$$

Then Eq. (3.144) can be written in a matrix notation similar to Eq. (3.140) as

$$\delta_q = \|\boldsymbol{\lambda}^{1/q} \circ [\mathbf{B}(\Theta) - \mathbf{B}_d(\Theta)]\|_q, \quad (3.147)$$

where “ \circ ” denotes the element-by-element multiplication of two vectors. $\boldsymbol{\lambda} = [\lambda_1, \dots, \lambda_j, \dots, \lambda_J]$ is the non-negative weighting coefficients vector. Correspondingly, $\boldsymbol{\lambda}^{1/q} = [\lambda_1^{1/q}, \dots, \lambda_j^{1/q}, \dots, \lambda_J^{1/q}]$.

Define the array manifold matrix as

$$\mathbf{P}(\Theta) = [\mathbf{p}(\theta_1), \dots, \mathbf{p}(\theta_j), \dots, \mathbf{p}(\theta_J)], \quad \theta_j \in \Theta. \quad (3.148)$$

Then, Eq. (3.145) can be written as

$$\mathbf{B}(\Theta) = \mathbf{w}^H \mathbf{P}(\Theta). \quad (3.149)$$

3.4.2 Least Squares Error Pattern Synthesis

If we choose $q = 2$, Eq. (3.147) becomes

$$\delta_2 = \|\lambda^{1/2} \circ (\mathbf{B} - \mathbf{B}_d)\|_2 = \left(\|\lambda^{1/2} \circ (\mathbf{w}^H \mathbf{P} - \mathbf{B}_d)\|^2 \right)^{1/2}, \quad (3.150)$$

where the Θ dependence have been suppressed.

Then, the least squares error pattern synthesis problem can be formulated as

$$\min_{\mathbf{w}} \|\lambda^{1/2} \circ (\mathbf{w}^H \mathbf{P}) - \lambda^{1/2} \circ \mathbf{B}_d\|^2. \quad (3.151)$$

Let

$$\check{\mathbf{P}} = (\mathbf{1}_{M \times 1} \lambda^{1/2}) \circ \mathbf{P}, \quad (3.152)$$

$$\check{\mathbf{B}}_d = \lambda^{1/2} \circ \mathbf{B}_d, \quad (3.153)$$

where $\mathbf{1}_{M \times 1}$ is an $M \times 1$ column vector of ones. The solution to the optimization problem Eq. (3.151) is given by

$$\mathbf{w}_{\text{opt}} = \left(\check{\mathbf{P}} \check{\mathbf{P}}^H \right)^{-1} \check{\mathbf{P}} \check{\mathbf{B}}_d^H. \quad (3.154)$$

When we use the unit weighting, i.e.,

$$\lambda = \mathbf{1}_{1 \times J}, \quad (3.155)$$

the solution is given by

$$\mathbf{w}_{\text{opt}} = (\mathbf{P} \mathbf{P}^H)^{-1} \mathbf{P} \mathbf{B}_d^H. \quad (3.156)$$

Using the least squares error pattern synthesis method, the low-sidelobe beam pattern can be designed by choosing an appropriate desired beam pattern.

Consider a 12-element ULA. Assume that the desired beam response is 1 at $\theta_s = 0^\circ$ and 0 in the sidelobe region $\Theta_{\text{SL}} = [-90^\circ, -\theta_p] \cup [\theta_p, 90^\circ]$, as shown in Fig. 3.20a.

Let $\theta_p = 15^\circ$ and $\Theta = \theta_s \cup \Theta_{\text{SL}}$, which is discretized using a uniform grid of 1° . The least squares solution in Eq. (3.156) is used. The resulting beam pattern is shown in Fig. 3.20b.

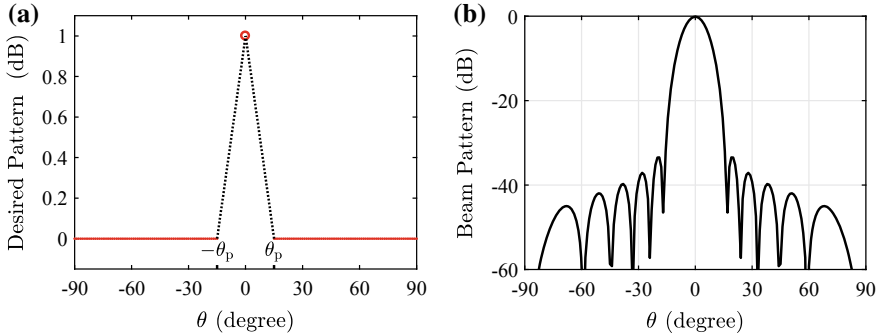
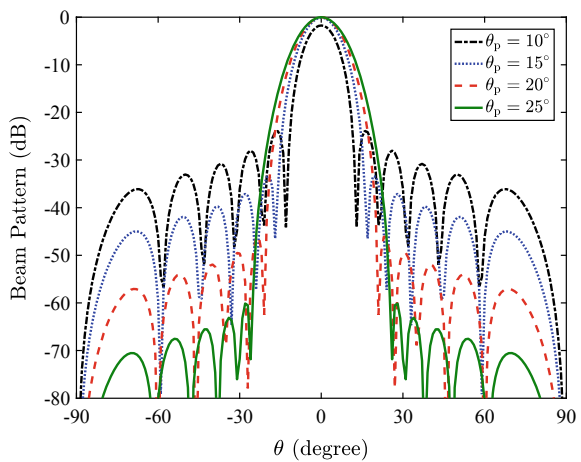


Fig. 3.20 Least squares error pattern synthesis. **a** Desired beam pattern. **b** Synthesized beam pattern

Fig. 3.21 The effect of θ_p on the beamformer design precision



By changing the value of θ_p , different approximation precision can be obtained. The beam patterns for various values of θ_p are shown in Fig. 3.21.

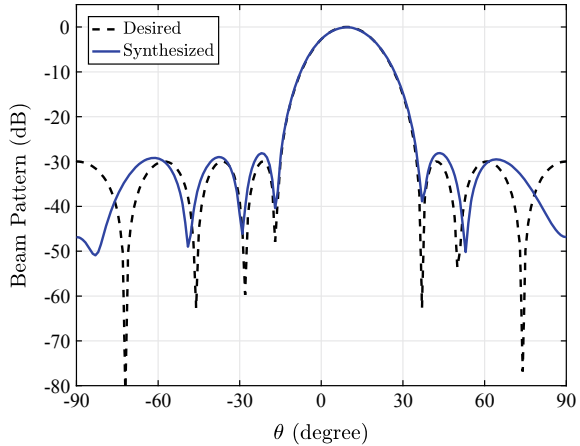
It is seen from Fig. 3.21 that, as the value of θ_p increases, the approximation error between the synthesized beam pattern and the desired one decreases.

Consider a 12-element ULA with a half-wavelength spacing at f_0 . Assume that the desired signal direction is $\theta_s = 10^\circ$. The method in Eq. (3.99) is used to design the beam pattern for frequency $f_0/2$, where we have controlled the sidelobes to be below -30 dB over the sidelobe region $\Theta_{SL} = [-90^\circ, -15^\circ] \cup [35^\circ, 90^\circ]$. The resulting beam pattern is chosen as the desired beam pattern, as shown in Fig. 3.22 by the dashed line.

Design the beam pattern for frequency f_0 using the method in Eq. (3.156) for finding the least squares error approximation to the desired beam pattern. The resulting beam pattern is shown by the solid line in Fig. 3.22.

It is seen from Fig. 3.22 that, the synthesized beam pattern approximates the desired one over the entire visible region $[-90^\circ, 90^\circ]$, but there is approximation

Fig. 3.22 Pattern synthesis using least squares error approximation over $[-90^\circ, 90^\circ]$



error. In addition, it is clearly seen that the sidelobe level of the synthesized beam pattern increases compared to the desired one.

3.4.3 Minimum-Norm Pattern Synthesis

By minimizing the ℓ_∞ -, ℓ_1 - and ℓ_2 -norms of the synthesis error between the synthesized beam pattern and the desired one, respectively, the minimum-norm pattern synthesis problems under the three criteria can be formulated as

$$\min_{\mathbf{w}} \max_{j=1, \dots, J} [\lambda_j |\mathbf{w}^H \mathbf{p}(\theta_j) - B_d(\theta_j)|], \quad \theta_j \in \Theta, \quad (3.157)$$

$$\min_{\mathbf{w}} \sum_{j=1}^J [\lambda_j |\mathbf{w}^H \mathbf{p}(\theta_j) - B_d(\theta_j)|], \quad \theta_j \in \Theta, \quad (3.158)$$

$$\min_{\mathbf{w}} \sum_{j=1}^J [\lambda_j |\mathbf{w}^H \mathbf{p}(\theta_j) - B_d(\theta_j)|^2], \quad \theta_j \in \Theta. \quad (3.159)$$

The ℓ_∞ -norm criterion is also referred to as the Minimax criterion or Chebyshev criterion, and the ℓ_2 -norm criterion is also referred to as the least squares criterion, which leads to a quadratic minimization problem.

For the optimization problem in Eq. (3.157), introducing a new variable δ , it can be rewritten as

$$\min_{\mathbf{w}} \delta, \quad \lambda_j |\mathbf{w}^H \mathbf{p}(\theta_j) - B_d(\theta_j)| \leq \delta, \quad \theta_j \in \Theta, j = 1, \dots, J. \quad (3.160)$$

For the optimization problem Eq. (3.158), introducing new variables δ_j , $j = 1, \dots, J$, it can be rewritten as

$$\min_{\mathbf{w}} \sum_{j=1}^J \delta_j, \quad \lambda_j |\mathbf{w}^H \mathbf{p}(\theta_j) - B_d(\theta_j)| \leq \delta_j, \quad \theta_j \in \Theta, \quad j = 1, \dots, J. \quad (3.161)$$

For the optimization problem Eq. (3.159), introducing a new variable δ , it can be rewritten as

$$\min_{\mathbf{w}} \delta^2, \quad \left(\sum_{j=1}^J \left| \lambda_j^{1/2} \mathbf{w}^H \mathbf{p}(\theta_j) - \lambda_j^{1/2} B_d(\theta_j) \right|^2 \right)^{1/2} \leq \delta, \quad \theta_j \in \Theta, \quad (3.162)$$

which is equivalent to the following SOCP problem

$$\min_{\mathbf{w}} \delta, \quad \left\| \begin{array}{l} \lambda_1^{1/2} \mathbf{w}^H \mathbf{p}(\theta_1) - \lambda_1^{1/2} B_d(\theta_1) \\ \lambda_2^{1/2} \mathbf{w}^H \mathbf{p}(\theta_2) - \lambda_2^{1/2} B_d(\theta_2) \\ \vdots \\ \lambda_J^{1/2} \mathbf{w}^H \mathbf{p}(\theta_J) - \lambda_J^{1/2} B_d(\theta_J) \end{array} \right\| \leq \delta, \quad \theta_j \in \Theta. \quad (3.163)$$

Alternatively, the optimization problem in Eq. (3.159) can also be formulated as another SOCP problem. Introducing new variables δ_j^2 , $j = 1, \dots, J$, Eq. (3.159) can be rewritten as

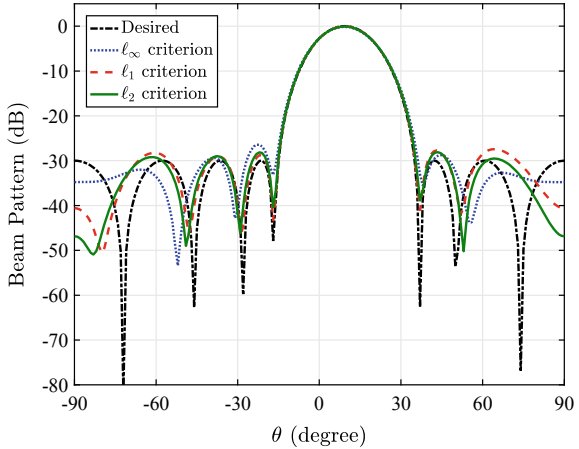
$$\begin{aligned} & \min_{\mathbf{w}} \sum_{j=1}^J (\lambda_j \delta_j^2), \\ & \text{subject to } |\mathbf{w}^H \mathbf{p}(\theta_j) - B_d(\theta_j)|^2 \leq \delta_j^2, \quad \theta_j \in \Theta. \end{aligned} \quad (3.164)$$

Since

$$\begin{aligned} & |\mathbf{w}^H \mathbf{p}(\theta_j) - B_d(\theta_j)|^2 \leq \delta_j^2 \\ & \Leftrightarrow |2B_d(\theta_j) - 2\mathbf{w}^H \mathbf{p}(\theta_j)|^2 \leq 4\delta_j^2 \\ & \Leftrightarrow |2B_d(\theta_j) - 2\mathbf{w}^H \mathbf{p}(\theta_j)|^2 + 1 + \delta_j^4 - 2\delta_j^2 \leq 1 + \delta_j^4 + 2\delta_j^2 \\ & \Leftrightarrow \left\| \begin{array}{l} 2B_d(\theta_j) - 2\mathbf{w}^H \mathbf{p}(\theta_j) \\ \delta_j^2 - 1 \end{array} \right\|^2 \leq (\delta_j^2 + 1)^2 \\ & \Leftrightarrow \left\| \begin{array}{l} 2B_d(\theta_j) - 2\mathbf{w}^H \mathbf{p}(\theta_j) \\ \delta_j^2 - 1 \end{array} \right\| \leq \delta_j^2 + 1, \end{aligned} \quad (3.165)$$

Equation (3.159) becomes

Fig. 3.23 Minimum-norm pattern synthesis



$$\begin{aligned}
 & \min_{\mathbf{w}} \sum_{j=1}^J \lambda_j \delta_j^2, \\
 \text{subject to} \quad & \left\| \frac{2B_d(\theta_j) - 2\mathbf{w}^H \mathbf{p}(\theta_j)}{\delta_j^2 - 1} \right\| \leq \delta_j^2 + 1, \quad \theta_j \in \Theta. \quad (3.166)
 \end{aligned}$$

Unlike the least squares method discussed in Sect. 3.4.2, an important advantage of the SOCP methods used here is that it is very convenient to include additional linear or convex quadratic constraints to the design problem. Thus, the norm constraint on the weight vector \mathbf{w} , i.e.,

$$\|\mathbf{w}\|^2 \leq \zeta_0 \quad (3.167)$$

can be imposed to the beam pattern synthesis problems to improve the robustness of the beamformer.

For the same cases as in Fig. 3.22, we choose $\lambda_j = 1$ and ignore the norm constraint on the weight vector temporarily. The resulting beam patterns designed using the minimum-norm pattern synthesis methods under three criteria are shown in Fig. 3.23.

It is seen from Fig. 3.23 that, the methods under the three criteria approximate the desired beam pattern with different fitting precision. Note that the synthesized beam pattern according to the ℓ_2 criterion is identical to that designed using the least squares method shown in Fig. 3.22.

The synthesis errors between the synthesized beam patterns obtained by the three criteria and the desired beam pattern, i.e., $|B(\theta_j) - B_d(\theta_j)|$, for $\theta_j \in \Theta$, are shown in Fig. 3.24.

Using Eq. (3.144), the ℓ_∞ -, ℓ_1 - and ℓ_2 -norms of the synthesis errors by the three criteria are calculated and shown in Table 3.1, where δ_2 is divided by \sqrt{J} to convert

Fig. 3.24 Synthesis errors between synthesized and desired beam patterns

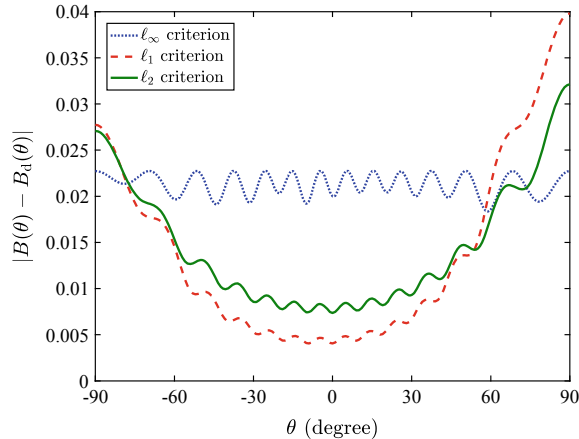


Table 3.1 Comparison of the norms of the synthesis errors by the three criteria

Methods	δ_∞	δ_1/J	δ_2/\sqrt{J}
ℓ_∞ criterion	0.0227	0.0213	0.0213
ℓ_1 criterion	0.0398	0.0138	0.0171
ℓ_2 criterion	0.0321	0.0145	0.0160

the ℓ_2 -norm of the error to the root-mean-square error, and δ_1 is divided by J to convert the ℓ_1 -norm of the error to the average value of the absolute error.

It is seen from Table 3.1 that, the value of δ_∞ by the ℓ_∞ criterion is the smallest among the three criteria, so do the value of δ_1 by the ℓ_1 criterion and the value of δ_2 by the ℓ_2 criterion, as indicated by the bold numbers in the table. The results meet the design requirements.

3.4.4 Mixed-Norm Pattern Synthesis

1. Problem formulation

In practice, we want the beam pattern to approximate the desired one over the mainlobe region, i.e.,

$$B(\theta) \approx B_d(\theta), \quad \forall \theta \in \Theta_{\text{ML}}, \quad (3.168)$$

where Θ_{ML} is the mainlobe region.

Compared to Eq. (3.142), the entire visible region Θ is replaced by the mainlobe region Θ_{ML} in Eq. (3.168). In this sense, the approximation methods discussed in Sect. 3.4.3 is equivalent to adding redundant constraints in the sidelobe region, which inevitably increases the synthesis error in the mainlobe region. Moreover, the

approximation methods there cannot strictly control the sidelobe level, as can be seen from Fig. 3.23.

Usually, we want to seek a beam pattern that minimizes the weighted approximation error over the mainlobe region subject to the sidelobes constraints, or that minimizes the sidelobe level subject to the weighted approximation error constraint over the mainlobe region. That is, different approximation criteria are respectively used in the mainlobe region and the sidelobe region. The mixed-norm criterion is a more reasonable criterion for the beam pattern synthesis problem.

Let

$$\theta_j \in \Theta_{\text{ML}}, \quad j = 1, \dots, N_{\text{ML}} \quad (3.169)$$

be the discretized direction grids in the mainlobe region.

Replacing the visible region Θ in Eq. (3.144) with the mainlobe region Θ_{ML} , the synthesis error norm over the mainlobe region is given by

$$\delta_q = \left(\sum_{j=1}^{N_{\text{ML}}} \lambda_j |B(\theta_j) - B_d(\theta_j)|^q \right)^{1/q},$$

$$\theta_j \in \Theta_{\text{ML}}, \quad j = 1, \dots, N_{\text{ML}}. \quad (3.170)$$

2. Sidelobe constrained mainlobe pattern synthesis

We consider the problem of finding the least squares error approximation to a desired pattern subject to the sidelobes and the WNG constraints. This pattern synthesis problem can be formulated as [12]

$$\min_{\mathbf{w}} \sum_{j=1}^{N_{\text{ML}}} \left[\lambda_j |\mathbf{w}^H \mathbf{p}(\theta_j) - B_d(\theta_j)|^2 \right], \quad \theta_j \in \Theta_{\text{ML}}, \quad j = 1, \dots, N_{\text{ML}},$$

$$\text{subject to} \quad |\mathbf{w}^H \mathbf{p}(\theta_j)| \leq \xi_{0i}, \quad \theta_i \in \Theta_{\text{SL}}, \quad i = 1, \dots, N_{\text{SL}},$$

$$\|\mathbf{w}\|^2 \leq \zeta_0, \quad (3.171)$$

where ξ_{0i} ($i = 1, \dots, N_{\text{SL}}$) are the specified values to control the sidelobes. This method is referred to as the sidelobe constrained least squares mainlobe method.

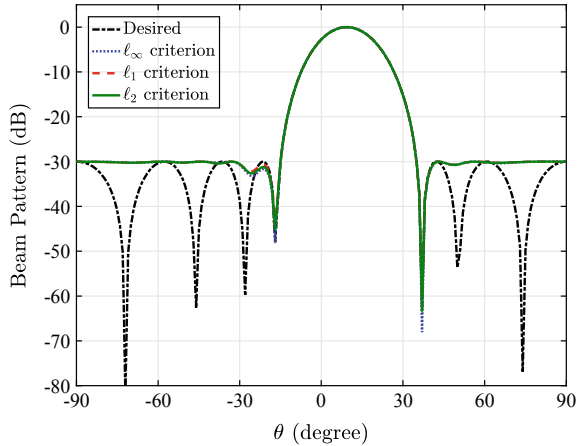
Alternatively, we can seek a beam pattern that minimizes the maximum weighted approximation error subject to the sidelobes and WNG constraints. This problem can be formulated as

$$\min_{\mathbf{w}} \max_{j=1, \dots, N_{\text{ML}}} |\mathbf{w}^H \mathbf{p}(\theta_j) - B_d(\theta_j)|, \quad \theta_j \in \Theta_{\text{ML}},$$

$$\text{subject to} \quad |\mathbf{w}^H \mathbf{p}(\theta_j)| \leq \xi_{0i}, \quad \theta_i \in \Theta_{\text{SL}}, \quad i = 1, \dots, N_{\text{SL}},$$

$$\|\mathbf{w}\| \leq \sqrt{\zeta_0}. \quad (3.172)$$

Fig. 3.25 Sidelobe constrained minimum mainlobe pattern synthesis



3. Mean-square mainlobe constrained minimum sidelobes

Minimizing the sidelobe level subject to the mainlobe mean-square error constraint gives another pattern synthesis problem [12]

$$\begin{aligned}
 & \min_{\mathbf{w}} \max_{j=1, \dots, N_{\text{SL}}} \mathbf{w}^H \mathbf{p}(\theta_j), \quad \theta_j \in \Theta_{\text{SL}}, \\
 & \text{subject to} \quad \sum_{j=1}^{N_{\text{ML}}} \left[\lambda_j |\mathbf{w}^H \mathbf{p}(\theta_j) - B_d(\theta_j)|^2 \right] \leq \delta_0^2, \quad \theta_j \in \Theta_{\text{ML}}, \quad j = 1, \dots, N_{\text{ML}}, \\
 & \quad \|\mathbf{w}\| \leq \sqrt{\zeta_0},
 \end{aligned} \tag{3.173}$$

where δ_0^2 is the specified upper bound on the sum of squared mainlobe errors. This method is referred to as the mean-square mainlobe constrained minimum sidelobes method.

Consider the same cases as in Fig. 3.22. The mainlobe beam pattern there is chosen as the desired mainlobe beam pattern. We seek a beam pattern for frequency f_0 that minimizes the approximation error over the mainlobe region subject to the sidelobes constraints. We choose $\Theta_{\text{ML}} = [-13^\circ, 33^\circ]$ and $\Theta_{\text{SL}} = [-90^\circ, -15^\circ] \cup [35^\circ, 90^\circ]$, which is discretized using a uniform grid of 1° . The desired sidelobe level is -30 dB. The ℓ_1 , ℓ_2 and ℓ_∞ criteria are respectively used for the mainlobe approximation.

The resulting beam patterns are shown in Fig. 3.25. It is seen that, the synthesized beam patterns designed using the three criteria approximate the desired one well in the mainlobe region, and their sidelobes are strictly controlled to be below -30 dB, which fully meets the design requirements.

The synthesis errors between the synthesized beam patterns obtained by the three criteria and the desired beam pattern in the mainlobe region, i.e., $|B(\theta_j) - B_d(\theta_j)|$, for $\theta_j \in \Theta_{\text{ML}}$, are shown in Fig. 3.26.

Fig. 3.26 Synthesis errors between synthesized and desired beam patterns in mainlobe region

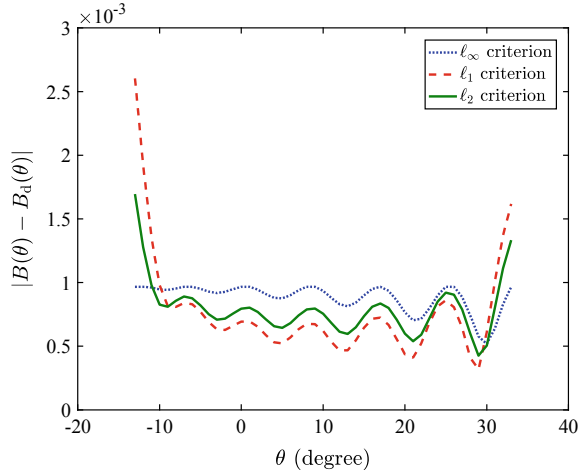


Table 3.2 Comparison of the norms of the mainlobe synthesis errors by the three criteria

Methods	$\delta_\infty (\times 10^{-3})$	$\delta_1 / N_{ML} (\times 10^{-3})$	$\delta_2 / \sqrt{N_{ML}} (\times 10^{-3})$
ℓ_∞ criterion	0.9668	0.8839	0.8903
ℓ_1 criterion	2.6037	0.7708	0.8697
ℓ_2 criterion	1.6945	0.7919	0.8201

It is seen that the mainlobe approximation errors by the mixed-norm methods shown in Fig. 3.26 are much smaller than those by the minimum-norm methods shown in Fig. 3.24. This can also be seen from the error norms of the design results using the three mainlobe approximation criteria shown in Table 3.2.

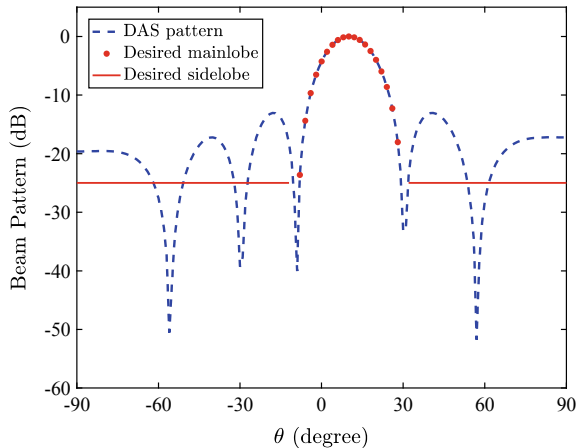
3.4.5 Frequency-Invariant Beam Pattern

Recall that the beamwidth of the DAS beam pattern increases as the frequency decreases, which will cause the signals arrived from the outer portions of the mainlobe to low-pass filtering and lead to distorted signal spectra. In order to avoid the signal spectra distortion behavior, the mainlobe is required to be constant over the frequency band of interest. This kind of beamformer is referred to as the constant-mainlobe beamformer, or frequency-invariant beamformer.

The mainlobe pattern synthesis methods discussed in this section can be used to design the constant-mainlobe beamformer. The design steps are as follows.

Step 1. Choose a desired beam pattern $B_d(\theta)$. The desired beam pattern can be either a conventional beam pattern corresponding to a reference frequency or an optimal beam pattern designed using some optimization criteria.

Fig. 3.27 Desired beam pattern



- Step 2. Decompose the frequency band of interest into K subbands. The center frequencies of each subband are $f_k \in [f_l, f_u]$, $k = 1, \dots, K$. Ensure that each subband satisfies the narrowband condition.
- Step 3. For each subband, the weight vector $\mathbf{w}(f_k)$ can be designed using the mainlobe pattern synthesis methods such that the synthesized beam pattern $B(f_k, \theta)$ approximates the desired beam pattern $B_d(\theta)$ over the mainlobe region Θ_{ML} .
- Step 4. The frequency-domain implementation of the broadband beamformer discussed in Chap. 2 is utilized. The resulting broadband beamformer has the constant mainlobe pattern over the frequency band of interest.

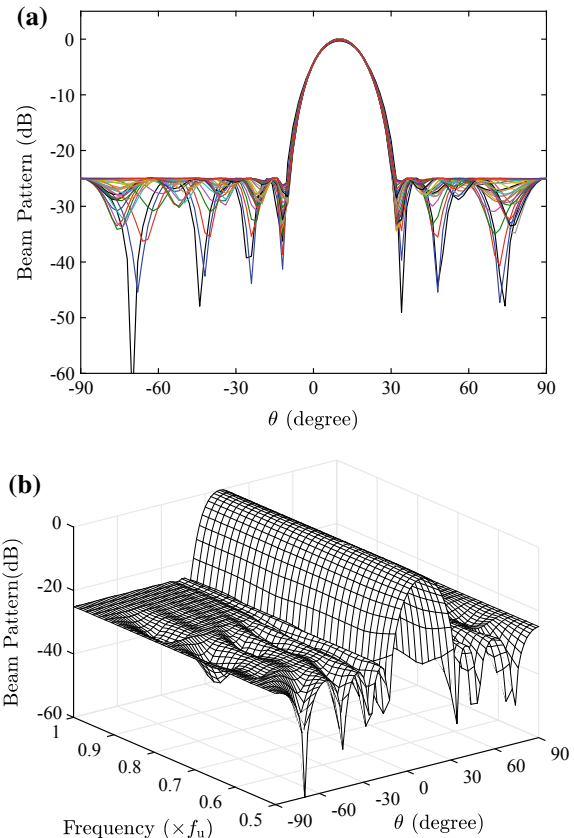
Consider a 12-element ULA with a half-wavelength spacing at f_0 . Assuming that the frequency band of interest is $[f_l, f_u] = [f_0/2, f_0]$ and the beamformer is steered to 10° . Choose the mainlobe response of conventional DAS beam pattern at $f_0/2$ as the desired mainlobe pattern and control the sidelobe level to be below -25 dB, as shown in Fig. 3.27.

The frequency band of interest is decomposed into 33 subbands uniformly. A uniform grid of 2° is used to discretize the visible region. Let $\Theta_{ML} = [-8^\circ, 28^\circ]$ and $\Theta_{SL} = [-90^\circ, -12^\circ] \cup [32^\circ, 90^\circ]$, and choose the weight vector norm constraint value $\zeta_0 = 10^{-7.5/10}$.

For each subband, the sidelobe constrained least squares mainlobe method shown in Eq. (3.171) are used to design the weight vectors. The resulting beam patterns are shown in Fig. 3.28. Figure 3.28a is the superposition plot of the 33 beam patterns and Fig. 3.28b is the corresponding three-dimensional plot.

It is seen from Fig. 3.28 that, the mainlobe patterns are almost constant over the frequency band of interest. The sidelobes of the 33 synthesized beam patterns are strictly controlled to be below -25 dB. Further investigation shows that, the weight vector norms of these beamformers also satisfy the design requirement $\|\mathbf{w}(f_k)\| \leq 10^{-7.5/20} = 0.4217$, for $k = 1, \dots, 33$.

Fig. 3.28 Frequency-invariant beam patterns for broadband array,
a superposition plot,
b three-dimensional plot



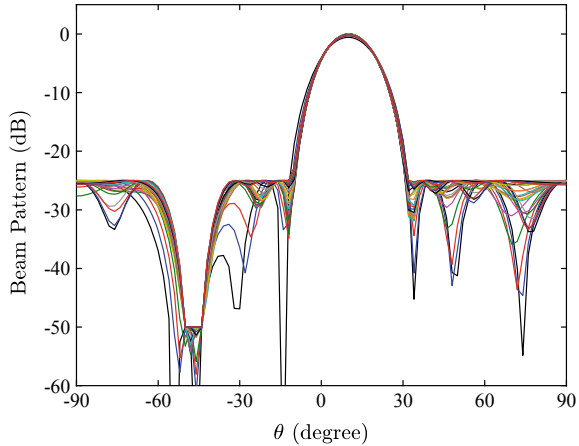
Assume that while designing the sidelobe constrained frequency-invariant beam patterns, the beamformer is required to place a notch with a depth of -50 dB in the sector $[-50^\circ, -44^\circ]$. Keeping the other parameters unchanged, the resulting beam patterns are shown in Fig. 3.29. The results satisfy the design requirements strictly.

3.5 Multiple-Objective Design

In practice, an optimal beamformer design which considers multiple objectives may be desired. This design involves trade-offs among the array gain, the robustness, the sidelobe level, the mainlobe pattern, as well as a number of other performance measures.

The beamformer design can be formulated as a multiply constrained design problem

Fig. 3.29 Superposition plot of frequency-invariant beam patterns with a notch



$$\min_w \mu_p, \quad p \in \{1, 2, 3, 4\}, \quad (3.174a)$$

$$\text{subject to} \quad \|\mathbf{B}(\Theta_{\text{ML}}) - \mathbf{B}_d(\Theta_{\text{ML}})\|_{q_1} \leq \mu_1, \quad (3.174b)$$

$$\|\mathbf{B}(\Theta_{\text{SL}})\|_{q_2} \leq \mu_2, \quad (3.174c)$$

$$\mathbf{w}^H \mathbf{R} \mathbf{w} \leq \mu_3, \quad (3.174d)$$

$$\|\mathbf{w}\| \leq \mu_4, \quad (3.174e)$$

where \mathbf{R} is the data covariance matrix, and the definitions of $\mathbf{B}(\Theta_{\text{ML}})$ and $\mathbf{B}(\Theta_{\text{SL}})$ are similar to Eq. (3.149).

In Eq. (3.174a), any chosen three of μ_p are the specified constraint values, and the other one is the optimization objective. Note that the constraint values cannot be chosen too small, otherwise there may be no solution to the optimization problem.

The constraint (3.174b) is used to control the mainlobe pattern, where $q_1 = 1, 2$ or ∞ , but commonly used value is $q_1 = 2$, which means that the synthesized beam pattern $\mathbf{B}(\Theta_{\text{ML}})$ will be the least squares approximation to the desired beam pattern $\mathbf{B}_d(\Theta_{\text{ML}})$. If $\mu_1 = 0$, the constraint (3.174b) will become the equality constraint $\mathbf{B}(\Theta_{\text{ML}}) = \mathbf{B}_d(\Theta_{\text{ML}})$, which can include the distortionless constraint as a special case.

The constraint (3.174c) is used to control the sidelobes, where $q_2 = 1, 2$ or ∞ . If $q_2 = \infty$, which is commonly used, the sidelobe level is controlled to be below $20 \lg \mu_2$ dB. If $q_2 = 2$, the sidelobes are constrained under the least squares criterion.

The constraint (3.174d) is used to control the beamformer output power for the purpose of increasing the array gain.

The constraint (3.174e) attempts to improve the robustness of the beamformer by constraining the norm of the weight vector, and the smaller the μ_4 , the more robust the beamformer.

The optimization method in Eq. (3.174) provides a unified framework for optimal design of narrowband beam patterns, which can be easily formulated as an SOCP problem for solution. This unified framework can include most of the existing methods, including the methods described earlier in this chapter, as its special cases, which leads to more flexible designs.

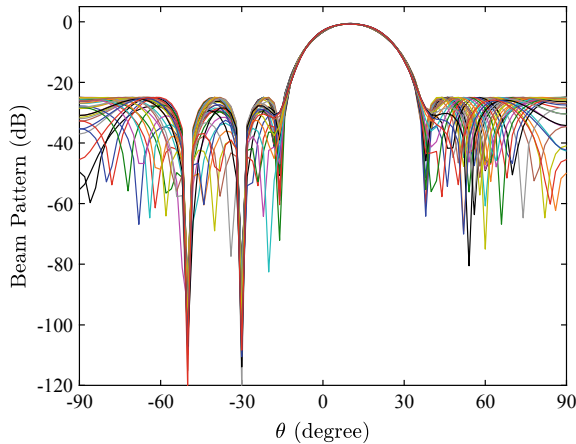
For the optimization problem in Eq. (3.174), the smaller the constraint value μ_p , the better the corresponding performance of the beamformer. However, these constraint values cannot be chosen too small, otherwise there may be no solution to the optimization problem. Thus the user should make a trade-off among multiple performances. In order to avoid the case when there is no solution, the values of each constraint can be chosen using the following steps.

- Step 1. First consider the problem of optimizing between two performances, i.e., there are only two constraints, such as (3.174c) and (3.174e).
- Step 2. Recalling the conclusion that $\min(\|\mathbf{w}\|) = 1/M$, we select suitable value of μ_4 , denoted by $\mu_{4\text{opt}}$, which satisfies $\mu_{4\text{opt}} \geq 1/M$.
- Step 3. Solve the optimization problem with two constraints and denote the obtained minimum value of μ_2 by $\mu_{2\text{min}}$. Check whether the value of $\mu_{2\text{min}}$ is satisfactory. If it is, choose $\mu_{2\text{opt}} = \mu_{2\text{min}}$. Otherwise, choose a more satisfactory value of $\mu_{2\text{opt}}$. Solve for the minimum value of μ_4 and denote it by $\mu_{4\text{min}}$, then check whether the value of $\mu_{4\text{min}}$ is satisfactory. Repeat the process until obtaining a set of satisfactory solutions and denote them by $\hat{\mu}_{4\text{opt}}$ and $\hat{\mu}_{2\text{opt}}$.
- Step 4. Add another constraint, such as (3.174b). Let $\mu_4 = \hat{\mu}_{4\text{opt}}$ and $\mu_2 = \hat{\mu}_{2\text{opt}}$. Solve the optimization problem for the minimum value of μ_1 and denote it by $\mu_{1\text{min}}$. Check whether the value of $\mu_{1\text{min}}$ is satisfactory. If it is, choose $\mu_{1\text{opt}} = \mu_{1\text{min}}$. Otherwise, choose a more satisfactory value of $\mu_{1\text{opt}}$. Keeping one of $\hat{\mu}_{4\text{opt}}$ and $\hat{\mu}_{2\text{opt}}$ unchanged, solve for the minimum value of the other, then check whether the new solution is satisfactory (In this process, when there is no solution, increase one or two of the three constraint values and repeat). Repeat this process until obtaining a set of satisfactory solutions and denote them by $\hat{\mu}_{4\text{opt}}$, $\hat{\mu}_{2\text{opt}}$ and $\hat{\mu}_{1\text{opt}}$.
- Step 5. Add one more constraint, repeat the above process until obtaining the best compromise among the four performances.

The steps above seem to be complicated, in practice, it is often only necessary to adjust two or three times to get a satisfactory compromise solution.

Consider a 12-element broadband ULA with a half-wavelength spacing at f_0 in the presence of spatially white Gaussian noise. A broadband plane-wave desired signal and two broadband plane-wave interferers arrive from 10° , -50° , and -30° with the signal(interference)-to-noise ratio at each sensor of 0, 30 and 30 dB, respectively. Assume that the desired signal, interferers and noise all have flat spectra over the frequency band of interest $[f_1, f_u] = [f_0/2, f_0]$.

Fig. 3.30 Superposition of beam patterns obtained by using multiple-objective design



The multiply constrained method in Eq. (3.174) is used to design the broadband robust frequency-invariant adaptive beamformer with sidelobe control.

The frequency band of interest is decomposed into $K = 33$ subbands uniformly. For each subband, the theoretical narrowband covariance matrices are used for convenience. A uniform grid of 2° is used to discretize the visible region $[-90^\circ, 90^\circ]$ and let $\Theta_{\text{ML}} = [-12^\circ : 2^\circ : 32^\circ]$ and $\Theta_{\text{SL}} = [-90^\circ : 2^\circ : -16^\circ] \cup [36^\circ : 2^\circ : 90^\circ]$.

The mainlobe of the Dolph-Chebyshev beam pattern (with specified sidelobe level of -25 dB) at f_i is chosen as the desired mainlobe pattern. The other parameters are chosen as follows: $p = 3$, $q_1 = 2$, $\mu_1 = 10^{-15/20}$, $q_2 = \infty$, $\mu_2 = 10^{-25/20}$, and $\mu_4 = 10^{-7.5/20}$.

The resulting beam patterns for the 33 subbands are plotted in Fig. 3.30.

It is seen from Fig. 3.30 that, the sidelobe levels of the subband beam patterns are strictly controlled to be below -25 dB, and nulls are placed at the directions of the interferers. It is verified that all constraints are met. The calculation results show that the average output SINR of each subband is about 8.34 dB. From the results above, the design capability of the multiply constrained method is fully demonstrated.

3.6 Summary

Several subband beamformer design methods are described in this chapter, including robust MVDR beamformer design, low-sidelobe beamformer design, mainlobe pattern synthesis, and multiple-objective beamformer design.

In the SMI implementation of the MVDR beamformer, the sample covariance matrix is estimated from a limited number of data samples, which leads to covariance matrix error. The covariance matrix mismatch caused a performance degradation similar to that in the steering vector mismatch case. The larger the error, the more severe the performance degradation. In the presence of desired signal, the SMI

beamformer treats the mismatched signal as an interferer and attempts to null it. As the SNR increases, the degradation due to mismatch increases and even a relatively small error can cause a significant degradation of the performance.

The LSMI method improves the robustness of the beamformer by diagonally loading the data sample covariance matrix. It can provide a trade-off between the MVDR beamformer and the DAS beamformer by adjusting the diagonal loading level. However, the disadvantage is that the diagonal loading level is difficult to determine.

The NC beamformer improves robustness of the beamformer by constraining the norm of the weight vector. The smaller the constraint value, the more robust the beamformer. The NC beamformer belongs to the class of diagonal loading methods. Unlike the LSMI method that use fixed loading, the diagonal loading level of the NC method varies with the input SNR.

In the WCC beamformer, the steering vector is assumed to belong to an elliptical uncertainty set and the worst-case output SINR is maximized. The WCC beamformer also belongs to the class of diagonal loading methods. Its advantage is that it can choose the diagonal loading level based on information about the uncertainty of the steering vector. The WCC beamformer offers robustness performance improvements relative to the LSMI and NC methods. It also provides excellent SOI power estimation performance. The techniques that used to improve robustness in the presence of steering vector mismatch will also improve robustness to covariance matrix mismatch.

The window technique can be used to reduce the sidelobes in classical array design. For a ULA with half-wavelength spacing, the Dolph-Chebyshev weighting provides minimum beamwidth for a given sidelobe level, or the minimum constant sidelobes for a given beamwidth. However, the window technique is mostly only suitable for uniform line arrays with isotropic element patterns.

For arrays with arbitrary geometry, the trade-off between the beamwidth and the sidelobe level, and between the high-gain and the sidelobes can both be expressed as a convex SOCP optimization problem. The weighted vector norm constraint can also be imposed to improve the robustness. The SOCP-based approach provides flexible design, high design precision and a wider range of applications.

The beam pattern degrades with respect to the nominal beam pattern in the presence of array manifold errors. A pattern synthesis technique is developed to optimize the worst case performance by minimizing the worst case sidelobe level while maintaining a distortionless response to the worst case signal steering vector. It provides good robustness in the presence of array manifold perturbations. The pattern synthesis parameters can be optimally chosen based on the uncertainty level of the array manifold vectors. A simple lower bound on the difference between the worst case sidelobe level of the robust beamformer and the sidelobe level of the nominal optimal beamformer has been derived.

Minimum-norm pattern synthesis techniques are developed to approximate the desired beam pattern by minimizing the ℓ_∞ -, ℓ_1 - or ℓ_2 -norm of the synthesis error between the synthesized beam pattern and the desired one. The mixed-norm criterion is a more reasonable criterion for pattern synthesis problem, in which various

approximation criteria are respectively used in the mainlobe region and the sidelobe region, and smaller mainlobe approximation error can be achieved. By specifying a desired pattern and then trying to approximate it in the frequency band of interest, these techniques can be easily used to design a broadband beamformer with frequency-invariant beam pattern.

The multiple-objective approach is presented for designing the weight vector that provides a suitable compromise among multiple conflicting array performances. It can provide beamformer design with a high level of detail in the specification of performance. The multiple-objective approach provides a unified framework for optimal design of narrowband beamformers, which includes most of the existing beamformer design methods as its special cases, and leads to more flexible designs. In addition, this is useful for analyzing and evaluating the advantages and disadvantages of various methods that can be regarded as its special cases. This is also useful for a thorough understanding of the subband beamformer design.

References

1. H. Cox, R.M. Zeskind, M.M. Owen, Robust adaptive beamforming. *IEEE Trans. Audio Speech Signal Process.* **35**(10), 1365–1376 (1987)
2. B.D. Carlson, Covariance-matrix estimation errors and diagonal loading in adaptive arrays. *IEEE Trans. Aerosp. Electron. Syst.* **24**(4), 397–401 (1988)
3. D.D. Feldman, L.J. Griffiths, A projection approach for robust adaptive beamforming. *IEEE Trans. Signal Process.* **42**(4), 867–876 (1994)
4. S.A. Vorobyov, A.B. Gershman, Z.Q. Luo, Robust adaptive beamforming using worst-case performance optimization: a solution to the signal mismatch problem. *IEEE Trans. Signal Process.* **51**(2), 313–324 (2003)
5. J. Li, P. Stoica, Z.S. Wang, On robust Capon beamforming and diagonal loading. *IEEE Trans. Signal Process.* **51**(7), 1702–1715 (2003)
6. R.G. Lorenz, S.R. Boyd, Robust minimum variance beamforming. *IEEE Trans. Signal Process.* **53**(5), 1684–1696 (2005)
7. J. Li, P. Stoica, *Robust Adaptive Beamforming* (Wiley, New Jersey, 2006)
8. C.A. Olen, R.T. Compton, A numerical pattern synthesis algorithm for arrays. *IEEE Trans. Antennas Propag.* **38**(10), 1666–1676 (1990)
9. J. Liu, A.B. Gershman, Z.Q. Luo, K.M. Wong, Adaptive beamforming with sidelobe control: a second-order cone programming approach. *IEEE Signal Process. Lett.* **10**(11), 331–334 (2003)
10. C.Y. Tseng, L.J. Griffiths, A simple algorithm to achieve desired patterns for arbitrary arrays. *IEEE Trans. Signal Process.* **40**(11), 2737–2746 (1992)
11. B.P. Ng, M.H. Er, C. Kot, A flexible array synthesis method using quadratic-programming. *IEEE Trans. Antennas Propag.* **41**(11), 1541–1550 (1993)
12. S. Yan, Y. Ma, Frequency invariant beamforming via optimal array pattern synthesis and FIR filters design. *Chin. J. Acoust.* **24**(3), 202–211 (2005)
13. I.S. Reed, J.D. Mallett, L.E. Brennan, Rapid convergence rate in adaptive arrays. *IEEE Trans. Aerosp. Electron. Syst.* **10**(6), 853–863 (1974)
14. E.J. Kelly, Performance of an adaptive detection algorithm—rejection of unwanted signals. *IEEE Trans. Aerosp. Electron. Syst.* **25**(2), 122–133 (1989)
15. S. Yan, Y. Ma, Robust supergain beamforming for circular array via second-order cone programming. *Appl. Acoust.* **66**(9), 1018–1032 (2005)
16. J.F. Sturm, Using SeDuMi 1.02, a MATLAB toolbox for optimization over symmetric cones. *Optim. Methods Soft.* **11–12**(1–4), 625–653 (1999)

17. J.E. Hudson, *Adaptive Array Principles* (Peter Peregrinus, London, 1981)
18. Z. Tian, K.L. Bell, H.L. Van Trees, A recursive least squares implementation for LCMP beam-forming under quadratic constraint. *IEEE Trans. Signal Process.* **49**(6), 1138–1145 (2001)
19. J. Li, P. Stoica, Z.S. Wang, Doubly constrained robust Capon beamformer. *IEEE Trans. Signal Process.* **52**(9), 2407–2423 (2004)
20. P. Stoica, Z.S. Wang, J. Li, Robust Capon beamforming. *IEEE Signal Process. Lett.* **10**(6), 172–175 (2003)
21. C.L. Dolph, A current distribution for broadside arrays which optimizes the relationship between beam width and side-lobe level. *Proc. IRE* **34**(6), 335–348 (1946)
22. S. Yan, Y. Ma, C. Sun, Optimal beamforming for arbitrary arrays using second-order cone programming. *Chin. J. Acoust.* **24**(1), 1–9 (2005)
23. S. Yan, J.M. Hovem, Array pattern synthesis with robustness against manifold vectors uncertainty. *IEEE J. Ocean. Eng.* **33**(4), 405–413 (2008)
24. A. Mutapcic, S.J. Kim, S. Boyd, Beamforming with uncertain weights. *IEEE Signal Process. Lett.* **14**(5), 348–351 (2007)

Chapter 4

Time-Domain Broadband Beamforming



4.1 Introduction

In Chap. 2, the frequency-domain snapshot model is used and the frequency-domain implementation becomes a straightforward extension of the narrowband beamforming to broadband beamforming.

In the frequency-domain broadband beamformer, the broadband array signals are first decomposed into narrower frequency bins by DFT. Within each frequency bin, the narrowband condition is satisfied and the narrowband beamformers discussed in Chap. 3 can be used directly. An IDFT is then performed to obtain the time-domain output. The procedure of frequency-domain broadband beamforming is block processing, which requires a block of snapshots to perform DFT. However, it is not suitable in many applications due to its associated time delay resulting from the block processing.

Recall from Chap. 1 that in a narrowband beamformer, we weight the signals arriving at each sensor and sum the results to obtain an output signal, while in the broadband case, we filter the signals and sum the results to obtain the output signal. Thus, a time-domain broadband beamformer can be implemented by placing a tapped delay line or FIR filter at the output of each sensor. The responses of these FIR filters at a frequency is actually the complex weightings corresponding to that frequency. An important advantage of the time-domain implementation is that the beamformer can be updated when each new snapshot arrives.

This time-domain implementation of a broadband beamformer is also referred to as an FIR beamformer. The Frost processor [1] is a traditional FIR beamformer. However, the mainlobe pattern was not taken into account and the sidelobes were not controlled, which can lead to severe performance degradation in the case of unexpected (i.e., suddenly appearing) interferers. An important issue in FIR beamformer design is how to choose the FIR filter impulse response, which is also termed as the tap weights, to achieve the desired frequency-wavenumber response.

The rest of this chapter is organized as follows. In Sect. 4.2, we introduce the FIR beamforming structure. In Sect. 4.3, a filter design method for FIR beamformer via

IFFT is introduced. In Sect. 4.4, an optimization method for designing an FIR filter with an arbitrary frequency response is presented. In Sect. 4.5, we discuss the design of an FIR beamformer by separately designing the subband beamformers and the corresponding FIR filters for each sensor. A brief summary of this chapter is given in Sect. 4.6.

4.2 FIR Beamforming

In 1972, Frost proposed a time-domain broadband beamforming method based on FIR filters. The Frost beamforming structure is shown in Fig. 4.1.

We now rewrite the broadband array data model. Consider an M -element array with a known arbitrary geometry. Assume that $D + 1 < M$ broadband plane waves impinge on the array from directions $\theta_0, \theta_1, \dots, \theta_d, \dots, \theta_D$. The time series received at the m th sensor can be modeled as

$$x_m(t) = \beta s_0[t - \tau_m(\theta_0)] + \sum_{d=1}^D s_d[t - \tau_m(\theta_d)] + n_m(t), \quad m = 1, \dots, M, \quad (4.1)$$

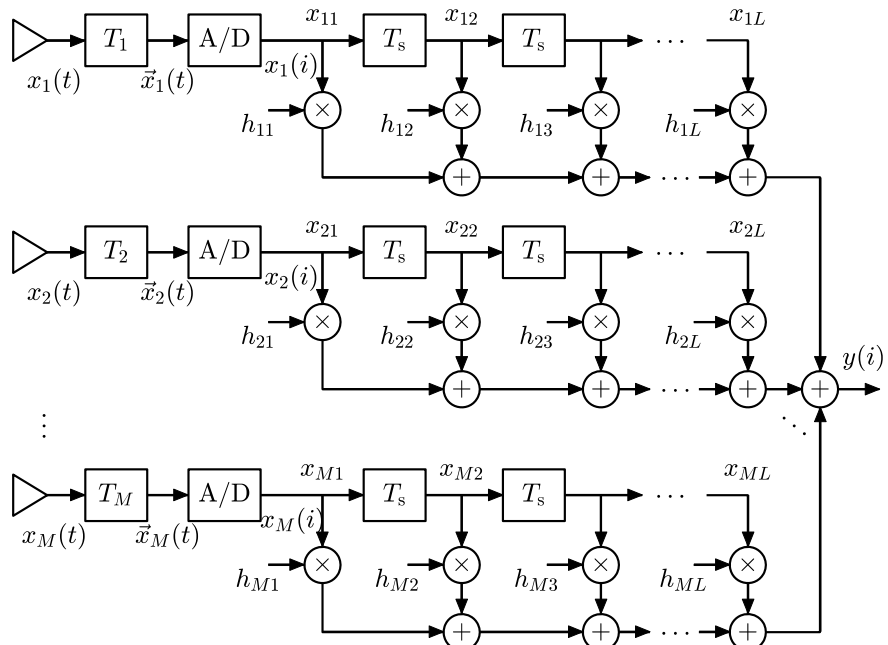


Fig. 4.1 Frost beamformer

where $\{s_d\}_{d=0}^D$ are the $D+1$ source signals observed at an arbitrarily chosen reference point, $\tau_m(\theta_d)$ is the propagation delay between the m th sensor and the reference point associated with the d th source, and $n_m(t)$ is the additive noise at the m th sensor. We assume that the first term in Eq. (4.1) corresponds to the signal of interest and the second term to D interferences. β is a binary parameter indicating whether the SOI is present in the training snapshots.

In the Frost beamformer, the steering direction θ_o is assumed to be exactly equal to the desired signal direction θ_0 , i.e. $\theta_o = \theta_0$, and the pre-steering delay is used to align the signals to the steering direction, i.e.,

$$T_m = -\tau_m(\theta_0), \quad m = 1, \dots, M. \quad (4.2)$$

Since the pre-delays T_m are usually not integers, mechanical or electronic pre-steering is usually applied. The pre-delayed sampled data from the m th sensor is given by

$$x_m(i) = \vec{x}_m(t)|_{t=iT_s} = x_m(t - T_m)|_{t=iT_s}. \quad (4.3)$$

Note that the digital signal $x_m(i)$ here is obtained by sampling the signal after the received signal $x_m(t)$ is delayed by T_m , instead of directly sampling $x_m(t)$.

Then the sampled data of each sensor pass through a transversal FIR filter respectively. Assume that the length of each filter is L . Since the time delay between any two adjacent taps is T_s , the input data of each tap are given by

$$x_{ml}(i) = x_m[i - (l - 1)] = x_m[t - T_m - (l - 1)T_s]|_{t=iT_s}, \quad m = 1, \dots, M, \quad l = 1, \dots, L. \quad (4.4)$$

The impulse responses of the FIR filters are also referred to as the tap weights. Let h_{ml} be the adjustable weight of the l th tap following behind the m th sensor. All the data samples are weighted (or filtered) and summed to obtain the desired beamformer output signal. The time series of the beamformer output is given by

$$y(i) = \sum_{m=1}^M \sum_{l=1}^L h_{ml} x_{ml}(i) = \sum_{m=1}^M \sum_{l=1}^L h_{ml} x_{ml}(i). \quad (4.5)$$

Now define two $M \times L$ matrices

$$X(i) = \begin{bmatrix} x_{11}(i) & \cdots & x_{1l}(i) & \cdots & x_{1L}(i) \\ \vdots & \ddots & \vdots & & \vdots \\ x_{m1}(i) & \cdots & x_{ml}(i) & \cdots & x_{mL}(i) \\ \vdots & & \vdots & \ddots & \vdots \\ x_{M1}(i) & \cdots & x_{Ml}(i) & \cdots & x_{ML}(i) \end{bmatrix} \quad (4.6)$$

and

$$\mathbf{H} = \begin{bmatrix} h_{11} & \cdots & h_{1l} & \cdots & h_{1L} \\ \vdots & \ddots & \vdots & & \vdots \\ h_{m1} & \cdots & h_{ml} & \cdots & h_{mL} \\ \vdots & & \vdots & \ddots & \vdots \\ h_{M1} & \cdots & h_{Ml} & \cdots & h_{ML} \end{bmatrix}. \quad (4.7)$$

We introduce the notations

$$\mathbf{x}(i) = \text{vec}\{\mathbf{X}(i)\}, \quad (4.8)$$

$$\mathbf{h} = \text{vec}\{\mathbf{H}\}, \quad (4.9)$$

where $\text{vec}\{\cdot\}$ denotes the vectorization operator which stacks the columns of a matrix on top of each other, and $\mathbf{x}(i)$ represents the i th snapshot.

Then, Eq. (4.5) can be written as

$$\mathbf{y}(i) = \mathbf{h}^T \mathbf{x}(i), \quad (4.10)$$

which is the expression of the time-domain beamformer output.

4.3 FIR Beamformer Design via FFT

Assume that the input sample data of the DFT beamformer and the Frost FIR beamformer are both pre-scanned delayed data, and they are identical. Let the input sample length (i.e., buffer length) of the DFT beamformer (see Eq. 2.38) and the filter length of the FIR beamformer (see Eq. 4.6) be both equal to L . Since the index corresponding to the latest time sample in Eq. (2.38) is $L - 1$ while that in Eq. (4.6) is $l = 1$, $x_m^{(n)}(l)$ in Eq. (2.38) and $x_{ml}(i)$ in Eq. (4.6) have the following relationship:

$$x_m^{(n=0)}(l) = x_{m(L-l)}(i = 0), l = 0, \dots, L - 1. \quad (4.11)$$

Substituting Eq. (4.11) into Eq. (2.19) gives

$$\begin{aligned} X_m^{(n=0)}(k) &= \sum_{l=0}^{L-1} x_{m(L-l)}(i = 0) \exp(-i2\pi kl/L) \\ &\stackrel{l'=L-l}{\Rightarrow} \sum_{l'=1}^L x_{ml'}(i = 0) \exp(-i2\pi k(L - l')/L) \end{aligned}$$

$$\stackrel{l=l'}{\Rightarrow} \sum_{l=1}^L x_{ml}(i=0) \exp(-i2\pi k(L-l)/L), \quad k = 0, \dots, L-1. \quad (4.12)$$

If we want the latest output of the DFT beamformer be equal to that of the FIR beamformer, we only need to let $n = 0$ and $l = L - 1$ in Eq. (2.44) and $i = 0$ in Eq. (4.5). Then we have

$$y^{(n=0)}(l)|_{l=L-1} = y(i)|_{i=0}. \quad (4.13)$$

Using Eqs. (2.44), (4.5) and (4.13), we have

$$\frac{1}{L} \sum_{k=0}^{L-1} Y^{(n=0)}(k) \exp\left[\frac{i2\pi k(L-1)}{L}\right] = \sum_{m=1}^M \sum_{l=1}^L h_{ml} x_{ml}(i=0). \quad (4.14)$$

Substituting Eqs. (2.41) and (4.12) into the left side of Eq. (4.14) gives

$$\begin{aligned} & \sum_{m=1}^M \sum_{l=1}^L h_{ml} x_{ml}(i=0) \\ &= \frac{1}{L} \sum_{k=0}^{L-1} Y^{(n=0)}(k) \exp[i2\pi k(L-1)/L] \\ &= \frac{1}{L} \sum_{k=0}^{L-1} \left\{ \left[\left(\sum_{m=1}^M w_m^*(f_k) X_m^{(n=0)}(k) \right) \right] \exp[i2\pi k(L-1)/L] \right\} \\ &= \frac{1}{L} \sum_{k=0}^{L-1} \left\{ \left[\left(\sum_{m=1}^M w_m^*(f_k) \left(\sum_{l=1}^L x_{ml}(i=0) \exp\left[\frac{-i2\pi k(L-l)}{L}\right] \right) \right) \right] \exp\left[\frac{i2\pi k(L-1)}{L}\right] \right\} \\ &= \frac{1}{L} \sum_{k=0}^{L-1} \sum_{m=1}^M \left\{ w_m^*(f_k) \left[\sum_{l=1}^L x_{ml}(i=0) \exp\left[\frac{-i2\pi k(L-l)}{L}\right] \exp\left[\frac{i2\pi k(L-1)}{L}\right] \right] \right\} \\ &= \frac{1}{L} \sum_{k=0}^{L-1} \sum_{m=1}^M \left\{ w_m^*(f_k) \left[\sum_{l=1}^L x_{ml}(i=0) \exp\left[\frac{i2\pi k(l-1)}{L}\right] \right] \right\} \\ &= \sum_{m=1}^M \sum_{l=1}^L x_{ml}(i=0) \left[\frac{1}{L} \sum_{k=0}^{L-1} w_m^*(f_k) \exp\left[\frac{i2\pi k(l-1)}{L}\right] \right]. \end{aligned} \quad (4.15)$$

It is seen that if Eq. (4.16) is satisfied, Eq. (4.15) also holds.

$$\begin{aligned} h_{ml} &= \frac{1}{L} \sum_{k=1}^{L-1} w_m^*(f_k) \exp\left[\frac{i2\pi k(l-1)}{L}\right], \\ l &= 1, \dots, L, \quad k = 0, 1, \dots, L-1, \end{aligned} \quad (4.16)$$

i.e.,

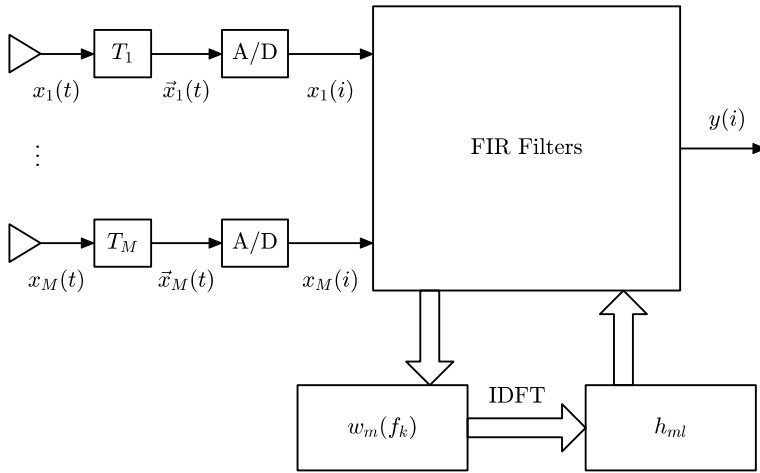


Fig. 4.2 FFT-based FIR broadband beamforming

$$h_{ml}(l = 1, 2, \dots, L) = \text{IDFT} \left\{ \frac{w_m^*(f_k)}{L}, (k = 0, 1, \dots, L-1) \right\}, \quad (4.17)$$

or

$$w_m^*(f_k), (k = 0, 1, \dots, L-1) = \text{DFT}\{h_{ml}, (l = 1, 2, \dots, L)\} \quad (4.18)$$

It is seen that the FIR filter tap weights of the time-domain beamformer and the frequency-domain weights of the DFT beamformer are a discrete Fourier transform pair when the length of each FIR filter is equal to the buffer length.

From Eq. (4.17), the FIR filter tap weights of the time-domain beamformer can be obtained by performing IDFT to the frequency-domain weights. This tap weight estimate scheme is referred to as the FFT-based FIR beamformer design scheme.

This result is different from the result in [2] where the tap weights are obtained by performing DFT but not IDFT to the frequency-domain weights. This is caused by the reverse ordering of the input data in this literature. However, the result in Eq. (4.17) is more intuitive.

Based on the discrete Fourier transform pair relationship between the frequency-domain weights and the FIR filters, the block diagram of the tap weight estimate scheme can be shown in Fig. 4.2.

The implementation of the FFT-based FIR broadband beamformer consists of the following steps.

Step 1. The broadband data received by the array are decomposed into a number of narrowband frequency bins. For each frequency bin, the subband data covariance matrix is estimated. This step can be omitted if there is no need to estimate the subband data covariance matrix.

- Step 2. Design the weight vectors $\mathbf{w}^H(f_k)$ for each frequency bin using the narrow-band beamformers design methods.
- Step 3. Calculate the FIR filter tap weights h_{ml} corresponding to each sensor using the discrete Fourier transform pair relationship between the frequency-domain weights and the FIR filters.
- Step 4. The time-domain data received by each sensor are filtered using the corresponding FIR filter and the results are summed to obtain the beamformer output time series.

This method avoids the $ML \times ML$ dimensional matrix inversion operation required in the Frost beamforming, which makes it computationally efficient. However, since the length of the FIR filters must be equal to the length of the DFT in this method, the increasing of the length of the DFT will also increase the length of the filter, thereby increasing the computational complexity.

Furthermore, from the Fourier transform pair relationship between the filter tap weights and the frequency-domain weights, we can see that the frequency response of the FIR filter for each sensor is exactly the weight of the DFT beamformer at the corresponding frequency for that sensor. From this point of view, the FIR filter design is simply obtained by performing inverse Fourier transform to the desired frequency response, however the design effect is not good.

4.4 FIR Filter Design for FIR Beamformer

Section 4.3 has pointed out that the objective of FIR beamformer design is to design a set of FIR filters whose frequency responses are identical to the weights of a DFT beamformer over the frequency band of interest.

The design of FIR filter with the desired frequency response is the core part of the FIR beamformer design. In this section, we focus on the FIR filter design problem.

Assume that an FIR filter of length L has an impulse response (or tap weights)

$$\mathbf{h} = [h(1), \dots, h(l), \dots, h(L)]^T. \quad (4.19)$$

The frequency response of the FIR filter can be given by

$$H(f) = \sum_{l=1}^L h(l) e^{-i2\pi(l-1)f/f_s} = \mathbf{e}^T(f) \mathbf{h} = \mathbf{h}^T \mathbf{e}(f), \quad (4.20)$$

where $\mathbf{e}(f) = [1, e^{-i2\pi f/f_s}, \dots, e^{-i2\pi(L-1)f/f_s}]^T$ with f_s being the sampling frequency.

It is seen that Eq. (4.20) has a similar form to the expression for beam pattern. In fact, the filtering in time-domain processing is analogous to the beamforming in spatial processing. Some of the analogy relationships between them are listed in Table 4.1.

Table 4.1 Analogy relationship between time-domain and spatial processing

Time-domain processing	Spatial processing
FIR filter	Beamformer
Filtering	Beamforming (or spatial filtering)
Frequency response $H(f)$	Beam pattern $B(\theta)$
Tap weights \mathbf{h}	Weight vector \mathbf{w}
Frequency response vector $\mathbf{e}(f)$	Array response vector $\mathbf{p}(\theta)$
Filter design	Beamformer design
Power spectrum	Spatial spectrum

There are also some differences between the filters and the beamformers, e.g., the weight vector of the beamformer is complex, while the tap weights of the FIR filter are usually real.

Utilizing the analog between the FIR filter and the beamformer, the techniques developed for array pattern synthesis can be modified for FIR filter design [3].

4.4.1 Minimum-Norm Filter Design

FIR filter design is to choose the tap weights to achieve the desired frequency response. This can be obtained by minimizing the norm of the error between the frequency response of the designed FIR filter and the desired frequency response.

Let $H_d(f)$ be the desired frequency response. The norm of the error between the frequency response of the designed filter and the desired frequency response is given by

$$\delta_q = \left(\int_F \lambda(f) |\mathbf{e}^T(f) \mathbf{h} - H_d(f)|^q df \right)^{1/q}, \quad (4.21)$$

where $F = [0, f_s/2]$ is the entire frequency band, and $\lambda(f)$ is a non-negative weighting function used for adjusting the fitting precision at various frequencies. Typically, $q = \infty, 1$ or 2 , which corresponds to the ℓ_∞ -, ℓ_1 -, and ℓ_2 -norms of the error, respectively.

We can choose a set of frequencies $f_1, \dots, f_k, \dots, f_K$ ($f_k \in F, k = 1, 2, \dots, K$) to discretize the frequency set F . Similar to Eq. (3.147), the discretized error norm is given by

$$\delta_q = \|\lambda^{1/q} \circ (\mathbf{H} - \mathbf{H}_d)\|_q, \quad (4.22)$$

where $\lambda = [\lambda_1, \dots, \lambda_k, \dots, \lambda_K]$ is the non-negative weighting coefficient, $\mathbf{H} = [H(f_1), H(f_2), \dots, H(f_K)]$ and $\mathbf{H}_d = [H_d(f_1), H_d(f_2), \dots, H_d(f_K)]$ are respectively the designed and desired frequency responses.

By minimizing the ℓ_∞ -, ℓ_1 - and ℓ_2 -norms of the error between the designed and the desired frequency responses, respectively, the minimum-norm FIR filter design under the three criteria can be formulated as (see also [4])

$$\min_{\mathbf{h}} \max_{k=1, \dots, K} [\lambda_k |e^T(f_k) \mathbf{h} - H_d(f_k)|], \quad f_k \in F, \quad (4.23)$$

$$\min_{\mathbf{h}} \sum_{k=1}^K [\lambda_k |e^T(f_k) \mathbf{h} - H_d(f_k)|], \quad f_k \in F, \quad (4.24)$$

$$\min_{\mathbf{h}} \sum_{k=1}^K [\lambda_k |e^T(f_k) \mathbf{h} - H_d(f_k)|^2], \quad f_k \in F. \quad (4.25)$$

Clearly, these three optimization problems can be solved using the similar methods as the weight vector design methods in Sect. 3.4.3.

Some useful FIR filters are designed below.

In many applications of signal processing, there is a need for a delay, which may be a fraction of the sampling period T_s .

When the analytic expression for a broadband discrete signal is unknown, a fractional delay FIR filter can be used to filter the discrete signal to achieve a fractional-delayed version of the input signal. Since the integer taps delay can be directly achieved using the tapped delay line, the delay time of the fractional delay filter only needs to be in the range of $[-0.5T_s, 0.5T_s]$.

Consider a real-valued FIR filter. Since the inherent group delay of an FIR filter of length L is $(L - 1)T_s/2$, the design accuracy can be improved when the desired delay approaches this value.

Thus, the desired frequency response of a fractional delay filter can be given by

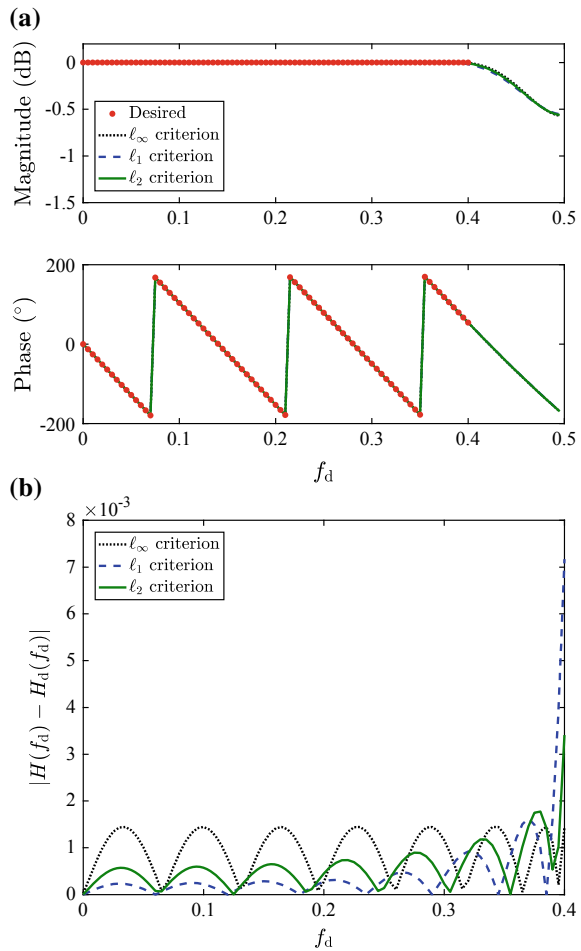
$$H_d(f_d) = e^{-i2\pi f(DT_s + \tau)} = e^{-i2\pi f_d(D + \tau/T_s)}, \quad f_d \in F_{PB}, \quad (4.26)$$

where $f_d = f/f_s$ is the digital frequency, or normalized frequency, F_{PB} is the passband that satisfies $F_{PB} \subset [0, 0.5]$. $\tau \in [-0.5T_s, 0.5T_s]$ is the desired time delay. D is an integer that is given by

$$D = \begin{cases} (L - 1)/2, & L \text{ odd}, \quad \tau \in [-0.5T_s, 0.5T_s] \\ L/2 - 1, & L \text{ even}, \quad \tau \in [0, 0.5T_s] \\ L/2, & L \text{ even}, \quad \tau \in [-0.5T_s, 0) \end{cases}. \quad (4.27)$$

From Eq. (4.26), the actual time delay produced by the FIR filter is $DT_s + \tau$. Therefore, in order to delay the broadband signal only by τ , it is necessary to reverse delay the filtered broadband signal by D taps using the tapped delay line. In practice,

Fig. 4.3 Results of fractional delay FIR filter.
a Frequency responses.
b Design errors



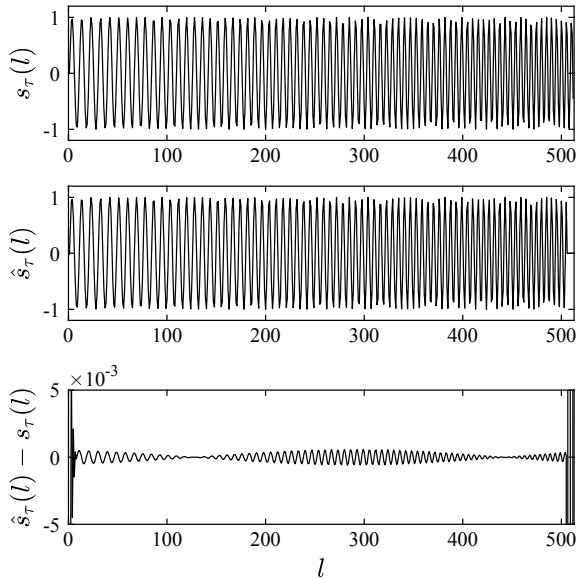
we don't really need to perform the reverse delay because in most cases a integer taps delay between the beamformer output and the input does not affect its performance.

Assume that we would like to design a fractional delay filter of length $L = 15$. The desired delay is $\tau = 0.12345T_s$, and the cut-off frequency is $0.4f_s$, i.e., the passband is $F_{PB} = [0, 0.4]$.

The frequency band $[0, 0.5]$ is uniformly discretized with 100 frequency grids. The desired frequency response of the fractional delay filter can be given from Eq. (4.26), as shown in Fig. 4.3a by dots. The weighting coefficients λ_k are chosen to be 1 for the frequency band $[0, 0.4]$ and 0 otherwise.

The FIR filter tap weights are designed using the three criteria respectively. The frequency responses (magnitude and phase responses) of the designed three FIR filters are shown in Fig. 4.3a. The corresponding design errors are shown in Fig. 4.3b.

Fig. 4.4 Effect of fractional delay FIR filter



It is seen that the frequency responses of the designed filters under three criteria all approximate the desired frequency response well. The errors of these three filters are different. These three filters are the optimum solutions in the sense of three minimum-norm criteria.

We next verify the performance of the designed fractional delay filter.

The expression of a continuous LFM waveform, $s(t)$, has been given by Eq. (2.49). The sampled version of it, i.e., $s(l) = s(t)|_{t=lT_s}$, was shown in Fig. 2.5a.

Assuming a delay of $\tau = 0.12345T_s$, the delayed version of the continuous LFM waveform is $s(t - \tau)$. The sampled version of it is $s_\tau(l) = s(t - \tau)|_{t=lT_s}$, which can also be calculated using Eq. (2.49), as shown in the upper plot of Fig. 4.4.

Now suppose that we don't know the expression $s(t)$ of the LFM waveform, but just know its sampled version $s(l)$. We want to obtain its delayed version, $\hat{s}_\tau(l)$, with a delay of τ by filtering $s(l)$ using the fractional delay filter shown in Fig. 4.3a.

Use the fractional delay filter designed using the ℓ_2 criterion shown in Fig. 4.3a to filter $s(l)$ and inversely delay the result by $D = 7$ taps. The resulting waveform $\hat{s}_\tau(l)$ is shown in the middle plot of Fig. 4.4.

The lower plot of Fig. 4.4 shows the error between $s_\tau(l)$ and $\hat{s}_\tau(l)$. It is seen that only the errors at both ends are relatively large. The error at the head is due to the sudden appearance of the source signal and the error at the tail is due to the zero padding at the tail of the filtered signal. In practice we can remove the head and the tail directly. Except for both ends, the error between $s_\tau(l)$ and $\hat{s}_\tau(l)$ is very small. This verifies that the design precision of the fractional delay FIR filter is very high.

Since the fractional delay filter can perform precise fractional time delay to a broadband signal of unknown expression, we can simulate the broadband signal received by the array using the fractional delay filters. The steps are as follows.

- Step 1. Choosing a reference point, calculate the propagation delay $\tau_m(\theta)$ ($m = 1, \dots, M$) of the signal arriving from θ between each sensor and the reference point using the method introduced in Chap. 1.
- Step 2. Simulate the broadband source signal, i.e., the signal that would be received at the reference point. The broadband signal can be either a deterministic signal or a band-limited broadband random process. In the latter case, it can be obtained by passing a broadband random process through a bandpass filter.
- Step 3. For each sensor, we design a fractional delay FIR filter with a desired time delay of $\tau_m(\theta)$, which is used to filter the broadband source signal to obtain the signal that would be received by the sensor.
- Step 4. For the case of multiple source signals, we can repeat the above process to obtain the array signal due to other source signals.
- Step 5. The broadband background noise received by the sensor array can be obtained by passing a set of broadband random processes through a bandpass filter. Generally, the background noise is required to be uncorrelated with the signals.
- Step 6. The simulated background noise is added to the array signal in a certain ratio to obtain the broadband array data received by the array.

4.4.2 Mixed-Norm Filter Design

Similar to the design of beamformer with desired mainlobe pattern, in some situations, we need to impose some constraints on the error norm at some frequencies while minimizing the error norm at the other frequencies [4]. The FIR filter design problem can be given by

$$\begin{aligned} & \min_{f \in F_1} \delta_{q_1}, \\ & \text{subject to } \delta_{q_2} \leq \xi_0, \quad f \in F_2, \end{aligned} \quad (4.28)$$

where $q_1, q_2 \in \{\infty, 1, 2\}$, $F_1, F_2 \subset F$, ξ_0 is a non-negative value specifying the desired constraints on the error measure. The set F_1 contains the frequencies where a minimization of the error measure is desired. The set F_2 contains the frequencies where bounds on the errors are imposed. The sets F_1 and F_2 need not be disjoint.

The design criterion used in Eq. (4.28) is referred to as the mixed-norm criterion. FIR filter design problem under various mixed-norm criteria can be formulated by choosing various cost functions and constraints. For example, the stopband peak error constrained weighted least square error passband FIR filter design problem can be written as

$$\begin{aligned} \min_{\mathbf{h}} \sum_{k=1}^K \left[\lambda_k |\mathbf{e}^T(f_k) \mathbf{h} - H_d(f_k)|^2 \right], \quad f_k \in F_{\text{PB}}, \\ \text{subject to } \max_{p=1, \dots, P} [\lambda_p |\mathbf{e}^T(f_p) \mathbf{h} - H_d(f_p)|] \leq \xi_0, \quad f_p \in F_{\text{SB}}, \end{aligned} \quad (4.29)$$

where $f_k \in F_{\text{PB}}$ ($k = 1, \dots, K$) are the frequency grids in the passband, and $f_p \in F_{\text{SB}}$ ($p = 1, \dots, P$) are the frequency grids in the stopband. The optimization problem in Eq. (4.29) is equivalent to choosing $q_1 = 2$ and $q_2 = \infty$ in Eq. (4.28).

If F_{PB} and F_{SB} are the same frequency set, it becomes the peak constrained weighted least square error filter design.

The FIR filter design problem that minimizes the maximum error in the stopband subject to a weighted squared error constraint in the passband can be formulated as

$$\begin{aligned} \min_{\mathbf{h}} \max_{p=1, \dots, P} [\lambda_p |\mathbf{e}^T(f_p) \mathbf{h} - H_d(f_p)|], \quad f_p \in F_{\text{SB}}, \\ \text{subject to } \sum_{k=1}^K \left[\lambda_k |\mathbf{e}^T(f_k) \mathbf{h} - H_d(f_k)|^2 \right] \leq \delta_0^2, \quad f_k \in F_{\text{PB}}, \end{aligned} \quad (4.30)$$

where δ_0^2 is the specified maximum passband squared error. The optimization problem in Eq. (4.30) is equivalent to choosing $q_1 = \infty$ and $q_2 = 2$ in Eq. (4.28).

The design problem that minimizes the weighted squared error in the passband subject to the weighted squared error constraint in the stopband can be formulated as

$$\begin{aligned} \min_{\mathbf{h}} \sum_{k=1}^K \left[\lambda_k |\mathbf{e}^T(f_k) \mathbf{h} - H_d(f_k)|^2 \right], \quad f_k \in F_{\text{PB}}, \\ \text{subject to } \sum_{p=1}^P \left[\lambda_p |\mathbf{e}^T(f_p) \mathbf{h} - H_d(f_p)|^2 \right] \leq \delta_0^2, \quad f_p \in F_{\text{SB}}. \end{aligned} \quad (4.31)$$

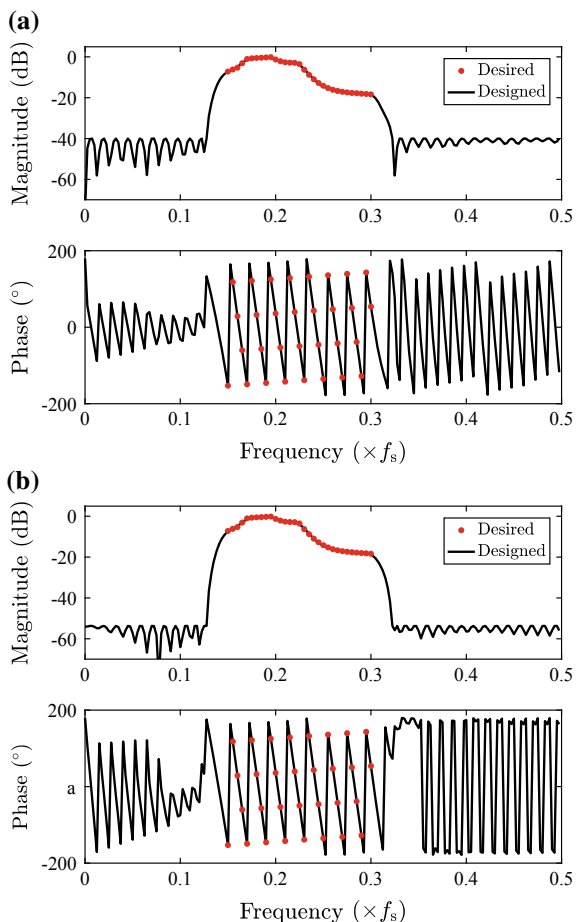
These optimization problems can be reformulated as SOCP problems that are computationally tractable. Note that the tap weights of the FIR filters are real, in contrast to the array pattern synthesis problems, in which the weight vectors are complex.

Assume that the desired frequency response of the FIR filter in the passband is shown by the dots in Fig. 4.5. The passband region is $F_{\text{PB}} = [0.15 : 0.005 : 0.3]$, which implies $K = 31$. The stopband region is chosen to be $F_{\text{SB}} = [0 : 0.0025 : 0.1275] \cup [0.3225 : 0.0025 : 0.4975]$, which implies $P = 123$. The desired response in the stopband is $H_d(f_p) = 0$. The length of the filter is $L = 80$.

First, the method in Eq. (4.29) is used to design the FIR filter. Assume that the attenuation in the stopband is specified to be -40 dB, i.e., $\xi_0 = 0.01$. We choose $\lambda_k = 1$ ($k = 1, \dots, K$) and $\lambda_p = 1$ ($p = 1, \dots, P$). The magnitude and phase responses of the designed FIR filters are shown by the solid lines in Fig. 4.5a.

It is seen that the magnitude and phase responses of the designed filter approximate the desired values well in the passband and the resulting stopband level is

Fig. 4.5 Results of FIR filter using mixed-norm criteria, **a** stopband peak constrained least square error passband design, **b** passband squared error constrained minimum stopband design



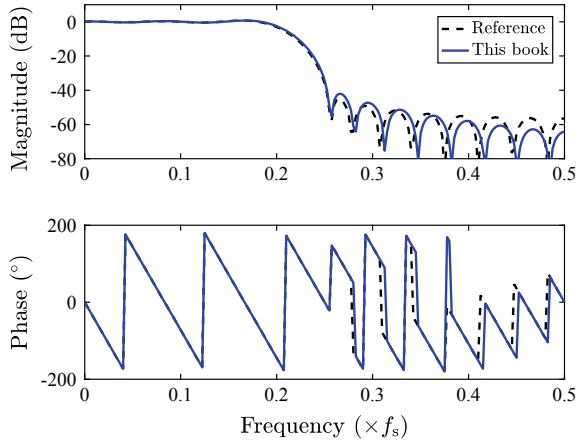
exactly -40 dB. Calculation results show that the obtained root-mean-square error in the passband is 0.0202. The obtained filter meets the design requirements well.

Next, we design the FIR filter using the method in Eq. (4.30). The constraint value on the root-mean-square error in the passband is chosen to be 0.0210, which is a little larger than that obtained in Fig. 4.5a. The other parameters remain unchanged. The magnitude and phase responses of the designed FIR filter are shown in Fig. 4.5b.

The results show that the maximum squared error constraint in the passband is satisfied, and the maximum stopband attenuation that can be obtained is -53.7 dB, which is lower than that in Fig. 4.5a. In other words, a lower stopband attenuation is obtained when the allowable passband approximation error is slightly larger.

In Ref. [5], a mean-squared stopband constrained least-square passband filter is designed using the quadratic programming method. Here, this method is compared with the method in Eq. (4.31).

Fig. 4.6 Mean-squared stopband constrained least-square passband filter design



We want to design a low-pass FIR filter whose passband is $[0, 0.2]$ and stopband is $[0.25, 0.5]$. The mean-squared error constraint value in the stopband is chosen to be $\delta_0^2 = 10^{-5}$. A uniform grid of 0.0025 is used to discretize the entire frequency band $[0, 0.5]$. The length of the filter is $L = 25$.

The resulting frequency responses of the filters designed using the methods in Ref. [5] and in Eq. (4.31) are shown in Fig. 4.6.

For the FIR filter designed using the method in Ref. [5], the mean-squared error in the passband is 0.0042, and that in the stopband is 6.54×10^{-6} , which is lower than the specified value. For the FIR filter designed using the method in Eq. (4.31), however, the mean-squared error in the passband is 0.0034, and that in the stopband is 1.00×10^{-5} , which is exactly equal to the specified value. It is seen that the method in Eq. (4.31) can obtain a lower mean-squared error in the passband while satisfying the specified stopband constraint. Its design precision is higher than the method in Ref. [5].

4.5 FIR Beamformer via Subband Beamformers and FIR Filters Designs

4.5.1 Design Principles

From Sect. 4.3, the FIR beamformers can be designed using a two-stage method. We first design the frequency-domain subband beamformer weight vectors, and then design the FIR filters for each sensor by using the relationship between the frequency-domain weight vectors and the FIR filter tap weights.

In Sect. 4.3, the FIR filter tap weights are calculated by performing IDFT to the frequency-domain weights, which is very inefficient. In fact, our goal is to choose

the tap weights to achieve the desired frequency response that approximates the frequency-domain subband beamformer weights over the frequency band of interest for each sensor. Then the FIR filter design methods in Sect. 4.4 can be used.

Taking the m th sensor as an example, the tap weights corresponding to this sensor is \mathbf{h}_m , where

$$\mathbf{h}_m = [h_{m1}, \dots, h_{ml}, \dots, h_{mL}]^T, \quad (4.32)$$

whose desired response at frequency f_k , denoted by $H_{d,m}(f_k)$, is equal to the corresponding subband beamformer weight $w_m^*(f_k)$, i.e.,

$$H_{d,m}(f_k) = w_m^*(f_k), \quad k = 1, \dots, K, \quad m = 1, \dots, M, \quad (4.33)$$

where f_k is the central frequency of each subband within the frequency band of interest.

If the array data are pre-delayed by T_m before passing through the FIR filters, as shown in Fig. 4.1, then

$$w_m^*(f_k) = H_{d,m}(f_k) \exp(-i2\pi f_k T_m), \quad k = 1, 2, \dots, K, \quad m = 1, 2, \dots, M, \quad (4.34)$$

or

$$H_{d,m}(f_k) = w_m^*(f_k) \exp(i2\pi f_k T_m), \quad k = 1, 2, \dots, K, \quad m = 1, 2, \dots, M. \quad (4.35)$$

Recall from Eq. (4.2) that the pre-delay in the Frost beamformer is exactly chosen as $T_m = -\tau_m(\theta_0)$ so that the signals received by each sensor will have the identical phases. Since these pre-delays are usually not an integer, mechanical or electronic pre-steering is applied.

In fact, in the method described in this section, we do not require $T_m = -\tau_m(\theta_0)$. We only need to choose the integer tap pre-delay close to $-\tau_m(\theta_0)$, i.e.,

$$T_m = -\text{int}[\tau_m(\theta_0)/T_s] \cdot T_s, \quad (4.36)$$

where $\text{int}(\cdot)$ denotes round towards the nearest integer. The benefit of this is that the integer tap pre-delay can be implemented directly using the tapped delay line.

Thus, in this method, the pre-delay can be performed after sampling, which avoids the use of the expensive mechanical or electronic delay devices in the Frost method. The block diagram of this method is shown in Fig. 4.7.

Note that in this method, the digital signal is obtained by sampling the analog signal $x_m(t)$ directly, and is denoted by $x_m(i)$, which is different from the data model of the FIR beamformer shown in Fig. 4.1, where the digital signal $x_m(i)$ is obtained by sampling the pre-delayed analog signal.

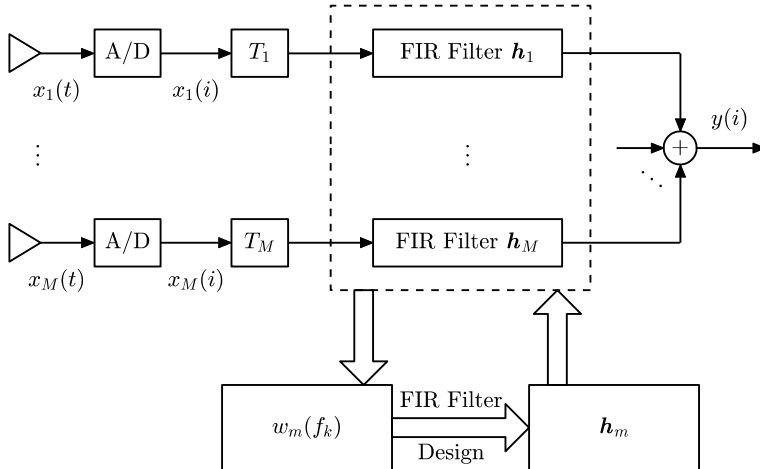


Fig. 4.7 Block diagram of two-stage method for FIR beamformer

The FIR filter tap weights are generally assumed to be real. It is known that the group delay of a real-valued FIR filter of length L is $(L - 1)T_s/2$. Thus, we can modify the required integer tap pre-delay as

$$T_m = -\text{int}[\tau_m(\theta_0)/T_s + (L - 1)/2] \cdot T_s, \quad m = 1, \dots, M, \quad (4.37)$$

where θ_0 is the steering direction. If the array is steered to the signal direction, then $\theta_0 = \theta_0$.

Note that T_m is not always positive. When T_m is negative, it is physically unrealizable. In practice, we can add a common integer tap delay in each channel so that all the delays are positive and the operations in Fig. 9.4 are physically realizable. This operation will cause a certain delay between the beamformer output and the input signals, however, this delay is very small and does not affect the beamformer performances.

In summary, the implementation of the two-stage method for the FIR beamformer consists of the following steps.

- Step 1. The operating frequency band F_{PB} is decomposed into a number of narrowband frequency bins $f_k \in F_{\text{PB}}$, $k = 1, 2, \dots, K$. For each frequency bin, we design the beamformer weight vectors $w(f_k) = [w_1(f_k), \dots, w_m(f_k), \dots, w_M(f_k)]$ using the methods discussed in Chap. 3.
- Step 2. The desired frequency response, $H_{d,m}(f_k)$, of the FIR filter corresponding to each sensor can be obtained using Eq. (4.35).
- Step 3. Design the FIR filter h_m corresponding to each sensor with desired frequency responses $H_{d,m}(f_k)$ using the methods described in Sect. 4.4.

Step 4. The output of each sensor is delayed by T_m and filtered using the corresponding FIR filter. The results are summed to obtain the broadband beamformer output time series, as shown in Eq. (4.10).

4.5.2 FIR Broadband Beamformer

1. Delay-and-sum beamformer

We design the time-domain broadband conventional beamformer using the two-stage method described in Sect. 4.5.1.

Consider a single plane-wave signal arriving from direction θ_0 . The propagation delay between the m th sensor and the reference point is $\tau_m(\theta_0)$. The array response vector for the signal is given by

$$\mathbf{p}(f_k, \theta_0) = [p_1(f_k, \theta_0), \dots, p_m(f_k, \theta_0), \dots, p_M(f_k, \theta_0)]^T, \quad (4.38)$$

where

$$p_m(f_k, \theta_0) = \exp[-i2\pi f_k \tau_m(\theta_0)]. \quad (4.39)$$

The weight vector of the conventional beamformer steering at θ_0 is given by

$$\mathbf{w}_c(f_k) = \mathbf{p}(f_k, \theta_0)/M. \quad (4.40)$$

The weight for the m th sensor is

$$\mathbf{w}_{c,m}(f_k) = \exp[-i2\pi f_k \tau_m(\theta_0)]/M. \quad (4.41)$$

Substituting Eq. (4.37) into Eq. (4.35) and suppressing θ_0 gives

$$\begin{aligned} H_{d,m}(f_k) &= \mathbf{w}_{c,m}^*(f_k) \exp\{-i2\pi f_k \text{int}[\tau_m/T_s + (L-1)/2] \cdot T_s\} \\ &= (1/M) \exp\{(-i2\pi f_k/T_s) [-\tau_m/T_s + \text{int}(\tau_m/T_s + (L-1)/2)]\}, \quad (4.42) \\ k &= 1, 2, \dots, K, \quad m = 1, 2, \dots, M. \end{aligned}$$

If L is odd (the derivation for L even is similar), letting $D = (L-1)/2$, Eq. (4.42) becomes

$$H_{d,m}(f_k) = (1/M) \exp\{(-i2\pi f_k/T_s) [-(\tau_m/T_s - \text{int}(\tau_m/T_s)) + D]\}. \quad (4.43)$$

Compared to Eq. (4.26), it is seen that this desired filter is exactly a fractional delay filter with delay $-(\tau_m/T_s - \text{int}(\tau_m/T_s))T_s + DT_s$, where $-(\tau_m/T_s - \text{int}(\tau_m/T_s))T_s \in [-0.5T_s, 0.5T_s]$.

From Fig. 4.7, the total delay of the m th sensor that consists of the pre-delay and the fractional delay is given by

$$T_m - [\tau_m/T_s - \text{int}(\tau_m/T_s)]T_s + DT_s = -\tau_m, \quad (4.44)$$

which is exactly the opposite of the propagation delay.

This shows that the time-domain broadband conventional beamformer designed by using the two-stage method is indeed the delay-and-sum beamformer.

Consider the array signal shown in Fig. 2.6. We design a time-domain broadband conventional beamformer using the two-stage method.

From the previous analysis, the desired filter for each channel is a fractional delay filter. The ℓ_2 criterion in Sect. 4.4.1 is used to design the FIR filters, where the length of each filter is chosen to be $L = 15$. The frequency band $[0, 0.5]$ is uniformly discretized with 160 frequency grids, and the operating frequency band $[f_l, f_u]$ includes 33 grids in total. The desired magnitude and phase responses and the resulting ones for the 2nd sensor are shown in Fig. 4.8a.

The beamformer output time series $y(i)$ is shown in the upper plot of Fig. 4.8b, and the error, $y(i) - s(i)$, between the beamformer output and the source signal is shown in the lower plot of Fig. 4.8b. It is seen that the error between the beamformer output and the source signal is very small except for both ends, reaching the level of 10^{-8} .

It is seen from Fig. 4.8a that the magnitude response of the designed filter is 0 dB over a broad frequency range. If we require the filter to suppress the out-of-band components while delaying the signal in the operating band, a mixed-norm criterion can be used.

Assume that the length of each filter is $L = 64$ and the specified stopband attenuation is -40 dB. The FIR filters are designed using the stopband peak constrained least square error passband method in Eq. (4.30). The desired magnitude and phase responses and the resulting ones for the 2nd sensor are shown in Fig. 4.9a.

The beamformer output time series $y(i)$ and its distortion $y(i) - s(i)$ are shown in Fig. 4.9b. It is seen that the distortion is larger than the result shown in Fig. 4.8b, but much lower than that of the DFT beamformer shown in Fig. 2.8, which is sufficient for practical applications.

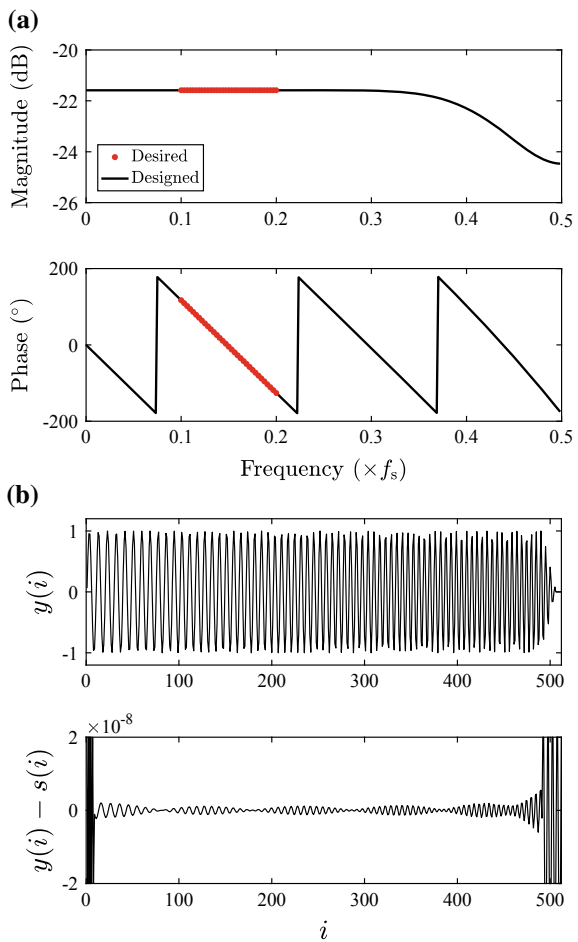
2. Frequency-invariant beamformer

We next design the frequency-invariant FIR beamformer using the two-stage method.

Consider a 12-element ULA with a half-wavelength spacing at f_0 . The operating frequency band is $[f_l, f_u] = [f_0/2, f_0]$. The sampling frequency is $f_s = 3.125f_0$, so the normalized operating frequency band is $[f_l/f_s, f_u/f_s] = [0.16, 0.32]$. The discretized frequency interval is 0.005, and the operating frequency band $[f_l, f_u]$ includes 33 frequency grids.

The two-stage method is used to design a frequency-invariant FIR beamformer with a steering direction of 10° . The length of each FIR filter is $L = 64$ and the desired stopband attenuation is -40 dB.

Fig. 4.8 Results of time-domain broadband conventional beamformer. **a** Desired and designed frequency responses corresponding to the 2nd sensor, **b** FIR beamformer output and the error between it and the source signal



The beam patterns for each frequencies within the operating frequency band are designed using the method described in Sect. 3.4.5, as shown in Fig. 3.28.

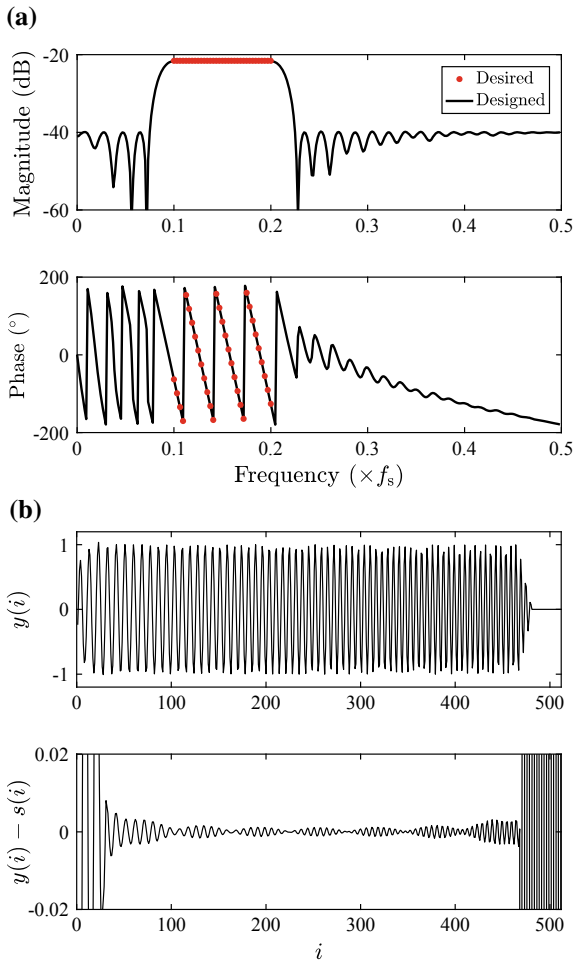
The FIR filters are designed using the stopband peak constrained least square error passband method as shown in Eq. (4.30). The desired magnitude and phase responses and the resulting ones for the 2nd sensor are shown in Fig. 4.10.

Using the FIR filter tap weights, the equivalent weight vector, denoted by $\hat{w}(f_k)$, of each subband of the FIR beamformer within the operating frequency band can be calculated.

From Eq. (4.20), the frequency response of filter with tap weights \mathbf{h}_m is given by

$$H_m(f_k) = \mathbf{h}_m^T \mathbf{e}(f_k). \quad (4.45)$$

Fig. 4.9 Results of time-domain broadband conventional beamformer with stopband suppression. **a** Desired and designed frequency responses corresponding to the 2nd sensor, **b** FIR beamformer output series and the error between it and the source signal



Using $H_m(f_k)$ instead of $H_{d,m}(f_k)$ in Eq. (4.34), the weights of the FIR beamformer at frequency f_k is given by

$$\hat{w}_m^*(f_k) = \mathbf{h}_m^T \mathbf{e}(f_k) \exp(-i2\pi f_k T_m), \quad k = 1, 2, \dots, K, \quad m = 1, 2, \dots, M. \quad (4.46)$$

Thus, the equivalent weight vector employed at frequency f_k is

$$\hat{\mathbf{w}}(f_k) = [\hat{w}_1(f_k), \dots, \hat{w}_m(f_k), \dots, \hat{w}_M(f_k)]^T. \quad (4.47)$$

Using the equivalent weight vector, the beam patterns of the FIR beamformer can be calculated for each frequency grid, as shown in Fig. 4.11.

Fig. 4.10 Desired and designed frequency responses corresponding to the 2nd sensor

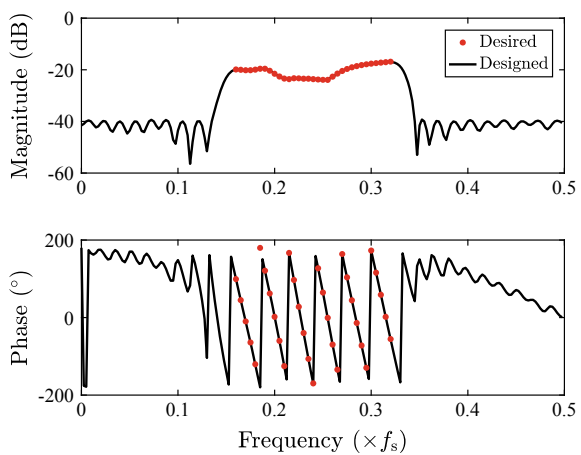
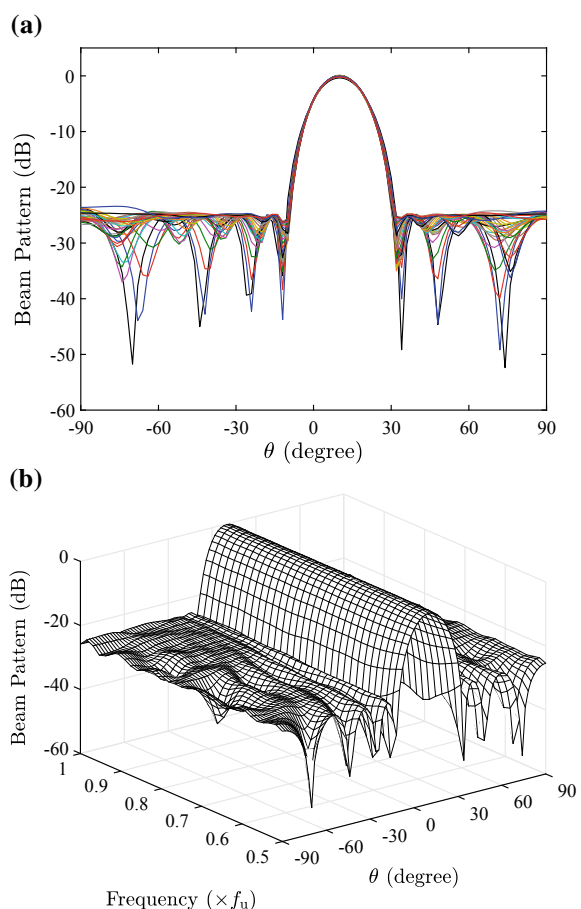


Fig. 4.11 Beam patterns of frequency-invariant FIR beamformer, **a** superposition plot, **b** three-dimensional plot



Comparing Fig. 4.11 to the subband beam patterns in Fig. 3.28, the sidelobe level of the FIR beamformer slightly increases, reaching about -23 dB. Calculation results show that the root-mean-square error between the designed and the desired mainlobe patterns of the subband beamformer is 0.0197, while that of the FIR beamformer increases slightly to 0.0199. The increasing of the sidelobe level and the mainlobe error is due to the FIR filter design error. However, this slight increase is acceptable in most cases.

3. High array gain with sidelobe control

For the above 12-element ULA, assume that an interferer arrives from 50° with the INR of 30 dB. The steering direction is 0° . We design the sidelobe constrained high array gain FIR beamformer using the two-stage method.

First, we design the RSLC beamformers for each subband using Eq. (3.98). The specified sidelobe level is -25 dB, and the WNG loss is chosen to be 2 dB. As the frequency increases, the mainlobe beamwidth is set to be linearly narrowed, with upper and lower bounds of 50° and 30° , respectively.

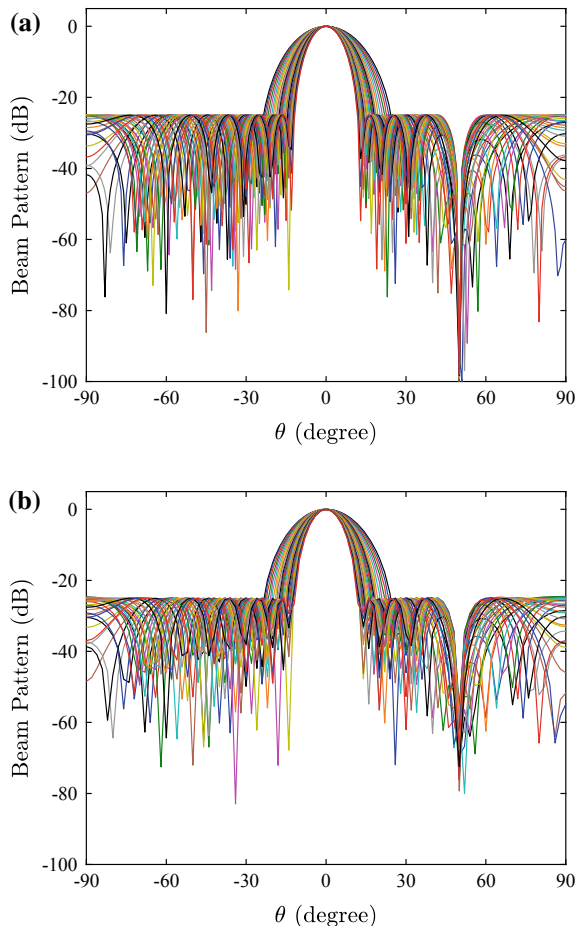
The superposition plot of the resulting beam patterns, i.e., the beam patterns of the DFT beamformer, at the 33 frequency grids are shown in Fig. 4.12a. It is seen that the sidelobes meet the design requirement and the beam patterns put perfect nulls in the interferer direction across the operating frequency band, with the depth from -100 dB to -92 dB.

In order to obtain the FIR beamformer, the FIR filters corresponding to each sensor are designed using the stopband peak constrained least square error passband method. We calculate the equivalent weight vector using Eqs. (4.46) and (4.47), and then calculate the beam patterns of the FIR beamformer at each frequency grid, as shown in Fig. 4.12b.

It is seen that the mainlobe patterns of the FIR beamformer are similar to those of the DFT beamformer. Due to the FIR filter design error, the sidelobe level of the FIR beam patterns slightly increases to about -24.5 dB. The depths of the nulls of the FIR beam pattern increase to a range from -79 to -55 dB.

When the sidelobe response is very small (the null can be viewed as a special sidelobe), even a small design error of the FIR filter can result in a significant increase in sidelobe response, which is one of the disadvantages of the two-stage method.

Fig. 4.12 Superposition plot of beam patterns of sidelobe constrained high array gain beamformer, **a** DFT beamformer, **b** FIR beamformer



4.6 Summary

The time-domain implementation of the broadband beamformer based on the filter-and-sum structure is studied in this chapter.

The time-domain broadband beamformer can be implemented by placing an FIR filter at the output of each sensor. The signals arriving at each sensor are pre-delayed and filtered, and the results are summed to obtain the output signal. This broadband beamformer is termed FIR beamformer.

The relationships between the weight vectors of a DFT beamformer and the tap weights of an FIR beamformer are derived. Letting the latest output of a DFT beamformer be equal to that of an FIR beamformer, when the length of each FIR filter is equal to the length of each buffer in the DFT beamformer, the FIR filter tap weights and the DFT beamformer weights are a discrete Fourier transform pair. This rela-

tionship can be used to calculate the FIR filter tap weights of the FIR beamformer designed by using the narrowband techniques.

This technique has potential for computational saving to calculate the tap weights of the FIR beamformer. Consider that in an FIR beamformer, the frequency response of the FIR filter (including pre-delay) is actually the corresponding frequency-domain weights. This technique estimate the tap weights by simply performing IDFT to the frequency-domain weights, which is very inefficient. Moreover, the algorithm may lead to large number of taps, since it requires that the number of taps be equal to the length of the buffer in the DFT beamformer.

FIR filter design is an important part of the FIR beamformer design. The FIR filter design is analogous to the optimal array pattern synthesis for spatial filter except that the filter coefficients are generally real. Therefore, the methods discussed in Sect. 3.4 for mainlobe pattern synthesis can be modified for FIR filter design. The minimum-norm and mixed-norm criteria have been used in FIR filter design with good results.

The FIR beamformers can be designed using a two-stage method. In the first stage, we design the narrowband beamformers for a number of frequency grids in the operating frequency band. In the second stage, the FIR filter corresponding to each sensor is designed such that its frequency response approximates the complex weights of the DFT beamformer for the sensor over the operating frequency band. The resulting beam patterns of the FIR beamformer in the operating frequency band approximates those of the DFT beamformers.

References

1. O.L. Frost, An algorithm for linearly constrained adaptive array processing. *Proc. IEEE* **60**(8), 926–935 (1972)
2. L.C. Godara, Application of the fast Fourier-transform to broad-band beamforming. *J. Acoust. Soc. Am.* **98**(1), 230–240 (1995)
3. S. Yan, Y. Ma, Optimal design and verification of temporal and spatial filters using second-order cone programming approach. *Sci. China Ser. F: Inf. Sci.* **49**(2), 235–253 (2006)
4. S. Yan, Y. Ma, A unified framework for designing FIR filters with arbitrary magnitude and phase response. *Digit. Signal Process.* **14**(6), 510–522 (2004)
5. M.H. Er, C.K. Siew, Design of FIR filters using quadratic-programming approach. *IEEE Trans. Circuits Syst. II: Analog. Digit. Signal Process.* **42**(3), 217–220 (1995)

Chapter 5

Optimal Design of Time-Domain Broadband Beamformers



5.1 Introduction

In Chap. 4, the time-domain implementation of a broadband beamformer is presented. It is based on a real-valued filter-and-sum structure, in which the output of each sensor are filtered using an FIR filter and the results are summed to obtain the beamformer output. The FIR-based time-domain beamformer are designed by separately designing the subband beamformers for each frequency bin and the FIR filters corresponding to each sensor.

This method is referred to as a two-stage design method. In the first stage, the narrowband beamformers are designed for a number of grid points over the operating frequency band using the methods discussed in Chap. 3. In the second stage, the FIR filter corresponding to each sensor is optimally designed such that it has a response that approximates the complex weights of the subband beamformers for the sensor over the operating frequency band.

The advantage of the two-stage design method is the ease of design and the low computational complexity. The two-stage design method can obtain the optimal solutions to narrowband array pattern synthesis and FIR filter design separately. However, it cannot guarantee to obtain the global optimum solution to the FIR beamformer design problem. The main disadvantages are that the approximation error between the weights generated by the FIR filter and those of the frequency-domain narrowband beamformer causes an error in the resulting broadband beam pattern, the stopband attenuation of the FIR filter is difficult to determine, and the sidelobes at the transition frequency band are difficult to be controlled.

By writing the expressions for the broadband beam response and the beamformer performance measures in terms of the tap weights of the FIR filters corresponding to the sensors, the techniques that are developed for the narrowband beamformers can be extended to the broadband case. An optimization problem can then be formulated to obtain the tap weights, in which the beam responses can be jointly optimized to satisfy some spatial and frequency-domain specifications [1].

The rest of this chapter is organized as follows. In Sect. 5.2, we design the FIR beamformer by jointly optimizing the spatial and frequency responses of the beamformer. In Sect. 5.3, an adaptive FIR beamformer with sidelobe control is designed. In Sect. 5.4, a method for designing the FIR beamformer with frequency-invariant patterns is presented by minimizing the mainlobe spatial response variation. In Sect. 5.5, a unified framework for designing FIR beamformers is presented using the multiple-objective design method. A brief summary of this chapter is given in Sect. 5.6.

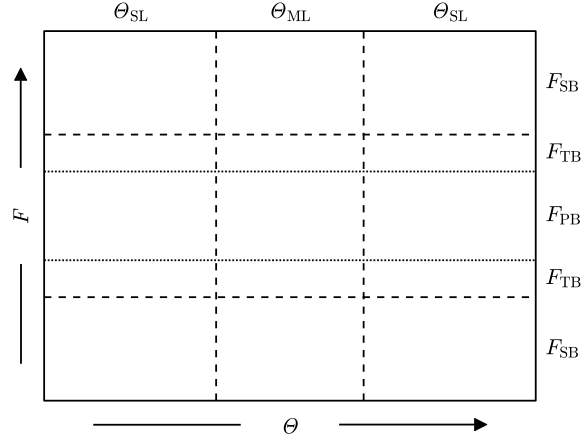
5.2 Jointly Spatial and Frequency Responses Optimization

5.2.1 Drawback of Two-Stage Method

Define the entire frequency band as $F \triangleq [0, f_s/2)$ and the entire visible region as Θ . Assume that the operating frequency band is $F_{PB} \triangleq [f_l, f_u] \subset F$ and the stopband is $F_{SB} \subset F$. The frequency band between the stopband and the operating band is the transition band, which is defined as $F_{TB} \subset F$. Then we have $F = F_{PB} \cup F_{SB} \cup F_{TB}$. The sidelobe region and mainlobe region are denoted by $\Theta_{SL} \subset \Theta$ and $\Theta_{ML} \subset \Theta$, respectively. The division of the visible region and the frequency band is shown in Fig. 5.1.

In the two-stage method, the FIR beamformer consists of the subband beamformer design and the FIR filter design. In the subband beamformer design stage, the sidelobes of the beam pattern within the operating frequency band can be controlled. In the FIR filter design stage, the stopband of the FIR filter suppresses the beam patterns in the stopband region. The beam patterns in the stopband region are referred to as the stopband sidelobes in this book. In summary, the region in which the beam patterns can be controlled are shown by the shading in Fig. 5.2a.

Fig. 5.1 Division of visible region and frequency band



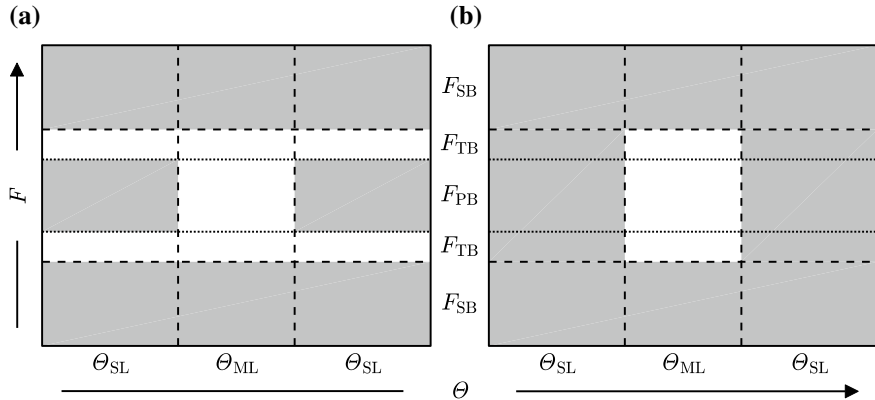


Fig. 5.2 The region in which the beam patterns can be controlled for **a** two-stage method, and **b** global optimization method

It is seen from Fig. 5.2a that, this method does not control the sidelobes in the transition band, which may result in high sidelobes in this region. In fact, the region in which the sidelobes are really required to be controlled is the shaded region in Fig. 5.2b, which is exactly the region in which the sidelobes to be controlled by the global optimization method to be introduced later.

Moreover, due to the FIR filter design error, the sidelobes of the FIR beam patterns in the operating band are slightly higher than that of the subband beam pattern, and the mainlobe pattern synthesis accuracy is slightly reduced. In addition, it is difficult to determine the desired stopband attenuation of the FIR filter based on the desired stopband sidelobe level.

5.2.2 FIR Beamformer Pattern

In the previous sections, we have introduced the block diagram of the FIR beamformer, as shown in Fig. 5.3.

The FIR filter tap weights corresponding to the m th sensor is given by

$$\mathbf{h}_m = [h_{m1}, \dots, h_{ml}, \dots, h_{mL}]^T. \quad (5.1)$$

From Eq. (4.46), the equivalent weight vector, denoted by $\hat{\mathbf{w}}(f)$, of the FIR beamformer at frequency f is given by

$$\hat{\mathbf{w}}(f) = [\hat{w}_1(f), \dots, \hat{w}_m(f), \dots, \hat{w}_M(f)]^T, \quad (5.2)$$

where

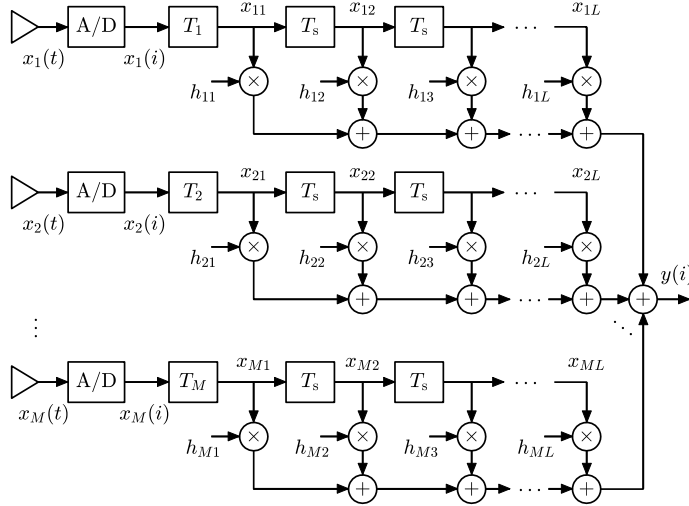


Fig. 5.3 Block diagram of FIR beamformer

$$\hat{w}_m(f) = \text{conj}[\mathbf{h}_m^T \mathbf{e}(f) \exp(-i2\pi f T_m)], m = 1, 2, \dots, M, \quad (5.3)$$

with $\mathbf{e}(f) = [1, \exp(-i2\pi f T_s), \dots, \exp(-i(L-1)2\pi f T_s)]^T$.

Let $\kappa_m(f) = \exp(-i2\pi f T_m)$, we have

$$\begin{aligned} \hat{w}^*(f) &= [\hat{w}_1^*(f), \dots, \hat{w}_m^*(f), \dots, \hat{w}_M^*(f)]^T \\ &= [\mathbf{h}_1^T \mathbf{e}(f) \kappa_1(f), \dots, \mathbf{h}_m^T \mathbf{e}(f) \kappa_m(f), \dots, \mathbf{h}_M^T \mathbf{e}(f) \kappa_M(f)]^T \\ &= \{[\mathbf{h}_1, \dots, \mathbf{h}_m, \dots, \mathbf{h}_M]^T \mathbf{e}(f)\} \circ \kappa(f) \\ &= [\mathbf{H} \mathbf{e}(f)] \circ \kappa(f), \end{aligned} \quad (5.4)$$

where “ \circ ” denotes the Hadamard product of two vectors, i.e., the element-by-element multiplication of two vectors, and

$$\begin{aligned} \mathbf{H} &= [\mathbf{h}_1, \dots, \mathbf{h}_m, \dots, \mathbf{h}_M]^T \\ &= \begin{bmatrix} h_{11} & \dots & h_{1L} & \dots & h_{1L} \\ \vdots & \ddots & \vdots & & \vdots \\ h_{m1} & \dots & h_{ml} & \dots & h_{mL} \\ \vdots & & \vdots & \ddots & \vdots \\ h_{M1} & \dots & h_{Ml} & \dots & h_{ML} \end{bmatrix}, \end{aligned} \quad (5.5)$$

$$\kappa(f) = [\kappa_1(f), \dots, \kappa_m(f), \dots, \kappa_M(f)]^T. \quad (5.6)$$

Thus, the beam pattern of the FIR beamformer is given by

$$\begin{aligned} B(f, \theta) &= \hat{\mathbf{w}}^H(f) \mathbf{p}(f, \theta) \\ &= \mathbf{p}^T(f, \theta) \hat{\mathbf{w}}^*(f) \\ &= [\mathbf{p}(f, \theta) \circ \kappa(f)]^T \mathbf{H} \mathbf{e}(f). \end{aligned} \quad (5.7)$$

Introducing the operation

$$\mathbf{h} = \text{vec}\{\mathbf{H}\}, \quad (5.8)$$

where $\text{vec}\{\cdot\}$ denotes the vectorization operator which stacks the columns of a matrix on top of each other, Eq. (5.7) becomes

$$\begin{aligned} B(f, \theta) &= \{\mathbf{e}(f) \otimes [\mathbf{p}(f, \theta) \circ \kappa(f)]\}^T \mathbf{h} \\ &= \mathbf{u}^T(f, \theta) \mathbf{h} = \mathbf{h}^T \mathbf{u}(f, \theta), \end{aligned} \quad (5.9)$$

where \otimes denotes the Kronecker product and $\mathbf{u}(f, \theta) = \mathbf{e}(f) \otimes [\mathbf{p}(f, \theta) \circ \kappa(f)]$. It is seen that $\mathbf{u}(f, \theta)$ is the array manifold vector corresponding to the stacked vector \mathbf{h} , which can be viewed as the broadband response vector of the FIR beamformer, and is given by

$$\mathbf{u}(f, \theta) = \text{vec}\{\mathbf{U}(f, \theta)\}, \quad (5.10)$$

where $\mathbf{U}(f, \theta)$ is an $M \times L$ matrix, whose (m, l) th element is given by

$$[\mathbf{U}(f, \theta)]_{m,l} = \exp\{-i2\pi f[T_m + \tau_m(\theta) + (l-1)T_s]\}. \quad (5.11)$$

The expression in Eq. (5.9) has a form that resembles that for a narrowband beam pattern in Eq. (1.44), as well as that for an FIR filter response in Eq. (4.20). Therefore, the narrowband beamformer design methods discussed in Chap. 3 and the FIR filter design methods discussed in Sect. 4.4 can be extended to the FIR beamformer design.

5.2.3 Frequency-Invariant FIR Beamformer

We discretize the frequency band and the visible region.

Assume that the discretized frequency grids within the operating frequency band are $f_k \in F_{\text{PB}}, k = 1, 2, \dots, K$, those in the stopband are $f_p \in F_{\text{SB}}, p = 1, 2, \dots, P$, and those in the transition band are

$$f_t \in F_{\text{TB}}, t = 1, 2, \dots, T, \quad (5.12)$$

where F_{TB} is the transition frequency band.

Discretize the visible region Θ as

$$\theta_q \in \Theta, q = 1, 2, \dots, N_{\text{FOV}}, \quad (5.13)$$

where N_{FOV} is the number of the direction grids. The direction grids within the sidelobe region and the mainlobe region are $\theta_i \in \Theta_{\text{SL}}$ ($i = 1, 2, \dots, N_{\text{SL}}$) and $\theta_j \in \Theta_{\text{ML}}$ ($j = 1, 2, \dots, N_{\text{ML}}$), respectively.

Controlling the spatial domain and the frequency-domain sidelobes of the beamformer and letting the mainlobe pattern approximate the desired one within the operating frequency band, the global optimization problem of the frequency-invariant FIR beamformer design under the minimax criterion can be formulated as

$$\begin{aligned} & \min_{\mathbf{h}} \max_{k,j} |B(f_k, \theta_j) - B_d(\theta_j)|, f_k \in F_{\text{PB}}, \theta_j \in \Theta_{\text{ML}}, \\ & \text{subject to } |B(f_k, \theta_i)| \leq \xi_{0ki}, f_k \in F_{\text{PB}}, \theta_i \in \Theta_{\text{SL}}, \\ & \quad |B(f_t, \theta_i)| \leq \xi_{0ti}, f_t \in F_{\text{TB}}, \theta_i \in \Theta_{\text{SL}}, \\ & \quad |B(f_p, \theta_q)| \leq \xi_{0pq}, f_p \in F_{\text{SB}}, \theta_q \in \Theta, \end{aligned} \quad (5.14)$$

where $B_d(\theta_j)$, $\theta_j \in \Theta_{\text{ML}}$ is the desired beam response at θ_j within the operating frequency band and the mainlobe region, $B(f, \theta) = \mathbf{u}^T(f, \theta)\mathbf{h}$ is the beam response of the designed beamformer at f and θ . ξ_{0ki} , ξ_{0ti} and ξ_{0pq} are the prescribed constraint values on the sidelobes within the operating frequency band, the sidelobes within the transition band, and the beam responses within the stopband (i.e., the stopband sidelobes), respectively. Moreover, different constraint values can be chosen for different frequencies and directions.

Clearly, this constrained optimization problem can be formulated as an SOCP problem for solution.

Compared to the two-stage method, the global optimization method in Eq. (5.14) can strictly control the spatial domain and the frequency-domain sidelobes, thereby improving the design precision.

Recall the discussion in Chap. 3 that the robustness of the narrowband beamformer can be improved by constraining the norm of the weight vector. We can also improve the robustness of the FIR beamformer by constraining the norm of the filter tap weights to some known constant $\Delta_0 > 0$, i.e.,

$$\sum_{m=1}^M \sum_{l=1}^L \|h_{ml}\|^2 \leq \Delta_0^2, \quad (5.15)$$

or

$$\|\mathbf{h}\| \leq \Delta_0. \quad (5.16)$$

The smaller the specified value Δ_0 , the higher the robustness. Imposing this constraint to Eq. (5.14), the resulting optimization problem can also be solved using SOCP.

If we try to approximate the desired mainlobe pattern in a least squares sense, the optimization problem becomes

$$\begin{aligned} \min_{\mathbf{h}} \sum_{j=1}^{N_{\text{ML}}} \sum_{k=1}^K |B(f_k, \theta_j) - B_d(\theta_j)|^2, \quad f_k \in F_{\text{PB}}, \theta_j \in \Theta_{\text{ML}}, \\ \text{subject to } |B(f_k, \theta_i)| \leq \xi_{0ki}, \quad f_k \in F_{\text{PB}}, \theta_i \in \Theta_{\text{SL}}, \\ |B(f_t, \theta_i)| \leq \xi_{0ti}, \quad f_t \in F_{\text{TB}}, \theta_i \in \Theta_{\text{SL}}, \\ |B(f_p, \theta_q)| \leq \xi_{0pq}, \quad f_p \in F_{\text{SB}}, \theta_q \in \Theta, \\ \|\mathbf{h}\| \leq \Delta_0. \end{aligned} \quad (5.17)$$

Similar to Eq. (3.163), the objective function in Eq. (5.17) can be converted to the following form:

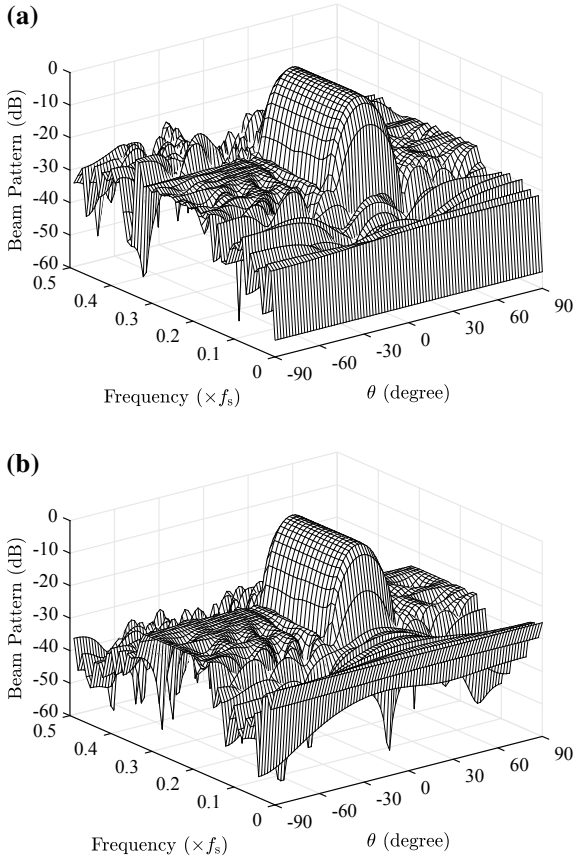
$$\begin{aligned} & \sum_{j=1}^{N_{\text{ML}}} \sum_{k=1}^K |B(f_k, \theta_j) - B_d(\theta_j)|^2 \\ &= \sum_{j=1}^{N_{\text{ML}}} \sum_{k=1}^K |\mathbf{u}^T(f_k, \theta_j) \mathbf{h} - B_d(\theta_j)|^2 \\ &= \left\| \begin{array}{c} \mathbf{u}^T(f_1, \theta_1) \mathbf{h} - B_d(\theta_1) \\ \vdots \\ \mathbf{u}^T(f_1, \theta_j) \mathbf{h} - B_d(\theta_j) \\ \vdots \\ \mathbf{u}^T(f_1, \theta_{N_{\text{ML}}}) \mathbf{h} - B_d(\theta_{N_{\text{ML}}}) \\ \vdots \\ \mathbf{u}^T(f_k, \theta_j) \mathbf{h} - B_d(\theta_j) \\ \vdots \\ \mathbf{u}^T(f_K, \theta_{N_{\text{ML}}}) \mathbf{h} - B_d(\theta_{N_{\text{ML}}}) \end{array} \right\|^2, \end{aligned} \quad (5.18)$$

where the total number of rows are $K \cdot N_{\text{ML}}$.

The methods in Eqs. (5.14) and (5.17) are referred to as the global optimization methods in this book.

Consider the same cases as in Fig. 4.11, that is, a 12-element ULA with a half-wavelength spacing at f_0 . The operating frequency band is $[f_1, f_u] = [f_0/2, f_0]$. The sampling frequency is $f_s = 3.125f_0$, so the normalized operating frequency band is $[f_1/f_s, f_u/f_s] = [0.16, 0.32]$. The steering direction is 10° and the length of each FIR filter is $L = 64$.

Fig. 5.4 Frequency-invariant broadband beam pattern. **a** Two-stage method. **b** Global optimization method



The frequency band and the visible region are discretized using 0.01 and 2° grids, respectively. $F_{\text{PB}} = [0.16 : 0.01 : 0.32]$, $F_{\text{SB}} = [0 : 0.01 : 0.13] \cup [0.35 : 0.01 : 0.50]$, $F_{\text{TB}} = [0.14 : 0.01 : 0.15] \cup [0.33 : 0.01 : 0.34]$, $\Theta = [-90^\circ : 2^\circ : 90^\circ]$, $\Theta_{\text{ML}} = [-8^\circ : 2^\circ : 28^\circ]$, $\Theta_{\text{SL}} = [-90^\circ : 2^\circ : -12^\circ] \cup [32^\circ : 2^\circ : 90^\circ]$.

First, the two-stage method is used to design an FIR beamformer with frequency-invariant pattern, where the parameters are chosen to be the same as those in Fig. 4.11 except for the discretized frequency grid. After obtaining the FIR filters, the beam patterns of the FIR beamformer at the discretized frequency and direction grids are calculated using Eq. (5.9) and shown in Fig. 5.4a.

It is seen that the maximum sidelobe of this broadband beam pattern within the passband is -24.1 dB, which is slightly higher than the desired value -25 dB. The sidelobe level in the transition band is -15.1 dB and the maximum magnitude of the pattern in the stopband (i.e., the stopband sidelobe level) is -21.9 dB. These results are consistent with the previous analyses. Calculation results show that the norm of the FIR filter tap weights is $\|\mathbf{h}\| = 0.25$.

Table 5.1 Performance comparison of broadband beamformers

Broadband beamformers	Passband SL (dB)	Transition band SL (dB)	Stopband SL (dB)	$\ \mathbf{h}\ $	RMS error
DFT beamformer	-25.0	-	-	-	0.0204
Two-stage	-24.1	-15.1	-21.9	0.25	0.0205
Global optimization	-25.0	-25.0	-25.0	0.25	0.0197

Next, we design the frequency-invariant FIR beamformer using the least-square global optimization method in Eq. (5.17), where the prescribed sidelobe level is chosen to be -25 dB. The constraint value on the filter norm is $\Delta_0 = 0.25$, which is equal to that of the two-stage method. The beam patterns of the obtained FIR beamformer at the frequency and direction grids are calculated, as shown in Fig. 5.4b.

It is seen that the beamformer sidelobes in the passband and the transition band, as well as the beam response amplitude in the stopband region are all strictly below -25 dB.

The performance comparisons of the FIR beamformers using the two-stage method and the global optimization method in terms of the mainlobe approximation precision (root-mean-square error, or RMS error), sidelobe level (SL), and filter norm are listed in Table 5.1. The relevant performances of the DFT beamformer are also listed in Table 5.1.

It is seen from Table 5.1 that the root-mean-square error of the mainlobe of the FIR beamformer designed using the global optimization method is smaller than that of the two-stage method. Compared to the two-stage method, the global optimization method can not only strictly control the sidelobes, but also achieve a higher mainlobe approximation precision. However, the computational complexity of the global optimization method is higher than that of the two-stage method.

Note that the root-mean-square error of the mainlobe of the FIR beamformer using the global optimization method is even smaller than that of the DFT beamformer. The reason for this is that the global optimization method only constrains the norm of the FIR filter tap weights, while in the DFT beamformer, the norm of each subband weight vector is constrained, which is a more strict constraint. This can be clearly seen in the analysis results below.

The weight vector norms $\|\mathbf{w}(f_k)\|$ (or $\|\hat{\mathbf{w}}(f_k)\|$), of the three beamformers (DFT beamformer, FIR beamformer using two-stage method and FIR beamformer using global optimization method) as functions of grid index k are shown in Fig. 5.5a.

It is seen that, at these frequency grids, the weight vector norms of the DFT beamformer are strictly controlled below the prescribed value $\sqrt{\zeta_0} = 0.4217$. The weight vector norm of the FIR beamformer using two-stage method approximates that of the DFT beamformer. For the FIR beamformer using global optimization method, the weight vector norms of the first three frequency grids are larger than those of the DFT beamformer.

Fig. 5.5 Performance comparison of DFT beamformer, FIR beamformer using two-stage method and FIR beamformer using global optimization method. **a** Weight vector norm. **b** Root-mean-square error of the mainlobe

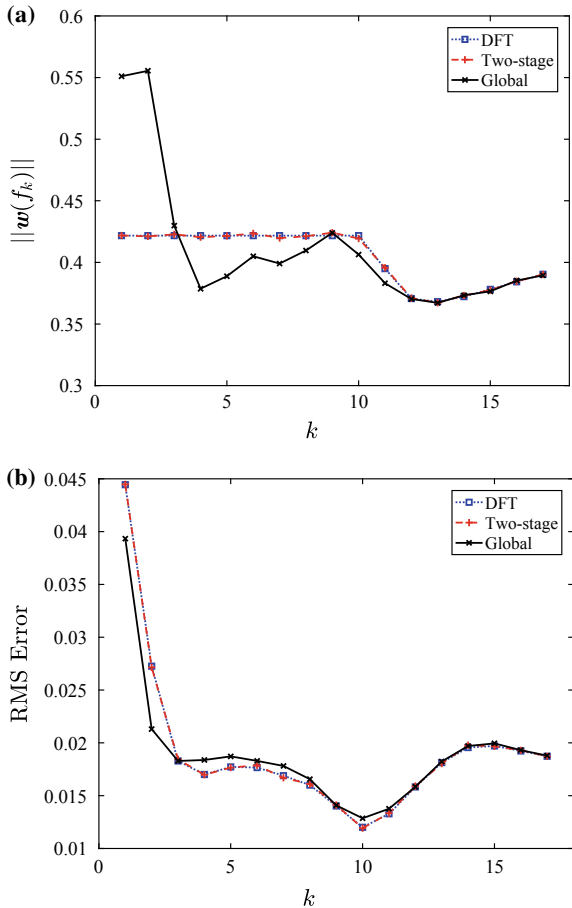


Figure 5.5b shows the root-mean-square errors of the mainlobe of the three beamformers as functions of k . It is seen that the root-mean-square errors of the mainlobe of the two-stage method are roughly equivalent to those of the DFT beamformer. Calculation results show that the former is slightly higher than the latter due to the design error of the FIR filters. For the FIR beamformer using global optimization method, at the frequency grid where its weight vector norm is larger than that of the DFT beamformer, the corresponding root-mean-square error of the mainlobe is smaller than that of the DFT beamformer.

From the previous analysis, Eq. (5.16) only constrains the filter tap weights norm and the equivalent weight vector norm of the designed FIR beamformer may be higher than that of the DFT beamformer at some frequency grids. If necessary, when designing the FIR beamformer, we can constrain the equivalent weight vector norm of each frequency grid separately, i.e.,

$$\|\hat{\mathbf{w}}(f_k)\| \leq \sqrt{\zeta_{0k}}, f_k \in F_{\text{PB}}, k = 1, 2, \dots, K, \quad (5.19)$$

where $\sqrt{\zeta_{0k}}$ is the constraint value on the weight vector norm for the k th frequency grid.

From Eq. (5.4), we have

$$\hat{\mathbf{w}}^*(f) = [\mathbf{H}\mathbf{e}(f)] \circ \kappa(f). \quad (5.20)$$

Then

$$\|\hat{\mathbf{w}}^*(f_k)\| = \|[\mathbf{H}\mathbf{e}(f_k)] \circ \kappa(f_k)\| = \|\mathbf{H}\mathbf{e}(f_k)\| = \|[\mathbf{e}^T(f_k) \otimes \mathbf{I}_{M \times M}] \mathbf{h}\|. \quad (5.21)$$

Therefore, the equivalent weight vector norm constraint of the FIR beamformer becomes

$$\|[\mathbf{e}^T(f_k) \otimes \mathbf{I}_{M \times M}] \mathbf{h}\| \leq \sqrt{\zeta_{0k}}, f_k \in F_{\text{PB}}, k = 1, 2, \dots, K, \quad (5.22)$$

which can be used to replace the tap weights norm constraint in Eq. (5.16).

In summary, the implementation of the frequency-invariant FIR beamformer using global optimization method consists of the following steps.

- Step 1. Discretize the entire frequency band F and divide them into the operating frequency band F_{PB} , the stopband F_{SB} and the transition band F_{TB} . Discretize the visible region Θ and divide them into the mainlobe region Θ_{ML} and the sidelobe region Θ_{SL} .
- Step 2. Calculate the broadband response vector $\mathbf{u}(f, \theta)$ of the FIR beamformer at a number of frequency and direction grids using Eq. (5.10).
- Step 3. Choose a desired mainlobe pattern $B_d(\theta_j), \theta_j \in \Theta_{\text{ML}}$, and specify a desired sidelobe level. Choose Eq. (5.16) or (5.22) as the robustness constraint of the FIR beamformer.
- Step 4. Formulate the optimization problem using the minimax criterion in Eq. (5.14) or the least-square criterion in Eq. (5.17), then solve the filter \mathbf{h} using SOCP. Extract the FIR filter \mathbf{h}_m corresponding to each sensor using Eqs. (5.8) and (5.5).
- Step 5. Delay the output of each sensor by an integer tap T_m and then pass them through the corresponding FIR filter \mathbf{h}_m . The outputs of each filter are summed to obtain the broadband beamformer output time series.
- Step 6. Calculate the beam pattern of the FIR beamformer at the frequency and direction grids using Eq. (5.9).

5.3 Adaptive FIR Beamformer

The expression for the FIR beamforming has been presented in Sect. 4.2. Equation (4.10) gives the relationship between the output and input of the FIR beamformer, which is rewritten here as follows:

$$y(i) = \mathbf{h}^T \mathbf{x}(i). \quad (5.23)$$

5.3.1 Data Covariance Matrix

Similar to the narrowband data model introduced in Chap. 1, let \mathbf{R}_t be the $ML \times ML$ theoretical covariance matrix corresponding to the stacked vector \mathbf{x} , i.e.,

$$\mathbf{R}_t = E[\mathbf{x}(i)\mathbf{x}^H(i)], \quad (5.24)$$

where the subscript “t” denotes time domain.

It is worth noting that the $ML \times ML$ covariance matrix \mathbf{R}_t here is different from the narrowband (or frequency-domain subband) $M \times M$ covariance matrix \mathbf{R} introduced in previous chapters. For convenience, in what follows we sometimes use \mathbf{R} instead of \mathbf{R}_t when there is no ambiguity.

We now consider two cases when the stacked vector is real or complex. In order to avoid ambiguity, the real covariance matrix is denoted by \mathbf{R} , and the complex covariance matrix is denoted by $\tilde{\mathbf{R}}$.

First, consider the special case of the complex stacked vector. Assume that the signal and the noise are statistically independent of each other and the noise received by each sensor are uncorrelated with each other. Then, the theoretical covariance matrix has the form

$$\tilde{\mathbf{R}} = \sum_{d=0}^D \tilde{\mathbf{R}}_d + \tilde{\mathbf{R}}_n, \quad (5.25)$$

where $\tilde{\mathbf{R}}_d$ is the broadband data covariance matrix corresponding to the d th signal. $d = 0$ corresponds to the broadband desired signal and $d = 1, \dots, D$ corresponds to the broadband interferers. $\tilde{\mathbf{R}}_n$ is the broadband noise covariance matrix.

Consider the single plane-wave signal case. Taking the d th signal as an example, assume that the signal direction is θ_d . Similar to the narrowband data model, the spatial spectral matrix of this plane wave is given by

$$\mathbf{S}_d(f) = S_d(f) \mathbf{u}(f, \theta_d) \mathbf{u}^H(f, \theta_d), \quad (5.26)$$

where $S_d(f)$ is the power spectrum of the d th signal, $\mathbf{u}(f, \theta_d)$ is the response vector of the FIR beamformer obtained by replacing θ in Eq. (5.10) with θ_d .

Assume that the broadband signal has a limited frequency band of $[f_l, f_u]$. Then its covariance matrix $\tilde{\mathbf{R}}_d$ can be written as

$$\tilde{\mathbf{R}}_d = \int_{f_l}^{f_u} S_d(f) df = \int_{f_l}^{f_u} S_d(f) \mathbf{u}(f, \theta_d) \mathbf{u}^H(f, \theta_d) df. \quad (5.27)$$

Assume that the total power of the signal is σ_s^2 and it has a flat spectrum over the frequency band of interest, then we have

$$\tilde{\mathbf{R}}_d = \frac{\sigma_s^2}{f_u - f_l} \int_{f_l}^{f_u} \mathbf{u}(f, \theta_d) \mathbf{u}^H(f, \theta_d) df. \quad (5.28)$$

From Eqs. (5.10) and (5.11), the $(m + (l - 1)M)$ th element of $\mathbf{u}(f, \theta_d)$ has the form

$$[\mathbf{u}(f, \theta_d)]_{m+(l-1)M} = \exp(-i2\pi f \tau_{ml}), \quad (5.29)$$

where $\tau_{ml} = T_m + \tau_m(\theta_d) + (l - 1)T_s$.

Thus, the $(m + (l - 1)M, \check{m} + (\check{l} - 1)M)$ th element of $\tilde{\mathbf{R}}_d$ (where $\check{m} = 1, 2, \dots, M$, $\check{l} = 1, 2, \dots, L$) is given by

$$\begin{aligned} [\tilde{\mathbf{R}}_d]_{m+(l-1)M, \check{m}+(\check{l}-1)M} &= \frac{\sigma_s^2}{f_u - f_l} \int_{f_l}^{f_u} \exp\left[-i2\pi f \left(\tau_{ml} - \tau_{\check{m}\check{l}}\right)\right] df \\ &= \frac{\sigma_s^2}{B_s} \text{sinc}\left[\pi B_s \left(\tau_{ml} - \tau_{\check{m}\check{l}}\right)\right] \exp\left[-i2\pi f_c \left(\tau_{ml} - \tau_{\check{m}\check{l}}\right)\right], \end{aligned} \quad (5.30)$$

where $B_s = f_u - f_l$ is the signal bandwidth and $f_c = (f_u + f_l)/2$ is the central frequency.

Assume that the noise has a flat spectrum over the same frequency band, and the total noise power is σ_n^2 . The noise received by each sensor are assumed to be uncorrelated with each other. Then, the $(m + (l - 1)M, \check{m} + (\check{l} - 1)M)$ th element of the noise covariance matrix $\tilde{\mathbf{R}}_n$ is given by

$$\begin{aligned}
[\tilde{\mathbf{R}}_n]_{m+(l-1)M, \tilde{m}+(\tilde{l}-1)M} &= \frac{\sigma_n^2}{B_s} \delta_{m\tilde{m}} \int_{f_1}^{f_u} \exp \left[-i2\pi f (l - \tilde{l}) T_s \right] df \\
&= \frac{\sigma_n^2}{B_s} \delta_{m\tilde{m}} \operatorname{sinc} \left[\pi B_s (l - \tilde{l}) T_s \right] \exp \left[-i2\pi f_c (l - \tilde{l}) T_s \right],
\end{aligned} \tag{5.31}$$

$$\text{where } \delta_{m\tilde{m}} = \begin{cases} 0, & m \neq \tilde{m} \\ 1, & m = \tilde{m} \end{cases}.$$

Substituting Eqs. (5.30) and (5.31) into Eq. (5.25) gives the theoretical complex data covariance matrix $\tilde{\mathbf{R}}$.

Next, consider the real value case. The real data has both positive frequency and negative frequency. Thus, the frequency band of the broadband signal becomes $[-f_u, -f_1] \cup [f_1, f_u]$. Assuming that the signal has a total power of σ_s^2 and a flat spectrum over the limited frequency band, the real covariance matrix corresponding to Eq. (5.30) is given by

$$\begin{aligned}
[\mathbf{R}_d]_{m+(l-1)M, \tilde{m}+(\tilde{l}-1)M} &= \frac{\sigma_s^2/2}{f_u - f_1} \int_{f_1}^{f_u} \exp \left[-i2\pi f (\tau_{ml} - \tau_{\tilde{m}\tilde{l}}) \right] df \\
&\quad + \frac{\sigma_s^2/2}{f_u - f_1} \int_{-f_u}^{-f_1} \exp \left[-i2\pi f (\tau_{ml} - \tau_{\tilde{m}\tilde{l}}) \right] df \\
&= \frac{\sigma_s^2}{B_s} \operatorname{sinc} \left[\pi B_s (\tau_{ml} - \tau_{\tilde{m}\tilde{l}}) \right] \cos \left[2\pi f_c (\tau_{ml} - \tau_{\tilde{m}\tilde{l}}) \right].
\end{aligned} \tag{5.32}$$

It is seen that

$$\mathbf{R}_d = \operatorname{Re}(\tilde{\mathbf{R}}_d), \tag{5.33}$$

where $\operatorname{Re}(\cdot)$ denotes the real part of its argument.

The real noise covariance matrix is given by

$$\begin{aligned}
[\mathbf{R}_n]_{m+(l-1)M, \tilde{m}+(\tilde{l}-1)M} &= \frac{\sigma_n^2}{B_s} \delta_{m\tilde{m}} \operatorname{sinc} \left[\pi B_s (l - \tilde{l}) T_s \right] \cos \left[2\pi f_c (l - \tilde{l}) T_s \right] \\
&= \operatorname{Re}(\tilde{\mathbf{R}}_n).
\end{aligned} \tag{5.34}$$

Replace $\tilde{\mathbf{R}}_d$ and $\tilde{\mathbf{R}}_n$ with \mathbf{R}_d and \mathbf{R}_n , respectively. Similar to Eq. (5.25), the real theoretical data covariance matrix \mathbf{R} is given by

$$\mathbf{R} = \sum_{d=0}^D \mathbf{R}_d + \mathbf{R}_n. \quad (5.35)$$

In what follows, when there is no ambiguity, the complex covariance matrix $\tilde{\mathbf{R}}$ in Eq. (5.25) and the real data covariance matrix \mathbf{R} are both denoted by \mathbf{R} . While whether \mathbf{R} is the complex model or the real model can be determined from the context.

In practical applications, whether the data is real or complex, we do not really require the signal, interferences and noise to have flat spectra. Actually, our beamformer is a data-based adaptive beamformer, which do not need any priori information of the spectral density. In practice, the theoretical data covariance matrix \mathbf{R} is unavailable, thus the sample covariance matrix $\hat{\mathbf{R}}$ is always applied, which can be estimated from the data samples

$$\hat{\mathbf{R}} = \frac{1}{N} \sum_{i=1}^N \mathbf{x}(i) \mathbf{x}^H(i), \quad (5.36)$$

where N is the length of the samples.

5.3.2 Design of Adaptive FIR Beamformer

The output power of the FIR broadband beamformer is given by

$$P_{\text{out}} = \mathbb{E}[y(i)y^*(i)] = \mathbb{E}[\mathbf{h}^T \mathbf{x}(i) \mathbf{x}^H(i) \mathbf{h}^*] = \mathbf{h}^T \mathbf{R} \mathbf{h}^*. \quad (5.37)$$

The output SINR of the FIR broadband beamformer can be calculated as

$$\text{SINR}_{\text{out}} = \frac{\mathbf{h}^T \mathbf{R}_0 \mathbf{h}^*}{\mathbf{h}^T \left(\sum_{d=1}^D \mathbf{R}_d + \mathbf{R}_n \right) \mathbf{h}^*}. \quad (5.38)$$

Similar to the narrowband adaptive beamformer, the design problem of the adaptive FIR beamformer is to minimize the beamformer output power subject to the distortionless constraint on the desired signal.

In order to improve the robustness of the beamformer, the broadband white noise gain constraint can be imposed, i.e., constrain the norm of the tap weights.

Thus, the beamformer design problem can be formulated as

$$\begin{aligned} & \min_{\mathbf{h}} \mathbf{h}^T \mathbf{R} \mathbf{h}^*, \\ & \text{subject to } \mathbf{u}^T(f, \theta_s) \mathbf{h} = 1, \forall f \in [f_l, f_u], \\ & \quad \|\mathbf{h}\| \leq \Delta_0, \end{aligned} \quad (5.39)$$

where θ_s is the direction of the desired signal.

The method for solving the problem in Eq. (5.39) can be referred to Sect. 5.3.3. In fact, this adaptive FIR beamformer is the extension of the MVDR beamformer to broadband case.

The main difference between this adaptive FIR beamformer and the conventional Frost beamformer is that the pre-delay of the latter is exactly $T_m = -\tau_m(\theta_0)$. Since this pre-delay is usually not an integer, expensive mechanical or electronic pre-steering is applied. However, the pre-delay of the FIR beamforming method presented in this section can be chosen as an integer times of the sampling period, which can be simply achieved using the tapped delay line, thus it is more convenient than the Frost beamformer. In addition, the FIR beamforming method presented in this section can control the norm of the filter tap weights, thereby improving the robustness of the beamformer.

Consider a 12-element ULA with a half-wavelength spacing at f_0 . The frequency band of interest is $[f_l, f_u] = [f_0/2, f_0]$. A broadband plane-wave desired signal and an broadband plane-wave interfering signal arrive from $\theta_0 = 10^\circ$ and $\theta_1 = -40^\circ$ with the SNR (or INR) at each sensor of 0 dB and 30 dB, respectively. The sampling frequency is $f_s = 3.125 f_0$.

We assume that the data is complex. Correspondingly, the FIR filter tap weights \mathbf{h} are also complex. Assumed that the length of each FIR filter is $L = 8$. It is worth noting that when the complex-valued filter is used, the pre-delay is different from that of the real case, i.e., there is no inherent group delay of $(L - 1)T_s/2$.

The frequency band of interest $[f_l, f_u]$ is decomposed into $K = 33$ subbands uniformly. Assume that the constraint value on the norm of the filter tap weights is $\Delta_0 = 1$. The visible region $[-90^\circ, 90^\circ]$ is discretized using 2° grids. In what follows, unless otherwise stated, the theoretical covariance matrix \mathbf{R} is used in the simulation for convenience.

Assume that the array is steered to the desired signal direction. The broadband beam pattern of the FIR beamformer is shown in Fig. 5.6. It puts null at the interferer direction. Its sidelobe level is about -12.5 dB. The output SINR from Eq. (5.38) is 10.75 dB.

5.3.3 Adaptive FIR Beamformer with Sidelobe Control

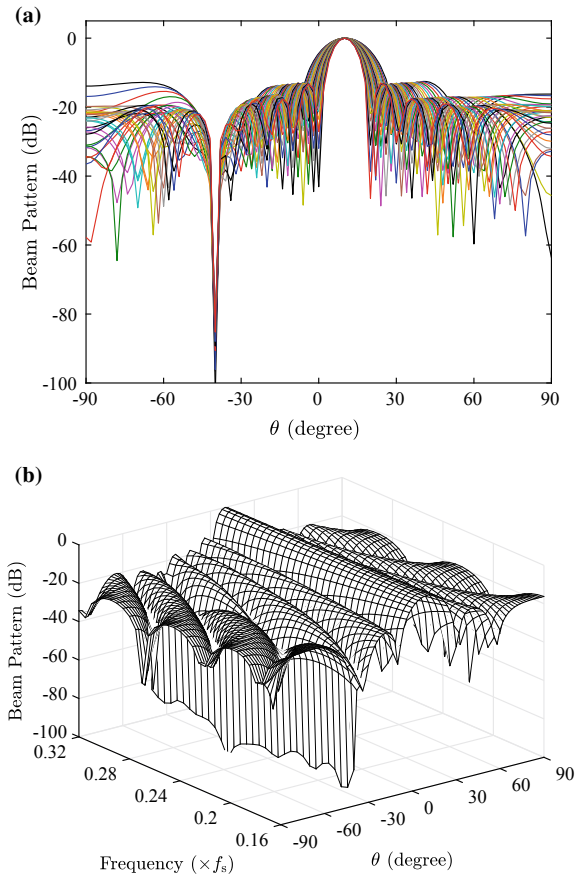
In order to control the sidelobes, the constraints on the sidelobes can be added to the adaptive FIR beamforming problem in Eq. (5.39) as

$$\min_{\mathbf{h}} \mathbf{h}^T \mathbf{R} \mathbf{h}^*, \quad (5.40a)$$

$$\text{subject to } \mathbf{u}^T(f, \theta_s) \mathbf{h} = 1, \forall f \in [f_l, f_u], \quad (5.40b)$$

$$|\mathbf{u}^T(f, \theta) \mathbf{h}| \leq \xi_0, \forall \theta \in \Theta_{SL}, \forall f \in [f_l, f_u], \quad (5.40c)$$

Fig. 5.6 Broadband beam pattern of the adaptive FIR beamformer in complex case. **a** Superposition plot. **b** Three-dimensional plot



$$\|\mathbf{h}\| \leq \Delta_0, \quad (5.40d)$$

where ξ_0 is the prescribed constraint value on the sidelobes, Θ_{SL} is the sidelobe region, which can be chosen to vary with frequency.

Discretize the frequency band of interest $[f_l, f_u]$ into a number of frequency grids, i.e., $f_k \in [f_l, f_u]$, $k = 1, \dots, K$.

Perform the Cholesky decomposition to \mathbf{R} , i.e., $\mathbf{R} = \mathbf{V}^H \mathbf{V}$. Then

$$\mathbf{h}^T \mathbf{R} \mathbf{h}^* = (\mathbf{V}^* \mathbf{h})^T (\mathbf{V}^* \mathbf{h})^* = \|\mathbf{V}^* \mathbf{h}\|^2. \quad (5.41)$$

Note that minimizing $\|\mathbf{V}^* \mathbf{h}\|^2$ is equivalent to minimizing $\|\mathbf{V}^* \mathbf{h}\|$. Introducing a new variable γ , Eq. (5.40a, 5.40b, 5.40c, 5.40d) can be reformulated as

$$\begin{aligned}
& \min_{\mathbf{h}} \gamma, \\
& \text{subject to } \|\mathbf{V}^* \mathbf{h}\| \leq \gamma, \\
& \quad \mathbf{u}^T(f_k, \theta_s) \mathbf{h} = 1, \quad f_k \in [f_l, f_u], \quad k = 1, \dots, K, \\
& \quad |\mathbf{u}^T(f_k, \theta_{i,k}) \mathbf{h}| \leq \xi_0, \quad \theta_{i,k} \in \Theta_{SL,k}, \quad i = 1, \dots, N_{SL,k}, \\
& \quad f_k \in [f_l, f_u], \quad k = 1, \dots, K, \\
& \quad \|\mathbf{h}\| \leq \Delta_0,
\end{aligned} \tag{5.42}$$

where $\Theta_{SL,k}, k = 1, \dots, K$ are the sidelobe regions corresponding to f_k , and $\theta_{i,k} \in \Theta_{SL,k}, i = 1, \dots, N_{SL,k}$ are the direction grids, where the value of $N_{SL,k}$ is determined by the required approximation precision.

The optimization problem in Eq. (5.42) can be formulated as a convex SOCP problem that is computationally tractable. The reader is referred to Ref. [2] for further discussion.

Consider the same case as in Fig. 5.6. We design the FIR beamformer by solving Eq. (5.42). Assume that the beamwidth narrows as the frequency increases. The sidelobe regions corresponding to the frequencies f_l and f_u are chosen as $[-90^\circ, -15^\circ] \cup [35^\circ, 90^\circ]$ and $[-90^\circ, -5^\circ] \cup [25^\circ, 90^\circ]$, respectively. The sidelobe regions corresponding to other frequency grids are obtained by performing linear interpolation. We choose $\xi_0 = \sqrt{0.001}$, i.e., the desired sidelobe level is -30 dB.

We first assume that the FIR filter tap weights are complex. The FIR beamformer is designed, whose beam patterns at the frequency and direction grids are shown in Fig. 5.7.

Different from Fig. 5.6, this method guarantees that the obtained sidelobe level is strictly below -30 dB, while the mainlobes of the beam patterns are slightly widened.

Both the beam patterns shown in Figs. 5.6 and 5.7 form nulls in the direction of interferer across the frequency band of interest. The depths of the nulls of the two beam patterns are shown in Fig. 5.8.

It is seen that the null depth shallows after imposing the sidelobe constraint, which will reduce the output SINR. From Eq. (5.38), the output SINR of the FIR beamformer with sidelobe control is 10.08 dB, which is 0.67 dB lower than that of the FIR beamformer without sidelobe control. In other words, the beamformer decreases the sidelobes at the cost of reducing the output SINR.

We next assume that the array data are real. Correspondingly, the real-valued FIR filter tap weights are applied. In order to ensure that the FIR filter have the same degree of freedom, we assume that the filter length is $L = 16$.

Proceeding in a similar manner to the complex case above, the broadband beam patterns of the FIR beamformer without sidelobe control and with sidelobe control are shown in Fig. 5.9a and b respectively.

The depths of the nulls of the two beam patterns are shown in Fig. 5.10. Calculation results show that the output SINR of the two FIR beamformers are 10.76 and 10.10 dB, respectively.

Fig. 5.7 Broadband beam pattern of the adaptive FIR beamformer with sidelobe control in complex case.
a Superposition plot.
b Three-dimensional plot

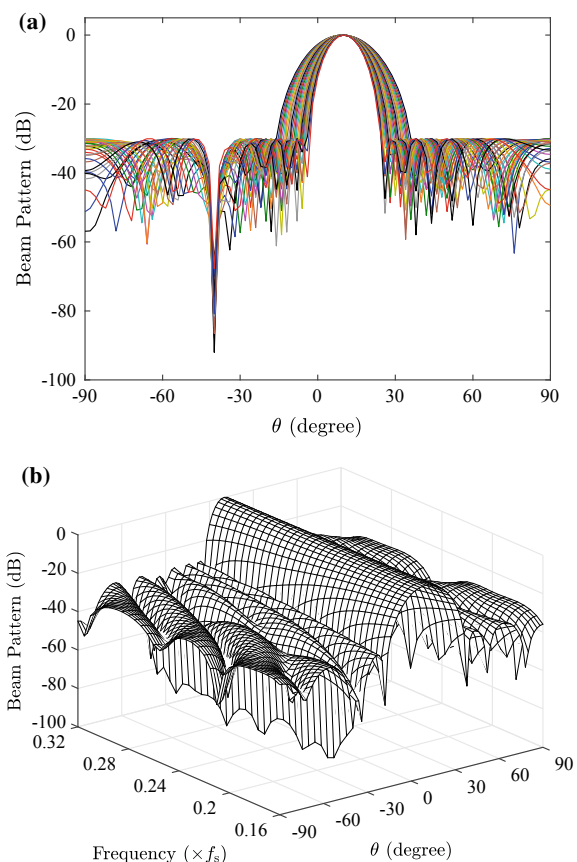


Fig. 5.8 Null depths at the interference direction of two FIR beamformers in complex case

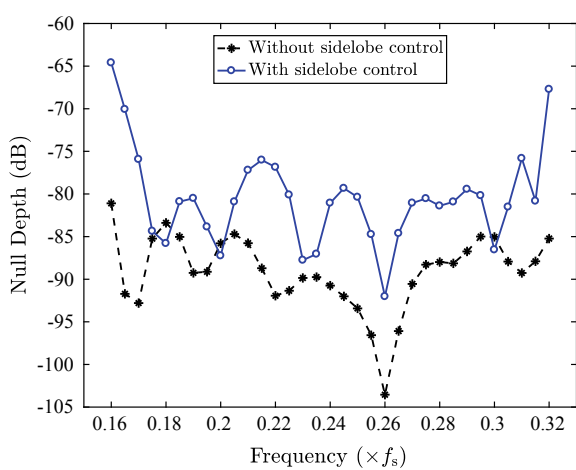


Fig. 5.9 Broadband beam pattern of FIR beamformers in real case **a** without sidelobe control, **b** with sidelobe control

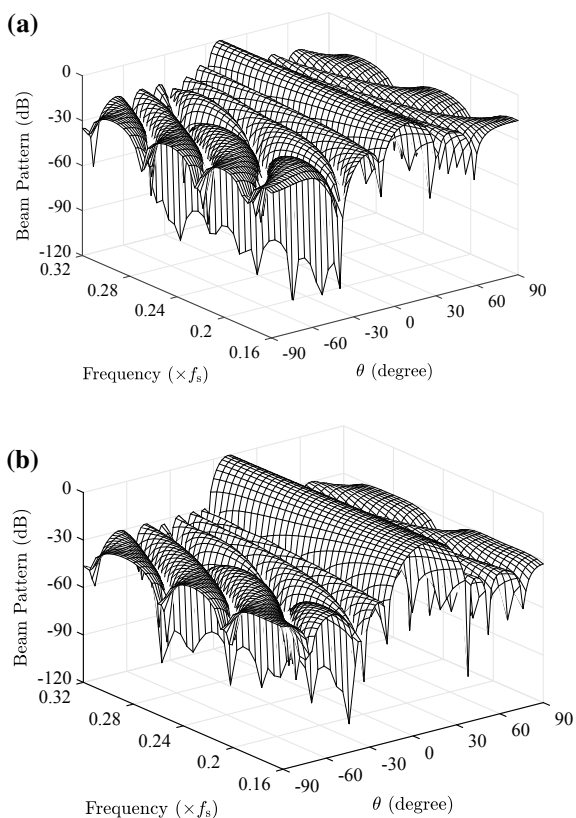


Fig. 5.10 Null depths at the interference direction of two FIR beamformers in real case

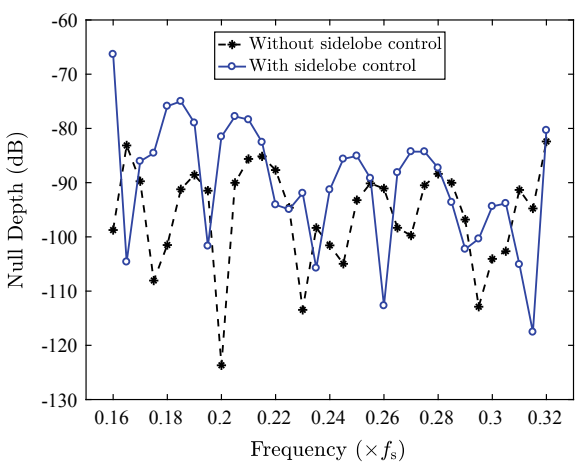
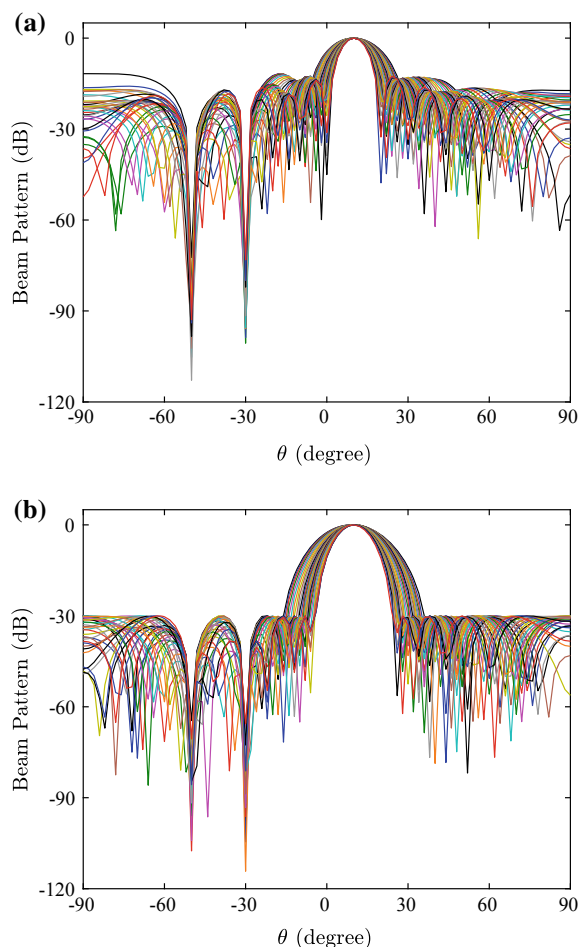


Fig. 5.11 FIR beam pattern in the presence of two interferers. **a** Without sidelobe control. **b** With sidelobe control



Consider the case of multiple interferers.

Assume that a broadband plane-wave desired signal and two broadband plane-wave interferers arrive from 10° , -50° and -30° with the SNR (or INR) of 0 dB, 30 dB and 30 dB, respectively.

Proceeding in a similar manner, the broadband beam patterns of the FIR beamformer without sidelobe control and with sidelobe control are shown in Fig. 5.11a and b, respectively.

Both beam patterns place deep nulls at the interferer directions. Calculation results show that the output SINR of the two beamformers are 10.73 dB and 10.03 dB, respectively.

5.4 Minimum Mainlobe Spatial Pattern Variation Design

Assuming that the beam patterns in the stopband are temporarily ignored, the global optimization problem in Eq. (5.14) can be reformulated as

$$\begin{aligned} & \min_{\mathbf{h}} \max_{k,j} |\mathbf{u}^T(f_k, \theta_j) \mathbf{h} - B_d(\theta_j)|, \quad f_k \in [f_l, f_u], \theta_j \in \Theta_{ML}, \\ & \text{subject to } |\mathbf{u}^T(f_k, \theta_i) \mathbf{h}| \leq \xi_0, \quad f_k \in F_{PB}, \theta_i \in \Theta_{SL}. \end{aligned} \quad (5.43)$$

The sidelobe constraint value ξ_0 is chosen as a constant in Eq. (5.43) for convenience.

This method requires specifying a desired mainlobe pattern $B_d(\theta_j)$ and then approximating the designed mainlobe pattern to the desired one. We would anticipate that an inappropriate desired mainlobe pattern will lead to large synthesis error in the designed mainlobe pattern, which is a drawback of this method.

5.4.1 Mainlobe Spatial Response Variation

We hereby introduce the mainlobe spatial response variation (MSRV), as a measure of the mainlobe pattern variation of the broadband beamformer.

The error between the beam pattern at f_k and θ_j and that at the reference frequency and the same direction is defined as

$$\begin{aligned} \delta_{MSRV}(f_k, \theta_j) &= |B(f_k, \theta_j) - B(f_0, \theta_j)| \\ &= |\mathbf{u}^T(f_k, \theta_j) \mathbf{h} - \mathbf{u}^T(f_0, \theta_j) \mathbf{h}|, \end{aligned} \quad (5.44)$$

where f_0 is the reference frequency, which can be chosen as any frequency within the frequency band $[f_l, f_u]$. $B(f_0, \theta_j)$ is the reference beam pattern. Different from the specified desired beam pattern $B_d(\theta_j)$ in the objective function in Eq. (5.43), the reference beam pattern here is a function of the optimization variable \mathbf{h} .

Thus, the frequency-invariant beamformer design is to minimize the MSRV of the broadband beamformer at each frequency.

The methods for frequency-invariant FIR beamformer design using several different criteria are presented below. We assume that both the sampled data and the filter tap weights are real in this section.

5.4.2 Peak Sidelobes Constrained Minimax MSRV

The maximum MSRV of a broadband beamformer is defined as

$$\delta_{\max} = \max_{k,j} |\mathbf{u}^T(f_k, \theta_j) \mathbf{h} - \mathbf{u}^T(f_0, \theta_j) \mathbf{h}|$$

$$= \max_{k,j} \left| [\mathbf{u}(f_k, \theta_j) - \mathbf{u}(f_0, \theta_j)]^T \mathbf{h} \right| \\ f_k \in [f_1, f_u], k = 1, 2, \dots, K, \theta_j \in \Theta_{ML}, j = 1, \dots, N_{ML}. \quad (5.45)$$

Replacing the maximum mainlobe synthesis error in Eq. (5.43) by maximum MSRV defined in Eq. (5.45), and imposing the distortionless constraint on the SOI at the reference frequency f_0 , gives the peak sidelobes constrained minimax MSRV beamformer design

$$\begin{aligned} & \min_{\mathbf{h}} \delta_{\max}, \\ & \text{subject to } \mathbf{u}^T(f_0, \theta_s) \mathbf{h} = 1, \\ & \quad \left| \mathbf{u}^T(f_k, \theta_i) \mathbf{h} \right| \leq \xi_0, f_k \in [f_1, f_u], \theta_i \in \Theta_{SL}. \end{aligned} \quad (5.46)$$

Comparing Eqs. (5.46) and (5.43), it is seen that, the desired beam pattern $B_d(\theta_j)$ in Eq. (5.43) is difficult to choose, while no specifying desired beam pattern is required in Eq. (5.46), which implies that an optimal desired beam pattern can be chosen automatically. This means that the method in Eq. (5.46) can obtain smaller mainlobe pattern synthesis error.

Introducing a new non-negative variable δ , Eq. (5.46) can be converted into the following form:

$$\begin{aligned} & \min_{\mathbf{h}} \delta, \\ & \text{subject to } \mathbf{u}^T(f_0, \theta_s) \mathbf{h} = 1, \\ & \quad \left| [\mathbf{u}(f_k, \theta_j) - \mathbf{u}(f_0, \theta_j)]^T \mathbf{h} \right| \leq \delta, f_k \in [f_1, f_u], \theta_i \in \Theta_{ML}, \\ & \quad \left| \mathbf{u}^T(f_k, \theta_i) \mathbf{h} \right| \leq \xi_0, f_k \in [f_1, f_u], \theta_i \in \Theta_{SL}. \end{aligned} \quad (5.47)$$

The peak sidelobe power of the resulting FIR beamformer is defined as

$$\sigma_{\max SL} = \max_{f_k \in [f_1, f_u], \theta_i \in \Theta_{SL}} \left| \mathbf{u}^T(f_k, \theta_i) \mathbf{h} \right|. \quad (5.48)$$

5.4.3 Peak Sidelobes Constrained Least-Square MSRV

Consider the mean-squared MSRV relative to the response at the reference frequency f_0 , which is defined as

$$\begin{aligned} \delta_{\text{rms}}^2 &= \frac{1}{N_{ML}} \sum_{j=1}^{N_{ML}} \frac{1}{K} \sum_{k=1}^K \left[\left| \mathbf{u}^T(f_k, \theta_j) \mathbf{h} - \mathbf{u}^T(f_0, \theta_j) \mathbf{h} \right|^2 \right] \\ &= \frac{1}{N_{ML} K} \sum_{j=1}^{N_{ML}} \sum_{k=1}^K \left\{ \mathbf{h}^T [\mathbf{u}(f_k, \theta_j) - \mathbf{u}(f_0, \theta_j)] [\mathbf{u}(f_k, \theta_j) - \mathbf{u}(f_0, \theta_j)]^H \mathbf{h} \right\}, \\ f_k &\in [f_1, f_u], k = 1, 2, \dots, K, \theta_j \in \Theta_{ML}, j = 1, 2, \dots, N_{ML}. \end{aligned} \quad (5.49)$$

It takes the form

$$\delta_{\text{rms}}^2 = \mathbf{h}^T \boldsymbol{\Omega} \mathbf{h}, \quad (5.50)$$

where $\boldsymbol{\Omega}$ is an $ML \times ML$ matrix,

$$\boldsymbol{\Omega} = \frac{1}{N_{\text{ML}} K} \sum_{j=1}^{N_{\text{ML}}} \sum_{k=1}^K \left\{ [\mathbf{u}(f_k, \theta_j) - \mathbf{u}(f_0, \theta_j)] [\mathbf{u}(f_k, \theta_j) - \mathbf{u}(f_0, \theta_j)]^H \right\}. \quad (5.51)$$

Note that the matrix $\boldsymbol{\Omega}$ is Hermitian and the vector \mathbf{h} is real-valued. Hence, Eq. (5.50) can be rewritten as

$$\delta_{\text{rms}}^2 = \mathbf{h}^T \boldsymbol{\Omega}_R \mathbf{h}, \quad (5.52)$$

where $\boldsymbol{\Omega}_R = \text{Re}(\boldsymbol{\Omega})$, i.e., the real part of $\boldsymbol{\Omega}$.

By constraining the mean-squared MSRV to be less than a small non-negative value, we can restrict the synthesized pattern at different frequencies to be similar to some extent. The constraint is

$$\mathbf{h}^T \boldsymbol{\Omega}_R \mathbf{h} \leq \delta^2, \quad (5.53)$$

where δ is a small positive variable. This constraint can be rewritten as

$$\left\| \boldsymbol{\Omega}_R^{1/2} \mathbf{h} \right\| \leq \delta. \quad (5.54)$$

Therefore, our peak sidelobes constrained least-square MSRV beamformer design problem can be formulated as

$$\begin{aligned} & \min_{\mathbf{h}} \delta, \\ & \text{subject to } \mathbf{u}^T(f_0, \theta_s) \mathbf{h} = 1, \\ & \left\| \boldsymbol{\Omega}_R^{1/2} \mathbf{h} \right\| \leq \delta, \\ & \left| \mathbf{u}^T(f_k, \theta_i) \mathbf{h} \right| \leq \xi_0, \quad f_k \in [f_1, f_u], \theta_i \in \Theta_{\text{SL}}. \end{aligned} \quad (5.55)$$

Comparing Eqs. (5.55) and (5.47), it can be noted that after replacing the maximum MSRV with the mean-squared MSRV, Eq. (5.55) reduces significantly the number of constraints and the computational complexity.

5.4.4 Mean-Squared MSRV Constrained Least-Square Sidelobes

It is seen from Eq. (5.55) that there are so many sidelobe constraints, which may still be computationally expensive for most applications. We hereby present a mean-squared MSRV constrained least-square sidelobes beamformer design method, which uses the mean-squared sidelobes constraint to replace the peak sidelobes constraint in Eq. (5.55). It is more computationally efficient than Eq. (5.55) because the sidelobe constraints are reduced.

The mean-squared sidelobe power of the FIR beamformer can be defined as

$$\sigma_{\text{rmsSL}}^2 = \frac{1}{N_{\text{SL}}} \sum_{i=1}^{N_{\text{SL}}} \left\{ \frac{1}{K} \sum_{k=1}^K \left[|\mathbf{u}^T(f_k, \theta_i) \mathbf{h}|^2 \right] \right\},$$

$$f_k \in [f_l, f_u], k = 1, 2, \dots, K, \theta_i \in \Theta_{\text{SL}}, i = 1, 2, \dots, N_{\text{SL}}. \quad (5.56)$$

Similar to Eq. (5.50), it takes the form

$$\sigma_{\text{rmsSL}}^2 = \mathbf{h}^T \boldsymbol{\Psi}_R \mathbf{h}, f_k \in [f_l, f_u], \theta_i \in \Theta_{\text{SL}}, \quad (5.57)$$

where $\boldsymbol{\Psi}_R$ is an $ML \times ML$ matrix,

$$\boldsymbol{\Psi}_R = \frac{1}{N_{\text{SL}} K} \sum_{i=1}^{N_{\text{SL}}} \sum_{k=1}^K \text{Re}[\mathbf{u}(f_k, \theta_i) \mathbf{u}^H(f_k, \theta_i)]. \quad (5.58)$$

Hence, the mean-squared sidelobe constraint can be stated as

$$\left\| \boldsymbol{\Psi}_R^{1/2} \mathbf{h} \right\| \leq \xi, \quad (5.59)$$

where ξ is a small positive variable.

Then, the broadband array pattern synthesis problem can be written as

$$\begin{aligned} & \min_{\mathbf{h}} \xi, \\ & \text{subject to } \mathbf{u}^T(f_0, \theta_s) \mathbf{h} = 1, \\ & \quad \left\| \boldsymbol{\Omega}_R^{1/2} \mathbf{h} \right\| \leq \delta_0, \\ & \quad \left\| \boldsymbol{\Psi}_R^{1/2} \mathbf{h} \right\| \leq \xi, \end{aligned} \quad (5.60)$$

where δ_0 is a prescribed value to control the MSRV.

It is worth noting that when the MSRV or mean-squared sidelobe is used as a constraint in the optimization, it is not necessary to use too small grid spacing in angles due to the correlations between responses at neighboring directions. This can reduce the computational complexity when calculating $\boldsymbol{\Omega}_R$ in Eq. (5.51) and $\boldsymbol{\Psi}_R$ in Eq. (5.58).

5.4.5 Frequency-Invariant Beamformer with Interference Rejection

The sidelobe constrained adaptive FIR beamformer design method has been presented in Sect. 5.3. This method can suppress strong broadband interferences, thereby increasing the output SINR. Here, we impose the MSRV constraint to this method such that the obtained FIR beamformer not only has a constant mainlobe pattern, but also has the capability to suppress interferences.

Assuming that the mean-squared sidelobe constraint is applied, this optimization problem can be formulated as

$$\begin{aligned} & \min_{\mathbf{h}} \mathbf{h}^T \mathbf{R} \mathbf{h}, \\ & \text{subject to } \mathbf{u}^T(f_0, \theta_s) \mathbf{h} = 1, \\ & \quad \left\| \boldsymbol{\Omega}_R^{1/2} \mathbf{h} \right\| \leq \delta_0, \\ & \quad \left\| \boldsymbol{\Psi}_R^{1/2} \mathbf{h} \right\| \leq \xi_0, \end{aligned} \quad (5.61)$$

where ξ_0 is a prescribed value to control the mean-squared sidelobes.

Clearly, we have

$$\mathbf{h}^T \mathbf{R} \mathbf{h} = \left\| \mathbf{R}^{1/2} \mathbf{h} \right\|^2. \quad (5.62)$$

Noting that minimizing $\left\| \mathbf{R}^{1/2} \mathbf{h} \right\|^2$ is equivalent to minimizing $\left\| \mathbf{R}^{1/2} \mathbf{h} \right\|$ and introducing a new auxiliary variable γ , we can rewrite Eq. (5.61) as

$$\begin{aligned} & \min_{\mathbf{h}} \gamma, \\ & \text{subject to } \mathbf{u}^T(f_0, \theta_s) \mathbf{h} = 1, \\ & \quad \left\| \mathbf{R}^{1/2} \mathbf{h} \right\| \leq \gamma, \\ & \quad \left\| \boldsymbol{\Omega}_R^{1/2} \mathbf{h} \right\| \leq \delta_0, \\ & \quad \left\| \boldsymbol{\Psi}_R^{1/2} \mathbf{h} \right\| \leq \xi_0. \end{aligned} \quad (5.63)$$

In addition, the FIR filter tap weights norm constraint in Eq. (5.16) can be imposed to Eqs. (5.47), (5.55), (5.60) and (5.63) to improve the robustness of the four frequency-invariant beamformers. The reader is referred to Ref. [3] for further discussion.

Now, several numerical examples are provided to illustrate the performance of the frequency-invariant FIR beamformer design methods.

Consider the above 12-element broadband ULA. Assume that the steering direction is $\theta_0 = 10^\circ$. The length of each FIR filter is $L = 15$. The normalized frequency band of interest $[f_l, f_u] = [0.16, 0.32]$ is decomposed into $K = 33$ subbands uniformly and the visible region $[-90^\circ, 90^\circ]$ is discretized using 2° grids.

First, we design the frequency-invariant FIR beamformer using the method in Eq. (5.43). The desired sidelobe level is -30 dB. We choose the mainlobe pattern of the DAS beamformer at reference frequency $f_0 = (f_l + f_u)/2 = 0.24$ and $f_0 = f_l = 0.16$ as the desired mainlobe patterns, respectively.

When the reference frequency is chosen to be $f_0 = f_l$, assume that the mainlobe region is $\Theta_{ML} = [-8^\circ : 2^\circ : 28^\circ]$ and the sidelobe region is $\Theta_{SL} = [-90^\circ : 2^\circ : -12^\circ] \cup [32^\circ : 2^\circ : 90^\circ]$. Consider that as the frequency increases, the beamwidth of the DAS beam pattern decreases. Thus, a narrower mainlobe region $\Theta_{ML} = [-2^\circ : 2^\circ : 22^\circ]$ is chosen when the reference frequency is $f_0 = (f_l + f_u)/2$. The desired mainlobe patterns and the prescribed sidelobe level are shown in Fig. 5.12a for the two cases.

We solve the optimization problem (5.43) to obtain the FIR beamformers corresponding to the two desired mainlobe patterns. The beam pattern as a function of the frequency and direction are calculated on the grids using Eq. (5.9). The superposition of the achieved beam patterns at the 33 subbands for the case $f_0 = 0.16$ and $f_0 = 0.24$ are shown in Fig. 5.12b and c respectively.

It is seen from Fig. 5.12 that, when we choose $f_0 = (f_l + f_u)/2$, the resulting mainlobe pattern is severely distorted and the mainlobe synthesis error is very large. When $f_0 = f_l$ is chosen, the resulting beam pattern within the mainlobe is approximately constant over the frequency band of interest and the sidelobes are strictly guaranteed to be below -30 dB.

From this example, we can conclude that the performance of this array pattern synthesis method depends on the choosing of desired mainlobe pattern. An arbitrarily chosen desired mainlobe pattern can result in very poor synthesized pattern. Therefore, how to choose an optimal desired beam pattern is the main limitation of this method.

We then apply the peak sidelobes constrained minimax MSRV beamformer design method shown in Eq. (5.47) to design the frequency-invariant FIR beamformer. We choose $\Theta_{ML} = [-8^\circ : 2^\circ : 28^\circ]$ and $\Theta_{SL} = [-90^\circ : 2^\circ : -12^\circ] \cup [32^\circ : 2^\circ : 90^\circ]$. Assume that the center frequency is chosen as the reference frequency, i.e., $f_0 = (f_l + f_u)/2$.

The resulting beam patterns at the 33 subbands are shown in Fig. 5.13. It is seen that the mainlobe pattern is approximately constant and the sidelobes are strictly guaranteed to be below -30 dB.

The maximum MSRV of the array patterns in Fig. 5.12b and that in Fig. 5.13 are calculated using Eq. (5.45). The maximum MSRV in dB (i.e., $20\lg\delta_{\max}$) of the former is -21.4 dB and that of the latter is -42.6 dB, which is much smaller than that of the former. As expected, the method in Eq. (5.47) outperforms the method in Eq. (5.43).

We next apply the peak sidelobes constrained least-square MSRV beamformer design method shown in Eq. (5.55). The resulting beam patterns at the 33 subbands are shown in Fig. 5.14. The root-mean-square MSRV of the beam patterns in dB (i.e., $10\lg\delta_{rms}^2$) from Eq. (5.49) is -51.2 dB.

Finally, we apply the mean-squared MSRV constrained least-square sidelobes beamformer design method shown in Eq. (5.60), in which δ_0 is chosen to be $20\lg\delta_0 =$

Fig. 5.12 Frequency-invariant FIR beamformer design using Eq. (5.43). **a** Desired mainlobe patterns and sidelobe level when choosing $f_0 = 0.24$ and $f_0 = 0.16$, respectively. **b** Superposition of all 33 beam patterns for the case $f_0 = f_l$. **c** Superposition of all 33 beam patterns for the case $f_0 = (f_l + f_u)/2$

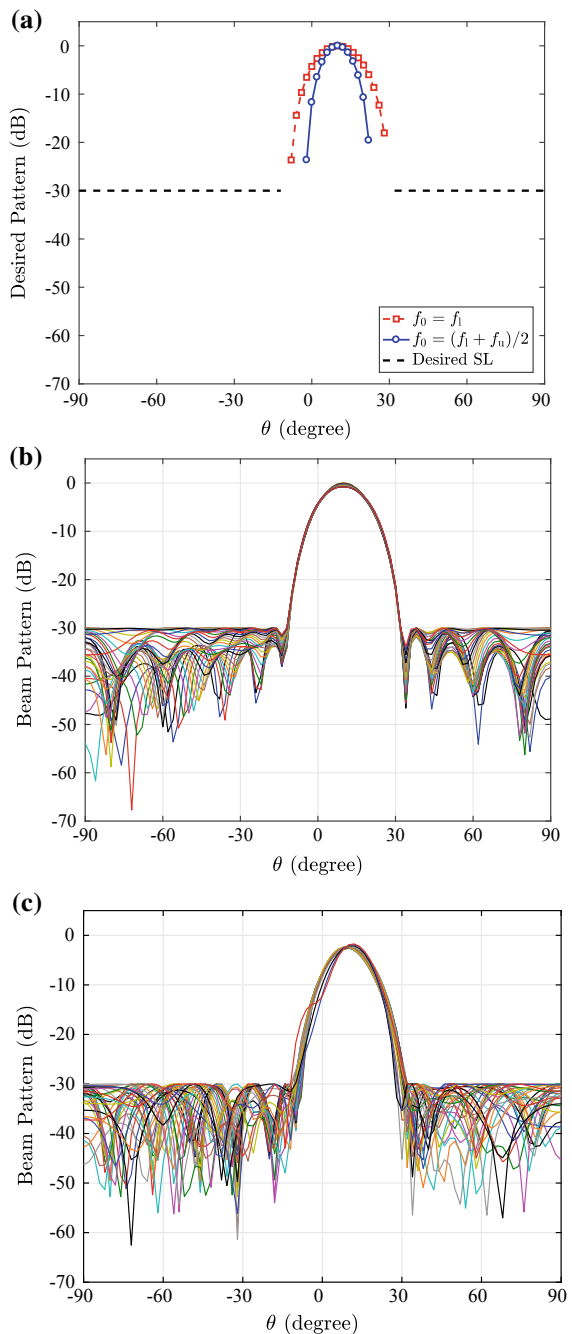


Fig. 5.13 Superposition of 33 beam patterns using peak sidelobes constrained minimax MSRV design method in Eq. (5.47)

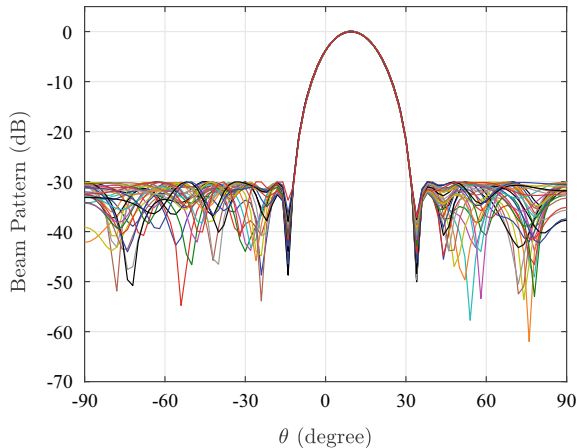
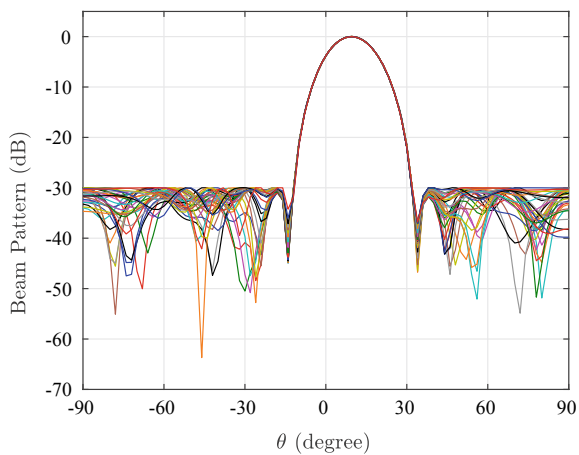


Fig. 5.14 Superposition of 33 beam patterns using peak sidelobes constrained least-square MSRV design method in Eq. (5.55)



–51.2 dB such that the designed beam patterns have the same root-mean-square MSRV as those in Fig. 5.14.

The resulting beam patterns at the 33 subbands are shown in Fig. 5.15. The resulting root-mean-square sidelobe from Eq. (5.57) is $10\lg\sigma_{\text{rmsSL}}^2 = -36.2$ dB.

For the above 12-element ULA. Assume that a signal and two interferers impinge on the array from 10° , -30° and -50° with the SNR (INR) at each sensor of 0 dB, 30 dB, and 30 dB, respectively. The signal, interferers, and noise are assumed to be bandpass white Gaussian process with flat spectral density over the frequency band $[f_l, f_u]$.

We design the FIR beamformer using the method in Eq. (5.63). The theoretical array covariance matrix \mathbf{R} in Eq. (5.35) is used. We choose $20\lg\delta_0 = -51.2$ dB and $20\lg\xi_0 = -33.2$ dB, which is 3 dB higher than the resulting root-mean-square sidelobe of the fixed beamformer in Fig. 5.15.

Fig. 5.15 Superposition of 33 beam patterns using mean-squared MSRV constrained least-square sidelobes design method in Eq. (5.60)

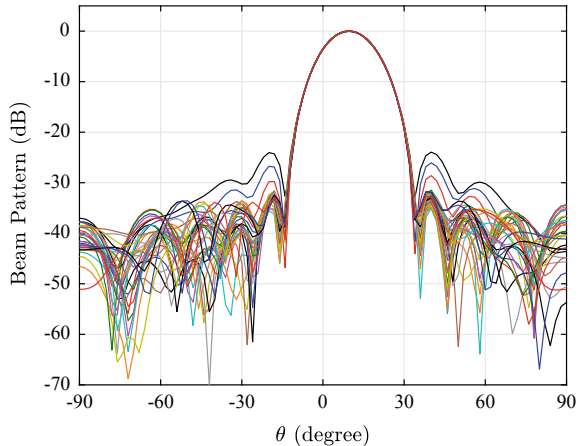
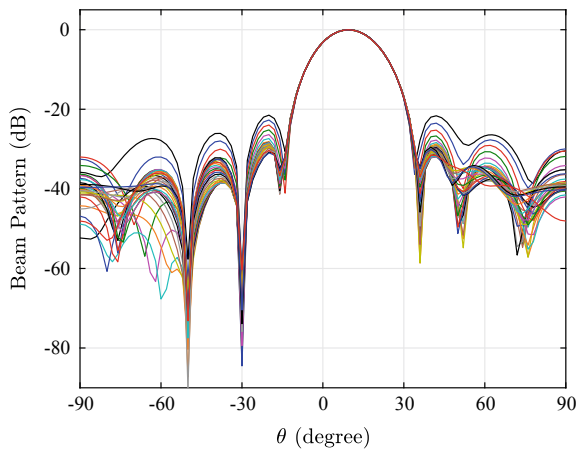


Fig. 5.16 Superposition of 33 beam patterns using frequency-invariant beamformer with interference rejection method in Eq. (5.63)



The resulting beam patterns at the 33 subbands are shown in Fig. 5.16. As expected, the beam patterns have constant mainlobe responses and deep nulls in the directions of the interferers.

To compare the performances of the 5 broadband array pattern synthesis methods introduced in this section, Table 5.2 lists the maximum MSRV in dB $20\lg\delta_{\max}$, root-mean-square MSRV in dB $20\lg\delta_{\text{rms}}$, peak sidelobe level in dB $20\lg\sigma_{\max\text{SL}}$, root-mean-square sidelobe level in dB $20\lg\sigma_{\text{rmsSL}}$, and the CPU time spent in solving the 5 optimization problem using SeDuMi for the above-mentioned examples.

From Table 5.2, it is seen that the method in Eq. (5.47) has both smaller δ_{\max} and δ_{rms} than the method in Eq. (5.43) with the same $\sigma_{\max\text{SL}}$. Obviously, the method in Eq. (5.47) outperforms the method in Eq. (5.43). As expected, the method in Eq. (5.55) has smaller δ_{rms} but a little larger δ_{\max} than the method in Eq. (5.47) with the same $\sigma_{\max\text{SL}}$, and also spends shorter CPU time. The method in Eq. (5.60)

Table 5.2 Performance comparison of the beamformers using different criteria

Method	Beam patterns	20lg δ_{\max} (dB)	20lg δ_{rms} (dB)	20lg $\sigma_{\max\text{SL}}$ (dB)	20lg $\sigma_{\text{rms}\text{SL}}$ (dB)	CPU time (s)
Equation (5.43)	Figure 5.12b	-21.4	-23.9	-30.0	-33.1	19.5
Equation (5.47)	Figure 5.13	-42.6	-45.5	-30.0	-32.3	10.1
Equation (5.55)	Figure 5.14	-35.7	-51.2	-30.0	-32.1	7.8
Equation (5.60)	Figure 5.15	-35.8	-51.2	-23.9	-36.2	0.22
Equation (5.63)	Figure 5.16	-37.0	-51.2	-21.5	-33.2	0.28

has smaller $\sigma_{\text{rms}\text{SL}}$ than the method in Eq. (5.55) with the same δ_{rms} , and spends the shortest CPU time, although it has a little higher $\sigma_{\max\text{SL}}$. We observe that the method in Eq. (5.60) offers computational advantages over the other methods, whose CPU time is reduced by 90 times to that of the method in Eq. (5.43). The method in Eq. (5.63) can provide good interference rejection ability at the cost of slightly increased sidelobes and computation load when comparing with the method in Eq. (5.60).

5.5 Multiple-Objective Design of FIR Beamformers

Define a $K \times N_{\text{ML}}$ matrix $\boldsymbol{\Gamma}(F_{\text{PB}}, \Theta_{\text{ML}})$, whose (k, j) th element is given by

$$[\boldsymbol{\Gamma}(F_{\text{PB}}, \Theta_{\text{ML}})]_{k,j} = \delta_{\text{MSRV}}(f_k, \theta_j), \quad (5.64)$$

where $\delta_{\text{MSRV}}(f_k, \theta_j)$ is defined in Eq. (5.44).

Let

$$\boldsymbol{\gamma}(F_{\text{PB}}, \Theta_{\text{ML}}) = \text{vec}\{\boldsymbol{\Gamma}(F_{\text{PB}}, \Theta_{\text{ML}})\}, \quad (5.65)$$

then the maximum MSRV and root-mean-square MSRV in Eqs. (5.45) and (5.49) are respectively given by

$$\delta_{\max} = \|\boldsymbol{\gamma}(F_{\text{PB}}, \Theta_{\text{ML}})\|_{\infty}, \quad (5.66)$$

$$\delta_{\text{rms}}^2 = \frac{1}{N_{\text{ML}}K} \boldsymbol{\gamma}(F_{\text{PB}}, \Theta_{\text{ML}}) \|\boldsymbol{\gamma}(F_{\text{PB}}, \Theta_{\text{ML}})\|_2^2. \quad (5.67)$$

Define a $K \times N_{\text{ML}}$ matrix $\mathbf{B}(F_{\text{PB}}, \Theta_{\text{SL}})$, whose (k, i) -th element is given by

$$[\mathbf{B}(F_{\text{PB}}, \Theta_{\text{SL}})]_{k,i} = B(f_k, \theta_i), f_k \in F_{\text{PB}}, \theta_i \in \Theta_{\text{SL}}, \quad (5.68)$$

and let

$$\mathbf{b}(F_{\text{PB}}, \Theta_{\text{SL}}) = \text{vec}\{\mathbf{B}(F_{\text{PB}}, \Theta_{\text{SL}})\}. \quad (5.69)$$

Then, using the derivation in this chapter, the multiply constrained broadband FIR beamformer optimization problem can be formulated as

$$\begin{aligned} & \min_{\mathbf{h}} \mu_p, p \in \{1, 2, 3, 4\}, \\ & \text{subject to } \mathbf{y}(F_{\text{PB}}, \Theta_{\text{ML}})_{q_1} \leq \mu_1, \\ & \quad \mathbf{b}(F_{\text{PB}}, \Theta_{\text{ML}})_{q_2} \leq \mu_2, \\ & \quad \mathbf{h}^T \mathbf{R}_t \mathbf{h} \leq \mu_3, \\ & \quad \mathbf{h} \leq \mu_4, \\ & \quad \mathbf{u}^T (f_0, \theta_s) \mathbf{h} = 1, \end{aligned} \quad (5.70)$$

where any chosen three of $\mu_p, p \in \{1, 2, 3, 4\}$ are the specified constraint values, and the other one is the optimization objective. $q_1, q_2 \in \{\infty, 1, 2\}$. \mathbf{R}_t is the $ML \times ML$ time-domain broadband data covariance matrix defined in Eq. (5.24) or its estimate. The notation \mathbf{R} is not used here to avoid confusion with the frequency-domain narrowband data covariance matrix \mathbf{R} in expressions such as Eq. (3.174).

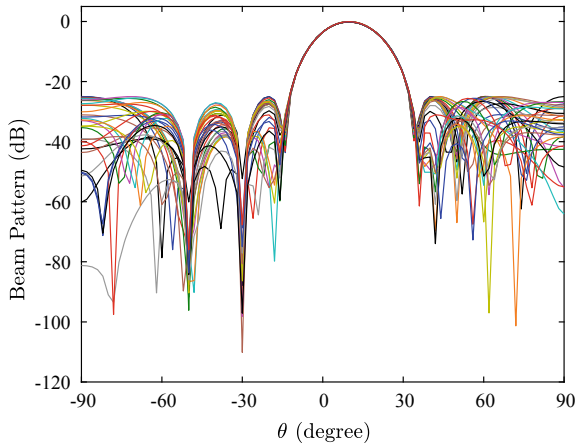
Obviously, the optimization problems in Eqs. (5.39), (5.40a, 5.40b, 5.40c, 5.40d), (5.46), (5.55), (5.60) and (5.61) are all special cases of the optimization problem in Eq. (5.70). The optimization method in Eq. (5.70) provides a unified framework for optimal design of broadband FIR beam patterns, which can be easily formulated as an SOCP problem for solution. Equation (5.70) can be viewed as extension of the unified narrowband beamformer design method in Eq. (3.174) to broadband case.

Consider the same case as in Fig. 3.30. We design the robust sidelobe constrained frequency-invariant adaptive FIR beamformer using the method in Eq. (5.70).

Assume $\theta_s = 10^\circ$. A uniform grid of 2° is used to discretize the visible region $[-90^\circ, 90^\circ]$ and let $\Theta_{\text{ML}} = [-12^\circ : 2^\circ : 32^\circ]$ and $\Theta_{\text{SL}} = [-90^\circ : 2^\circ : -16^\circ] \cup [36^\circ : 2^\circ : 90^\circ]$. The theoretical covariance matrix \mathbf{R} shown in Eq. (5.35) is used for convenience. The length of each filter is $L = 32$. The frequency band of interest $[f_l, f_u]$ is decomposed into $K = 33$ uniform subbands. Other parameters are set as follows: $p = 3, q_1 = 2, \mu_1 = 10^{-15/20}, q_2 = \infty, \mu_2 = 10^{-25/20}, \mu_4 = 10^{-10/20}, f_0 = (f_l + f_u)/2$.

The optimization problem in Eq. (5.70) is solved to obtain the FIR filter corresponding to each sensor. The beam pattern as a function of the frequency and direction grids are calculated. The superposition of the beam patterns for the 33 subbands are shown in Fig. 5.17. It is seen that the design result satisfies the constraints, and deep nulls are formed in the directions of the interferers. Calculation results show that the

Fig. 5.17 Superposition of beam patterns using multiple-objective design



output SINR of the FIR beamformer is 9.02 dB. From the results above, the design capability of the multiply constrained method is fully demonstrated.

5.6 Summary

The optimal design methods for time-domain implementation of broadband beamformer based on FIR filters (also called FIR beamformer) are presented in this chapter.

The two-stage design method for the FIR beamformer separately designs the narrowband beamformers and the FIR filters, which is easy in design and low in computational complexity. However, there is error between the beam pattern of the time-domain implementation and that of the frequency-domain implementation, although the error may be small. The stopband attenuation of the FIR filter is difficult to determine, and the sidelobes at the transition frequency band are difficult to be controlled.

The beam response and several commonly used performance measures can be expressed in terms of the FIR filter tap weights. These expressions have the forms that are similar to those for the narrowband beamformers, so the techniques from narrowband beamformer design problems can be used. The beam pattern can be optimally designed to satisfy some spatial and frequency-domain specifications. This method improves the design accuracy at the cost of increased computational complexity.

A method for designing broadband adaptive FIR beamformer has been proposed. This method minimizes the beamformer output power, while maintaining the distortionless response in the signal direction. The tap weights are determined adaptively from the array data. This method can be viewed as an extension of the MVDR beamformer to time-domain broadband case. It can place perfect nulls adaptively at the directions of interferers. Norm constraint on tap weights can be imposed to improve

the robustness of the beamformer. The sidelobes can also be controlled strictly to be below a specified threshold.

A broadband array pattern synthesis method has been presented for designing FIR beamformer with frequency-invariant mainlobe patterns. This method optimally designs the FIR filters of the beamformer by imposing constraint on the MSRV over the frequency band of interest. For this method, no preliminary desired beam pattern is required and the beam responses' variation constraint is employed only in the mainlobe region, which improves the constant mainlobe pattern synthesis accuracy. Several criteria and the corresponding computational complexities are given, which is helpful for us to choose suitable criteria for various application requirements.

The multiple-objective approach is presented for designing the tap weights of the FIR beamformer that provides a suitable trade-off among multiple conflicting array performances such as the array gain, the robustness, the sidelobe level, the frequency invariance, etc. It can provide FIR beamformer design with a high level of detail in the specification of performance and allows great design flexibility. The multiple-objective approach provides a unified framework for optimal design of broadband FIR beamformers, which is an extension of the unified framework for narrowband beamformer to the broadband case.

References

1. S. Yan, Optimal design of FIR beamformer with frequency invariant patterns. *Appl. Acoust.* **67**(6), 511–528 (2006)
2. S. Yan, C. Hou, X. Ma, Y. Ma, Convex optimization based time-domain broadband beamforming with sidelobe control. *J. Acoust. Soc. Am.* **121**(1), 46–49 (2007)
3. S. Yan, Y. Ma, C. Hou, Optimal array pattern synthesis for broadband arrays. *J. Acoust. Soc. Am.* **122**(5), 2686–2696 (2007)

Chapter 6

Modal Beamforming for Circular Arrays



6.1 Introduction

In Chaps. 1–5 we discussed narrowband and broadband beamformer design techniques, most of which can be applied to arrays with arbitrary geometry. In this chapter and Chaps. 7–9, we will restrict our attention to two types of symmetrical array geometries: circular arrays and spherical arrays.

All of the processing that we have discussed up to this point is element-space processing, in which the signals arriving at each of the elements are weighted (or filtered in the broadband case) and summed to obtain an output signal. From this chapter, in addition to the element-space beamforming, we focus on the modal beamforming problems. In this chapter and Chap. 7, we study the modal beamforming problem for circular arrays, and the modal beamforming problem for spherical arrays will be studied in Chaps. 8 and 9.

Because of the symmetric geometry, circular arrays are often used in applications where we want identical beam pattern in all directions of the plane in which the circular located. Moreover, the processing problem can be greatly simplified due to the circular symmetry property. As a result, circular arrays have attracted a significant amount of interest over the past few decades [1].

Modal beamforming applies the notion of spatial harmonic decomposition of the sound field and the composition of eigenbeams [2]. On the basis of the principles of wave propagation and wave scattering, the modal array signal processing algorithms were derived from the fundamental solutions of the acoustic wave equation [3]. Phase-mode beamformer is a famous modal beamformer.

Modal beamforming for circular arrays is also referred to as the circular-harmonics-domain (CHD) beamforming, which is based on decomposing the sound field into a series of circular harmonics with circular arrays. Phase-mode beamformer has better resolution and lower sidelobes than DAS beamforming by selectively processing a different number of phase modes. However, the low-frequency performance of phase-mode beamformer is limited by measurement noise and microphone place-

ment error due to the fact that large equalization coefficients introduced by circular harmonics beamforming will cause a huge amount of noise amplification.

Using the circular Fourier transform, the element-space data received by a UCA can be transformed into circular harmonics domain, thus the beamforming operation can be performed in the circular harmonics domain. The techniques for element-space beamformer design can then be extended to the circular harmonics domain in a straightforward manner. By deriving the expressions for the CHD beam response, covariance matrix, array gain, WNG, etc. in terms of the CHD weight vector, the CHD beamformer can be designed.

The rest of this chapter is organized as follows. In Sect. 6.2, we study the continuous circular arrays and the corresponding element-space DAS beamformer and phase-mode beamformer. The general formulation of the element-space beamformer and CHD beamformer for UCAs are studied in Sect. 6.3, where several commonly used CHD performance measures are derived. In Sect. 6.4, we develop the optimal design methods of CHD beamformer for UCAs. In Sect. 6.5, the frequency-domain implementation of the broadband CHD beamformer is presented. A brief summary of this chapter is given in Sect. 6.6.

6.2 Continuous Circular Arrays (Apertures)

We consider continuous circular arrays in this section. The continuous circular arrays are also referred to as circular (or ring) apertures.

Consider a circular aperture of radius r located in the xy -plane with its center at the origin of the coordinate system, as shown in Fig. 6.1.

For an observation point (r, ϑ) (in polar coordinates) on the circular aperture, the position vector is given by

$$\mathcal{P}_\vartheta = [r \cos \vartheta, r \sin \vartheta, 0]^T. \quad (6.1)$$

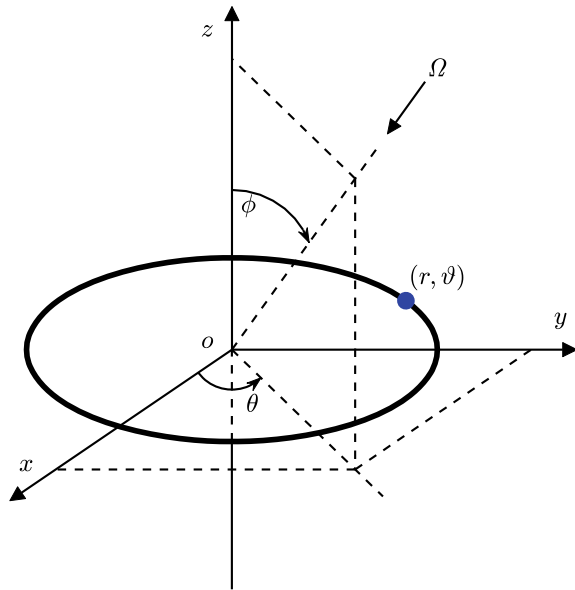
The manifold function, which is analogous to the array manifold vector in an array, of the aperture can be given by

$$p_\vartheta(\mathbf{k}) = \exp(-i\mathbf{k}^T \mathcal{P}_\vartheta) = \exp(ikr \sin \phi \cos(\vartheta - \theta)). \quad (6.2)$$

The manifold function can be interpreted as the sensor's response to a unit plane wave as a function of its wavenumber \mathbf{k} .

For a single-frequency sound field, assuming a unit-amplitude plane wave impinging on the circular aperture from the direction $\Omega_s = (\theta_s, \phi_s)$, the sound pressure received at the point (r, ϑ) can be written as

$$p(kr, \vartheta, \Omega_s) = \exp(ikr \sin \phi_s \cos(\vartheta - \theta_s)). \quad (6.3)$$

Fig. 6.1 Circular aperture

Let $w_a^*(\vartheta)$ be the weighting function at position \mathcal{P}_ϑ . The frequency-wavenumber response is given by

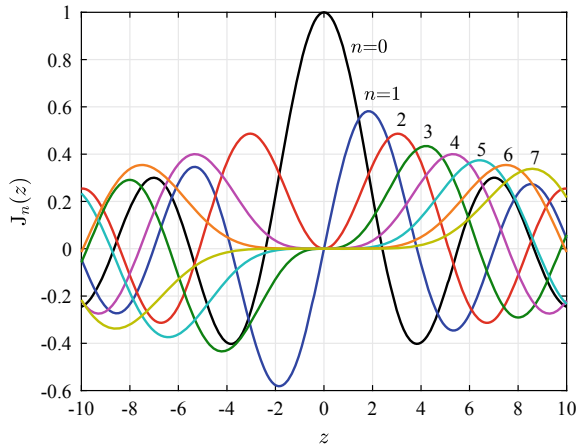
$$\begin{aligned} Y(\omega, \mathbf{k}) &= \frac{1}{2\pi} \int_0^{2\pi} w_a^*(\vartheta) p_\vartheta(\mathbf{k}) d\vartheta \\ &= \frac{1}{2\pi} \int_0^{2\pi} w_a^*(\vartheta) e^{ikr \sin \phi \cos(\vartheta - \theta)} d\vartheta. \end{aligned} \quad (6.4)$$

Writing Eq. (6.4) as a beam pattern

$$B(kr, \Omega) = \frac{1}{2\pi} \int_0^{2\pi} w_a^*(\vartheta) e^{ikr \sin \phi \cos(\vartheta - \theta)} d\vartheta. \quad (6.5)$$

6.2.1 Uniform Weighting

Define

Fig. 6.2 Bessel functions

$$P_n \triangleq \frac{1}{2\pi} \int_0^{2\pi} e^{ikr \sin \phi \cos(\vartheta - \theta)} e^{-in\vartheta} d\vartheta. \quad (6.6)$$

Letting $\psi = \vartheta - \theta$, Eq. (6.6) becomes

$$\begin{aligned} P_n &= \frac{1}{2\pi} \int_0^{2\pi} e^{ikr \sin \phi \cos \psi} e^{-in(\psi + \theta)} d\psi \\ &= e^{-in\theta} \frac{1}{2\pi} \int_0^{2\pi} e^{ikr \sin \phi \cos \psi} e^{-in\psi} d\psi. \end{aligned} \quad (6.7)$$

We know that the Bessel function of the first kind of order n is defined as

$$J_n(z) = \frac{1}{2\pi i^n} \int_0^{2\pi} e^{i(z \cos \psi + n\psi)} d\psi, \quad n = 0, \pm 1, \pm 2, \dots \quad (6.8)$$

The Bessel functions $J_n(z)$ versus z for various orders of n are plotted in Fig. 6.2. It is seen that as n increases, $\max|J_n(z)|$ decreases. When the order n exceeds $|z|$, the amplitude value $|J_n(z)|$ of the Bessel function is relatively small.

Using Eq. (6.8), Eq. (6.7) can be written as

$$P_n = i^{-n} J_{-n}(kr \sin \phi) e^{-in\theta}. \quad (6.9)$$

Using the relation

$$J_{-n}(z) = (-1)^n J_n(z), \quad (6.10)$$

Equation (6.9) can be written as

$$P_n = i^n J_n(kr \sin \phi) e^{-in\theta}. \quad (6.11)$$

Assume that the uniform aperture weighting

$$w_a^*(\vartheta) = 1, \quad \vartheta \in [0, 2\pi] \quad (6.12)$$

is used. Substituting it into Eq. (6.5), we obtain

$$B(kr, \Omega) = \frac{1}{2\pi} \int_0^{2\pi} e^{ikr \sin \phi \cos(\vartheta - \theta)} d\vartheta. \quad (6.13)$$

Using Eqs. (6.6) and (6.11), and letting $n = 0$, Eq. (6.13) can be written as

$$B(kr, \Omega) = J_0(kr \sin \phi). \quad (6.14)$$

This beam response is independent of the horizontal angle θ , indicating that the beam response is rotationally symmetric with respect to the z -axis.

We observe that for a circular aperture, the function $J_0(\cdot)$ plays the same role as the function $\text{sinc}(\cdot)$ did for a linear aperture. The first sidelobe occurs at $kr \sin \phi = 3.83$ and its height is -7.90 dB, in contrast to a linear aperture, whose sidelobe height is -13.26 dB.

Using Eq. (6.14), the beam pattern of a uniformly weighted circular aperture with $kr = 2\pi$ over the entire visible region $\theta \in [0^\circ, 360^\circ)$ and $\phi \in [0^\circ, 180^\circ]$ is shown in Fig. 6.3.

The beam patterns versus the vertical angle ϕ over the range $\phi \in [0^\circ, 180^\circ]$ for various values of $kr \in [0, 10]$ are shown in Fig. 6.4. As the frequency decreases, the beam broadens. When the frequency drops to 0, the beam pattern becomes a circle, i.e., there is no directivity.

The beam pattern of a uniformly weighted circular aperture is a 0-order Bessel function. This is contrast to the uniformly weighted linear aperture, whose beam pattern is a sinc function.

6.2.2 Conventional Beamformer

The conventional DAS beamformer is applied. Assume that the steering direction is $\Omega_o = (\theta_o, \phi_o)$. Using Eq. (6.2), the manifold function at direction Ω_o is given by

Fig. 6.3 Beam pattern of uniformly weighted circular aperture with $kr = 2\pi$

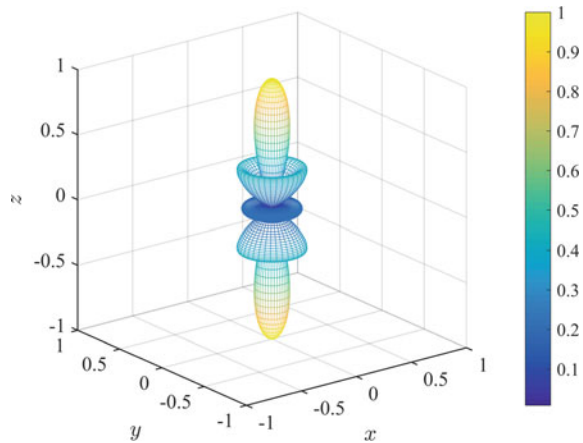
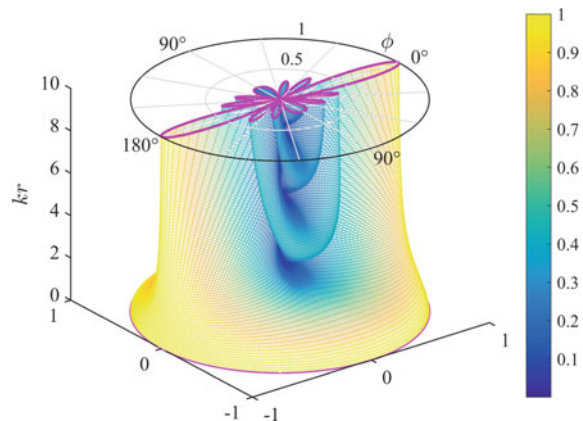


Fig. 6.4 Beam pattern of uniformly weighted circular aperture, $kr \in [0, 10]$, $\phi \in [0^\circ, 180^\circ]$



$$p_\vartheta(\Omega_o) = \exp(ikr \sin \phi_o \cos(\vartheta - \theta_o)). \quad (6.15)$$

The aperture weighting function of the DAS beamformer can be given by

$$w_a^*(\vartheta) = p_\vartheta^*(\Omega_o) = \exp(-ikr \sin \phi_o \cos(\vartheta - \theta_o)). \quad (6.16)$$

Substituting Eq. (6.16) into Eq. (6.5) gives the DAS beam pattern of the circular aperture

$$B(kr, \Omega) = \frac{1}{2\pi} \int_0^{2\pi} e^{ikr(\sin \phi \cos(\vartheta - \theta) - \sin \phi_o \cos(\vartheta - \theta_o))} d\vartheta. \quad (6.17)$$

In the exponential term in Eq. (6.17), define

$$\begin{aligned}
z &= \sin \phi \cos(\vartheta - \theta) - \sin \phi_0 \cos(\vartheta - \theta_0) \\
&= \sin \phi (\cos \vartheta \cos \theta + \sin \vartheta \sin \theta) - \sin \phi_0 (\cos \vartheta \cos \theta_0 + \sin \vartheta \sin \theta_0) \\
&= \cos \vartheta (\sin \phi \cos \theta - \sin \phi_0 \cos \theta_0) + \sin \vartheta (\sin \phi \sin \theta - \sin \phi_0 \sin \theta_0), \quad (6.18)
\end{aligned}$$

and let

$$\cos \beta = (\sin \phi \cos \theta - \sin \phi_0 \cos \theta_0) / \rho, \quad (6.19)$$

$$\sin \beta = (\sin \phi \sin \theta - \sin \phi_0 \sin \theta_0) / \rho. \quad (6.20)$$

Using the relation $\cos^2 \beta + \sin^2 \beta = 1$, we have

$$\begin{aligned}
\rho &= \sqrt{(\sin \phi \cos \theta - \sin \phi_0 \cos \theta_0)^2 + (\sin \phi \sin \theta - \sin \phi_0 \sin \theta_0)^2} \\
&= \sqrt{\sin^2 \phi + \sin^2 \phi_0 - 2 \sin \phi \sin \phi_0 \cos(\theta - \theta_0)} \\
&= \sqrt{(\sin \phi - \sin \phi_0)^2 + 4 \sin \phi \sin \phi_0 \sin^2 \frac{\theta - \theta_0}{2}}. \quad (6.21)
\end{aligned}$$

Then, Eq. (6.18) reduces to

$$z = \rho \cos(\vartheta - \beta). \quad (6.22)$$

And Eq. (6.17) can be rewritten as

$$B(kr, \Omega) = \frac{1}{2\pi} \int_0^{2\pi} e^{i\rho kr \cos(\vartheta - \beta)} d\vartheta = J_0(\rho kr), \quad (6.23)$$

where $\rho = \sqrt{(\sin \phi - \sin \phi_0)^2 + 4 \sin \phi \sin \phi_0 \sin^2[(\theta - \theta_0)/2]}$.

It is seen from Eq. (6.23) that, the DAS beam pattern of a circular aperture is also a 0-order Bessel function.

Since $\sin(180^\circ - \phi) = \sin \phi$, we have $B(kr, (\theta, 180^\circ - \phi)) = B(kr, (\theta, \phi))$, which implies that DAS beam pattern of the circular aperture is symmetrical with respect to the plane of the aperture.

When $\phi_0 = 0^\circ$, Eq. (6.23) reduces to

$$B(kr, \phi) = J_0(kr \sin \phi), \quad (6.24)$$

which is the same as Eq. (6.14).

If the steering direction Ω_0 and the signal direction Ω are both on the plane passing the z -axis, let $\theta = \theta_0$, Eq. (6.23) reduces to

$$B(kr, \phi) = J_0(kr(\sin \phi - \sin \phi_0)). \quad (6.25)$$

Alternatively, when $\phi = \phi_0 = \pi/2$, Eq. (6.23) reduces to

$$B(kr, \theta) = J_0(2kr \sin[(\theta - \theta_0)/2]). \quad (6.26)$$

Using Eq. (6.23), the DAS beam pattern of a circular aperture with $kr = 2\pi$ is plotted in Fig. 6.5 for three steering directions: $\Omega_0 = (\theta_0, \phi_0) = (0^\circ, 30^\circ), (0^\circ, 60^\circ)$ and $(0^\circ, 90^\circ)$. The beam pattern with respect to the steering direction $\Omega_0 = (0^\circ, 0^\circ)$ has been shown in Fig. 6.3.

As the beam is steered from the positive z -axis ($\phi_0 = 0^\circ$) toward the positive x -axis ($\phi_0 = 90^\circ$), the beam broadens.

Using Eq. (6.26) with the assumption that $\phi = \phi_0 = 90^\circ$, the DAS beam patterns versus θ over the range $\theta \in [-180^\circ, 180^\circ]$ for various values of $kr \in [0, 10]$ are shown in Fig. 6.6. The sidelobe level is approximately -7.9 dB, which is consistent with the theoretical value of the zero-order Bessel function.

6.2.3 Phase Mode Excitation

A function on the unit circle in polar coordinates, $g(\vartheta)$, can be represented using a circular Fourier series expansion as

$$g(\vartheta) = \sum_{n=-\infty}^{\infty} G_n e^{in\vartheta}, \quad (6.27)$$

where the coefficients G_n are given by

$$G_n = \frac{1}{2\pi} \int_0^{2\pi} g(\vartheta) e^{-in\vartheta} d\vartheta. \quad (6.28)$$

Equations (6.28) and (6.27) are referred to as the circular Fourier transform pair. They are also referred to as the circular harmonics transform pair.

In general, any function that is square-integrable over a unit circle can be expanded into a series of circular harmonics using the inverse circular Fourier transform.

The aperture weighting function $w_a(\vartheta)$ can be represented by a Fourier series as

$$w_a(\vartheta) = \sum_{n=-\infty}^{\infty} W_n e^{in\vartheta}. \quad (6.29)$$

where W_n is given by

Fig. 6.5 DAS beam pattern of circular aperture with $kr = 2\pi$ for
a $\Omega_0 = (0^\circ, 30^\circ)$,
b $\Omega_0 = (0^\circ, 60^\circ)$,
c $\Omega_0 = (0^\circ, 90^\circ)$

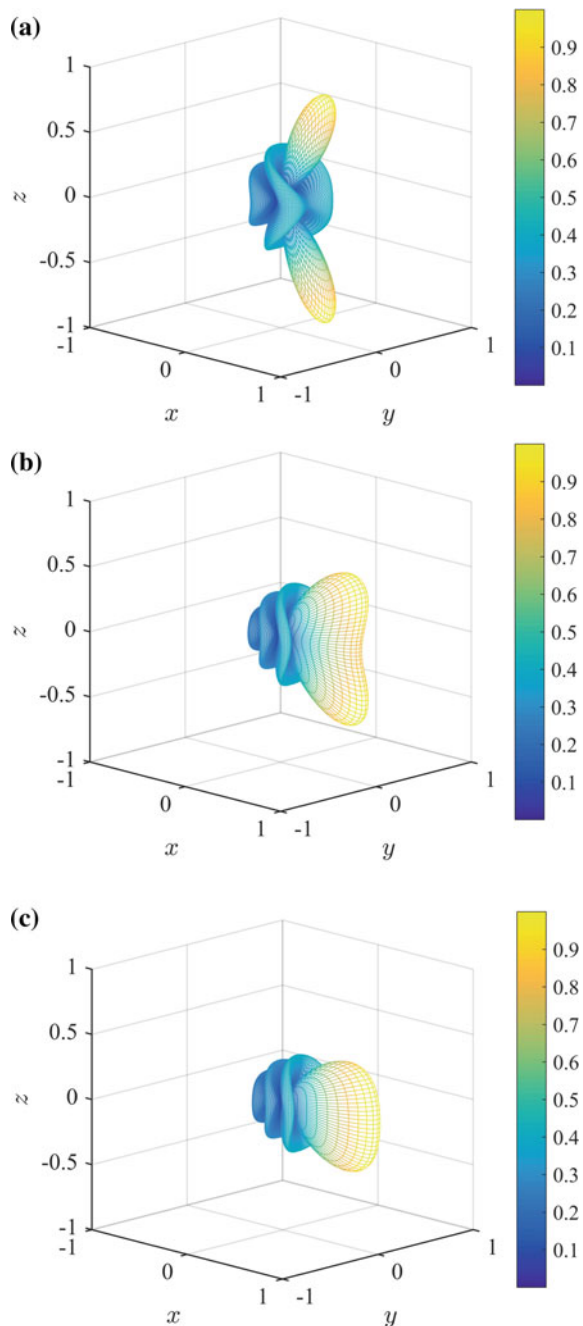
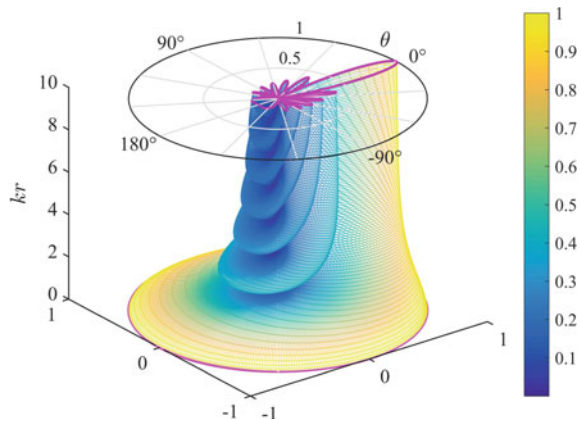


Fig. 6.6 DAS beam pattern of circular aperture



$$W_n = \frac{1}{2\pi} \int_0^{2\pi} w_a(\vartheta) e^{-in\vartheta} d\vartheta, \quad (6.30)$$

of which each term is called a phase mode excitation of the aperture.

Using Eq. (6.29), we have

$$w_a^*(\vartheta) = \sum_{n=-\infty}^{\infty} W_n^* e^{-in\vartheta}. \quad (6.31)$$

Substituting Eq. (6.31) into Eq. (6.5) gives

$$\begin{aligned} B(kr, \Omega) &= \frac{1}{2\pi} \int_0^{2\pi} \left(\sum_{n=-\infty}^{\infty} W_n^* e^{-in\vartheta} \right) e^{ikr \sin \phi \cos(\vartheta - \theta)} d\vartheta \\ &= \frac{1}{2\pi} \sum_{n=-\infty}^{\infty} W_n^* \int_0^{2\pi} e^{ikr \sin \phi \cos(\vartheta - \theta)} e^{-in\vartheta} d\vartheta. \end{aligned} \quad (6.32)$$

From Eq. (6.6), Eq. (6.32) can be written as

$$B(kr, \Omega) = \sum_{n=-\infty}^{\infty} W_n^* P_n = \sum_{n=-\infty}^{\infty} W_n^* i^n J_n(kr \sin \phi) e^{-in\theta}. \quad (6.33)$$

It is seen that each phase mode excitation term gives rise to a spatial harmonic in the beam pattern. The beamforming technique that represents the beam pattern as a sum of several order harmonics is referred to as the modal beamforming.

Especially, letting

$$W_n^* = \begin{cases} 1, & n = 0 \\ 0, & n \neq 0 \end{cases}, \quad (6.34)$$

Equation (6.33) can be written as

$$B(kr, \Omega) = P_0 = J_0(kr \sin \phi). \quad (6.35)$$

From Eq. (6.31), the aperture weighting function corresponding to Eq. (6.34) is uniform weighting, i.e.,

$$w_a^*(\vartheta) = 1, \quad (6.36)$$

which is the same as the result of Eq. (6.14).

6.2.4 Circular Mode

Using the circular Fourier transform introduced in Eq. (6.27), the sound pressure in Eq. (6.3) can be written in Fourier series expansion as

$$p(kr, \vartheta, \Omega_s) = \sum_{n=-\infty}^{\infty} P_n(kr, \Omega_s) e^{in\vartheta}, \quad (6.37)$$

where the Fourier coefficients $P_n(kr, \Omega_s)$ are given by

$$P_n(kr, \Omega_s) = \frac{1}{2\pi} \int_0^{2\pi} p(kr, \vartheta, \Omega_s) e^{-in\vartheta} d\vartheta \quad (6.38)$$

and $e^{in\vartheta}$ is the circular harmonics (CH).

The polar plot of the real part of the circular harmonics, i.e., $|\cos(n\vartheta)|$, versus ϑ over the range $0^\circ \leq \theta < 360^\circ$ for various values of n are shown in Fig. 6.7.

The circular harmonics transform pair Eqs. (6.38) and (6.37) can also be interpreted as the decomposition and synthesis of the sound field using circular harmonics.

The circular harmonics satisfy the orthogonal property

$$\frac{1}{2\pi} \sum_{n=-\infty}^{\infty} e^{in\theta} e^{-in\theta_0} = \delta(\theta - \theta_0), \quad (6.39)$$

where $\delta(\theta - \theta_0)$ is the delta function, which is also referred to as the Dirac function. It has a unit impulse at $\theta = \theta_0$ and zero otherwise. The integral area of the delta function is 1, i.e.,

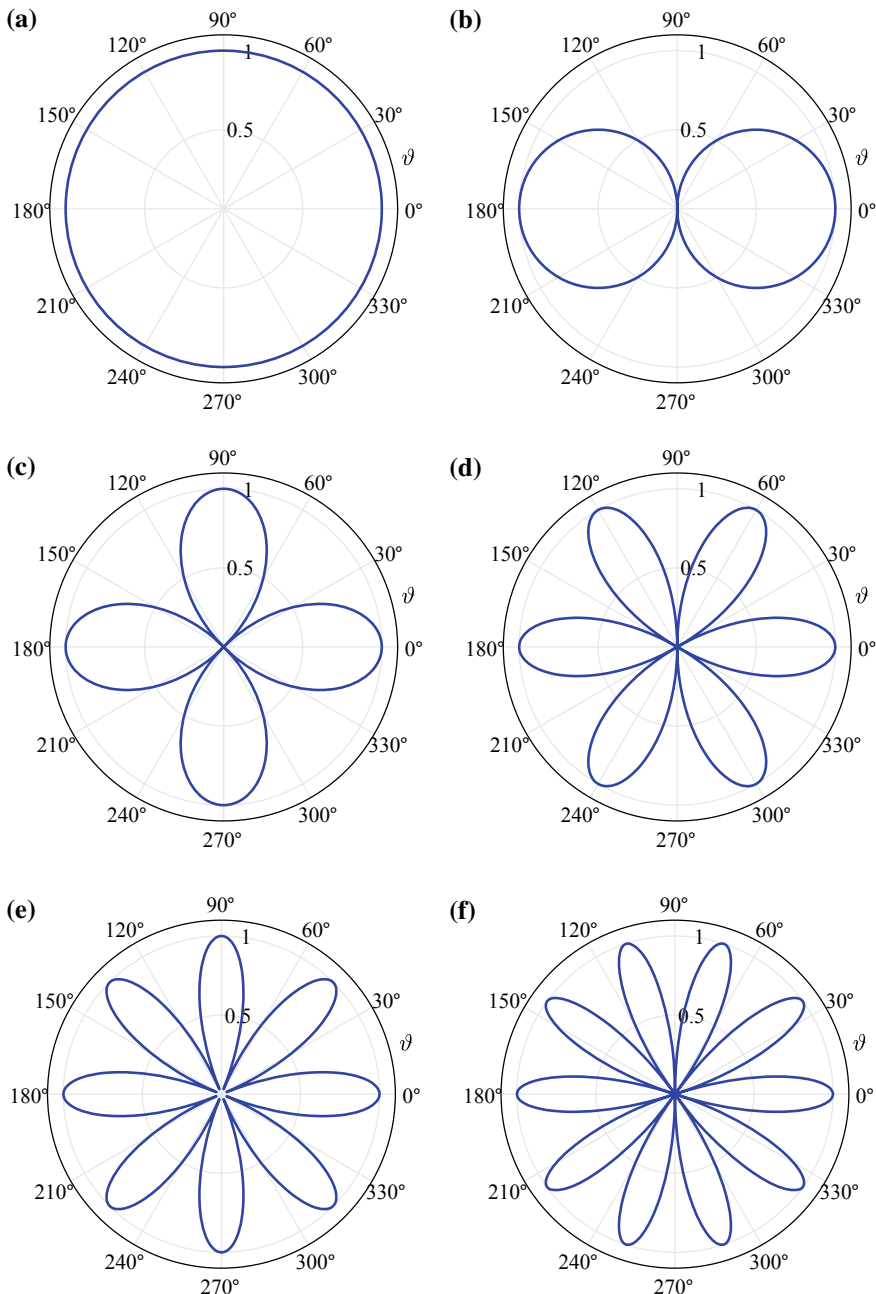


Fig. 6.7 Polar plot of $|\cos(n\vartheta)|$ for **a** $n = 0$, **b** $n = 1$, **c** $n = 2$, **d** $n = 3$, **e** $n = 4$, **f** $n = 5$

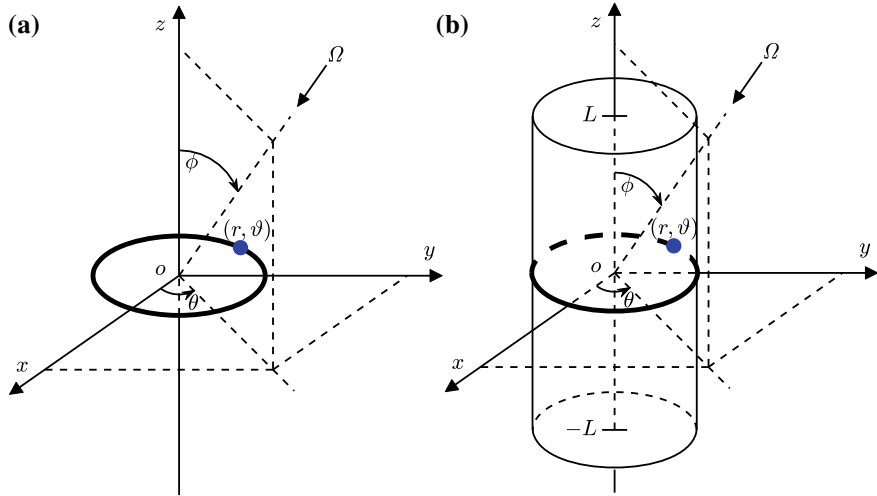


Fig. 6.8 Circular apertures. **a** Unbaffled, and **b** baffled by a rigid cylinder

$$\int_0^{2\pi} \delta(\theta - \theta_0) d\theta = 1. \quad (6.40)$$

Substituting Eq. (6.3) into Eq. (6.38) gives

$$P_n(kr, \Omega_s) = \frac{1}{2\pi} \int_0^{2\pi} \exp(ikr \sin \phi_s \cos(\vartheta - \theta_s)) e^{-in\vartheta} d\vartheta. \quad (6.41)$$

Consider an acoustic transparent circular aperture, or a circular aperture in free field, as shown in Fig. 6.8a. The acoustic transparent circular aperture (or array) is also termed as an unbaffled circular aperture (or array) in this book.

Using Eq. (6.11), Eq. (6.41) can be written as

$$P_n(kr, \Omega_s) = i^n J_n(kr \sin \phi_s) e^{-in\theta_s} = C_{n,\text{unbaff}}(kr) e^{-in\theta_s}, \quad (6.42)$$

where the coefficients P_n are usually referred to as the eigenbeams, and

$$C_{n,\text{unbaff}}(kr) \triangleq i^n J_n(kr \sin \phi_s) \quad (6.43)$$

is referred to as the circular modal response, and the subscript “unbaff” denotes the aperture in free field.

Equation (6.42) can also be viewed as the CHD expression for the sound pressure $p(kr, \vartheta, \Omega_s)$ received by the unbaffled circular aperture.

Substituting Eq. (6.42) into Eq. (6.37) gives

$$p(kr, \vartheta, \Omega_s) = \sum_{n=-\infty}^{\infty} C_{n,\text{unbaff}}(kr) e^{-in\theta_s} e^{in\vartheta}. \quad (6.44)$$

In the following discussions, unless otherwise stated, only the incident signals on the plane where the circular aperture located are considered for simplicity, i.e., $\phi_s = \pi/2$ (or 90°). Then Ω_s can be replaced by θ_s , and the aforementioned sound pressure $p(kr, \vartheta, \Omega_s)$ and its CHD representation $P_n(kr, \Omega_s)$ can be rewritten as $p(kr, \vartheta, \theta_s)$ and $P_n(kr, \theta_s)$, respectively.

Thus, for the aforementioned circular aperture, Eq. (6.43) reduces to

$$C_{n,\text{unbaff}}(kr) \triangleq i^n J_n(kr). \quad (6.45)$$

Next consider the case when the circular aperture is baffled by an acoustically rigid cylinder of length $2L$, as shown in Fig. 6.8b.

For a circular aperture baffled by an infinitely long acoustically rigid cylinder (i.e., $L \rightarrow \infty$), the corresponding circular modal response becomes [3]

$$C_{n,\text{baff}}(kr) \triangleq i^n \left(J_n(kr) - \frac{J'_n(kr)}{H'_n(kr)} H_n(kr) \right), \quad (6.46)$$

where the subscript “baff” indicates baffled aperture, H_n is the n th-order Hankel function of the second kind, and J'_n and H'_n are the derivatives of J_n and H_n with respect to their arguments, respectively. The first item in the brackets of Eq. (6.46) describes the incident wave, which is identical to that of the unbaffled circular aperture as shown in Eq. (6.45). And the second item describes the scattered wave.

It is worth noting that, in some literatures where the single-frequency plane wave $s(t)$ is expressed as $\exp(-i\omega t)$ rather than the expression of $\exp(i\omega t)$ used in this book, the n th-order Hankel function of the second kind H_n in Eq. (6.46) needs to be replaced by the n th-order Hankel function of the first kind.

The Bessel functions have the properties

$$J'_n(kr) = [J_{n-1}(kr) - J_{n+1}(kr)]/2, \quad (6.47)$$

$$H_n(kr) = J_n(kr) - iY_n(kr), \quad (6.48)$$

$$H'_n(kr) = J'_n(kr) - iY'_n(kr), \quad (6.49)$$

where Y_n is the n th-order Bessel function of the second kind.

Applying Wronskian identity

$$J_n(kr)Y'_n(kr) - Y_n(kr)J'_n(kr) = 2/(\pi kr), \quad (6.50)$$

gives

$$\begin{aligned} J_n(kr)H_n'(kr) - H_n(kr)J_n'(kr) &= -i \left[J_n(kr)Y_n'(kr) - Y_n(kr)J_n'(kr) \right] \\ &= -2i/(\pi kr). \end{aligned} \quad (6.51)$$

Thus

$$H_n'(kr) = \left[-2i/(\pi kr) + H_n(kr)J_n'(kr) \right] / J_n(kr), \quad (6.52)$$

and

$$\begin{aligned} J_n(kr) - \frac{J_n'(kr)}{H_n'(kr)} H_n(kr) &= \frac{-2i/(\pi kr)}{H_n'(kr)} \\ &= \frac{-J_n(kr)2i/(\pi kr)}{-2i/(\pi kr) + H_n(kr)J_n'(kr)} \\ &= \frac{-4J_n(kr)i}{-4i + \pi kr H_n(kr)[J_{n-1}(kr) - J_{n+1}(kr)]}. \end{aligned} \quad (6.53)$$

Then, Eq. (6.46) can be rewritten as

$$C_{n,\text{baff}}(kr) = \frac{-4i^{n+1}J_n(kr)}{-4i + \pi kr H_n(kr)[J_{n-1}(kr) - J_{n+1}(kr)]}. \quad (6.54)$$

Combining Eqs. (6.42), (6.45) and (6.46), the CHD representation of the sound pressure received by the circular aperture can be written as

$$P_n(kr, \theta_s) = C_n(kr)e^{-in\theta_s}, \quad (6.55)$$

where the circular modal response is given by

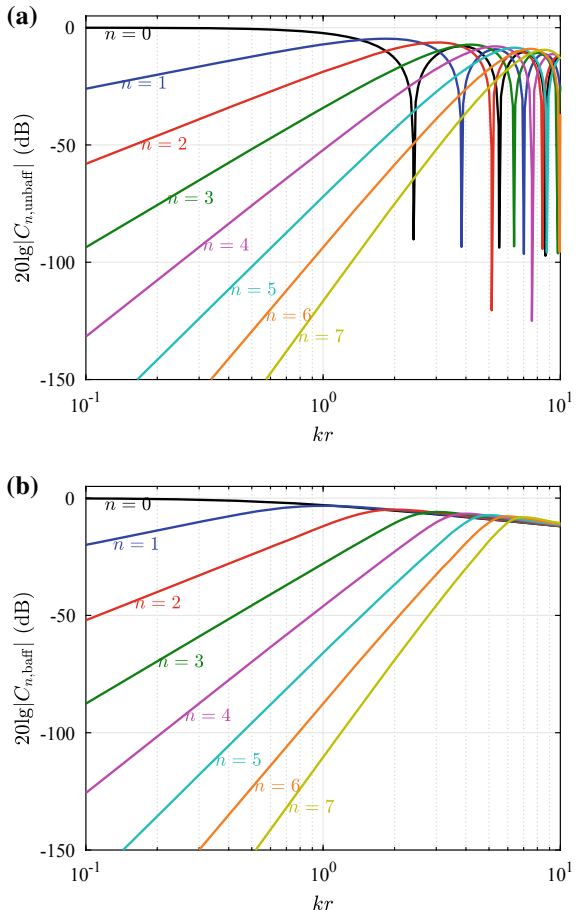
$$C_n(kr) = \begin{cases} i^n J_n(kr), & \text{unbaffled circular aperture,} \\ i^n \left(J_n(kr) - \frac{J_n'(kr)}{H_n'(kr)} H_n(kr) \right), & \text{baffled circular aperture.} \end{cases} \quad (6.56)$$

It is worth noting that, in practical applications, there is only a slight performance variation between the circular apertures mounted into a rigid cylindrical baffle with an infinite length and a finite length of [4]

$$2L \geq 2.8r. \quad (6.57)$$

Using Eqs. (6.45) and (6.54), the modal magnitude response in dB of an unbaffled circular aperture and a circular aperture mounted into an infinite-length rigid cylindri-

Fig. 6.9 Modal magnitude responses of **a** an unbaffled circular aperture, and **b** a circular aperture mounted into an infinite-length rigid cylindrical baffle

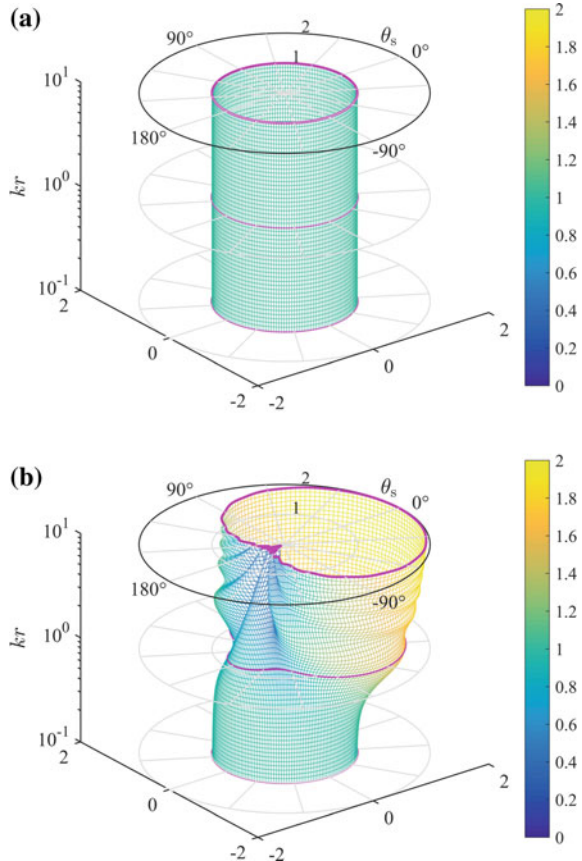


cal baffle, i.e., $20\lg|C_{n,\text{unbaff}}(kr)|$ and $20\lg|C_{n,\text{baff}}(kr)|$, versus kr for various values of n are plotted in Fig. 6.9a and b, respectively.

It is seen that the higher-order terms of the coefficients $C_n(kr)$ contribute significantly less than the lower-order terms when the order n exceeds kr . For the unbaffled circular aperture as shown in Fig. 6.9a, it is also seen that some coefficients $C_n(kr)$ are zero for some values of kr due to the zeros of the Bessel functions. For the baffled circular aperture, the zeros in the modal magnitude response disappear.

Substituting Eq. (6.55) into Eq. (6.37), the sound pressure received at the point (r, ϑ) for the unit-amplitude single-frequency plane-wave signal from θ_s , i.e., $p(kr, \vartheta, \theta_s)$, can be obtained. It is defined as the manifold function for the point (r, ϑ) , which is analogous to the array manifold vector in an array. It can be written as

Fig. 6.10 Manifold function $|p(kr, 0^\circ, \theta_s)|$ over the range $\theta_s \in [-180^\circ, 180^\circ]$ and $kr \in [0.1, 10]$ for
a unbaffled and **b** baffled circular apertures



$$p(kr, \vartheta, \theta_s) = \sum_{n=-\infty}^{\infty} C_n(kr) e^{-in\theta_s} e^{in\vartheta}. \quad (6.58)$$

Using Eq. (6.58) with the terms up to order $n = 20$ and letting $\vartheta = 0^\circ$, the manifold function $p(kr, \vartheta, \theta_s)$ versus kr in the range $[0.1, 10]$ and θ_s in the range $[-180^\circ, 180^\circ]$ for the unbaffled and baffled circular apertures are plotted in Fig. 6.10.

For the baffled circular aperture as shown in Fig. 6.10b, the magnitude of the manifold function for the point $(r, \vartheta = 0^\circ)$ varies very little with the signal direction θ_s at low frequencies (when the value of kr is small), which indicates that the scattering of the cylindrical baffle is negligible at low frequencies.

At high frequencies (when the value of kr is large), when the direction of the signal and the sensor are in the same side of the circular aperture (sunny side), the magnitude of the manifold is larger (close to 2 when $kr = 10$). However, due to acoustic scattering, when the sensor is located at the nightside of the signal direction,

the magnitude of the manifold is smaller. This indicates that the baffled aperture has a non-isotropic element pattern, especially at high frequencies.

6.2.5 Phase-Mode Beamformer

Assume that the circular aperture has a weighting function $w^*(kr, \vartheta)$ corresponding to the point (r, ϑ) . The frequency-wavenumber response (or beam response) function, denoted by $B(kr, \theta)$, can be given by

$$B(kr, \theta) = \frac{1}{2\pi} \int_0^{2\pi} p(kr, \vartheta, \theta) w^*(kr, \vartheta) d\vartheta. \quad (6.59)$$

Let W_n be the circular harmonics transform of w , i.e., w and W_n are a circular harmonics transform pair. Then

$$w(kr, \vartheta) = \sum_{n=-\infty}^{\infty} W_n(kr) e^{in\vartheta}, \quad (6.60)$$

$$W_n(kr) = \frac{1}{2\pi} \int_0^{2\pi} w(kr, \vartheta) e^{-in\vartheta} d\vartheta. \quad (6.61)$$

Substituting Eqs. (6.37) and (6.60) into Eq. (6.59) gives the beam response function

$$B(kr, \theta) = \frac{1}{2\pi} \int_0^{2\pi} \left(\sum_{n=-\infty}^{\infty} P_n(kr, \theta) e^{in\vartheta} \right) \left(\sum_{n=-\infty}^{\infty} W_n^*(kr) e^{-in\vartheta} \right) d\vartheta. \quad (6.62)$$

Use the orthogonality

$$\frac{1}{2\pi} \int_0^{2\pi} e^{in\vartheta} e^{-i\tilde{n}\vartheta} d\vartheta = \delta_{n\tilde{n}}, \quad (6.63)$$

where $\delta_{n\tilde{n}}$ is Kronecker delta function, which is 1 at $n = \tilde{n}$, and 0 otherwise, i.e.,

$$\delta_{n\tilde{n}} = \begin{cases} 1, & n = \tilde{n} \\ 0, & n \neq \tilde{n} \end{cases}. \quad (6.64)$$

Then, Eq. (6.62) can be written as

$$B(kr, \theta) = \sum_{n=-\infty}^{\infty} P_n(kr, \theta) W_n^*(kr). \quad (6.65)$$

Equation (6.65) shows that the beam response function of circular aperture can be expressed as the form of CHD weighted summation. This form of CHD beamformer is referred to as the eigen-beamformer. The element-space beamformer shown in Eq. (6.59) is equivalent to the CHD beamformer shown in Eq. (6.65).

Substituting Eq. (6.42) into Eq. (6.65) gives

$$B(kr, \theta) = \sum_{n=-\infty}^{\infty} W_n^*(kr) C_n(kr) e^{-in\theta}. \quad (6.66)$$

Using the relationship of the circular harmonics transform pair gives

$$W_n(kr) C_n^*(kr) = \frac{1}{2\pi} \int_0^{2\pi} B^*(kr, \theta) e^{-in\theta} d\theta. \quad (6.67)$$

Thus, if the desired beam response of the circular aperture is $B_d(kr, \theta)$, the CHD weighting function can be calculated using Eq. (6.67) as

$$W_n(kr) = \frac{1}{2\pi} \frac{1}{C_n^*(kr)} \int_0^{2\pi} B_d^*(kr, \theta) e^{-in\theta} d\theta. \quad (6.68)$$

Ideally, a pencil beam is required, i.e.,

$$B_d(kr, \theta) = \delta(\theta - \theta_o). \quad (6.69)$$

The modal beamformer with the ideal pencil beamshape shown in Eq. (6.69) is referred to as the ideal phase-mode (PM) beamformer. In order to distinguish from the phase-mode beamformer for spherical arrays, the phase-mode beamformer for circular arrays is referred to as the CH-PM beamformer in this book. For convenience, it is sometimes called the PM beamformer in this chapter when there is no ambiguity.

Substituting Eq. (6.69) into Eq. (6.68) gives the ideal phase-mode beamformer weighting function

$$W_{n,PM}(kr) = \frac{1}{2\pi} \frac{1}{C_n^*(kr)} \int_0^{2\pi} \delta(\theta - \theta_o) e^{-in\theta} d\theta = \frac{e^{-in\theta_o}}{2\pi C_n^*(kr)}, \quad (6.70)$$

or

$$W_{n,PM}^*(kr) = \frac{e^{in\theta_0}}{2\pi C_n(kr)}, \quad (6.71)$$

where the subscript ‘‘PM’’ denotes the phase-mode beamformer.

Note that C_n appears in the denominator of the weights shown in Eq. (6.71), i.e., the weights are inversely proportional to C_n . Recalling Fig. 6.9, it is seen that the magnitude of C_n decreases significantly with increasing order n at low frequencies, that is, the magnitude of the ideal phase-mode weighting function shown in Eq. (6.71) increases significantly as the order n increases.

This implies that the contribution of the high-order circular harmonics in the ideal phase-mode beamformer is significantly higher than that of the low-order circular harmonics at low frequencies. Recall that, the larger the weights, the higher the sensitivity of the beamformer to mismatches and the poorer the robustness. In other words, the robustness of the beamformer containing high-order modes degrades significantly. In addition, for the unbaffled circular aperture as shown in Fig. 6.9a, C_n is zero at some frequencies, which results in infinite weights at these frequencies that cannot be achieved in reality.

Substituting Eq. (6.71) into Eq. (6.66) gives

$$B_{PM}(kr, \theta) = \frac{1}{2\pi} \sum_{n=-\infty}^{\infty} e^{-in(\theta-\theta_0)} = \delta(\theta - \theta_0), \quad (6.72)$$

which is equal to the ideal phase-mode beam response shown in Eq. (6.69).

6.2.6 Modal Representation of DAS Beamformer

In the element-space DAS beamforming case, the inputs from each sensor are shifted so that the signals are aligned in time and then summed to obtain the beamformer output.

For an unbaffled circular aperture, assuming that a plane wave impinges from $(\theta_s, \phi_s = \pi/2)$ and the steering direction is $(\theta_0, \phi_0 = \pi/2)$, the output of the DAS beamformer can be given by

$$y(kr, \theta_s) = \frac{1}{2\pi} \int_0^{2\pi} e^{ikr \cos(\vartheta - \theta_s)} e^{-ikr \cos(\vartheta - \theta_0)} d\vartheta. \quad (6.73)$$

From Eq. (6.26), the element-space DAS beamformer response is

$$B_{DAS}(kr, \theta) = J_0\left(2kr \sin \frac{\theta - \theta_0}{2}\right). \quad (6.74)$$

Using Eqs. (6.3), (6.42) and (6.44), Eq. (6.73) can be rewritten as

$$y(kr, \theta_s) = \frac{1}{2\pi} \int_0^{2\pi} \sum_{n=-\infty}^{\infty} C_n(kr) e^{-in\theta_s} e^{in\vartheta} \cdot \sum_{n=-\infty}^{\infty} C_n^*(kr) e^{in\theta_o} e^{-in\vartheta} d\vartheta. \quad (6.75)$$

Using Eq. (6.63), Eq. (6.75) reduces to

$$\begin{aligned} y(kr, \theta_s) &= \sum_{n=-\infty}^{\infty} C_n(kr) e^{-in\theta_s} C_n^*(kr) e^{in\theta_o} \\ &= \sum_{n=-\infty}^{\infty} P_n(kr, \theta_s) C_n^*(kr) e^{in\theta_o}, \end{aligned} \quad (6.76)$$

which is the CHD representation of the DAS beamformer.

According to the definition of the beam response function, the CHD beam response can be obtained by replacing the θ_s in Eq. (6.76) with θ as

$$B(kr, \theta) = \sum_{n=-\infty}^{\infty} P_n(kr, \theta) C_n^*(kr) e^{in\theta_o}. \quad (6.77)$$

Comparing Eqs. (6.77) and (6.65), the CHD weights of the DAS beamformer can be given by

$$W_{n, \text{DAS}}^*(kr) = C_n^*(kr) e^{in\theta_o}. \quad (6.78)$$

Substituting Eq. (6.78) into Eq. (6.66) gives

$$B_{\text{DAS}}(kr, \theta) = \sum_{n=-\infty}^{\infty} |C_n(kr)|^2 e^{-in(\theta-\theta_o)}, \quad (6.79)$$

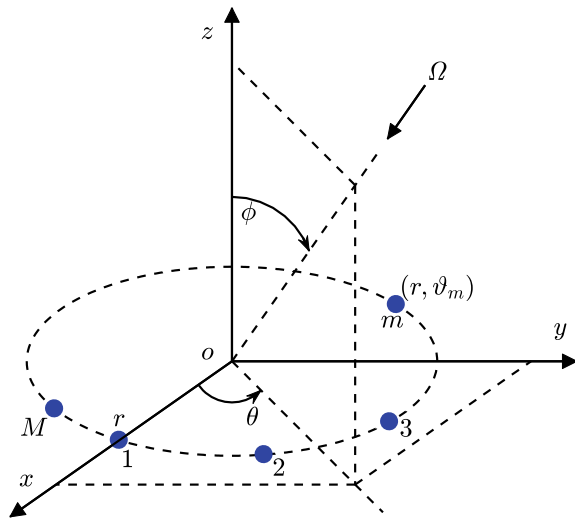
which is the CHD representation of the DAS beamformer response.

This DAS beamformer implemented in the circular harmonics domain is referred to as the CH-DAS beamformer.

Using the fact that $\sum_{n=-\infty}^{\infty} |J_n|^2 = 1$, for the case of unbaffled circular aperture, $\lim_{N \rightarrow \infty} \sum_{n=-N}^N |C_n|^2 = 1$. Accordingly, the beam pattern at the steering direction is $B_{\text{DAS}}(kr, \theta_o) = 1$.

It is worth noting that, the derivation results of the DAS beamformer above are based on the unbaffled circular aperture. For a baffled circular aperture, the results are different.

Fig. 6.11 Uniform circular array



6.3 Uniform Circular Arrays

In practical applications, the circular apertures are sampled by means of a finite number of sensors. In this chapter, we assume that this sampling is performed by equispaced omnidirectional microphones array, i.e., uniform circular array.

Consider an M -element UCA of radius r located in the xy -plane with its center at the origin of the coordinate system. The m th element is placed at angle $\vartheta_m = 2\pi(m-1)/M$, $m = 1, \dots, M$, as shown in Fig. 6.11.

The position vector for an element at (r, ϑ_m) is

$$\mathbf{p}_m = [r \cos(\vartheta_m), r \sin(\vartheta_m), 0]^T, \quad m = 1, \dots, M. \quad (6.80)$$

6.3.1 Element-Space Beamformer

For a plane wave arriving from $\Omega = (\theta, \phi)$, the array manifold vector is given by

$$\mathbf{p}(\Omega) = [e^{ikr \sin \phi \cos(\vartheta_1 - \theta)}, e^{ikr \sin \phi \cos(\vartheta_2 - \theta)}, \dots, e^{ikr \sin \phi \cos(\vartheta_M - \theta)}]^T. \quad (6.81)$$

Assuming that the steering direction is $\Omega_o = (\theta_o, \phi_o)$, the DAS beamformer weight vector is given by

$$\mathbf{w}_c = \mathbf{p}(\Omega_o)/M. \quad (6.82)$$

Thus the beam pattern is given by

$$B(\vartheta) = \mathbf{w}_c^H \mathbf{p}(\vartheta)/M = \mathbf{p}^H(\vartheta_0) \mathbf{p}(\vartheta)/M. \quad (6.83)$$

Assume that the signal direction and the steering direction are in the xy -plane, i.e., $\phi = \phi_0 = \pi/2$. The array manifold vector reduces to

$$\mathbf{p}(\theta) = [e^{ikr \cos(\vartheta_1 - \theta)}, e^{ikr \cos(\vartheta_2 - \theta)}, \dots, e^{ikr \cos(\vartheta_M - \theta)}]^T. \quad (6.84)$$

Accordingly, the beam pattern becomes

$$B(\theta) = \mathbf{w}_c^H \mathbf{p}(\theta)/M = \mathbf{p}^H(\theta_0) \mathbf{p}(\theta)/M. \quad (6.85)$$

Substituting Eq. (6.84) into Eq. (6.85), the beam pattern of the UCA can be written as

$$B(\theta) = \frac{1}{M} \sum_{m=1}^M \exp(ikr(\cos(\vartheta_m - \theta) - \cos(\vartheta_m - \theta_0))). \quad (6.86)$$

Due to the relationship of $\cos(\vartheta_m - \theta) - \cos(\vartheta_m - \theta_0) = -2 \sin \frac{\theta - \theta_0}{2} \sin \left(\frac{\theta + \theta_0}{2} - \vartheta_m \right)$, we have

$$\begin{aligned} B(\theta) &= \frac{1}{M} \sum_{m=1}^M \exp \left(-2ikr \sin \frac{\theta - \theta_0}{2} \sin \left(\frac{\theta + \theta_0}{2} - \vartheta_m \right) \right) \\ &= \frac{1}{M} \sum_{m=1}^M \exp(-iz \sin(\beta - \vartheta_m)), \end{aligned} \quad (6.87)$$

where $z = 2kr \sin \frac{\theta - \theta_0}{2}$ and $\beta = \frac{\theta + \theta_0}{2}$.

Using the Jacobi-Anger identity

$$\exp(iz \sin \alpha) = \sum_{n=-\infty}^{\infty} J_n(z) \exp(in \alpha), \quad (6.88)$$

Equation (6.87) can be written as

$$\begin{aligned} B(\theta) &= \frac{1}{M} \sum_{m=1}^M \sum_{n=-\infty}^{\infty} J_n(z) \exp(-in(\beta - \vartheta_m)) \\ &= \frac{1}{M} \sum_{m=1}^M \sum_{n=-\infty}^{\infty} J_n(z) \exp \left(-in \left(\beta - 2\pi \frac{m-1}{M} \right) \right). \end{aligned} \quad (6.89)$$

Exchanging the order of summation gives

$$B(\theta) = \sum_{n=-\infty}^{\infty} J_n(z) \exp(-in\beta) \frac{1}{M} \sum_{m=1}^M \exp[2\pi i(m-1)n/M]. \quad (6.90)$$

For the term $\frac{1}{M} \sum_{m=1}^M \exp[2\pi i(m-1)n/M]$, if n/M is an integer, letting $n/M = \ell$ with ℓ being an integer, gives

$$\frac{1}{M} \sum_{m=1}^M \exp[2\pi i(m-1)n/M] = 1. \quad (6.91)$$

Otherwise, if n/M is not an integer, the sum of the geometric series can be written as

$$\frac{1}{M} \sum_{m=1}^M \exp[2\pi i(m-1)n/M] = \frac{1 - \exp(i2\pi n)}{1 - \exp(i2\pi n/M)} = 0. \quad (6.92)$$

Using Eqs. (6.91) and (6.92), Eq. (6.90) can be written as

$$B(\theta) = \sum_{\ell=-\infty}^{\infty} J_{\ell M}(z) \exp(-i\ell M\beta). \quad (6.93)$$

If M is even, using Eq. (6.10), we have $J_{-\ell M}(z) = J_{\ell M}(z)$. Equation (6.93) can then be written as

$$\begin{aligned} B(\theta) &= J_0(z) + \sum_{\ell=1}^{\infty} J_{\ell M}(z) [\exp(-i\ell M\beta) + \exp(i\ell M\beta)] \\ &= J_0(z) + 2 \sum_{\ell=1}^{\infty} J_{\ell M}(z) \cos(\ell M\beta). \end{aligned} \quad (6.94)$$

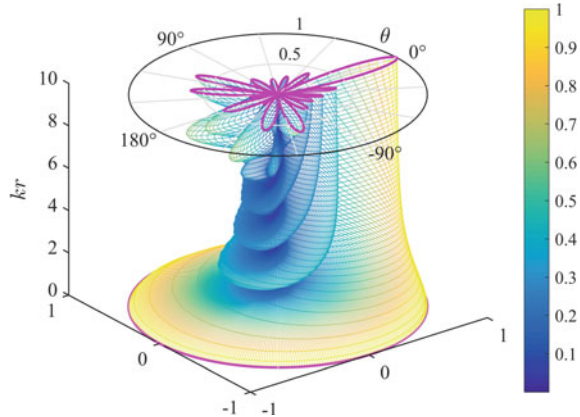
The first term in Eq. (6.94) corresponds to the conventional DAS beam pattern of an circular aperture as shown in Eq. (6.26). We observe from Fig. 6.2 that, when the number of elements M exceeds a certain value, the second item in Eq. (6.94) is very small and can be ignored. That is to say, as M increases, the beam pattern of the UCA approximates that of the circular aperture.

In addition, we observe from Fig. 6.2 that, $|J_n(z)|$ is relatively small when n exceeds $|z|$. Therefore, in order to ensure that the beam pattern error between the UCA and the circular aperture is small enough, i.e., the second item in Eq. (6.94) is small, we require

$$M \geq \max(|z|) = 2kr \quad (6.95)$$

or

Fig. 6.12 DAS beam patterns for a 16-element UCA over the range of $kr \in [0, 10]$



$$2\pi r/M \leq \lambda/2, \quad (6.96)$$

which implies that the interelement spacing along the arc of the circle should be less than half of the wavelength.

Assume that $M = 16$, using Eq. (6.93), the beam patterns over the frequency range $kr \in [0, 10]$ are shown in Fig. 6.12. It is seen that the beam patterns of the UCA are not much different from the circular aperture when $kr < M/2$, and that the sidelobes rise when $kr > M/2$, which is consistent with the theoretical analysis of Eq. (6.95).

The modal order n for the circular aperture is infinite. However, for a UCA, the highest order N of the circular harmonics that can be effectively extracted and used is limited by the maximum wavenumber k_{\max} and the radius r . It is seen from Fig. 6.9 that, when $kr < n$, the magnitude of the high-order $C_n(kr)$ is much smaller than that of the low-order and thus can be neglected. As a rule of thumb, we often choose [4, 5]

$$N \approx k_{\max}r = 2\pi r/\lambda_{\min}, \quad (6.97)$$

where λ_{\min} is the wavelength corresponding to the maximum wavenumber k_{\max} .

Note that the spatial sampling procedure implies an error in the circular harmonics, which is referred to as modal aliasing. Modal aliasing cannot be entirely avoided, however, by judiciously choosing the number of microphones, these distorting modes can be made as small as desired. In order to extract the N th-order harmonic, it is generally required that the number of sensors M satisfies

$$M \geq 2N. \quad (6.98)$$

From Eqs. (6.97) and (6.98), in order to avoid modal aliasing, the highest frequency is required to satisfy $2\pi f_{\max}r/c = k_{\max}r \leq M/2$, which is the same as Eq. (6.95).

We assume the plane of interest is the xy -plane, i.e., $\phi = \pi/2$. Letting $w^*(kr, \vartheta_m)$ being the weighting corresponding to the m th element and using the summation instead of the integral in Eq. (6.59), the beam pattern of the UCA can be written as

$$\begin{aligned} B(kr, \theta) &= \frac{1}{M} \sum_{m=1}^M p(kr, \vartheta_m, \theta) w^*(kr, \vartheta_m) \\ &= \frac{1}{M} \sum_{m=1}^M p_m(kr, \theta) w_m^*(kr) \\ &= \mathbf{w}_e^H(kr) \mathbf{p}_e(kr, \theta), \end{aligned} \quad (6.99)$$

where $w_m(kr) \triangleq w(kr, \vartheta_m)$, $p_m(kr, \theta) \triangleq p(kr, \vartheta_m, \theta)$, $m = 1, \dots, M$, the subscript “e” denotes the element-space. $\mathbf{w}_e(kr)$ and $\mathbf{p}_e(kr)$ are respectively the element-space weight vector and array manifold vector and are given by

$$\mathbf{w}_e(kr) \triangleq \frac{1}{M} [w_1(kr), \dots, w_m(kr), \dots, w_M(kr)]^T, \quad (6.100)$$

$$\mathbf{p}_e(kr, \theta) \triangleq [p_1(kr, \theta), \dots, p_m(kr, \theta), \dots, p_M(kr, \theta)]^T. \quad (6.101)$$

Note the $1/M$ term in Eq. (6.100), which is different from the definition of other vectors.

Recall that the sensitivity decreases as the white noise array gain increases. The design of an element-space beamformer with the maximum WNG can be formulated as

$$\begin{aligned} &\min_{\mathbf{w}_e(kr)} \mathbf{w}_e^H(kr) \mathbf{w}_e(kr), \\ &\text{subject to } \mathbf{w}_e^H(kr) \mathbf{p}_e(kr, \theta_0) = 1. \end{aligned} \quad (6.102)$$

The solution to the optimization problem is

$$\mathbf{w}_{e, \text{MWNG}}(kr) = \frac{\mathbf{p}_e(kr, \theta_0)}{\mathbf{p}_e^H(kr, \theta_0) \mathbf{p}_e(kr, \theta_0)} = \frac{\mathbf{p}_e(kr, \theta_0)}{\|\mathbf{p}_e(kr, \theta_0)\|^2}. \quad (6.103)$$

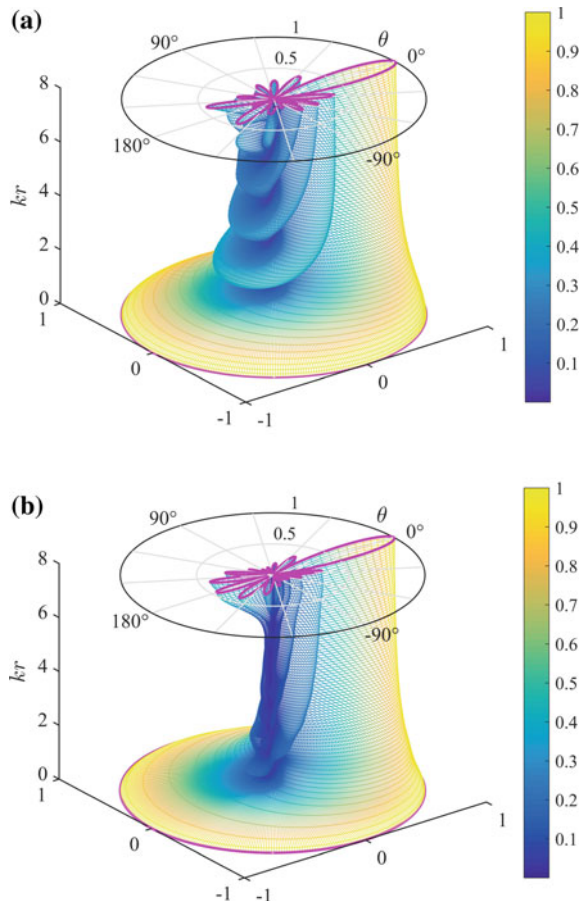
where the subscript “MWNG” denotes the maximum WNG. This beamformer is referred to as an MWNG beamformer.

For the case of unbaffled circular array where $|p_m(kr, \theta)| = 1$ and $\|\mathbf{p}_e(kr, \theta_0)\|^2 = M$, the weight vector reduces to

$$\mathbf{w}_{e, \text{MWNG}} = \mathbf{p}_e(kr, \theta_0) / M, \quad (6.104)$$

which corresponds to a conventional DAS beamformer.

Fig. 6.13 MWNG beam patterns of 16-element UCA.
a Unbaffled, **b** baffled



The MWNG beam patterns for an unbaffled UCA and a baffled UCA with 16 sensors are shown in Fig. 6.13a and b, respectively.

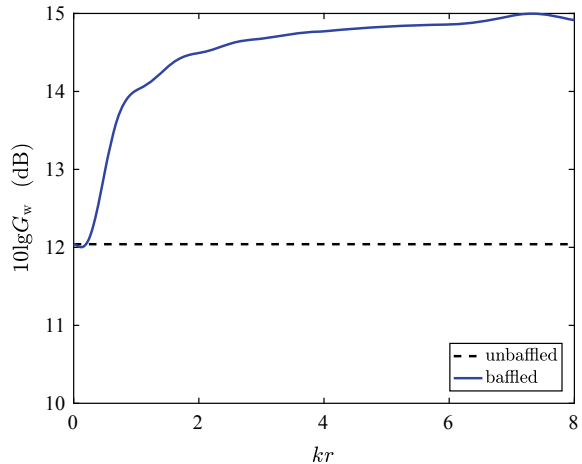
Compared with the beam patterns of the circular aperture shown in Fig. 6.6, it is seen that when $kr \leq 7$, the difference between the beam patterns of the unbaffled UCA and that of the unbaffled circular aperture is very small, and when $kr > 7$, the sidelobe height of the UCA increases.

Compared with the unbaffled UCA, the beamwidth of the baffled UCA is narrower and the sidelobes are lower.

The resulting WNGs of both UCAs are shown in Fig. 6.14.

The maximum WNG of the unbaffled UCA is a constant value of $10 \lg M = 12.04$ dB over the frequency band of interest. For the baffled UCA, the WNG is equal to that of the unbaffled UCA when $kr = 0$ and increases roughly as the frequency increases, up to about 3 dB higher than that of the unbaffled UCA. Therefore, the baffled circular array has higher robustness than the unbaffled circular array.

Fig. 6.14 WNG of MWNG beamformers for 16-element UCAs



6.3.2 Circular-Harmonics-Domain (CHD) Beamformer

By replacing the integral in the circular harmonics transform for circular aperture shown in Eq. (6.38) with the summation, the circular harmonics transform for uniform circular array becomes

$$\widehat{P}_n(kr, \theta) = \frac{1}{M} \sum_{m=1}^M p_m(kr, \theta) e^{-in\vartheta_m},$$

$$n = 0, 1, 2, \dots, N, \quad N < M/2, \quad (6.105)$$

where \widehat{P}_n is the estimate of the CHD data P_n .

Equation (6.105) is referred to as the discrete circular harmonics transform. Due to the limited number of circular harmonics that can be obtained, by replacing the symbol “ ∞ ” by “ N ”, the corresponding discrete inverse circular harmonics transform is given by

$$p_m(kr, \theta) \approx \hat{p}_m(kr, \theta) = \sum_{n=-N}^N \widehat{P}_n(kr, \theta) e^{in\vartheta_m}. \quad (6.106)$$

Let $\widehat{W}_n(kr)$ be the discrete circular harmonics transform of $w_m(kr)$ in Eq. (6.99), we have the discrete circular harmonics transform pair

$$\widehat{W}_n(kr) = \frac{1}{M} \sum_{m=1}^M w_m(kr) e^{-in\vartheta_m}, \quad (6.107)$$

$$w_m(kr) \approx \hat{w}_m(kr) = \sum_{n=-N}^N \hat{W}_n(kr) e^{in\vartheta_m}. \quad (6.108)$$

Substituting Eqs. (6.106) and (6.108) into Eq. (6.99) gives the beam pattern

$$B(kr, \theta) \approx \frac{1}{M} \sum_{m=1}^M \left(\sum_{n=-N}^N \hat{P}_n(kr, \theta) e^{in\vartheta_m} \right) \left(\sum_{n=-N}^N \hat{W}_n^*(kr) e^{-in\vartheta_m} \right). \quad (6.109)$$

Using the orthogonality

$$\frac{1}{M} \sum_{m=1}^M e^{in\vartheta_m} e^{-i\tilde{n}\vartheta_m} = \delta_{n\tilde{n}}, \quad (6.110)$$

Equation (6.109) becomes

$$B(kr, \theta) \approx \sum_{n=-N}^N \hat{P}_n(kr, \theta) \hat{W}_n^*(kr) \triangleq \hat{B}_h(kr, \theta), \quad (6.111)$$

where $\hat{B}_h(kr, \theta)$ is the CHD beam pattern and the subscript “h” denotes the circular harmonics domain.

Now define the vectors

$$\hat{\mathbf{w}}_h(kr) \triangleq \left[\hat{W}_{-N}(kr), \dots, \hat{W}_0(kr), \dots, \hat{W}_N(kr) \right]^T, \quad (6.112)$$

$$\hat{\mathbf{p}}_h(kr, \theta) \triangleq \left[\hat{P}_{-N}(kr, \theta), \dots, \hat{P}_0(kr, \theta), \dots, \hat{P}_N(kr, \theta) \right]^T, \quad (6.113)$$

then Eq. (6.111) can be written as

$$\hat{B}_h(kr, \theta) = \hat{\mathbf{w}}_h^H(kr) \hat{\mathbf{p}}_h(kr, \theta). \quad (6.114)$$

It is worthwhile noting that, $w_m(kr)$ and $\hat{W}_n(kr)$ in Eqs. (6.107) and (6.108) are a discrete circular harmonics transform pair. However, due to the factor $1/M$ in Eq. (6.100) which defines $\mathbf{w}_e(kr)$, $M\mathbf{w}_e(kr)$ and $\hat{\mathbf{w}}_h(kr)$ are a discrete circular harmonics transform pair.

We next define

$$\mathbf{E}_n \triangleq \frac{1}{M} [e^{in\vartheta_1}, \dots, e^{in\vartheta_m}, \dots, e^{in\vartheta_M}]^T, \quad (6.115)$$

then Eq. (6.105) can be written as

$$\hat{P}_n(kr, \theta) = \mathbf{E}_n^H \mathbf{p}_e(kr, \theta). \quad (6.116)$$

Thus, an $M \times (2N + 1)$ circular harmonics transform matrix can be defined as

$$\mathbf{T} \triangleq [\mathbf{E}_{-N}, \dots, \mathbf{E}_0, \dots, \mathbf{E}_N], \quad (6.117)$$

then, from Eq. (6.116)

$$\hat{\mathbf{p}}_h(kr, \theta) = \mathbf{T}^H \mathbf{p}_e(kr, \theta). \quad (6.118)$$

It is worth noting that, the circular harmonics transform matrix \mathbf{T} is independent of kr .

Similarly, the inverse circular Fourier transform matrix, denoted by $\check{\mathbf{T}}$, can be defined as

$$\check{\mathbf{T}} \triangleq \begin{bmatrix} e^{-i(-N)\vartheta_1} & \dots & e^{-i(-N)\vartheta_m} & \dots & e^{-i(-N)\vartheta_M} \\ \vdots & \ddots & \vdots & \dots & \vdots \\ e^{-in\vartheta_1} & \dots & e^{-in\vartheta_m} & \dots & e^{-in\vartheta_M} \\ \vdots & \dots & \vdots & \ddots & \vdots \\ e^{-iN\vartheta_1} & \dots & e^{-iN\vartheta_m} & \dots & e^{-iN\vartheta_M} \end{bmatrix} = M\mathbf{T}^H. \quad (6.119)$$

Then,

$$\check{\mathbf{T}}^H \mathbf{T}^H = \frac{2N+1}{M} \mathbf{I}_M \approx \mathbf{I}_M, \quad (6.120)$$

where \mathbf{I}_M is an M -by- M identity matrix. When $M = 2N + 1$, we have

$$\check{\mathbf{T}}^H \mathbf{T}^H = \mathbf{I}_M. \quad (6.121)$$

From Eqs. (6.118) and (6.120),

$$\mathbf{p}_e(kr, \theta) \approx \check{\mathbf{T}}^H \hat{\mathbf{p}}_h(kr, \theta). \quad (6.122)$$

Substituting Eq. (6.118) into Eq. (6.114) gives

$$\hat{B}_h(kr, \theta) = \hat{\mathbf{w}}_h^H(kr) \mathbf{T}^H \mathbf{p}_e(kr, \theta). \quad (6.123)$$

For notational simplicity, in what follows we no longer distinguish between the circular harmonics transform and the discrete circular harmonics transform. Thus, by removing the hat, Eq. (6.114) can be written as

$$B_h(kr, \theta) = \mathbf{w}_h^H(kr) \mathbf{p}_h(kr, \theta). \quad (6.124)$$

It is seen from Eqs. (6.99) and (6.124) that the element-space beamformer output $B(kr, \theta)$ is equivalent to the CHD beamformer output $B_h(kr, \theta)$, i.e.,

$$B_h(kr, \theta) = \mathbf{w}_h^H(kr) \mathbf{p}_h(kr, \theta) \approx \mathbf{w}_e^H(kr) \mathbf{p}_e(kr, \theta) = B(kr, \theta), \quad (6.125)$$

with equality if the order N approaches infinite. Moreover, the term $\mathbf{p}_h(kr, \theta)$ in Eq. (6.125) can be viewed as the CHD array manifold vector.

6.3.3 Performance Measures in Circular Harmonics Domain

1. Data Covariance Matrix

Consider an M -element uniform circular array. A plane-wave signal and D plane-wave interferers arrive from directions θ_s and $\theta_d, d = 1, \dots, D$, respectively. Assume that the desired signal, interferers, and noise are uncorrelated with each other. Using the frequency-domain snapshot model, the sound pressure spectrum at the m th sensor can be written as

$$\begin{aligned} x_m(kr) \triangleq x(kr, \vartheta_m) &= \beta p(kr, \vartheta_m, \theta_s) S_s(\omega) \\ &+ \sum_{d=1}^D p(kr, \vartheta_m, \theta_d) S_d(\omega) + N(kr, \vartheta_m), \end{aligned} \quad (6.126)$$

where $S_s(\omega)$, $\{S_d(\omega)\}_{d=1}^D$, and $N(kr, \vartheta_m)$ are the spectra of the desired signal, the interferers and the noise, respectively. β is a binary parameter indicating whether the desired signal is present or not.

The element-space array data can be written in vector notation as

$$\mathbf{x}_e(kr) \triangleq [x_1(kr), \dots, x_m(kr), \dots, x_M(kr)]^T. \quad (6.127)$$

Using the circular harmonics transform, Eq. (6.126) can be expressed in the circular harmonics domain as

$$X_n(kr) = \beta P_n(kr, \theta_s) S_s(\omega) + \sum_{d=1}^D P_n(kr, \theta_d) S_d(\omega) + N_n(kr), \quad (6.128)$$

where $N_n(kr)$ is the CHD representation of the noise.

Then, the CHD array data vector can be defined as

$$\mathbf{x}_h(kr) \triangleq [X_{-N}(kr), \dots, X_0(kr), \dots, X_N(kr)]^T, \quad (6.129)$$

and the corresponding data covariance matrix is given by

$$\begin{aligned}
\mathbf{R}_h(kr) &= E[\mathbf{x}_h(kr)\mathbf{x}_h^H(kr)] \\
&= \beta^2 \sigma_s^2 \mathbf{p}_h(kr, \theta_s) \mathbf{p}_h^H(kr, \theta_s) \\
&\quad + \sum_{d=1}^D \sigma_d^2 \mathbf{p}_h(kr, \theta_d) \mathbf{p}_h^H(kr, \theta_d) + \mathbf{Q}_{hn}(kr),
\end{aligned} \tag{6.130}$$

where $E[\cdot]$ denotes the statistical expectation of the quantity in the brackets, σ_s^2 and $\{\sigma_d^2\}_{d=1}^D$ are respectively the variances (powers) of the desired signal and the interferers, $\mathbf{Q}_{hn} = \sigma_n^2 \rho_{hn}(kr)$ is the CHD noise covariance matrix with σ_n^2 being the power of the noise and $\rho_{hn}(kr)$ being the normalized CHD noise covariance matrix.

Performing the weighted summation to the CHD data gives the CHD beamformer output

$$y(kr) = \mathbf{w}_h^H(kr) \mathbf{x}_h(kr) = \sum_{n=-N}^N W_n^*(kr) X_n(kr). \tag{6.131}$$

The beamformer output power can then be written as

$$\begin{aligned}
P_h(kr) &= E[y(kr)y^*(kr)] \\
&= \mathbf{w}_h^H(kr) E[\mathbf{x}_h(kr)\mathbf{x}_h^H(kr)] \mathbf{w}_h(kr) \\
&= \mathbf{w}_h^H(kr) \mathbf{R}_h(kr) \mathbf{w}_h(kr).
\end{aligned} \tag{6.132}$$

In practical applications, the CHD data \mathbf{x}_h can be estimated using discrete circular harmonics transform as

$$\hat{\mathbf{x}}_h(kr) = \mathbf{T}^H \mathbf{x}_e(kr), \tag{6.133}$$

where $\hat{\mathbf{x}}_h(kr) \triangleq \left[\hat{X}_{-N}(kr), \dots, \hat{X}_0(kr), \dots, \hat{X}_N(kr) \right]^T$ is the estimate of \mathbf{x}_h .

Similar to the element-space processing, the theoretical CHD covariance matrix \mathbf{R}_h in Eq. (6.130) is unavailable. Therefore, the CHD covariance matrix is always estimated using a segment of the sampled data as

$$\begin{aligned}
\hat{\mathbf{R}}_h(kr) &= \frac{1}{\mathcal{L}} \sum_{\ell=1}^{\mathcal{L}} \hat{\mathbf{x}}_h(kr, \ell) \hat{\mathbf{x}}_h^H(kr, \ell) \\
&= \mathbf{T}^H \left[\frac{1}{\mathcal{L}} \sum_{\ell=1}^{\mathcal{L}} \mathbf{x}_e(kr, \ell) \mathbf{x}_e^H(kr, \ell) \right] \mathbf{T},
\end{aligned} \tag{6.134}$$

where \mathcal{L} is the number of training snapshots (also termed the training sample size), and $\hat{\mathbf{x}}_h(kr, \ell)$ and $\mathbf{x}_e(kr, \ell)$ are the ℓ th snapshot of $\hat{\mathbf{x}}_h(kr)$ and $\mathbf{x}_e(kr)$, respectively.

2. Noise Covariance Matrix

We derive the CHD noise covariance matrix. Three types of noise field are mainly considered: spherically isotropic noise field, planarly isotropic noise field and spatially white noise field.

First, the spherically isotropic noise field can be viewed as that there are an infinite number of uncorrelated plane waves arriving at the circular array from all directions with uniform power density. Thus, by integrating the CHD covariance matrix over a sphere, the normalized CHD spherically isotropic noise covariance matrix, denoted by $\rho_{\text{hspf}}(kr)$, can be given by

$$\rho_{\text{hspf}}(kr) = \frac{1}{4\pi} \int_0^\pi \int_0^{2\pi} \mathbf{p}_h(kr, \Omega) \mathbf{p}_h^H(kr, \Omega) d\theta \sin \phi d\phi. \quad (6.135)$$

Substituting Eqs. (6.42) and (6.113) into Eq. (6.135), and using the orthonormal property shown in Eq. (6.63), the CHD covariance matrix $\rho_{\text{hspf}}(kr)$ in Eq. (6.135) is a $(2N + 1) \times (2N + 1)$ diagonal matrix that takes the form of

$$\rho_{\text{hspf}}(kr) = \text{diag}(Q_{-N}, \dots, Q_0, \dots, Q_N), \quad (6.136)$$

where $\text{diag}(\cdot)$ denotes a square matrix with the elements of its arguments on the diagonal.

The term Q_n in Eq. (6.136) can be calculated as follows. As we know from Chap. 1 that, in spherically isotropic noise field, the correlation coefficient between two elements with distance of d is

$$\rho(kd) = \sin(kd)/kd = \text{sinc}(kd). \quad (6.137)$$

The distance between the m th and the \tilde{m} th sensors of the UCA is given by

$$d_{m,\tilde{m}} = 2r \sin\left(\pi|m - \tilde{m}|/M\right) = 2r \sin(\pi\Delta m/M) \triangleq d_{\Delta m}, \quad (6.138)$$

where $\Delta m = |m - \tilde{m}|$ with range $0 \leq \Delta m \leq M - 1$. Due to the circular symmetry, we have $d_{M-\Delta m} = d_{\Delta m}$.

Let $\rho_{\text{esph}}(kr)$ be the normalized element-space spherically isotropic noise covariance matrix, whose (m, \tilde{m}) -th element is given by

$$[\rho_{\text{esph}}(kr)]_{m,\tilde{m}} = \rho_{m,\tilde{m}} = \text{sinc}(kd_{\Delta m}) \triangleq \rho_{\Delta m}. \quad (6.139)$$

Thus, $\rho_{\text{esph}}(kr)$ can be given by

$$\rho_{\text{esph}}(kr) = \begin{bmatrix} \rho_0 & \rho_1 & \cdots & \rho_{M-1} \\ \rho_1 & \rho_0 & \cdots & \rho_{M-2} \\ \vdots & \vdots & \ddots & \vdots \\ \rho_{M-1} & \rho_{M-2} & \cdots & \rho_0 \end{bmatrix}, \quad (6.140)$$

with $\rho_{M-\Delta m} = \rho_{\Delta m}$ due to the circular symmetry.

Using Eq. (6.134), the CHD spherically isotropic noise covariance matrix ρ_{hsp} can be calculated as

$$\rho_{\text{hsp}}(kr) \approx \mathbf{T}^H \rho_{\text{esph}}(kr) \mathbf{T}. \quad (6.141)$$

Using the circulant property of ρ_{esph} , the diagonal elements of $\rho_{\text{hsp}}(kr)$ are given by

$$\begin{aligned} Q_n &= \frac{1}{M^2} \sum_{m=1}^M \sum_{\bar{m}=1}^M \rho_{m\bar{m}} e^{jn(\vartheta_{\bar{m}} - \vartheta_m)} \\ &= \frac{1}{M} \sum_{\Delta m=0}^{M-1} \rho_{\Delta m} e^{jn2\pi\Delta m/M}, \quad n = -N, \dots, 0, \dots, N, \end{aligned} \quad (6.142)$$

which is substituted into Eq. (6.136) to obtain ρ_{hsp} .

Next, the planarly isotropic noise with a unit power spectral density can be viewed as the situation where there are an infinite number of uncorrelated plane waves coming from all directions on the median plane with uniform power density. Thus, by integrating the CHD covariance matrix over all directions on the median plane, the normalized CHD planarly isotropic noise covariance matrix, denoted by ρ_{hpla} , can be given by

$$\rho_{\text{hpla}}(kr) = \frac{1}{2\pi} \int_0^{2\pi} \mathbf{p}_h(kr, \theta) \mathbf{p}_h^H(kr, \theta) d\theta. \quad (6.143)$$

Using Eq. (6.55), and employing the orthogonal property in Eq. (6.63), Eq. (6.143) can be written as

$$\rho_{\text{hpla}}(kr) = \text{diag}\{|C_{-N}(kr)|^2, \dots, |C_0(kr)|^2, \dots, |C_N(kr)|^2\}. \quad (6.144)$$

Clearly, it has a very concise form.

Let $\rho_{\text{epla}}(kr)$ be the normalized element-space planarly isotropic noise covariance matrix. Similar to Eq. (6.141), we have

$$\rho_{\text{hpla}}(kr) \approx \mathbf{T}^H \rho_{\text{epla}}(kr) \mathbf{T}. \quad (6.145)$$

From Eq. (6.120)

$$\boldsymbol{\rho}_{\text{epla}}(kr) \approx \check{\mathbf{T}}^H \boldsymbol{\rho}_{\text{hpla}}(kr) \check{\mathbf{T}}. \quad (6.146)$$

The higher is the order N of the applied circular harmonics, the higher is the calculation accuracy of $\boldsymbol{\rho}_{\text{epla}}$.

Finally, in order to ensure the integrity of the content, the CHD spatially white noise covariance matrix with unit power spectral density derived later in Eq. (6.160) is listed here. The normalized CHD white noise covariance matrix, denoted by $\boldsymbol{\rho}_{\text{hw}}(kr)$, is given by

$$\boldsymbol{\rho}_{\text{hw}}(kr) = \frac{\mathbf{I}_{2N+1}}{M}, \quad (6.147)$$

where \mathbf{I}_{2N+1} is a $(2N + 1)$ -by- $(2N + 1)$ identity matrix. Note that $\boldsymbol{\rho}_{\text{hw}}(kr)$ is not a unit matrix as in element-space spatially white noise field, but has a factor $1/M$.

3. Array Gain

Similar to the element-space processing, the array gain of the CHD beamformer is defined as the ratio of the SINR of the array output to that of a single input sensor

$$G(kr) = \frac{\sigma_s^2 |\mathbf{w}_h^H(kr) \mathbf{p}_h(kr, \theta_s)|^2}{\mathbf{w}_h^H(kr) \mathbf{R}_{h,i+n}(kr) \mathbf{w}_h(kr)} \Big/ \frac{\sigma_s^2}{\sum_{d=1}^D \sigma_d^2 + \sigma_n^2}, \quad (6.148)$$

where $\mathbf{R}_{h,i+n}(kr)$ is the CHD interference-plus-noise covariance matrix.

Let $\boldsymbol{\rho}_h(kr)$ be the normalized CHD interference-plus-noise covariance matrix, i.e.,

$$\boldsymbol{\rho}_h(kr) = \mathbf{R}_{h,i+n}(kr) / \left(\sum_{d=1}^D \sigma_d^2 + \sigma_n^2 \right), \quad (6.149)$$

which will be reduced to $\boldsymbol{\rho}_{\text{hspa}}(kr)$ as shown in Eq. (6.136) in spherically isotropic noise field, and to $\boldsymbol{\rho}_{\text{hpla}}(kr)$ as shown in Eq. (6.144) in planarly isotropic noise field, and to $\boldsymbol{\rho}_{\text{hw}}(kr)$ as shown in Eq. (6.147) in spatially white noise field.

Thus, Eq. (6.148) can be written as

$$G(kr) = \frac{|\mathbf{w}_h^H(kr) \mathbf{p}_h(kr, \theta_s)|^2}{\mathbf{w}_h^H(kr) \boldsymbol{\rho}_h(kr) \mathbf{w}_h(kr)}. \quad (6.150)$$

From Eq. (6.125), the element-space distortionless response constraint is equivalent to the following CHD distortionless response constraint

$$\mathbf{w}_h^H(kr) \mathbf{p}_h(kr, \theta_s) = 1. \quad (6.151)$$

Thus, Eq. (6.150) can be written as

$$G(kr) = \frac{1}{\mathbf{w}_h^H(kr) \boldsymbol{\rho}_h(kr) \mathbf{w}_h(kr)}. \quad (6.152)$$

4. White Noise Gain

It is known that the WNG of the element-space beamformer is

$$G_w(kr) = \frac{1}{\mathbf{w}_e^H(kr) \mathbf{w}_e(kr)}. \quad (6.153)$$

Applying the Parseval's relation to the discrete circular harmonics transform in Eq. (6.107), we have

$$\frac{1}{M} \sum_{m=1}^M |w_m(kr)|^2 \approx \sum_{n=-N}^N |W_n(kr)|^2, \quad (6.154)$$

where $w_m(kr)$ and $W_n(kr)$ are a discrete circular harmonics transform pair.

Replacing $\widehat{W}_n(kr)$ in Eq. (6.112) with $W_n(kr)$, i.e.,

$$\mathbf{w}_h(kr) \triangleq [W_{-N}(kr), \dots, W_0(kr), \dots, W_N(kr)]^T, \quad (6.155)$$

and using Eq. (6.100), Eq. (6.154) can be written in vector notation as

$$\mathbf{w}_e^H(kr) \mathbf{w}_e(kr) \approx \frac{1}{M} \mathbf{w}_h^H(kr) \mathbf{w}_h(kr), \quad (6.156)$$

or

$$\|\mathbf{w}_e(kr)\|^2 \approx \|\mathbf{w}_h(kr)\|^2 / M. \quad (6.157)$$

Substituting Eq. (6.156) into Eq. (6.153), the WNG of the beamformer is given by

$$G_w(kr) = \frac{M}{\mathbf{w}_h^H(kr) \mathbf{w}_h(kr)}. \quad (6.158)$$

On the other hand, using the CHD white noise covariance matrix $\boldsymbol{\rho}_{hw}(kr)$ instead of $\boldsymbol{\rho}_h(kr)$ in (6.152), the WNG is given by

$$G_w(kr) = \frac{1}{\mathbf{w}_h^H(kr) \boldsymbol{\rho}_{hw}(kr) \mathbf{w}_h(kr)}. \quad (6.159)$$

Using Eqs. (6.158) and (6.159), the CHD white noise covariance matrix $\boldsymbol{\rho}_{hw}$ is given by

$$\boldsymbol{\rho}_{\text{hw}}(kr) = \frac{\mathbf{I}_{2N+1}}{M}, \quad (6.160)$$

where \mathbf{I}_{2N+1} is a $(2N + 1)$ -by- $(2N + 1)$ identity matrix.

5. Directivity Index

It is known that the directivity of a beamformer is equivalent to the array gain against spherically isotropic noise. Thus, using $\boldsymbol{\rho}_{\text{hsp}}^{\text{h}}$ instead of $\boldsymbol{\rho}_{\text{h}}(kr)$ in Eq. (6.152), the directivity of the beamformer can be given by

$$G_{\text{D}}(kr) = \frac{1}{\mathbf{w}_{\text{h}}^{\text{H}}(kr) \boldsymbol{\rho}_{\text{hsp}}^{\text{h}}(kr) \mathbf{w}_{\text{h}}(kr)}. \quad (6.161)$$

The directivity is frequently expressed in dB and is referred to as the directivity index,

$$DI(kr) = 10 \lg G_{\text{D}}(kr). \quad (6.162)$$

6.4 Design of CHD Beamformers

In this section, the design methods of the CHD beamformer are derived and their performances are analyzed. The argument dependence will be suppressed in the notation for convenience when the variable is clear.

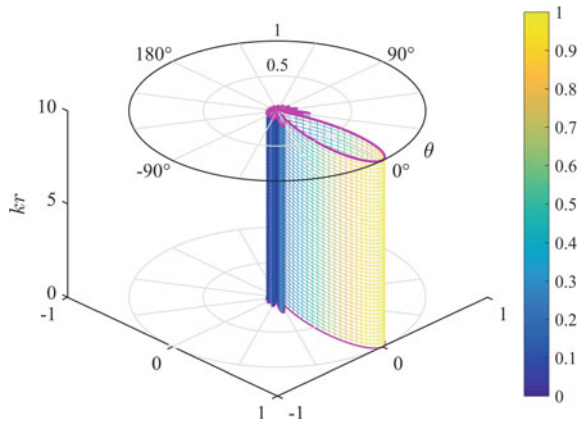
6.4.1 Phase-Mode Beamformer

Assume that the highest order of the circular harmonics that can be obtained and used is N . Using the symbol “ N ” instead of “ ∞ ” in Eq. (6.72), and normalizing the response at the steering direction to unity, the phase-mode beam pattern of the UCA is given by

$$\begin{aligned} B_{\text{PM},N}(kr, \theta) &= \frac{1}{2N+1} \sum_{n=-N}^N e^{-in(\theta-\theta_0)} \\ &= \begin{cases} \frac{\sin[(2N+1)(\theta-\theta_0)/2]}{(2N+1)\sin[(\theta-\theta_0)/2]}, & \theta \neq \theta_0 \\ 1, & \theta = \theta_0 \end{cases}. \end{aligned} \quad (6.163)$$

It is seen that the numerator and denominator of the beam pattern shown in Eq. (6.163) are both sin functions, which is analogous to the beam pattern of a uniformly weighted ULA.

Fig. 6.15 Phase-mode beam patterns $|B_{PM,7}(kr, \theta)|$ for $N = 7$ over $kr \in [0.1, 10]$



It is seen from Eqs. (6.72) and (6.163) that, the beam pattern is independent of kr and is identical over the frequencies, i.e., frequency-invariant. Moreover, since the phase-mode beam pattern is independent of C_n , the baffled and the unbaffled circular arrays have the same phase-mode beam patterns.

Comparing the phase-mode beam pattern of the circular aperture in Eq. (6.72) and that of the uniform circular array in Eq. (6.163), and referring to the weight vector for the circular aperture shown in Eq. (6.70), the phase-mode weight vector for the uniform circular array is given by

$$W_{n,PM}(kr) = \frac{1}{2N+1} \frac{e^{-in\theta_0}}{C_n^*(kr)}. \quad (6.164)$$

Using Eq. (6.163) and choosing $\theta_0 = 0^\circ$, the cylindrical plot of the magnitude of the beam pattern, i.e., $|B_{PM,N}(kr, \theta)|$, versus θ over the range $kr \in [0.1, 10]$ for $N = 7$ is shown in Fig. 6.15. It is seen that the phase-mode beamformer has a property of frequency-invariant beam pattern.

The polar plots of $|B_{PM,N}(kr, \theta)|$ versus θ for various values of N are shown in Fig. 6.16.

It is seen that, when $N = 0$, the beam pattern is a unit circle, i.e., there is no directivity. As N increases, the mainlobe beamwidth gradually decreases and the beam pattern approaches the ideal pencil beam. To obtain a sharp pencil beam, the required highest order N should be very large.

The robustness of the phase-mode beamformer of circular array is investigated below by its WNG.

Assuming that $kr \in [1, 7]$, the weights of the phase-mode beamformer are calculated using Eq. (6.164). Then its WNG is calculated using Eq. (6.158).

For the unbaffled circular array case, the resulting WNG versus kr for various values of N are shown in Fig. 6.17a. The maximum WNG $G_{w,max}$ calculated using Eq. (6.176) is also shown in this figure.

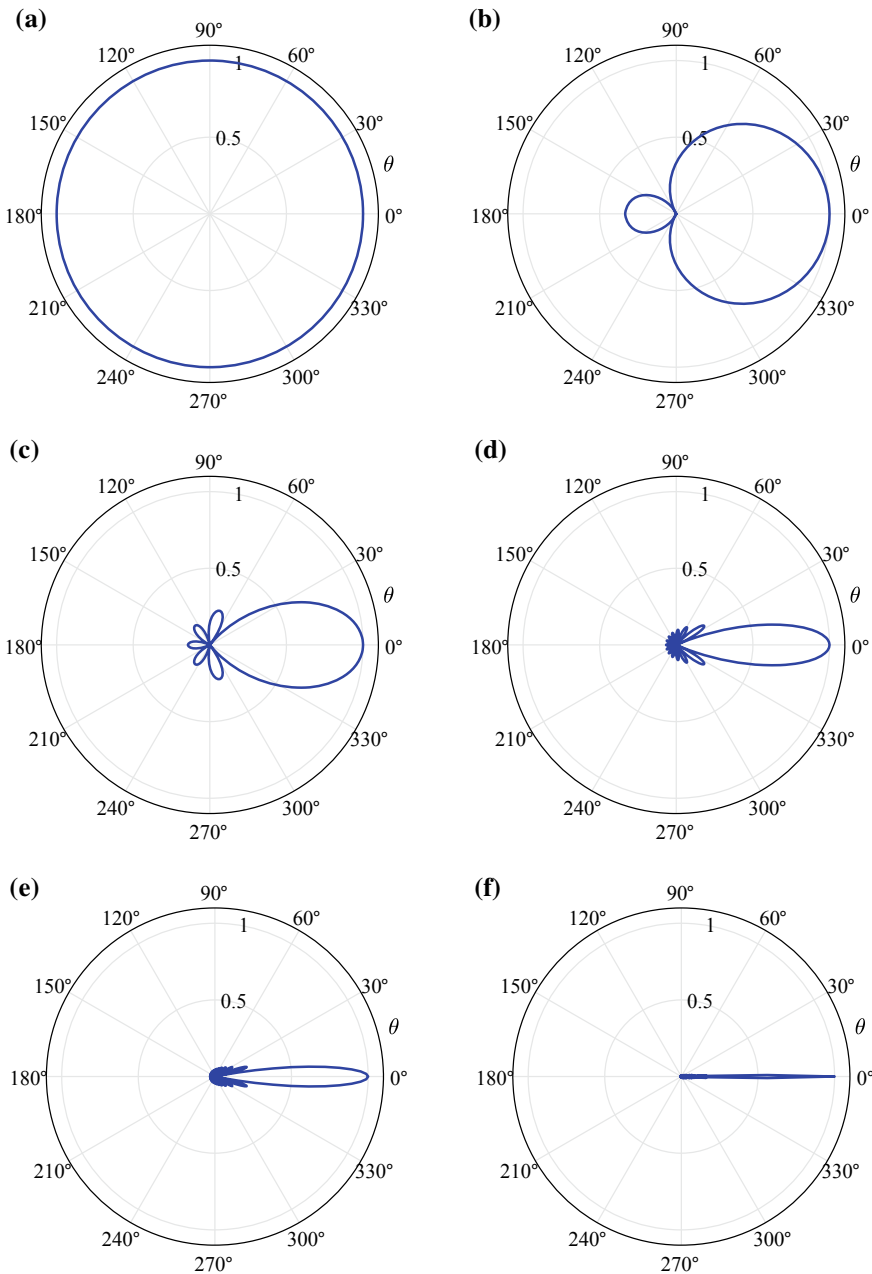
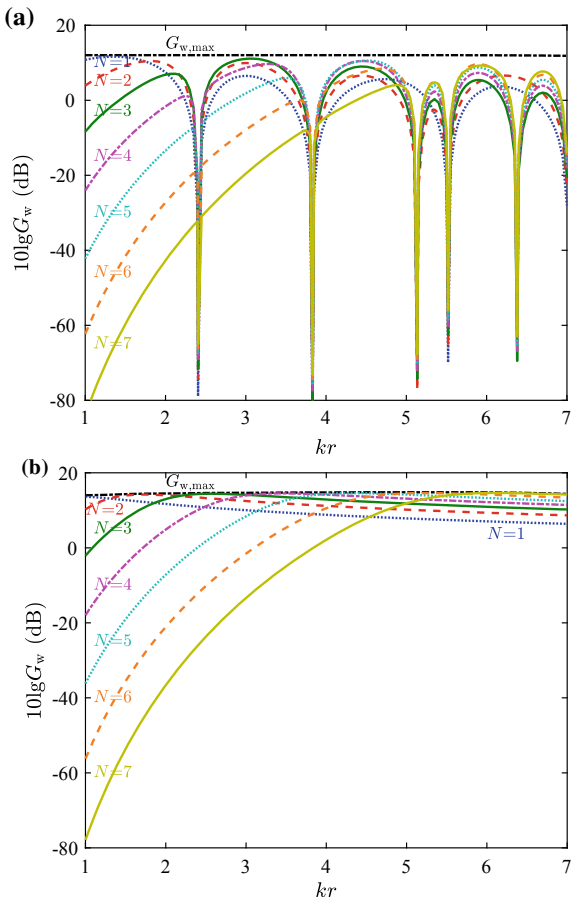


Fig. 6.16 Magnitude of phase-mode beam pattern $|B_{PM,N}(kr, \theta)|$. **a** $N = 0$, **b** $N = 1$, **c** $N = 3$, **d** $N = 7$, **e** $N = 15$, **f** $N = 100$

Fig. 6.17 WNG of phase-mode beamformer versus kr for various values of N for **a** unbaffled and **b** baffled UCA



It is seen that, the WNGs of the CHD beamformer have nulls near several values of kr due to the zeros of $C_{n,\text{unbaff}}(kr)$. In addition, the WNG is small at low frequencies. In general, the higher is the order N , the lower is the WNG.

For the baffled circular array case, the corresponding WNGs are shown in Fig. 6.17b. The WNGs no longer have nulls. The values of the WNG approach those of the unbaffled circular array at low frequencies.

This implies that the phase-mode beamformer has poor robustness at low frequencies regardless of whether there is a baffle. The higher is the order N , the poorer is the robustness. Due to the zeros of $C_{n,\text{unbaff}}(kr)$, the unbaffled circular array is less robust at several frequencies, and this can be avoided by using a baffled circular array.

6.4.2 CHD DAS Beamformer

By replacing “ ∞ ” with “ N ”, the CH-DAS beam pattern shown in Eq. (6.79) becomes

$$B_{\text{DAS},N}(kr, \theta) = \sum_{n=-N}^N |C_n(kr)|^2 e^{-in(\theta-\theta_0)}. \quad (6.165)$$

Note that, as N approaches infinity, the beam pattern in Eq. (6.165) approaches the ideal beam pattern as shown in Eq. (6.74).

The relationship between the CH-DAS beam pattern $B_{\text{DAS},N}(kr, \theta)$ and the used highest order N is investigated below.

Consider the unbaffled circular array. Using Eq. (6.165), the magnitude of the CH-DAS beam patterns, i.e., $|B_{\text{DAS},N}(kr, \theta)|$, versus kr and θ over the range $kr \in [0, 10]$ and $\theta \in [-180^\circ, 180^\circ]$ for various values of N are shown in Fig. 6.18. The case of “ $N = \infty$ ” corresponds to the beam patterns of the unbaffled circular aperture that are calculated using Eq. (6.74), as shown in Fig. 6.18f, which is the pseudocolor plot of Fig. 6.6.

It is seen from Fig. 6.18 that, as the highest order N increases, the beam pattern approaches the beam pattern of the unbaffled circular aperture shown in Fig. 6.18f. For a given order N , a good approximation is obtained for $kr \leq N$. In other words, in order to obtain the beam pattern at kr , the highest order is required to satisfy $N \geq kr$.

6.4.3 CHD MVDR Beamformer

The MVDR beamformer attempts to minimize the output power while maintaining the distortionless response in the steering direction, which will obtain the highest array gain. Applying the MVDR method to the design of CHD beamformer, the CHD MVDR beamformer can be obtained. The optimization problem can be formulated as

$$\begin{aligned} & \min_{\mathbf{w}_h(kr)} \mathbf{w}_h^H(kr) \mathbf{R}_h(kr) \mathbf{w}_h(kr), \\ & \text{subject to } \mathbf{w}_h^H(kr) \mathbf{p}_h(kr, \theta_0) = 1. \end{aligned} \quad (6.166)$$

Using the analogy to the element-space MVDR beamformer, the solution to Eq. (6.166) can be obtained as

$$\mathbf{w}_{h,\text{MVDR}} = \frac{\mathbf{R}_h^{-1} \mathbf{p}_h}{\mathbf{p}_h^H \mathbf{R}_h^{-1} \mathbf{p}_h}, \quad (6.167)$$

where the argument dependence is suppressed for convenience. This beamformer is referred to as the CH-MVDR beamformer.

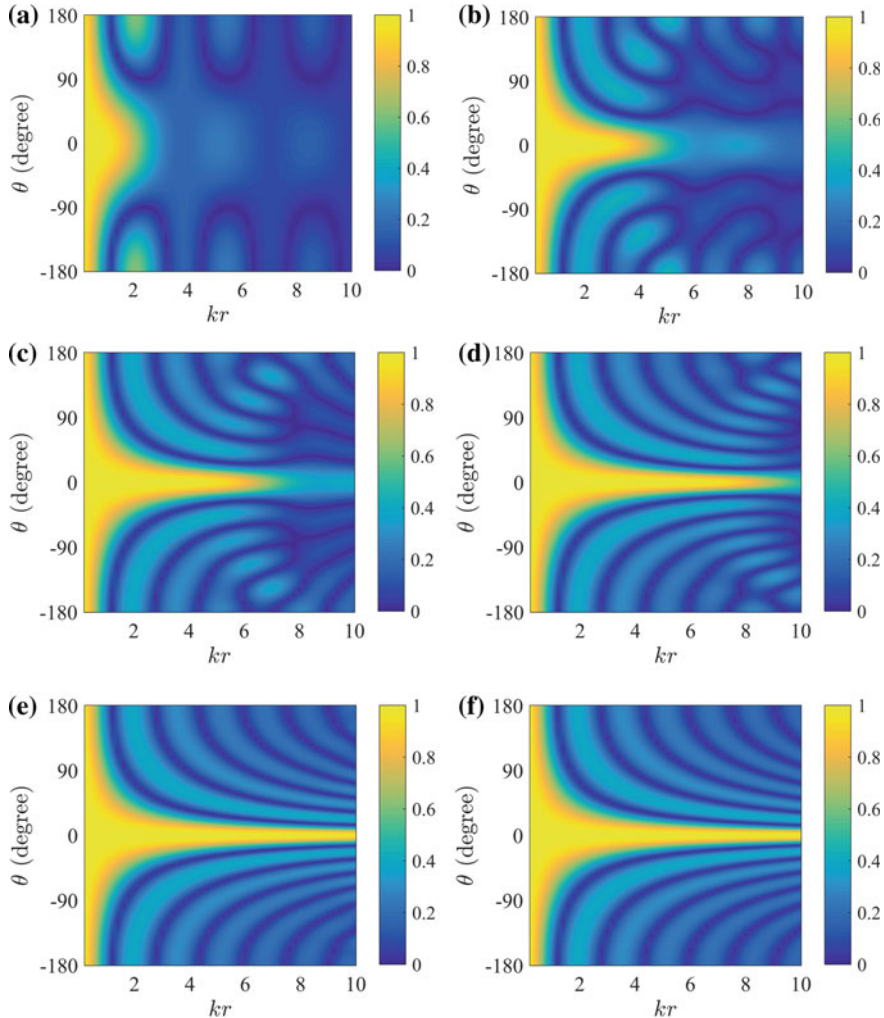


Fig. 6.18 Magnitude of CH-DAS beam patterns of unbaffled UCA $|B_{\text{DAS},N}(kr, \theta)|$. **a** $N = 1$, **b** $N = 3$, **c** $N = 5$, **d** $N = 7$, **e** $N = 10$, **f** $N = \infty$

6.4.4 Maximum-Directivity-Index (MDI) Beamformer

The directivity of a beamformer is equivalent to the array gain against spherically isotropic noise. The beamformer with the maximum directivity can be obtained by replacing \mathbf{R}_h in Eq. (6.167) with the CHD spherically isotropic noise covariance matrix ρ_{hsp} shown in Eq. (6.136). The weight vector is given by

$$\mathbf{w}_{h,MDI} = \frac{\boldsymbol{\rho}_{hsp}^{-1} \mathbf{p}_h}{\mathbf{p}_h^H \boldsymbol{\rho}_{hsp}^{-1} \mathbf{p}_h}. \quad (6.168)$$

This beamformer is referred to as the CHD maximum-directivity-index (MDI) beamformer, or CH-MDI beamformer for short.

Substituting Eq. (6.168) into Eq. (6.161) gives the directivity of the CH-MDI beamformer

$$G_{D,max} = \mathbf{p}_h^H \boldsymbol{\rho}_{hsp}^{-1} \mathbf{p}_h = \sum_{n=-N}^N \frac{|P_n|^2}{Q_n} = \sum_{n=-N}^N \frac{|C_n|^2}{Q_n}. \quad (6.169)$$

Substituting Eqs. (6.116) and (6.142) into Eq. (6.169), and replacing P_n with \hat{P}_n gives

$$G_{D,max} \approx \sum_{n=-N}^N \frac{\left| \frac{1}{M} \sum_{m=1}^M p_m(kr, \theta) e^{-in\vartheta_m} \right|^2}{\frac{1}{M} \sum_{m=0}^{M-1} \rho_m e^{in2\pi m/M}}, \quad (6.170)$$

which is identical to the so-called high-order superdirective of a circular array (see Eq. (24) of Ref. [6]). However, our results in Eq. (6.169) are more straightforward.

6.4.5 MVDR Beamformer in Planarly Isotropic Noise Field

Assuming that the noise field is a planarly isotropic noise field, the CHD MVDR beamformer against planarly isotropic noise can be obtained by replacing \mathbf{R}_h in Eq. (6.167) with the CHD planarly isotropic noise covariance matrix $\boldsymbol{\rho}_{hpla}$ shown in Eq. (6.144). The weight vector is

$$\mathbf{w}_{h,pla} = \frac{\boldsymbol{\rho}_{hpla}^{-1} \mathbf{p}_h}{\mathbf{p}_h^H \boldsymbol{\rho}_{hpla}^{-1} \mathbf{p}_h}, \quad (6.171)$$

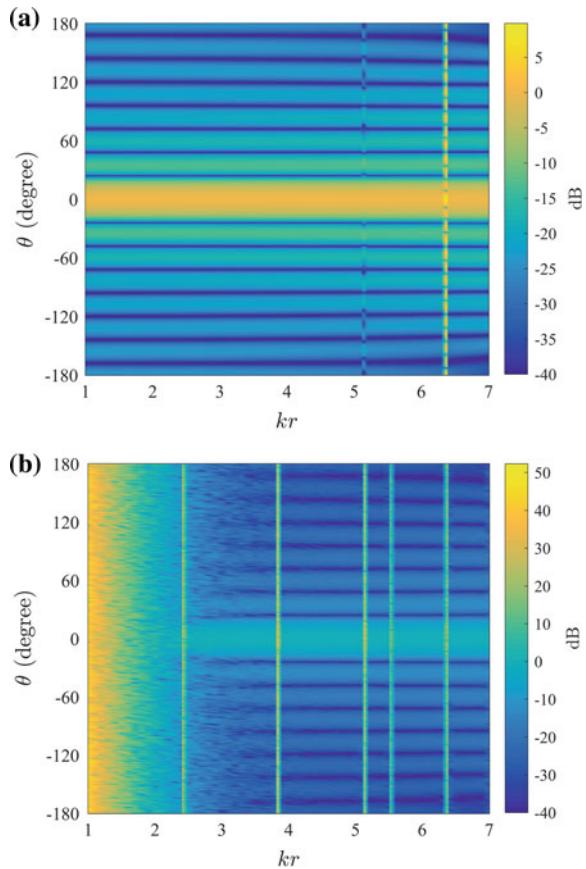
whose n th element is given by

$$W_{n,pla}(kr) = \frac{1}{2N+1} \frac{e^{-in\theta_0}}{C_n^*(kr)}. \quad (6.172)$$

This beamformer is referred to as the CHD maximum planar directivity index (MPDI) beamformer, or CH-MPDI beamformer for short.

Interestingly, the weights shown in Eq. (6.172) are identical to those shown in Eq. (6.164). That is to say, the ideal phase-mode beamformer for circular arrays is equivalent to the CHD MVDR beamformer against planarly isotropic noise.

Fig. 6.19 Beam patterns of CHD MVDR beamformer for 16-element unbaffled UCA in planarly isotropic noise with $N = 7$. **a** In the absence of array manifold mismatch, **b** in the presence of 1% array manifold mismatch



Substituting Eq. (6.172) into Eq. (6.152), the array gain of the CH-MPDI beamformer is given by

$$G_{\text{pla}}(kr) = 2N + 1, \quad (6.173)$$

which is equal to the total number of the used modes.

Considering a 16-element unbaffled uniform circular array in planarly isotropic noise. Assume that $kr \in [1, 7]$, $\theta_0 = 0^\circ$, and up to $N = 7$ order circular harmonics are used. The weight vector of the CH-MPDI beamformer is calculated using Eq. (6.171), which is substituted into Eq. (6.124) to obtain the beam pattern.

The resulting beam responses are shown in Fig. 6.19a. It is seen that the beam patterns are almost identical over the frequency band of interest. In addition, the vertical distortion lines can be clearly seen in the beam patterns near $kr = 5.14$ and 6.38 due to the zeros of $C_{n,\text{unbaff}}(kr)$.

Next, assume that there is a 1% error in array manifold. The beam patterns obtained using the same method are shown in Fig. 6.19b. Besides the more obvious beam pattern distortion around several values of kr , the beam pattern is severely distorted when kr is small (i.e., at low frequencies). This phenomenon can be explained by the WNG of the beamformer shown in Fig. 6.17a. The lower is the WNG, the poorer is the robustness of the beamformer and the severer the distortion of the beam pattern in the presence of array manifold mismatch.

Therefore, in order to improve the robustness at low frequencies, one way is to reduce the value of N . However, it is known from Eq. (6.173) that doing so will also reduce the array gain. The robustness of the beamformer decreases around the frequencies where the WNG exhibits zeros. One way to avoid this problem is to employ a baffled circular array rather than an unbaffled array.

6.4.6 Maximum WNG Beamformer

It is known that, in the white noise environment, the MVDR beamformer reduces to a beamformer with the maximum WNG. Replacing \mathbf{R}_h in Eq. (6.167) with the CHD white noise covariance matrix ρ_{hw} shown in Eq. (6.160), the CHD weight vector becomes

$$\mathbf{w}_{h,MWNG} = \frac{\mathbf{p}_h}{\mathbf{p}_h^H \mathbf{p}_h}, \quad (6.174)$$

whose n th element is

$$W_{n,MWNG} = \frac{C_n e^{-in\theta_0}}{\sum_{n=-N}^N |C_n|^2}. \quad (6.175)$$

This beamformer is referred to as the CHD MWNG beamformer, or CH-MWNG beamformer for short.

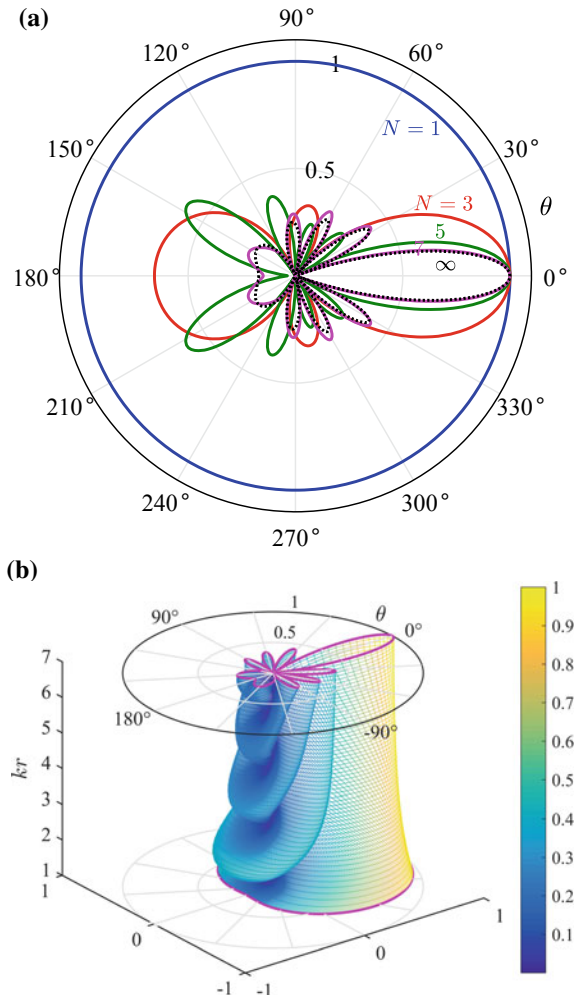
As expected, for the unbaffled circular array, the CH-MWNG beamformer is equivalent to the CH-DAS beamformer. The weights of the CH-MWNG beamformer in Eq. (6.175) are identical to those of the CH-DAS beamformer shown in Eq. (6.78), except for a scalar factor $1/\sum_{n=-N}^N |C_n|^2$ that is chosen to satisfy the distortionless constraint.

It is worth noting that, for a baffled circular array, the CH-DAS beamformer is no longer equivalent to the CH-MWNG beamformer.

Substituting Eq. (6.175) into Eq. (6.158) gives the maximum WNG

$$G_{w,\max} = M \sum_{n=-N}^N |C_n|^2. \quad (6.176)$$

Fig. 6.20 CH-MWNG beam patterns for 16-element unbaffled UCA. **a** $kr = 7$, $N = 1, 3, 5, 7, \infty$. **b** $kr \in [0, 7]$, $N = 7$



For the case of unbaffled circular array, we have $\lim_{N \rightarrow \infty} \sum_{n=-N}^N |C_n|^2 = 1$. Thus

$$G_{w,\max} \approx M, \quad (6.177)$$

which is a well-known result for the element-space DAS beamformer.

For the 16-element UCA, the CH-MWNG beam patterns at $kr = 7$ for various values of N are shown in Fig. 6.20a. It is seen that as N increases, the beam pattern approaches the beam pattern of the unbaffled circular aperture ($N = \infty$), and when $N = kr = 7$, the approximation accuracy is very high.

In the examples considered below, unless noted, we always assume that the 16-element UCA can decompose the sound field into up to $N = 7$ order circular harmonics, and all of them are used to calculate the CHD weight vector.

The CH-MWNG beam patterns for $N = 7$ over the range $kr \in [1, 7]$ are shown in Fig. 6.20b. It is seen that the CHD beam patterns shown in Fig. 6.20b are similar to the element-space MWNG beam patterns shown in Fig. 6.13a over the range $kr \in [0, 7]$. In other words, the CHD beam pattern is equivalent to the element-space beam pattern.

6.4.7 Multiply Constrained CHD Beamformer

The robustness of a CHD beamformer can also be improved by imposing the WNG constraint, or the weight vector norm constraint.

It is seen from Eq. (6.157) that the CHD weight vector norm $\|\mathbf{w}_h\|$ is \sqrt{M} times of the element-space weight vector norm $\|\mathbf{w}_e\|$. Therefore, the CHD weight vector norm constraint can be written as

$$\|\mathbf{w}_h(kr)\| \leq \sqrt{M} \cdot \sqrt{\xi_0} = \sqrt{M\xi_0}, \quad (6.178)$$

where ξ_0 is the specified constraint value. From Eqs. (6.158) and (6.177), we have

$$\min(\|\mathbf{w}_h(kr)\|^2) \approx 1, \quad (6.179)$$

therefore, the specified constraint value is required to satisfy $\xi_0 \geq 1/M$, with equality corresponding to the CH-DAS beamformer.

Similar to the element-space processing, the WNG loss can be defined as

$$G_{wd}(kr) = 10\lg[\|\mathbf{w}_h(kr)\|^2/\min(\|\mathbf{w}_h(kr)\|^2)]. \quad (6.180)$$

Using Eq. (6.178) gives

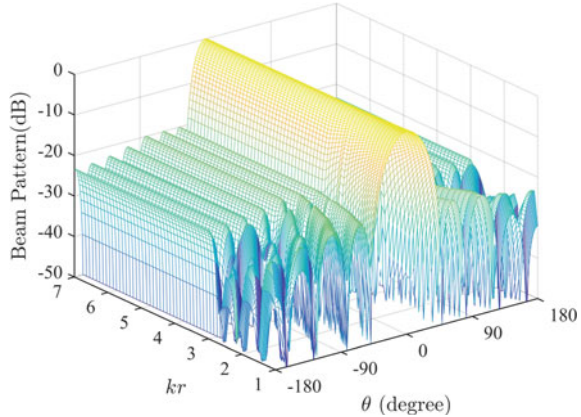
$$G_{wd} \leq 10\lg M + 10\lg(\xi_0) \triangleq G_{wd0}, \quad (6.181)$$

where G_{wd0} is the WNG loss value. Clearly, $G_{wd} \geq 0$, with equality corresponding to the CH-DAS beamformer.

Then, the weight vector norm constraint Eq. (6.178) can be added to Eq. (6.166) to obtain another optimization problem

$$\begin{aligned} & \min_{\mathbf{w}_h(kr)} \mathbf{w}_h^H(kr) \mathbf{R}_h(kr) \mathbf{w}_h(kr), \\ & \text{subject to } \mathbf{w}_h^H(kr) \mathbf{p}_h(kr, \theta_0) = 1, \\ & \quad \|\mathbf{w}_h(kr)\| \leq \sqrt{M\xi_0}. \end{aligned} \quad (6.182)$$

Fig. 6.21 Beam patterns of CHD beamformer with multiple constraints.
 $\zeta_0 = 100, \xi = 0.1$



The optimization problem in Eq. (6.182) is a CHD norm constrained MVDR beamformer design problem. The obtained beamformer is referred to as the CH-NC beamformer.

Sidelobe control is another important issue in array processing. The sidelobes can be controlled by imposing the following multiple constraints to the above optimization problem

$$|\mathbf{w}_h^H(kr) \mathbf{p}_h(kr, \theta_i)| \leq \xi_i, \quad \theta_i \in \Theta_{SL}, \quad i = 1, 2, \dots, N_{SL}, \quad (6.183)$$

where $\xi_i (i = 1, 2, \dots, N_{SL})$ are the specified constraint values on the sidelobes, Θ_{SL} is the sidelobe region, and $\theta_i (i = 1, 2, \dots, N_{SL})$ are a finite number of grid points in the sidelobe region.

The CHD beamformer with multiple constraints is referred to as the CH-MC beamformer [7].

It can be seen from the above derivation that the CHD beamformer design problem is identical in form to the element-space beamformer design problem, thus the element-space beamformer design methods discussed in Chap. 3 can be applied to CHD beamformer design.

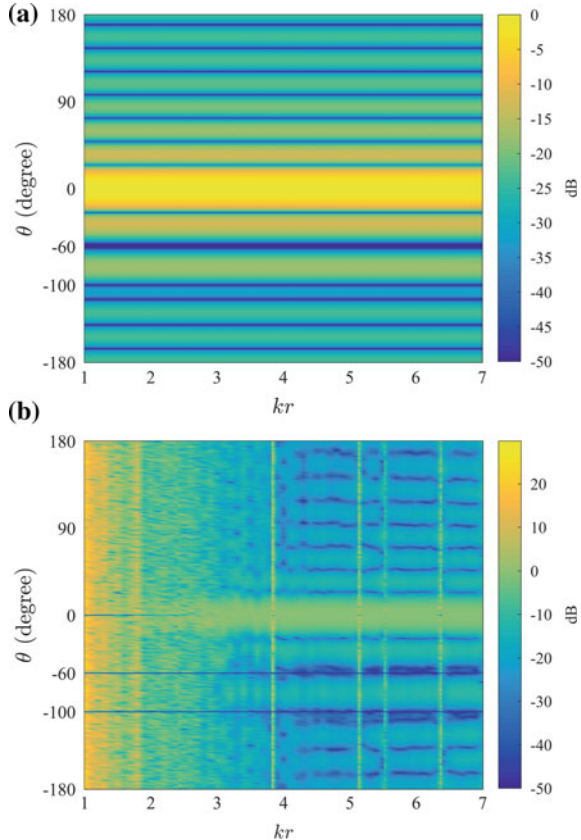
Assume that the constraint on the norm of the weight vector is $\zeta_0 = 100$ and the sidelobe level is chosen as -20 dB, i.e., $\xi_i = 0.1$. The beamwidth BW_{SL} is chosen to have different values across the frequency band of interest $kr \in [1, 7]$. It varies from 90° to 70° in the range $kr \in [1, 3]$ and is a constant value of 70° across $kr \in [3, 7]$.

The resulting beam patterns versus θ over the range $kr \in [1, 7]$ are shown in Fig. 6.21. It is seen that, the sidelobe level is below -20 dB as specified.

Assume that a desired signal and two interferers arrive from 0° , -60° , and -100° with the signal(interference)-to-noise ratio at each sensor of -6 dB, 20 dB and 20 dB, respectively. The CH-MVDR beamformer is designed using Eq. (6.167).

In the absence of array manifold error, the pseudocolor plot of the resulting beam patterns is shown in Fig. 6.22a. It is seen that the beamformer puts perfect nulls adap-

Fig. 6.22 Beam patterns of CH-MVDR beamformer in the **a** absence, and **b** presence of 1% array manifold mismatch



tively in the interferer directions across the frequency band to suppress undesirable interferences, which is similar to the element-space MVDR beamformer.

In the presence of 1% array manifold errors, the resulting beam patterns are shown in Fig. 6.22b. It is seen that the beamformer gives distorted mainlobes and high sidelobes, which means this beamformer is very sensitive to manifold mismatch. At low frequencies, the beamformer even places a null at the mainlobe attempting to null out the mismatched signal. At high frequencies, high sidelobes appear at several frequencies due to the effect of Bessel zeros.

The values of the WNG of the CH-MVDR beamformer from Eq. (6.158) are shown by the dashed line in Fig. 6.23. It is seen that the WNG is low at low frequencies and nulls occur at multiple frequency points at high frequencies. The results are useful to understand the beamformer behavior.

The WNG of the CH-MWNG beamformer shown in Fig. 6.20b is also plotted in Fig. 6.23 with a dotted line. It has the highest WNG and therefore the best robustness.

The CH-NC beamformer shown in Eq. (6.182) is used, in which we choose $\zeta_0 = 0.5$. From Eq. (6.158), this value corresponds to a 3-dB WNG constraint.

Fig. 6.23 WNG of CHD beamformers for 16-element unbaffled UCA

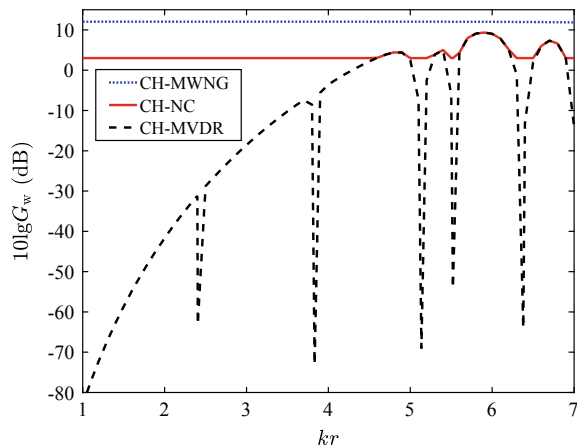
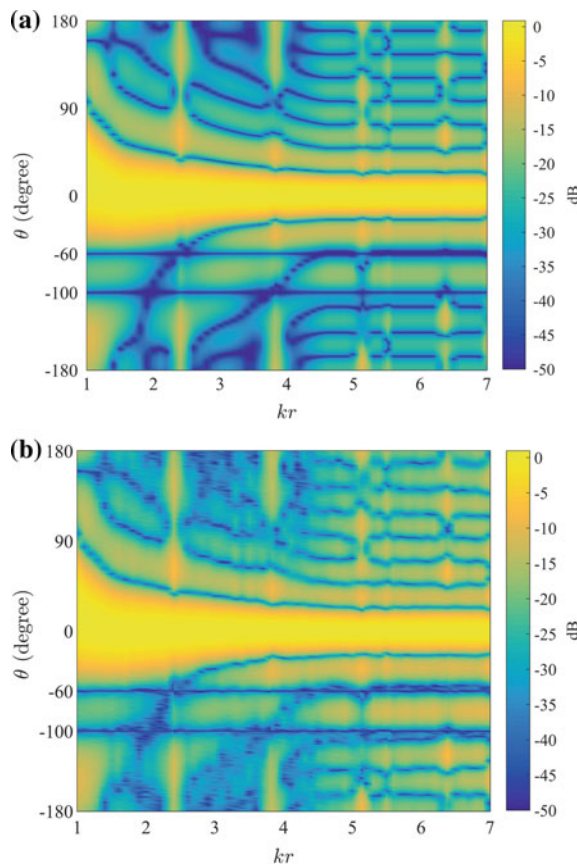


Fig. 6.24 Beam patterns of CH-NC beamformer in the **a** absence, and **b** presence of 1% array manifold mismatch



The WNG of the resulting beamformer is plotted in Fig. 6.23 with a solid line. As expected, the WNG strictly exceeds 3 dB at all frequencies.

The beam patterns in the absence and presence of 1% array manifold errors are shown in Fig. 6.24a and b, respectively.

It is seen that, the beam patterns put perfect nulls adaptively in the interferer directions. And when errors occur in array manifold, the beam patterns are still similar to those in the absence of manifold error, which indicates that the beamformer has good robustness.

The mainlobe beamwidth of this beamformer at low frequencies is wider than that of the CH-MVDR beamformer shown in Fig. 6.22a, but narrower than that of the MWNG beamformer shown in Fig. 6.20b. This indicates that the CH-NC beamformer can provide a trade-off between the CH-MVDR and the CH-MWNG beamformers.

6.5 Frequency-Domain Broadband CHD Beamforming

6.5.1 Implementation of CHD Beamformer

The aforementioned CHD beamformer focuses on the narrowband model and uses the frequency-domain snapshots. The frequency-domain implementation of the broadband CHD beamformer is a straightforward extension of the narrowband results. The basic principle is to decompose the received broadband signals into narrower frequency bins using DFT, and transform the frequency-domain snapshots to the circular harmonics domain using the circular harmonics transform, narrowband CHD beamforming is then performed on discrete frequency bins, and the outputs of different frequency bins are combined to synthesize the output signal.

Assume that the sampled broadband time series received at the m th sensor is

$$x_m(i) = x_m(t)|_{t=iT_s}, \quad (6.184)$$

where T_s is the sampling interval and i is the index of the time series.

Here, $x_m(i)$ is the time-domain representation of the frequency-domain snapshot data $x_m(kr)$ shown in Eq. (6.126).

A broadband uniform circular array using frequency-domain CHD beamforming is shown in Fig. 6.25.

The implementation of the frequency-domain broadband CHD beamformer consists of the following steps.

- Step 1. Sample the data received by each sensor to obtain the time series $x_m(i)$, $m = 1, \dots, M$, as shown in Eq. (6.184).
- Step 2. For each sensor, we buffer L samples and take the DFT of the L samples to obtain the subband frequency-domain samples $x_m(kr)$.
- Step 3. The element-space array sample vectors $x_e(kr)$ corresponding to each frequency bin in the range $k \in [k_l, k_u]$ are obtained, as shown in Eq. (6.127).

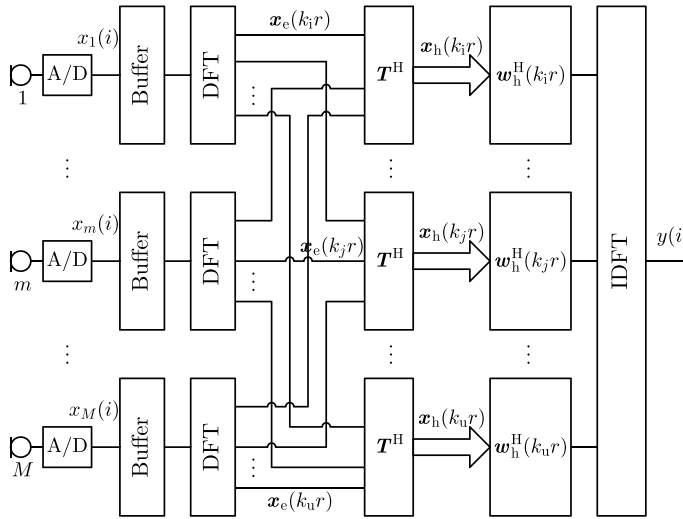


Fig. 6.25 Frequency-domain implementation of broadband CHD beamformer

Here k_l and k_u are the wavenumbers corresponding to the lowest and the highest frequencies, respectively.

- Step 4. Use the circular harmonics transform matrix T shown in Eq. (6.117) to transform the element-space data vector into the circular harmonics domain, as shown in Eq. (6.133).
- Step 5. The methods developed in Sect. 6.4 are used to design the CHD weight vector $w_h(kr)$ for $k \in [k_l, k_u]$.
- Step 6. Weighted combinations of the CHD sample vector at each frequency bin are formed to obtain the subband beamformer output $y(kr)$ for $k \in [k_l, k_u]$, as shown in Eq. (6.131).
- Step 7. The IDFT is performed on the narrowband beamformer outputs in all frequency bins to obtain the output samples $y(i)$.

We now consider several examples to illustrate the frequency-domain broadband CHD beamforming operation.

Consider a UCA with $M = 16$ elements. A far field LFM broadband plane wave impinges on the array from $\theta_s = 0^\circ$. The frequency band of interest is $kr = 2\pi fr/c \in [3.5, 7]$ and the sampling frequency f_s satisfies $k_s r = 2\pi f_s r/c = 30$. The sample length is 512.

The LFM waveform is generated using Eq. (2.49) and is shown in Fig. 6.26a. Here, we use “ i ” as the index of the time series. For the cases of the unbaffled and the baffled UCAs, the signals received by the 16 sensors are shown in Fig. 6.26b and c, respectively.

The frequency-domain implementations of the CH-PM, CH-MVDR, CH-MDI, CH-MWNG, CH-NC, and CH-MC beamformers are referred to as the CH-FPM,

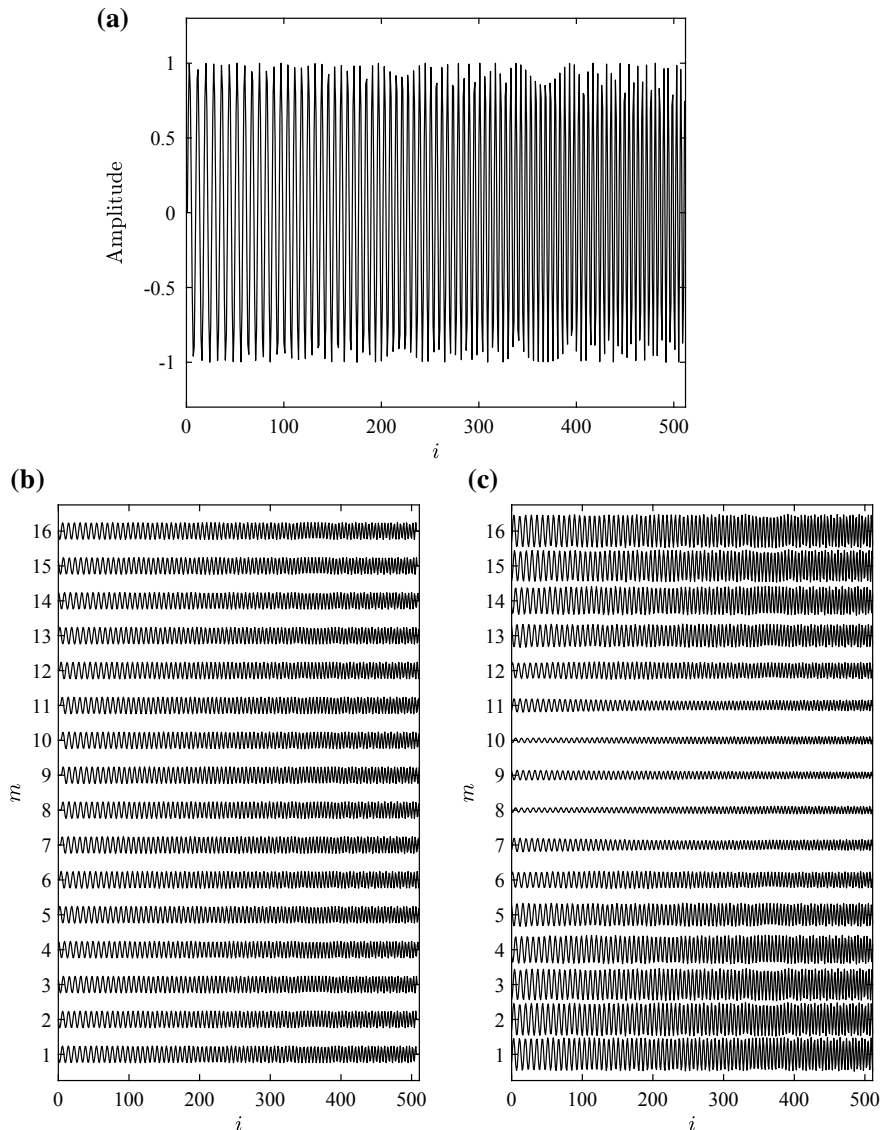


Fig. 6.26 Waveforms **a** of the source signal, **b** received by an unbaffled UCA, and **c** received by a baffled UCA

CH-FMVDR, CH-FMDI, CH-FMWNG, CH-FNC, and CH-FMC beamformers in this book, respectively, and are also referred to as the FPM, FMVDR, FMDI, FMWNG, FNC, and FMC beamformers for short in this chapter.

The behavior of the frequency-domain broadband CHD beamformer for the cases of the unbaffled and the baffled UCAs are illustrated in Sect. 6.5.2 and Sect. 6.5.3, respectively.

6.5.2 Unbaffled Circular Array

Consider the 16-element unbaffled UCA. Assume that the steering direction is $\theta_o = 0^\circ$ and up to $N = 7$ order circular harmonics are used to design the CHD weights.

The output waveforms of the FMWNG, FPM and FNC beamformers are shown in Fig. 6.27a, c and e, respectively.

It is seen that the output waveforms of the three beamformers are similar to the waveform of the sound signal shown in Fig. 6.26a except for both ends. This is because only a limited number of subbands in the frequency band of interest are processed, which is equivalent to using a frequency-domain rectangular window. The effect of the window is to reduce the amplitudes of the waveforms at both ends.

It is also seen that the error between the FPM beamformer output shown in Fig. 6.27c and the source signal is slightly larger when comparing to the other two beamformers.

Assume that the steering direction moves to $\theta_o = 18^\circ$, which implies that the signal arrives inside the main beam but not along the main response axis. The output waveforms of the three frequency-domain CHD beamformers are shown in Fig. 6.27b, d and f, respectively.

For the FMWNG beamformer output shown in Fig. 6.27b, the signal is low-pass filtered because the beamwidth becomes narrower as the frequency increases, which can be seen from Fig. 6.20b.

The amplitudes of the outputs of the FPM and FNC beamformers shown in Fig. 6.27d, f are smaller than that of the FMWNG beamformer. And the amplitude of the FPM beamformer output is independent of frequency across the operating frequency band.

We next evaluate the robustness of the three beamformers in the presence of white noise. Assume that $SNR = 0$ dB and $\theta_o = 0^\circ$.

The output waveforms of the three beamformers are shown in Fig. 6.28a, b and c, respectively.

It is seen that the FPM beamformer output shown in Fig. 6.28b is severely distorted. This indicates that the FPM beamformer is very sensitive to even very small errors generated from the circular harmonics transform. The FMWNG and FNC beamformers, however, maintain good robustness.

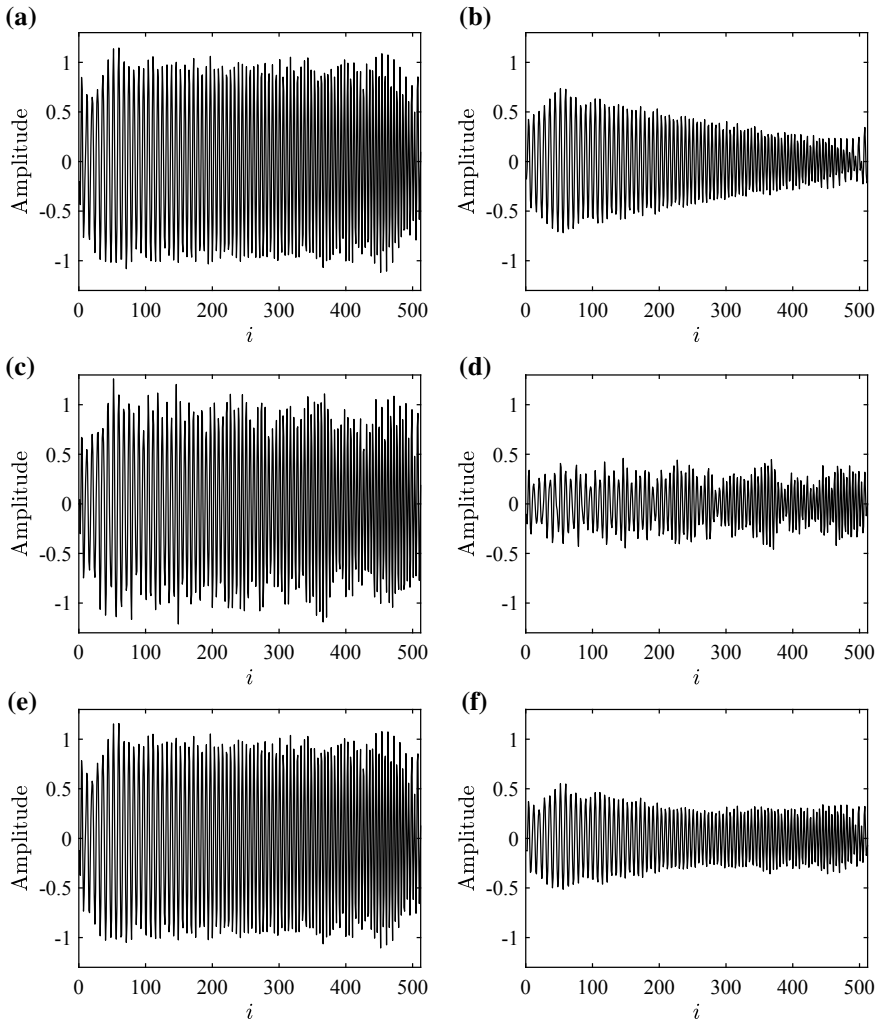


Fig. 6.27 Output waveforms of frequency-domain broadband CHD beamformers for unbaffled UCA. **a** FMWNG, $\theta_0 = 0^\circ$, **b** FMWNG, $\theta_0 = 18^\circ$, **c** FPM, $\theta_0 = 0^\circ$, **d** FPM, $\theta_0 = 18^\circ$, **e** FNC, $\theta_0 = 0^\circ$, **f** FNC, $\theta_0 = 18^\circ$

6.5.3 Baffled Circular Array

Consider the 16-element baffled UCA and repeat the above process.

When $\theta_0 = 0^\circ$ and $\theta_0 = 18^\circ$, the output waveforms of the FMWNG, FPM and FNC beamformers are shown in Fig. 6.29. It is seen that similar results follow for the baffled circular array. In addition, the signal distortion in Fig. 6.29d is smaller than that in Fig. 6.27d.

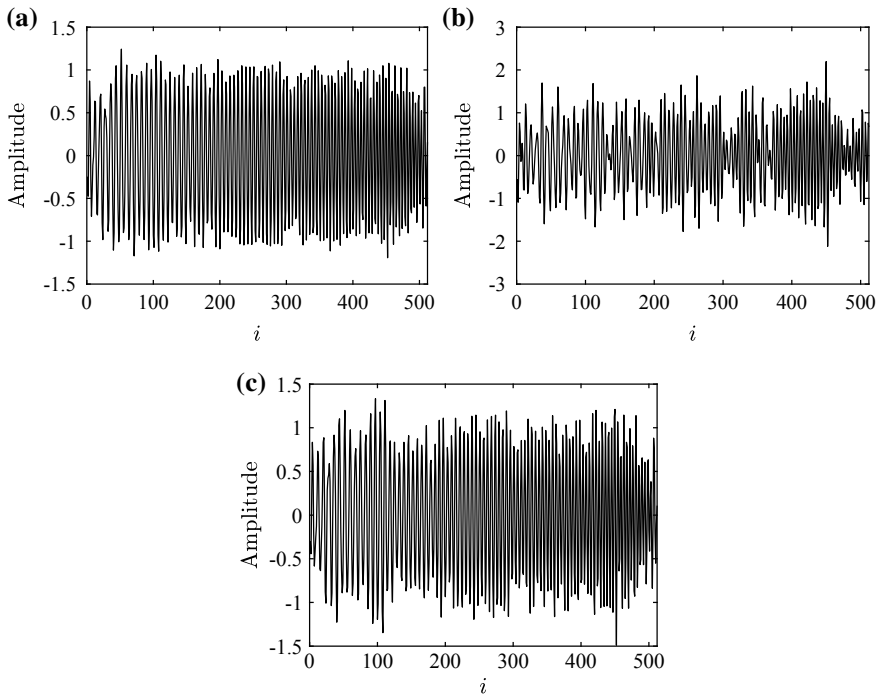


Fig. 6.28 Output waveforms of frequency-domain broadband CHD beamformers for unbaffled UCA for $SNR = 0$ dB and $\theta_o = \theta_s = 0^\circ$. **a** FMWNG, **b** FPM, **c** FNC

The output waveforms of the three beamformers when $SNR = 0$ dB and $\theta_o = 0^\circ$ are shown in Fig. 6.30. The signal distortion in Fig. 6.30b is much smaller than that in Fig. 6.28b and the signal distortion in Fig. 6.30c is even smaller.

The results indicate that the baffled circular array is more robust than the unbaffled circular array. Moreover, the robustness of the beamformer is improved by incorporating additional constraint on the norm of the weight vector in the FNC beamformer.

6.6 Summary

In this chapter, we mainly discussed the beamforming problem for circular arrays, focusing on the problem of modal beamforming. The optimal design and frequency-domain implementation of modal beamformer were presented.

The conventional beam pattern of an acoustic transparent circular aperture is a zero-order Bessel function $J_0(\cdot)$, which plays the same role as the function $\text{sinc}(\cdot)$ did for a linear aperture. This indicates that the conventional sidelobe level of a

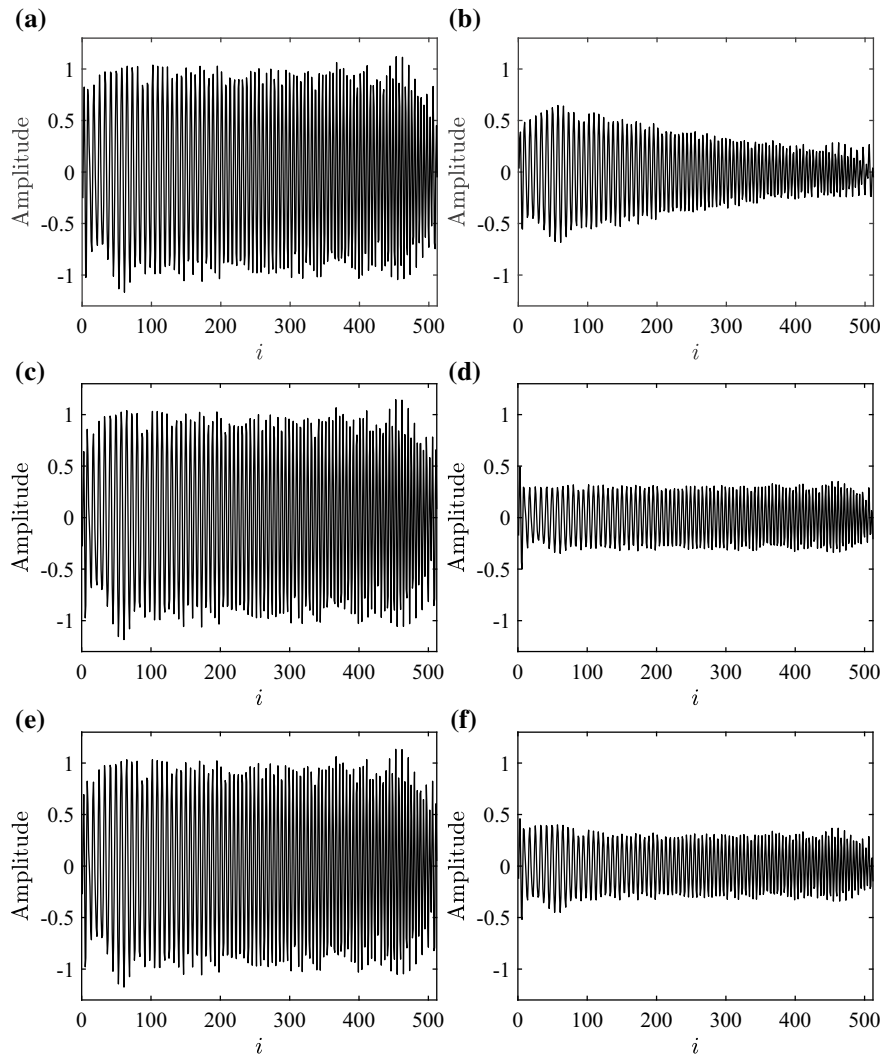


Fig. 6.29 Output waveforms of frequency-domain broadband CHD beamformers for baffled UCA. **a** FMWNG, $\theta_0 = 0^\circ$, **b** FMWNG, $\theta_0 = 18^\circ$, **c** FPM, $\theta_0 = 0^\circ$, **d** FPM, $\theta_0 = 18^\circ$, **e** FNC, $\theta_0 = 0^\circ$, **f** FNC, $\theta_0 = 18^\circ$

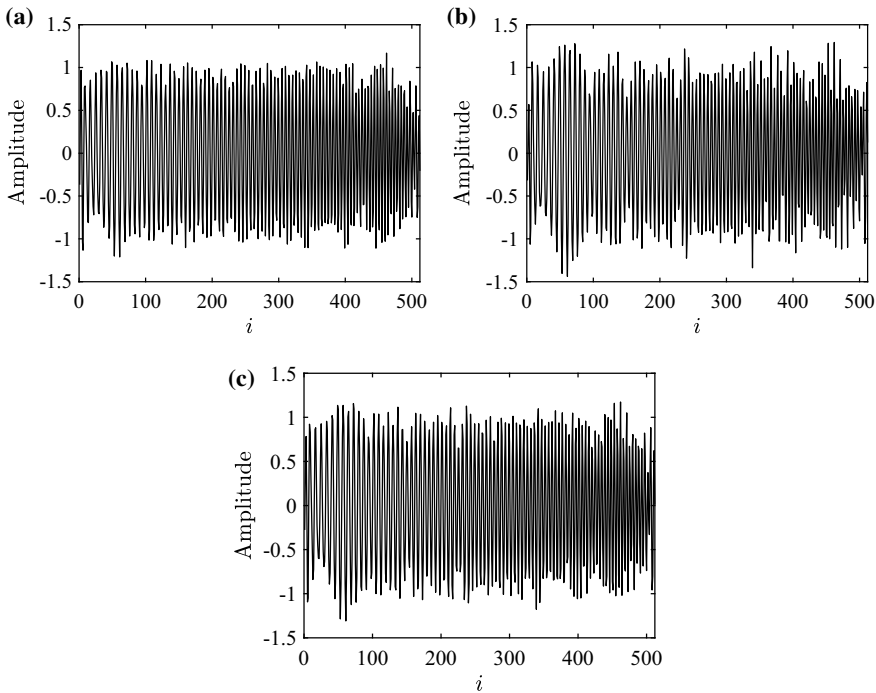


Fig. 6.30 Output waveforms of frequency-domain broadband CHD beamformers for baffled UCA for $SNR = 0$ dB and $\theta_0 = \theta_s = 0^\circ$. **a** FMWNG, **b** FPM, **c** FNC

circular aperture is about -7.90 dB, which is higher than that of the linear aperture of -13.26 dB.

Using the circular harmonics transform pair, the sound pressure received by a circular aperture can be expressed as a Fourier series expansion, in which the Fourier coefficients can be obtained by integrating the sound pressure over the circle. This process can be interpreted as the decomposition and synthesis of the sound field using circular harmonics.

Accordingly, the beamforming operation for the circular apertures can be performed in circular harmonics domain. The CHD beamformer output is equivalent to the element-space beamformer output. The well-known phase-mode beamformer and DAS beamformer for circular apertures can both be represented in the form of CHD beamformer.

In the real-world case, the circular apertures are sampled using UCAs. The beam pattern of a UCA approximates that of the circular aperture with the same radius. In order to ensure that the beam pattern approximation error is small enough, we require that the interelement spacing along the arc be less than half-wavelength.

For an M -element UCA, the highest order of the circular harmonics that can be extracted should satisfy $N \leq M/2$ to avoid modal aliasing. Due to the high-order

truncation approximation, a slight error occurs between the CHD beamformer and the element-space beamformer for UCA.

By deriving the expressions for the CHD beam response, covariance matrix, array gain, WNG, etc. in terms of the CHD weight vector, the techniques for element-space beamformer design can be applied to the CHD beamformer design.

It is found that the phase-mode beamformer for circular arrays can be regarded as an ideal CHD MVDR beamformer against the planarly isotropic noise. This interesting result helps understand the behavior of phase-mode beamformers, analyze its sensitivity to model perturbations, and propose improved methods.

A multiply constrained CHD beamformer is presented, which leads to very flexible designs. It can not only include most of the modal beamformers, such as the phase-mode beamformer and the DAS beamformer, as its special cases, but also can be used to examine the advantages and disadvantages of these beamformers. This is useful for a thorough understanding of the CHD beamformer design.

References

1. J. Benesty, J. Chen, I. Cohen, *Design of Circular Differential Microphone Arrays* (Springer, Switzerland, 2015)
2. E.G. Williams, *Fourier Acoustics: Sound Radiation and Nearfield Acoustical Holography* (Academic Press, New York, 1999)
3. H. Teutsch, *Modal Array Signal Processing: Principles and Applications of Acoustic Wavefield Decomposition* (Springer, Berlin, Germany, 2007)
4. H. Teutsch, W. Kellermann, Acoustic source detection and localization based on wavefield decomposition using circular microphone arrays. *J. Acoust. Soc. Am.* **120**(5), 2724–2736 (2006)
5. C.P. Mathews, M.D. Zoltowski, Eigenstructure techniques for 2-D angle estimation with uniform circular arrays. *IEEE Trans. Signal Process.* **42**(9), 2395–2407 (1994)
6. Y. Ma, Y. Yang, Z. He, K. Yang, C. Sun, Y. Wang, Theoretical and practical solutions for high-order superdirective of circular sensor arrays. *IEEE Trans. Ind. Electron.* **60**(1), 203–209 (2013)
7. S. Yan, Optimal design of modal beamformers for circular arrays. *J. Acoust. Soc. Am.* **138**(4), 2140–2151 (2015)

Chapter 7

Time-Domain Modal Beamforming for Circular Arrays



7.1 Introduction

The uniform circular arrays have been widely used because they are convenient for forming almost uniform beam patterns over 360° azimuthal directions and the signal processing can be greatly simplified due to the symmetry property.

The design and frequency-domain implementation of modal beamformer for circular arrays, namely CHD beamformer, have been studied in Chap. 6, in which a multiply constrained CHD beamformer was presented. This multiply constrained approach can include DAS beamformer and ideal phase-mode circular harmonics beamformer as special cases. The relationship among the array gain, the order of harmonics, and the sensitivity can thus be well understood.

Modal beamformer is a two-stage beamformer, in which a decomposer is used to perform the spatial decomposition of the sound field into circular harmonics and an actual beamformer is used to form the beam by combining the circular harmonics. One advantage of modal beamforming is that the actual beamformer is decoupled from the sensor locations, which allows a very efficient implementation.

The modal beamformer discussed in Chap. 6 mainly uses a frequency-domain snapshot model, and broadband beamforming is implemented in the frequency domain. Consider that the frequency-domain implementation is not suitable in many applications due to its associated time delay resulting from block processing. This chapter focuses on the time-domain implementation of broadband CHD beamforming. This method extends the time-domain element-space beamformer discussed in Chap. 5 to the CHD beamformer. An advantage of the time-domain implementation is that we can update the beamformer when each new snapshot arrives, in contrast to the frequency-domain beamformer, which requires a block of snapshots to perform the DFT. For convenience, we only consider the time-domain modal beamformer design problem with symmetric beam patterns, however, this method can be easily extended to the case of asymmetric beam patterns design.

This beamformer consists of a circular harmonics transforming and steering unit, followed by a pattern generation unit implemented using a set of FIR filters, in which

the beam pattern design is decoupled from beam pattern steering. The problem of FIR filter tap weights design is formulated as a constrained optimization problem that is computationally tractable. The array performance measures such as array gain, sensitivity, sidelobes, and mainlobe variation can be taken into consider, which is very important in practical applications.

The rest of this chapter is organized as follows. In Sect. 7.2, we develop the CHD beamformer with symmetric beam patterns by decoupling the steering and the shaping of the patterns. In Sect. 7.3, we present the time-domain implementation structure for symmetric-pattern beamformer consisting of a time-domain circular harmonics transform and steering unit and a pattern generation unit. The design of FIR filters for pattern generation is presented in Sect. 7.4, in which the beamformer performance measures are expressed in terms of the filter tap weights and then an optimization problem is formulated to obtain the tap weights. Several examples are considered to illustrate the time-domain broadband CHD beamforming behavior in Sect. 7.5. A brief summary of this chapter is given in Sect. 7.6.

7.2 Beamformer with Symmetric Patterns

In the CHD beamformer methods mentioned above, steering was achieved by directly changing the weight vector \mathbf{w}_h . In this section, a method that can decouple the steering and the shaping is introduced.

7.2.1 Design of Weight Vector

Assume that the weights of a CHD beamformer take the form

$$W_{n,\text{sym}}^*(kr) \triangleq d_n(kr)e^{in\theta_0}, \text{ with } d_n(kr) = d_{-n}(kr), \quad (7.1)$$

where $d_n(kr)$ is a specified value and the subscript “sym” denotes symmetry. The reason for this name will be clear after we derive the beamformer.

Clearly, the phase-mode beamformer shown in Eq. (6.71), the CH-DAS beamformer shown in Eq. (6.78), and their equivalent beamformers shown in Eqs. (6.164) and (6.175) can all be written in the form of Eq. (7.1). Thus they all belong to this type of beamformer.

For the phase-mode beamformer shown in Eq. (6.71), we have

$$d_n(kr) = \frac{1}{2\pi C_n(kr)}. \quad (7.2)$$

For the CH-DAS beamformer shown in Eq. (6.78), we have

$$d_n(kr) = C_n^*(kr). \quad (7.3)$$

For the phase-mode beamformer shown in Eq. (6.164) and the CH-MVDR beamformer against planarly isotropic noise shown in Eq. (6.172), we have

$$d_n(kr) = \frac{1}{(2N+1)C_n(kr)}. \quad (7.4)$$

For the CH-MWNG beamformer shown in Eq. (6.175), we have

$$d_n(kr) = \frac{C_n^*(kr)}{\sum_{n=-N}^N |C_n(kr)|^2}. \quad (7.5)$$

Substituting Eqs. (7.1) and (6.55) into Eq. (6.124), the beam pattern can be written as

$$\begin{aligned} B(kr, \theta) &= \sum_{n=-N}^N C_n(kr) e^{-in\theta} W_{n,\text{sym}}^*(kr) \\ &= \sum_{n=-N}^N C_n(kr) d_n(kr) e^{in(\theta_0 - \theta)} \\ &= \sum_{n=0}^N \overline{\overline{d}_n}(kr) \overline{\overline{P}_n}(kr, \psi), \end{aligned} \quad (7.6)$$

where $\psi = \theta - \theta_0$, and

$$\overline{\overline{d}}_n(kr) = \begin{cases} d_0(kr), & n = 0 \\ \sqrt{2}d_n(kr), & n \neq 0 \end{cases}, \quad (7.7)$$

$$\overline{\overline{P}}_n(kr, \psi) = \begin{cases} C_0(kr), & n = 0 \\ \sqrt{2}C_n(kr) \cos n\psi, & n \neq 0 \end{cases}. \quad (7.8)$$

Defining

$$\overline{\overline{\mathbf{d}}} \triangleq \left[\overline{\overline{d}}_0, \dots, \overline{\overline{d}}_n, \dots, \overline{\overline{d}}_N \right]^T, \quad (7.9)$$

and

$$\overline{\overline{\mathbf{p}}} \triangleq \left[\overline{\overline{P}}_0, \dots, \overline{\overline{P}}_n, \dots, \overline{\overline{P}}_N \right]^T, \quad (7.10)$$

Equation (7.6) can be rewritten as

$$B(kr, \theta) = \overline{\overline{\mathbf{d}}}^T(kr) \overline{\overline{\mathbf{p}}}(kr, \psi). \quad (7.11)$$

In Eq. (7.11), $\bar{\bar{\mathbf{d}}}$ can be viewed as the weight vector, and $\bar{\bar{\mathbf{p}}}$ is the corresponding array manifold vector. Note that the weight vector here is not conjugated.

It is seen from Eq. (7.6) that the beam pattern is a function of ψ , and

$$B(kr, \theta_0) = \bar{\bar{\mathbf{d}}}^T(kr) \bar{\bar{\mathbf{p}}}(kr, 0), \quad (7.12)$$

$$B(kr, \theta_0 + \psi) = B(kr, \theta_0 - \psi). \quad (7.13)$$

This indicates that the beam pattern $B(kr, \theta)$ is symmetric with respect to the steering direction θ_0 . The CHD beamformer whose weight vector has the form of Eq. (7.1) is referred to as the CHD symmetric-pattern beamformer in this book.

By changing the value of θ_0 , the beam pattern $B(kr, \theta_0 \pm \psi)$ itself does not change, but is steered such that $\psi = 0$ coincides with $\theta = \theta_0$. In other words, if the value of θ_0 is changed, the steering direction will change to θ_0 , but the shape of the beam pattern is unchanged.

A beam pattern function as a function of ψ can then be defined as

$$\tilde{B}(kr, \psi) = B(kr, \theta)|_{\theta=\theta_0+\psi} = \bar{\bar{\mathbf{d}}}^T(kr) \bar{\bar{\mathbf{p}}}(kr, \psi). \quad (7.14)$$

Obviously, the main response axis of the beam pattern is at $\psi = 0$.

Now define

$$\mathbf{w}_{h,\text{sym}} \triangleq [W_{-N,\text{sym}}, \dots, W_{0,\text{sym}}, \dots, W_{N,\text{sym}}]^T, \quad (7.15)$$

$$\mathbf{\Lambda} \triangleq \begin{bmatrix} 0 & \dots & 0 & 1 & 0 & \dots & 0 \\ \vdots & & 0 & \frac{\sqrt{2}}{2}e^{-i\theta_0} & 0 & \frac{\sqrt{2}}{2}e^{i\theta_0} & 0 \\ 0 & \ddots & 0 & \vdots & 0 & \ddots & 0 \\ \frac{\sqrt{2}}{2}e^{-iN\theta_0} & 0 & 0 & 0 & 0 & 0 & \frac{\sqrt{2}}{2}e^{iN\theta_0} \end{bmatrix}, \quad (7.16)$$

then, Eq. (7.1) can be rewritten in matrix notation as

$$\mathbf{w}_{h,\text{sym}} = \mathbf{\Lambda}^H \bar{\bar{\mathbf{d}}}^*, \quad (7.17)$$

and

$$\mathbf{\Lambda} \mathbf{\Lambda}^H = \mathbf{I}_{N+1}, \quad (7.18)$$

$$\bar{\bar{\mathbf{d}}}^* = \mathbf{\Lambda} \mathbf{w}_{h,\text{sym}}, \quad (7.19)$$

where \mathbf{I}_{N+1} is an $(N+1)$ -by- $(N+1)$ identity matrix.

Using $\mathbf{w}_{h,\text{sym}}$ in Eq. (7.17) instead of \mathbf{w}_h in Eq. (6.132), the beamformer output power is given by

$$\begin{aligned}
P_{\text{out}} &= \mathbf{w}_{\text{h,sym}}^H \mathbf{R}_{\text{h}} \mathbf{w}_{\text{h,sym}} \\
&= \overline{\overline{\mathbf{d}}}^T \mathbf{\Lambda} \mathbf{R}_{\text{h}} \mathbf{\Lambda}^H \overline{\overline{\mathbf{d}}}^* \\
&= \overline{\overline{\mathbf{d}}}^T \overline{\overline{\mathbf{R}}}_{\text{d}} \overline{\overline{\mathbf{d}}}, \tag{7.20}
\end{aligned}$$

where

$$\overline{\overline{\mathbf{R}}}_{\text{d}} = \mathbf{\Lambda} \mathbf{R}_{\text{h}} \mathbf{\Lambda}^H \tag{7.21}$$

is the CHD covariance matrix with respect to the weight vector $\overline{\overline{\mathbf{d}}}$.

In the cases of spherically isotropic noise, the planarily isotropic noise and the spatially white noise, by replacing \mathbf{R}_{h} in Eq. (7.21) with the ρ_{hsp} shown in Eq. (6.136), ρ_{hpla} shown in Eq. (6.144), and ρ_{hw} shown in Eq. (6.160), respectively, the corresponding CHD covariance matrices with respect to $\overline{\overline{\mathbf{d}}}$ become

$$\begin{aligned}
\overline{\overline{\rho}}_{\text{hsp}}(kr) &= \mathbf{\Lambda} \rho_{\text{hsp}}(kr) \mathbf{\Lambda}^H \\
&= \text{diag}(\mathcal{Q}_0, \dots, \mathcal{Q}_N), \tag{7.22}
\end{aligned}$$

$$\begin{aligned}
\overline{\overline{\rho}}_{\text{hpla}}(kr) &= \mathbf{\Lambda} \rho_{\text{hpla}}(kr) \mathbf{\Lambda}^H \\
&= \text{diag}\{|C_0(kr)|^2, \dots, |C_N(kr)|^2\}. \tag{7.23}
\end{aligned}$$

$$\begin{aligned}
\overline{\overline{\rho}}_{\text{hw}}(kr) &= \mathbf{\Lambda} \rho_{\text{hw}}(kr) \mathbf{\Lambda}^H \\
&= \frac{\mathbf{\Lambda} \mathbf{\Lambda}^H}{M} = \frac{\mathbf{I}_{N+1}}{M}. \tag{7.24}
\end{aligned}$$

Thus, similar to Eq. (6.166), the CHD MVDR beamformer in this case can be formulated as

$$\begin{aligned}
&\min_{\overline{\overline{\mathbf{d}}}(kr)} \overline{\overline{\mathbf{d}}}^T(kr) \overline{\overline{\mathbf{R}}}_{\text{d}}(kr) \overline{\overline{\mathbf{d}}}(kr), \\
&\text{subject to } \overline{\overline{\mathbf{d}}}^T(kr) \overline{\overline{\mathbf{p}}}(kr, 0) = 1. \tag{7.25}
\end{aligned}$$

The solution to Eq. (7.25) is given by

$$\overline{\overline{\mathbf{d}}}^*(kr) = \frac{\overline{\overline{\mathbf{R}}}_{\text{d}}^{-1}(kr) \overline{\overline{\mathbf{p}}}(kr, 0)}{\overline{\overline{\mathbf{p}}}^H(kr, 0) \overline{\overline{\mathbf{R}}}_{\text{d}}^{-1}(kr) \overline{\overline{\mathbf{p}}}(kr, 0)}. \tag{7.26}$$

From Eq. (7.26), it is seen that the weight vector $\overline{\overline{\mathbf{d}}}$ is independent of the steering direction θ_o . In other words, the beamformer decouples the shaping and the steering of array patterns, i.e., in Eq. (7.1), the weights are decomposed into two parts, where

$d_n(kr)$ is used to design the shape of the beam pattern and $e^{in\theta_0}$ is used to adjust the steering direction.

For the case of planarly isotropic noise, using $\overline{\rho_{\text{hpla}}}$ in Eq. (7.23) instead of $\overline{\mathbf{R}_d}$ in Eq (7.26), the weight vector is given by

$$\overline{\overline{\mathbf{d}}}_{\text{pla}}^* = \frac{1}{1+2N} \left[\frac{1}{C_0^*}, \frac{\sqrt{2}}{C_1^*}, \frac{\sqrt{2}}{C_2^*}, \dots, \frac{\sqrt{2}}{C_N^*} \right]^T. \quad (7.27)$$

For the case of spatially white noise, using $\overline{\overline{\rho_{\text{hw}}}}$ in Eq. (7.24) instead of $\overline{\mathbf{R}_d}$ in Eq. (7.26), the weight vector becomes

$$\overline{\overline{\mathbf{d}}}_{\text{MWNG}}^* = \frac{1}{|C_0|^2 + 2 \sum_{n=1}^N |C_n|^2} \left[C_0, \sqrt{2}C_1, \sqrt{2}C_2, \dots, \sqrt{2}C_N \right]^T. \quad (7.28)$$

It is straightforward to verify that by replacing $\overline{\overline{\mathbf{d}}}$ in Eq. (7.17) with $\overline{\overline{\mathbf{d}}}_{\text{pla}}^*$ shown in Eq. (7.27) and $\overline{\overline{\mathbf{d}}}_{\text{MWNG}}^*$ shown in Eq. (7.28), respectively, the resulting CHD weight vectors are equal to those in Eqs. (6.171) and (6.174).

Using $\mathbf{w}_{\text{h,sym}}$ in Eq. (7.17) instead of \mathbf{w}_h in Eq. (6.158), the WNG of the symmetric-pattern beamformer is given by

$$G_w(kr) = \frac{M}{\overline{\overline{\mathbf{d}}}^T(kr) \overline{\overline{\mathbf{d}}}(kr)}. \quad (7.29)$$

In order to improve the robustness of the beamformer, the following constraint on the norm of the weight vector can be imposed to Eq. (7.25):

$$\left\| \overline{\overline{\mathbf{d}}}(kr) \right\| \leq \sqrt{M\xi_0}. \quad (7.30)$$

The sidelobes of the symmetric-pattern beamformer can be controlled by adding the constraints to the optimization problem

$$\overline{\overline{\mathbf{d}}}^T(kr) \overline{\overline{\mathbf{p}}}(kr, \psi_i) \leq \xi_i, \quad \psi_i \in \Psi_{\text{SL}}, \quad i = 1, 2, \dots, N_{\text{SL}}, \quad (7.31)$$

where $\xi_i (i = 1, 2, \dots, N_{\text{SL}})$ are the specified constraint values on the sidelobes, Ψ_{SL} is the sidelobe region, and $\psi_i (i = 1, 2, \dots, N_{\text{SL}})$ are the grid points in the sidelobe region. It is worth noting that, due to the symmetry of the beam pattern, the sidelobe region Ψ_{SL} only needs to be selected as one of the two symmetrical sidelobe regions.

In summary, the symmetric-pattern beamformer design problem can be formulated as

$$\min_{\overline{\overline{\mathbf{d}}}(kr)} \overline{\overline{\mathbf{d}}}^T(kr) \overline{\overline{\mathbf{R}_d}}(kr) \overline{\overline{\mathbf{d}}}(kr),$$

$$\begin{aligned}
& \text{subject to } \bar{\bar{\bar{d}}}^T(kr) \bar{\bar{p}}(kr, 0) = 1, \\
& \left\| \bar{\bar{\bar{d}}}(kr) \right\| \leq \sqrt{M\zeta_0} \\
& \bar{\bar{\bar{d}}}^T(kr) \bar{\bar{p}}(kr, \psi_i) \leq \xi, \quad \psi_i \in \Psi_{\text{SL}}, \quad i = 1, 2, \dots, N_{\text{SL}}. \quad (7.32)
\end{aligned}$$

The optimization problem can be solved using the method similar to that of the element-space beamformer introduced in Chap. 3.

7.2.2 Symmetric-Pattern Beamforming

Substituting Eqs. (6.133) and (7.1) into Eq. (6.131), the output of the symmetric-pattern beamformer is given by

$$\begin{aligned}
y(kr) &= \sum_{n=-N}^N W_n^*(kr) \hat{X}_n(kr) \\
&= \sum_{n=-N}^N d_n(kr) e^{in\theta_0} \frac{1}{M} \sum_{m=1}^M x_m(kr) e^{-in\vartheta_m} \\
&= \frac{\bar{\bar{d}}_0(kr)}{M} \sum_{m=1}^M x_m(kr) + \sum_{n=1}^N \frac{\bar{\bar{d}}_n(kr)}{M} \sum_{m=1}^M \left\{ x_m(kr) \sqrt{2} \cos[n(\theta_0 - \vartheta_m)] \right\} \\
&= \sum_{n=0}^N \bar{\bar{d}}_n(kr) X_n(kr, \theta_0), \quad (7.33)
\end{aligned}$$

where

$$X_n(kr, \theta_0) = \begin{cases} \frac{1}{M} \sum_{m=1}^M x_m(kr), & n = 0 \\ \frac{1}{M} \sum_{m=1}^M \left\{ x_m(kr) \sqrt{2} \cos[n(\theta_0 - \vartheta_m)] \right\}, & n \neq 0 \end{cases}. \quad (7.34)$$

The transform in Eq. (7.34) is referred to as the symmetric circular harmonics transform, where the element-space data $x_m(kr)$ are transformed into the CHD data $X_n(kr, \theta_0)$.

From Eq. (7.33), the implementation of the symmetric-pattern beamformer is shown in Fig. 7.1. It consists of two parts: symmetric circular harmonics transform and CHD weighted summation.

Note that the symmetric-pattern beamformer in Eq. (7.33) only requires $N + 1$ weights, in contrast to the CHD beamformer in Eq. (6.131), which requires $2N + 1$

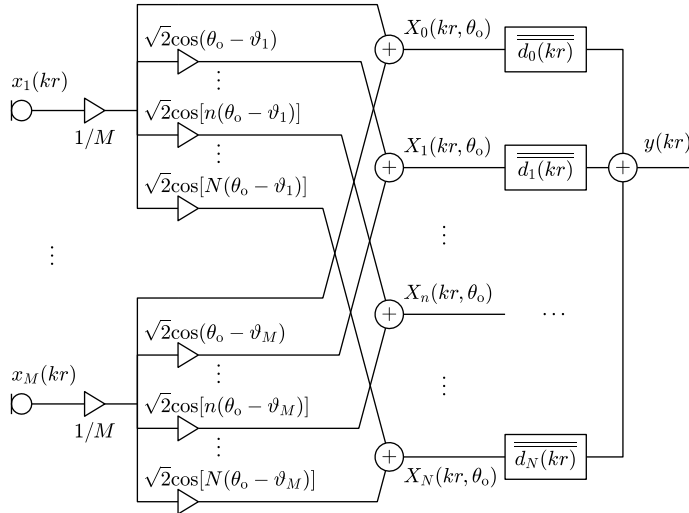


Fig. 7.1 Structure of symmetric-pattern beamforming

weights. However, this method is not suitable in the presence of strong interferers because it is difficult to use adaptive methods to suppress interferers.

7.3 Time-Domain CHD Beamforming Structure

Recall the discussion in Chaps. 4–5 that the broadband beamformers can be implemented in the time-domain using FIR filters [1, 2]. The techniques can be extended to the broadband CHD beamformers. In order to make this chapter more compact, only the time-domain implementation of CHD symmetric-pattern beamformer is considered. In this case, the beam steering can be decoupled from array beam pattern design. For the problem of asymmetric CHD beamformer, the reader is referred to the similar design procedures, which will not be described in detail in this book.

Note that in the discrete circular harmonics transform Eq. (6.105), $e^{-in\vartheta_m}$ is independent of frequency. Thus, the broadband time-domain data can be converted into circular harmonics domain using the same transformation

$$\widehat{X}_n(i) = \frac{1}{M} \sum_{m=1}^M x_m(i) e^{-in\vartheta_m}, \quad (7.35)$$

where $x_m(i)$ is the element-space broadband time-domain data and $\widehat{X}_n(i)$ is the CHD broadband time-domain data. And $\widehat{X}_n(i)$ can be viewed as the time-domain representation of $\widehat{X}_n(kr)$ in Eq. (6.133).

Then, for the symmetric-pattern beamforming problem presented in Sect. 7.2, using the same symmetric circular harmonic form as in Eq. (7.34), the time-domain representation of $X_n(kr, \theta_0)$ is given by

$$X_n(i, \theta_0) = \begin{cases} \frac{1}{M} \sum_{m=1}^M x_m(i), & n = 0 \\ \frac{1}{M} \sum_{m=1}^M x_m(i) \sqrt{2} \cos[n(\theta_0 - \vartheta_m)], & n \neq 0 \end{cases}. \quad (7.36)$$

Clearly, $X_n(i, \theta_0)$ is a real-valued function.

The filter-and-sum structure can be applied to the CHD beamformer. Assume that the impulse response (or tap weights) of the real-valued FIR filter corresponding to the n th-order circular harmonic is $\mathbf{h}_n = [h_{n1}, \dots, h_{nl}, \dots, h_{nL}]^T$, $n = 0, 1, \dots, N$, where L is the length of each filter.

Similar to the element-space FIR broadband beamformer, the frequency responses of each FIR filter \mathbf{h}_n are applied to act as the role of complex weighting \overline{d}_n over the frequency band of interest. These FIR filters are referred to as the pattern generation filters in this book.

The convolution theorem states that point-wise multiplication in the frequency domain equals convolution in the time domain. Therefore, the time-domain representation of the frequency-domain output $y(kr)$ shown in Eq. (7.33) is given by

$$y(i) = \sum_{n=0}^N \sum_{l=1}^L h_{nl} X_n(i - l + 1, \theta_0), \quad (7.37)$$

where $y(i)$ is the beamformer output time series.

We can define an $L \times 1$ column vector $\mathbf{X}_n(i, \theta_0)$ as

$$\mathbf{X}_n(i, \theta_0) \triangleq [X_n(i - L + 1, \theta_0), X_n(i - L + 2, \theta_0), \dots, X_n(i, \theta_0)]^T. \quad (7.38)$$

Then, from Eq. (7.37), we can obtain the time-domain implementation of the broadband CHD beamformer based on FIR filters, as shown in Fig. 7.2.

This beamformer structure consists of two parts: the time-domain circular harmonics transform and steering unit and the pattern generation unit. The function of the former is to implement the real-valued time-domain circular harmonics transform as shown in Eq. (7.36) and the beam steering. The latter consists of a set of real-valued FIR filters, where the time-domain CHD data for each order of the former are filtered and then added to obtain the beamformer output time series, as shown in Eq. (7.37).

The beamformer structure shown in Fig. 7.2 is the time-domain implementation of the symmetric-pattern beamformer shown in Fig. 7.1. Similar to the element-space

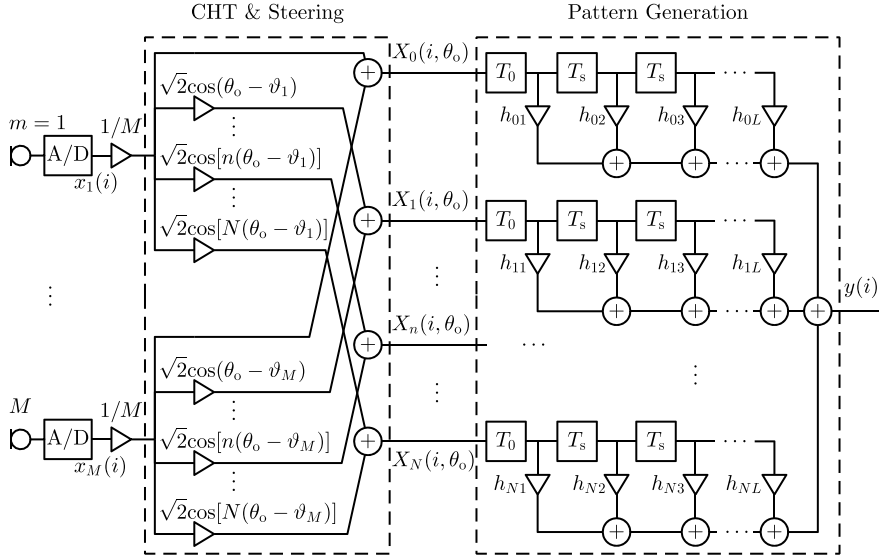


Fig. 7.2 Time-domain implementation of broadband CHD symmetric-pattern beamformer

FIR beamformer, in order to reduce the difficulty of the FIR filter design, pre-delay units can be attached before each FIR filter to compensate the inherent group delay. In Fig. 7.2, the pre-delay of each FIR filter can be chosen as $T_0 = -(L - 1)T_s/2$.

7.4 Design of FIR Filters for Pattern Generation

Then, our goal is to design the tap weights of these pattern generation filters as shown in Fig. 7.2 to achieve the desired beam pattern. The basic idea is as follows. First, derive the expressions of the beam pattern and other performance measures in terms of the filter tap weights \mathbf{h}_n . Then, an optimization problem can be formulated to obtain the tap weights.

We observe that, for the n th-order CHD data $X_n(i, \theta_o)$, the weighting function generated by the pre-delay and the pattern generation filter, which is used to take the place of complex weighting \bar{d}_n , is given by

$$\begin{aligned}\widehat{d}_n(kr) &= e^{-i2\pi f T_0} \mathbf{h}_n^T \mathbf{e}(f) \\ &= \eta \mathbf{h}_n^T \mathbf{e}(f), \quad n = 0, 1, \dots, N,\end{aligned}\quad (7.39)$$

where $\eta = e^{-i2\pi f T_0}$, $\mathbf{e}(f) = [1, e^{-i2\pi f T_s}, \dots, e^{-i(L-1)2\pi f T_s}]^T$.

In order to ensure that the results of the time-domain and frequency-domain beamformers are identical, the time-domain weighting function $\widehat{d}_n(kr)$ should be equivalent to the frequency-domain weighting function $\overline{\overline{d}}_n(kr)$.

Thus, using $\widehat{d}_n(kr)$ in Eq. (7.39) instead of $\overline{\overline{d}}_n(kr)$ in Eq. (7.14) gives the beam pattern

$$\tilde{B}(kr, \psi) = \sum_{n=0}^N \eta \mathbf{h}_n^T \mathbf{e}(f) \overline{\overline{P}}_n(kr, \psi). \quad (7.40)$$

Letting $a_n(kr, \psi) = \eta \overline{\overline{P}}_n(kr, \psi)$, $\mathbf{a} = [a_0, \dots, a_n, \dots, a_N]^T$, and defining an $(N+1)L \times 1$ column vector $\mathbf{h} = [\mathbf{h}_0^T, \mathbf{h}_1^T, \dots, \mathbf{h}_N^T]^T$, Eq. (7.40) can be rewritten as

$$\begin{aligned} \tilde{B}(kr, \psi) &= \sum_{n=0}^N a_n(kr, \psi) \mathbf{h}_n^T \mathbf{e}(f) \\ &= \mathbf{h}^T [\mathbf{a}(kr, \psi) \otimes \mathbf{e}(f)] \\ &= \mathbf{h}^T \mathbf{u}(kr, \psi), \end{aligned} \quad (7.41)$$

where “ \otimes ” denotes the Kronecker product, and $\mathbf{u}(kr, \psi) = \mathbf{a}(kr, \psi) \otimes \mathbf{e}(f)$.

The beam pattern is now expressed in terms of the FIR filter tap weights, where $\psi = 0$ corresponds to the main response axis direction. Thus, the distortionless constraint on the desired signal can be given by

$$\tilde{B}(kr, 0) = \mathbf{h}^T \mathbf{u}(kr, 0) = 1. \quad (7.42)$$

According to Eq. (7.39), define

$$\widehat{\mathbf{d}}(kr) \triangleq [\widehat{d}_0(kr), \dots, \widehat{d}_n(kr), \dots, \widehat{d}_N(kr)]^T, \quad (7.43)$$

then we have

$$\widehat{\mathbf{d}}(kr) = \eta [\mathbf{I}_{N+1} \otimes \mathbf{e}(f)]^T \mathbf{h}. \quad (7.44)$$

The beamformer output power can also be written in terms of the filter tap weights. We now consider the noise-only beamformer output power. The planarily isotropic noise and spatially white noise are considered as special cases. Other cases such as the spherically isotropic noise follow the same procedure.

We first consider the case of planarily isotropic noise. It is seen from Eq. (7.20) that the noise-only beamformer output power for planarily isotropic noise with a unit power spectral density can be given by

$$P_{\text{pla}}(kr) = \mathbf{w}_{\text{h,sym}}^H(kr) \boldsymbol{\rho}_{\text{hpla}}(kr) \mathbf{w}_{\text{h,sym}}(kr)$$

$$\begin{aligned}
&= \hat{\mathbf{d}}^T(kr) \overline{\overline{\rho_{\text{hpla}}}}(kr) \hat{\mathbf{d}}^*(kr) \\
&= \mathbf{h}^T \widetilde{\rho_{\text{hpla}}}(kr) \mathbf{h},
\end{aligned} \tag{7.45}$$

where $\overline{\overline{\rho_{\text{hpla}}}}(kr)$ is the unit power planarly isotropic noise covariance matrix associated with $\hat{\mathbf{d}}^*(kr)$ given by Eq. (7.23), and

$$\widetilde{\rho_{\text{hpla}}}(kr) = [\mathbf{I}_{N+1} \otimes \mathbf{e}(f)] \overline{\overline{\rho_{\text{hpla}}}}(kr) [\mathbf{I}_{N+1} \otimes \mathbf{e}(f)]^H \tag{7.46}$$

is the unit power planarly isotropic noise covariance matrix associated with \mathbf{h} .

Then, the array gain of the time-domain CHD beamformer against planarly isotropic noise can be written as the ratio of the beamformer output power for a unit power signal to that for a unit power noise, i.e.,

$$G_{\text{pla}}(kr) = \frac{|\mathbf{h}^T \mathbf{u}(kr, 0)|^2}{P_{\text{pla}}(kr)} = \frac{1}{\mathbf{h}^T \widetilde{\rho_{\text{hpla}}}(kr) \mathbf{h}}. \tag{7.47}$$

For other noise fields, the array gain can be calculated by replacing $\widetilde{\rho_{\text{hpla}}}(kr)$ in Eq. (7.47) with the corresponding noise covariance matrix.

For the broadband planarly isotropic noise case, by integrating $\widetilde{\rho_{\text{hpla}}}(kr)$ over the frequency band of interest, the broadband noise covariance matrix is given by

$$\overleftrightarrow{\rho_{\text{hpla}}} = \int_{k_l}^{k_u} \widetilde{\rho_{\text{hpla}}}(kr) dk, \tag{7.48}$$

where k_l and k_u are the wavenumbers corresponding to the lowest frequency f_l and the highest frequency f_u , i.e., $k_l = 2\pi f_l/c$ and $k_u = 2\pi f_u/c$. The integration can be approximated by summation in practice.

Then, the broadband planarly isotropic noise-only beamformer output power can be written as

$$\overleftrightarrow{P_{\text{pla}}} = \mathbf{h}^T \overleftrightarrow{\rho_{\text{hpla}}} \mathbf{h}. \tag{7.49}$$

Next, we consider the case of spatially white noise. Proceeding in a manner similar to the planarly isotropic noise, the noise-only beamformer output power for spatially white noise with a unit power spectral density is given by

$$\begin{aligned}
P_w(kr) &= \hat{\mathbf{d}}^T(kr) \overline{\overline{\rho_{\text{hw}}}}(kr) \hat{\mathbf{d}}^*(kr) \\
&= \mathbf{h}^T \widetilde{\rho_{\text{hw}}}(kr) \mathbf{h},
\end{aligned} \tag{7.50}$$

where $\widetilde{\rho_{\text{hw}}}$ can be obtained by replacing $\overline{\overline{\rho_{\text{hpla}}}}$ in Eq. (7.46) with $\overline{\overline{\rho_{\text{hw}}}}$ as

$$\widetilde{\rho_{\text{hw}}}(kr) = [\mathbf{I}_{N+1} \otimes \mathbf{e}(f)] \overline{\overline{\rho_{\text{hw}}}}(kr) [\mathbf{I}_{N+1} \otimes \mathbf{e}(f)]^H$$

$$= \frac{1}{M} [\mathbf{I}_{N+1} \otimes \mathbf{e}(f)] [\mathbf{I}_{N+1} \otimes \mathbf{e}(f)]^H. \quad (7.51)$$

Substituting Eq. (7.51) into (7.50) gives

$$P_w(kr) = \frac{\sum_{n=0}^N |\mathbf{h}_n^T \mathbf{e}(f)|^2}{M}. \quad (7.52)$$

Similar to Eq. (7.47), the array gain of the time-domain CHD beamformer against spatially white noise can be calculated as

$$G_w(kr) = \frac{1}{P_w(kr)} = \frac{M}{\sum_{n=0}^N |\mathbf{h}_n^T \mathbf{e}(f)|^2}. \quad (7.53)$$

This result is identical to the WNG calculated by replacing $\bar{\bar{\mathbf{d}}}(kr)$ in Eq. (7.29) with $\hat{\mathbf{d}}(kr)$ in Eq. (7.43).

Assume that the spatially white noise has a flat spectral density over the entire frequency band $[0, f_s/2]$, where f_s is the sampling frequency. By integrating the beamformer output power $P_w(kr)$ over $[0, f_s/2]$, the broadband beamformer output power is given by

$$\begin{aligned} \overleftrightarrow{P_w} &= \int_0^{f_s/2} P_w(kr) df \\ &= \frac{1}{M} \sum_{n=0}^N \int_0^{f_s/2} |\mathbf{h}_n^T \mathbf{e}(f)|^2 df. \end{aligned} \quad (7.54)$$

Applying Parseval's relation, Eq. (7.54) can be rewritten as

$$\overleftrightarrow{P_w} = \frac{\mathbf{h}^T \mathbf{h}}{M}. \quad (7.55)$$

The broadband white noise gain (BWNG), denoted by $\overleftrightarrow{G_w}$, can then be defined as

$$\overleftrightarrow{G_w} = \frac{M}{\mathbf{h}^T \mathbf{h}}. \quad (7.56)$$

Thus the sensitivity function is the inverse of the broadband white noise gain and is proportional to the norm of the filter tap weights \mathbf{h} . As the norm of the filter tap weights increases, the sensitivity to array perturbations increases.

The optimal design problem for time-domain CHD beamformer can be formulated to achieve various objectives, such as maximum robustness, maximum array gain or

directivity, minimum sidelobe level, minimum MSRV, or optimal trade-off among them.

We discretize the wavenumber band $[k_l, k_u]$ using a finite number of grids $k_j \in [k_l, k_u]$, $j = 1, 2, \dots, N_k$. The distortionless constraint can be imposed to each frequency bin. With the aim of offering maximum robustness, using Eq. (7.56), the time-domain maximum-white-noise-gain CHD beamformer (or CH-TMWNG beamformer for short) can be formulated as

$$\begin{aligned} & \min_{\mathbf{h}} \mathbf{h}^T \mathbf{h}, \\ & \text{subject to } \mathbf{h}^T \mathbf{u}(k_j r, 0) = 1, \\ & \quad k_j \in [k_l, k_u], \quad j = 1, 2, \dots, N_k. \end{aligned} \quad (7.57)$$

Recall the discussion in Sect. 6.4 that the well-known ideal phase-mode beamformer for circular array is equivalent to the CHD MVDR beamformer against planarly isotropic noise. For the broadband case, the optimal design problem for time-domain CHD MVDR beamformer against planarly isotropic noise can be formulated as

$$\begin{aligned} & \min_{\mathbf{h}} \mathbf{h}^T \overleftrightarrow{\rho}_{\text{hpla}} \mathbf{h}, \\ & \text{subject to } \mathbf{h}^T \mathbf{u}(k_j r, 0) = 1, \\ & \quad k_j \in [k_l, k_u], \quad j = 1, 2, \dots, N_k. \end{aligned} \quad (7.58)$$

This beamformer is referred to as the time-domain phase-mode beamformer in this book, or CH-TPM beamformer for short.

Similar to the narrowband CHD beamformer design problem, in order to improve the robustness of the FIR beamformer, the broadband WNG shown in Eq. (7.56) should be constrained, which is equivalent to impose the constraint on the filter tap weights norm, i.e.,

$$\|\mathbf{h}\| \leq \Delta_h, \quad (7.59)$$

where Δ_h is the specified upper bound on the norm of the filter tap weights.

The sidelobe constraints can also be imposed to the optimization problem to control the sidelobes,

$$\mathcal{L}_q \left\{ \left[\mathbf{h}^T \mathbf{u}(k_j r, \psi_i) \right]_{k_j \in [k_l, k_u], \psi_i \in \Psi_{\text{SL}}} \right\} \leq \varepsilon, \quad (7.60)$$

where $\mathcal{L}_q \{\cdot\}$ stands for the ℓ_q -norm of the vector in its arguments, where $q = 2$ and $q = \infty$ represent the Euclidean and Chebyshev norms, respectively, and ε is the specified constraint value on the sidelobes.

In addition, if a broadband beamformer with a constant mainlobe pattern is required, similar to the element-space FIR beamformer design presented in Chap. 5, the CHD MSRV constraint

$$\mathcal{L}_q \left\{ [\mathbf{h}^T \mathbf{u}(k_j r, \psi_l) - \mathbf{h}^T \mathbf{u}(k_0 r, \psi_l)]_{k_j \in [k_l, k_u], \psi_l \in \Psi_{ML}} \right\} \leq \delta \quad (7.61)$$

can be imposed to the optimization problem. Here δ is the specified threshold of the MSRV, k_0 is the chosen reference wavenumber, Ψ_{ML} is the mainlobe region and $\psi_l \in \Psi_{ML}$ are the grid points in the mainlobe region.

Then, imposing the constraints Eqs. (7.59)–(7.61) to the optimization problem Eq. (7.58), gives the time-domain broadband CHD multiply constrained beamformer design problem

$$\begin{aligned} & \min_{\mathbf{h}} \mathbf{h}^T \overleftrightarrow{\rho}_{hpla} \mathbf{h}, \\ & \text{subject to } \mathbf{h}^T \mathbf{u}(k_j r, 0) = 1, \quad k_j \in [k_l, k_u], \quad j = 1, 2, \dots, N_k, \\ & \mathcal{L}_q \left\{ [\mathbf{h}^T \mathbf{u}(k_j r, \psi_l)]_{k_j \in [k_l, k_u], \psi_l \in \Psi_{SL}} \right\} \leq \varepsilon, \\ & \mathcal{L}_q \left\{ [\mathbf{h}^T \mathbf{u}(k_j r, \psi_l) - \mathbf{h}^T \mathbf{u}(k_0 r, \psi_l)]_{k_j \in [k_l, k_u], \psi_l \in \Psi_{ML}} \right\} \leq \delta, \\ & \|\mathbf{h}\| \leq \Delta_h. \end{aligned} \quad (7.62)$$

This optimization problem is a CHD extension of the FIR broadband beamformer presented in Chap. 5, which can be solved using a similar method, and will not be discussed here for simplicity.

It is worth noting that the time-domain broadband modal beamformer developed in this section has a symmetric beam pattern. It is also not suitable in the presence of strong interferers. For the case when strong interferences exist, the reader is referred to the similar design procedures, which will not be described in detail in this book.

We now consider several examples to illustrate the FIR filters based time-domain CHD beamforming operation.

Consider an unbaffled UCA with $M = 16$ elements in the planarly isotropic noise environment and assume that the steering direction is $\theta_0 = 0^\circ$. The FIR filter length is chosen as $L = 65$ and up to $N = 7$ order circular harmonics are used. The frequency band of interest satisfies $kr = 2\pi f r / c \in [k_l r, k_u r] = [1, 7]$ and the sampling frequency f_s satisfies $k_s r = 2\pi f_s r / c = 21$.

The CH-TMWNG beamformer is used. The filter \mathbf{h} and its subvectors $\mathbf{h}_0, \dots, \mathbf{h}_n, \dots, \mathbf{h}_N$ are determined by solving the optimization problem in Eq. (7.57). The obtained tap weights of each FIR filter are shown in Fig. 7.3a.

Substituting the obtained filter tap weights \mathbf{h}_n into Eq. (7.39) gives the weighting functions of the CH-TMWNG beamformer, $\widehat{d}_n(kr)$, as functions of kr , as shown in Fig. 7.3b in dB. For comparison purposes, the weighting functions of CHD frequency-domain MWNG beamformer (i.e., CH-FMWNG beamformer), $\overline{\widehat{d}}_n(kr)$, for selected kr grids are calculated using Eqs. (7.5) and (7.7) and are also shown in this figure.

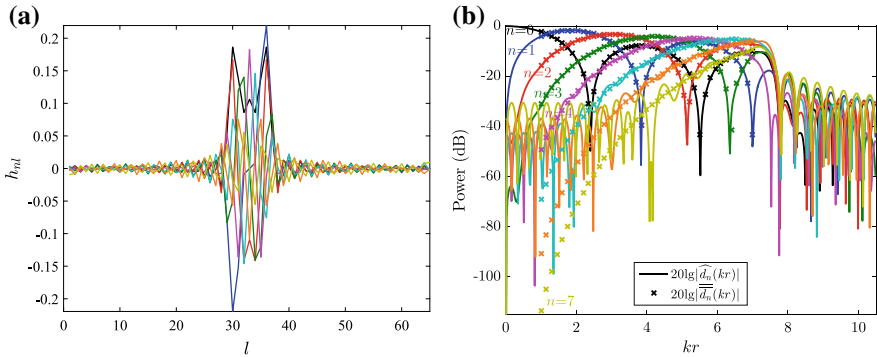
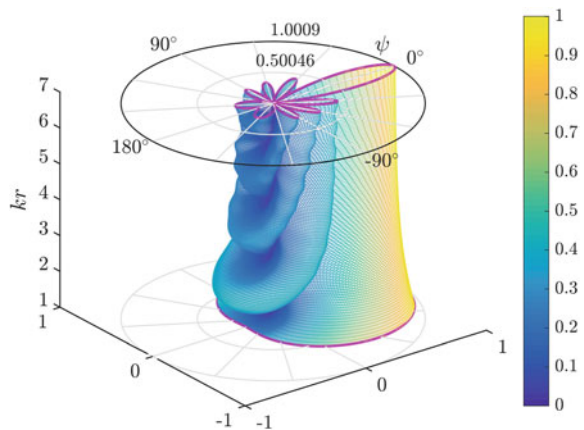


Fig. 7.3 Results of CH-TMWNG beamformer for 16-element unbaffled UCA. **a** Pattern generation filters h_{nl} . **b** Weights as a function of kr for both CH-TMWNG and CH-FMWNG beamformers. The CH-TMWNG method approximates the CH-FMWNG method

Fig. 7.4 CH-TMWNG beam patterns of 16-element unbaffled UCA

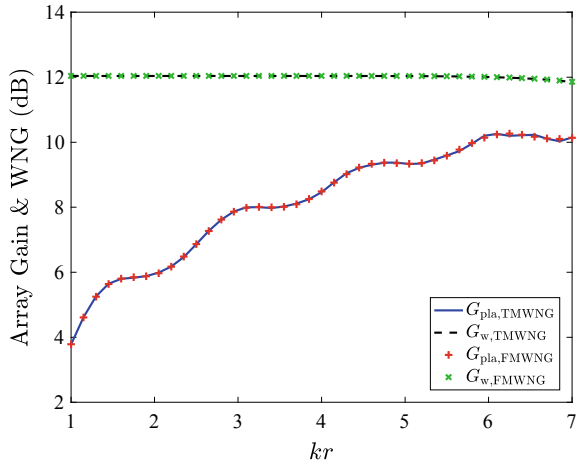


It is seen that the weights of the CH-TMWNG beamformer, $\widehat{d}_n(kr)$, approximate that of the CH-FMWNG beamformer, $\overline{\overline{d}}_n(kr)$, at each wavenumber bin within the wavenumber passband $[k_l, k_u]$.

The beam patterns of the CH-TMWNG beamformer are calculated using Eq. (7.41) on a grid of points in kr and direction, as shown in Fig. 7.4. These beam patterns approximate well those of the CH-FMWNG beamformer shown in Fig. 6.20b, which indicates that the time-domain beamformer is equivalent to the frequency-domain beamformer.

Using Eqs. (7.47) and (7.53), the array gain against planarly isotropic noise and the WNG are calculated, respectively, for selected kr grids. For comparison purposes, those of the CH-FMWNG beamformer are also calculated using Eqs. (6.152) and (7.29), respectively. The results are shown in Fig. 7.5, where we have added the sub-

Fig. 7.5 The values of array gain and WNG versus kr for CH-TMWNG and CH-FMWNG beamformers for 16-element unbaffled UCA. The results demonstrate the equivalence of time-domain and frequency-domain processing



scripts “TMWNG” and “FMWNG” to denote the CH-FMWNG and CH-FMWNG beamformers, respectively.

It is seen that the CH-TMWNG and CH-FMWNG beamformers can achieve nearly identical array gain and WNG performances, which also demonstrates the equivalence of the time-domain processing and the frequency-domain processing.

Recall that for an unbaffled M -element UCA, the maximum WNG is M and corresponds to the uniform weighting in element-space processing. In the CHD processing case, we observe from Eq. (6.177) that the MWNG beamformer can obtain a maximum WNG approaching M . From Fig. 7.5, it is seen that the values of WNG for both CH-TMWNG and CH-FMWNG beamformers go from 12.04 dB (i.e., $10 \lg M$, the maximum WNG available) at $kr = 1$ to 11.85 dB at $kr = 7$, which indicates that the beamformers have good robustness. The values of array gain against planarly isotropic noise for both CH-TMWNG and CH-FMWNG beamformers roughly increase as the frequency increases. At the low-frequency end ($kr = 1$), the array gain is about 3.78 dB.

Next, we use the time-domain phase-mode beamformer (i.e., CH-TPM beamformer) described in Eq. (7.58). The results are shown in Fig. 7.6. Figure 7.6a shows the pattern generation filters corresponding to each circular harmonic. Comparing the filters with those in Fig. 7.3a, we observe that the coefficients in Fig. 7.6a have increased to a very significant level, which will lead to a very small value of BWNG shown in Eq. (7.56). We would anticipate that the beamformer would be very sensitive to mismatches between the actual environment and the model used to derive the optimal beamformer.

Substituting the filter coefficients \mathbf{h}_n corresponding to each circular harmonic into Eq. (7.39) gives the weighting functions of time-domain phase-mode beamformer, $\widehat{d}_n(kr)$, as shown in Fig. 7.6b. Its frequency-domain counterpart, i.e., the weighting functions of frequency-domain phase-mode beamformer (or CH-FPM beamformer for short), $\overline{d}_n(kr)$, calculated using Eqs. (7.4) and (7.7) are also shown in this figure.

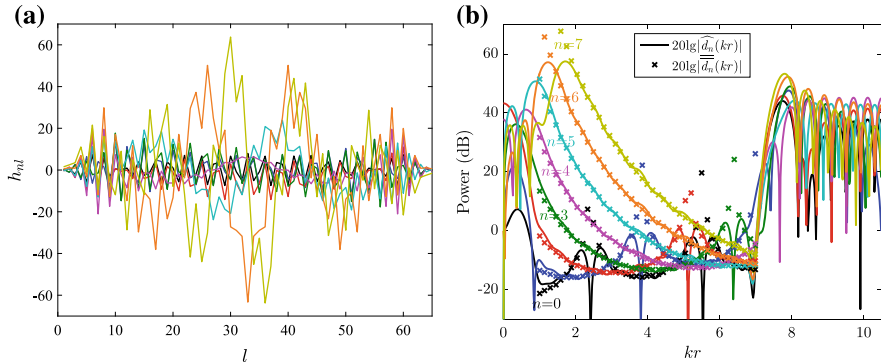
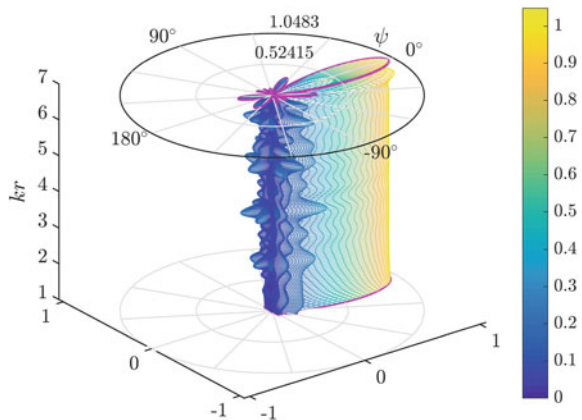


Fig. 7.6 Results of CH-TPM beamformer for 16-element unbaffled UCA. **a** Pattern generation filters h_n , **b** Weights for both CH-TPM and CH-FPM beamformers

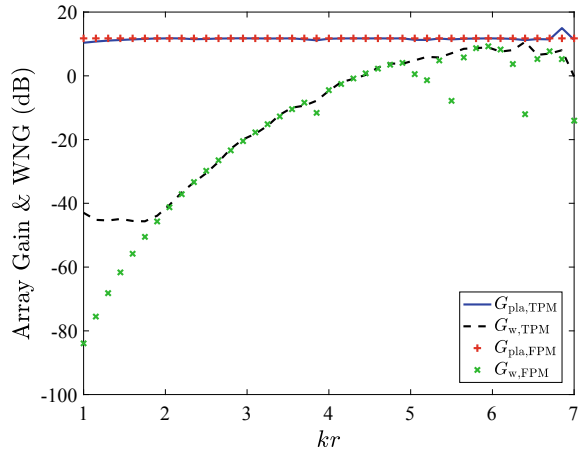
Fig. 7.7 Beam patterns of CH-TPM beamformer for 16-element unbaffled UCA in the absence of array manifold mismatch



It is seen that the dynamic range of $\widehat{d}_n(kr)$ and $\overline{\overline{d}}_n(kr)$ is quite large. The weighting functions $\widehat{d}_n(kr)$ approximate $\overline{\overline{d}}_n(kr)$ well, except at the low-frequency end and around frequencies where the peaks of $\overline{\overline{d}}_n(kr)$ appear due to the zeros of $C_n(kr)$. Outside the operating frequency band, the frequency responses of these FIR filters are very high, reaching about 40 dB. This is due to the aforementioned large filter coefficients, which also leads to considerable noise amplification at out-of-band frequencies, thereby will cause significant degradation to the beam pattern.

The resulting beam patterns of the CH-TPM beamformer calculated using Eq. (7.41) are shown in Fig. 7.7. It is already known that the CH-FPM beamformer is equivalent to the CHD MVDR beamformer against planarly isotropic noise, whose beam patterns are shown in Fig. 6.19a. Comparing Fig. 7.7 with Fig. 6.19a, it is seen that the beam patterns degrade significantly even by some slight mismatches between $\widehat{d}_n(kr)$ and $\overline{\overline{d}}_n(kr)$. The CH-TPM beam patterns are not frequency-invariant any more and the sidelobe height increases.

Fig. 7.8 Array gain and WNG of CH-TPM and CH-FPM beamformers for 16-element unbaffled UCA



The values of array gain against planarly isotropic noise and WNG versus kr are calculated for both CH-TPM and CH-FPM beamformers, as shown in Fig. 7.8, where we have added the subscripts “TPM” and “FPM” to denote the CH-TPM and CH-FPM beamformers, respectively.

Recall from Fig. 7.6b that at frequencies where zeros appear in $C_n(kr)$, the weight-ing functions $\widehat{d}_n(kr)$ no longer have peaks as $\overline{d}_n(kr)$ do, due to the smoothing effect of the FIR filter response. As a result, the CH-TPM beamformer has higher WNG than the CH-FPM beamformer at these frequencies, so does at low frequencies. We observe that both CH-TPM and CH-FPM beamformers achieve poor WNG at low values of kr , which indicates that both beamformers are sensitive to manifold per-turbations at the lower frequencies and cannot be applied in practical applications.

We next evaluate the robustness of the CH-TPM beamformer in the presence of array manifold mismatch. The beam patterns of the CH-TPM beamformer in the presence of 1% manifold perturbations are shown in Fig. 7.9. Compared to Fig. 7.7, the beam patterns shown in Fig. 7.9 are distorted significantly at the lower frequencies, and small mismatches lead to unacceptable performance.

We now consider the design of time-domain broadband CHD MVDR beam-former with multiple constraints. Assume that we want to synthesize a frequency-invariant mainlobe pattern over the frequency band corresponding to $kr \in [3.5, 7]$. The robustness constraint Eq. (7.59) and the MSRV constraint Eq. (7.61) are imposed. The resulting beamformer is referred to as the CHD time-domain robust frequency-invariant beamformer, or CH-TRFI beamformer for short.

Consider an unbaffled and a baffled 16-element UCA in the planarly isotropic noise environment, respectively.

Assume that the steering direction is $\theta_0 = 0^\circ$, the length of the FIR filter is $L = 65$, $k_s r = 2\pi f_s r / c = 21$, and up to $N = 7$ order circular harmonics are used.

The method in Eq. (7.62) is used, in which we choose $\Psi_{\text{ML}} = [0^\circ : 1^\circ : 30^\circ]$, $\delta = 0.01$, $q = 2$, $\varepsilon = \infty$.

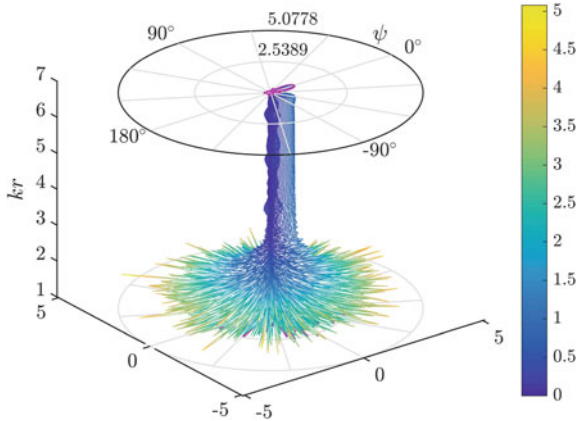


Fig. 7.9 Beam patterns of CH-TPM beamformer for 16-element unbaffled UCA in the presence of 1% array manifold mismatch

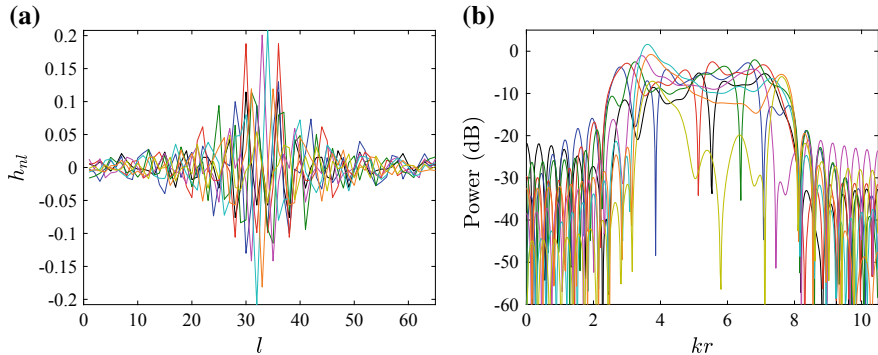


Fig. 7.10 Results of CH-TRFI beamformer for 16-element unbaffled UCA. **a** Pattern generation filters \mathbf{h}_n . **b** Equivalent weighting functions $\hat{d}_n(kr)$

For the case of unbaffled UCA, we choose $\Delta_h = 10^{-1/20}$. The resulting FIR filters \mathbf{h}_n are shown in Fig. 7.10a. It is seen that these filter tap weights are much smaller than those in Fig. 7.6a. We would anticipate that this beamformer would provide improved robustness.

Substituting the obtained filter tap weights \mathbf{h}_n into Eq. (7.39) gives the equivalent weighting functions $\hat{d}_n(kr)$ of the CH-TRFI beamformer for selected kr grids, as shown in Fig. 7.10b in dB. It is seen that most of the values of the weighting functions are less than 0 dB, and the stopband suppression is below -20 dB.

The beam patterns in the absence of manifold mismatch are shown in Fig. 7.11. It is seen that the mainlobe remains almost unchanged over the operating frequency band, and the distortion of the sidelobes is small. The design results meet the design requirements.

Fig. 7.11 Beam patterns of CH-TRFI beamformer for 16-element unbaffled UCA in the absence of array manifold mismatch

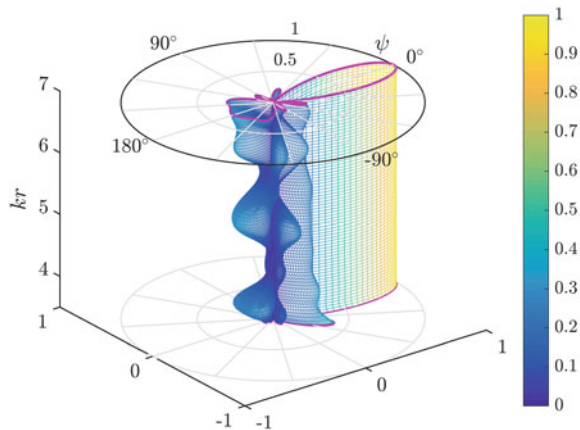
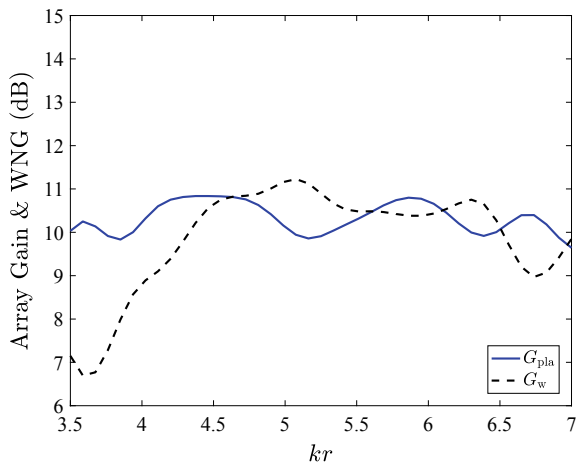


Fig. 7.12 Array gain and WNG of CH-TRFI beamformer for 16-element unbaffled UCA



The values of array gain and WNG against planarly isotropic noise versus kr are shown in Fig. 7.12. It is seen that the array gains are approximately between 10–11 dB, and the values of WNG within the operating frequency band all exceed 6 dB, which are much higher than those in Fig. 7.8. We would anticipate that this beamformer would have good robustness.

The beam patterns of the CH-TRFI beamformer in the presence of 5% manifold perturbations are shown in Fig. 7.13. Compared to Fig. 7.11, the CH-TRFI beamformer suffers very little performance degradation in the presence of manifold mismatch.

The results show that the multiply constrained method provides a good trade-off among multiple performance measures.

For the case of baffled UCA, we choose $\Delta_h = 10^{-3/20}$ and repeat the above process.

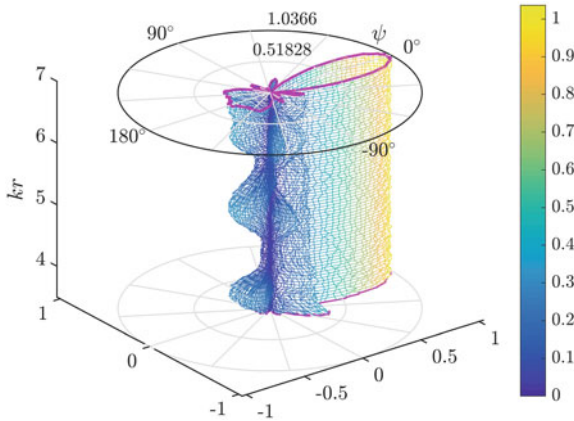


Fig. 7.13 Beam patterns of CH-TRFI beamformer for 16-element unbaffled UCA in the presence of 5% array manifold mismatch

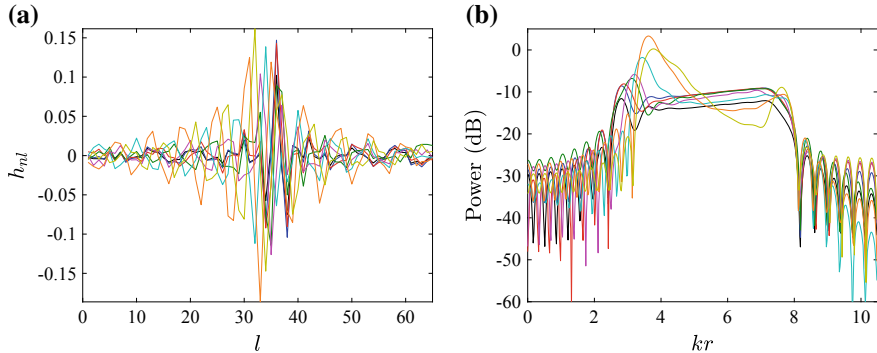


Fig. 7.14 Results of CH-TRFI beamformer for 16-element baffled UCA. **a** Pattern generation filters h_n . **b** Equivalent weighting functions $\hat{d}_n(kr)$

The resulting FIR filters and their equivalent weighting functions are shown in Fig. 7.14a and b respectively. It is seen that the filter tap weights are slightly smaller than those in Fig. 7.10a, and the stopband attenuation is also smaller.

The beam patterns in the absence of manifold mismatch are shown in Fig. 7.15. Compared to Fig. 7.11, the mainlobe beamwidth in Fig. 7.15 is narrower and the sidelobes are lower.

The values of array gain and WNG against planarly isotropic noise versus kr are shown in Fig. 7.16. It is seen that the array gains are approximately between 11–11.6 dB, which is very close to the highest array gain derived from Eq. (6.173), i.e., $10\lg(2N + 1) = 11.76$ dB. The values of the WNG in the operating frequency band all exceed 6 dB. When $kr > 5$, the WNG is approximately between 14–15 dB, which is higher than that of the unbaffled circular array as shown in Fig. 7.12.

Fig. 7.15 Beam patterns of CH-TRFI beamformer for 16-element baffled UCA in the absence of array manifold mismatch

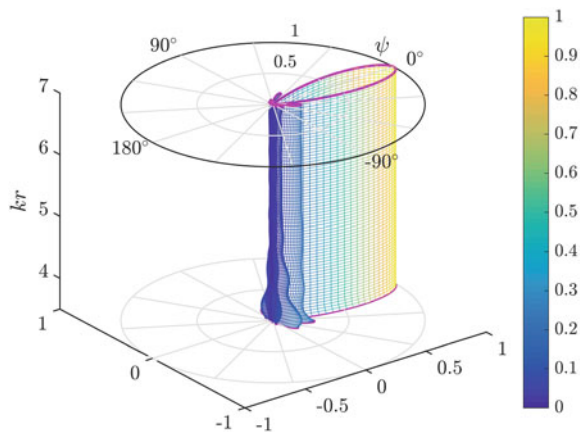
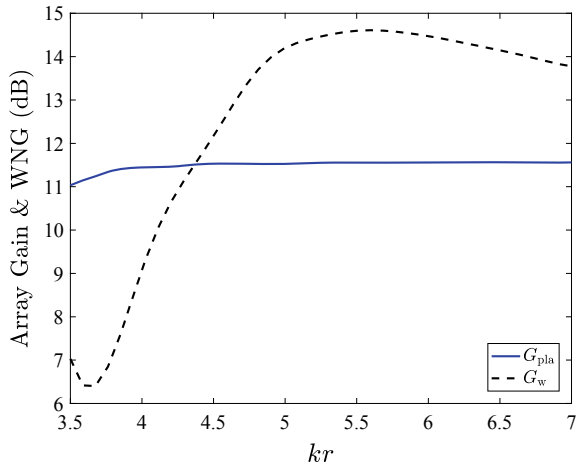


Fig. 7.16 Array gain and WNG of CH-TRFI beamformer for baffled UCA



In summary, the baffled circular array has better comprehensive performance than the unbaffled circular array in terms of mainlobe beamwidth, sidelobe level, array gain, robustness, etc.

7.5 Time-Domain Broadband CHD Beamforming

Several examples are considered to illustrate the behavior of the time-domain CHD beamforming.

Consider the same cases as in Fig. 6.26. For an unbaffled and a baffled 16-element broadband UCA, a far field LFM broadband plane wave impinges on the arrays from

$\theta_s = 0^\circ$. The waveforms received by the two UCAs have been shown in Fig. 6.26b and c respectively.

The CH-TMWNG, CH-TPM, and CH-TRFI beamformers are used to perform the beamforming on the received array data. Assume that the length of each FIR filter is $L = 65$. For the CH-TRFI beamformer, we choose $\Psi_{ML} = [0^\circ : 1^\circ : 30^\circ]$, $\delta = 0.01$, $q = 2$, $\Delta_h = 10^{-1/20}$, $\varepsilon = \infty$. The beamformer output time series are calculated using Eq. (7.37).

We first consider the 16-element unbaffled UCA.

Assume that the steering direction is $\theta_o = 0^\circ$. The output waveforms of the CH-TMWNG, CH-TPM, and CH-TRFI beamformers for the noise-free inputs are shown in Fig. 7.17a, c and e respectively. Figure 7.18 is the zoomed-in plot of the waveform shown in Fig. 7.17c.

It is seen from Fig. 7.17a, e that, the output waveforms of the CH-TMWNG and CH-TRFI beamformers are almost identical to the source signal shown in Fig. 6.26a except for both head and tail ends. Compared to the frequency-domain beamformer output shown in Fig. 6.27, it is seen that the error between the time-domain beamformer output shown in Fig. 7.17 and the source signal is even smaller.

The output waveform of the CH-TPM beamformer in Figs. 7.17c and 7.18 is also almost identical to the source signal except for both ends. However, the amplitude of the head of the waveform is more than 10 times of the normal value. This is due to the large FIR filter coefficients, which leads to considerable error amplification.

Assume that the steering direction moves to $\theta_o = 18^\circ$, which implies that the signal arrives inside the main beam but not along the main response axis. The output waveforms of the CH-TMWNG, CH-TPM, and CH-TRFI beamformers are shown in Fig. 7.17b, d and f respectively.

From Fig. 7.17b, it is seen that the CH-TMWNG beamformer output is large at low frequencies and small at high frequencies, i.e., the signal is low-pass filtered. This is similar to the result of the frequency-domain beamforming shown in Fig. 6.27b.

The CH-TPM beamformer output shown in Fig. 7.17d is distorted, especially in both ends. In the ideal case, the CH-TPM beamformer should have a frequency-invariant mainlobe pattern. This indicates that the CH-TPM beamformer has poor robustness and a small design error can cause significant degradation in the performance.

The output waveform of the CH-TRFI beamformer in Fig. 7.17f is similar to that in Fig. 7.17e, with a constant but reduced amplitude. This is because the CH-TRFI beamformer has a constant mainlobe pattern over the operating frequency band, which is an advantage of a frequency-invariant beamformer.

Consider the case when noise exists. Assume that, in addition to the desired signal, each sensor receives Gaussian noise which is uncorrelated with the signal, and the SNR at each sensor is 10 dB. The waveform of the signal received by a single input sensor (e.g., the 5th sensor, whose time delay relative to the reference point is 0) is shown in Fig. 7.19a.

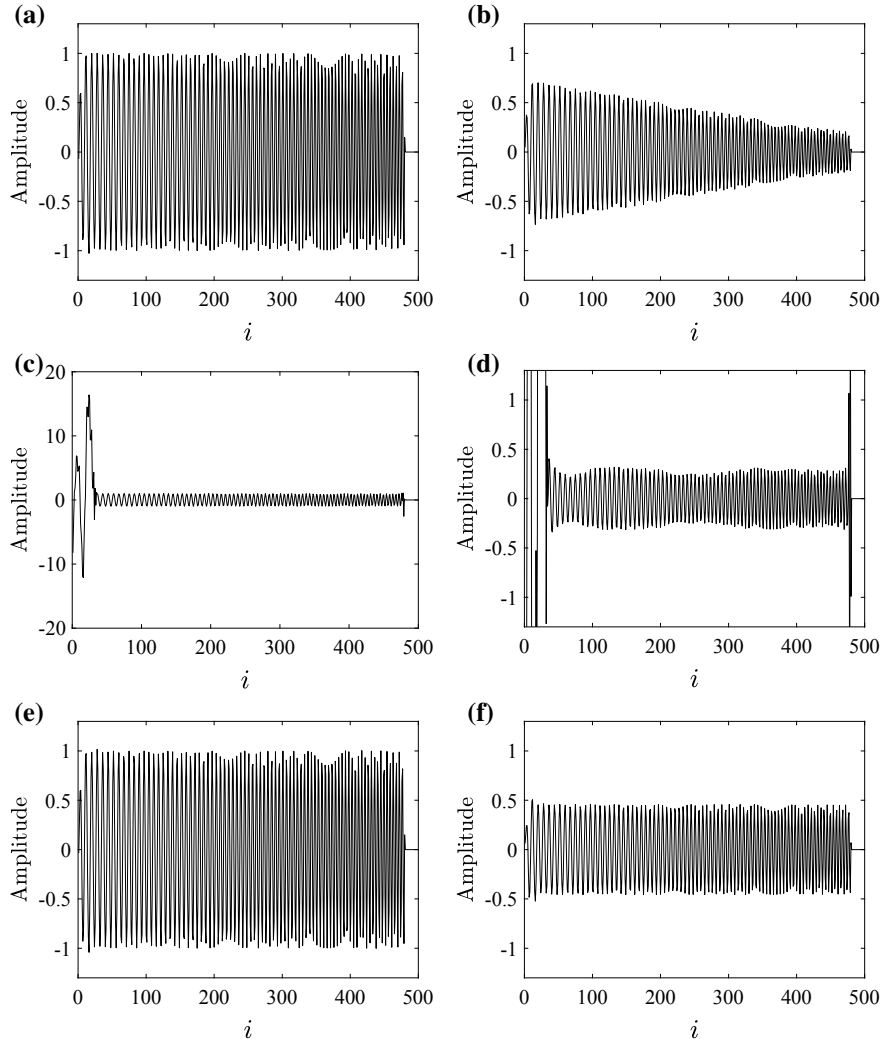


Fig. 7.17 Output waveforms of time-domain broadband CHD beamformers for unbaffled UCA. **a** CH-TMWNG, $\theta_0 = 0^\circ$, **b** CH-TMWNG, $\theta_0 = 18^\circ$, **c** CH-TPM, $\theta_0 = 0^\circ$, **d** CH-TPM, $\theta_0 = 18^\circ$, **e** CH-TRFI, $\theta_0 = 0^\circ$, **f** CH-TRFI, $\theta_0 = 18^\circ$

Using the CH-TMWNG, CH-TPM and CH-TRFI beamformers with $\theta_0 = 0^\circ$ designed above, the obtained outputs of the three beamformers are shown in Fig. 7.19b, c and d respectively.

Compared to the waveform shown in Fig. 7.19a, the output waveforms of the CH-TMWNG and CH-TRFI beamformers shown in Fig. 7.19b, d both suppress noise and improve the SNR. The amplitude of the CH-TPM beamformer output shown in Fig. 7.19c is very large and the waveform is completely distorted, which indicates that

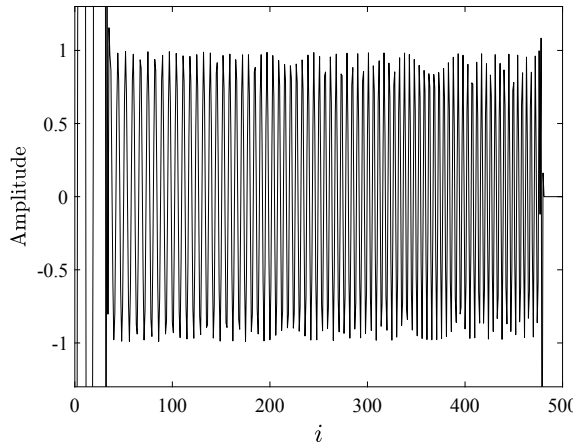


Fig. 7.18 Zoomed-in plot of the waveform shown in Fig. 7.17c

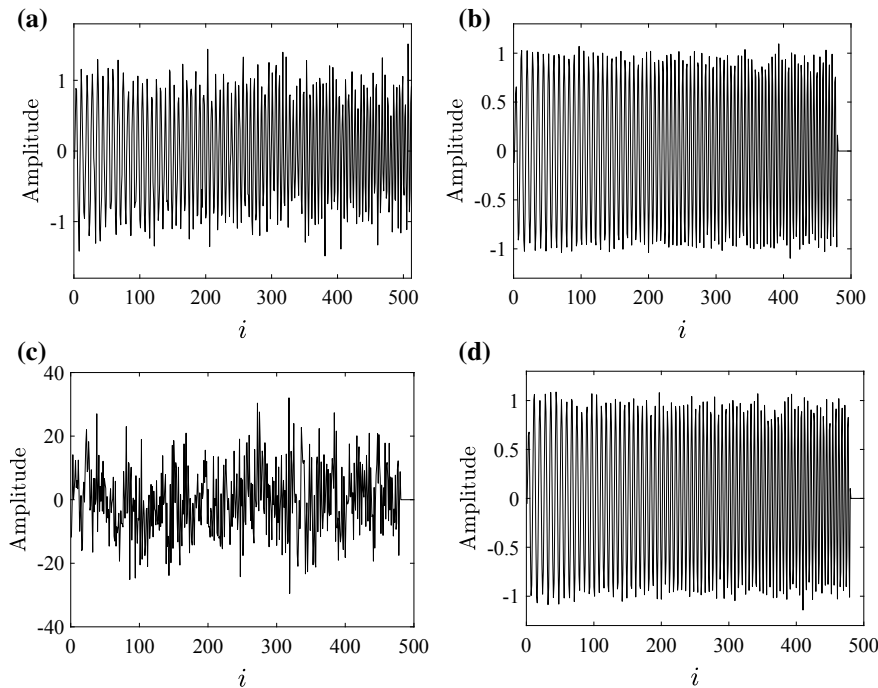


Fig. 7.19 Results of time-domain CHD beamformer for unbaffled UCA for $SNR = 10$ dB and $\theta_0 = 0^\circ$. **a** Waveform received by the 5th sensor. **b** Output waveform of CH-TMWNG beamformer. **c** Output waveform of CH-TPM beamformer. **d** Output waveform of CH-TRFI beamformer

the CH-TPM beamformer has poor robustness. This is due to the large coefficients of its pattern generation FIR filters, which leads to considerable noise amplification, thereby causing severe distortion in the output waveform.

We next consider the 16-element baffled UCA. The parameters are chosen to be the same as the unbaffled circular array above when designing the beamformers.

In the absence of noise, when the steering direction is at $\theta_o = 0^\circ$, the output waveforms of the CH-TMWNG, CH-TPM and CH-TRFI beamformers are shown in Fig. 7.20a, c and e respectively. The output waveforms of the CH-TMWNG and CH-TRFI beamformers shown in Fig. 7.20a, e are almost identical to the source signal shown in Fig. 6.26a. However, the output waveform of the CH-TPM beamformer shown in Fig. 7.20c is distorted compared to the source signal, which indicates that the CH-TPM beamformer has poor robustness.

When the steering direction moves to $\theta_o = 18^\circ$, the output waveforms of the three beamformers are shown in Fig. 7.20b, d and f respectively. It is seen from Fig. 7.20b that the signal is low-pass filtered by the CH-TMWNG beamformer. The output waveform of the CH-TPM beamformer shown in Fig. 7.20d is distorted, which indicates that the CH-TPM beamformer has poor robustness. The amplitude of the CH-TRFI beamformer output shown in Fig. 7.20f is constant, and the waveform is almost identical to the beamformer output shown in Fig. 7.20e except that the amplitude is reduced, which indicates that the CH-TRFI beamformer has a constant mainlobe pattern. In addition, the amplitudes of the output waveforms shown in Fig. 7.20b, f are both slightly smaller than the corresponding results for the unbaffled circular array case shown in Fig. 7.17b, f, which indicates that the mainlobe beamwidth of the baffled circular array is slightly narrower than that of the unbaffled circular array.

In the presence of spatially white noise, the power of the noise received by each sensor is assumed to be the same as that in the unbaffled circular array case, i.e., the SNR is 10 dB. Note that since the amplitudes of the desired signal received by each sensor of the baffled circular array are different from each other, the SNR at each sensor is not identical. The waveform received by the 5th sensor is shown in Fig. 7.21a.

Using the CH-TMWNG, CH-TPM and CH-TRFI beamformers for the baffled circular array with steering direction $\theta_o = 0^\circ$, the obtained outputs are shown in Fig. 7.21b, c and d respectively.

The results in Fig. 7.21 are similar to those for the unbaffled circular array case in Fig. 7.19. Compared to the waveform shown in Fig. 7.21a, the output waveforms of the CH-TMWNG and CH-TRFI beamformers shown in Fig. 7.21b, d both suppress noise and increase the SNR. The output waveform of the CH-TPM beamformer shown in Fig. 7.21c is distorted, which indicates that the CH-TPM beamformer has poor robustness. However, the amplitude of the beamformer output in Fig. 7.21c is smaller than that in Fig. 7.19c, which indicates that the baffled circular array is slightly more robust than the unbaffled circular array.

In summary, the results shown in Figs. 7.17, 7.18, 7.19, 7.20 7.21 verify the following conclusions. The CH-TMWNG and CH-TRFI beamformers have good robustness. The mainlobe beamwidth of the CH-TMWNG beamformer narrows with increasing frequency. The mainlobe pattern of the CH-TRFI beamformer remains

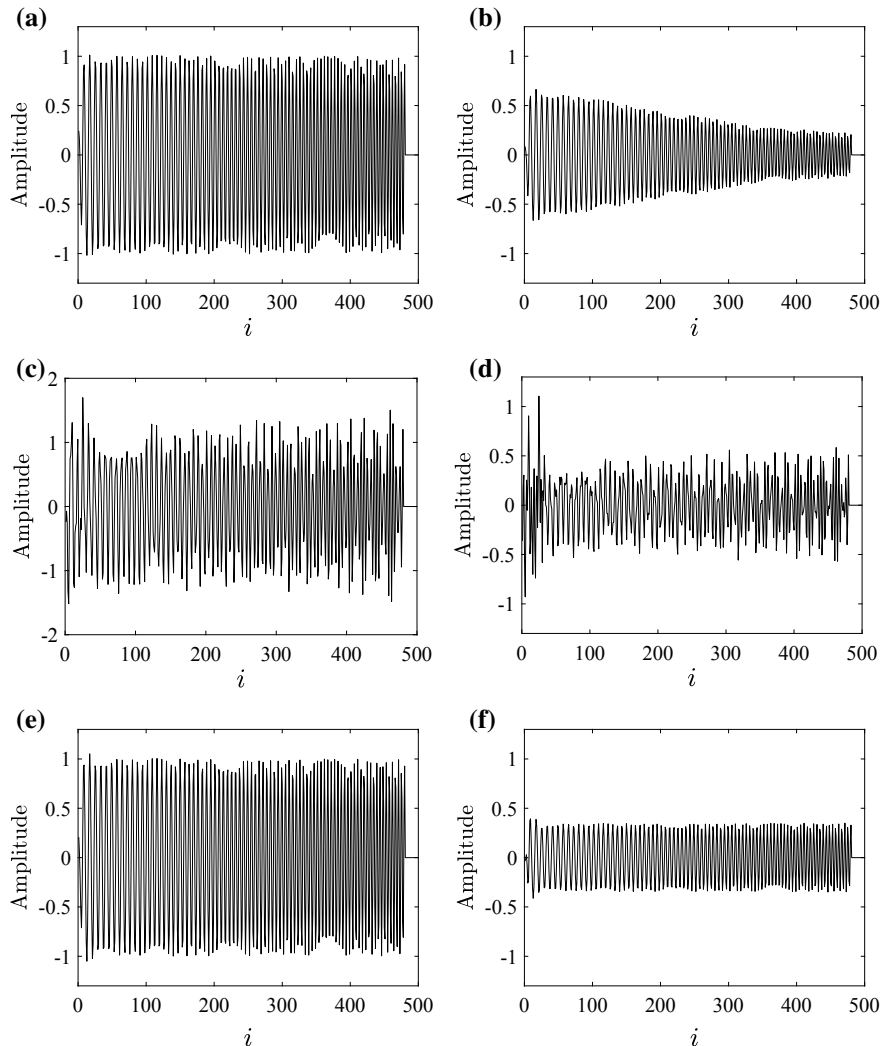


Fig. 7.20 Output waveforms of time-domain broadband CHD beamformers for baffled UCA. **a** CH-TMWNG, $\theta_0 = 0^\circ$, **b** CH-TMWNG, $\theta_0 = 18^\circ$, **c** CH-TPM, $\theta_0 = 0^\circ$, **d** CH-TPM, $\theta_0 = 18^\circ$, **e** CH-TRFI, $\theta_0 = 0^\circ$, **f** CH-TRFI, $\theta_0 = 18^\circ$

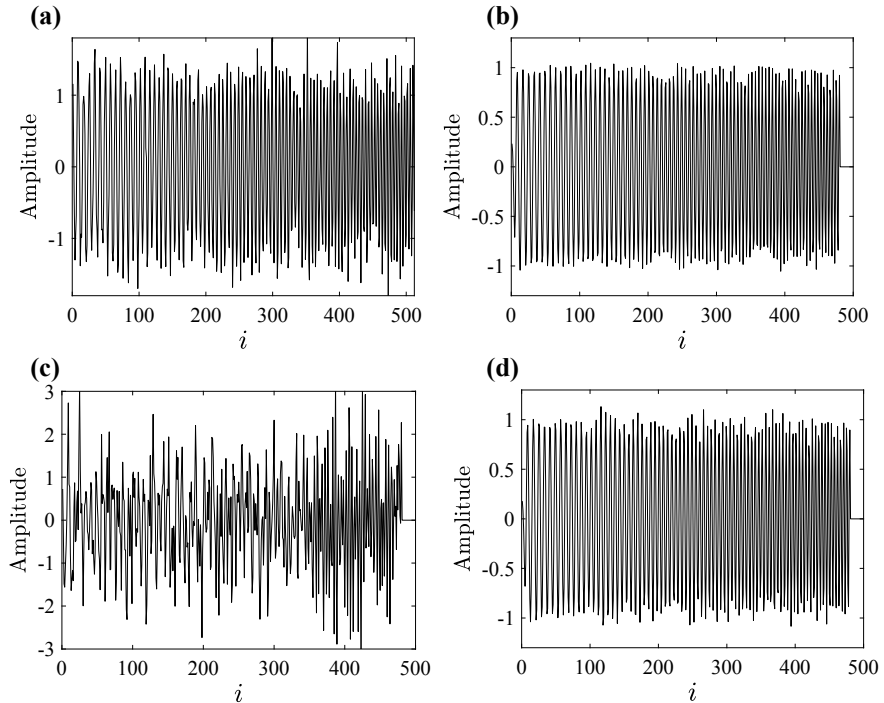


Fig. 7.21 Results of time-domain CHD beamformer for baffled UCA for $SNR = 10$ dB and $\theta_0 = 0^\circ$. **a** Waveform received by the 5th sensor. **b** Output waveform of CH-TMWNG beamformer. **c** Output waveform of CH-TPM beamformer. **d** Output waveform of CH-TRFI beamformer

constant over the frequency band of interest. Due to the large coefficients of the pattern generation FIR filters, the CH-TPM beamformer has small WNG and poor robustness, and suffers severe performance degradation in the presence of small mismatches and noise. The robustness of the beamformer for baffled circular array is slightly higher than that of the un baffled circular array.

7.6 Summary

The time-domain implementation of the broadband CHD beamformer for circular arrays has been presented.

The frequency-domain beamformer requires a block of snapshots to perform the DFT, which leads to associated delay. In order to avoid the associated delay, the time-domain implementation is required, in which we can update the beamformer output when each new snapshot arrives.

The circular arrays presented in this chapter employed beam patterns that are symmetric about the steering direction. The advantages of these beam patterns are the low computational complexity and the flexibility of beam steering, which is decoupled from beam pattern design. However, in some applications that an asymmetric beam pattern is required, the methods developed in Chap. 6 can be used.

The implementation of the CHD beamformer consists of two parts: circular harmonics transform and CHD beamforming. Similar to the element-space beamforming, the CHD broadband beamformer can be implemented either in the frequency domain or in the time domain, and the outputs of both implementations are equivalent.

In order to make this chapter more compact, only the time-domain implementation of the CHD symmetric-pattern beamformer is considered. For the problem of asymmetric CHD beamformer, the reader is referred to the similar design procedures, which is not described in this book.

In the time-domain broadband CHD beamformer, the element-space array data are first converted to the circular harmonics domain using real-valued circular harmonics transform, and then steered to the look direction, followed by a real-valued filter-and-sum structure to achieve the beamformer output time series.

By deriving the expressions for the array response, array gain, white noise gain, and MSRV in terms of the filter tap weights, the pattern generation filter design is formulated as an optimization problem that is computationally tractable. Additional constraints such as robustness constraint, sidelobe constraint and mainlobe variation constraint can also be imposed. The resulting beamformer can provide a suitable trade-off among multiple conflicting array performance measures, which is very useful in practical applications.

The performance of the proposed approach is demonstrated by a number of simulations. The results show that the time-domain and frequency-domain implementations can obtain nearly identical performances. In addition, the circular arrays baffled by an acoustically rigid cylinder have the potential to achieve narrower mainlobe beamwidth, lower sidelobe levels, higher array gain, and higher robustness than the acoustic transparent circular arrays. In other words, the baffled circular arrays have better comprehensive performance than the unbaffled circular arrays.

References

1. S. Yan, C. Hou, X. Ma, Y. Ma, Convex optimization based time-domain broadband beamforming with sidelobe control. *J. Acoust. Soc. Am.* **121**(1), 46–49 (2007)
2. S. Yan, Y. Ma, C. Hou, Optimal array pattern synthesis for broadband arrays. *J. Acoust. Soc. Am.* **122**(5), 2686–2696 (2007)

Chapter 8

Modal Beamforming for Spherical Arrays



8.1 Introduction

The designs and implementations of modal beamformers for broadband circular arrays have been studied in Chaps. 6 and 7.

The spherical symmetry of the spherical microphone array is very advantageous for three-dimensional sound field analysis. Spherical array beamforming technology has recently become an important research issue [1].

Meyer and Elko [2] presented an elegant modal beamformer structure for spherical microphone arrays based on the spherical harmonics decomposition (also known as the spherical Fourier transform [3]), which is referred to as the phase-mode processing [4].

The phase-mode processing provides frequency-independent spatial resolution and seems to offer a useful framework for spherical arrays, but care must be taken at low frequencies for noise amplification and spatial aliasing [5] at frequencies where the average microphone spacing exceeds one-half of the wavelength. It is then necessary to reduce the highest spherical harmonics order used, at the cost of reduced array gain and spatial resolution.

The phase-mode processing decouples the shaping and the steering of a beam pattern and produces a beam pattern that is axis-symmetric with respect to the steering direction. This beamforming structure makes the processing simple, but it cannot deal with the situation where there is interference. The nulls in the beam pattern cannot be adaptively formed and steered to suppress dynamic interferences coming from arbitrary outside beam directions. In some applications, a beam pattern that is not rotationally symmetric may be desired.

The author and his collaborators proposed an approach to optimal design of spherical-harmonics-domain (SHD) beamformer in the previous papers [6–9]. The element-space data received by a spherical array are transformed into spherical harmonics domain using the spherical Fourier transform, and then the beamforming operation is performed in the spherical harmonics domain. By utilizing the equivalence relation between the SHD processing and the element-space processing and

deriving the expressions for the SHD array performance measures, the techniques for element-space beamformer design can then be extended to the spherical harmonics domain.

The rest of this chapter is organized as follows. In Sect. 8.2, we introduce the spherical harmonics, the phase-mode beamforming for spherical arrays, and the modal representation of DAS beamformer. The general formulation of the SHD beamformer for spherical arrays are studied in Sect. 8.3, where several commonly used SHD performance measures are derived. In Sect. 8.4, we develop the optimal design methods of SHD beamformer for spherical arrays. In Sect. 8.5, the frequency-domain implementation of the broadband SHD beamformer is presented. A brief summary of this chapter is given in Sect. 8.6.

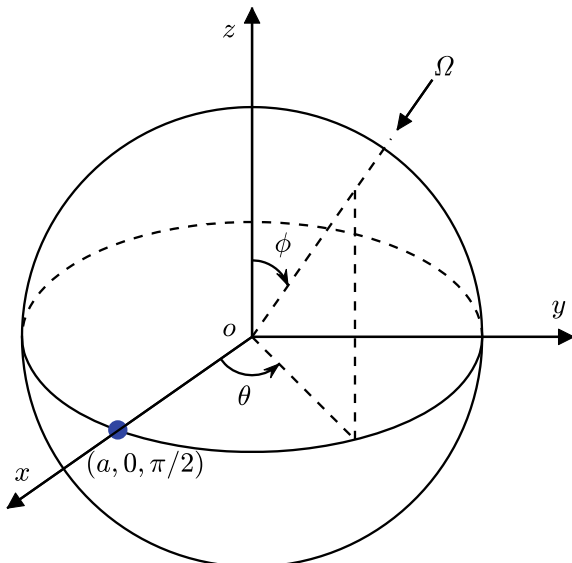
8.2 Continuous Spherical Arrays (Apertures)

8.2.1 Spherical Apertures

In this chapter, we consider the spherical arrays in a plane-wave sound field. The standard Cartesian (x, y, z) and spherical (r, θ, ϕ) coordinate systems are used.

The continuous spherical array (or spherical aperture) of interest is shown in Fig. 8.1. Let a be the radius of the sphere. A position on the sphere can be denoted in the spherical coordinates by (a, ϑ, φ) or (a, Φ) , where $\Phi = (\vartheta, \varphi)$ is the spherical angle with ϑ and φ be the azimuth and the elevation angles, respectively.

Fig. 8.1 A sphere in three-dimensional coordinate system



A position (a, ϑ, φ) represented in the spherical coordinates can also be denoted in the Cartesian coordinates by \mathcal{P}_ϑ or $\mathcal{P}_{(\vartheta, \varphi)}$, where

$$\mathcal{P}_\vartheta = \mathcal{P}_{(\vartheta, \varphi)} = [a \sin \varphi \cos \vartheta, a \sin \varphi \sin \vartheta, a \cos \varphi]^T. \quad (8.1)$$

From Eq. (8.1), we have

$$\mathcal{P}_{(\vartheta + \pi, -\varphi)} = \mathcal{P}_{(\vartheta, \varphi)}. \quad (8.2)$$

Equation (8.2) indicates that we can choose an appropriate spherical coordinates representation for convenience.

For example, a plane containing the z -axis can be represented by $\vartheta = \vartheta_0$ or $\vartheta = \vartheta_0 + \pi$, where ϑ_0 is the azimuth angle of the projection of the plane on the xy -plane. A cut of the sphere through the plane $\vartheta = \vartheta_0$ is a circle. The angles on this circle can be denoted by the set $(\vartheta, \varphi) = \{(\vartheta_0, \varphi) | \varphi \in [0, \pi]\} \cup \{(\vartheta_0 + \pi, \varphi) | \varphi \in [0, \pi]\}$. From Eq. (8.2), since $\{(\vartheta_0 + \pi, \varphi) | \varphi \in [0, \pi]\} = \{(\vartheta_0, \varphi) | \varphi \in [-\pi, 0]\}$, these angles can also be denoted by the set $(\vartheta, \varphi) = \{(\vartheta_0, \varphi) | \varphi \in [-\pi, \pi]\}$. Obviously, the latter representation is more convenient to use.

Consider an acoustic transparent spherical aperture, or a spherical aperture in a free field. This spherical aperture is also termed as an open spherical aperture.

Assume a unit magnitude plane wave impinging on the aperture from direction $\Omega_s = (\theta_s, \phi_s)$. Using the frequency-domain snapshot model and suppressing the time factor $\exp(i\omega t)$, the sound pressure on the sphere surface at an observation point $\Phi = (\vartheta, \varphi)$ can be written as

$$p(ka, \Phi, \Omega_s) = \exp[-ik^T(\Omega_s)\mathcal{P}_\vartheta], \quad (8.3)$$

where $\mathbf{k}(\Omega_s) = -k[\sin \phi_s \cos \theta_s, \sin \phi_s \sin \theta_s, \cos \phi_s]^T$ is the wavenumber vector.

Since we have suppressed the time factor $\exp(i\omega t)$, Eq. (8.3) is actually the manifold function of the spherical aperture.

8.2.2 Spherical Mode

Recall the discussion in Chap. 6 that any function which is square-integrable over a unit circle can be expanded into a series of circular harmonics using the inverse circular Fourier transform. Similarly, a square-integrable function on a sphere can also be decomposed into a number of spherical harmonics using the spherical Fourier transform. Thus, the sound pressure $p(ka, \Phi, \Omega_s)$ on the sphere surface can be written in Fourier series expansion as [10]

$$p(ka, \Phi, \Omega_s) = \sum_{n=0}^{\infty} \sum_{m=-n}^n P_{nm}(ka, \Omega_s) Y_n^m(\Phi), \quad (8.4)$$

where $Y_n^m(\Phi)$ is the spherical harmonics (SH) of order n and degree m , and the Fourier coefficients $P_{nm}(ka, \Omega_s)$ are given by

$$P_{nm}(ka, \Omega_s) = \int_{\Phi \in S^2} p(ka, \Phi, \Omega_s) [Y_n^m(\Phi)]^* d\Phi, \quad (8.5)$$

where the integral $\int_{\Phi \in S^2} d\Phi = \int_0^{2\pi} \int_0^\pi \sin\varphi d\varphi d\vartheta$ covers the entire surface of the unit sphere S^2 .

Equation (8.5) is also referred to as the spherical harmonics transform, and Eq. (8.4) is its inverse transform, which is also referred to as the spherical harmonics decomposition.

Thus, $P_{nm}(ka, \Omega_s)$ can be viewed as the SHD representation of the sound pressure $p(ka, \Phi, \Omega_s)$.

The spherical harmonics $Y_n^m(\Phi)$ are the solutions to the wave equation, or the Helmholtz equation, in spherical coordinates. They are given by [3]

$$Y_n^m(\Phi) = Y_n^m(\vartheta, \varphi) = \sqrt{\frac{(2n+1)}{4\pi} \frac{(n-m)!}{(n+m)!}} P_n^m(\cos \varphi) e^{im\vartheta}, \quad (8.6)$$

where $P_n^m(\cdot)$ denotes the associated Legendre function.

The spherical harmonics functions $Y_n^m(\Phi)$ are orthonormal and satisfy

$$\int_{\Phi \in S^2} Y_{\tilde{n}}^{\tilde{m}}(\Phi) [Y_n^m(\Phi)]^* d\Phi = \delta_{n-\tilde{n}} \delta_{m-\tilde{m}}, \quad (8.7)$$

where $\delta_{n-\tilde{n}}$ is the Kronecker delta function, which is 1 at $n = \tilde{n}$ and zero otherwise.

The spherical harmonics functions $Y_n^m(\Phi)$ also satisfy

$$Y_n^{-m}(\Phi) = (-1)^m [Y_n^m(\Phi)]^*. \quad (8.8)$$

When $m = 0$, the corresponding spherical harmonics function $Y_n^0(\Phi)$ is a real-valued number.

Applying the spherical harmonics decomposition, the sound pressure on the sphere surface can be given by [3]

$$p(ka, \Phi, \Omega_s) = \sum_{n=0}^{\infty} b_n(ka) \sum_{m=-n}^n [Y_n^m(\Omega_s)]^* Y_n^m(\Phi), \quad (8.9)$$

and its SHD representation is given by

$$P_{nm}(ka, \Omega_s) = b_n(ka) [Y_n^m(\Omega_s)]^*, \quad (8.10)$$

where $b_n(ka)$ is the spherical modal response, which depends on the sphere configuration. For an open sphere, it is given by

$$b_{n,\text{open}}(ka) = 4\pi i^n j_n(ka), \quad (8.11)$$

where the subscript “open” denotes the open sphere and j_n is the n th-order spherical Bessel function of the first kind.

For an aperture mounted around a rigid sphere, the spherical modal response is given by [3]

$$b_{n,\text{rigid}}(ka) = 4\pi i^n \left(j_n(ka) - \frac{j'_n(ka)}{h'_n(ka)} h_n(ka) \right), \quad (8.12)$$

where the subscript “rigid” denotes the rigid sphere, h_n is the n th-order spherical Hankel function of the second kind, and j'_n and h'_n are the derivatives of j_n and h_n with respect to their arguments, respectively.

It is worth noting that, in some literatures where the time factor is denoted by $\exp(-i\omega t)$ rather than the expression of $\exp(i\omega t)$ used in this book, the n th-order spherical Hankel function of the second kind in Eq. (8.21) should be replaced by that of the first kind.

The first term of $b_{n,\text{rigid}}(ka)$ represents the incident sound field, which is identical to the open sphere, and the second term represents the scattered sound field, which is the sound field that is scattered from the rigid sphere due to the incident field.

The n th-order Bessel function J_n and spherical Bessel function j_n of the first kind have the relationship

$$j_n(ka) = \sqrt{\frac{\pi}{2ka}} J_{n+1/2}(ka). \quad (8.13)$$

Correspondingly, the n th-order Bessel function Y_n and spherical Bessel function y_n of the second kind have the relationship

$$y_n(ka) = \sqrt{\frac{\pi}{2ka}} Y_{n+1/2}(ka). \quad (8.14)$$

The spherical Bessel functions of the first kind and the second kind have the relationship

$$j_n(ka)y'_n(ka) - y_n(ka)j'_n(ka) = \frac{1}{(ka)^2}. \quad (8.15)$$

The spherical Hankel function of the second kind h_n and the spherical Bessel function j_n have the relationship

$$h_n(ka) = j_n(ka) - iy_n(ka). \quad (8.16)$$

From Eqs. (8.15) and (8.16), we have

$$j_n(ka)h'_n(ka) - h_n(ka)j'_n(ka) = \frac{-i}{(ka)^2}. \quad (8.17)$$

Since

$$h'_n(ka) = h_{n-1}(ka) - \frac{n+1}{ka}h_n(ka), \quad (8.18)$$

then,

$$\begin{aligned} j_n(ka) - \frac{j'_n(ka)}{h'_n(ka)}h_n(ka) &= \frac{-i}{(ka)^2 h'_n(ka)} \\ &= \frac{-i}{(ka)^2 [h_{n-1}(ka) - \frac{n+1}{ka}h_n(ka)]}. \end{aligned} \quad (8.19)$$

Substituting Eq. (8.19) into Eq. (8.12) gives the spherical modal response of the rigid sphere

$$b_{n,\text{rigid}}(ka) = \frac{-4\pi i^{n+1}}{(ka)^2 [h_{n-1}(ka) - \frac{n+1}{ka}h_n(ka)]}. \quad (8.20)$$

Combining Eqs. (8.11) and (8.12), we have

$$b_n(ka) = \begin{cases} 4\pi i^n j_n(ka), & \text{open sphere,} \\ 4\pi i^n \left(j_n(ka) - \frac{j'_n(ka)}{h'_n(ka)} h_n(ka) \right), & \text{rigid sphere.} \end{cases} \quad (8.21)$$

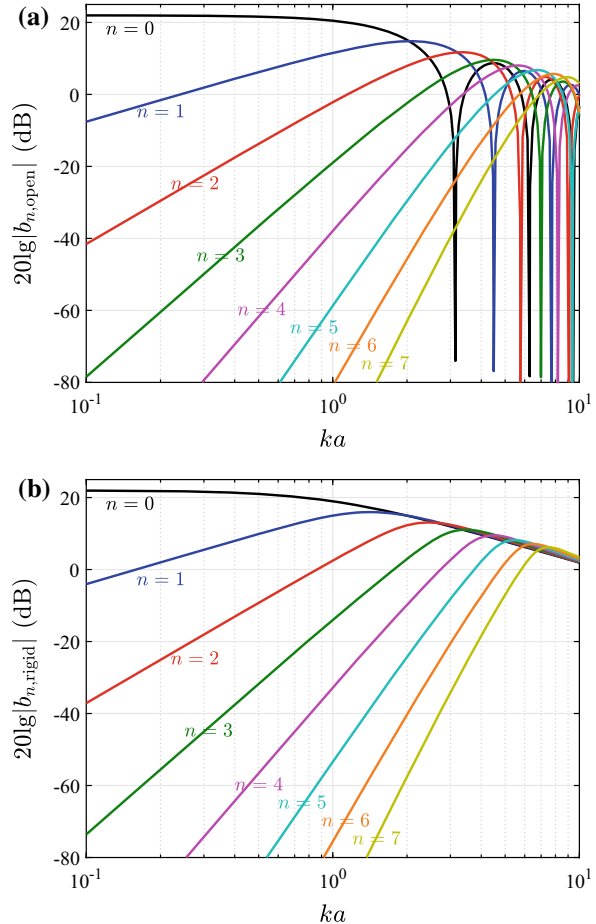
Using Eqs. (8.11) and (8.20), the modal magnitude response in dB of an open and a rigid spherical apertures, i.e., $20 \lg |b_{n,\text{open}}(ka)|$ and $20 \lg |b_{n,\text{rigid}}(ka)|$, versus ka in the range $[0.1, 10]$ for various values of n are plotted in Fig. 8.2a, b, respectively.

For the open spherical aperture, it is seen that for a small value of ka , the high-order terms of the coefficients $b_n(ka)$ contribute significantly less than the lower-order terms. We also observe that, some coefficients $b_n(ka)$ are zero for some values of ka due to the zeros of the spherical Bessel functions, which is similar to the unbaffled circular aperture introduced in Chap. 6.

For the rigid spherical aperture, the zeros in the spherical modal magnitude response disappear. It is also seen that the high-order terms of the coefficients $b_n(ka)$ contribute significantly less than the lower-order terms when the order n exceeds ka .

The real and imaginary parts of spherical harmonics functions $Y_n^m(\Phi)$ versus $\Phi = (\vartheta, \varphi)$ over the range $\vartheta \in [0, 2\pi]$ and $\varphi \in [0, \pi]$ for various values of n are shown in Fig. 8.3, where light shades indicate positive values and dark shades indicate negative values. Note that from Eq. (8.8), the values of $Y_n^m(\Phi)$ for $m = -n, \dots, -1$

Fig. 8.2 Modal magnitude responses $b_n(ka)$, of **a** open spherical array, and **b** rigid spherical array



can be calculated from the corresponding values for $m = 1, \dots, n$. Thus, we only need to calculate the spherical harmonics with m ranging from 0 to n .

The array manifold function of a spherical aperture, $p(ka, \Phi, \Omega_s)$, can be calculated by using Eq. (8.9). We assume that up to $n = 20$ order spherical harmonics are used. Letting $\Phi_0 = (\vartheta_0, \phi_0) = (0^\circ, 0^\circ)$ be the direction of the observation point, then the manifold function $p(ka, \Phi_0, \Omega_s)$ is independent of the azimuth angle θ_s .

The magnitude of the manifold function, $|p(ka, \Phi_0, \Omega_s)|$, versus ka in the range $[0.1, 10]$ and ϕ_s in the range $[-180^\circ, 180^\circ]$ for the open and the rigid spherical apertures are plotted in Fig. 8.4.

For the open spherical aperture, as shown in Fig. 8.4a, the magnitude response remains constant, which indicates that a sensor (or the observation point) on an open spherical array (or aperture) has an isotropic element pattern.

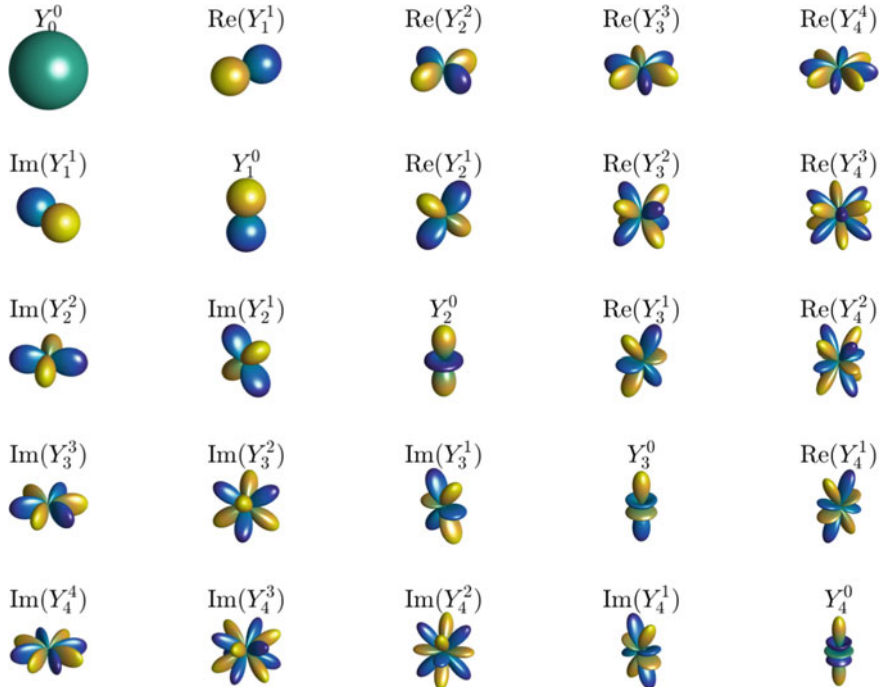


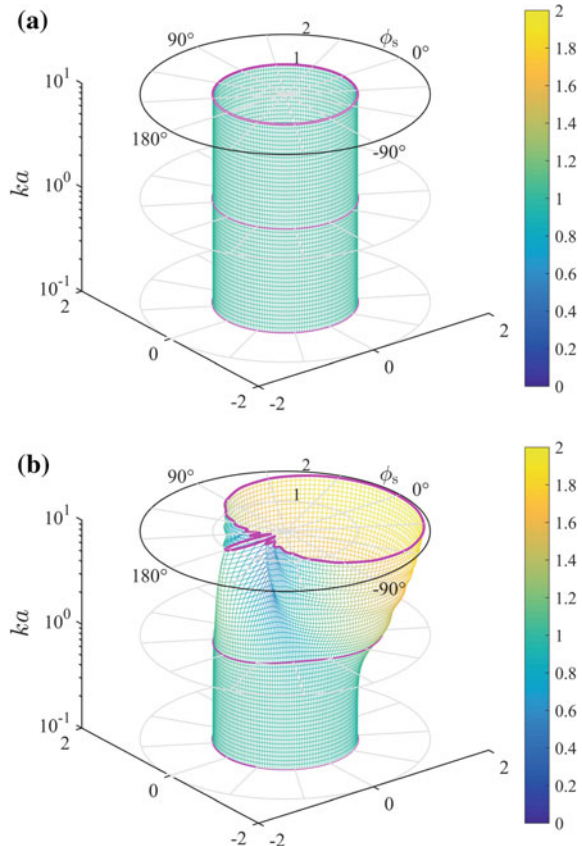
Fig. 8.3 Real and imaginary parts of the spherical harmonics function $Y_n^m(\phi)$ in the range $0 \leq n \leq 4$ with $0 \leq m \leq n$, with light shades indicating positive values and dark shades indicating negative values

For the rigid spherical aperture, as shown in Fig. 8.4b, the magnitude response remains almost constant at low frequencies (when the value of ka is small), which indicates that the scattering of the rigid sphere can be neglected in this case. At high frequencies, the magnitude response of the manifold function is larger (close to 2 at $ka = 10$) when the signal arrives from the sunny side ($\phi_s = 0^\circ$), while it is smaller when the sensor is in a different side of the signal direction due to the acoustic scattering. This indicates that a sensor on a rigid sphere has a non-isotropic element pattern, which is similar to the baffled circular array.

8.2.3 Phase-Mode Beamformer

Assume that the spherical aperture has a weighting function $w^*(ka, \Phi)$ corresponding to the point (a, Φ) . The frequency-wavenumber response (or beam response) function, denoted by $B(ka, \Omega)$, can be given by the integral of the product between the manifold function and the weighting function over the entire sphere surface S^2 , then

Fig. 8.4 Manifold function $|p(ka, \Phi_0, \Omega_s)|$ with $\Phi_0 = (0^\circ, 0^\circ)$ in the ranges $-180^\circ \leq \phi_s \leq 180^\circ$ and $0.1 \leq ka \leq 10$ for **a** open spherical aperture and **b** rigid spherical aperture



$$B(ka, \Omega) = \int_{\Phi \in S^2} p(ka, \Phi, \Omega) w^*(ka, \Phi) d\Phi. \quad (8.22)$$

Let W_{nm} be the spherical harmonics transform of w . Using the spherical harmonics transform pair described in Eqs. (8.4) and (8.5), we have

$$w(ka, \Phi) = \sum_{n=0}^{\infty} \sum_{m=-n}^n W_{nm}(ka) Y_n^m(\Phi), \quad (8.23)$$

$$W_{nm}(ka) = \int_{\Phi \in S^2} w(ka, \Phi) [Y_n^m(\Phi)]^* d\Phi. \quad (8.24)$$

Substituting Eqs. (8.23) and (8.9) into Eq. (8.22) gives

$$B(ka, \Omega) = \int_{\Phi \in S^2} \left\{ \sum_{n=0}^{\infty} \sum_{m=-n}^n b_n(ka) [Y_n^m(\Omega)]^* Y_n^m(\Phi) \right\} \cdot \left\{ \sum_{n=0}^{\infty} \sum_{m=-n}^n [W_{nm}(ka)]^* [Y_n^m(\Phi)]^* \right\} d\Phi. \quad (8.25)$$

Using the orthogonal property shown in Eq. (8.7), Eq. (8.25) can be written as

$$B(ka, \Omega) = \sum_{n=0}^{\infty} \sum_{m=-n}^n [W_{nm}(ka)]^* b_n(ka) [Y_n^m(\Omega)]^* \quad (8.26)$$

$$= \sum_{n=0}^{\infty} \sum_{m=-n}^n [W_{nm}(ka)]^* P_{nm}(ka, \Omega). \quad (8.27)$$

In Eq. (8.27), the beam response function of the spherical array has been expressed in the form of SHD weighted summation. Thus, the SHD beamformer in Eq. (8.27) is equivalent to the element-space beamformer shown in Eq. (8.22).

From Eq. (8.26), we know that $B^*(ka, \Omega)$ and $W_{nm}(ka)b_n^*(ka)$ are a spherical harmonics transform pair. Then

$$W_{nm}(ka)b_n^*(ka) = \int_{\Omega \in S^2} B^*(ka, \Omega) [Y_n^m(\Omega)]^* d\Omega. \quad (8.28)$$

Thus, if the desired beam response of the spherical aperture is $B_d(ka, \Omega)$, the SHD weighting function can be calculated using Eq. (8.28) as

$$W_{nm}(ka) = \frac{1}{b_n^*(ka)} \int_{\Omega \in S^2} B_d^*(ka, \Omega) [Y_n^m(\Omega)]^* d\Omega. \quad (8.29)$$

Ideally, a pencil beam is required, i.e.,

$$B_d(kr, \theta) = \delta(\Omega - \Omega_0). \quad (8.30)$$

The modal beamformer with the ideal pencil beamshape shown in Eq. (8.30) is referred to as the ideal phase-mode beamformer.

Substituting Eq. (8.30) into Eq. (8.29) gives the ideal phase-mode beamformer weighting function

$$W_{nm,PM}(ka) = \frac{[Y_n^m(\Omega_0)]^*}{b_n^*(ka)}, \quad (8.31)$$

or

$$W_{nm,PM}^*(ka) = \frac{Y_n^m(\Omega_o)}{b_n(ka)}, \quad (8.32)$$

where the subscript “PM” denotes the phase-mode beamformer.

In order to distinguish from the phase-mode beamformer for circular arrays in Chap. 6, the phase-mode beamformer for spherical arrays is referred to as the SH-PM beamformer in this book. For convenience, it is sometimes called the PM beamformer in this chapter when there is no ambiguity.

Substituting Eq. (8.32) into Eq. (8.26) gives the ideal phase-mode beam response

$$\begin{aligned} B_{PM}(ka, \Omega) &= \sum_{n=0}^{\infty} \sum_{m=-n}^n Y_n^m(\Omega_o) [Y_n^m(\Omega)]^* \\ &= \delta(\cos\phi - \cos\phi_o) \delta(\theta - \theta_o). \end{aligned} \quad (8.33)$$

In addition, the spherical harmonics $Y_n^m(\Omega)$ have the property

$$\sum_{m=-n}^n Y_n^m(\Omega_o) [Y_n^m(\Omega)]^* = \frac{2n+1}{4\pi} P_n(\cos\psi), \quad (8.34)$$

where ψ is the angle between Ω_o and Ω . $P_n(\cdot)$ is the Legendre polynomial, which satisfies $P_n(\cdot) = P_n^0(\cdot)$. Substituting Eq. (8.34) into Eq. (8.33) gives

$$B_{PM}(ka, \Omega) = \sum_{n=0}^{\infty} \frac{2n+1}{4\pi} P_n(\cos\psi). \quad (8.35)$$

It is seen from Eq. (8.35) that this beam pattern is a function of angle ψ and is independent of the direction Ω . In other words, we only need to change Ω_o to adjust the steering direction, i.e., the beamformer decouples the shaping and the steering of array patterns.

When the modal order is finite, assume that the highest modal order is N . Using “ N ” instead of “ ∞ ” in Eq. (8.35) gives

$$B_{PM,N}(ka, \Omega) = \sum_{n=0}^N \frac{2n+1}{4\pi} P_n(\cos\psi). \quad (8.36)$$

Letting $\Omega_o = (0^\circ, 0^\circ)$, then the angle between Ω_o and Ω is $\psi = \phi$, the elevation angle of Ω . Assume that the highest modal order is chosen to be $N = 0, 1, 2, 4, 8$ and 100 , respectively. Using Eq. (8.36), the magnitudes of the phase-mode beam patterns $|B_{PM,N}(ka, \Omega)|$ are calculated and normalized so that the responses on the steering direction are unity, as shown in Fig. 8.5.

It is seen that when $N = 0$, the beam pattern is a unit circle, i.e., there is no directivity. As N increases, the mainlobe pattern gradually narrows and approaches

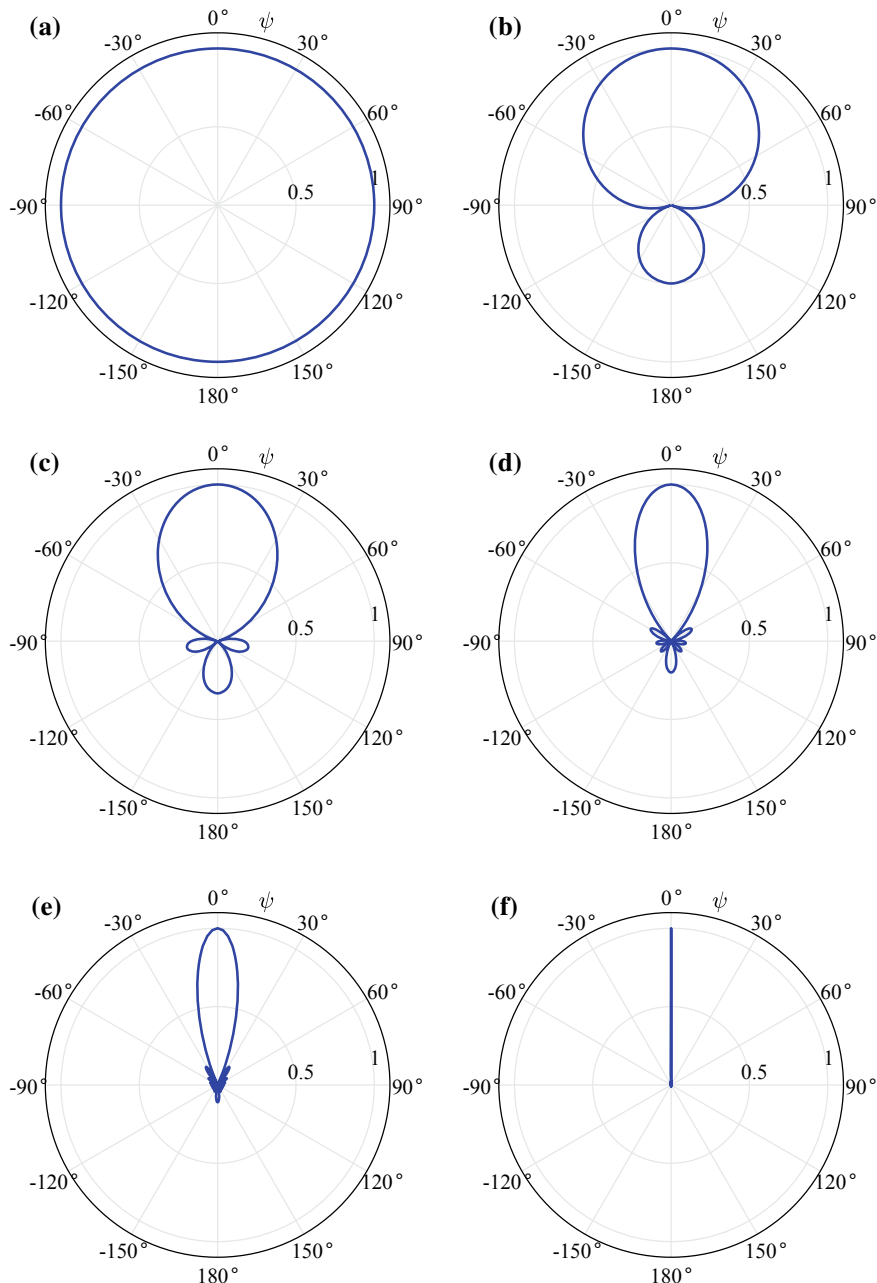
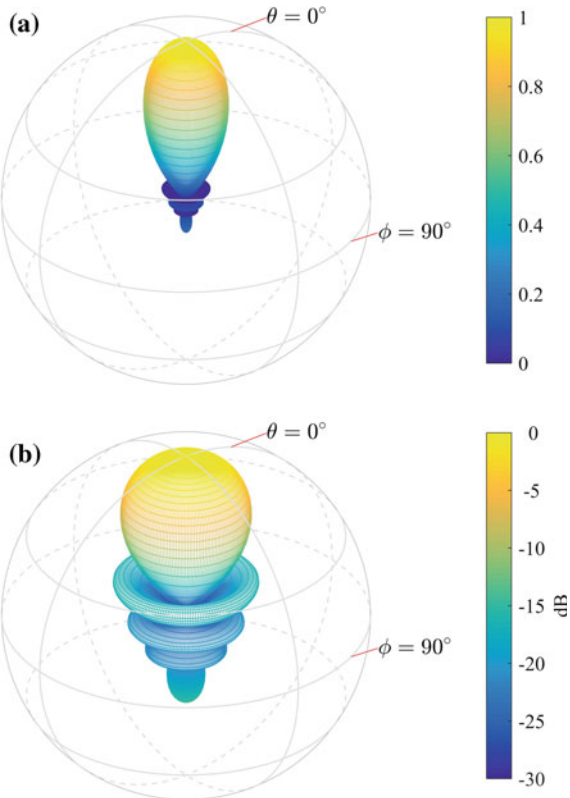


Fig. 8.5 Phase-mode beam pattern $|B_{PM,N}(ka, \Omega)|$ for **a** $N = 0$, **b** $N = 1$, **c** $N = 2$, **d** $N = 4$, **e** $N = 8$, **f** $N = 100$

Fig. 8.6 Phase-mode beam pattern $|B_{PM,4}(ka, \Omega)|$



the ideal pencil beam. In order to obtain a sharp pencil beam, a large value of N is required.

When $N = 4$, the three-dimensional plot of the phase-mode beam pattern $B_{PM,N}(ka, \Omega)$ is shown in Fig. 8.6a. The beam pattern is rotationally symmetric about the z -axis and is identical at all frequencies. The beam pattern in Fig. 8.6a is plotted in dB, as shown in Fig. 8.6b.

Note that b_n appears in the denominator of the weights in Eq. (8.32), which is similar to the phase-mode beamformer for circular array described in Chap. 6. Similar to the circular array, it is seen from Fig. 8.2 that the value of b_n decreases significantly as n increases at low frequencies. Thus, for the ideal phase-mode beamformer, the weights corresponding to the high-order spherical harmonics increase significantly at low frequencies, which results in a small WNG and poor robustness of the beamformer. In addition, for the open spherical aperture, b_n is 0 at some frequencies, which leads to infinite weights that cannot be achieved.

8.2.4 Modal Representation of DAS Beamformer

Consider the DAS beamformer for open spherical apertures. Assume that a plane wave impinges from $\Omega_s = (\theta_s, \phi_s)$ and the steering direction is $\Omega_o = (\theta_o, \phi_o)$. The sound pressure in Eq. (8.3) is delayed and then integrated over the sphere surface to obtain the beamformer output

$$y(ka, \Omega_s) = \int_{\Phi \in S^2} \exp[-ik^T(\Omega_s)\mathcal{P}_\Phi] \exp[ik^T(\Omega_o)\mathcal{P}_\Phi] d\Phi. \quad (8.37)$$

Using Eq. (8.9), we have

$$\exp[-ik^T(\Omega_s)\mathcal{P}_\Phi] = \sum_{n=0}^{\infty} b_n(ka) \sum_{m=-n}^n [Y_n^m(\Omega_s)]^* Y_n^m(\Phi), \quad (8.38)$$

where b_n is the modal response for the open sphere given in Eq. (8.11).

Using Eq. (8.38), Eq. (8.37) can be rewritten as [11]

$$y(ka, \Omega_s) = \int_{\Phi \in S^2} \left\{ \sum_{n=0}^{\infty} b_n(ka) \sum_{m=-n}^n [Y_n^m(\Omega_s)]^* Y_n^m(\Phi) \right\} \cdot \left\{ \sum_{n=0}^{\infty} b_n^*(ka) \sum_{m=-n}^n Y_n^m(\Omega_o) [Y_n^m(\Phi)]^* \right\} d\Phi. \quad (8.39)$$

Using the orthogonal property Eq. (8.7), Eq. (8.39) reduces to

$$y(ka, \Omega_s) = \sum_{n=0}^{\infty} |b_n(ka)|^2 \sum_{m=-n}^n [Y_n^m(\Omega_s)]^* Y_n^m(\Omega_o). \quad (8.40)$$

Using Eq. (8.34) gives

$$y(ka, \Omega_s) = \sum_{n=0}^{\infty} |b_n(ka)|^2 \frac{2n+1}{4\pi} P_n(\cos \psi_s), \quad (8.41)$$

where ψ_s is the angle between Ω_s and Ω_o .

According to the definition of the beam response function, the SHD beam response can be obtained by replacing the Ω_s in Eq. (8.40) with Ω as

$$B_{DAS}(ka, \Omega) = \sum_{n=0}^{\infty} \sum_{m=-n}^n \{b_n(ka)[Y_n^m(\Omega)]^*\} \{b_n^*(ka)Y_n^m(\Omega_o)\} \quad (8.42)$$

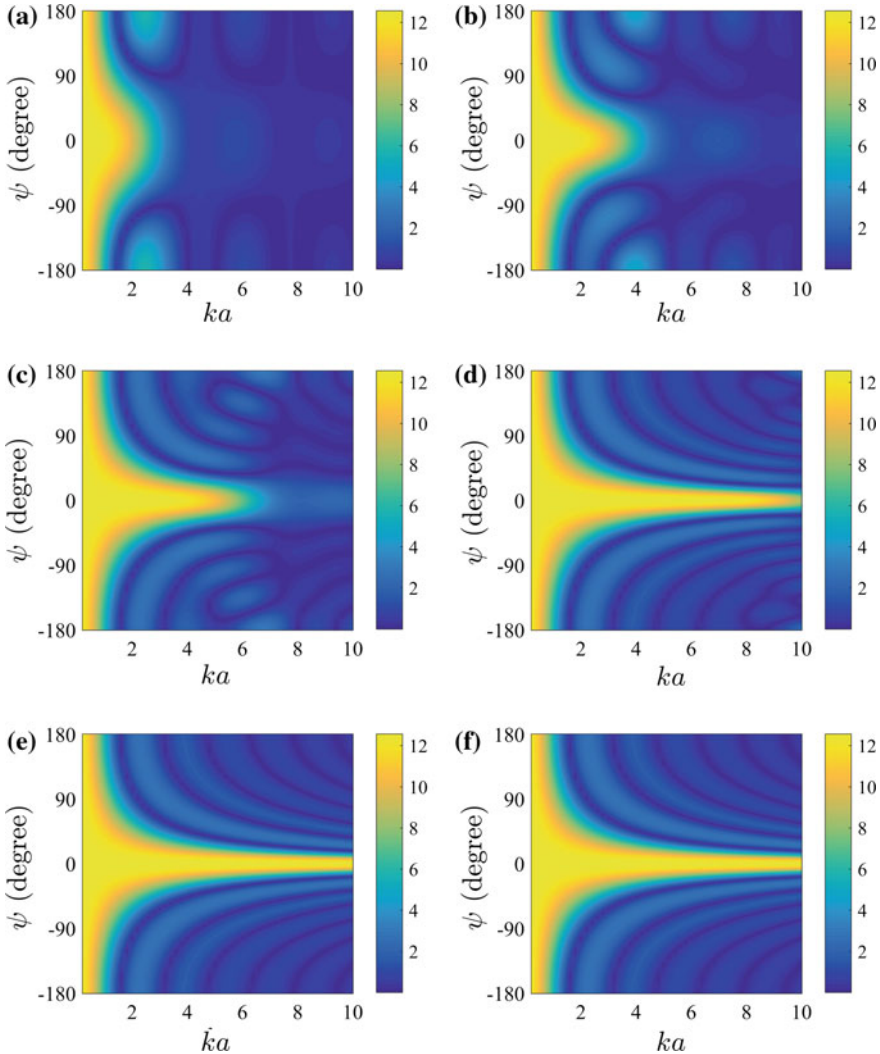


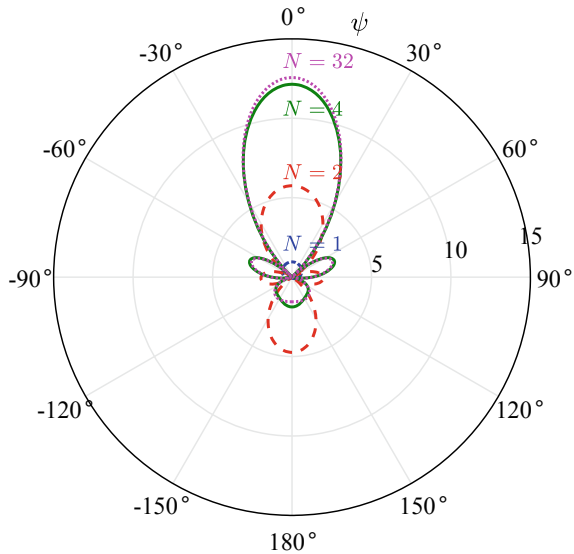
Fig. 8.7 SHD DAS beam patterns $|B_{\text{DAS},N}(ka, \Omega)|$. **a** $N = 1$, **b** $N = 2$, **c** $N = 4$, **d** $N = 8$, **e** $N = 16$, **f** $N = 32$

$$= \sum_{n=0}^{\infty} |b_n(ka)|^2 \frac{2n+1}{4\pi} P_n(\cos \psi), \quad (8.43)$$

where ψ is the angle between Ω and Ω_0 .

Comparing Eqs. (8.42) and (8.26), the SHD weights of the DAS beamformer can be given by

Fig. 8.8 SHD DAS beam pattern $|B_{\text{DAS},N}(ka, \Omega)|$ with $ka = 4$ and $N = 1, 2, 4, 32$



$$W_{nm,\text{DAS}}(ka) = b_n(ka) [Y_n^m(\Omega_0)]^* \quad (8.44)$$

Substituting Eq. (8.44) into Eq. (8.43) and using “ N ” instead of “ ∞ ” gives

$$B_{\text{DAS},N}(ka, \Omega) = \sum_{n=0}^N |b_n(ka)|^2 \frac{2n+1}{4\pi} P_n(\cos \psi), \quad (8.45)$$

which is the SHD representation of the DAS beamformer response.

Consider the open spherical aperture. Using Eq. (8.45), the magnitudes of the SHD DAS beam patterns, i.e., $|B_{\text{DAS},N}(ka, \Omega)|$, versus ka in the range $(0, 10]$ and ψ in the range $[-180^\circ, 180^\circ]$ for various values of N are shown in Fig. 8.7. Noting that the beam patterns here are not normalized.

It is seen from Fig. 8.7 that, as the highest order N increases, the beam pattern approaches the ideal beam pattern (for $N = \infty$). For a given order N , a good approximation is obtained for $ka \leq N$. In other words, in order to obtain the beam pattern at ka , the highest order is required to satisfy $N \geq ka$.

The beam patterns for $ka = 4$ are shown in Fig. 8.8, where the modal order is chosen as $N = 1, 2, 4, 32$, respectively. It is seen that as the order N increases, the beam pattern gradually converges. When $N = ka = 4$, the beam pattern approaches that with $N = 32$. Therefore, when calculating the SHD beam response, in order to ensure a certain accuracy, the highest order is generally chosen as $N = ka$.

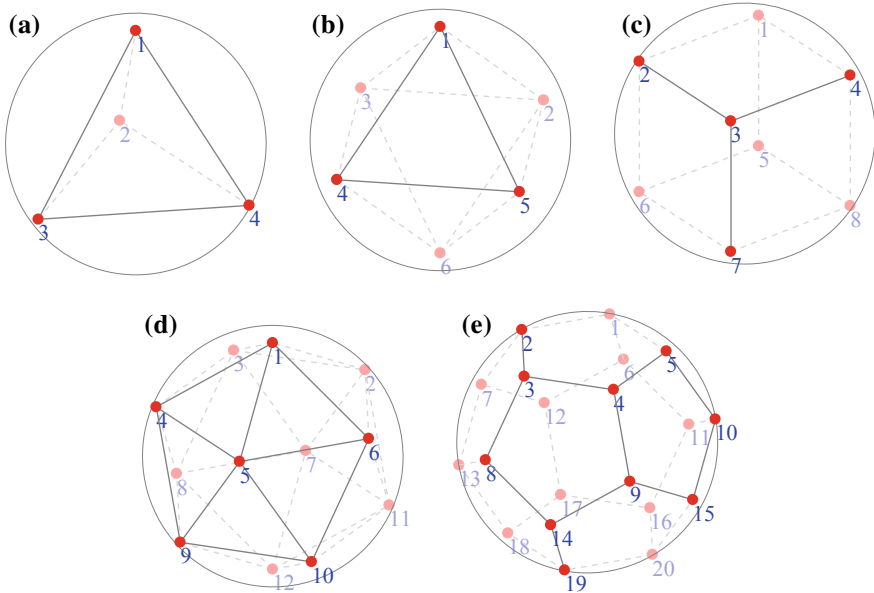


Fig. 8.9 Platonic solids. **a** tetrahedron ($M = 4$), **b** octahedron ($M = 6$), **c** cube ($M = 8$), **d** icosahedron ($M = 12$), **e** dodecahedron ($M = 20$)

8.3 Spherical Arrays

8.3.1 Nearly-Uniform Spherical Arrays

In practical applications, the continuous spherical arrays are sampled by means of a finite number of sensors. In this chapter, we assume that this sampling is performed by equispaced omnidirectional microphones.

In order to be able to extract three-dimensional sound field information well using the spherical array, it is generally desirable that the sensor be uniformly distributed on the spherical surface. It should be noted, however, that this can only be achieved for specific values of M , since the true equidistant spatial sampling is only possible for arrangements that are constructed according to the so-called Platonic solids or regular polyhedrons.

It has been proven that only five such geometries exist, i.e., tetrahedron ($M = 4$), octahedron ($M = 6$), cube ($M = 8$), icosahedron ($M = 12$), and dodecahedron ($M = 20$), as shown in Fig. 8.9. Note that each vertex of the cube is exactly at the direction of each face center of the octahedron, and vice versa. Each vertex of the dodecahedron is exactly at the direction of each face center of the icosahedron, and vice versa.

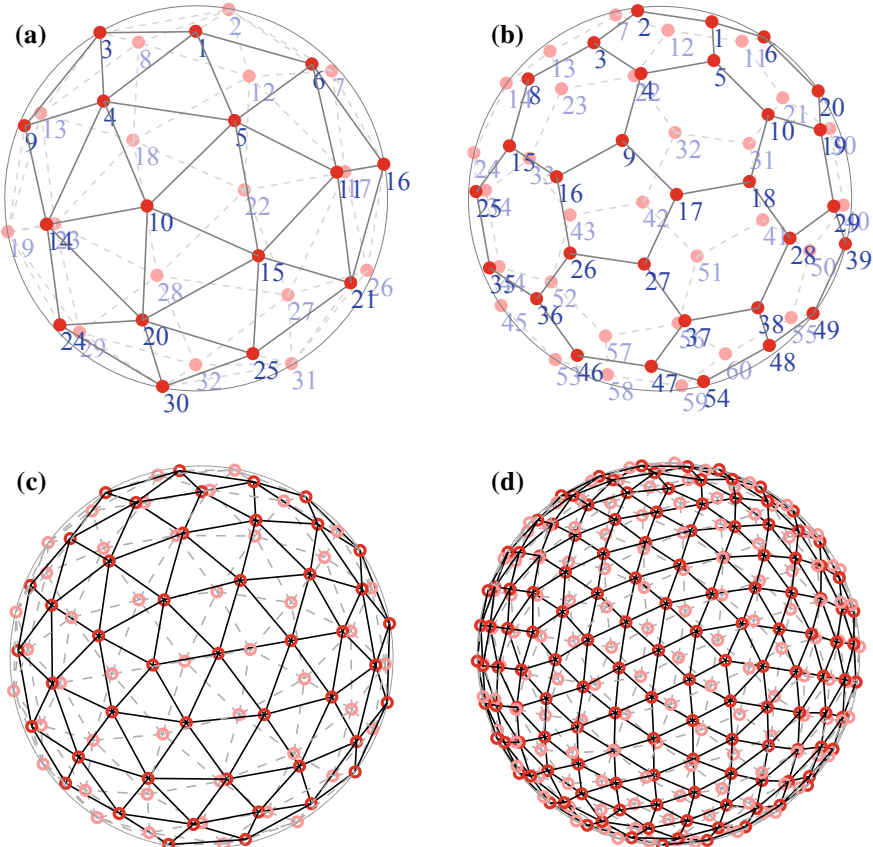
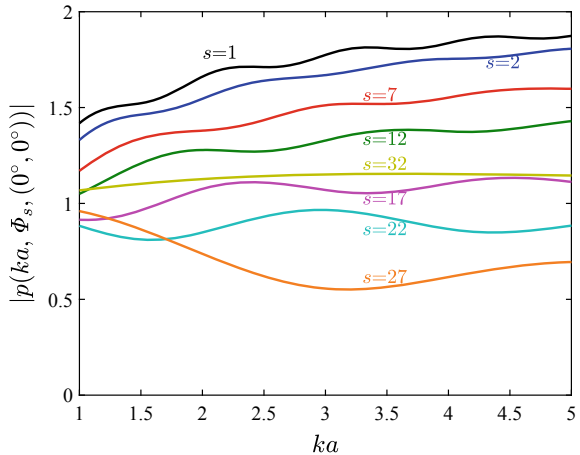


Fig. 8.10 Nearly-uniform sampling distribution. **a** $M = 32$, **b** $M = 60$, **c** $M = 92$, **d** $M = 272$

Several arrangements that provide a nearly-uniform sampling scheme are shown in Fig. 8.10. Figure 8.10b shows a truncated icosahedron, who has 32 faces (12 regular pentagonal faces and 20 regular hexagonal faces), 60 vertices and 90 edges. We can place $M = 32$ microphones at the centers of the faces of the truncated icosahedron, as shown in Fig. 8.10a, in which these 32 vertices also happen to be the 32 vertices obtained by combining Fig. 8.9d with Fig. 8.9e. By combining Fig. 8.10a, b, 92 vertices can be obtained, as shown in Fig. 8.10c. In Fig. 8.10d, there are 272 spherically uniformly distributed vertices.

Consider a 32-element rigid spherical array, as shown in Fig. 8.10a. The directions of the microphones on the spherical surface are $\Phi_s = (\vartheta_s, \varphi_s)$, $s = 1, \dots, M$. A far field broadband plane-wave signal impinges on the microphone array from $\Omega_s = (\theta_s, \phi_s) = (0^\circ, 0^\circ)$. The manifold response $p(ka, \Phi_s, \Omega_s)$ of the sensor at $\Phi_s = (\vartheta_s, \varphi_s)$ to a unit magnitude signal impinging from $\Omega_s = (0^\circ, 0^\circ)$ can be obtained using the same method as in Fig. 8.4b.

Fig. 8.11 Magnitude of manifold function $|p(ka, \Phi_s, (0^\circ, 0^\circ))|$ as a function of ka for rigid spherical array



The magnitude of the manifold function $|p(ka, \Phi_s, \Omega_s)|$ as a function of ka over the range $1 \leq ka \leq 5$ is plotted in Fig. 8.11. Due to the symmetry of the spherical array, only the manifold functions of 8 microphones (i.e., $s = 1, 2, 7, 12, 17, 22, 27$ and 32) are plotted in this figure.

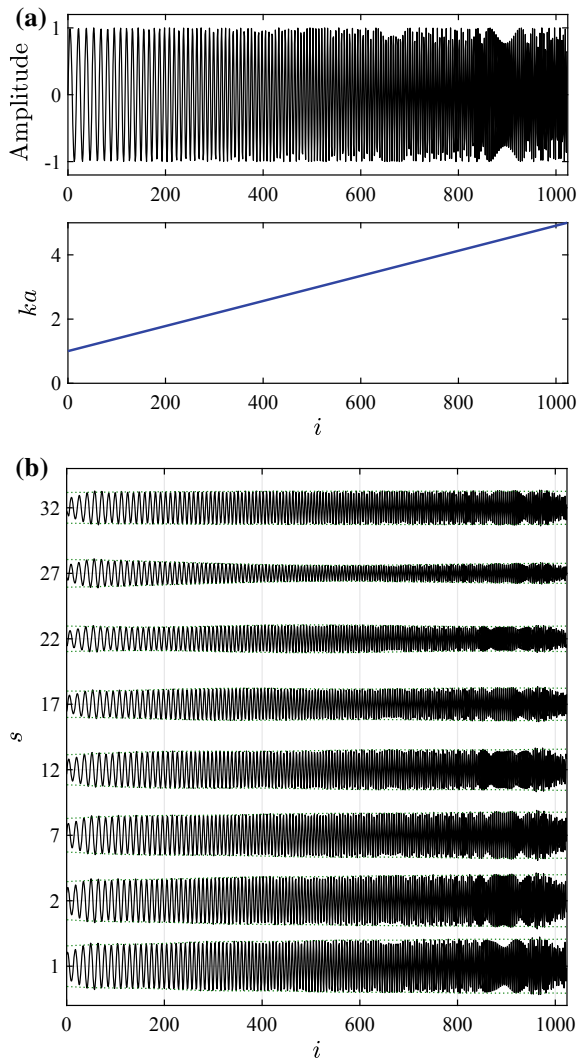
Assume that the far field plane-wave signal is an LFM signal, whose frequency f satisfies $ka = 2\pi f a/c \in [1, 5]$ and the sampling frequency f_s satisfies $2\pi f_s a/c = 18$. The sample length is $T \cdot f_s = 1024$. The waveform of the source signal generated using Eq. (2.49) is shown in the upper plot of Fig. 8.12a, and the corresponding instantaneous frequency is shown in the lower plot. Here, we use “ i ” as the index of the time series.

The waveforms of the signals received by the 8 microphones are calculated and shown in Fig. 8.12b. When the incident signal is an LFM signal, the magnitude responses of each microphone shown in Fig. 8.11 are exactly the ideal envelopes of the received signals. The envelopes are plotted in Fig. 8.12b by dashed lines. It is seen that most of the waveforms match the ideal envelope well except for both ends of the signal. The scattering effect of the rigid sphere can be observed clearly from Figs. 8.11 and 8.12.

8.3.2 Spherical-Harmonics-Domain (SHD) Beamformer

For the aforementioned spherical aperture, the received sound pressure can be converted into the spherical harmonics domain using the orthogonality of spherical harmonics shown in Eq. (8.7). However, for the spherical array, especially those whose elements are not strictly uniformly distributed, the orthogonality shown in Eq. (8.7) is no longer satisfied. In this case, in order to convert the received sound pressure into the spherical harmonics domain, some weighting operations are required to be

Fig. 8.12 Signals received by the rigid spherical array. **a** LFM source signal and the corresponding instantaneous frequency. **b** Waveforms received by 8 microphones ($s = 1, 2, 7, 12, 17, 22, 27$ and 32)



performed. We require that the sensor positions fulfill the discrete orthonormality condition

$$\sum_{s=1}^M \alpha_s Y_{\tilde{n}}^{\tilde{m}}(\Phi_s) [Y_n^m(\Phi_s)]^* = \delta_{n-\tilde{n}} \delta_{m-\tilde{m}}, \quad (8.46)$$

where α_s is a real value which depends on the sampling scheme. For uniform sampling, in order that

$$\sum_{s=1}^M \alpha_s = \int_{\Phi \in S^2} d\Phi = 4\pi, \quad (8.47)$$

it gives

$$\alpha_s = 4\pi/M. \quad (8.48)$$

To simplify the analysis, in this book, we assume that the microphones are equidistantly spaced and in this case, $\alpha_s = 4\pi/M$. For the spherical array using the nearly-uniform sampling scheme, we also use $\alpha_s = 4\pi/M$ to approximate.

In order to compute up to N th-order spherical harmonics, the number of sensors M should satisfy

$$M \geq (N + 1)^2 \quad (8.49)$$

to avoid spatial aliasing. The reader is referred to the paper by Rafaely et al. [5] for a comprehensive analysis of spatial aliasing. In this book, we assume that the aliasing is negligible, i.e., the higher orders in the spherical harmonics transform domain are not aliased onto the lower orders.

The first step in a spherical harmonics based array processing is to compute the spherical Fourier transform of the pressure on the sphere. From Eqs. (8.5) and (8.4), under the weighted orthonormality condition shown in Eq. (8.46), the spherical Fourier coefficients $P_{nm}(ka, \Omega)$ can be estimated as

$$\hat{P}_{nm}(ka, \Omega) = \sum_{s=1}^M \alpha_s p(ka, \Phi_s, \Omega) [Y_n^m(\Phi_s)]^*, \quad (8.50)$$

and

$$p(ka, \Phi_s, \Omega) \approx \sum_{n=0}^N \sum_{m=-n}^n \hat{P}_{nm}(ka, \Omega) Y_n^m(\Phi_s). \quad (8.51)$$

Equation (8.50) is referred to as the discrete spherical harmonics transform, and Eq. (8.51) is its inverse transform.

In what follows we no longer distinguish between $\hat{P}_{nm}(ka, \Omega)$ and $P_{nm}(ka, \Omega)$, and use “=” instead of “ \approx ” in Eq. (8.51) for simplicity.

Assume that $w^*(ka, \Phi_s)$ are the array weights and $W_{nm}^*(ka)$ are their spherical Fourier coefficients, i.e.,

$$W_{nm}(ka) = \sum_{s=1}^M \alpha_s w(ka, \Phi_s) [Y_n^m(\Phi_s)]^*, \quad (8.52)$$

$$w(ka, \Phi_s) = \sum_{n=0}^N \sum_{m=-n}^n W_{nm}(ka) Y_n^m(\Phi_s). \quad (8.53)$$

Then, the corresponding array output can be calculated by

$$\begin{aligned} & \sum_{s=1}^M \alpha_s p(ka, \Phi_s, \Omega) w^*(ka, \Phi_s) \\ &= \sum_{s=1}^M \alpha_s \left\{ \sum_{n=0}^N \sum_{m=-n}^n P_{nm}(ka, \Omega) Y_n^m(\Phi) \right\} \\ & \quad \cdot \left\{ \sum_{n=0}^N \sum_{m=-n}^n W_{nm}^*(ka) [Y_n^m(\Phi)]^* \right\} \\ &= \sum_{n=0}^N \sum_{m=-n}^n P_{nm}(ka, \Omega) W_{nm}^*(ka). \end{aligned} \quad (8.54)$$

The orthogonality shown in Eq. (8.46) has been used in the derivation in Eq. (8.54). It is seen from Eq. (8.54) that the element-space and the SHD weighted summations are equivalent.

The beam pattern can then be defined as

$$B(ka, \Omega) \triangleq \sum_{s=1}^M \alpha_s p(ka, \Phi_s, \Omega) w^*(ka, \Phi_s) \quad (8.55)$$

$$= \sum_{n=0}^N \sum_{m=-n}^n P_{nm}(ka, \Omega) W_{nm}^*(ka). \quad (8.56)$$

It is worth noting that there is a weighting factor α_s in the beam pattern expression in Eq. (8.55) compared to those in the previous chapters.

Define $w_s(ka) \triangleq w(ka, \Phi_s)$ and $p_s(ka, \Omega) \triangleq p(ka, \Phi_s, \Omega)$ for $s = 1, \dots, M$. We can further define three $M \times 1$ column vectors

$$\boldsymbol{\alpha} \triangleq [\alpha_1, \dots, \alpha_l, \dots, \alpha_M]^T, \quad (8.57)$$

$$\mathbf{w}_e(ka) \triangleq [w_1(ka), \dots, w_s(ka), \dots, w_M(ka)]^T, \quad (8.58)$$

$$\mathbf{p}_e(ka, \Omega) \triangleq [p_1(ka, \Omega), \dots, p_s(ka, \Omega), \dots, p_M(ka, \Omega)]^T, \quad (8.59)$$

where the subscript “e” denotes the element-space.

Equation (8.55) can then be rewritten as

$$B(ka, \Omega) = [\boldsymbol{\alpha} \circ \mathbf{w}_e(ka)]^H \mathbf{p}_e(ka, \Omega), \quad (8.60)$$

where “ \circ ” denotes the Hadamard product (i.e., the dot product) of two vectors. For the uniform spherical array, $\boldsymbol{\alpha} = (4\pi/M) \cdot \mathbf{1}_{M \times 1}$, where $\mathbf{1}_{M \times 1}$ is an $M \times 1$ column vector of ones.

Introduce an operator $\text{vec}(\cdot)$, which denotes stacking all the entries in the parentheses to obtain a column vector. Using this notation, we can further define two $(N+1)^2 \times 1$ column vectors

$$\begin{aligned} \mathbf{w}_h(ka) &\triangleq \text{vec}\left(\left\{[W_{nm}(ka)]_{m=-n}^n\right\}_{n=0}^N\right) \\ &= [W_{00}, W_{1-1}, W_{10}, W_{11}, \dots, W_{nm}, \dots, W_{NN}]^T, \end{aligned} \quad (8.61)$$

$$\mathbf{p}_h(ka, \Omega) \triangleq \text{vec}\left(\left\{[P_{nm}(ka, \Omega)]_{m=-n}^n\right\}_{n=0}^N\right), \quad (8.62)$$

where the subscript “ h ” denotes the spherical harmonics domain, \mathbf{w}_h and \mathbf{p}_h represent the SHD weight vector and array manifold vector, respectively. Then, Eq. (8.56) can be written in vector notation as

$$B(ka, \Omega) = \mathbf{w}_h^H(ka) \mathbf{p}_h(ka, \Omega). \quad (8.63)$$

Using Eqs. (8.60) and (8.63) gives

$$B(ka, \Omega) = [\boldsymbol{\alpha} \circ \mathbf{w}_e(ka)]^H \mathbf{p}_e(ka, \Omega) = \mathbf{w}_h^H(ka) \mathbf{p}_h(ka, \Omega). \quad (8.64)$$

Applying the Parseval’s relation for the discrete spherical harmonics transform to the weights, we have

$$\sum_{s=1}^M \alpha_s |w(ka, \Phi_s)|^2 \approx \sum_{n=0}^N \sum_{m=-n}^n |W_{nm}(ka)|^2. \quad (8.65)$$

Defining an $M \times 1$ column vector

$$\mathbf{Y}_n^m = [\alpha_1 Y_n^m(\Phi_1), \dots, \alpha_s Y_n^m(\Phi_s), \dots, \alpha_M Y_n^m(\Phi_M)]^T, \quad (8.66)$$

Equation (8.50) can be rewritten in matrix notation as

$$P_{nm}(ka, \Omega) = (\mathbf{Y}_n^m)^H \mathbf{p}_e(ka, \Omega). \quad (8.67)$$

We now define an $M \times (N+1)^2$ matrix

$$\mathbf{T} = [\mathbf{Y}_0^0, \mathbf{Y}_1^{-1}, \mathbf{Y}_1^0, \mathbf{Y}_1^1, \dots, \mathbf{Y}_n^m, \dots, \mathbf{Y}_N^N], \quad (8.68)$$

which is referred to as the spherical harmonics transform matrix.

Then, using Eqs. (8.62) and (8.67), we have

$$\mathbf{p}_h(ka, \Omega) = \mathbf{T}^H \mathbf{p}_e(ka, \Omega). \quad (8.69)$$

Substituting Eq. (8.69) into Eq. (8.63), gives

$$B(ka, \Omega) = \mathbf{w}_h^H(kr) \mathbf{T}^H \mathbf{p}_e(ka, \Omega). \quad (8.70)$$

Note that there is a weighting vector α in the element-space beam pattern expression in Eq. (8.60) compared to those in the previous chapters. In this book, we assume that $\alpha = (4\pi/M) \cdot \mathbf{1}_{M \times 1}$. In order to ensure the consistency of the book, from Eq. (8.60), the element-space distortionless constraint for spherical arrays can be rewritten as

$$B(ka, \Omega_0) = (4\pi/M) \mathbf{w}_e^H(ka) \mathbf{p}_e(ka, \Omega_0) = 4\pi/M. \quad (8.71)$$

Correspondingly, from Eq. (8.64), the SHD distortionless constraint becomes

$$B(ka, \Omega_0) = \mathbf{w}_h^H(ka) \mathbf{p}_h(ka, \Omega_0) = 4\pi/M. \quad (8.72)$$

Note that the right side of the SHD distortionless constraint shown in Eq. (8.72) is $4\pi/M$, in contrast to the conventional element-space case, which is 1.

8.3.3 SHD Beamformer Structure

Consider an M -element spherical array. A plane-wave desired signal and D plane-wave interfering signals arrive from directions Ω_s and Ω_d , $d = 1, \dots, D$, respectively. Adding uncorrelated noise, the sound pressure received by the s th microphone can be written as

$$\begin{aligned} x_s(ka) &\triangleq x(ka, \Phi_s) = \beta p(ka, \Phi_s, \Omega_s) S_s(\omega) \\ &\quad + \sum_{d=1}^D p(ka, \Phi_s, \Omega_d) S_d(\omega) + N(ka, \Phi_s), \end{aligned} \quad (8.73)$$

where $S_s(\omega)$ and $\{S_d(\omega)\}_{d=1}^D$ are the $D + 1$ source signal spectra, $N(ka, \Phi_s)$ is the additive noise spectrum, and β is a binary parameter indicating whether the SOI is present or not.

The element-space array data can be written in vector notation as

$$\mathbf{x}_e(ka) \triangleq [x_1(ka), \dots, x_s(ka), \dots, x_M(ka)]^T. \quad (8.74)$$

The SHD representation of Eq. (8.73) is given by

$$X_{nm}(ka) = \beta P_{nm}(ka, \Omega_s) S_s(\omega) + \sum_{d=1}^D P_{nm}(ka, \Omega_d) S_d(\omega) + N_{nm}(ka), \quad (8.75)$$

where $N_{nm}(ka)$ is the SHD representation of the noise.

For the spherical arrays, $X_{nm}(ka)$ can be obtained using the discrete spherical harmonics transform as

$$X_{nm}(ka) = \sum_{s=1}^M \alpha_s x_s(ka) [Y_n^m(\Phi_s)]^*. \quad (8.76)$$

Define an $(N + 1)^2 \times 1$ SHD array data vector

$$\mathbf{x}_h(ka) = \text{vec}\left(\{[X_{nm}(ka)]_{m=-n}^n\}_{n=0}^N\right), \quad (8.77)$$

then

$$\mathbf{x}_h(ka) = \mathbf{T}^H \mathbf{x}_e(ka), \quad (8.78)$$

where \mathbf{T} is the spherical harmonics transform matrix defined by Eq. (8.68).

The beamformer output of the spherical array can then be calculated in both element-space and spherical harmonics domain as

$$y(ka) = [\boldsymbol{\alpha} \circ \mathbf{w}_e(ka)]^H \mathbf{x}_e(ka) = \mathbf{w}_h^H(ka) \mathbf{x}_h(ka). \quad (8.79)$$

In summary, a general SHD beamformer structure can be obtained, as shown in Fig. 8.13. This structure consists of two parts: spherical harmonics transform (SHT) and SHD weighted summation.

8.3.4 Performance Measures in Spherical Harmonics Domain

1. Data Covariance Matrix

The beamformer output power is given by

$$\begin{aligned} P_{\text{out}}(ka) &= E[y(ka)y^*(ka)] \\ &= \mathbf{w}_h^H(ka) E[\mathbf{x}_h(ka) \mathbf{x}_h^H(ka)] \mathbf{w}_h(ka) \\ &= \mathbf{w}_h^H(ka) \mathbf{R}_h(ka) \mathbf{w}_h(ka), \end{aligned} \quad (8.80)$$

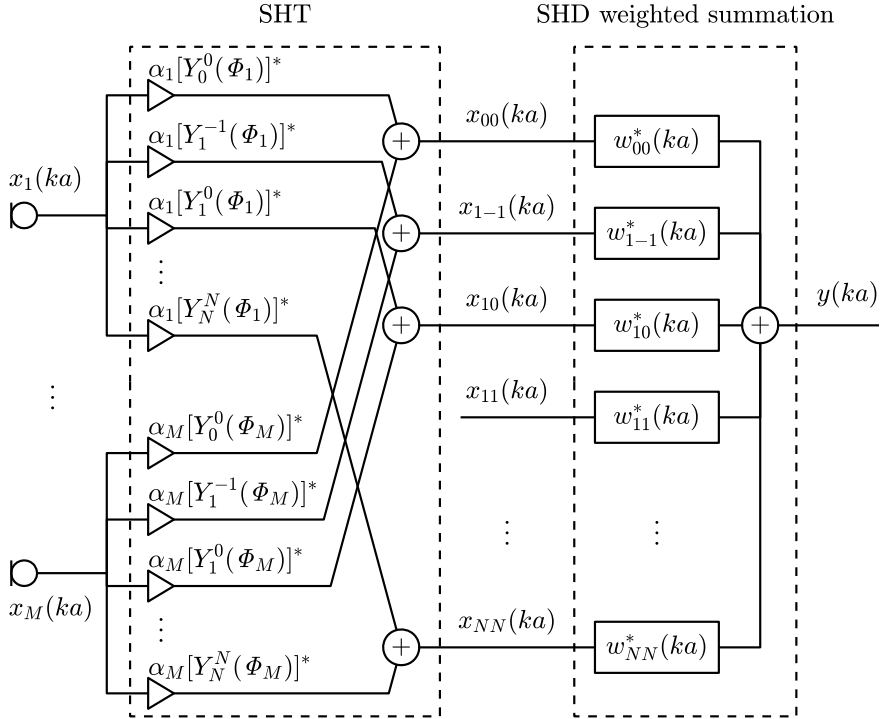


Fig. 8.13 SHD beamformer structure

where $\mathbf{R}_h(ka)$ is the $(N + 1)^2 \times (N + 1)^2$ covariance matrix (spectral matrix) of $\mathbf{x}_h(ka)$. Assuming that the signal sources are uncorrelated from each other, the covariance matrix has the following form:

$$\begin{aligned} \mathbf{R}_h(ka) &= E[\mathbf{x}_h(ka)\mathbf{x}_h^H(ka)] \\ &= \beta^2 \sigma_s^2 \mathbf{p}_h(ka, \Omega_s) \mathbf{p}_h^H(ka, \Omega_s) \\ &\quad + \sum_{d=1}^D \sigma_d^2 \mathbf{p}_h(ka, \Omega_d) \mathbf{p}_h^H(ka, \Omega_d) + \mathbf{Q}_{hn}(ka), \end{aligned} \quad (8.81)$$

where σ_s^2 and $\{\sigma_d^2\}_{d=1}^D$ are the variances (powers) of the $D + 1$ uncorrelated signal and interferers, and $\mathbf{Q}_{hn}(ka)$ is the SHD noise covariance matrix

$$\mathbf{Q}_{hn}(ka) = E[N(ka)N^H(ka)] = \sigma_n^2 \rho_{hn}(ka), \quad (8.82)$$

where σ_n^2 is the noise power, $\rho_{hn}(ka)$ is the SHD normalized noise covariance matrix, and

$$\mathbf{N} = \text{vec}\left(\left\{[N_{nm}]_{m=-n}^n\right\}_{n=0}^N\right). \quad (8.83)$$

In practical applications, the theoretical covariance matrix $\mathbf{R}_h(ka)$ is unavailable. Therefore, the sample covariance matrix

$$\begin{aligned} \widehat{\mathbf{R}}_h(ka) &= \frac{1}{\mathcal{L}} \sum_{\ell=1}^{\mathcal{L}} \mathbf{x}_h(ka, \ell) \mathbf{x}_h^H(ka, \ell) \\ &= \mathbf{T}^H \left[\frac{1}{\mathcal{L}} \sum_{\ell=1}^{\mathcal{L}} \mathbf{x}_e(ka, \ell) \mathbf{x}_e^H(ka, \ell) \right] \mathbf{T}, \end{aligned} \quad (8.84)$$

is usually used instead of Eq. (8.81). Here, \mathcal{L} is the number of training snapshots (also termed the training sample size), the argument “ ℓ ” denotes the time-domain sample (or snapshot) index, and $\mathbf{x}_h(ka, \ell)$ and $\mathbf{x}_e(ka, \ell)$ are the ℓ th snapshot of $\mathbf{x}_h(ka)$ and $\mathbf{x}_e(ka)$, respectively.

2. Noise Covariance Matrix

We derive the SHD noise covariance matrix. Two special cases of noise fields, i.e., spherically isotropic noise and spatially white noise are considered.

We first consider the spherically isotropic noise. Spherically isotropic noise with a unit power spectral density can be viewed as that there are an infinite number of uncorrelated plane waves arriving at the sphere from all directions with uniform power density $1/(4\pi)$. Thus, by integrating the covariance matrix over all directions, the normalized isotropic noise covariance matrix is given by

$$\boldsymbol{\rho}_{\text{iso}}(ka) = \frac{1}{4\pi} \int_{\Phi \in S^2} \mathbf{p}_h(ka, \Omega) \mathbf{p}_h^H(ka, \Omega) d\Omega. \quad (8.85)$$

Define $(N + 1)^2 \times 1$ column vectors

$$\mathbf{b}(ka) = \text{vec}\left(\left\{[b_n(ka)]_{m=-n}^n\right\}_{n=0}^N\right), \quad (8.86)$$

$$\mathbf{Y}(\Omega) = \text{vec}\left(\left\{[Y_n^m(\Omega)]_{m=-n}^n\right\}_{n=0}^N\right). \quad (8.87)$$

Note that in Eq. (8.86), \mathbf{b} has repetitions of b_n from entry $(n^2 + 1)$ through entry $(n + 1)^2$.

Using Eqs. (8.62), (8.86) and (8.87), Eq. (8.10) can be written in vector notation as

$$\mathbf{p}_h(ka, \Omega) = \mathbf{b}(ka) \circ \mathbf{Y}^*(\Omega). \quad (8.88)$$

Substituting Eq. (8.88) into Eq. (8.85) gives

$$\begin{aligned}
\rho_{\text{iso}}(ka) &= \frac{1}{4\pi} \int_{\phi \in S^2} \mathbf{p}_h(ka, \Omega) \mathbf{p}_h^H(ka, \Omega) d\Omega \\
&= \frac{1}{4\pi} \int_{\phi \in S^2} [\mathbf{b}(ka) \circ \mathbf{Y}^*(\Omega)] [\mathbf{b}(ka) \circ \mathbf{Y}^*(\Omega)]^H d\Omega \\
&= \frac{1}{4\pi} \text{diag}\{\mathbf{b}(ka) \circ \mathbf{b}^*(ka)\} \\
&= \frac{1}{4\pi} \text{diag}\{|b_0(ka)|^2, |b_1(ka)|^2, |b_1(ka)|^2, |b_1(ka)|^2, \dots, |b_N(ka)|^2\}.
\end{aligned} \tag{8.89}$$

Note that the spherical harmonic orthonormal property Eq. (8.7) has been employed in the above derivation.

In order to ensure the integrity of the content, the SHD spatially white noise covariance matrix with unit power spectral density derived later is listed here. From the derivation result in Eq. (8.101), the SHD white noise covariance matrix, denoted by $\rho_{\text{hw}}(ka)$, is given by

$$\rho_{\text{hw}}(ka) = \frac{4\pi}{M} \mathbf{I}_{(N+1)^2}, \tag{8.90}$$

where $\mathbf{I}_{(N+1)^2}$ is an $(N+1)^2 \times (N+1)^2$ identity matrix.

3. Array Gain

The array gain $G(ka)$ is defined to be the ratio of the SINR at the output of the array to the SINR at a single input sensor

$$\begin{aligned}
G(ka) &= \frac{\sigma_s^2 |\mathbf{w}_h^H(ka) \mathbf{p}_h(ka, \Omega_s)|^2}{\mathbf{w}_h^H(ka) \mathbf{R}_{h,i+n}(ka) \mathbf{w}_h(ka)} \Big/ \frac{\sigma_s^2}{\sum_{d=1}^D \sigma_d^2 + \sigma_n^2} \\
&= \frac{|\mathbf{w}_h^H(ka) \mathbf{p}_h(ka, \Omega_s)|^2}{\mathbf{w}_h^H(ka) \rho_h(ka) \mathbf{w}_h(ka)},
\end{aligned} \tag{8.91}$$

where $\mathbf{R}_{h,i+n}(ka)$ is the interference-plus-noise covariance matrix, and $\rho_h(ka)$ is the normalized interference-plus-noise covariance matrix, i.e.,

$$\rho_h(ka) = \frac{\mathbf{R}_{h,i+n}(ka)}{\sum_{d=1}^D \sigma_d^2 + \sigma_n^2}. \tag{8.92}$$

The directivity factor $G_D(ka)$, or directive gain, can be interpreted as the array gain against isotropic noise. Replacing $\rho_h(ka)$ in Eq. (8.91) by $\rho_{\text{iso}}(ka)$ gives the directivity factor

$$G_D(ka) = \frac{|\mathbf{w}_h^H(ka) \mathbf{p}_h(ka, \Omega_s)|^2}{\mathbf{w}_h^H(ka) \rho_{\text{iso}}(ka) \mathbf{w}_h(ka)}$$

$$= \frac{4\pi \left| \sum_{n=0}^N \sum_{m=-n}^n P_{nm}(ka, \Omega_s) W_{nm}^*(ka) \right|^2}{\sum_{n=0}^N |b_n(ka)|^2 \sum_{m=-n}^n |W_{nm}(ka)|^2}. \quad (8.93)$$

The directivity index is then defined as

$$DI(ka) = 10 \lg G_D(ka). \quad (8.94)$$

4. White Noise Gain

Recall that the element-space WNG is given by

$$G_w(ka) = \frac{1}{\mathbf{w}_e^H(ka) \mathbf{w}_e(ka)}. \quad (8.95)$$

Assume that the sensors are equidistantly spaced on the sphere surface, i.e., $\alpha_s = 4\pi/M$. From Eq. (8.65),

$$(4\pi/M) \mathbf{w}_e^H(ka) \mathbf{w}_e(ka) = \mathbf{w}_h^H(ka) \mathbf{w}_h(ka), \quad (8.96)$$

or

$$(4\pi/M) \|\mathbf{w}_e(ka)\|^2 = \|\mathbf{w}_h(ka)\|^2. \quad (8.97)$$

Then, the WNG can be rewritten as

$$G_w(ka) = \frac{4\pi/M}{\mathbf{w}_h^H(ka) \mathbf{w}_h(ka)} = \frac{4\pi/M}{\|\mathbf{w}_h(ka)\|^2}. \quad (8.98)$$

It is seen that the white noise gain is inversely proportional to the squared norm of the SHD weight vector. Thus, the white noise gain constraint is also equivalent to the SHD weight vector norm constraint.

In addition, replacing $\rho_h(ka)$ in Eq. (8.91) with the SHD white noise covariance matrix $\rho_{hw}(ka)$, gives the white noise gain

$$G_w(ka) = \frac{|\mathbf{w}_h^H(ka) \mathbf{p}_h(ka, \Omega_s)|^2}{\mathbf{w}_h^H(ka) \rho_{hw}(ka) \mathbf{w}_h(ka)}. \quad (8.99)$$

If the steering direction corresponds to the desired signal direction, i.e., $\Omega_o = \Omega_s$, for the uniform spherical array, using Eq. (8.72), the WNG shown in Eq. (8.99) becomes

$$G_w(ka) = \frac{(4\pi/M)^2}{\mathbf{w}_h^H(ka) \rho_{hw}(ka) \mathbf{w}_h(ka)}. \quad (8.100)$$

Using Eqs. (8.98) and (8.100), the SHD white noise covariance matrix $\rho_{hw}(ka)$ is given by

$$\rho_{hw}(ka) = \frac{4\pi}{M} I_{(N+1)^2}. \quad (8.101)$$

8.4 Design of SHD Beamformers

In this section, the design methods of the SHD beamformer are derived and their performances are analyzed. The argument dependence will be suppressed in the notation for convenience when the variable is clear.

8.4.1 Multiply Constrained SHD Beamformer

The design of beamformers to achieve certain performance criteria involves trade-offs among the array gain, beamwidth, sidelobe level, robustness, as well as a number of other factors.

Recall that the robustness of the beamformer can be improved by imposing the white noise gain constraint or weight vector norm constraint. It is known from Eq. (8.96) that the SHD weight vector norm $\|\mathbf{w}_h\|$ is $\sqrt{4\pi/M}$ times of the element-space weight vector norm $\|\mathbf{w}_e\|$. In order to ensure the consistency of the book, the SHD weight vector norm constraint can be written as

$$\|\mathbf{w}_h(ka)\| \leq \sqrt{4\pi/M} \cdot \sqrt{\xi_0} = \sqrt{4\pi\xi_0/M}, \quad (8.102)$$

where ξ_0 is the specified constraint value.

From Eq. (8.98), the weight vector norm constraint is equivalent to the white noise gain constraint

$$G_w(ka) \geq \frac{1}{\xi_0}. \quad (8.103)$$

Since $\min(\|\mathbf{w}_e(ka)\|^2) = 1/M$, from Eq. (8.96), we have

$$\min(\|\mathbf{w}_h(ka)\|^2) \approx 4\pi/M^2. \quad (8.104)$$

Similar to the element-space processing, the WNG loss can be defined as

$$G_{wd} = 10\lg\left(\frac{\|\mathbf{w}_h\|^2}{4\pi/M^2}\right). \quad (8.105)$$

Using Eq. (8.102) gives

$$G_{\text{wd}} \leq 10\lg M + 10\lg(\xi_0) \triangleq G_{\text{wd}0}, \quad (8.106)$$

where $G_{\text{wd}0}$ is the value of WNG loss. The user can determine ξ_0 by setting $G_{\text{wd}0}$. Clearly, $G_{\text{wd}} \geq 0$, thus $G_{\text{wd}0} \geq 0$, i.e., $\xi_0 \geq 1/M$. Therefore, the minimum value of ξ_0 is $1/M$, which corresponds to the maximum-WNG beamformer to be described later.

The beamformer design optimization problem where the output power is minimized subject to a distortionless constraint on the SOI and possibly sidelobes and robustness constraints can be formulated as [6]

$$\begin{aligned} & \min_{\mathbf{w}_h^H(ka)} \mathbf{w}_h^H(ka) \mathbf{R}_h(ka) \mathbf{w}_h(ka), \\ & \text{subject to } \mathbf{w}_h^H(ka) \mathbf{p}_h(ka, \Omega_o) = 4\pi/M, \\ & \quad \mathbf{w}_h^H(ka) \mathbf{p}_h(ka, \Omega_i) \leq \xi \cdot 4\pi/M, \quad \Omega_i \in \Theta_{\text{SL}}, \quad i = 1, 2, \dots, N_{\text{SL}}, \\ & \quad \|\mathbf{w}_h(ka)\| \leq \sqrt{4\pi\xi_0/M}, \end{aligned} \quad (8.107)$$

where ξ and ξ_0 are user parameters to control the sidelobes and the WNG, respectively, Θ_{SL} is the sidelobe region, and $\Omega_i (i = 1, 2, \dots, N_{\text{SL}})$ are the direction grids in the sidelobe region.

This beamformer is referred to as the SHD multiply constrained beamformer in this book, or SH-MC beamformer for short.

The SHD multiply constrained optimization problem shown in Eq. (8.107) provides a unified method for SHD beamformer design. We now consider several useful special cases of this optimization problem.

8.4.2 SHD MVDR Beamformer

Let $\xi = \infty$ and $\xi_0 = \infty$, which implies that the latter two inequality constraints in Eq. (8.107) are always inactive and can be ignored. The optimization problem in this case resembles a Capon beamformer, or an MVDR beamformer in element-space array processing, i.e.,

$$\begin{aligned} & \min_{\mathbf{w}_h^H(ka)} \mathbf{w}_h^H(ka) \mathbf{R}_h(ka) \mathbf{w}_h(ka), \\ & \text{subject to } \mathbf{w}_h^H(ka) \mathbf{p}_h(ka, \Omega_o) = 4\pi/M. \end{aligned} \quad (8.108)$$

This beamformer is referred to as the SHD MVDR beamformer, or SH-MVDR beamformer for short. The solution to Eq. (8.108) is easily derived as

$$\begin{aligned} \mathbf{w}_{h,\text{MVDR}}(ka) &= \frac{(4\pi/M)\mathbf{R}_h^{-1}(ka)\mathbf{p}_h(ka, \Omega_o)}{\mathbf{p}_h^H(ka, \Omega_o)\mathbf{R}_h^{-1}(ka)\mathbf{p}_h(ka, \Omega_o)} \\ &= \frac{(4\pi/M)\mathbf{R}_{i+n}^{-1}(ka)\mathbf{p}_h(ka, \Omega_o)}{\mathbf{p}_h^H(ka, \Omega_o)\mathbf{R}_{i+n}^{-1}(ka)\mathbf{p}_h(ka, \Omega_o)}. \end{aligned} \quad (8.109)$$

8.4.3 Maximum-Directivity-Index Beamformer

The directivity factor can be interpreted as the array gain against isotropic noise.

We use Eq. (8.109) with \mathbf{R}_h replaced by the isotropic noise covariance matrix $\boldsymbol{\rho}_{\text{iso}}$ shown in Eq. (8.89) to obtain the weight vector

$$\mathbf{w}_{h,\text{MDI}}(ka) = \frac{(4\pi/M)\boldsymbol{\rho}_{\text{iso}}^{-1}(ka)\mathbf{p}_h(ka, \Omega_o)}{\mathbf{p}_h^H(ka, \Omega_o)\boldsymbol{\rho}_{\text{iso}}^{-1}(ka)\mathbf{p}_h(ka, \Omega_o)}, \quad (8.110)$$

where the subscript ‘‘MDI’’ denotes maximum directivity index. This beamformer is referred to as the SHD MDI beamformer, or SH-MDI beamformer for short.

Substituting Eqs. (8.10) and (8.89) into Eq. (8.110) gives

$$\mathbf{w}_{h,\text{MDI}}(ka) = \frac{\boldsymbol{\rho}_{\text{iso}}^{-1}(ka)\mathbf{p}_h(ka, \Omega_o)}{M \sum_{n=0}^N \sum_{m=-n}^n Y_n^m(\Omega_o)[Y_n^m(\Omega_o)]^*}. \quad (8.111)$$

Using the fact that

$$\sum_{n=0}^N \sum_{m=-n}^n Y_n^m(\Omega_o)[Y_n^m(\Omega_o)]^* = \sum_{n=0}^N \frac{2n+1}{4\pi} P_n(\cos 0) = \frac{(N+1)^2}{4\pi}, \quad (8.112)$$

Equation (8.110) can be further transformed to the following form:

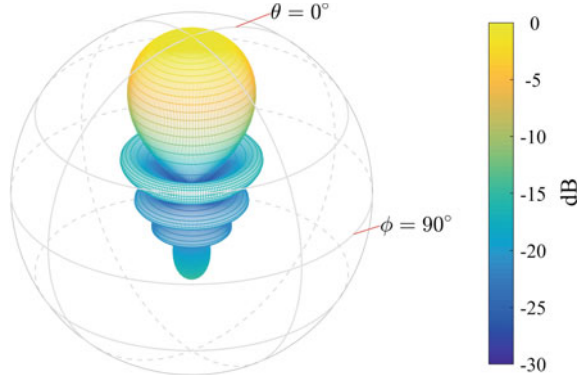
$$\mathbf{w}_{h,\text{MDI}}(ka) = \frac{(4\pi)^2}{M(N+1)^2} \mathbf{Y}^*(\Omega_o) \oslash \mathbf{b}^*(ka), \quad (8.113)$$

where ‘‘ \oslash ’’ denotes element-by-element division. The elements of the weight vector $\mathbf{w}_{h,\text{MDI}}$ are

$$W_{nm,\text{MDI}}(ka) = \frac{(4\pi)^2}{M(N+1)^2} \frac{[Y_n^m(\Omega_o)]^*}{b_n^*(ka)}. \quad (8.114)$$

It is seen that the weights in Eq. (8.114) are identical to the weights of an ideal phase-mode beamformer given in Eq. (8.31) except for a scalar multiplier $(4\pi)^2/[M(N+1)^2]$, which doesn’t affect the array gain. In other words, the ideal

Fig. 8.14 SH-MDI beam pattern



phase-mode spherical sensor array is an MVDR beamformer in the spherical harmonics domain in the case of isotropic noise.

Substituting Eq. (8.113) into Eq. (8.93) gives the directivity factor

$$\begin{aligned}
 G_{D,MDI}(ka) &= \frac{(4\pi/M)^2}{\mathbf{w}_h^H(ka)\rho_{iso}(ka)\mathbf{w}_h(ka)} \\
 &= \frac{(N+1)^4}{4\pi \sum_{n=0}^N \sum_{m=-n}^n Y_n^m(\Omega_o) [Y_n^m(\Omega_o)]^*} \\
 &= (N+1)^2.
 \end{aligned} \tag{8.115}$$

Thus, the directivity index is given by

$$DI_{MDI}(ka) = 20 \lg(N+1), \tag{8.116}$$

which is frequency-independent.

Substituting Eq. (8.113) into Eq. (8.98) gives the WNG

$$G_{w,MDI}(ka) = \frac{4\pi/M}{\mathbf{w}_h^H(ka)\mathbf{w}_h(ka)} = \frac{M}{(4\pi)^2} \frac{(N+1)^4}{\sum_{n=0}^N [(2n+1)/|b_n(ka)|^2]}. \tag{8.117}$$

Consider a uniform open spherical array in the spherically isotropic noise environment. Assume that $ka = 3$, and the steering direction is $\Omega_o = [0^\circ, 0^\circ]$. Up to $N = 4$ spherical harmonics are used and $M = (N+1)^2 = 25$ is chosen (although a uniform 25-element spherical array does not exist in practice).

Substituting Eqs. (8.113) and (8.88) into Eq. (8.63), the obtained SH-MDI beam pattern is shown in Fig. 8.14 in dB. The beam pattern is identical to the result shown in Fig. 8.6b, which verifies that the phase-mode beamformer for a spherical array is actually the SH-MDI beamformer.

Using Eqs. (8.116) and (8.117), the directivity index and the WNG of this beamformer are $DI_{MDI} = 13.98$ dB and $G_{w,MDI}(3) = 6.27$ dB, respectively.

8.4.4 Maximum WNG Beamformer

In Eq. (8.107), let $\mathbf{R}_h(ka) = \mathbf{I}$, $\xi = \infty$, and $\zeta_0 = \infty$. The optimization problem in this case becomes a problem of minimizing the weighted vector norm, i.e.,

$$\begin{aligned} & \min_{\mathbf{w}_h(ka)} \|\mathbf{w}_h(ka)\|^2, \\ & \text{subject to } \mathbf{w}_h^H(ka) \mathbf{p}_h(ka, \Omega_o) = 4\pi/M. \end{aligned} \quad (8.118)$$

The obtained beamformer has the maximum WNG and the highest robustness, which is referred to as the SHD maximum WNG beamformer in this book, or SH-MWNG beamformer for short.

With ρ_{iso} in Eq. (8.110) replaced by \mathbf{I} , the solution in this case is found to be

$$\begin{aligned} \mathbf{w}_{h,MWNG}(ka) &= \frac{(4\pi/M) \mathbf{p}_h(ka, \Omega_o)}{\mathbf{p}_h^H(ka, \Omega_o) \mathbf{p}_h(ka, \Omega_o)} \\ &= \frac{(4\pi)^2 \mathbf{b}(ka) \circ \mathbf{Y}^*(\Omega_o)}{M \sum_{n=0}^N |b_n(ka)|^2 (2n+1)}, \end{aligned} \quad (8.119)$$

whose elements are given by

$$W_{nm,MWNG}(ka) = \frac{(4\pi)^2 b_n(ka) [Y_n^m(\Omega_o)]^*}{M \sum_{n=0}^N |b_n(ka)|^2 (2n+1)}, \quad (8.120)$$

where the subscript ‘‘MWNG’’ denotes maximum WNG.

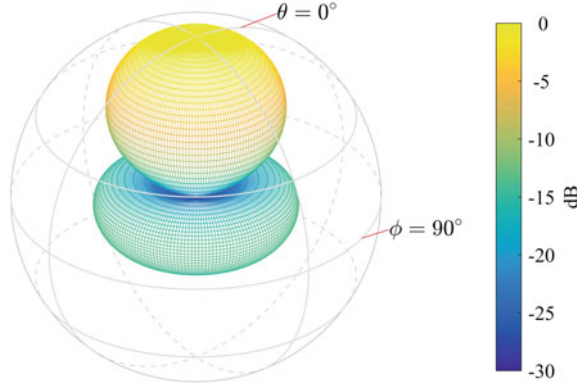
It is seen that the weights in Eq. (8.120) are identical to the weights of the SHD DAS beamformer given in Eq. (8.44) except for a scalar multiplier. This means that the SH-MWNG beamformer is identical to the SHD representation of the DAS beamformer for open spherical arrays.

Substituting Eq. (8.119) into Eq. (8.93) gives the directivity factor

$$\begin{aligned} G_{D,MWNG}(ka) &= \frac{\left[\sum_{n=0}^N |b_n(ka)|^2 (2n+1) \right]^2}{4\pi \sum_{n=0}^N |b_n(ka)|^4 Y_n^m(\Omega_o) [Y_n^m(\Omega_o)]^*} \\ &= \frac{\left[\sum_{n=0}^N |b_n(ka)|^2 (2n+1) \right]^2}{\sum_{n=0}^N |b_n(ka)|^4 (2n+1)}. \end{aligned} \quad (8.121)$$

The directivity index is then given by

Fig. 8.15 SH-MWNG beam pattern



$$DI_{\text{MWNG}}(ka) = 10 \lg G_{\text{D,MWNG}}(ka). \quad (8.122)$$

Substituting Eq. (8.119) into Eq. (8.98) gives the WNG

$$\begin{aligned} G_{\text{w,MWNG}}(ka) &= \frac{4\pi/M}{\mathbf{w}_{\text{h,MWNG}}^H(ka)\mathbf{w}_{\text{h,MWNG}}(ka)} \\ &= \frac{\left[M \sum_{n=0}^N |b_n(ka)|^2 (2n+1) \right]^2 4\pi/M}{(4\pi)^4 \sum_{n=0}^N |b_n(ka)|^2 Y_n^m(\Omega_o) [Y_n^m(\Omega_o)]^*} \\ &= \frac{M}{(4\pi)^2} \sum_{n=0}^N |b_n(ka)|^2 (2n+1). \end{aligned} \quad (8.123)$$

This WNG is the maximum WNG that an SHD beamformer can obtain.

For the open spherical array, we have $\lim_{N \rightarrow \infty} \sum_{n=0}^N |b_n(ka)|^2 (2n+1) = (4\pi)^2$. Thus, the maximum WNG that can be obtained for an open spherical array is

$$\lim_{N \rightarrow \infty} G_{\text{w,MWNG}} = M. \quad (8.124)$$

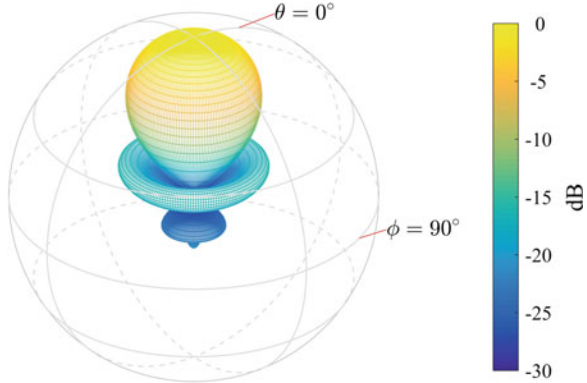
This result is consistent with the result for the element-space DAS beamformer.

For the same case as in Fig. 8.14, the SH-MWNG beam pattern is obtained by substituting Eqs. (8.88) and (8.119) into Eq. (8.63), as shown in Fig. 8.15 in dB.

Compared to Fig. 8.14, the beam pattern shown in Fig. 8.15 has a wider mainlobe width and slightly higher sidelobes.

Using Eqs. (8.122) and (8.123), the directivity index and the WNG of this beamformer are $DI_{\text{MWNG}}(3) = 10.61 \text{ dB}$ and $G_{\text{w,MWNG}}(3) = 13.97 \approx 10 \lg 25 \text{ dB}$, respectively.

Fig. 8.16 SH-NC beam pattern with $\xi_0 = 4/M$



8.4.5 Norm Constrained SHD Beamformer

Letting $\xi = \infty$ in Eq. (8.107), the optimization problem has a form that resembles a norm constrained MVDR beamformer design problem, i.e.,

$$\begin{aligned} & \min_{\mathbf{w}_h(ka)} \mathbf{w}_h^H(ka) \mathbf{R}_h(ka) \mathbf{w}_h(ka), \\ & \text{subject to } \mathbf{w}_h^H(ka) \mathbf{p}_h(ka, \Omega_o) = 4\pi/M, \\ & \|\mathbf{w}_h(ka)\| \leq \sqrt{4\pi\xi_0/M}. \end{aligned} \quad (8.125)$$

The solution to this optimization problem can be obtained using the similar algorithm as discussed in Sect. 3.2.2.

This beamformer is referred to as the SHD NC beamformer in this book, or SH-NC beamformer for short.

Furthermore, with $\mathbf{R}_h = \rho_{iso}$ and adjusting the value of ξ_0 in the range $(1/M, \infty)$, a trade-off between the ideal phase-mode (or SH-MDI) and the SHD DAS (or SH-MWNG) beamformers can be obtained. When $\xi_0 = 1/M$, it reduces to the SH-MWNG beamformer, and when $\xi_0 = \infty$, it corresponds to the SH-MDI beamformer.

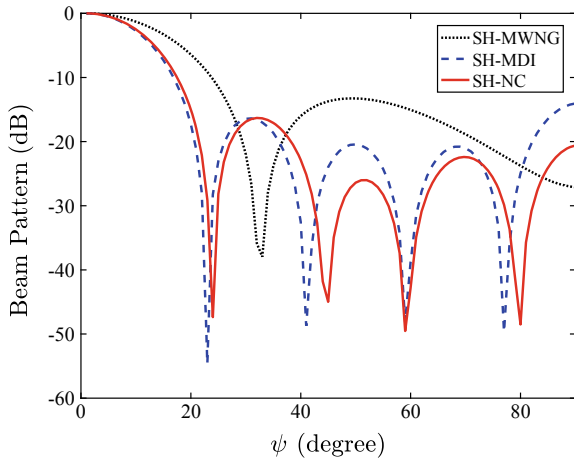
For the same case as in Fig. 8.14, the SH-NC beamformer is designed using Eq. (8.125), in which we choose $\xi_0 = 4/M$.

From Eq. (8.103), the WNG constraint becomes $G_w(ka) \geq M/4$, i.e., 7.96 dB. Using Eq. (8.106), the corresponding WNG loss is $G_{w,0} = 10\lg M + 10\lg(\xi_0) = 10\lg(4) = 6.02$ dB.

The resulting beam pattern is shown in Fig. 8.16. The directivity index is $DI_{NC}(3) = 13.84$ dB, and the WNG is $G_{w,NC}(3) = 7.96$ dB. The WNG loss is $10\lg 25 - 7.96 = 6.02$ dB, which meets the design requirements.

The beam patterns shown in Figs. 8.14, 8.15 and 8.16 are all rotationally symmetric about the steering direction. The three beam patterns as functions of angle ψ are shown in Fig. 8.17. The SH-MWNG beamformer has the widest mainlobe, the SH-

Fig. 8.17 Beam patterns of SH-MWNG, SH-MDI and SH-NC ($\zeta_0 = 4/M$) beamformers



MDI beamformer has the narrowest mainlobe, and the SH-NC beamformer provides a trade-off between them.

The performances of the three beamformers are compared by investigating their DIs and WNGs.

Assume that the frequency band of interest is $ka \in [0, 5]$. The DIs and WNGs of these three beamformers are calculated and shown in Fig. 8.18a, b, respectively.

It is seen that the SH-MDI beamformer has the highest directivity index, which is a constant value of $10 \lg(N + 1)^2 = 13.98$ dB. However, its WNG is small at low frequencies and several high frequencies. We would anticipate that this beamformer has poor robustness at the frequencies where the WNG is small.

The SH-MWNG beamformer has the highest WNG, which approaches $10 \lg M = 13.98$ dB. However, its DI is relatively small, which approaches 0 dB at low frequencies.

The WNG of the SH-NC beamformer strictly exceeds $10 \lg M/4 = 7.96$ dB, which meets the design requirements. Its DI is much higher than that of the SH-MWNG beamformer. In addition, in some frequency bands the WNG of the SH-NC beamformer is equal to that of the SH-MDI beamformer. At these frequencies the SH-MDI beamformer already has a sufficiently high WNG, and the weight vector norm constraint of the SH-NC beamformer is inactive. The SH-NC beamformer reduces to the SH-MDI beamformer at these frequencies.

Consider a 25-element uniform open spherical array in a spherically isotropic noise environment. A plane-wave signal and two plane-wave interferers impinge on the array from $(0^\circ, 0^\circ)$, $(-90^\circ, 60^\circ)$ and $(180^\circ, 60^\circ)$ with the signal (interference)-to-noise ratio at each sensor of 0, 20, and 20 dB, respectively.

We assume that the DOAs of the interferences are unknown to the beamformer, the steering direction is $\Omega_o = (0^\circ, 0^\circ)$, and up to $N = 4$ order spherical harmonics are used. The SH-NC beamformer is designed, in which we choose $\zeta_0 = 4/M$. The resulting beam patterns for $ka = 3$ is shown in Fig. 8.19.

Fig. 8.18 Performance comparison for SH-MDI, SH-MWNG and SH-NC ($\zeta_0 = 4/M$) beamformers.
a DI. **b** WNG

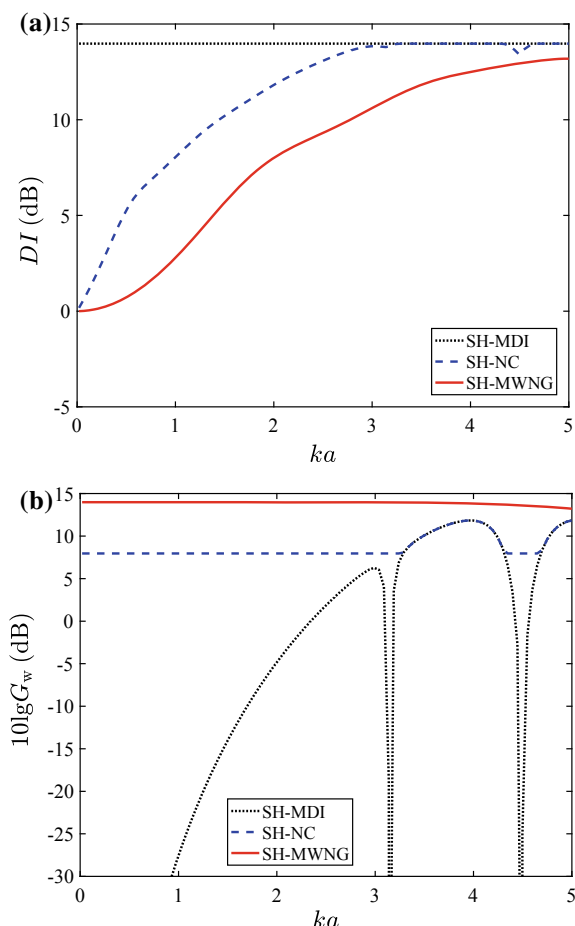
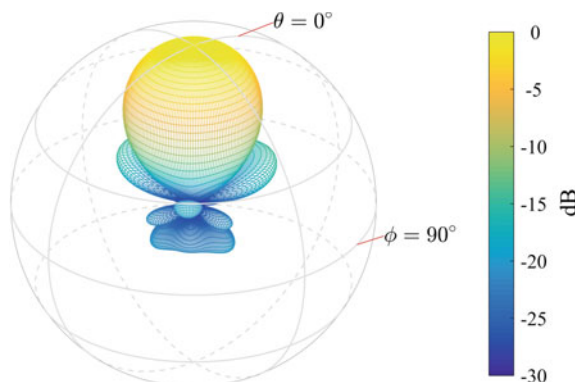


Fig. 8.19 Beam pattern of an SH-NC beamformer with $\zeta_0 = 4/M$ and $ka = 3$



As expected, the nulls are formed adaptively in the DOAs of the interferences. The beam pattern is no longer rotationally symmetric about the steering direction, unlike those of the ideal phase-mode beamformer and the SHD DAS beamformer.

In addition, the WNG of this beamformer is $G_w = 7.96$ dB, which satisfies the WNG constraint (or weight vector norm constraint). The resulting DI is $DI = 13.59$ dB, which approaches that in Fig. 8.16. This indicates that this beamformer can suppress interferences while maintaining good robustness and high directivity.

The sidelobe levels of the beam patterns shown in Figs. 8.14, 8.15, 8.16 and 8.19 are from -16.3 to -13.2 dB, which may be too high for many applications. Next, we consider the issue of sidelobe control.

Consider the 25-element uniform open spherical array in the spherically isotropic noise environment. Assume that $ka = 3$ and the steering direction is $\Omega_o = [0^\circ, 0^\circ]$. The robust high-directivity beamformer with sidelobe control is designed using the method in Eq. (8.107).

Let $\zeta_0 = 4/M$. The desired sidelobe level is chosen to be -20 dB, i.e., $\xi = 0.1$. The sidelobe region is defined as $\Theta_{SL} = \{(\theta, \phi) | \phi \geq 45^\circ\}$, which is sampled at 2° intervals along both θ and ϕ .

The resulting beam pattern is shown in Fig. 8.20a. It is seen that the sidelobe level is below -20 dB and the WNG is 7.96 dB, which meets the design requirements. The DI is about 13.72 dB, which is relatively high.

Consider now that in addition to sidelobe control, we want to design a notch around the direction $(-90^\circ, 60^\circ)$ with a depth of -40 dB and a width of 30° .

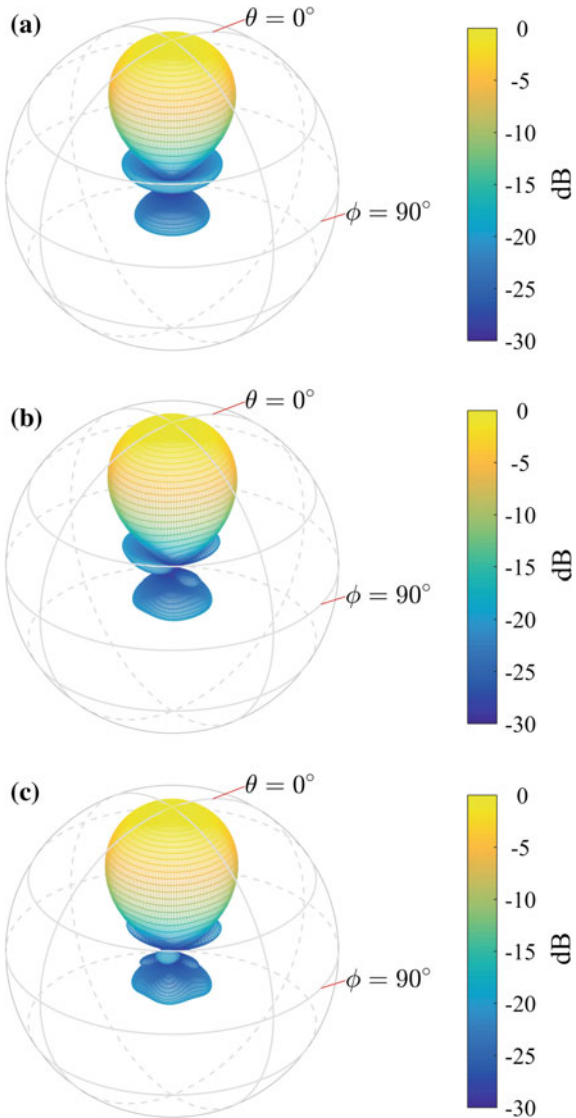
In this case, the desired sidelobe structure is direction-dependent. By choosing $\xi = 0.01$ in the desired notch region while maintaining $\xi = 0.1$ for other sidelobe regions, and solving the optimization problem, the resulting array pattern is shown in Fig. 8.20b.

It is seen that the prescribed notch is formed and the low sidelobe level of -20 dB is achieved. The WNG is 7.96 dB, and the DI is 13.57 dB.

It is worth noting that this beamformer is a data-independent beamformer, and that in order to form notches around the interferences, we need to know the a priori DOAs of the interferences. This is different from the adaptive beamformer in Fig. 8.19.

Finally, consider the SHD sidelobe constrained robust adaptive beamformer design problem, i.e., imposing the sidelobe constraint to the beamformer in Fig. 8.19. Assume that we want to control the sidelobes to be below -20 dB, i.e., $\xi = 0.1$. We keep the other parameters the same as those used in Fig. 8.19. The resulting array pattern is shown in Fig. 8.20c. It is seen that the sidelobes by this method are strictly below -20 dB besides the nulls in the DOAs of the interferences. The WNG is 7.96 dB, and the DI is 13.57 dB.

Fig. 8.20 SHD beam patterns with sidelobe control (-20 dB) for $ka = 3$. **a** DI is maximized. **b** A -40 dB-notch is formed at $(-90^\circ, 60^\circ)$. **c** Output SINR is maximized, which forms nulls adaptively in the DOAs of interferences



8.5 Frequency-Domain Broadband SHD Beamforming

The frequency-domain implementations of the broadband SHD beamformer is discussed in this section.

Assume that the sampled broadband time series received at the s th sensor is

$$x_s(i) = x_s(t)|_{t=iT_s}, \quad (8.126)$$

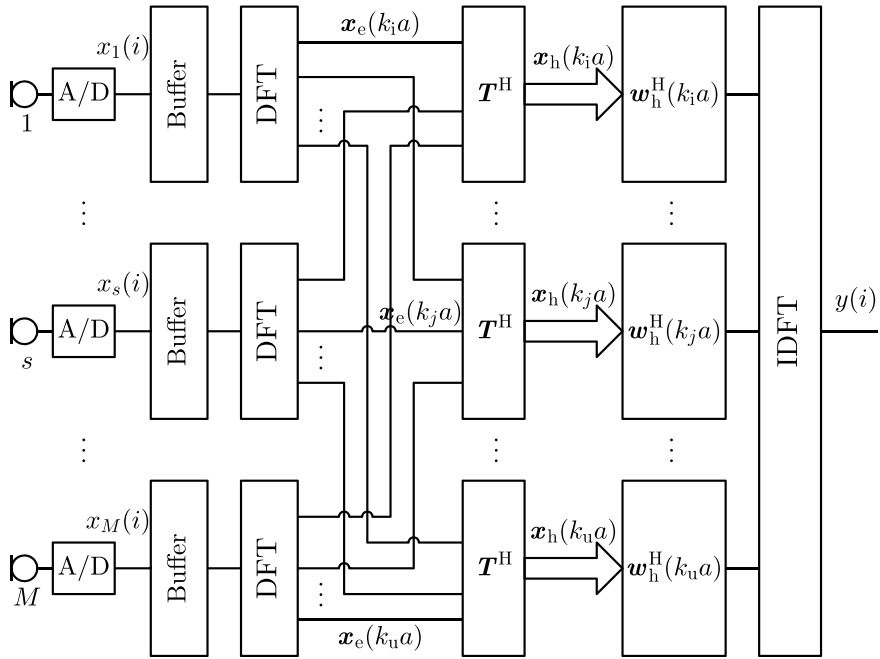


Fig. 8.21 Frequency-domain implementation of broadband SHD beamformer

where T_s is the sampling interval and i is the index of the time series. Here, $x_s(i)$ is actually the time-domain representation of the frequency-domain snapshot data $x_s(ka)$ shown in Eq. (8.73).

Similar to the frequency-domain broadband CHD beamformer, the implementation structure of a broadband SHD beamformer is shown in Fig. 8.21.

The frequency-domain implementation of the broadband SHD beamformer consists of the following steps.

- Step 1. Sample the data received by each sensor to obtain the time series $x_s(i)$, $s = 1, \dots, M$, as shown in Eq. (8.126).
- Step 2. For each sensor, we buffer L samples and take the DFT of the L samples to obtain the subband frequency-domain samples $x_s(ka)$.
- Step 3. The element-space array sample vectors $x_e(ka)$ corresponding to each frequency bin in the range $k \in [k_l, k_u]$ are obtained, as shown in Eq. (8.74).
- Step 4. Use the spherical harmonics transform matrix T shown in Eq. (8.68) to transform the element-space data vector into the spherical harmonics domain, as shown in Eq. (8.78).
- Step 5. The methods developed in Sect. 8.4 are used to design the SHD weight vector $w_h(ka)$ for $k \in [k_l, k_u]$.

- Step 6. Weighted combinations of the SHD sample vector at each frequency bin are formed to obtain the subband beamformer output $y(ka)$ for $k \in [k_l, k_u]$, as shown in Eq. (8.79).
- Step 7. The IDFT is performed on the narrowband beamformer outputs in all frequency bins to obtain the output samples $y(i)$.

The frequency-domain implementation of the SH-PM, SH-MVDR, SH-MDI, SH-MWNG, SH-NC, and SH-MC beamformers are referred to as the SH-FPM, SH-FMVDR, SH-FMDI, SH-FMWNG, SH-FNC, and SH-FMC beamformers in this book, respectively.

8.6 Summary

In this chapter, we discussed the modal beamforming problem for spherical arrays. The optimal design and frequency-domain implementation of SHD beamformer were presented.

Using the spherical harmonics transform pair, the sound pressure received by a spherical aperture can be expressed as a Fourier series expansion, in which the Fourier coefficients can be obtained by integrating the sound pressure over the surface of the sphere. This process can be interpreted as the decomposition and synthesis of the sound field using spherical harmonics.

Accordingly, the beamforming operation for the spherical apertures can be performed in spherical harmonics domain. The SHD beamformer output is equivalent to the element-space beamformer output. The well-known phase-mode beamformer and DAS beamformer for circular apertures can both be represented in the form of SHD beamformer.

In the real-world case, the spherical apertures are sampled using spherical arrays. It is generally desirable that the sensor be uniformly distributed on the spherical surface. There are only five geometries exist for true equidistant spatial sampling. For a nearly-uniform sampling, some weighting operations are required in spherical harmonics transform.

As a rule of thumb, the highest order N of spherical harmonics that can be effectively used is often chosen as $N = k_{\max}a$. For an M -element spherical array, in order to extract up to N th-order spherical harmonics, the number of sensors M should be larger than or equal to $(N + 1)^2$ to avoid spatial aliasing.

By deriving the expressions for the SHD beam response, covariance matrix, array gain, WNG, etc. in terms of the SHD weight vector, the techniques for element-space beamformer design can be applied to the SHD beamformer design.

A multiply constrained SHD beamformer was developed and several useful special cases were presented. It is found that the phase-mode beamformer for spherical arrays can be regarded as an ideal SHD MVDR beamformer against the spherically isotropic noise. This interesting result helps understand the behavior of phase-mode

beamformers, analyze its sensitivity to model perturbations, and propose improved methods.

The multiply constrained method provides a unified framework for SHD beamformer design, which leads to very flexible designs. Since this unified framework can include most of the SHD beamformers as its special cases, it can be used to analyze the advantages and disadvantages of various SHD beamformers. This is very useful for a thorough understanding of the SHD beamformer.

References

1. B. Rafaely, *Fundamentals of Spherical Array Processing* (Springer, Berlin, 2015)
2. J. Meyer, G. Elko, A highly scalable spherical microphone array based on an orthonormal decomposition of the soundfield. *Proc. ICASSP* **2**, 1781–1784 (2002)
3. E.G. Williams, *Fourier Acoustics: Sound Radiation and Nearfield Acoustical Holography* (Academic Press, New York, 1999)
4. E. De Witte, H.D. Griffiths, P.V. Brennan, Phase mode processing for spherical antenna arrays. *Electron. Lett.* **39**(20), 1430–1431 (2003)
5. B. Rafaely, B. Weiss, E. Bachmat, Spatial aliasing in spherical microphone arrays. *IEEE Trans. Signal Process.* **55**(3), 1003–1010 (2007)
6. S. Yan, H. Sun, U.P. Svensson, X. Ma, J.M. Hovem, Optimal modal beamforming for spherical microphone arrays. *IEEE Trans. Audio Speech Lang. Process.* **19**(2), 361–371 (2011)
7. S. Yan, H. Sun, X. Ma, U.P. Svensson, C. Hou, Time-domain implementation of broadband beamformer in spherical harmonics domain. *IEEE Trans. Audio Speech Lang. Process.* **19**(5), 1221–1230 (2011)
8. H. Sun, S. Yan, U.P. Svensson, Robust minimum sidelobe beamforming for spherical microphone arrays. *IEEE Trans. Audio Speech Lang. Process.* **19**(4), 1045–1051 (2011)
9. H. Sun, S. Yan, U.P. Svensson, Optimal higher order ambisonics encoding with predefined constraints. *IEEE Trans. Audio Speech Lang. Process.* **20**(3), 742–754 (2012)
10. J.R. Driscoll, D.M. Healy Jr., Computing Fourier Transforms and Convolutions on the 2-Sphere. *Adv. Appl. Math.* **15**(2), 202–250 (1994)
11. B. Rafaely, Phase-mode versus delay-and-sum spherical microphone array processing. *IEEE Signal Process. Lett.* **12**(10), 713–716 (2005)

Chapter 9

Time-Domain Modal Beamforming for Spherical Arrays



9.1 Introduction

The design and frequency-domain implementation of modal beamformer for spherical arrays, namely SHD beamformer, have been studied in Chap. 8, in which a multiply constrained SHD beamformer was presented.

The modal beamformer discussed in Chap. 8 mainly uses a frequency-domain snapshot model, where complex-valued spherical harmonics transform and array processing is employed. In order to achieve a broadband beamformer, the frequency-domain implementation was employed as a straightforward extension of the narrowband results. Since the frequency-domain implementation is performed with block processing, it might be unsuitable for time-critical speech and audio applications due to its associated time delay.

In Chap. 7, the broadband CHD beamformer is implemented in the time domain using circular harmonics transform and filter-and-sum structure, in which the data are manipulated into a form where real computations can be utilized. The spherical array modal beamformer can also be implemented in the time domain with the real-valued modal transformation and the filter-and-sum beamforming structure.

Meyer and Elko presented a time-domain implementation structure for a spherical array modal beamformer [1], within the spherical harmonics framework. The real and imaginary parts of the spherical harmonics are employed as the spherical Fourier transform basis to convert the time-domain broadband signals to the real-valued spherical harmonics domain, and the steering direction of the beamformer can be tactfully decoupled from its beam pattern shape. To achieve a frequency-independent beam pattern, Meyer and Elko proposed to employ inverse filters to decouple the frequency-dependent components in each signal channel. However, such kind of inverse filtering could damage the system robustness.

The author and his collaborators proposed a broadband SHD beamforming framework implemented in the time domain based on the modified filter-and-sum modal beamforming structure [2]. By deriving the expressions for the array performance measures in terms of the FIR filter tap weights, the design problem is then

formulated as a multiple-constraint optimization problem with the aim of achieving a suitable trade-off among multiple conflicting performance measures.

The rest of this chapter is organized as follows. In Sect. 9.2, the SHD beamformer with axis-symmetric beam patterns is introduced, which decouple the steering and the shaping of the patterns. In Sect. 9.3, we present the time-domain implementation that uses real operations for symmetric-pattern beamformer, which consists of a real spherical harmonics transform unit, a steering unit and a pattern generation unit. The design of FIR Filters for pattern generation is presented in Sect. 9.4, in which the beamformer performance measures are expressed in terms of the filter tap weights and then an optimization problem is formulated to obtain the tap weights. Several examples are considered to illustrate the time-domain broadband SHD beamforming behavior in Sect. 9.5. A brief summary of this chapter is given in Sect. 9.6.

9.2 Rotationally Symmetric SHD Beamformer

As can be seen from the diagram of the frequency-domain broadband SHD beamformer shown in Fig. 8.13, if the steering direction is to be adjusted, the weight vector \mathbf{w}_h needs to be redesigned. This section describes an SHD beamformer that decouples the steering and the shaping of the beam pattern.

9.2.1 Beamforming Structure

Assume that the weights of an SHD beamformer take the form

$$W_{nm,\text{sym}}^*(ka) \triangleq \tilde{c}_n(ka) Y_n^m(\Omega_0), \quad (9.1)$$

where $\tilde{c}_n(ka)$ is a specified value and the subscript “sym” denotes symmetry. The reason for this name can be known after we study the beamformer.

Clearly, the phase-mode beamformer for spherical arrays shown in Eq. (8.32) and the SHD DAS beamformer shown in Eq. (8.44) both belong to this type of beamformer.

Letting $c_n = \sqrt{(2n+1)/4\pi} \tilde{c}_n$, then Eq. (9.1) becomes

$$W_{nm,\text{sym}}^*(ka) \triangleq \sqrt{4\pi/(2n+1)} c_n(ka) Y_n^m(\Omega_0). \quad (9.2)$$

In Eq. (9.2), the weights consist of two parts, where $\sqrt{4\pi/(2n+1)} Y_n^m(\Omega_0)$ is the steering unit to adjust the steering direction Ω_0 , and $c_n(ka)$ is used to synthesize the shape of the beam pattern.

Substituting Eqs. (8.10) and (9.1) into Eq. (8.56) gives

$$\begin{aligned}
B(ka, \Omega) &= \sum_{n=0}^N \sum_{m=-n}^n b_n(ka) [Y_n^m(\Omega)]^* \sqrt{\frac{4\pi}{2n+1}} c_n(ka) Y_n^m(\Omega_o) \\
&= \sum_{n=0}^N \sqrt{\frac{4\pi}{2n+1}} c_n(ka) b_n(ka) \sum_{m=-n}^n [Y_n^m(\Omega)]^* Y_n^m(\Omega_o) \\
&= \sum_{n=0}^N c_n(ka) b_n(ka) \sqrt{(2n+1)/4\pi} P_n(\cos \psi),
\end{aligned} \tag{9.3}$$

where ψ is the angle between Ω and Ω_o .

It is seen from Eq. (9.3) that the beam pattern is only related to the angle ψ , which indicates that the beam pattern is rotationally symmetric about the steering direction Ω_o .

The SHD beamformer whose weight vector has the form of Eq. (9.1) is referred to as the SHD rotationally symmetric pattern beamformer in this book.

A beam pattern function as a function of ψ can then be defined as

$$\tilde{B}(ka, \psi) = \sum_{n=0}^N c_n(ka) b_n(ka) \sqrt{(2n+1)/4\pi} P_n(\cos \psi). \tag{9.4}$$

Clearly, the main response axis of the beam pattern is at $\psi = 0$.

Equation (9.2) can be rewritten in vector notation as

$$\mathbf{w}_{h,sym}(ka) \triangleq \text{vec} \left(\left\{ [W_{nm,sym}(ka)]_{m=-n}^n \right\}_{n=0}^N \right). \tag{9.5}$$

Substituting Eq. (9.5) into Eq. (8.98) gives the WNG

$$\begin{aligned}
G_{w,sym}(ka) &= \frac{4\pi/M}{\mathbf{w}_{h,sym}^H(ka) \mathbf{w}_{h,sym}(ka)} \\
&= \frac{4\pi/M}{\sum_{n=0}^N \tilde{c}_n(ka) \tilde{c}_n^*(ka) \sum_{m=-n}^n Y_n^m(\Omega_o) [Y_n^m(\Omega_o)]^*} \\
&= \frac{4\pi/M}{\sum_{n=0}^N \tilde{c}_n(ka) \tilde{c}_n^*(ka) [(2n+1)/4\pi]} \\
&= \frac{4\pi/M}{\sum_{n=0}^N c_n(ka) c_n^*(ka)} \\
&= \frac{4\pi/M}{\mathbf{c}^H(ka) \mathbf{c}(ka)},
\end{aligned} \tag{9.6}$$

where $\mathbf{c} = [c_0, \dots, c_n, \dots, c_N]^T$ is an $(N+1) \times 1$ column vector.

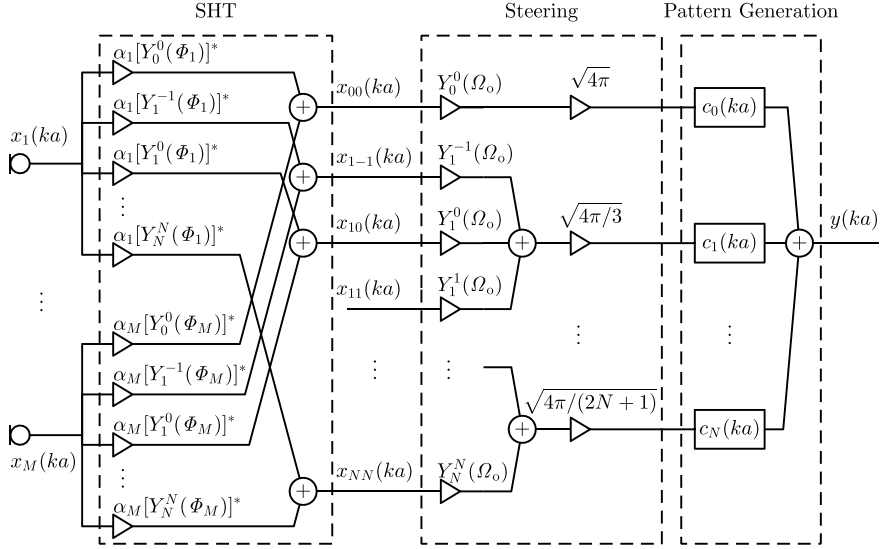


Fig. 9.1 Structure of rotationally symmetric pattern beamforming

Defining $\bar{\bar{P}}_n(ka, \psi) = b_n(ka)\sqrt{(2n+1)/4\pi}P_n(\cos \psi)$ and $\bar{\bar{p}} \triangleq \left[\bar{\bar{P}}_0, \dots, \bar{\bar{P}}_n, \dots, \bar{\bar{P}}_N\right]^T$, Eq. (9.4) can be written in vector notation as

$$\tilde{B}(ka, \psi) = \mathbf{c}^T(ka)\bar{\bar{p}}(ka, \psi). \quad (9.7)$$

Substituting Eq. (9.2) into Eq. (8.79), the output of the beamformer is given by

$$\begin{aligned} y(ka) &= \sum_{n=0}^N \sqrt{\frac{4\pi}{2n+1}} c_n(ka) \sum_{m=-n}^n x_{nm}(ka) Y_n^m(\Omega_o) \\ &= \sum_{n=0}^N \sqrt{\frac{4\pi}{2n+1}} c_n(ka) \sum_{m=-n}^n \left\{ \sum_{s=1}^M \alpha_s x_s(ka) [Y_n^m(\Phi_s)]^* \right\} Y_n^m(\Omega_o). \end{aligned} \quad (9.8)$$

From Eq. (9.8), the implementation of the rotationally symmetric pattern beamformer is shown in Fig. 9.1. First, the received data $x_s(ka)$ is converted to the spherical harmonics domain using the spherical harmonics transform. Then, we input the SHD data $x_{nm}(ka)$ to an SHD beamformer to obtain the output time series, wherein the SHD beamformer consists of a steering unit and a pattern generation unit.

The SHD beamforming diagram shown in Fig. 9.1 is somewhat different from that proposed by Meyer and Elko [3] (see Fig. 9.2).

In Fig. 9.2, in order to calculate the spherical harmonics $\hat{Y}_n^m(\Omega_s)$, the SHD data needs to be divided by $b_n(ka)$, which cannot be achieved at some frequencies

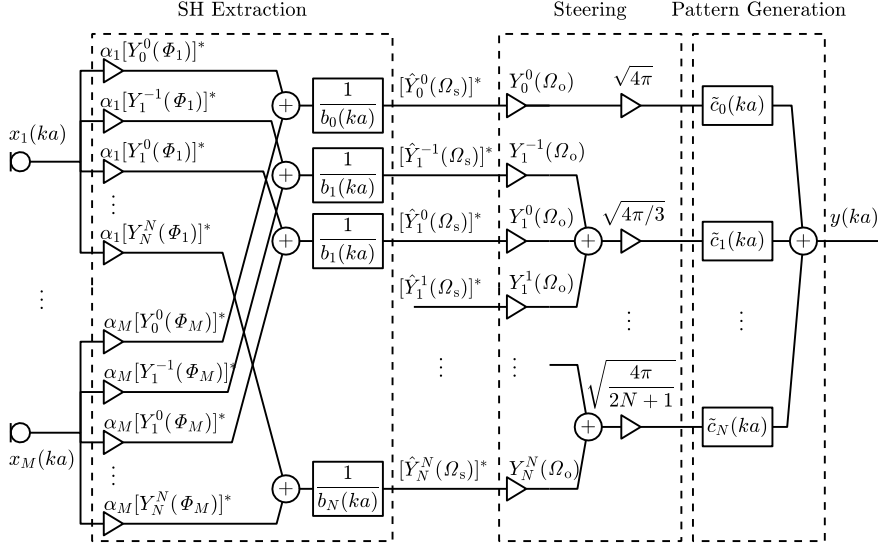


Fig. 9.2 Structure of modal beamforming by Meyer and Elko

where the values of b_n are 0. In addition, small $b_n(ka)$ will cause poor robustness of the beamformer. In Fig. 9.1, however, we perform the weighted summation on the SHD data directly. Thus, as long as the weights $c_n(ka)$ are designed appropriately, the degradation of the beamformer robustness can be avoided.

9.2.2 Design of Weight Vector

In this section, the design methods for the SHD rotationally symmetric pattern beamformer are deduced in detail.

Consider the noise-only input. Two special cases of noise fields, spherically isotropic noise and spatially white noise, are considered.

For the case of spherically isotropic noise, substituting Eq. (9.5) into Eq. (8.80) and letting $\mathbf{R}_h(ka) = \rho_{\text{iso}}(ka)$, the beamformer output power can be obtained using Eq. (8.89) as

$$\begin{aligned}
 P_{\text{isoout}}(ka) &= \mathbf{w}_{h,\text{sym}}^H(ka) \rho_{\text{iso}}(ka) \mathbf{w}_{h,\text{sym}}(ka) \\
 &= \sum_{n=0}^N \sum_{m=-n}^n W_{nm,\text{sym}}^*(ka) \frac{|b_n(ka)|^2}{4\pi} W_{nm,\text{sym}}(ka) \\
 &= \sum_{n=0}^N \frac{|b_n(ka)|^2}{2n+1} c_n(ka) c_n^*(ka) \sum_{m=-n}^n Y_n^m(\Omega_o) [Y_n^m(\Omega_o)]^*
 \end{aligned}$$

$$\begin{aligned}
&= \sum_{n=0}^N \frac{|b_n(ka)|^2}{4\pi} c_n(ka) c_n^*(ka) \\
&= \mathbf{c}^T(ka) \boldsymbol{\rho}_{\text{ciso}}(ka) \mathbf{c}^*(ka),
\end{aligned} \tag{9.9}$$

where $\boldsymbol{\rho}_{\text{ciso}}(ka)$ is the normalized SHD isotropic noise covariance matrix associated with \mathbf{c} , which is given by

$$\begin{aligned}
\boldsymbol{\rho}_{\text{ciso}}(ka) &= \frac{1}{4\pi} \text{diag}\{|b_0(ka)|^2, |b_1(ka)|^2, \dots, |b_N(ka)|^2\} \\
&= \frac{1}{4\pi} \text{diag}\{\mathbf{b}_c(ka) \circ \mathbf{b}_c^*(ka)\},
\end{aligned} \tag{9.10}$$

where $\mathbf{b}_c(ka) = [b_0(ka), b_1(ka), b_2(ka), \dots, b_N(ka)]^T$.

Using Eq. (9.9) and the distortionless constraint Eq. (8.72), the directivity of the beamformer can be calculated using Eq. (8.93) as

$$G_{\text{D,sym}}(ka) = \frac{(4\pi/M)^2}{\mathbf{c}^T(ka) \boldsymbol{\rho}_{\text{ciso}}(ka) \mathbf{c}^*(ka)}. \tag{9.11}$$

Correspondingly, the DI is $DI_{\text{sym}}(ka) = 10\lg G_{\text{D,sym}}(ka)$.

For the case of spatially white noise, using $\boldsymbol{\rho}_{\text{hw}}(ka)$ in Eq. (8.90) instead of $\boldsymbol{\rho}_{\text{iso}}(ka)$ in Eq. (9.9), the noise-only beamformer output power becomes

$$\begin{aligned}
P_{\text{wout}}(ka) &= \mathbf{w}_{\text{h,sym}}^H(ka) \boldsymbol{\rho}_{\text{hw}}(ka) \mathbf{w}_{\text{h,sym}}(ka) \\
&= \frac{4\pi}{M} \sum_{n=0}^N \sum_{m=-n}^n W_{nm,\text{sym}}^*(ka) W_{nm,\text{sym}}(ka) \\
&= \frac{4\pi}{M} \sum_{n=0}^N \frac{4\pi}{2n+1} c_n(ka) c_n^*(ka) \sum_{m=-n}^n Y_n^m(\Omega_o) [Y_n^m(\Omega_o)]^* \\
&= \frac{4\pi}{M} \sum_{n=0}^N c_n(ka) c_n^*(ka) \\
&= \mathbf{c}^T(ka) \boldsymbol{\rho}_{\text{cw}}(ka) \mathbf{c}^*(ka),
\end{aligned} \tag{9.12}$$

where $\boldsymbol{\rho}_{\text{cw}}(ka) = \frac{4\pi}{M} \mathbf{I}_{N+1}$ is the normalized SHD spatially white noise covariance matrix associated with \mathbf{c} .

The design of beamformer with maximum DI (i.e., MDI beamformer) can be formulated as

$$\begin{aligned}
&\min_{\mathbf{c}(ka)} \mathbf{c}^T(ka) \boldsymbol{\rho}_{\text{ciso}}(ka) \mathbf{c}^*(ka), \\
&\text{subject to } \mathbf{c}^T(ka) \bar{\bar{\mathbf{p}}}(ka, 0) = 4\pi/M.
\end{aligned} \tag{9.13}$$

Similar to the MVDR beamformer, the solution to Eq. (9.13) is given by

$$\mathbf{c}_{\text{MDI}}^*(ka) = \frac{(4\pi/M)\rho_{\text{ciso}}^{-1}(ka)\bar{\mathbf{p}}(ka, 0)}{\bar{\mathbf{p}}^H(ka, 0)\rho_{\text{ciso}}^{-1}(ka)\bar{\mathbf{p}}(ka, 0)}, \quad (9.14)$$

whose elements are respectively given by

$$c_{n,\text{MDI}}^*(ka) = \frac{4\pi\sqrt{4\pi(2n+1)}}{M(N+1)^2b_n^*(ka)}. \quad (9.15)$$

It is straightforward to verify that by substituting Eq. (9.15) into Eq. (9.2), the results are equal to those in Eq. (8.114). Therefore, this beamformer is also termed as the SH-MDI beamformer.

Substituting Eqs. (9.14) and (9.10) into Eq. (9.11), the directivity of the rotationally symmetric pattern beamformer is given by

$$\begin{aligned} G_{\text{D,sym,MDI}}(ka) &= \frac{(4\pi/M)^2}{\sum_{n=0}^N \left(\frac{4\pi\sqrt{4\pi(2n+1)}}{M(N+1)^2} \cdot \frac{1}{4\pi} \cdot \frac{4\pi\sqrt{4\pi(2n+1)}}{M(N+1)^2} \right)} \\ &= \frac{(N+1)^4}{\sum_{n=0}^N (2n+1)} = (N+1)^2, \end{aligned} \quad (9.16)$$

which is identical to the result in Eq. (8.115).

Substituting Eq. (9.14) into Eq. (9.6), the WNG of the rotationally symmetric pattern beamformer is given by

$$\begin{aligned} G_{\text{w,sym,MDI}}(ka) &= \frac{4\pi/M}{\sum_{n=0}^N \left(\frac{4\pi\sqrt{4\pi(2n+1)}}{M(N+1)^2b_n^*(ka)} \cdot \frac{4\pi\sqrt{4\pi(2n+1)}}{M(N+1)^2b_n(ka)} \right)} \\ &= \frac{M}{(4\pi)^2} \frac{(N+1)^4}{\sum_{n=0}^N [(2n+1)/|b_n(ka)|^2]}, \end{aligned} \quad (9.17)$$

which is identical to the result in Eq. (8.117).

In order to improve the robustness of the beamformer, the norm constraint on the weight vector $\mathbf{c}(ka)$ can be imposed to Eq. (9.13), i.e.,

$$\|\mathbf{c}(ka)\| \leq \sqrt{4\pi\xi_0/M}, \quad (9.18)$$

where ξ_0 is a specified value.

The sidelobes of the rotationally symmetric pattern beamformer can be controlled by adding the constraints to the optimization problem

$$\mathbf{c}^T(ka)\bar{\mathbf{p}}(ka, \psi_i) \leq \xi \cdot 4\pi/M, \quad \psi_i \in \Psi_{\text{SL}}, \quad i = 1, 2, \dots, N_{\text{SL}}, \quad (9.19)$$

where ξ is the specified constraint value on the sidelobes, Ψ_{SL} is the sidelobe region, and $\psi_i (i = 1, 2, \dots, N_{\text{SL}})$ are the grid points in the sidelobe region.

Using $\rho_{\text{cw}}(ka)$ instead of $\rho_{\text{ciso}}(ka)$ in Eq. (9.14) results in an MWNG beamformer, whose weight vector is given by

$$\mathbf{c}_{\text{MWNG}}^*(ka) = \frac{(4\pi/M)\rho_{\text{cw}}^{-1}(ka)\bar{\mathbf{p}}(ka, 0)}{\bar{\mathbf{p}}^H(ka, 0)\rho_{\text{cw}}^{-1}(ka)\bar{\mathbf{p}}(ka, 0)}, \quad (9.20)$$

whose elements are given by

$$c_{n, \text{MWNG}}^*(ka) = \frac{4\pi\sqrt{(2n+1)4\pi}b_n(ka)}{M\sum_{n=0}^N(2n+1)|b_n(ka)|^2}. \quad (9.21)$$

It is easy to verify that the result obtained by substituting Eq. (9.21) into Eq. (9.2) is identical to the result in Eq. (8.120). Therefore, this beamformer is also termed as the SH-MWNG beamformer.

Substituting Eqs. (9.21) and (9.10) into Eq. (9.11) gives the directivity of the MWNG beamformer

$$\begin{aligned} G_{\text{D,sym,MWNG}}(ka) &= \frac{(4\pi/M)^2}{\sum_{n=0}^N \frac{(4\pi)^2(2n+1)|b_n(ka)|^4}{\left[M\sum_{n=0}^N(2n+1)|b_n(ka)|^2\right]^2}} \\ &= \frac{\left[\sum_{n=0}^N(2n+1)|b_n(ka)|^2\right]^2}{\sum_{n=0}^N(2n+1)|b_n(ka)|^4}, \end{aligned} \quad (9.22)$$

which is identical to the result in Eq. (8.121).

Substituting Eq. (9.21) into Eq. (9.6) gives the WNG of the MWNG beamformer

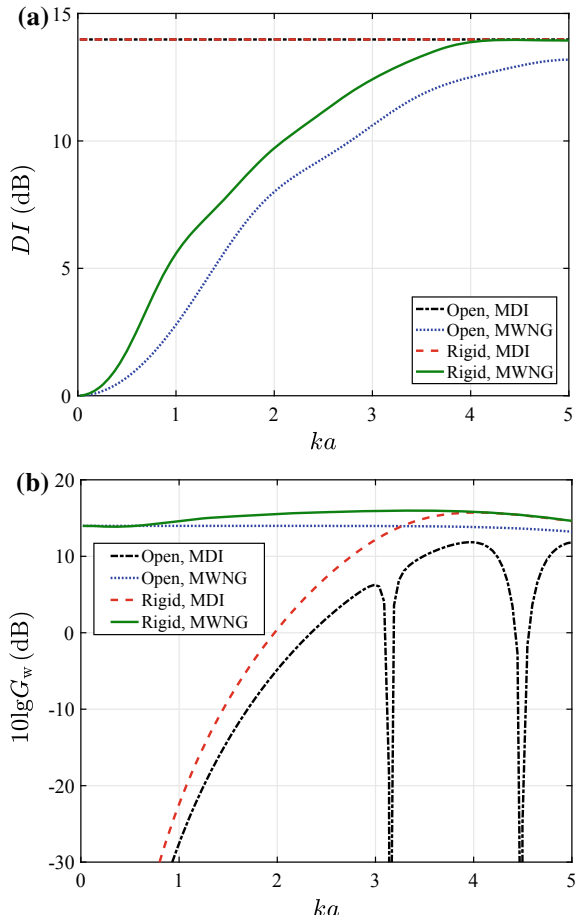
$$\begin{aligned} G_{\text{w,sym,MWNG}}(ka) &= \frac{\left[M\sum_{n=0}^N(2n+1)|b_n(ka)|^2\right]^2 4\pi/M}{(4\pi)^3 \sum_{n=0}^N(2n+1)|b_n(ka)|^2} \\ &= \frac{M\sum_{n=0}^N(2n+1)|b_n(ka)|^2}{(4\pi)^2}, \end{aligned} \quad (9.23)$$

which is identical to the result in Eq. (8.123).

Consider a uniform open spherical array and a uniform rigid spherical array, respectively, both with $M = 25$ elements. Assume that the frequency band of interest is $ka \in [0, 5]$ and up to $N = 4$ order spherical harmonics are used. The MDI and MWNG beamformers are applied and their DIs and WNGs are investigated.

The spherical modal responses of the two spherical arrays are given in Eq. (8.21), which are substituted into Eqs. (9.14) and (9.20), respectively, to obtain the weight vectors of the MDI and MWNG beamformers. Using Eq. (9.11), the DIs of the two beamformers for two arrays can be calculated. The results are shown in Fig. 9.3a.

Fig. 9.3 DI and WNGs of two beamformers for open and rigid spherical arrays
a DI. **b** WNG



It is seen that, whether for the open or the rigid spherical array, the MDI beamformer achieves the same DI, i.e., $20\lg(N + 1) = 13.98$ dB, which is consistent with the result in Eq. (9.16). The DI of the MWNG beamformer approaches 0 dB when the frequency approaches 0 and increases as the frequency increases. The DI of the MWNG beamformer for the rigid spherical array is slightly higher than that of the open spherical array, and it approaches the maximum DI at high frequencies.

Substituting the weights of the two beamformers for the two spherical arrays into Eqs. (9.17) and (9.23), respectively, the obtained WNGs are shown in Fig. 9.3b.

For the MDI beamformer, both spherical arrays achieve small WNG at low frequencies, which indicates that they have poor robustness in this case. At high frequencies, there are two deep notches in the WNG of the open spherical array, i.e., the beamformer cannot work at these two frequencies. The rigid spherical array has high WNG at high frequencies and therefore achieves good robustness.

For the MWNG beamformer, the WNGs of both spherical arrays exceed 13 dB, and the WNG of the rigid spherical array is slightly higher than that of the open one. Both arrays achieve good robustness.

9.3 Time-Domain SHD Beamforming Structure

Since the real-valued coefficients are more suitable for a time-domain implementation, the following discussion focuses on the design and implementation of time-domain SHD beamformer based on real coefficients. Note that in Fig. 9.1 the complex model are used, we have to reformulate our algorithms in order to actually implement the processors using real arithmetic.

We observe from the spherical harmonics transform in Eq. (8.76) that, $Y_n^m(\Phi_s)$ is independent of frequency. Therefore, we can perform the spherical harmonics transform on broadband signals in the same manner. Then

$$x_{nm}(i) = \sum_{s=1}^M \alpha_s x_s(i) [Y_n^m(\Phi_s)]^*, \quad i = 1, 2, \dots, \quad (9.24)$$

where $x_{nm}(i)$ is the time-domain representation of $X_{nm}(ka)$ in Eq. (8.76).

The time-domain implementations of the element-space and CHD broadband beamformers based on FIR filters have been presented in Chaps. 4 and 7, respectively. These techniques can be extended to the broadband SHD beamformers. In order to make this chapter more compact, only the time-domain implementation of the SHD rotationally symmetric pattern beamformer is considered. For the problem of asymmetric SHD beamformer, the reader is referred to the similar design procedures, which will not be described in detail in this book.

The basic idea is to design a bank of real-valued FIR filters that act as the role of complex weighting $c_n(ka)$ shown in Fig. 9.1 over the frequency band of interest.

An advantage of this rotationally symmetric modal beamformer is that it is computationally efficient since only $N+1$ FIR filters are required, in contrast to the classical element-space beamformer which requires M filters. Note that $(N+1)^2 \leq M$.

Let \mathbf{h}_n be the impulse response of the FIR filter corresponding to the spherical harmonics of order n , i.e., $\mathbf{h}_n = [h_{n1}, h_{n2}, \dots, h_{nL}]^T$, $n = 0, 1, \dots, N$. Here, L is the length of each FIR filter.

The frequency-domain SHD beamformer output shown in Eq. (9.8) can be rewritten as

$$y(ka) = \sum_{n=0}^N c_n(ka) x_n(ka, \Omega_0), \quad (9.25)$$

where

$$x_n(ka, \Omega_o) = \sqrt{\frac{4\pi}{2n+1}} \sum_{m=-n}^n \left\{ \sum_{s=1}^M \alpha_s x_s(ka) [Y_n^m(\Phi_s)]^* \right\} Y_n^m(\Omega_o). \quad (9.26)$$

Using Eq. (9.24), the time-domain representation of Eq. (9.26) is given by

$$\begin{aligned} x_n(i, \Omega_o) &= \sqrt{\frac{4\pi}{2n+1}} \sum_{m=-n}^n \left\{ \sum_{s=1}^M \alpha_s x_s(i) [Y_n^m(\Phi_s)]^* \right\} Y_n^m(\Omega_o) \\ &= \sqrt{\frac{4\pi}{2n+1}} \left\{ \tilde{x}_{n0}(i) Y_n^0(\Omega_o) + 2 \sum_{m=1}^n \tilde{x}_{nm}(i) \operatorname{Re}[Y_n^m(\Omega_o)] \right. \\ &\quad \left. + 2 \sum_{m=1}^n \check{x}_{nm}(i) \operatorname{Im}[Y_n^m(\Omega_o)] \right\}, \end{aligned} \quad (9.27)$$

where $\operatorname{Re}(\cdot)$ and $\operatorname{Im}(\cdot)$ denote the real part and the imaginary part of their arguments, respectively, and

$$\tilde{x}_{nm}(i) = \sum_{s=1}^M \alpha_s x_s(i) \operatorname{Re}[Y_n^m(\Phi_s)], \quad (9.28)$$

$$\check{x}_{nm}(i) = \sum_{s=1}^M \alpha_s x_s(i) \operatorname{Im}[Y_n^m(\Phi_s)]. \quad (9.29)$$

Note that the property $Y_n^{-m}(\Omega) = (-1)^m [Y_n^m(\Omega)]^*$ has been used in the above derivation.

Equations (9.28) and (9.29) are referred to as the real spherical harmonics transform (real SHT).

Substituting Eq. (8.6) into Eq. (9.27) gives

$$\begin{aligned} x_n(i, \Omega_o) &= \tilde{x}_{n0}(i) P_n^0(\cos \phi_o) \\ &\quad + 2 \sum_{m=1}^n \sqrt{\frac{(n-m)!}{(n+m)!}} P_n^m(\cos \phi_o) \left[\tilde{x}_{nm}(i) \cos(m\theta_o) + \check{x}_{nm}(i) \sin(m\theta_o) \right]. \end{aligned} \quad (9.30)$$

The convolution theorem states that point-wise multiplication in the frequency domain is equal to the convolution in the time domain. Since the time-domain representation of $x_n(ka, \Omega_o)$ is $x_n(i, \Omega_o)$ and the frequency response of \mathbf{h}_n is approximate to $c_n(ka)$, the time-domain representation of Eq. (9.25) can be given by

$$y(i) = \sum_{n=0}^N \sum_{l=1}^L h_{nl} x_n(i-l+1, \Omega_o). \quad (9.31)$$

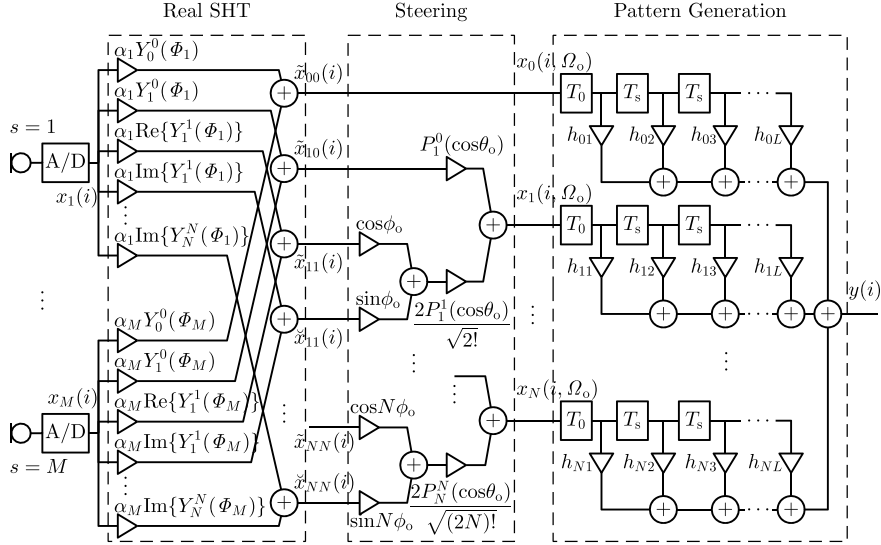


Fig. 9.4 Time-domain implementation of broadband SHD beamformer

We can define an $L \times 1$ column vector $\mathbf{x}_n(i, \Omega_o)$ as

$$\mathbf{x}_n(i, \Omega_o) = [x_n(i - L + 1, \Omega_o), x_n(i - L + 2, \Omega_o), \dots, x_n(i, \Omega_o)]^T. \quad (9.32)$$

According to Eqs. (9.28) to (9.31), the time-domain implementation of the broadband SHD beamformer can be given in Fig. 9.4. This beamformer structure consists of three units: a real spherical harmonics transform unit, a steering unit, and a pattern generation unit. Note that all the coefficients in the three units are real, which allows the use of real calculation.

Note that the pre-delay T_0 is attached before the FIR filters for each harmonic. This pre-delay is used to compensate the inherent group delay of an FIR filter, which is typically chosen as $T_0 = -(L - 1)T_s/2$. Note that the pre-delay is negative, which is physically unrealizable. In practice, we can add a common delay, e.g., $(L - 1)T_s/2$, in each channel so that the operations in Fig. 9.4 are physically realizable. Note, however, that in the derivation of Eq. (9.33) below, the pre-delay $T_0 = -(L - 1)T_s/2$ is not negligible.

Our goal is then to choose the impulse responses (or tap weights) of these FIR filters \mathbf{h}_n to achieve the desired beam pattern of the SHD beamformer.

9.4 Design of FIR Filters for Pattern Generation

In Fig. 9.4, the total weighting function, denoted by $\hat{c}_n(ka)$, that generated by the pre-delay and the pattern generation filter corresponding to the n th order spherical harmonics, is given by

$$\hat{c}_n(ka) = \eta \mathbf{h}_n^T \mathbf{e}(f), \quad n = 0, 1, \dots, N, \quad (9.33)$$

where $\eta = e^{-i2\pi f T_0}$ and $\mathbf{e}(f) = [1, e^{-i2\pi f T_s}, \dots, e^{-i(L-1)2\pi f T_s}]^T$.

Using $\hat{c}_n(ka)$ in Eq. (9.33) instead of $c_n(ka)$ in Eq. (9.4) gives

$$\tilde{B}(ka, \psi) = \sum_{n=0}^N b_n(ka) \sqrt{(2n+1)/4\pi} P_n(\cos \psi) \eta \mathbf{h}_n^T \mathbf{e}(f). \quad (9.34)$$

Let $a_n(ka, \psi) = b_n(ka) \sqrt{(2n+1)/4\pi} P_n(\cos \psi) \eta$, $\mathbf{a} = [a_0, \dots, a_n, \dots, a_N]^T$, and define an $(N+1)L \times 1$ composite vector $\mathbf{h} = [\mathbf{h}_0^T, \mathbf{h}_1^T, \dots, \mathbf{h}_N^T]^T$. Equation (9.34) takes the form

$$\begin{aligned} \tilde{B}(ka, \psi) &= \sum_{n=0}^N a_n(ka, \psi) \mathbf{h}_n^T \mathbf{e}(f) \\ &= [\mathbf{a}(ka, \psi) \otimes \mathbf{e}(f)]^T \mathbf{h} \\ &= \mathbf{u}^T(ka, \psi) \mathbf{h} \\ &= \mathbf{h}^T \mathbf{u}(ka, \psi), \end{aligned} \quad (9.35)$$

where $\mathbf{u}(ka, \psi) = \mathbf{a}(ka, \psi) \otimes \mathbf{e}(f)$ with “ \otimes ” denoting the Kronecker product.

Recall that the main response axis of the rotationally symmetric pattern corresponds to $\psi = 0$. Therefore, the distortionless constraint in the spherical harmonics domain becomes

$$\tilde{B}(ka, 0) = \mathbf{h}^T \mathbf{u}(ka, 0) = 4\pi/M. \quad (9.36)$$

For a broadband beamformer, this distortionless constraint is required to be satisfied at all frequencies over the frequency band of interest.

Using Eq. (9.33) and defining $\hat{\mathbf{c}}(ka) = [\hat{c}_0(ka), \dots, \hat{c}_n(ka), \dots, \hat{c}_N(ka)]^T$, we have

$$\begin{aligned} \hat{\mathbf{c}}(ka) &= [\eta \mathbf{h}_0^T \mathbf{e}(f), \dots, \eta \mathbf{h}_n^T \mathbf{e}(f), \dots, \eta \mathbf{h}_N^T \mathbf{e}(f)]^T \\ &= \eta [\mathbf{I}_{N+1} \otimes \mathbf{e}(f)]^T \mathbf{h}. \end{aligned} \quad (9.37)$$

Using $\hat{\mathbf{c}}(ka)$ instead of $\mathbf{c}(ka)$ in Eq. (9.9) gives

$$P_{\text{isoout}}(ka) = \mathbf{c}^T(ka) \boldsymbol{\rho}_{\text{ciso}}(ka) \mathbf{c}^*(ka)$$

$$\begin{aligned}
&= \mathbf{h}^T [\mathbf{I}_{N+1} \otimes \mathbf{e}(f)] \boldsymbol{\rho}_{\text{ciso}}(ka) [\mathbf{I}_{N+1} \otimes \mathbf{e}(f)]^H \mathbf{h} \\
&= \mathbf{h}^T \boldsymbol{\rho}_{\text{hiso}}(ka) \mathbf{h},
\end{aligned} \tag{9.38}$$

where

$$\boldsymbol{\rho}_{\text{hiso}}(ka) = [\mathbf{I}_{N+1} \otimes \mathbf{e}(f)] \boldsymbol{\rho}_{\text{ciso}}(ka) [\mathbf{I}_{N+1} \otimes \mathbf{e}(f)]^H \tag{9.39}$$

is the SHD normalized isotropic noise covariance matrix associated with \mathbf{h} .

The directivity factor equals to the array gain against isotropic noise, which is given by

$$G_D(ka) = \frac{(4\pi/M)^2}{\mathbf{h}^T \boldsymbol{\rho}_{\text{hiso}}(ka) \mathbf{h}}. \tag{9.40}$$

The directivity index is then defined as

$$DI(ka) = 10 \lg G_D(ka). \tag{9.41}$$

For a broadband isotropic noise that occupies a broadband frequency band corresponding to $[k_l, k_u]$, where k_l and k_u are respectively the wavenumbers corresponding to the lower and upper bound frequencies, the broadband covariance matrix, denoted by $\overleftrightarrow{\boldsymbol{\rho}}_{\text{hiso}}$, can be given by performing the integration with respect to k over the region $[k_l, k_u]$

$$\overleftrightarrow{\boldsymbol{\rho}}_{\text{hiso}} = \int_{k_l}^{k_u} \boldsymbol{\rho}_{\text{hiso}}(ka) dk, \tag{9.42}$$

where the integration can be approximated by performing summation.

Thus, the broadband isotropic noise-only beamformer output power is

$$\overleftrightarrow{P}_{\text{isoout}} = \mathbf{h}^T \overleftrightarrow{\boldsymbol{\rho}}_{\text{hiso}} \mathbf{h}. \tag{9.43}$$

For the spatially white noise case, using $\hat{\mathbf{c}}(ka)$ instead of $\mathbf{c}(ka)$ in Eq. (9.12) gives the spatially white noise-only beamformer output power

$$\begin{aligned}
P_{\text{wout}}(ka) &= \mathbf{c}^T(ka) \boldsymbol{\rho}_{\text{cw}}(ka) \mathbf{c}^*(ka) \\
&= \mathbf{h}^T [\mathbf{I}_{N+1} \otimes \mathbf{e}(f)] \boldsymbol{\rho}_{\text{cw}}(ka) [\mathbf{I}_{N+1} \otimes \mathbf{e}(f)]^H \mathbf{h} \\
&= \mathbf{h}^T \boldsymbol{\rho}_{\text{hw}}(ka) \mathbf{h},
\end{aligned} \tag{9.44}$$

where $\boldsymbol{\rho}_{\text{hw}}(ka)$ is the SHD normalized white noise covariance matrix associated with \mathbf{h} , which is given by

$$\begin{aligned}\rho_{\text{hw}}(ka) &= [\mathbf{I}_{N+1} \otimes \mathbf{e}(f)] \rho_{\text{cw}}(ka) [\mathbf{I}_{N+1} \otimes \mathbf{e}(f)]^H \\ &= \frac{4\pi}{M} [\mathbf{I}_{N+1} \otimes \mathbf{e}(f)] [\mathbf{I}_{N+1} \otimes \mathbf{e}(f)]^H.\end{aligned}\quad (9.45)$$

Substituting Eq. (9.45) into Eq. (9.44) gives

$$P_{\text{wout}}(ka) = \frac{4\pi}{M} \sum_{n=0}^N |\mathbf{h}_n^T \mathbf{e}(f)|^2. \quad (9.46)$$

Assume that the spatially white noise has a flat spectrum over the entire frequency band $[0, f_s/2]$, where f_s is the sampling frequency. The broadband beamformer output power, denoted by $\overleftrightarrow{P}_{\text{wout}}$, is given by

$$\begin{aligned}\overleftrightarrow{P}_{\text{wout}} &= \int_0^{f_s/2} P_{\text{wout}}(ka) df \\ &= \int_0^{f_s/2} \frac{4\pi}{M} \sum_{n=0}^N |\mathbf{h}_n^T \mathbf{e}(f)|^2 df \\ &= \frac{4\pi}{M} \sum_{n=0}^N \mathbf{h}_n^T \mathbf{h}_n \\ &= \frac{4\pi}{M} \mathbf{h}^T \mathbf{h}.\end{aligned}\quad (9.47)$$

The broadband WNG, denoted by \overleftrightarrow{G}_w , is then defined as

$$\overleftrightarrow{G}_w = \frac{(4\pi/M)^2}{\overleftrightarrow{P}_{\text{wout}}} = \frac{4\pi/M}{\mathbf{h}^T \mathbf{h}} = \frac{4\pi/M}{\|\mathbf{h}\|^2}. \quad (9.48)$$

It is seen that the broadband white noise gain is inversely proportional to $\|\mathbf{h}\|^2$, which is similar to the result for narrowband beamformers.

In many applications, it is required that the mainlobe response of the beamformer is constant over the frequency band of interest, i.e., frequency-invariant. The MSRV is defined as

$$\gamma_{\text{MSRV}}(ka, \psi) = |\mathbf{h}^T \mathbf{u}(ka, \psi) - \mathbf{h}^T \mathbf{u}(k_0 a, \psi)|, \quad (9.49)$$

where k_0 is the wavenumber corresponding to a chosen reference frequency.

Let $k_j \in [k_l, k_u]$, $j = 1, 2, \dots, N_k$, $\psi_l \in \Psi_{\text{ML}}$ ($l = 1, \dots, N_{\text{ML}}$), and $\psi_i \in \Psi_{\text{SL}}$ ($i = 1, \dots, N_{\text{SL}}$) be the chosen (uniform or nonuniform) grids that approximate the wavenumber band $[k_l, k_u]$, the mainlobe region Ψ_{ML} , and the sidelobe region Ψ_{SL} , respectively.

Define an $N_{\text{ML}}N_{\text{k}} \times 1$ column vector $\boldsymbol{\gamma}_{\text{MSRV}}$ whose $(j + (l - 1)N_{\text{k}})$ th element is given by

$$[\boldsymbol{\gamma}_{\text{MSRV}}]_{j+(l-1)N_{\text{k}}} = \gamma_{\text{MSRV}}(k_j a, \psi_l). \quad (9.50)$$

Then, the norm of $\boldsymbol{\gamma}_{\text{MSRV}}$, i.e., $\|\boldsymbol{\gamma}_{\text{MSRV}}\|_q$, can be used as a measure of the frequency-invariant approximation of the synthesized broadband beam pattern over frequencies. The subscript $q \in \{2, \infty\}$ stands for the ℓ_2 (Euclidean) and ℓ_∞ (Chebyshev) norm, respectively.

Define an $N_{\text{SL}}N_{\text{k}} \times 1$ column vector $\boldsymbol{B}_{\text{SL}}$ whose $(j + (i - 1)N_{\text{k}})$ th element is given by

$$[\boldsymbol{B}_{\text{SL}}]_{j+(i-1)N_{\text{k}}} = \tilde{B}(k_j a, \psi_i). \quad (9.51)$$

Similarly, $\|\boldsymbol{B}_{\text{SL}}\|_q$ is a measure of sidelobe behavior.

With the expressions for the array pattern (Eq. (9.35)), broadband isotropic noise-only beamformer output power (Eq. (9.43)), broadband WNG (Eq. (9.48)), MSRV (Eq. (9.50)) and sidelobe measure (Eq. (9.51)) in hand, the design of FIR filters for pattern generation can be formulated as a multiply constrained design problem

$$\begin{aligned} & \min_{\boldsymbol{h}, \mu_\ell} \mu_\ell, \quad \ell \in \{1, 2, 3, 4\}, \\ & \text{subject to } \tilde{B}(k_j a, 0) = 4\pi/M, \quad k_j \in [k_{\text{l}}, k_{\text{u}}], \quad j = 1, 2, \dots, N_{\text{k}}, \\ & \quad \overleftarrow{\overrightarrow{P}_{\text{isoout}}} \leq \mu_1, \\ & \quad \overleftarrow{\overrightarrow{G}_{\text{w}}}^{-1} \leq \mu_2, \\ & \quad \|\boldsymbol{\gamma}_{\text{MSRV}}\|_{q_1} \leq \mu_3, \\ & \quad \|\boldsymbol{B}_{\text{SL}}\|_{q_2} \leq \mu_4, \end{aligned} \quad (9.52)$$

where $q_1, q_2 \in \{2, \infty\}$, and $\{\mu_\ell\}_{\ell=1}^4$ include a cost function and three user parameters.

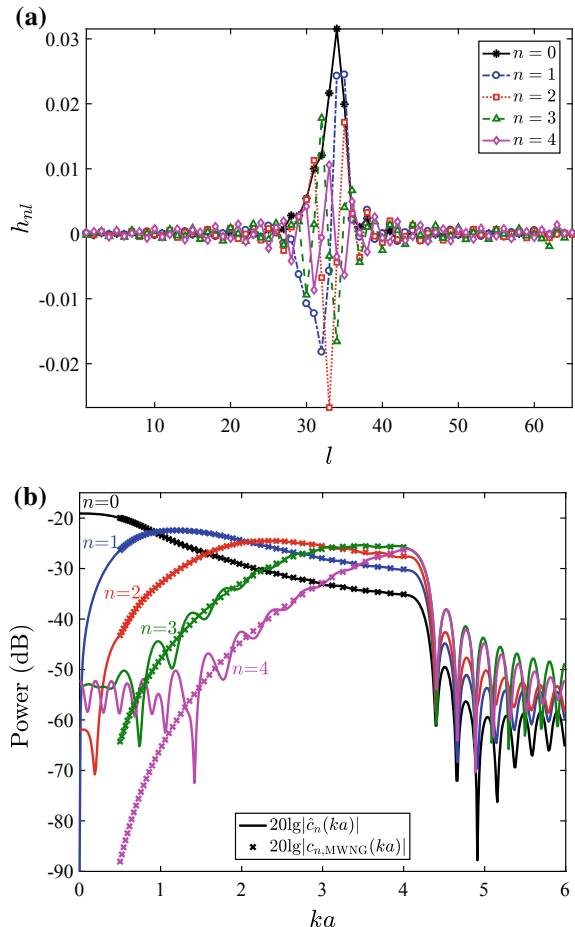
This method is referred to as the SHD time-domain multiply constrained beamformer, or SH-TMC beamformer for short.

Several examples are considered to illustrate the time-domain broadband SHD beamforming operation.

Let $\ell = 2$, $\mu_1 = \infty$, $\mu_3 = \infty$, and $\mu_4 = \infty$ in Eq. (9.52). The optimization problem becomes

$$\begin{aligned} & \min_{\boldsymbol{h}} \boldsymbol{h}^T \boldsymbol{h}, \\ & \text{subject to } \boldsymbol{h}^T \boldsymbol{u}(k_j a, 0) = 4\pi/M, \\ & \quad k_j \in [k_{\text{l}}, k_{\text{u}}], \quad j = 1, 2, \dots, N_{\text{k}}. \end{aligned} \quad (9.53)$$

Fig. 9.5 Results of SH-TMWNG beamformer. **a** Pattern generation filters \mathbf{h}_n . **b** Weighting function $\hat{c}_n(ka)$ and $c_{n,MWNG}(ka)$

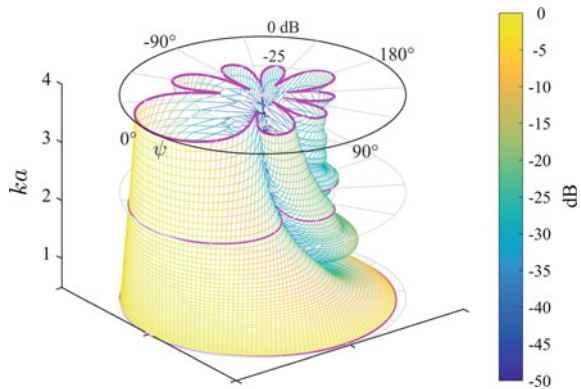


From Eq. (9.48), the cost function in Eq. (9.53) maximizes the broadband WNG, resulting in a beamformer that achieves the highest robustness. This beamformer is referred to as the SHD time-domain maximum-WNG (TMWNG) beamformer, or SH-TMWNG beamformer for short.

Consider a rigid spherical array with $M = 32$ sensors located at the center of the faces of a truncated icosahedron, as shown in Fig. 8.10a. Let $\alpha_s = 4\pi/M$. From Eq. (8.49), the highest order of the spherical harmonics that can be obtained by the 32-element spherical array is $N = 4$. The frequency band of interest is $ka = 2\pi fa/c \in [0.5, 4]$, which is discretized using 51 frequency grids, and the sampling frequency f_s satisfies $2\pi f_s a/c = 12$.

The SH-TMWNG beamformer is used. Assume that the length of each FIR filter is $L = 65$. The FIR filter \mathbf{h} is solved using Eq. (9.53) and its subvectors $\mathbf{h}_0, \dots, \mathbf{h}_n, \dots, \mathbf{h}_N$ are shown in Fig. 9.5a.

Fig. 9.6 Beam pattern of SH-TMWNG beamformer



Substituting \mathbf{h}_n into Eq. (9.33) gives the weighting function of the SH-TMWNG beamformer $\hat{c}_n(ka)$, as shown in Fig. 9.5b. For comparison purposes, its frequency-domain counterpart $c_{n,\text{MWNG}}(ka)$ from Eq. (9.21) is also shown in this figure.

It is seen that $\hat{c}_n(ka)$ approximate $c_{n,\text{MWNG}}(ka)$ within the frequency band of interest. When $c_{n,\text{MWNG}}(ka)$ is too small (e.g., the low frequency end for $n = 4$), $\hat{c}_n(ka)$ cannot approximate $c_{n,\text{MWNG}}(ka)$, however, the approximation error in this case is below -40 dB, which is acceptable.

Using Eq. (9.35), the beam pattern as a function of ka and ψ is calculated on a grid of points in frequency and angle. The resulting beam patterns are shown in Fig. 9.6, where we have included a normalization factor $M/4\pi$ so that the amplitudes of the patterns at the steering direction are equal to unity (or to 0 dB). It is seen that the mainlobe beamwidth widens as the frequency decreases.

The DI and WNG of the SH-TMWNG beamformer are calculated by using Eqs. (9.11) and (9.6), respectively. Those of the SH-FMWNG beamformer (i.e., frequency-domain SHD MWNG beamformer) are also calculated for comparison purposes. These results are shown in Fig. 9.7 in dB for various frequencies, where we have added the subscripts “TMWNG” and “FMWNG” to denote the SH-TMWNG and SH-FMWNG beamformers, respectively.

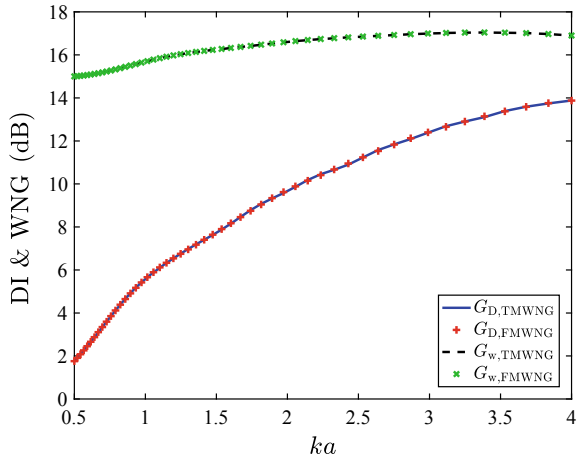
It is seen that the results of the time-domain method approximate that of the frequency-domain method well, and the WNGs are from 15.0 to 17.0 dB within the frequency band of interest, which indicates that the beamformer has good robustness.

Letting $\ell = 1$, $\mu_2 = \infty$, $\mu_3 = \infty$, and $\mu_4 = \infty$, the optimization problem in Eq. (9.52) becomes a maximum directivity design problem

$$\begin{aligned} & \min_{\mathbf{h}} \mathbf{h}^T \overleftrightarrow{\rho}_{\text{hiso}} \mathbf{h}, \\ & \text{subject to } \mathbf{h}^T \mathbf{u}(k_j a, 0) = 4\pi/M, \\ & \quad k_j \in [k_l, k_u], \quad j = 1, 2, \dots, N_k. \end{aligned} \quad (9.54)$$

The resulting beamformer is referred to as the SHD time-domain MDI beamformer, or SH-TMDI beamformer for short.

Fig. 9.7 DI and WNG versus ka for SH-TMWNG and SH-FMWNG beamformers



For the above 32-element rigid spherical array, the SH-TMDI beamformer is designed using Eq. (9.54). The resulting FIR filters $\mathbf{h}_0, \dots, \mathbf{h}_n, \dots, \mathbf{h}_N$ are shown in Fig. 9.8a.

Compared with the filter coefficients in Fig. 9.5a, it is found that the magnitudes of the filter coefficients in Fig. 9.8a are thousands of times higher than those of the former, especially for the FIR filter coefficients corresponding to high-order spherical harmonics, which will lead to small WNG and poor robustness.

The weighting function $\hat{c}_n(ka)$ from Eq. (9.33) as a function of ka is shown in Fig. 9.8b. For comparison purposes, its frequency-domain counterpart $c_{n,\text{MDI}}(ka)$ from Eq. (9.15) is also shown in the figure.

It is seen that $\hat{c}_n(ka)$ closely approximate $c_{n,\text{MDI}}(ka)$ within the operating frequency band. At high frequencies outside the operating frequency band, the values of $\hat{c}_n(ka)$ are much larger than those at frequencies within the operating frequency band, i.e., the pattern generation filters act as band-stop filters that suppress the signal in the operating frequency band. This will lead to considerable noise amplification at high frequencies outside the operating frequency band, thereby will cause significant degradation in performance.

The resulting beam pattern of the SH-TMDI beamformer from Eq. (9.35) is shown in Fig. 9.9, where the magnitudes have been normalized. It is seen that the mainlobe beamwidth is almost constant over the frequency band of interest.

The values of DI and WNG versus ka for both time-domain and frequency-domain SHD MDI beamformers (i.e., SH-TMDI and SH-FMDI beamformers) are plotted in dB in Fig. 9.10, where we have added the subscripts “TMDI” and “FMDI” to denote the SH-TMDI and SH-FMDI beamformers, respectively.

It is seen that the results of the SH-TMDI beamformer approach those of the SH-FMDI beamformer.

Comparing Fig. 9.7 with Fig. 9.10, it is seen that the former achieves high WNGs, but the DIs are small, especially at low frequencies. The latter has high DIs, but

Fig. 9.8 Results of SH-TMDI beamformer. **a** Pattern generation filters h_n . **b** Weighting functions $\hat{c}_n(ka)$ and $c_{n,MDI}(ka)$

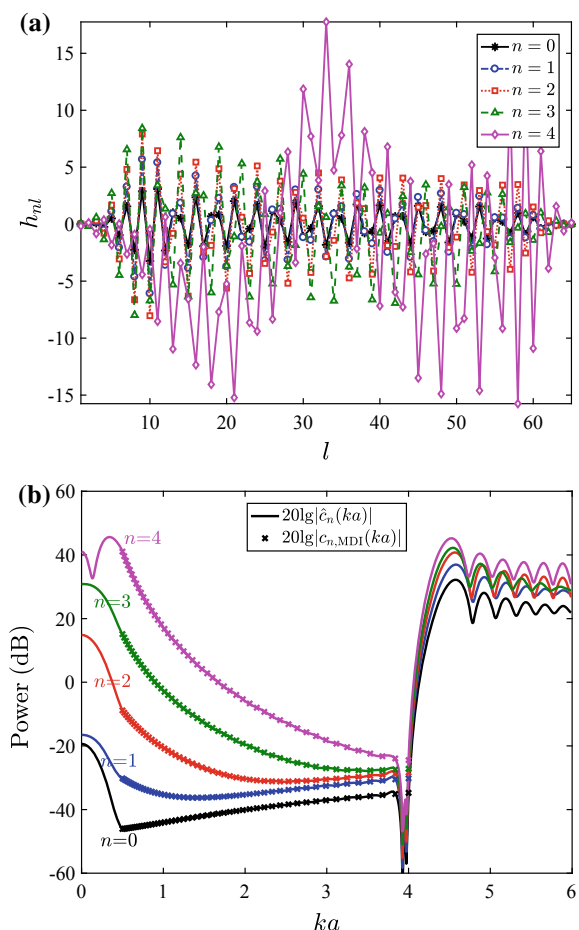


Fig. 9.9 Beam pattern of SH-TMDI beamformer

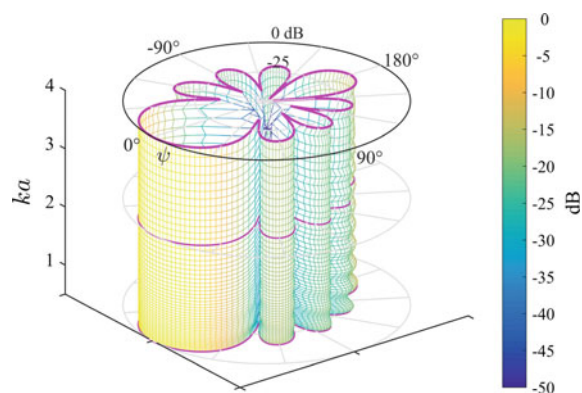
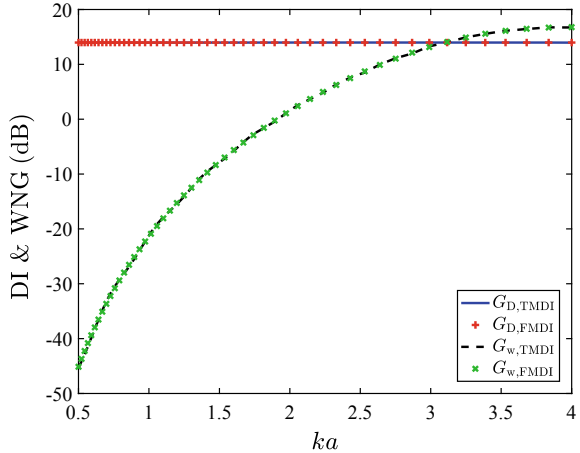


Fig. 9.10 DI and WNG versus ka for SH-TMDI and SH-FMDI beamformers



the WNGs at low frequencies are small. The results show that the former has good robustness and the latter is less robust.

In order to solve this problem, we need to find a trade-off between the DI and the robustness. In order to improve the robustness of the beamformer, a broadband WNG constraint can be imposed.

Let $\ell = 1$, $\mu_3 = \infty$, $\mu_4 = \infty$, and μ_2 be a user parameter, the optimization problem in Eq. (9.52) becomes

$$\begin{aligned} & \min_{\mathbf{h}} \mathbf{h}^T \overleftrightarrow{\rho}_{\text{hiso}} \mathbf{h}, \\ & \text{subject to } \mathbf{h}^T \mathbf{u}(k_j a, 0) = 4\pi/M, \quad k_j \in [k_l, k_u], \quad j = 1, 2, \dots, N_k, \\ & \quad \overleftrightarrow{G}_w^{-1} \leq \mu_2. \end{aligned} \quad (9.55)$$

The resulting beamformer is referred to as an SHD time-domain robust high-directivity-index beamformer, or SH-TRHDI beamformer for short.

For the above 32-element rigid spherical array, the SH-TRHDI beamformer is designed using Eq. (9.55), where we choose $\mu_2 = 4\pi/M$.

The resulting FIR filters $\mathbf{h}_0, \dots, \mathbf{h}_n, \dots, \mathbf{h}_N$ and the weighting functions $\hat{c}_n(ka)$ are shown in Fig. 9.11a, b, respectively. Compared with Fig. 9.8, the FIR filter coefficients in Fig. 9.11a are much smaller, and the weights in Fig. 9.11b at out-of-band frequencies decrease significantly. These filters have better stop-band rejection performance, reduce the noise gain outside the operating frequency band, and improve the SNR.

The resulting beam pattern of the SH-TRHDI beamformer is shown in Fig. 9.12, where the magnitudes have been normalized. It is seen that the mainlobe beamwidth in Fig. 9.12 is narrower than that of the SH-TMWNG beamformer in Fig. 9.6, but unlike the SH-TMDI beamformer in Fig. 9.9 which has a constant mainlobe.

The values of DI and WNG are shown in Fig. 9.13. It is seen that the WNG of this beamformer exceeds -3 dB over the frequency band of interest, and the DI is

Fig. 9.11 Results of SH-TRHDI beamformer. **a** Pattern generation filters h_n . **b** Weighting functions $\hat{c}_n(ka)$

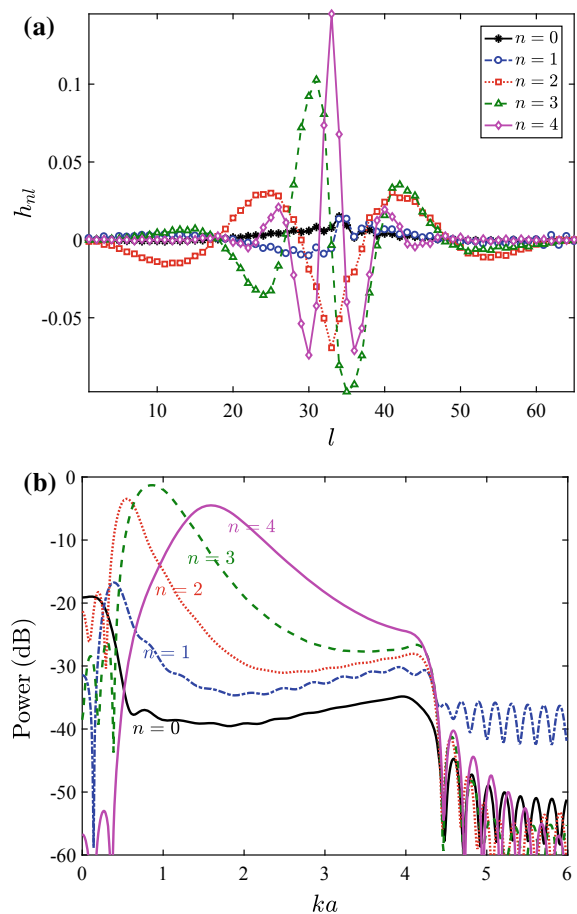


Fig. 9.12 Beam pattern of SH-TRHDI beamformer

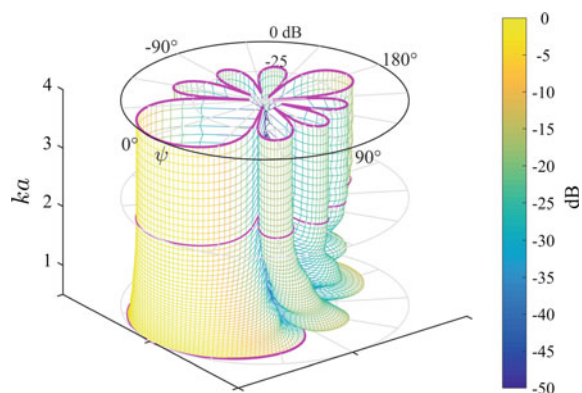
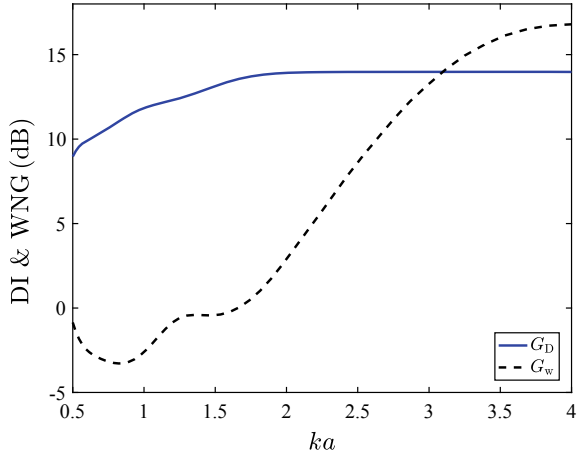


Fig. 9.13 DI and WNG of SH-TRHDI beamformer



much higher than that in Fig. 9.7 at low frequencies. Hence, the results show that this design provides a good trade-off between the directivity and the robustness.

If we want to synthesize a frequency-invariant mainlobe pattern over the frequency band of interest, the MSRV constraint can be imposed. Letting $\ell = 1$, $q_1 = 2$, and $\mu_4 = \infty$, the optimization problem in Eq. (9.52) becomes

$$\begin{aligned} & \min_{\mathbf{h}} \mathbf{h}^T \overleftrightarrow{\rho}_{\text{hiso}} \mathbf{h}, \\ & \text{subject to } \mathbf{h}^T \mathbf{u}(k_j a, 0) = 4\pi/M, \quad k_j \in [k_l, k_u], \quad j = 1, 2, \dots, N_k, \\ & \quad \overleftrightarrow{G}_w^{-1} \leq \mu_2, \\ & \quad \|\boldsymbol{\gamma}_{\text{MSRV}}\|_2 \leq \mu_3. \end{aligned} \quad (9.56)$$

The resulting beamformer is referred to as the SHD time-domain robust frequency-invariant beamformer, or SH-TRFI beamformer for short.

For the above 32-element rigid spherical array, assume that we want to synthesize a frequency-independent broadband beam pattern. Considering that it is practically impossible to synthesize a frequency-independent beam pattern over a frequency band of up to three octaves and at the same time with a good robustness, we reduce the bandwidth to two octaves so that $ka \in [1, 4]$.

The SH-TRFI beamformer is designed using Eq. (9.56), in which we choose $\mu_2 = 10^{-3/10} \cdot 4\pi/M = 2\pi/M$, $\mu_3 = 10^{-1.5} \cdot 4\pi/M$ and $\Psi_{\text{ML}} = [0^\circ : 2^\circ : 180^\circ]$. The resulting FIR filters $\mathbf{h}_0, \dots, \mathbf{h}_n, \dots, \mathbf{h}_N$ and their equivalent weighting functions $\hat{c}_n(ka)$ are shown in Fig. 9.14.

It is seen from Fig. 9.14a that the coefficients are relatively small, especially for the highest order spherical harmonic ($n = 4$). Moreover, Fig. 9.14b shows that these filters have good stop-band rejection performance.

The resulting normalized beam pattern of the SH-TRFI beamformer is shown in Fig. 9.15. It is seen that the beam pattern is constant over two-octave frequency band.

Fig. 9.14 Results of SH-TRFI beamformer. **a** Pattern generation filters h_n . **b** Weighting functions $\hat{c}_n(ka)$

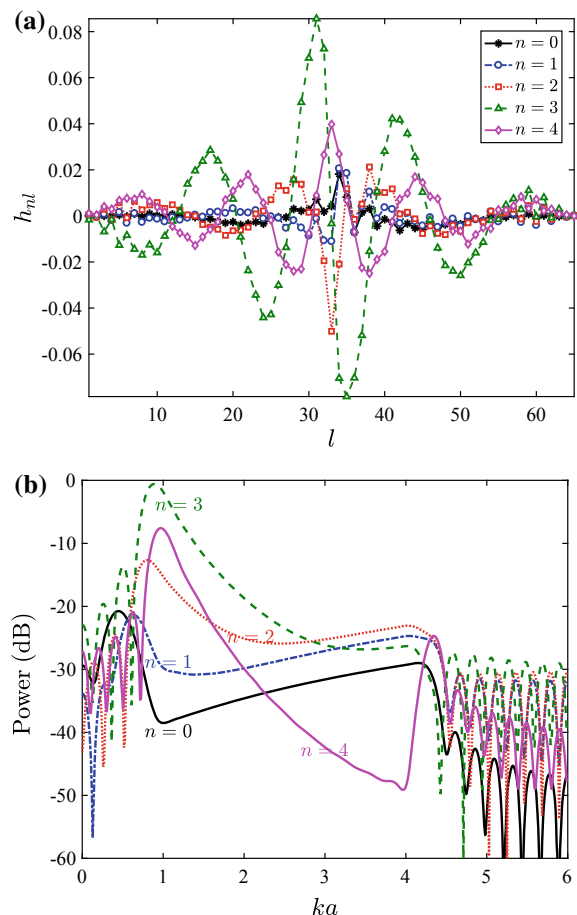


Fig. 9.15 Beam pattern of SH-TRFI beamformer

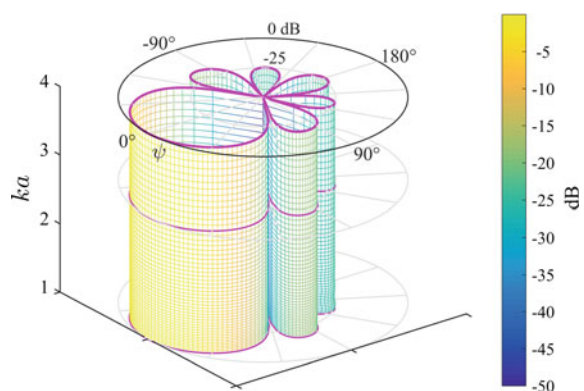
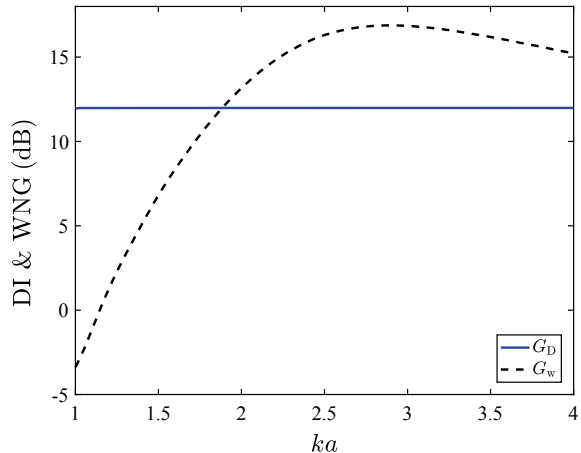


Fig. 9.16 DI and WNG of SH-TRFI beamformer



The values of DI and WNG versus ka are shown in Fig. 9.16. It is seen that the WNG exceeds -3 dB over the frequency band of interest, which indicates that the beamformer has good robustness.

For the above 32-element rigid spherical array, assume that we want to design an SHD time-domain robust frequency-invariant beamformer with sidelobe control.

This beamformer is an SH-TMC beamformer that can be designed using Eq. (9.52), in which we choose $\ell = 1$, $\mu_2 = 10^{-3/10} \cdot 4\pi/M$, $\mu_3 = 0.1 \cdot 4\pi/M$, $q_1 = 2$, $\mu_4 = 10^{-22/20} \cdot 4\pi/M$, $q_2 = \infty$, $\Psi_{\text{ML}} = [0^\circ : 2^\circ : 46^\circ]$ and $\Psi_{\text{SL}} = [56^\circ : 2^\circ : 180^\circ]$.

The resulting FIR filters $\mathbf{h}_0, \dots, \mathbf{h}_n, \dots, \mathbf{h}_N$ and their equivalent weighting functions $\hat{c}_n(ka)$ are shown in Fig. 9.17.

The normalized beam pattern of the resulting SH-TMC beamformer is shown in Fig. 9.18. It is seen that the sidelobes are controlled to be below -22 dB as required by μ_4 , and the mainlobe pattern is constant over the frequency band of interest.

The values of DI and WNG versus ka are shown in Fig. 9.19.

The calculation results show that all constraints are met. This beamformer provides a suitable trade-off among multiple performance measures.

9.5 Time-Domain Broadband SHD Beamforming

Several examples are considered to illustrate the time-domain broadband SHD beamforming behavior.

Consider the rigid spherical array with $M = 32$ elements, as shown in Fig. 8.10a. A far field LFM broadband plane wave impinges on the array from $\Omega_s = (\theta_s, \phi_s) = (0^\circ, 0^\circ)$. The frequency band of interest is $ka = 2\pi f a/c \in [2, 4]$, which covers an octave, and the sampling frequency f_s satisfies $k_s a = 2\pi f_s a/c = 18$. The sample

Fig. 9.17 Results of SH-TMC beamformer. **a** Pattern generation filters h_n . **b** Weighting functions $\hat{c}_n(ka)$

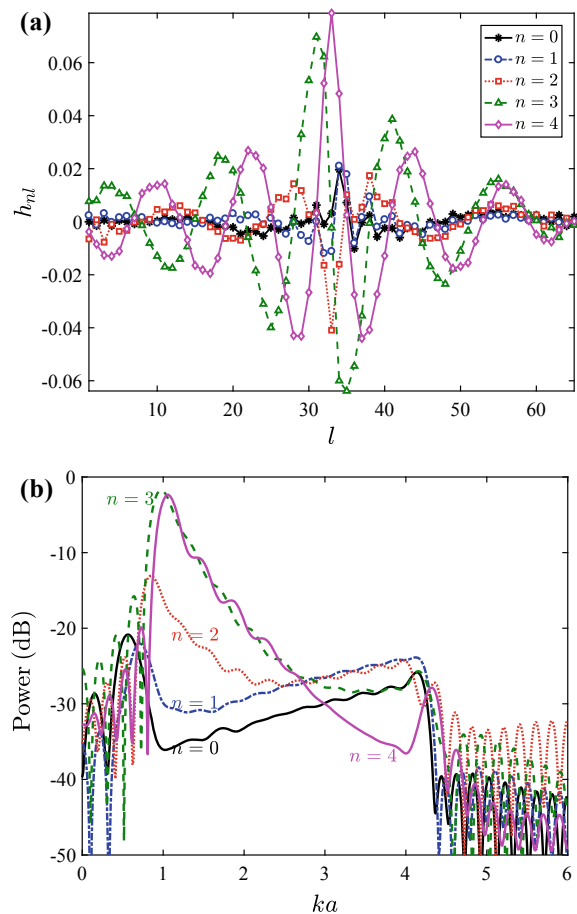


Fig. 9.18 Beam pattern of SH-TMC beamformer

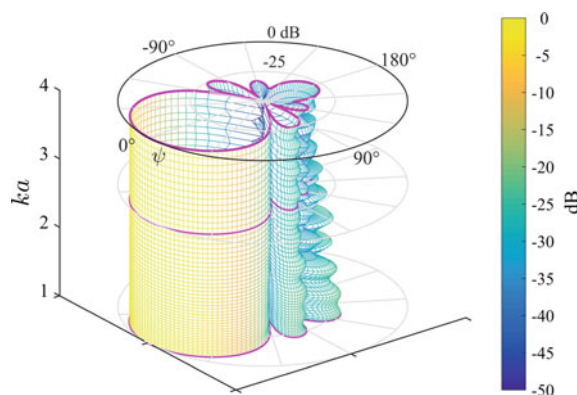
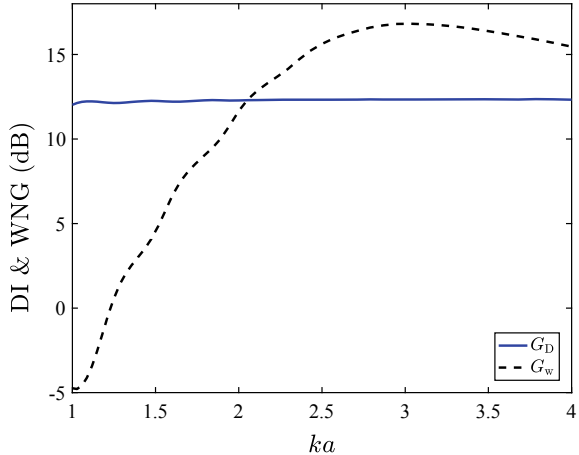


Fig. 9.19 DI and WNG of SH-TMC beamformer



length is 1024. The waveform and the instantaneous frequency of this LFM signal are shown in Fig. 9.20a.

The waveforms of the signals received by each sensor are generated using the same method as in Fig. 8.12, and 8 of which ($s = 1, 2, 7, 12, 17, 22, 27$ and 32) are shown in Fig. 9.20b.

Let $N = 4$ and $L = 65$. The SH-TMWNG, SH-TMDI, and SH-TMC beamformers are designed. For the SH-TMC beamformer, we have chosen $\ell = 1$, $\mu_2 = 10^{-15/10} \cdot 4\pi/M$, $\mu_3 = 0.1 \cdot 4\pi/M$, $q_1 = 2$, $\mu_4 = 0.1 \cdot 4\pi/M$, $q_2 = \infty$, $\Psi_{ML} = [0^\circ : 2^\circ : 46^\circ]$, and $\Psi_{SL} = [56^\circ : 2^\circ : 180^\circ]$.

Assume the steering direction is $\Omega_o = (\theta_o, \phi_o) = (0^\circ, 0^\circ)$. The time-domain beamforming structure in Fig. 9.4 is applied.

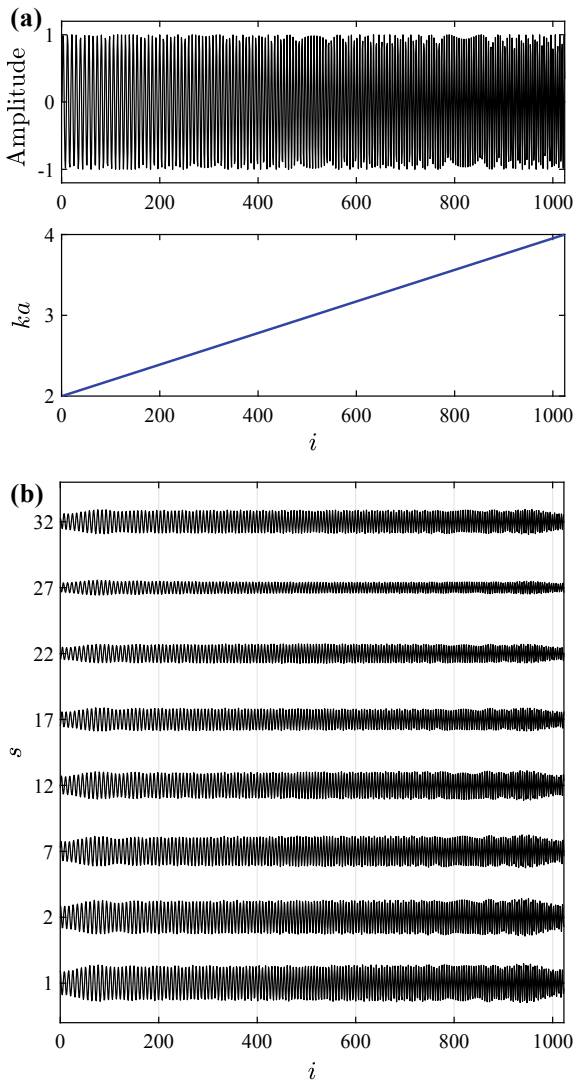
In the noise-free case, the output waveforms of the three beamformers are shown in Fig. 9.21a, c, e, respectively. It is seen that the output waveforms are all identical to the source signal shown in Fig. 9.20a.

Assuming that the beamformers are steered to $\Omega_o = (0^\circ, 30^\circ)$, the output waveforms of the three beamformers are shown in Fig. 9.21b, d, f, respectively.

It is seen that the amplitude of the SH-TMWNG beamformer output decreases as the frequency increases. The output waveforms of the SH-TMDI and SH-TMC beamformers have a constant amplitude over the frequency band, and the amplitude of the SH-TMDI beamformer output is smaller than that of the SH-TMC beamformer. This indicates that the mainlobe beamwidth of the SH-TMWNG beamformer narrows as the frequency increases, and the SH-TMDI and SH-TMC beamformers have constant mainlobe patterns while the mainlobe beamwidth of the SH-TMDI beamformer is narrower than that of the SH-TMC beamformer.

Assume that, in addition to the desired signal, each sensor receives Gaussian noise that is uncorrelated with the signal, and the SNR at each sensor is 0 dB. The waveforms of the signal received by the 8 sensors ($s = 1, 2, 7, 12, 17, 22, 27$ and 32)

Fig. 9.20 Signals received by the rigid spherical array.
a LFM source signal and the corresponding instantaneous frequency.
b Waveforms received by 8 microphones ($s = 1, 2, 7, 12, 17, 22, 27$ and 32)



are shown in Fig. 9.22. As can be seen from the figure, the source signals have been masked by noise.

Using the SH-TMWNG, SH-TMDI and SH-TMC beamformers with $\Omega_0 = (0^\circ, 0^\circ)$ designed above, the outputs of the three beamformers are shown in Fig. 9.23a–c, respectively.

It is seen that both SH-TMWNG and SH-TMC beamformers improve the SNR and recover the source signal well, while the TMDI beamformer output waveform is very messy. This indicates that the TMWNG and TMC beamformers have good

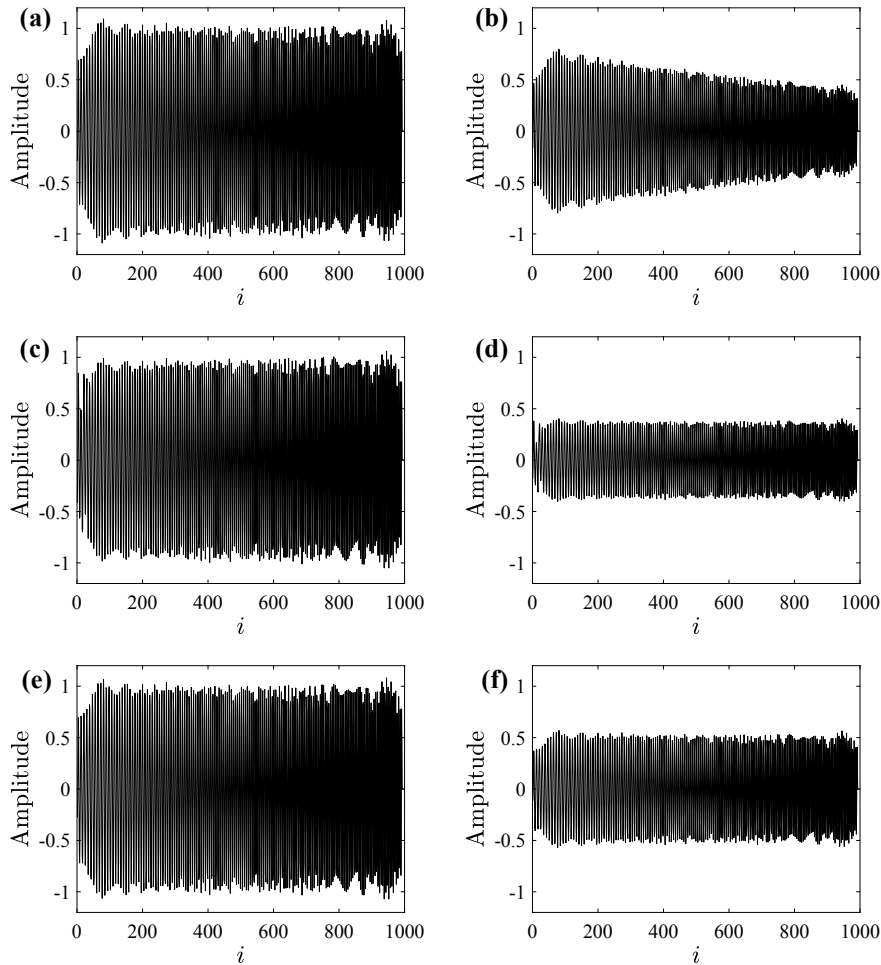
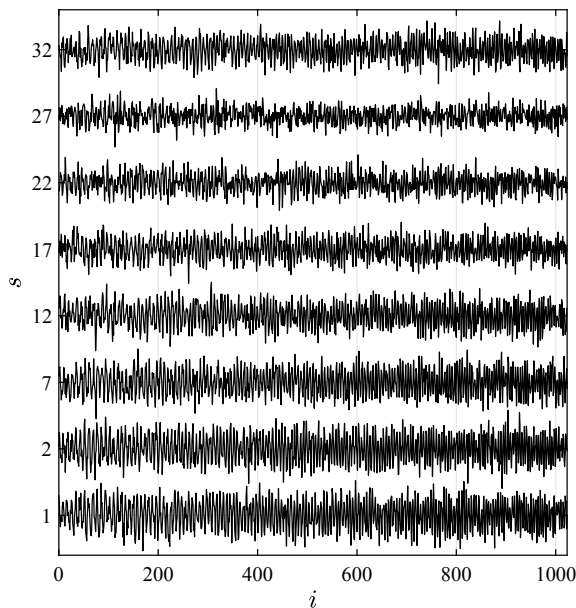


Fig. 9.21 Output waveforms of time-domain broadband SHD beamformers for rigid spherical array. **a** SH-TMWNG, $\Omega_o = (0^\circ, 0^\circ)$, **b** SH-TMWNG, $\Omega_o = (0^\circ, 30^\circ)$, **c** SH-TMDI, $\Omega_o = (0^\circ, 0^\circ)$, **d** SH-TMDI, $\Omega_o = (0^\circ, 30^\circ)$, **e** SH-TMC, $\Omega_o = (0^\circ, 0^\circ)$, **f** SH-TMC, $\Omega_o = (0^\circ, 30^\circ)$

robustness, while the robustness of the TMDI beamformer is poor, which causes severe distortion in the output waveform.

The above results verify the performances of time-domain SHD beamformers, which are consistent with the theoretical results.

Fig. 9.22 Waveforms received by 8 sensors ($s = 1, 2, 7, 12, 17, 22, 27$ and 32), $SNR = 0$ dB



9.6 Summary

The time-domain implementation of the broadband SHD beamformer for spherical arrays has been presented.

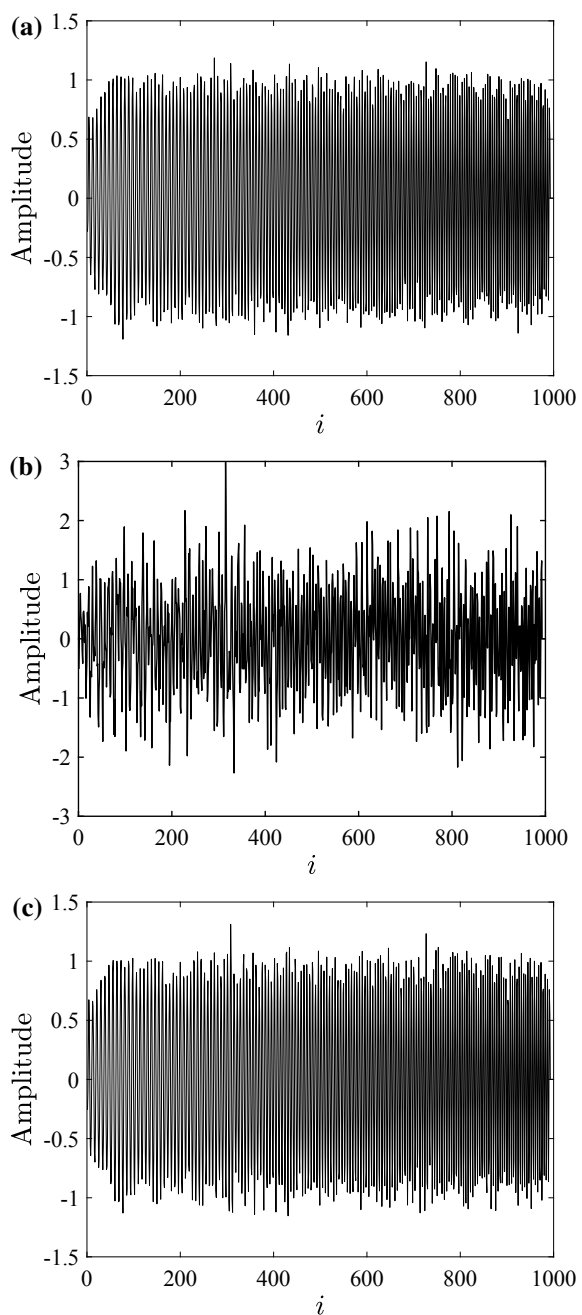
The spherical-harmonics-based spherical arrays presented in this chapter employed beam patterns that are rotationally symmetric about the steering direction. The advantage is that the beam steering can be decoupled from the beam pattern design, which makes the beam design and implementation simple. However, in some applications, a beam pattern that is not rotationally symmetric may be desired, the methods developed in Chap. 8 can be applied.

The implementation of the SHD beamformer consists of three parts: spherical harmonics transform, beam steering, and pattern generation. The SHD broadband beamformer can be implemented either in the frequency domain or in the time domain, and the outputs of both implementations are equivalent.

In order to make this chapter more compact, only the time-domain implementation of the SHD beamformer with rotationally symmetric patterns is considered. A time-domain broadband SHD beamforming structure that utilizes real arithmetic is derived. The element-space array data are first converted to the spherical harmonics domain using real spherical harmonics transform, and then steered to the look direction, followed by a real-valued filter-and-sum structure to achieve the beamformer output time series.

The broadband array response, the beamformer output power against both spherically isotropic noise and spatially white noise, and the MSRV are all expressed as the

Fig. 9.23 Output waveforms of **a** SH-TMWNG, **b** SH-TMDI, and **c** SH-TMC beamformers with $\Omega_0 = (0^\circ, 0^\circ)$



functions of the pattern generation filter tap weights. The filters design problem is formulated as a multiply constrained problem, which ensures that the resulting beamformer can provide a suitable trade-off among multiple conflicting array performance measures such as directivity, MSRV, sidelobe level, and robustness.

For the obtained time-domain beamformer, weighting functions generated by the pre-delay and the pattern generation filter are approximately equal to those of a frequency-domain beamformer based on the same design criteria. This indicates that the time-domain and frequency-domain implementations can obtain nearly identical performances.

The performance of the time-domain broadband modal beamforming approach is demonstrated by a number of simulations. The results also show that the rigid spherical arrays have better comprehensive performance than the open spherical arrays.

References

1. G.W. Elko, R.A. Kubli, J. Meyer, Audio system based on at least second-order eigenbeam. United States Patent WO 03/061336 A1 (2003)
2. S. Yan, H. Sun, X. Ma, U.P. Svensson, C. Hou, Time-domain implementation of broadband beamformer in spherical harmonics domain. *IEEE Trans. Audio Speech Lang. Process.* **19**(5), 1221–1230 (2011)
3. J. Meyer, G. Elko, A highly scalable spherical microphone array based on an orthonormal decomposition of the soundfield. *Proc. ICASSP* **2**, 1781–1784 (2002)

Glossary

Acronyms

BWNG Broadband white noise gain

CH Circular harmonics

CHD Circular-harmonics-domain

CH-DAS CHD DAS

CH-FMC CHD FMC

CH-FMDI CHD FMDI

CH-FMVDR CHD FMVDR

CH-FMWNG CHD FMWNG

CH-FNC CHD FNC

CH-FPM CHD FPM

CH-MC CHD MC

CH-MDI CHD MDI

CH-MPDI CHD MPDI

CH-MVDR CHD MVDR

CH-MWNG CHD MWNG

CH-NC CHD NC

CH-PM CHD PM

CH-TMWNG CHD TMWNG

CH-TPM CHD TPM

CH-TRFI CHD TRFI

CMP Constant mainlobe pattern

DAS Delay-and-sum

DFT Discrete Fourier transform

DI Directivity index

FFT Fast Fourier transform

FI Frequency-invariant

FIR Finite impulse response

FMC Frequency-domain MC

FMDI Frequency-domain MDI

FMVDR Frequency-domain MVDR

FMWNG Frequency-domain MWNG

FNC Frequency-domain NC

FOV Field of view

FPM Frequency-domain PM

IDFT Inverse DFT

INR Interference-to-noise ratio

LFM Linear frequency-modulated

LNR Load-to-white-noise ratio

LSMI Loaded sample matrix inversion

MC Multiply constrained

MDI Maximum-directivity-index

MPDI Maximum planar directivity index

MRA Main response axis

MSL Minimum-sidelobe

MSRV Mainlobe spatial pattern variation

MVDR Minimum variance distortionless response

MWNG Maximum WNG

NC Norm constrained

PM Phase-mode

RMSL Robust minimum-sidelobe

RSLC Robust sidelobe constrained

SH Spherical harmonics

SHD Spherical-harmonics-domain

SHT Spherical harmonics transform

SH-FMC SHD FMC

SH-FMDI SHD FMDI

SH-FMVDR SHD FMVDR

SH-FMWNG SHD FMWNG

SH-FNC SHD FNC

SH-FPM SHD FPM

SH-MC SHD MC

SH-MDI SHD MDI

SH-MVDR SHD MVDR

SH-MWNG SHD MWNG

SH-NC SHD NC

SH-PM SHD PM

SH-TMC SHD TMC

SH-TMDI SHD TMDI

SH-TMWNG SHD TMWNG

SH-TRFI SHD TRFI

SH-TRHDI SHD TRHDI

SINR Signal-to-interference-plus-noise ratio

SMI Sample matrix inversion

SNR Signal-to-noise ratio

SOCP Second-order cone programming

SOI Signal of interest

SL Sidelobe level

TMC Time-domain MC

TMDI Time-domain MDI

TMWNG Time-domain MWNG

TPM Time-domain PM

TRFI Time-domain robust frequency-invariant

TRHDI Time-domain robust high-directivity-index

UCA Uniform circular array

ULA Uniform linear array

WCC Worst-case constrained

WNG White noise gain